

Alma Mater Studiorum – Università di Bologna

DOTTORATO DI RICERCA IN
Scienze Biomediche e Neuromotorie

Ciclo XXXII

Settore Concorsuale: 06/N1

Settore Scientifico Disciplinare: MED/50

**PERI-IMPLANT AND PERIAPICAL ORAL BONE DEFECTS: CLINICAL
STRATEGIES TO ACHIEVE ALVEOLAR BONE STABILITY AND
EXPERIMENTAL BONE REGENERATION PROCEDURES.**

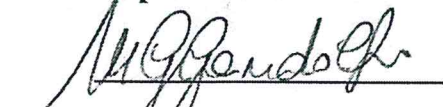
Presentata da: **Fausto Zamparini**

Coordinatore Dottorato

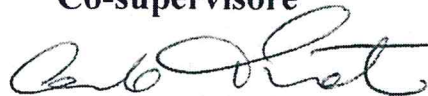
Prof. Pietro Cortelli



Supervisore


Prof.ssa Maria Giovanna Gandolfi

Co-supervisore



Prof. Carlo Prati

Esame finale anno 2019

Summary

Peri implant and periapical bone defects are widespread in the world population. Considering the high number of implant placement and root canal treatment performed every year, resolution of these bone defects will be of predominant interest in the next future.

The present project has several aims:

The first part of the project aimed to investigate how and what factors affect peri implant bone remodeling process. Microchemical analysis of the peri implant bone interface of retrieved human dental implants was performed. In addition, prospective clinical studies were carried out to evaluate the factors mostly related to peri implant bone loss.

The second part of the project aimed to evaluate chemical physical and micromorphological properties of hydraulic calcium silicates based materials (CaSi), which gained a particular attention in the endodontic field. Use of these materials claimed to resolve several complex endodontic complications, however few information is present in literature. These materials were compared with different “gold standard” bioinert materials.

Given the attractive biointeractive properties of CaSi based materials, the last part of the study will focus on the design and characterization of new mineral based scaffolds, aimed to be applied in future bone regeneration procedures. Scaffolds, composed of a polymeric matrix were doped with CaSi and calcium phosphates, in order to increase the materials biointeractive properties. A complete characterization of their chemical-physical-mechanical-thermal properties was performed, as well as the evaluation of apatite forming ability (bioactivity) and biocompatibility of these mineral based scaffolds. The combination of Human Periapical-cysts Mesenchymal Stem Cells (hPC-MSCs) as a potential strategy to achieve periapical bone regeneration was also evaluated. Finally, the angiogenesis potential of these scaffolds was investigated through the growth and proliferation of porcine vascular wall mesenchymal stem cells (pVW-MSCs) was performed.

1. Peri-implant bone remodeling and clinical strategies to achieve soft and hard tissue stability

1.1 BONE REMODELLING AT THE PERI-IMPLANT BONE INTERFACE

1.1.1 Microchemical and micromorphologic ESEM-EDX analysis of bone mineralization at the thread interface in human dental implants retrieved for mechanical complications after 2 months to 17 years

1.1.2 Esem-Edx Microanalysis Of The Bone-Implant Interface Around Loaded And Unloaded Retrieved Dental Implants.

1.2 CLINICAL STRATEGIES TO ACHIEVE (ALVEOLAR PERI IMPLANT) BONE STABILITY

1.2.1 Factors affecting soft and hard tissues around over tissue level hyperbolic neck implants. A three-year prospective cohort study

1.2.2 A multi-level analysis of platform-switching flapless implants placed tissue-level: 4-year prospective cohort study

2. Endodontic-related periapical bone defects and new biomaterials for periapical bone regeneration

2.1 ENDODONTIC-RELATED PERIAPICAL BONE DEFECTS

2.1.1 The fate of root canals obturated with Thermafil: 10-year data for patients treated in a master's program

2.1.2 A 20-year historical prospective cohort study of root canal treatments. A Multilevel analysis

2.2 NEW BIOMATERIALS FOR PERIAPICAL BONE REGENERATION

2.2.1 Properties of a novel polydimethylsiloxane endodontic sealers

2.2.2 Properties of bioroot RCS, a tricalcium silicate endodontic sealer modified with povidone and polycarboxylate

2.2.3 Properties of calcium silicate-monobasic calcium phosphate materials for endodontics containing tantalum pentoxide and zirconium oxide

3. Tissue engineering approaches for experimental bone regeneration procedures

3.1 DEVELOPMENT OF EXPERIMENTAL MINERAL DOPED POLYMERIC SCAFFOLDS

3.1.1 Polylactic Acid-Based Porous Scaffolds Doped With Calcium Silicate And Dicalcium Phosphate Dihydrate Designed For Biomedical Application

3.1.2 Highly Porous Polycaprolactone Scaffolds Doped With Calcium Silicate And Dicalcium Phosphate Dihydrate Designed For Bone Regeneration

3.2 CHARACTERIZATION OF EXPERIMENTAL MINERAL DOPED POLYMERIC SCAFFOLDS

3.2.1 Pla-Based Mineral-Doped Scaffolds Seeded With Human Periapical Cyst-Derived Mscs: A Promising Tool For Regenerative Healing In Dentistry

3.2.2 Culture Of Porcine Vascular Wall - Mesenchymal Stem Cells On 3d Biodegradable Highly Porous Mineral Doped Poly (a-Hydroxy) Acids Scaffolds

4. Conclusions

1. Peri-implant bone remodeling and clinical strategies to achieve soft and hard tissue stability

Dental implants have become an attractive treatment to restore edentulism allowing the preservation of natural adjacent teeth (Jivray & Chen 2006), restoring edentulous jaws, masticatory function and quality of life (Jofre *et al.* 2013; Hartlev *et al.* 2014). A high % of survival has been described in literature, with values over 90% (Lang & Berghlund 2011, Buser *et al.* 2012, Degidi *et al.* 2012, Gottfredsen *et al.* 2012, Jemt 2016).

A substantial increase in the world proportion of individuals receiving implants has been observed. Every year, more than 1.8 million implant surgeries are performed in the European Union (Dental Implants Market to 2027 - Global Analysis and Forecasts by Product; Material; End User and Geography); this number is expected to increase due to the significant increase of the elderly population. A quarter of the whole European population will be over 60 years of age by 2020. (Market research report 2018).

Annually, more than 800,000 individual implants are placed in the United States. This country already faced a significant increase of implant placement in the last years, from 0.7% of the whole population in 1999 to 5.7% to 2016. Considering that the greater increase was observed in elderly patients, population with at least one dental implant rehabilitation is expected to jump over 17 % by 2026 (Elani *et al.* 2018).

It is important to investigate and monitor the bone levels in the first year from implant insertion. Several biological processes start immediately after implant insertion; these events bring to the formation of new bone tissue close to the implant surface (osseointegration) (Albrektsson & Johansson 2001). This process follows the traditional intrabony wound healing phases: hemostasis (minutes to first hours), inflammatory phase (first hours to days), proliferative days (days to 3 weeks) and remodeling phase (from 3 weeks to years) (Terheyden *et al.* 2012).

Different circumstances may occur in this period and are critical for long-term success, as may trigger bone level alterations (Galindo Moreno *et al.* 2014). Indeed, early implant failures have been described in literature in approx. 3-6 % of the cases (Berghlund *et al.* 2002; Carr *et al.* 2019). Initial breakdown of the implant-tissue interface generally begins at the crestal region in successfully osseointegrated endosteal implants. In these cases, bone loss beyond the first thread of dental implants may be detected radiographically during the first year of function. (Oh *et al.* 2002).

The present chapter will first focus on the bone remodeling processes at the peri implant bone interface. Then, several clinical strategies will be explored to maintain bone level stability during the first months from implant placement.

REFERENCES

- Albrektsson T, Johansson C. Osteoinduction, osteoconduction and osseointegration. *Eur Spine J.* 2001 Oct;10 Suppl 2:S96-101.
- Berglundh T, Persson L, Klinge B. A systematic review of the incidence of biological and technical complications in implant dentistry reported in prospective longitudinal studies of at least 5 years. *J Clin Periodontol* 2002, 29, 197-212.
- Buser D, Janner SF, Wittneben JG, Bragger U, Ramseier CA, Salvi GA. 10-year survival and success rates of 511 titanium implants with a sandblasted and acid-etched surface: a retrospective study in 303 partially edentulous patients. *Clin Implant Dent Relat Res* 2012; 14: 839–851.
- Carr AB, Sinha N, Lohse CM, Muller OM, Salinas TJ. Association Between Early Implant Failure and Prosthodontic Characteristics. *J Prosthodont.* 2019 Jan;28(1):30-35.
- Degidi M, Nardi D, Piattelli A. 10-year follow-up of immediately loaded implants with TiUnite porous anodized surface. *Clin Implant Dent Relat Res* 2012; 14: 828–838.
- Dental Implants Market to 2027 - Global Analysis and Forecasts by Product; Material; End User and Geography.
- Elani HW, Starr JR, Da Silva JD, Gallucci GO. Trends in Dental Implant Use in the U.S., 1999-2016, and Projections to 2026. *J Dent Res.* 2018 Dec;97(13):1424-1430.
- Fischer K, Stenberg T. Prospective 10-year cohort study based on a randomized controlled trial (RCT) on implantsupported full-arch maxillary prostheses. Part 1: sandblasted and acid-etched implants and mucosal tissue. *Clin Implant Dent Relat Res* 2012; 14: 808–815.
- Galindo-Moreno P, León-Cano A, Ortega-Oller I, Monje A, O Valle F, Catena A. Marginal bone loss as success criterion in implant dentistry: beyond 2 mm. *Clin Oral Implants Res.* 2015 Apr;26(4):e28-e34.
- Gotfredsen K. A 10-year prospective study of single tooth implants placed in the anterior maxilla. *Clin Implant Dent Relat Res* 2012; 14: 80–87.
- Hartlev, J, Kohberg, P, Ahlmann, S, Andersen, NT, Schou, S, Isidor, F. 2014. Patient satisfaction and esthetic outcome after immediate placement and provisionalization of single-tooth implants involving a definitive individual abutment. *Clin Oral Implants Res.* 25(11):1245–1250.

Jemt T. Single-implant survival: more than 30 years of clinical experience. *Int J Prosthodont* 2016; 30: 551–558.

Jepsen S, Berglundh T, Genco R, et al. Primary prevention of peri-implantitis: managing peri-implant mucositis. *J Clin Periodontol*. 2015;42 Suppl. 16:S152–157.

Jivraj S, Chee W. Rationale for dental implants. *Br Dent J*. 2006 200(12):661–665.

Jofre J, Castiglioni X, Lobos CA. Influence of minimally invasive implant-retained overdenture on patients' quality of life: a randomized clinical trial. *Clin Oral Implants Res*. 2013 24(10):1173–1177.

Lang NP, Berglundh T, Working Group 4 of Seventh European Workshop on P. Periimplant diseases: where are we now?—Consensus of the Seventh European Workshop on Periodontology. *J Clin Periodontol*. 2011;38 Suppl. 11:178–181.

Market research report. Dental Implants Market Size, Share & Trends Analysis Report By Product (Titanium Implants, Zirconium Implants), By Region (North America, Europe, Asia Pacific, Latin America, MEA), And Segment Forecasts, 2018 – 2024; ID GVR-1-68038-566-3.

Sanz M, Chapple IL, Working Group 4 of the VEWoP. Clinical research on peri-implant diseases: consensus report of Working Group 4. *J Clin Periodontol*. 2012;39 Suppl 12:202–206.

1.1 Bone remodelling at the peri-implant bone interface

Bone is a dynamic, highly vascularized connective tissue with the unique capacity to heal and remodel depending of physiological load (Jayakumar & Di Silvio, 2010). Modifications in response to mechanical demands lead to significative variations of mineral and organic content (Davies 2014).

Oral bone remodeling processes close to the implant threads gained a particular interest in modern implantology, as a stable peri-implant bone tissue is essential to achieve long term results (Davies *et al.* 2003, Qian *et al.* 2012). Numerous factors may affect peri-implant bone stability and during the first months from insertion, including surgical techniques (De Bruyn *et al.* 2014, Prati *et al.* 2016), implant placement timing (Lang *et al.* 2012, Zhao *et al.* 2016, Prati *et al.* 2017), surgical trauma, occlusal overload (Oh *et al.* 2002), implant insertion depth (Hermann *et al.* 1997, Sanz *et al.* 2015) and design of implant system (Araujo & Lindhe 2018). Towards all these factors, mechanical loading is considered as the most critical (Davies *et al.* 2003, Halldin *et al.* 2014, Araujo & Lindhe 2018). Interfacial stress of the implants is mainly located at the interface between the implants and the surrounding bone, thus possibly induce bone resorption and remodelling in this critical area (Chen *et al.* 2011).

The peri-implant bone interface has been investigated mostly on animal models (Palmquist 2009, 2010). Histological and histomorphometric studies evidenced a tight bone to implant contact with the implant and bone and high percentages of bone to implant contact were related to implant stability and success (Palmquist 2009 and 2010).

However, *in-vivo* peri-implant bone interface may be highly heterogeneous and may include mineralised, partially mineralised (osteoid), and unmineralised areas (Haiat *et al.* 2014). To date very few studies analysed the degree of mineralization at the peri-implant bone interface around human dental implants, for it is very difficult to obtain the sample histology (Shah *et al.* 2014 and 2019, Mangano *et al.* 2015, Iezzi *et al.* 2016).

Environmental scanning electron microscope (ESEM) is a useful nondestructive investigation able to analyse mineralized tissue micromorphology without sample manipulation or deterioration (Gandolfi *et al.* 2017 and 2018) and may result attractive in the investigation of the peri-implant bone interface.

Energy-dispersive x-ray spectroscopy (EDX) is useful for studying the composition of mineralized tissues or mineral (apatitic) deposits and the mineralization degree of bone by calculating the element ratios (atomic or weight) and it allows detection of elements that may have migrated from an implanted material into the bone tissue.

Calcium-to- phosphorous (Ca/P) ratio has been used in several studies to assess bone mineralization (Bigi *et al.* 1997, Kourkoumelis *et al.* 2012). Likewise, atomic calcium-to-nitrogen (Ca/N) and phosphorus-to-nitrogen (P/N) ratios have been used to investigate the degree of mineralization by evaluation of organic components in dentin and bone tissue (Engfeldt 1974, Eliades *et al.* 2013, Gandolfi *et al.* 2018).

In the following studies, the peri implant bone interface of different retrieved dental implants was investigated using a non-destructive methodology, which allowed assessing the degree of mineralization and the presence of metal contaminants in such critical area.

The first study focused on bone remodelling events at different retrieval time (from 2 months to 17 years).

The second study aimed to investigate the role of loading on peri implant bone remodelling events.

REFERENCES

Araujo MG, Lindhe J. Peri-implant health. *Journal of Clinical Periodontology* 2018;45:S230-S236.

Bigi A, Cojazzi G, Panzavolta S, Ripamonti A, Roveri N, Romanello M, Noris Suarez K, Moro L. Chemical and structural Characterization of the Mineral Phase from Cortical and Trabecular Bone. *J Inorg Biochem* 1997;68:45-51.

Chen LJ, He H, Li YM, Li T, Guo XP, RF Wang. Finite element analysis of stress at implant–bone interface of dental implants with different structures. *Transactions of Nonferrous Metals Society of China* 2011;21: 1602-1610.

Davies JE, Mendes VC, Ko JC, Ajami E. Topographic scale-range synergy at the functional bone/implant interface. *Bio materials* 2014;35:25–35.

Davies JE. Understanding peri-implant endosseous healing. *J Dent Educ.* 2003;67:932-49.

De Bruyn H, Atashkadeh M, Cosyn J, van de Velde T. Clinical outcome and bone preservation of single TiUnite™ implants installed with flapless or flap surgery. *Clin Implant Dent Relat Res* 2011; 13:175–183.

Eliades G, Mantzourani M, Labella R, Mutti B, Sharma D. Interactions of dentine desensitisers with human dentine: morphology and composition. *J Dent* 2013;41:S28-S39.

Engfeldt B, Hjerpe A. Density gradient fractionation of dentine and bone powder. *Calcif Tissue Res* 1974;16:261-275.

Gandolfi MG, Iezzi G, Piattelli A, Prati C, Scarano A. Osteoinductive potential and bone-bonding ability of ProRoot MTA, MTA Plus and Biodentine in rabbit intramedullary model: Microchemical characterization and histological analysis. *Dent Mater* 2017;33:221-238.

Gandolfi MG, Zamparini F, Iezzi G, Degidi M, Botticelli D, Piattelli A, et al. Microchemical and micromorphologic ESEM-EDX analysis of bone mineralization at the thread interface in human dental implants retrieved for mechanical complications after 2 months to 17 years. *Int J Periodontics Restorative Dent* 2018;38:431-441.

Haïat G, Wang HL, Brunski J. Effects of biomechanical properties of the bone-implant interface on dental implant stability: from in silico approaches to the patient's mouth. *Annu Rev Biomed Eng.* 2014 Jul 11;16:187-213.

Halldin A, Jimbo R, Johansson CB, Wennerberg A, Jacobsson M, Albrektsson T, Hansson S. Implant stability and bone remodeling after 3 and 13 days of implantation with an initial static strain. *Clin Implant Dent Relat Res.* 2014;16:383-93.

Hermann JS, Cochran DL, Nummikoski PV, Buser D. Crestal bone changes around titanium implants. A radiographic evaluation of unloaded nonsubmerged and submerged implants in the canine mandible. *J Periodontol.* 1997;68:1117-1130.

Iezzi G, Piattelli A, Mangano C, Degidi M, Testori T, Vantaggiato G, Fiera E, Frosecchi M, Floris P, Perroni R, Ravera L, Moreno GG, De Martinis E, Perrotti V. Periimplant bone response in human-retrieved, clinically stable, successful, and functioning dental implants after a long-term loading period: A report of 17 cases from 4 to 20 years. *Implant Dent* 2016;25:380-386.

Jayakumar P, Di Silvio L. Osteoblasts in bone tissue engineering. *Proc Inst Mech Eng H.* 2010 Dec;224(12):1415-40.

Kourkoumelis N, Balatsoukas I, Tzaphlidou M. Ca/P concentration ratio at different sites of normal and osteoporotic rabbit bones evaluated by Auger and energy dispersive X-ray spectroscopy. *J Biol Phys* 2012;38:279-291.

Lang NP, Pun L, Lau KY, Li KY, Wong MC. A systematic review on survival and success rates of implants placed immediately into fresh extraction sockets after at least 1 year. *Clin Oral Implants Res* 2012;23:39-66.

Mangano C, Piattelli A, Mortellaro C, Mangano F, Perrotti V, Iezzi G. Evaluation of Peri-Implant Bone Response in Implants Retrieved for Fracture After More Than 20 Years of Loading: A Case Series. *J Oral Implantol.* 2015 ;41:414-418.

Oh TJ, Yoon J, Misch CE, Wang HL. The causes of early implant bone loss: myth or science? *J Periodontol* 2002;73:322-333.

Palmquist A, Lindberg F, Emanuelsson L, Branemark R, Engqvist H, Thomsen P. Biomechanical, histological, and ultrastructural analyses of laser micro and nano-structured titanium alloy implants: a study in rabbit. *J Biomed Mater Res A* 2010;92:1476-1486.

Palmquist, A, Lindberg F, Emanuelsson, L, Branemark, R, Engqvist H, Thomsen P. Morphological studies on machined implants of commercially pure titanium and titanium alloy (Ti6Al4V) in the rabbit. *J Biomed Mater Res B* 2009 91B, 309 –319.

Prati C, Zamparini F, Scialabba VS, Gatto MR, Piattelli A, Montebugnoli L, et al. A 3-year prospective cohort study on 132 calcium phosphate-blasted implants: Flap vs flapless technique. *Int J Oral Maxillofac Implants* 2016;31:413-423.

Prati C, Zamparini F, Pirani C, Gatto MR, Piattelli A, Gandolfi MG. Immediate Early and Delayed Implants: A 2- Year Prospective Cohort Study of 131 Transmucosal Flapless Implants Placed in Sites With Different Pre-extractive Endodontic Infections. *Impl Dent* 2017; 26:654-663.

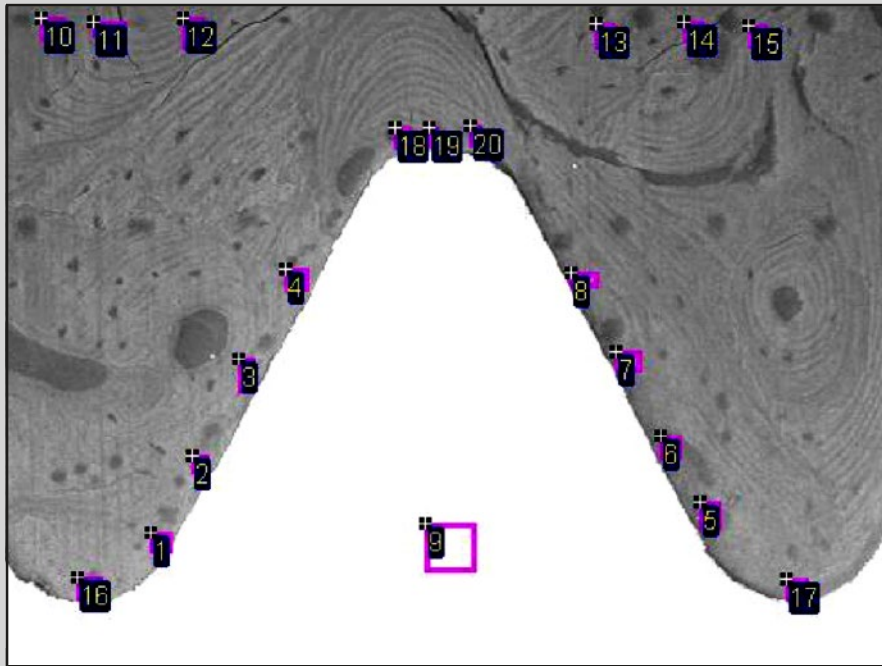
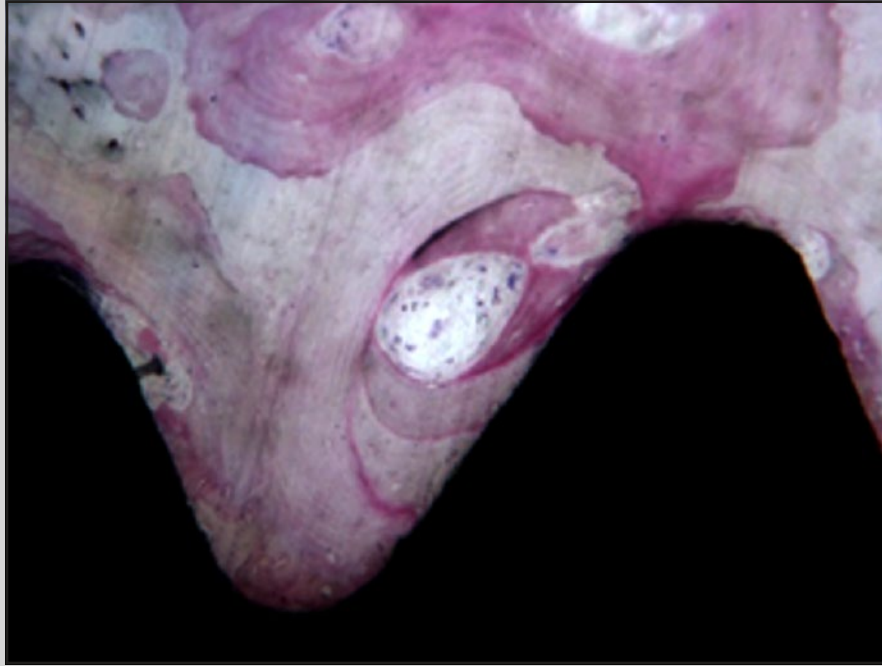
Qian J, Wennerberg A, Albrektsson T. Reasons for Marginal Bone Loss around Oral Implants. *Clin Implant Dent Relat Res* 2012;14:792-807.

Sanz M, Ivanoff C, Weingart D, Wiltfang J, Gahlert M, Cordaro L, et al. Clinical and radiologic outcomes after submerged and transmucosal implant placement with two-piece implants in the anterior maxilla and mandible: 3-year results of a randomized controlled clinical trial. *Clin Implant Dent Relat Res* 2015;17:234-246.

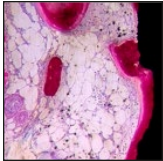
Shah FA, Nilson B, Brånemark R, Thomsen P, Palmquist A. The bone-implant interface nanoscale analysis of clinically retrieved dental implants. *Nanomedicine* 2014;10:1729-1737.

Shah FA, Thomsen P, Palmquist A. Osseointegration and current interpretations of the bone-implant interface. *Acta Biomater.* 2019;84:1-15.

Zhao D, Wu Y, Xu C, Zhang F. Immediate dental implant placement into infected vs. non-infected sockets: a meta-analysis. *Clin Oral Implants Res* 2016;27:1290-1296.



Microchemical and Micromorphologic ESEM-EDX Analysis of Bone Mineralization at the Thread Interface in Human Dental Implants Retrieved for Mechanical Complications After 2 Months to 17 Years



Maria Giovanna Gandolfi, DBiol, M Biol, PhD¹
 Fausto Zamparini, DDS, MEndo²/Giovanna Iezzi, DDS, PhD³
 Marco Degidi, MD, DDS⁴/Daniele Botticelli, MD, DDS, PhD⁵
 Adriano Piattelli, MD, DDS⁶/Carlo Prati, MD, DDS, PhD⁷

The aim of this study was to analyze the degree of mineralization around nine clinically stable titanium dental implants retrieved after 2 months to 17 years for mechanical complications from five patients. The micromorphology and microchemistry of the interface bone at the coronal and apical sides of the threads were analyzed by environmental scanning electron microscope and energy-dispersive X-ray spectroscopy (EDX) on histologic samples. Mineralization was investigated by atomic calcium-to-nitrogen (Ca/N), phosphorous-to-nitrogen (P/N), and calcium-to-phosphorous (Ca/P) ratio evaluation (statistical analysis by two-way analysis of variance with Student-Newman-Keuls; $P < .05$). EDX showed higher Ca/N, P/N, and Ca/P values for the bone at the coronal side compared to the apical side of the threads in the long-term (≥ 14 years) samples. The two most significant findings were that (1) the interface bone located at the coronal side of the implant threads was generally more mineralized than the interface bone located at the apical side, and (2) the mineralization of the peri-implant bone at the interface increased over time. A higher degree of mineralization was found at 2 months in an immediately loaded implant when compared to the 2-month submerged unloaded control, likely related to the different remodeling events (coronal vs apical side of the implant threads) due to the direction of the loading forces. *Int J Periodontics Restorative Dent* 2018;38:431–441. doi: 10.11607/prd.3503

Dental implants usually appear to be osseointegrated, demonstrating a mineralized interface on the metal surface.^{1–4} Bone is a dynamic tissue, continuously modified in response to mechanical demands.^{5,6} Bone remodeling leads to considerable variations in terms of mineral (calcium phosphates) and organic (bone matrix, mainly composed of collagen-1) content.

Environmental scanning electron microscope (ESEM) allows investigation of the bone tissue morphology and the bone-implant interface.^{1,7–10} Energy-dispersive x-ray spectroscopy (EDX) is useful for studying the composition of mineralized tissues or mineral (apatitic) deposits¹¹ and the mineralization degree of bone by calculating the element ratios (atomic or weight),^{2,6,10,12,13} and it allows detection of elements that may have migrated from an implanted material into the bone tissue.^{10,14} Calcium-to-phosphorous (Ca/P) ratio has been used in several studies to assess bone mineralization.^{6,10,13} Likewise, atomic calcium-to-nitrogen (Ca/N) and phosphorus-to-nitrogen (P/N) ratios have been used to investigate the degree of mineralization by evaluation of organic components in dentin and bone tissue.^{10,12,15}

Some histomorphometric analyses of bone-implant contact in a large number of dental implants retrieved for various causes have

¹Professor, Laboratory of Biomaterials and Oral Pathology, School of Dentistry, Department of Biomedical and Neuromotor Sciences, University of Bologna, Bologna, Italy.

²PhD Student, Laboratory of Biomaterials and Oral Pathology, School of Dentistry, Department of Biomedical and Neuromotor Sciences, University of Bologna, Bologna, Italy.

³Professor, Department of Medical, Oral and Biotechnological Sciences, University of Chieti-Pescara, Chieti, Italy.

⁴Private Practice, Bologna, Italy.

⁵ARDEC, Rimini, Italy.

⁶Clinical Professor, Department of Medical, Oral and Biotechnological Sciences, University of Chieti-Pescara, Chieti, Italy.

⁷Clinical Professor, School of Dentistry, Department of Biomedical and Neuromotor Sciences, University of Bologna, Bologna, Italy.

Correspondence to: Prof Maria Giovanna Gandolfi, Via san Vitale 59, 40125, Bologna, Italy. Phone: +39 0512088176. Fax: +39 051 225208. Email: mgiovanna.gandolfi@unibo.it

©2018 by Quintessence Publishing Co Inc.

Table 1 Implant Distribution According to Retrieval Time, Implant Type, Implant Location, and Reason for Retrieval

Sample (code)	Retrieval time	Implant type	Implant location	Reason for retrieval
1 (6357/1)	17 y	TiOblast	Anterior mandible	Implant fracture
2 (6357/2)	17 y	TiOblast	Anterior mandible	Implant fracture
3 (6357/3)	14 y	TiOblast	Anterior mandible	Implant fracture
4 (6357/4)	14 y	TiOblast	Anterior mandible	Implant fracture
5 (6223)	14 y	Unknown	Posterior maxilla	Implant fracture
6 (6090)	8 y	Unknown	Posterior mandible	Implant fracture
7 (5933)	4 y	Oral-Plant	Posterior mandible	Implant fracture
8 (3892)	2 mo (IL)	Ankylos Plus	Posterior mandible	Part of a clinical histologic study
9 (3893)	2 mo (UL)	Ankylos Plus	Posterior maxilla	Part of a clinical histologic study

IL = immediately loaded; UL = unloaded.

been published.^{16–18} Few studies, however, have investigated by scanning electron microscopy (SEM) the bone-implant interface of implants retrieved from humans¹ or analyzed by EDX the bone Ca/P around clinically stable dental implants in humans because of the difficulty of gathering and processing these samples.⁷ Therefore, the purpose of this study was to analyze the degree of mineralization of the interface bone at the coronal and apical sides of the threads of stable titanium dental implants retrieved for mechanical complications at different time periods (2 months to 17 years).

Materials and Methods

Nine implants were retrieved from five patients (three men and two women; mean age 59 years, range 41 to 68 years). Nine biopsy samples were obtained and analyzed. Some histologic histomorphometric data on these samples have been previously published.^{19–23} Table 1 reports implant location, implant type, time

of implant retrieval, and reason for retrieval. Histologic preparation was performed using the present authors' well-recognized protocol.²² The specimens were sectioned longitudinally with a high-precision diamond-coated steel disc along the major axis of the implant at approximately 150 μ m and ground down to approximately 30 μ m.²²

ESEM-EDX microanalyses were performed following the well-recognized protocol.^{9,10} The histologic samples were observed under ESEM in their entirety, from the coronal to the most apical portion of the implant, at $\times 500$ magnification. Microchemical analysis was then performed in a thread where bone tissue was present on both sides. EDX was performed to evaluate the qualitative and semiquantitative (weight % and atomic %) element content on the sample area. Analyses were carried out at areas approximately $30 \times 30 \mu$ m in three different regions of interest: bone adjacent to the coronal side of the implant thread, bone adjacent to the apical side of the implant thread,

and remote bone located at about 300 to 500 μ m from the implant thread. For all the acquired spectra, the atomic Ca/N, P/N, and Ca/P ratios were calculated.¹⁰ Punctual EDX was also carried out on the implant section to evaluate the presence of contaminant elements (ie, Fe⁺⁺). Ca/N, P/N, and Ca/P mean values were statistically analyzed using two-way analysis of variance followed by Student-Newman-Keuls test. *P* value was previously set at .05.

Results

Histologic Evaluation

All implants were surrounded by mineralized bone tissue, most of which was in close contact with the metal surface. In the specimens retrieved after many years (samples 1 to 7) the bone was more mature, with small osteocyte lacunae and small marrow spaces, and no fibrous connective tissue was observed at the interface. In the specimens retrieved after 2 months (samples 8

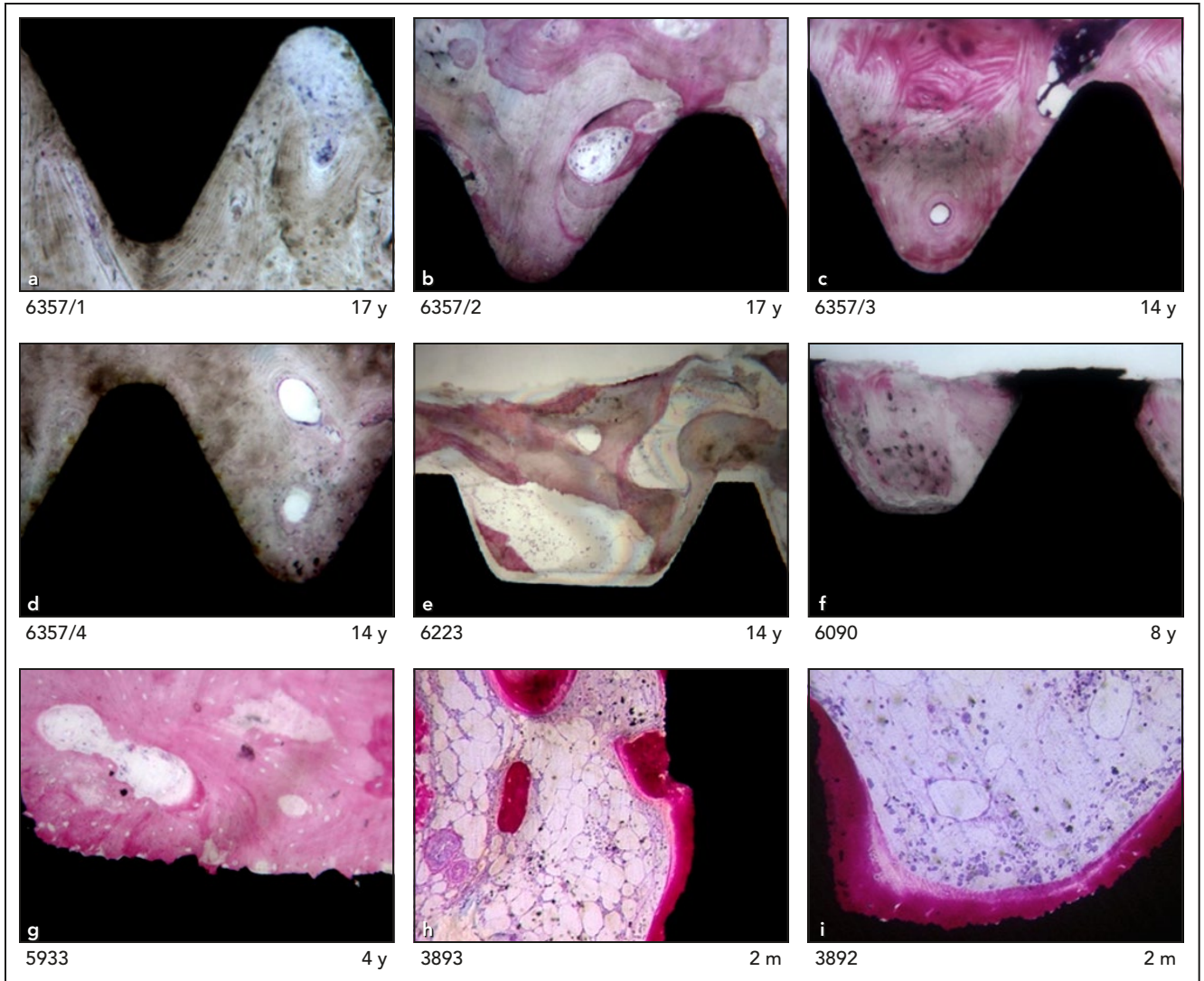


Fig 1 (a, b) In the 17-year samples, compact mature lamellar bone with small marrow spaces was present around the implant surface. Remodeling areas were present close to the implant surface. (c to e) In the 14-year samples, osteons were present in the proximity of the implant body. Mature old bone was in close contact with the implant surface. Trabecular mature bone could be detected at the interface of the implant. (f) In the 8-year sample, lamellar bone with a low affinity for the staining could be distinguished. (g) In the 4-year sample, bone was in tight contact with the implant surface and adapted to all its microirregularities. (h) Signs of bone formation were present inside the concavity of an implant thread in the sample retrieved after 2 months. (i) Newly formed bone was present along the perimeter of the unloaded implant retrieved after 2 months. Many blood vessels were evident in the marrow spaces. (Toluidine blue and acid fuchsin; magnification $\times 40$ and $\times 100$.)

and 9), the interface was characterized by diffuse presence of connective tissue. No inflammatory infiltrate was present at the bone-implant interface or at the level of the marrow spaces. No foreign body reaction cells or epithelial downgrowth were present (Fig 1).

ESEM-EDX Analysis

Sample 1 (6357/1): Retrieved After 17 Years

ESEM analysis of a thread located at the middle part of the implant showed a compact and mature cortical bone tissue (Fig 2a, Table 2).

Osteon bone lamellae were arranged concentrically in the areas between threads. Osteocyte lacunae closer to the implant surface were disposed near the interface and followed the thread contour. Some small, dense metal fragments, evident at higher magnifications

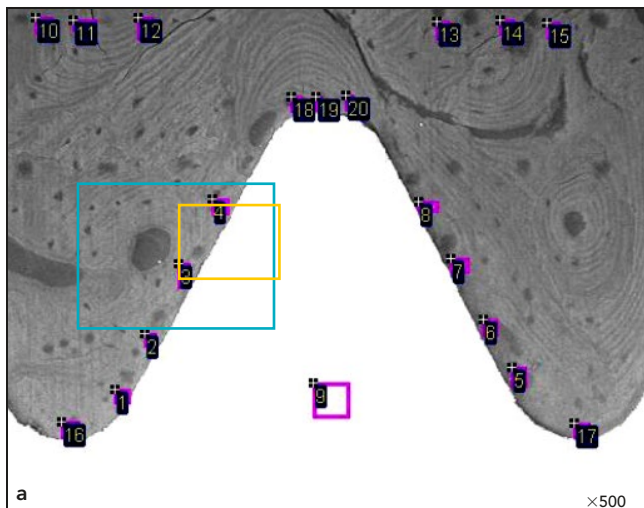


Fig 2 ESEM images of Sample 1 (6357/1). (a) Compact cortical bone showing close bone-implant contact, well evident at higher magnifications (b, c). Osteocyte lacunae closer to the implant surface were arranged following the implant thread design.

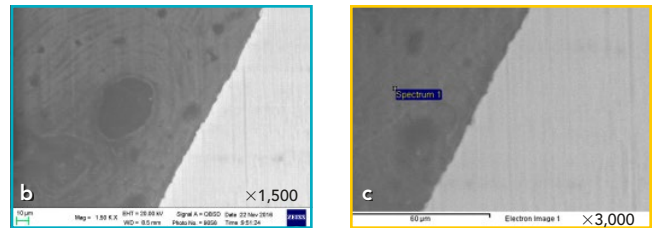


Table 2 Atomic Percentages and Ratios Obtained by EDX Analysis on Sample 1 (6357/1)

Spectrum	C	N	O	Na	Mg	P	S	Cl	Ca	Ti	Ca/N	P/N	Ca/P
1	48.47	15.61	20.56	0.21	0.08	2.62	0.12		3.50	8.83	0.22	0.17	1.33
2	51.01	15.17	19.92	0.24	0.07	2.73	0.12		3.51	7.22	0.23	0.18	1.28
3	53.31	13.79	19.49	0.26	0.09	2.83	0.13		3.70	6.41	0.26	0.21	1.31
4	53.13	14.52	20.00	0.27	0.09	20.81	0.11		3.68	5.39	0.25	0.19	1.31
5	58.14	16.13	14.21	0.24		1.96	0.13		2.38	6.81	0.15	0.12	1.21
6	59.41	16.54	13.56	0.28		1.88	0.11		2.25	5.97	0.14	0.11	1.19
7	50.78	14.48	22.28	0.36	0.06	2.69	0.16		3.26	5.92	0.19	0.19	1.21
8	51.95	13.80	22.17	0.38	0.07	2.74	0.15		3.36	5.36	0.25	0.20	1.22
9	27.33	10.88	17.85			0.58			0.62	42.74			
10	57.67	11.34	21.48	0.33		2.97	0.31		3.97	1.92	0.35	0.26	1.33
11	54.27	12.53	22.68	0.39	0.07	3.42	0.16		4.58	1.89	0.36	0.27	1.34
12	52.41	12.39	24.95	0.37		3.29	0.26		4.38	1.95	0.35	0.27	1.33
13	55.39	11.69	22.86	0.44	0.06	3.31	0.17		4.19	1.89	0.36	0.28	1.26
14	53.45	14.25	22.45	0.45		3.21	0.18		4.23	1.78	0.30	0.22	1.32
15	57.66	13.32	20.33	0.39		2.84	0.16	0.04	3.64	1.63	0.27	0.21	1.28
16	47.27	16.08	21.21	0.37	0.09	2.53	0.12		3.19	9.13	0.20	0.16	1.26
17	56.68	14.63	15.99	0.24		1.65	0.11		1.92	8.79	0.13	0.11	1.16
18	61.98	15.23	13.51	0.27		2.35	0.12		2.99	3.55	0.20	0.15	1.27
19	58.56	14.99	15.72	0.28		2.73	0.14		3.49	4.09	0.16	0.18	1.27
20	61.93	15.52	13.49	0.25		2.32	0.11		2.87	3.52	0.18	0.15	1.23

Table 3 Atomic Percentages and Ratios Obtained by EDX Analysis on Sample 1 (6357/1) in Focused Area (Frame 2c)

Spectrum 1	C	O	Na	P	S	Ca	Ti	Fe
	53.96	33.23	0.27	2.81	0.18	3.75	4.49	1.30

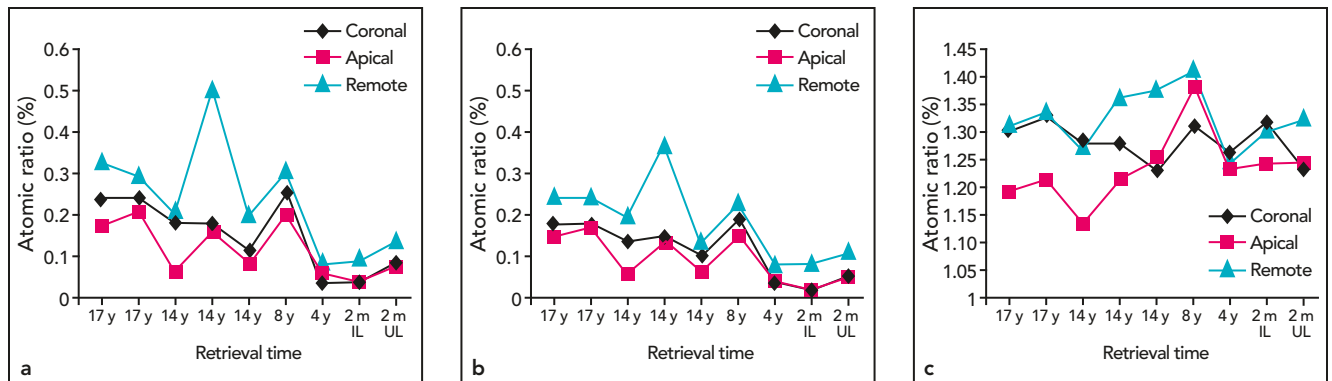


Fig 3 Mean values of Ca/N (a), P/N (b), and Ca/P (c) ratios of the examined bone samples. Ca/N and P/N values of the interface bone at the coronal side of the thread were higher compared to the apical side, and remote bone had the highest values. Ca/P was mainly higher on the coronal side with respect to the apical side; in the long-term samples, Ca/P had the same value in the coronal side and in remote bone. IL = immediately loaded; UL = unloaded.

Table 4 Ca/P, Ca/N, and P/N Atomic Ratios (Mean \pm SD) Calculated from EDX Analyses Carried Out in Bone at Coronal and Apical Sides Around Implant Thread and in Remote Bone

Sample (code)	Ca/P			Ca/N			P/N		
	Coronal	Apical	Remote bone	Coronal	Apical	Remote bone	Coronal	Apical	Remote bone
1 (6357/1)	1.30 \pm 0.02 ^{aA}	1.19 \pm 0.02 ^{aB}	1.31 \pm 0.02 ^{aA}	0.23 \pm 0.02 ^{aA}	0.17 \pm 0.05 ^{aA}	0.33 \pm 0.04 ^{aB}	0.18 \pm 0.02 ^{aA}	0.15 \pm 0.05 ^{aA}	0.25 \pm 0.03 ^{aB}
2 (6357/2)	1.33 \pm 0.05 ^{aA}	1.21 \pm 0.02 ^{aB}	1.33 \pm 0.02 ^{aA}	0.24 \pm 0.02 ^{aA}	0.21 \pm 0.01 ^{aA}	0.29 \pm 0.09 ^{aB}	0.18 \pm 0.02 ^{aA}	0.17 \pm 0.08 ^{aA}	0.25 \pm 0.02 ^{aB}
3 (6357/3)	1.28 \pm 0.02 ^{aA}	1.13 \pm 0.04 ^{aB}	1.27 \pm 0.04 ^{aA}	0.18 \pm 0.02 ^{aA}	0.06 \pm 0.04 ^{bB}	0.21 \pm 0.05 ^{bA}	0.14 \pm 0.02 ^{aA}	0.06 \pm 0.01 ^{bB}	0.20 \pm 0.02 ^{aC}
4 (6357/4)	1.28 \pm 0.09 ^{aA}	1.21 \pm 0.08 ^{aA}	1.36 \pm 0.07 ^{aB}	0.18 \pm 0.06 ^{aA}	0.16 \pm 0.08 ^{aA}	0.51 \pm 0.07 ^{cB}	0.15 \pm 0.05 ^{abA}	0.13 \pm 0.06 ^{aA}	0.37 \pm 0.05 ^{bB}
5 (6223)	1.23 \pm 0.04 ^{aA}	1.25 \pm 0.02 ^{aA}	1.37 \pm 0.03 ^{aB}	0.11 \pm 0.05 ^{abA}	0.07 \pm 0.05 ^{bA}	0.20 \pm 0.02 ^{bB}	0.10 \pm 0.04 ^{bAB}	0.06 \pm 0.04 ^{bA}	0.14 \pm 0.03 ^{cB}
6 (6090)	1.31 \pm 0.01 ^{aA}	1.38 \pm 0.06 ^{bB}	1.41 \pm 0.02 ^{bB}	0.25 \pm 0.06 ^{aAB}	0.20 \pm 0.02 ^{aA}	0.31 \pm 0.08 ^{aB}	0.19 \pm 0.04 ^{aAB}	0.15 \pm 0.02 ^{aA}	0.23 \pm 0.05 ^{aB}
7 (5933)	1.26 \pm 0.08 ^{aA}	1.23 \pm 0.06 ^{aA}	1.24 \pm 0.10 ^{cA}	0.03 \pm 0.01 ^{bA}	0.05 \pm 0.03 ^{bA}	0.08 \pm 0.04 ^{dA}	0.03 \pm 0.01 ^{cA}	0.04 \pm 0.02 ^{bAB}	0.08 \pm 0.02 ^{cB}
8 (3892)	1.32 \pm 0.01 ^{aA}	1.24 \pm 0.11 ^{aA}	1.30 \pm 0.04 ^{aA}	0.04 \pm 0.01 ^{bA}	0.03 \pm 0.02 ^{bA}	0.10 \pm 0.05 ^{dB}	0.04 \pm 0.01 ^{bcAB}	0.02 \pm 0.01 ^{bA}	0.08 \pm 0.05 ^{cB}
9 (3893)	1.23 \pm 0.01 ^{aA}	1.24 \pm 0.04 ^{aA}	1.32 \pm 0.02 ^{aB}	0.08 \pm 0.02 ^{bA}	0.07 \pm 0.01 ^{bA}	0.14 \pm 0.01 ^{dB}	0.06 \pm 0.01 ^{bcA}	0.05 \pm 0.02 ^{bA}	0.11 \pm 0.01 ^{cB}

Superscript letters represent statistically significant differences in the same row (*capital*) or in the same column (*lowercase*).

($\times 1,500$ and $\times 3,000$), were embedded in the peri-implant bone tissue (Figs 2b and 2c). EDX analysis showed higher Ca/N and especially Ca/P values at the coronal side (sites 1 to 4 and 16; Table 3) than at the

apical side (sites 5 to 8 and 17; Fig 3, Table 4), revealing a more mineralized and more mature bone at the coronal side of the thread. The highest Ca/N and P/N values (0.33 and 0.25, respectively) were measured

on remote bone (sites 10 to 15). EDX on the implant (site 9) showed Ti (71.68 weight %) with no Al, V, or Fe. Microanalysis on a metal fragment showed presence of Fe (4.21 weight %) (Fig 2c).

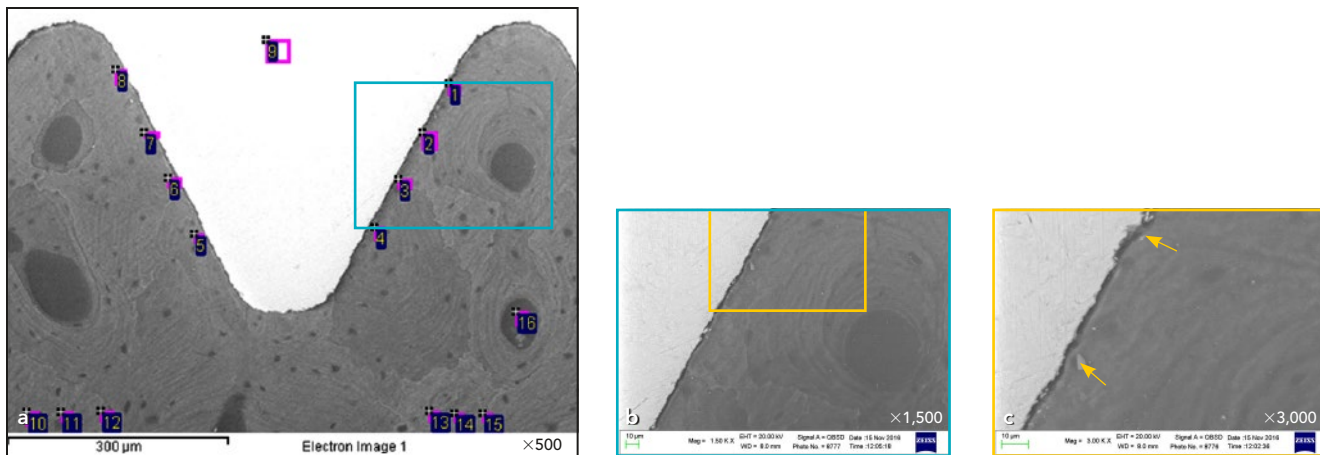


Fig 4 ESEM images of Sample 2 (6357/2). (a) Mature compact bone showing osteon lamellae concentrically arranged and close to the implant surface. (b,c) At higher magnifications, the interface appeared detached from bone tissue and small debris (arrows) and metal fragments were present.

Sample 2 (6357/2): Retrieved After 17 Years

ESEM analysis carried out in one area located at the middle portion of the implant showed a homogeneous bone-implant interface and uniform compact bone. Osteons close to but not in contact with the implant surface showed lamellae concentrically arranged (Fig 4a). Osteocyte lacunae closer to the implant surface followed the thread contour. At $\times 1,500$ and $\times 3,000$ magnification (Figs 4b and 4c), the bone at the apical side appeared to be detached from the implant surface and many metal fragments were observed near the interface. EDX revealed similar Ca/N and P/N ratios at the coronal (sites 5 to 8) and apical (sites 1 to 4) sides (Table 4, Fig 3), while the highest Ca/N and P/N values were observed on remote bone (sites 10 to 15). The Ca/P value was similar on the coronal side (1.33) and remote bone. EDX on the implant section (site 9) revealed Ti (74.67 weight %).

Sample 3 (6357/3): Retrieved After 14 Years

A thread located in the middle part of the implant was investigated. Compact bone with a close bone-implant contact was primarily present on the coronal side of the implant thread, where osteons were evident. Bone lamellae were concentrically arranged and followed the coronal implant surface. On the apical side, only small portions of compact bone were present at the implant interface and wide remodeling areas were visible. EDX showed markedly lower Ca/N, P/N, and Ca/P values at the apical side compared to the coronal side and especially to remote bone (Table 4, Fig 3). Ca/P values on the coronal side and on remote bone were similar. EDX on the implant section showed Ti (76.18 weight %).

Sample 4 (6357/4): Retrieved After 14 Years

ESEM analysis focused on one implant thread located at the middle-

apical portion of the implant showed mature compact bone tissue. Bone lamellae with numerous osteocyte lacunae were arranged concentrically. Osteocyte lacunae closer to the implant surface followed the implant thread design. Some osteons abutted the implant thread at the coronal and apical sides. EDX revealed differences in mineral content among the examined areas, showing markedly higher Ca/N and P/N in remote bone (Fig 3). Ca/N and P/N values were similar at both thread sides, revealing similar organic content; however, a higher atomic Ca/P ratio was detected on the coronal side compared to the apical side (Table 4). Microanalysis on the implant revealed Ti (89.24 weight %).

Sample 5 (6223): Retrieved After 14 Years

ESEM analysis of a thread located in the middle part of the implant revealed a mature trabecular bone. Bone lamellae were arranged fol-

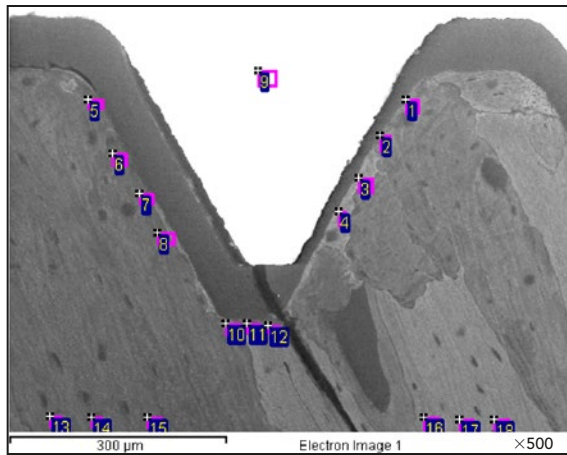


Fig 5 ESEM image of Sample 6 (6090). Bone tissue appeared compact with few Haversian channels and numerous osteocyte lacunae not uniformly disposed.

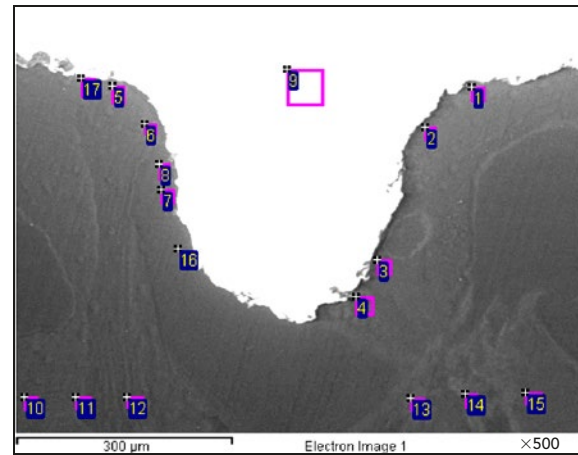


Fig 6 ESEM image of Sample 7 (5933). Bone lamellae followed the implant thread contour mostly on the coronal (left) side, while the structure appeared less organized on the apical (right) side.

lowing the contour of the implant thread, with a limited presence of osteocyte lacunae. More bone tissue was found on the coronal side of the implant thread, closely apposed to the metal implant surface. On the apical side, only small areas of bone tissue were in contact with the implant surface. EDX microanalysis revealed low Ca/N and P/N values on coronal and apical thread sides, revealing a bone tissue with a high organic component (Table 4, Fig 3). On remote bone, slightly higher Ca/N and P/N values showed a more mineralized structure, while markedly high Ca/P values revealed mature bone. EDX on the implant section revealed Ti (65.93 weight %) and traces of Fe (0.13 weight %).

Sample 6 (6090):

Retrieved After 8 Years

ESEM analyses of a thread located at the coronal-middle part of the implant body showed detachment of bone tissue from the implant sur-

face, likely attributable to the sample retrieval and/or histologic preparation procedures (Fig 5). A mature compact bone with few Haversian channels in the osteon structure was visible. Bone lamellae did not follow the implant thread design. Numerous osteocyte lacunae were identified but appeared not to have a uniform disposition. EDX revealed Ca/N and P/N values higher on the coronal side (sites 1–4) of the thread compared to the apical side (sites 5 to 8), revealing a more mineralized bone with a lower organic composition (Table 4, Fig 3).

Similar to the majority of the samples examined, the highest Ca/N and P/N values were registered in remote bone. Unlike the previously examined samples, the Ca/P values were very high, particularly for the apical side and remote bone (1.38 and 1.41, respectively). This indicated a mature bioapatite (Fig 3). EDX on the implant body (site 9) revealed Ti (69.81 weight %).

Sample 7 (5933):

Retrieved After 4 Years

ESEM of a thread located on the middle part of the implant showed a mature compact bone with a visible osteon at the apical side of the implant thread (Fig 6). Bone lamellae were well represented on the coronal side, which followed the margin of the implant thread, while on the apical side the structure appeared less organized (Fig 6). EDX analyses revealed similar Ca/P, Ca/N, and P/N values at the coronal (sites 5 to 8 and 17), apical (sites 1 to 4), and remote bone (sites 10 to 15) (Table 4, Fig 3), revealing a less mineralized tissue with a high presence of organic components. Ca/N and P/N values were lower compared to the previous (long-term) examined samples. Traces of Al ions on all the spectra were acquired at the bone-implant interface and on remote bone (site 14).

The analysis of the implant (site 9) revealed Ti (73.46 weight %) and

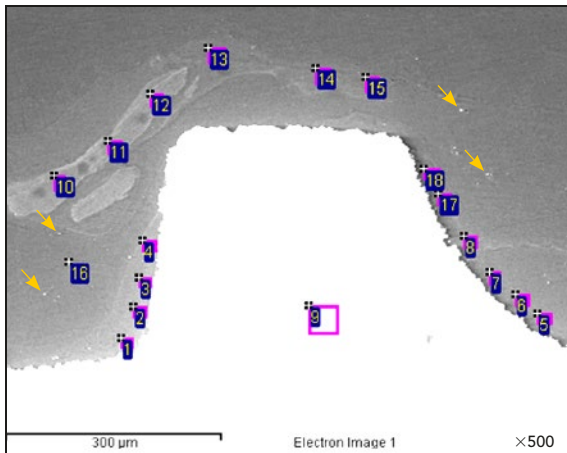


Fig 7 ESEM image of Sample 8 (3892), IL. An irregular bone-forming structure with few osteocyte lacunae was seen, with less dense areas around the thread at apical (right) and coronal (left) sides. A large number of small dense granules were also well evident (arrows).

Table 5 Atomic Percentages and Ratios Obtained by EDX Analysis on Sample 8 (3892), IL

Spectrum	C	N	O	Na	P	S	Ca	Ti	Ca/N	P/N	Ca/P
1	54.61	16.44	17.68	0.31	0.76	0.36	0.92	8.91	0.06	0.05	1.21
2	54.53	16.61	18.59	0.33	0.56	0.34	0.75	8.29	0.05	0.03	1.33
3	56.27	17.32	17.14	0.28	0.47	0.34	0.62	7.54	0.04	0.04	1.32
4	53.99	16.97	19.67	0.33	0.50	0.37	0.71	7.44	0.04	0.05	1.42
5	63.54	16.46	13.38	0.10	0.06	0.08	0.07	6.31	0.01	0.01	1.16
6	63.48	16.79	13.86	0.07	0.08	0.05	0.09	5.59	0.004	0.004	1.12
7	60.08	16.45	15.41	0.21	0.21	0.20	0.29	7.14	0.02	0.01	1.38
8	56.16	17.31	18.71	0.26	0.66	0.32	0.77	5.81	0.04	0.01	1.16
9	32.47	12.99	13.26		0.11		0.10	41.07			
10	53.56	17.85	21.21	0.39	1.71	0.25	2.26	2.77	0.13	0.01	1.32
11	54.90	16.02	21.27	0.38	1.82	0.25	2.41	2.94	0.15	0.10	1.32
12	54.12	16.21	22.01	0.42	1.89	0.24	2.50	2.62	0.15	0.11	1.33
13	57.57	17.44	20.23	0.35	0.79	0.36	0.99	2.26	0.06	0.12	1.30
14	57.09	17.67	19.93	0.40	0.74	0.38	0.91	2.88	0.05	0.05	1.22
15	57.40	17.59	19.60	0.36	0.69	0.37	0.92	3.07	0.05	0.04	1.33
16	63.57	16.41	14.83	0.14	0.16	0.13	0.17	4.58			
17	57.87	16.56	17.86	0.27	0.57	0.43	0.72	5.73	0.04	0.03	1.26
18	58.28	16.44	18.31	0.26	0.49	0.32	0.68	5.23	0.04	0.03	1.38

traces of Al (0.08 weight %); punctual EDX on a dense metal fragment (site 16) revealed the same Al content.

Sample 8 (3892): Retrieved After 2 Months Immediate Loading

The section, located on the middle-apical portion of the implant, showed the presence of less dense

bone tissue around the thread at apical (sites 1 to 4) and coronal (sites 5 to 8, 17, and 18) sides. This morphology suggested new bone formation (Fig 7, Table 5). Trabecular bone with many osteocyte lacunae could be found at about 50 to 100 μm from the coronal side of the thread. Small metal fragments

were observed in the bone (Fig 7) at coronal and apical sides. EDX analysis revealed a less mineralized and more immature peri-implant bone. Ca/N and P/N values were similarly low on coronal (sites 1 to 4) and apical (sites 5 to 8, 17, and 18) sides. Ca/P ratios were unexpectedly higher on the coronal side

Fig 8 ESEM image of Sample 9 (3893), UL. Bone tissue appeared less dense on apical (left) and coronal (right) sides, suggesting ongoing bone formation. Remote bone appeared more organized, with a larger number of osteocyte lacunae. Small dense granules were embedded into the bone structure.

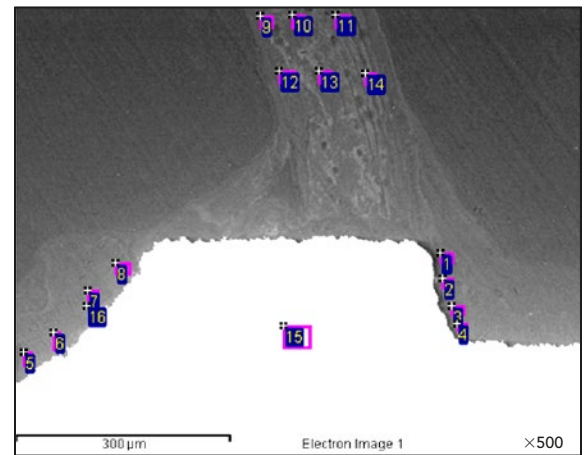


Table 6 Atomic Percentages and Ratios Obtained by EDX Analysis on Sample 9 (3893), UL

Spectrum	C	N	O	Na	Mg	P	S	Ca	Ti	Ca/N	P/N	Ca/P
1	58.81	15.91	15.50	0.35	0.04	1.33	0.33	1.66	6.07	0.10	0.08	1.24
2	56.66	18.12	14.80	0.25		1.26	0.22	1.55	7.13	0.09	0.07	1.23
3	59.74	18.07	12.36	0.23		0.86	0.28	1.06	7.41	0.06	0.05	1.23
4	59.54	17.65	12.05	0.22		0.96	0.28	1.16	8.15	0.07	0.05	1.21
5	56.79	16.88	16.10	0.33		0.88	0.35	1.07	7.60	0.06	0.05	1.22
6	57.09	17.25	15.96	0.30		0.85	0.35	1.04	7.15	0.06	0.05	1.22
7	53.38	17.48	19.51	0.37		0.85	0.40	1.11	6.90	0.06	0.05	1.30
8	55.63	16.60	18.54	0.32	0.04	1.01	0.25	1.25	6.35	0.08	0.06	1.23
9	56.89	17.15	19.59	0.31	0.05	1.68	0.26	2.18	1.89	0.12	0.10	1.29
10	55.22	18.24	19.75	0.32		1.84	0.26	2.48	1.88	0.14	0.10	1.34
11	56.73	17.52	18.90	0.30	0.05	1.84	0.24	2.46	1.94	0.14	0.11	1.34
12	56.25	17.15	19.73	0.36		1.70	0.25	2.21	2.34	0.13	0.10	1.30
13	55.18	17.97	19.95	0.34		1.75	0.26	2.33	2.21	0.13	0.09	1.33
14	55.87	16.86	19.58	0.35	0.05	2.01	0.25	2.66	2.37	0.16	0.12	1.32
15	30.24	13.44	12.59	0.14		0.24		0.25	43.10			
16	58.73	16.50	16.59	0.29		0.65	0.32	0.84	6.08			

(Table 4, Fig 3) compared to the apical portion. Remote bone (sites 10 to 15) showed a more mineralized structure with higher Ca/N and P/N values. Implant section (site 9) EDX showed Ti (71.30 weight %).

Sample 9 (3893): Retrieved After 2 Months Unloaded (Control)

ESEM microanalysis of a thread located on the middle portion of

the implant showed a low-density trabecular bone that suggested ongoing bone formation. Remote bone appeared to be more mature, with many osteocyte lacunae and some localized dense areas (Fig 8, Table 6). Some metal fragments were present in the bone tissue on both coronal and apical (sites 5 to 8) sides (Table 4, Fig 3). EDX microanalysis revealed extremely low

coronal (sites 1 to 4) and apical Ca/N and P/N values, suggesting a high presence of organic materials; low Ca/P values were detected. Remote bone (sites 9 to 14) showed markedly higher Ca/N, P/N, and Ca/P values. EDX of the implant (site 15) showed Ti (72.74 weight %).

Discussion

In the present study, ESEM-EDX analysis provided new information regarding peri-implant bone structure, its degree of mineralization, and its element composition, revealing some important features.

In the long-term samples (retrieved after 8 to 17 years) the Ca/N and P/N values (representing the mineral component with respect to the organic component) of the interface bone at the coronal side of the thread were higher with respect to the apical side, indicating more mineralized bone (Figs 3a and 3b). Ca/P ranged from 1.06 to 1.41, which is lower than the values reported in the literature (range: 1.37 to 1.62).⁷ This may be related to the fact that EDX analysis was performed on histologic samples, and the resin content likely contributed to the lower Ca/P ratios. Because of this, N rather than C has been used as an index of organic content to evaluate the mineralization degree of bone.

Four of the five implants retrieved after a long period (14 to 17 years) showed higher Ca/P ratios on the interface bone at the coronal side compared to the apical side of the thread (Fig 3c), with statistically significant differences in three of them ($P < .05$). One sample retrieved after 14 years (sample 5) showed a different Ca/P trend compared to the other implants. This may be related to implant placement, as this implant was retrieved from the maxilla while the other implants were retrieved from the mandible.

Implants retrieved after a shorter period (4 to 8 years) or during

osseointegration phases (2 months) showed a different mineralization pattern. Implants retrieved during osseointegration phases showed an increased presence of organic component, revealed by significantly low Ca/N and P/N values ($P < .001$) at both coronal and apical sides of the thread. The sample retrieved after 8 years showed an unexpectedly higher Ca/P ratio on the apical side than on the coronal side (Fig 3c), while the sample retrieved after 4 years showed the lowest (not statistically significant, with high SD) Ca/P value detected on remote bone among all the samples. Active bone remodeling on coronal and apical sides, as shown by ESEM morphologic analysis and confirmed by the high SD values, justifies these results of the implants retrieved after short periods. These findings may appear to be in contrast with data reported in the literature. In a recent study, 29 porous zirconia implants were retrieved for increased bone loss.²⁴ Through histologic evaluations, the authors found that the most compact bone was in the periapical region. These data are different from the results of the present study for several reasons. First, the implants were retrieved for increased bone loss (ie, peri-implantitis)²⁴ while in the present study the implants were retrieved for mechanical complications and not for infective processes. Second, the authors performed a histomorphometric analysis,²⁴ and bone mineralization was not qualitatively assessed as in the present study.

A recent study analyzed the soft tissue around dental implants

affected by peri-implantitis, describing the presence of metals/contaminants (Fe and Ti ions).¹⁴ Ti ionic leakage may occur around turned and rough-surface dental implants. No correlation between increasing roughness and ion release was found either in vitro or in vivo.²⁵ In the present study, metal fragments were found in two specimens and traces of Fe ions were detected with no presence of altered bone tissue/bone remodeling. It could be hypothesized that the presence of these metal fragments did not affect implant osseointegration processes; however, this aspect needs to be clarified in further studies.

Previous human histologic studies demonstrated continuous remodeling at the interface of dental implants.²⁶ Over time, the newly formed woven bone located around the implant perimeter undergoes remodeling, changing its structure to a more organized lamellar bone.²⁶ The hardness and the elastic modulus of the peri-implant bone tended to increase over time.²⁶ The present study is in accordance with a previous 12-month animal study²⁷ showing that removal torque (correlatable to the increased bone mineralization) increased over time. In two previous studies from the laboratory of the present authors,^{19,21} the number of osteocytes was found to increase in immediately loaded implants when compared with unloaded controls, and there was a statistically significant increase in osteocytes in the first few years after implant loading. This increase could be important for the mechanical competence of bone.^{19,21}

Conclusions

The two most significant findings were that the interface bone located at the coronal side of the implant threads was generally more mineralized than the interface bone at the apical side of the threads and that the mineralization of the peri-implant bone at the interface increased over time. These results could be related to the different remodeling events (apical versus coronal sides) due to the direction of the loading forces. Notable as a proof of principle was the unexpected finding of a higher degree of mineralization in the 2-month immediately loaded implant when compared to the 2-month submerged unloaded control.

Acknowledgments

The authors reported no conflicts of interest related to this study.

References

- Albrektsson T, Brånemark PI, Hansson HA, Lindström J. Osseointegrated titanium implants. Requirements for ensuring a long-lasting, direct bone-to-implant anchorage in man. *Acta Orthop Scand* 1981;52:155–170.
- Albrektsson T, Johansson C. Osteoinduction, osteoconduction and osseointegration. *Eur Spine J* 2001;10(suppl): s96–s101.
- Davies JE. Mechanisms of endosseous integration. *Int J Prosthodont* 1998;11: 391–401.
- Davies JE, Mendes VC, Ko JC, Ajami E. Topographic scale-range synergy at the functional bone/implant interface. *Biomaterials* 2014;35:25–35.
- Feng X, McDonald JM. Disorders of bone remodeling. *Annu Rev Pathol* 2011;6: 121–145.
- Kourkoumelis N, Balatsoukas I, Tzaphlidou M. Ca/P concentration ratio at different sites of normal and osteoporotic rabbit bones evaluated by Auger and energy dispersive x-ray spectroscopy. *J Biol Phys* 2012;38:279–291.
- Shah FA, Nilson B, Brånemark R, Thomsen P, Palmquist A. The bone-implant interface—Nanoscale analysis of clinically retrieved dental implants. *Nanomedicine* 2014;10:1729–1737.
- Palmquist A, Emanuelsson L, Sjövall P. Chemical and structural analysis of the bone-implant interface by TOF-SIMS, SEM, FIB and TEM: Experimental study in animal. *Appl Surf Sci* 2012;258: 6485–6494.
- Gandolfi MG, Taddei P, Siboni F, et al. Micro-topography and reactivity of implant surfaces: An in vitro study in simulated body fluid (SBF). *Microsc Microanal* 2015;21:190–203.
- Gandolfi MG, Iezzi G, Piattelli A, Prati C, Scarano A. Osteoinductive potential and bone bonding ability of ProRoot MTA, MTA Plus and Biodentine in rabbit intramedullary model: Microchemical characterization and histological analysis. *Dent Mater* 2017;33:e221–e238.
- Gandolfi MG, Spagnuolo G, Siboni F, et al. Calcium silicate/calcium phosphate biphasic cements for vital pulp therapy: Chemical-physical properties and human pulp cells response. *Clin Oral Invest* 2015;19:2075–2089.
- Engfeldt B, Hjerpe A. Density gradient fractionation of dentine and bone powder. *Calcif Tissue Res* 1974;16:261–275.
- Bigi A, Cozzani G, Panzavolta S, et al. Chemical and structural characterization of the mineral phase from cortical and trabecular bone. *J Inorg Biochem* 1997; 68:45–51.
- Fretwurst T, Buzanich G, Nahles S, Woelber JP, Riesemeier H, Nelson K. Metal elements in tissue with dental peri-implantitis: A pilot study. *Clin Oral Implants Res* 2016;27:1178–1186.
- Eliades G, Mantzourani M, Labella R, Mutti B, Sharma D. Interactions of dentine desensitizers with human dentine: Morphology and composition. *J Dent* 2013; 41(suppl):s28–s39.
- Bolind P. On 606 Retrieved Oral and Craniofacial Implants. An Analysis of Consecutively Received Human Specimens [thesis]. Gothenburg: University of Gothenburg, 2004.
- Bolind P, Johansson CB, Balshi TJ, Langer B, Albrektsson T. A study of 275 retrieved Brånemark oral implants. *Int J Periodontics Restorative Dent* 2005; 25:425–437.
- Bolind PK, Johansson CB, Becker W, Langer L, Sevetz EB Jr, Albrektsson TO. A descriptive study on retrieved non-threaded and threaded implant designs. *Clin Oral Implants Res* 2005;16:447–455.
- Barros RR, Degidi M, Novaes AB, Piattelli A, Shibli JA, Iezzi G. Osteocyte density in the peri-implant bone of immediately loaded and submerged dental implants. *J Periodontol* 2009;80:499–504.
- Degidi M, Piattelli A, Shibli JA, Perrotti V, Iezzi G. Bone formation around immediately loaded and submerged dental implants with a modified sand-blasted and acid-etched surface after 4 and 8 weeks: A human histologic and histomorphometric analysis. *Int J Oral Maxillofac Implants* 2009;24:896–901.
- Piattelli A, Artese L, Penitente E, et al. Osteocyte density in the peri-implant bone of implants retrieved after different time periods (4 weeks to 27 years). *J Biomed Mater Res B Appl Biomater* 2014;102:239–243.
- Iezzi G, Piattelli A, Mangano C, et al. Periimplant bone response in human-retrieved, clinically stable, successful, and functioning dental implants after a long-term loading period: A report of 17 cases from 4 to 20 years. *Implant Dent* 2016; 25:380–386.
- Botticelli D, Perrotti V, Piattelli A, Iezzi G. Four human stable and functioning dental implants retrieved for fracture after 14 and 17 years from the same patient: A histological and histomorphometrical report. *Int J Periodontics Restorative Dent* [in press].
- Kohal RJ, Schwindling FS, Bächle M, Spies BC. Peri-implant bone response to retrieved human zirconia oral implants after a 4-year loading period: A histologic and histomorphometric evaluation of 22 cases. *J Biomed Mater Res Part B Appl Biomater* 2016;104:1622–1631.
- Wennerberg A, Ide-Ektessabi A, Hatkamata S, et al. Titanium release from implants prepared with different surface roughness. *Clin Oral Implants Res* 2004;15:505–512.
- Gil LF, Suzuki M, Janal MN, et al. Progressive plateau root form dental implant osseointegration: A human retrieval study. *J Biomed Mater Res B Appl Biomater* 2015;103:1328–1332.
- Johansson C, Albrektsson T. Integration of screw implants in the rabbit: A 1-year follow-up of removal torque of titanium implants. *Int J Oral Maxillofac Implants* 1987;2:69–75.

1.1.2 Esem-Edx Microanalysis Of The Bone-Implant Interface Around Loaded And Unloaded Retrieved Dental Implants.

Prati Carlo¹, Zamparini Fausto^{1,2}, Botticelli Daniele³, Daichi Yonezawa⁴, Adriano Piattelli⁵, Gandolfi Maria Giovanna².

1. School of Dentistry, Department of Biomedical and Neuromotor Sciences, University of Bologna, Bologna, Italy
2. Laboratory of Biomaterials and Oral Pathology, School of Dentistry, Department of Biomedical and Neuromotor Sciences, University of Bologna, Bologna, Italy
3. Ardec Academy, Rimini, Italy
4. Clinical Assistant Professor, Department of Applied Prosthodontics, Graduate School of Biomedical Sciences, Nagasaki University
5. Department of Medical Oral and Biotechnological Sciences, University of Chieti - Italy

AIM

The aim of the present study is to analyse the mineralization degree at the bone implant interface and the effect of initial loading procedures around clinically stable retrieved dental implant before (4 months from insertion) and after 2 months of loading (4 months from insertion).

MATERIALS AND METHODS

The protocol of the study was approved by Ethical Committee of the Corporación Universitaria Rafael Núñez, Cartagena de Indias, Colombia. Detailed information on Material and Methods and histological data have been reported in a previous published paper (Yonezawa et al. 2018). Sixteen volunteers were included in the study and two mini implants were installed in a non-submerged fashion in the edentulous distal region of the jaws. After two months, one mini implant was randomly selected to be loaded with a single crown while the other mini implant was left unloaded. After 2 more months, both mini implants were removed with a trephine. Twenty biopsies retrieved from 10 volunteers were available for histological analysis. The biopsies were sectioned using a diamond steel disc along the major axis of the implants at approximately 150 mm and ground to about 30 microns. The sections were stained with acid fuchsin and toluidine blue. Ten ground sections from 5 patients were used for OM and ESEM-EDX Microanalysis.

OM and ESEM-EDX Microanalysis

The histological samples were observed under Optical microscopy (OM) to identify the macrostructure of the sample and bone macromorphology.

Then, ESEM observation were performed entirely, from the coronal to the most apical portion of the implant at 500x magnification. ESEM-EDX micro-analyses were performed following Gandolfi protocol (Gandolfi *et al.* 2017 and 2018). Briefly, micromorphological and microchemical analyses were performed at both coronal and apical sides of the **upper** (where bone was present) and **deep** threads of the implants and at 300 and 500 µm from the implant thread (distant bone as mineralization control of each sample).

EDX analyses were carried out at areas of approx. 30x30 microns (n=3 per thread side) and qualitative and semi-quantitative element (weight % and atomic %) content were investigated. For all the acquired spectra, the atomic Ca/N,

P/N and Ca/P ratios were calculated (as mean and standard deviation) to evaluate the degree of mineralization (Gandolfi *et al.* 2017 and 2018).

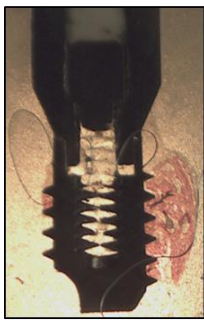
Statistical analysis

Ca/N, P/N and Ca/P mean values were statistically analyzed using two-way ANOVA followed by Student-Newman-Keuls test. P value was previously set at 0.05.

RESULTS

The investigated samples are reported in **Figure 1**. Out of 10 implants, 5 were retrieved after 4 months from placement (unloaded group) and 5 were retrieved after 6 months (loaded group, namely retrieved after 2 months of loading and 4 months healing period).

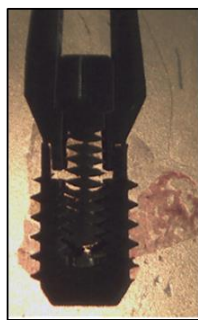
Loaded samples (2 months unloaded + 2 months loading)



Sample 6504



Sample 6508



Sample 6514



Sample 6517



Sample 6518

Unloaded samples (4 months unloaded)



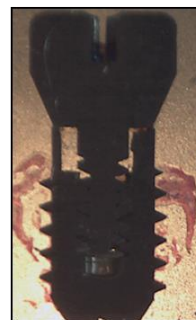
Sample 6507



Sample 6509



Sample 6516



Sample 6519

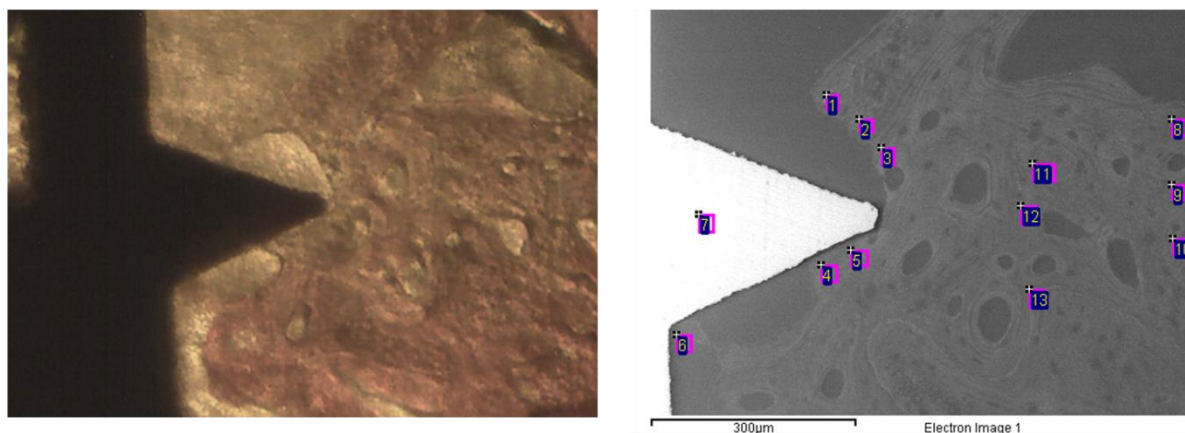


Sample 6521

Figure 1: Retrieved implants histology analysed in the present study. Five were retrieved after 4 months unloaded, the other five were retrieved after 4 months (2 months of loading).

Samples analysis was conducted as in **Figure 2**.

Sample 6504



Spectrum	C	N	O	Na	P	S	Ca	Ti	Ca/P	Ca/N	P/N
1	68.72	12.31	14.68	0.08	1.19	0.08	1.50	1.44	1.26	0.122	0.097
2	68.33	12.49	15.00	0.06	1.22	0.08	1.53	1.29	1.25	0.122	0.098
3	64.38	11.80	18.61		1.69	0.07	2.11	1.34	1.25	0.179	0.143
4	62.94	12.44	18.53	0.07	1.48	0.09	1.88	2.56	1.27	0.151	0.189
5	61.33	11.03	21.06	0.09	1.83	0.10	2.29	2.27	1.25	0.207	0.166
6	64.90	10.57	17.88		0.56	0.07	0.68	5.34	1.21	0.064	0.052
7	47.34		20.82		0.37		0.39	31.08	1.05		
8	66.46	12.96	16.63	0.06	1.54	0.10	1.95	0.28	1.27	0.151	0.119
9	66.25	13.29	16.41		1.59	0.10	2.06	0.30	1.30	0.155	0.120
10	66.17	13.26	16.41	0.07	1.61	0.09	2.10	0.29	1.30	0.158	0.121
11	66.22	12.40	16.90	0.07	1.66	0.10	2.14	0.51	1.29	0.101	0.081
12	64.12	12.97	18.03	0.07	1.77	0.11	2.35	0.59	1.33	0.181	0.136
13	64.87	13.30	17.18	0.06	1.68	0.10	2.22	0.58	1.32	0.167	0.127

All results in atomic%

Figure 2: ESEM microanalysis of one thread located on the upper portion revealed electron dense cortical bone tissue well-evident osteons and bone niches, indicating high bone remodelling activity. EDX microanalysis revealed similar Ca/N and P/N atomic ratios at both coronal and apical side of the thread.

Loaded samples (2 months unloaded + 2 months loading)

Sample 6504

OM revealed cortical bone tissue along all the specimen (**Table 1**). The first bone to implant contact was identified at thread 1.

ESEM microanalysis of the upper thread revealed **electron dense cortical bone** tissue with numerous osteons and bone niches, which suggest high bone remodelling activity. Bone tissue appeared in strict contact with the apical side of the thread, while few bone was present at the implant thread crest.

EDX revealed similar Ca/N and P/N atomic ratios at both coronal and apical side of the upper thread (mean values were 0.14 ± 0.03 and 0.14 ± 0.07). High standard deviation of the apical portion also suggests bone remodelling in this area

(Tables 2,4). Distant bone revealed higher values of Ca/N and P/N, with low SD values. Ca/P values were similar at coronal and apical side of the thread, both lower than Ca/P values of remote bone ($p<0.05$) (Tables 6,7).

	Upper thread	Bone remodeling	Deep thread	Bone remodeling
6504 L	C	+	C	-
6508 L	T	-	T	+
6514 L	C	+	C	+
6517 L	C	+	C	-
6518 L	C	+	T	+
6507 UL	T	-	T	-
6509 UL	C	-	T	-
6516 UL	C	+	C	-
6519 UL	T	-	T	-
6521 UL	C	+	T	+

L= loaded; UL= unloaded; C= cortical bone; T= Trabecular bone ; += presence of alveolar bone remodelling; -= low/absence bone remodelling

ESEM analysis on one deep thread revealed few **cortical bone** tissue with some osteocytes lacunae. Low-electron dense bone tissue was in strict contact with the implant surface, the bone lamellae are concentrically arranged following the implant thread design. No osteons were present close to the implant thread. Similarly low electron dense bone tissue was also identified on remote bone.

EDX microanalysis revealed significantly high Ca/N values on the coronal side with respect to the apical side ($p<0.05$), mean values were 0.17 ± 0.001 and 0.09 ± 0.02 respectively. Interestingly, P/N values followed a opposite trend, being that the apical portion revealed high P/N values when compared to the coronal side of the deep thread (mean P/N were 0.08 ± 0.02 and 0.03 ± 0.001). (Tables 3,5). Distant bone showed higher P/N and Ca/N values when compared to both apical and coronal side. Ca/P ratios on calculated on the apical side revealed statistically lower values compared to both coronal side and bone located at 300 and 500 micron ($p<0.05$) (Tables 6,7).

Table 2 Ca/N at upper thread (Mean \pm SD). Different letters represent statistically significant differences ($p < 0.05$) in the same horizontal row (capital letters) or in the same column (small letters)

	Coronal Side	Apical Side	300 micron	500 micron
6504 L	0.14 \pm 0.03 aA	0.14 \pm 0.07 aA	0.17 \pm 0.003 aA	0.15 \pm 0.01 aA
6508 L	0.07 \pm 0.05 aA	0.30 \pm 0.02 bB	0.35 \pm 0.02 bB	0.27 \pm 0.049 bB
6514 L	0.13 \pm 0.06 aA	0.23 \pm 0.02 cB	0.207 \pm 0.016 cB	0.27 \pm 0.01 bC
6517 L	0.15 \pm 0.06 aA	0.067 \pm 0.07 dB	0.2 \pm 0.001 cA	0.21 \pm 0.017 abA
6518 L	0.16 \pm 0.024 aA	0.178 \pm 0.06 aA	0.19 \pm 0.02 cA	0.15 \pm 0.01 aA
6507 UL	0.19 \pm 0.02 bA	0.21 \pm 0.01cA	0.14 \pm 0.04 aB	0.17 \pm 0.06 aAB
6509 UL	0.04 \pm 0.01 cA	0.12 \pm 0.08 aA	0.07 \pm 0.06 dA	0.12 \pm 0.03 aA
6516 UL	0.14 \pm 0.02 aA	0.27 \pm 0.01 bB	0.14 \pm 0.02 aA	0.21 \pm 0.01 abAB
6519 UL	0.20 \pm 0.01 bA	0.17 \pm 0.09 aA	0.13 \pm 0.02 aA	0.14 \pm 0.02 aA
6521 UL	0.13 \pm 0.01 aA	0.17 \pm 0.04 aA	0.16 \pm 0.01 aA	0.12 \pm 0.01 aA

Sample 6508

OM analysis revealed **trabecular bone** tissue along all the implant section. Bone tissue starts 300 micron over the upper thread. ESEM investigation on the **upper thread** showed close bone implant contact only on the apical side. Electron-dense bone tissue was observed with some osteocytes lacunae and few osteons, suggesting low bone remodelling activity.

EDX microanalysis revealed significantly high Ca/N and P/N ratios at the apical side of the implant thread, when compared to coronal side ($p < 0.05$), suggesting a more mineralized area. (**Tables 2,4**). No differences were observed between coronal and apical side of the thread in terms of Ca/P. (**Tables 6,7**).

ESEM investigation of one **deep thread** revealed the presence of **trabecular bone tissue with** numerous bone niches, and bone lamellae concentrically arranged following the thread contour and osteons located distant from the implant thread. Bone implant contact was scarce, only at the crest of the thread and in few areas of the coronal and apical side. EDX microanalysis revealed statistically ($p < 0.05$) high Ca/N and P/N values of the apical side of the thread when compared to the coronal side, mean values were 0.26 ± 0.01 and 0.196 ± 0.03 for Ca/N, 0.193 ± 0.031 and 0.149 ± 0.008 for P/N, respectively (**Tables 3,5**). No differences were observed between coronal and apical side of the thread in terms of Ca/P. (**Tables 6,7**).

Table 3 Ca/N at deep thread (Mean \pm SD). Different letters represent statistically significant differences ($p < 0.05$) in the same horizontal row (capital letters) or in the same column (small letters)

	Coronal Side	Apical Side	300 micron	500 micron
6504 L	0.17 \pm 0.001 aA	0.09 \pm 0.02 aB	0.11 \pm 0.01aB	0.10 \pm 0.01 aB
6508 L	0.196 \pm 0.031 aA	0.26 \pm 0.008 bB	0.232 \pm 0.03 bAB	0.222 \pm 0.07 bAB
6514 L	0.18 \pm 0.07 aA	0.206 \pm 0.03 bA	0.207 \pm 0.03 bA	0.267 \pm 0.04 bB
6517 L	0.088 \pm 0.015 bA	0.072 \pm 0.03 aA	0.135 \pm 0.012 aB	0.196 \pm 0.031 bC
6518 L	0.116 \pm 0.004 bA	0.099 \pm 0.006 aA	0.178 \pm 0.05 bB	0.172 \pm 0.013 bB
6507 UL	0.14 \pm 0.04 aA	0.24 \pm 0.03 bB	0.18 \pm 0.001 bA	0.18 \pm 0.018 bA
6509 UL	0.07 \pm 0.06 bA	0.02 \pm 0.001 cA	0.06 \pm 0.001 cA	0.06 \pm 0.001 cA
6516 UL	0.14 \pm 0.02 aA	0.27 \pm 0.029 bB	0.126 \pm 0.025 aA	0.205 \pm 0.003 bC
6519 UL	0.11 \pm 0.03 aA	0.12 \pm 0.04 aA	0.10 \pm 0.02 aA	0.11 \pm 0.01 aA
6521 UL	0.11 \pm 0.02 aA	0.17 \pm 0.04 aA	0.15 \pm 0.10 abA	0.14 \pm 0.02 aA

Sample 6514

At OM observation, bone tissue was present from thread 2, only around the top of the thread. Cortical bone was present along all the implant threads.

ESEM investigation on one upper thread revealed **cortical bone tissue with numerous osteocyte lacunae** and osteons. EDX microanalysis revealed higher Ca/N and P/N values on the apical side of the thread with respect to the coronal side, (Ca/N values were 0.23 ± 0.02 and 0.13 ± 0.06 respectively; P/N values were 0.16 ± 0.02 and 0.14 ± 0.02 respectively). Statistically significant differences were observed only on Ca/N values ($p < 0.05$) (**Tables 2,4**). High SD values suggested bone remodelling on the coronal side. Bone implant contact was evidenced on the root of thread 2 and 3 with numerous bone niches creating a strict bone-implant interface. Ca/P ratio was similar on both coronal and apical sides. (**Tables 6,7**).

ESEM analysis on one deep thread revealed electron dense **cortical bone** tissue with a large number of osteons and osteocytes lacunae disposed close to the apical side of the implant interface and on remote bone.

EDX microanalysis revealed higher Ca/N and P/N values on the apical side of the implant thread, when compared to the coronal side, (Ca/N values were 0.206 ± 0.03 and 0.18 ± 0.07 respectively; P/N values were 0.19 ± 0.03 and 0.10 ± 0.05 respectively) the values were statistically significant only for P/N values ($p < 0.05$) (**Tables 3,5**). Ca/P ratios were similar on coronal, apical side of the thread, statistically significant differences were observed only on remote bone (at 500 micron) ($p < 0.05$). (**Tables 6,7**).

Table 4	P/N at upper thread (Mean \pm SD). Different letters represent statistically significant differences ($p < 0.05$) in the same horizontal row (capital letters) or in the same column (small letters)			
	Coronal Side	Apical Side	300 micron	500 micron
6504 L	0.11 \pm 0.025 aA	0.11 \pm 0.05 aA	0.13 \pm 0.001 aA	0.12 \pm 0.005 aA
6508 L	0.05 \pm 0.04 bA	0.22 \pm 0.017 bB	0.245 \pm 0.015 bB	0.19 \pm 0.033 bB
6514 L	0.142 \pm 0.016 aA	0.16 \pm 0.017 aA	0.21 \pm 0.012 bB	0.235 \pm 0.008 bB
6517 L	0.12 \pm 0.01 aA	0.08 \pm 0.02 aA	0.153 \pm 0.02 aB	0.1519 \pm 0.025 aB
6518 L	0.128 \pm 0.016 aA	0.146 \pm 0.04 aA	0.144 \pm 0.008 aA	0.116 \pm 0.09 aA
6507 UL	0.15 \pm 0.023 abAB	0.17 \pm 0.03 aB	0.10 \pm 0.004 aA	0.13 \pm 0.009 aA
6509 UL	0.03 \pm 0.01 bA	0.12 \pm 0.08 aB	0.04 \pm 0.03 cA	0.09 \pm 0.02 aA
6516 UL	0.104 \pm 0.01 aA	0.208 \pm 0.011 bA	0.104 \pm 0.01 aA	0.149 \pm 0.016 aA
6519 UL	0.16 \pm 0.01 bA	0.14 \pm 0.01 aA	0.10 \pm 0.01 aA	0.11 \pm 0.02 aA
6521 UL	0.09 \pm 0.01 aA	0.13 \pm 0.03 aA	0.12 \pm 0.01 aA	0.16 \pm 0.01 aB

Sample 6517

Through OM, the peri-implant bone tissue was defined as cortical bone; no trabecular bone was identified.

ESEM analysis **on the upper thread** revealed cortical bone tissue with numerous osteons and osteocytes lacunae, which may indicate bone remodelling. First bone to implant contact starts on the apical side of the thread, while no bone tissue was identified on the coronal side. Thus, the EDX microanalysis was performed on bone closer to the coronal side of the thread.

EDX revealed significantly higher Ca/N and P/N values on the coronal side when compared to the apical side of the implant thread, which revealed a low mineralized area: Ca/N values were 0.15 \pm 0.06 and 0.07 \pm 0.07, the P/N values were 0.12 \pm 0.01 and 0.08 \pm 0.02 respectively (**Tables 2,4**). High SD confirms bone remodelling along the thread, while distant bone reveal high Ca/N and P/N values, with low SD values.

ESEM **on one deep thread** revealed cortical bone tissue with few osteon distant from the implant thread. Bone lamellae are hardly identified on distant bone, suggesting minimal alveolar bone remodelling in this area..

Ca/N and P/N ratios were similar on the apical and coronal portion of the implant thread (Mean Ca/N were 0.09 \pm 0.02 and 0.07 \pm 0.03), which may indicate low mineralized areas both sides of the thread (**Tables 3,5**). On distant bone, Ca/N values were significantly higher ($p < 0.05$), while P/N were similar ($P < 0.05$).

Sample 6518

OM investigation revealed compact bone tissue only at the first bone implant contact, located over thread 1 (thickness 300 micron). Differently trabecular bone tissue was observed along all the deeper threads. ESEM analysis on the implant **thread 1** revealed compact cortical bone over on the coronal side of the implant thread, while less regular bone

was present on the apical side of the thread. Some osteons were present close to the upper thread but few bone niches. Distant bone revealed more bone niches and less osteons.

EDX on the coronal thread showed similar but slightly higher Ca/N and P/N values on the apical side of the thread, the Ca/N values were 0.18 ± 0.06 and 0.16 ± 0.02 , the P/N values were 0.128 ± 0.016 and 0.146 ± 0.04 respectively. (Tables 2,4). The high SD suggest different mineralized areas on the apical side of the thread. Ca/P was similar on both coronal and apical side, even though the high SD of the apical thread may suggest an irregular bone tissue in this area. No differences were observed between coronal and apical side of the thread in terms of Ca/P. (Tables 6,7).

ESEM analysis on **one deep thread** revealed less electron dense bone tissue close to the implant interface, with numerous osteons and few osteocytes lacunae close to the implant thread.

EDX microanalysis revealed similar but slightly higher Ca/N and P/N values on the coronal side of the implant thread when compared to the apical side, the Ca/N values were 0.12 ± 0.01 and 0.10 ± 0.01 , while the P/N values were 0.09 ± 0.01 and 0.08 ± 0.01 respectively (Tables 3,5). Ca/P ratios revealed not statistically significant differences ($p > 0.05$), however high SD of both coronal and apical sides may suggest different bone tissue maturation. No differences were observed between coronal and apical side of the thread in terms of Ca/P. (Tables 6,7).

Table 5	P/N at deep thread (Mean \pm SD). Different letters represent statistically significant differences ($p < 0.05$) in the same horizontal row (capital letters) or in the same column (small letters)			
	Coronal Side	Apical Side	300 micron	500 micron
6504 L	0.03 ± 0.001 aA	0.08 ± 0.02 aB	0.081 ± 0.016 aB	0.09 ± 0.01 aB
6508 L	0.193 ± 0.031 bA	0.149 ± 0.008 bB	0.17 ± 0.01 bA	0.12 ± 0.05 aB
6514 L	0.104 ± 0.05 cA	0.185 ± 0.03 cB	0.161 ± 0.03 bB	0.20 ± 0.02 bB
6517 L	0.069 ± 0.012 aA	0.058 ± 0.02 aA	0.099 ± 0.01 aA	0.14 ± 0.024 abB
6518 L	0.09 ± 0.005 bA	0.084 ± 0.008 aA	0.132 ± 0.01 aA	0.126 ± 0.02 aA
6507 UL	0.119 ± 0.048 cA	0.198 ± 0.027 bB	0.14 ± 0.009 bA	0.14 ± 0.01 abA
6509 UL	0.06 ± 0.01 aA	0.01 ± 0.001 dB	0.04 ± 0.001 aA	0.05 ± 0.001 cA
6516 UL	0.169 ± 0.019 bA	0.126 ± 0.014 bB	0.11 ± 0.020 bB	0.12 ± 0.01 aB
6519 UL	0.08 ± 0.03 cA	0.10 ± 0.03 abA	0.07 ± 0.02 aA	0.08 ± 0.01 acA
6521 UL	0.08 ± 0.02 cA	0.13 ± 0.03 bA	0.11 ± 0.07 bA	0.13 ± 0.02 abA

Unloaded samples (retrieved 4 months from placement)

Sample 6507

OM investigation revealed trabecular bone tissue along all the implant threads. ESEM analysis **on the upper thread** revealed few bone, mostly located on the coronal side of the thread with some osteon, few osteocyte lacunae and well-evident bone lamellae, indicating limited bone remodelling in this area. Thin low electron dense bone tissue was identified close to the apical side of the thread, with no recognizable osteocyte lacunae.

EDX revealed similar but slightly higher Ca/N and P/N ratios (**Tables 2,4**) on the apical side of the thread, the Ca/N values were 0.21 ± 0.01 and 0.19 ± 0.02 , while P/N values were 0.17 ± 0.03 and 0.15 ± 0.02 respectively. These values were similar on distant bone. Low standard deviation calculated suggested limited bone remodelling at the implant thread. Ca/P ratios were similar on all the investigated areas, with no statistical differences ($p > 0.05$). (**Tables 6,7**).

ESEM on **one deep thread** revealed electron-dense dense bone tissue, with some osteocytes lacunae and evident bone lamellae concentrically arranged to the implant thread, equally distributed on both coronal and apical side, which may indicate limited bone remodelling events in this area. EDX revealed significantly high Ca/N and P/N values on the apical side of the thread, Ca/N values were 0.24 ± 0.03 and 0.14 ± 0.05 , while P/N were 0.20 ± 0.03 and 0.12 ± 0.05 respectively (**Tables 3,5**). The high standard deviation may suggest bone remodelling at the moment of implant retrieval. Ca/P was similar on both apical and coronal sides of the thread, which were statistically lower than that of remote bone ($p < 0.05$). (**Tables 6,7**).

Table 6 Ca/P at upper thread (Mean \pm SD). Different letters represent statistically significant differences ($p < 0.05$) in the same horizontal row (capital letters) or in the same column (small letters)

	Coronal Side	Apical Side	300 micron	500 micron
6504 L	1.25 ± 0.01 aA	1.25 ± 0.03 aA	1.31 ± 0.02 aB	1.29 ± 0.02 aB
6508 L	1.37 ± 0.04 bAB	1.34 ± 0.02 bA	1.39 ± 0.01 bB	1.40 ± 0.01 bB
6514 L	1.27 ± 0.01 aA	1.29 ± 0.01 aA	1.34 ± 0.002 cB	1.31 ± 0.01 aB
6517 L	1.27 ± 0.05 aA	1.26 ± 0.01 aA	1.33 ± 0.01 aB	1.36 ± 0.05 abB
6518 L	1.26 ± 0.02 aA	1.22 ± 0.07 acA	1.33 ± 0.02 aB	1.29 ± 0.07 aAB
6507 UL	1.25 ± 0.04 aA	1.27 ± 0.05 aA	1.28 ± 0.03 aA	1.29 ± 0.02 aA
6509 UL	1.40 ± 0.13 bA	1.10 ± 0.21 dB	1.39 ± 0.20 bA	1.54 ± 0.14 cA
6516 UL	1.34 ± 0.01 abA	1.30 ± 0.03 bA	1.34 ± 0.01 aB	1.38 ± 0.01 bC
6519 UL	1.24 ± 0.03 cA	1.19 ± 0.03 dA	1.31 ± 0.04 aB	1.32 ± 0.02 aB
6521 UL	1.32 ± 0.04 bA	1.33 ± 0.05 bAB	1.37 ± 0.01 bB	1.36 ± 0.02 abB

Sample 6509

At OM analysis, cortical bone tissue was evidenced around the first 2 implant threads, while trabecular bone morphology was observed on the last threads.

ESEM microanalysis was focused on the first thread, revealing a heterogeneous cortical bone tissue. The coronal side of the thread was in contact with low-electron dense bone, while the apical side revealed a more electron dense tissue. This tissue showed some osteocytes lacunae and bone lamellae concentrically arranged partially in contact with the apical side of the thread. Remote bone follows a similar thread, with irregular bone structures, suggesting few active bone remodelling at the moment of the sample retrieval.

EDX revealed statistically higher ($p < 0.05$) Ca/N and P/N values at the apical side of the thread, when compared to the coronal side of the thread (coronal Ca/N and P/N mean values were 0.04 ± 0.01 , 0.03 ± 0.01 and apical Ca/N and P/N values 0.12 ± 0.08 , 0.12 ± 0.08 , respectively) (**Tables 2,4**). Higher values were reported on distant bone, increasing with the distance from the bone interface. Statistically higher Ca/P values were found on the coronal side when compared to the apical side of the thread, suggesting different bone tissue maturation (**Tables 6,7**).

OM analysis on one deep thread revealed few islands of bone tissues (trabecular bone) with no signs of bone remodelling.

ESEM microanalysis on one deep thread showed few low dense bone equally distributed on both coronal and apical side of the thread. No relevant bone remodelling processes were observed, as confirmed with the absence of osteons or osteocytes lacunae in this area.

EDX revealed extremely low Ca/N and P/N values at the bone interface. Coronal side of the thread showed significantly higher values when compared to the apical side (coronal Ca/N and P/N mean values were 0.07 ± 0.06 , 0.06 ± 0.01 and apical Ca/N and P/N values 0.02 ± 0.001 , 0.01 ± 0.001 , respectively) (**Tables 3,5**). In this case, high SD at the coronal side may suggest irregular mineralization in this area. (**Tables 6,7**).

Table 7 Ca/P at deep thread (Mean \pm SD) Different letters represent statistically significant differences ($p < 0.05$) in the same horizontal row (capital letters) or in the same column (small letters)

	Coronal Side	Apical Side	300 micron	500 micron
6504 L	1.27 \pm 0.04 aA	1.17 \pm 0.01 aB	1.3 \pm 0.02 aA	1.27 \pm 0.03 aA
6508 L	1.37 \pm 0.016 bA	1.35 \pm 0.043 bA	1.39 \pm 0.036 bA	1.37 \pm 0.026 bA
6514 L	1.24 \pm 0.03 aA	1.24 \pm 0.001 cA	1.28 \pm 0.04 aA	1.32 \pm 0.01 abB
6517 L	1.24 \pm 0.017 aA	1.26 \pm 0.02 cA	1.34 \pm 0.061 abB	1.39 \pm 0.032 bB
6518 L	1.23 \pm 0.06 aA	1.18 \pm 0.06 acA	1.35 \pm 0.02 bB	1.35 \pm 0.07 abB
6507 UL	1.24 \pm 0.01 aA	1.24 \pm 0.02 Ca	1.31 \pm 0.002 aB	1.29 \pm 0.001 aB
6509 UL	1.35 \pm 0.08 bA	1.33 \pm 0.02 bA	1.35 \pm 0.02 bB	1.36 \pm 0.09 ab
6516 UL	1.29 \pm 0.02 aA	1.26 \pm 0.03 cA	1.34 \pm 0.02 bB	1.37 \pm 0.028 bB
6519 UL	1.38 \pm 0.19 bA	1.20 \pm 0.03 acB	1.33 \pm 0.03 abA	1.25 \pm 0.03 aB
6521 UL	1.30 \pm 0.05 aA	1.31 \pm 0.03 bA	1.34 \pm 0.07 abA	1.41 \pm 0.05 bB

Sample 6516

At OM bone tissue contact initiated from thread 3. **Cortical bone** tissue was present along all the implant surface. ESEM investigation on the upper thread revealed electron dense cortical bone with numerous osteons and bone niches close to the first bone implant contact, suggesting peri-implant bone remodeling. On distant sites (300 and 500 micron), numerous bone niches, but no osteons were identified. EDX microanalysis of the coronal side of the implant was performed on bone closer to the implant coronal side thread.

EDX revealed low Ca/N ratios on the apical side when compared to the coronal side of the thread and on remote bone, the mean values were 0.14 ± 0.02 and 0.27 ± 0.01 respectively. Interestingly, P/N ratios were lower on the coronal side, the values were 0.10 ± 0.01 and 0.21 ± 0.01 respectively. (**Tables 2,4**). No differences were observed between coronal and apical side of the thread in terms of Ca/P. (**Tables 6,7**).

ESEM on one deep thread revealed low electron dense bone tissue in contact with the implant thread, , with less osteons and with bone lamellae concentrically arranged to the apical and coronal threads. Few bone niches were present close to the implant thread, suggested limited bone remodelling in this area. Some metal fragments were identified on distant bone. EDX microanalysis revealed significantly high Ca/N values on the coronal side of the implant thread, the values were 0.22 ± 0.02 and 0.16 ± 0.02 respectively. (**Tables 3,5**) P/N ratios were higher on the coronal thread, the values were 0.17 ± 0.02 and 0.13 ± 0.01 respectively. Distant bone (sites at 300 and 500 microns) revealed similar values to that found on the apical side of the thread. No differences were observed between coronal and apical side of the thread in terms of Ca/P. (**Tables 6,7**).

Sample 6519

OM investigation revealed trabecular bone tissue along all the implant section, which appear more thick on coronal threads.

ESEM analysis performed **on one upper thread** revealed electron dense trabecular bone, which was evident at distant sites from the thread, with numerous bone niches and bone lamellae. Differently, limited bone tissue was evidenced on both coronal and apical sides with few osteocytes lacunae, suggesting limited bone remodelling.

EDX revealed higher Ca/N and P/N values on the coronal side of the thread when compared to the apical side, the Ca/N values were 0.20 ± 0.01 and 0.17 ± 0.01 , while P/N values were 0.16 ± 0.01 and 0.14 ± 0.01 . (**Tables 2,4**). No differences were observed between coronal and apical side of the thread in terms of Ca/P. (**Tables 6,7**).

ESEM **on one deep thread** revealed few bone tissues on both coronal and apical side of the thread. Bone lamellae were well identified on some islands of bone tissue located on distant bone and on the crest of the thread. However, few osteocytes lacunae were identified, suggesting limited bone remodelling in this area.

EDX microanalysis revealed similar Ca/N and P/N ratios comparing the coronal and apical side of the thread, the Ca/N values were 0.11 ± 0.03 and 0.12 ± 0.03 , while P/N values were 0.08 ± 0.03 and 0.09 ± 0.02 . (**Tables 3,5**).

Sample 6521

OM analysis was focused on one upper thread, which showed cortical bone tissue distributed along all the investigated thread.

ESEM microanalysis revealed that bone tissue was not uniform, with a higher electron dense bone present on the coronal side of the thread. Osteocyte lacunae and some osteons were identified close to the peri-implant bone interface, which may suggest bone remodelling.

EDX analysis revealed that Ca/N and P/N were higher at the apical side of the thread, when compared to the coronal side (but not statistically significant, $p>0.05$), the Ca/N and P/N coronal ratios values were 0.13 ± 0.01 and 0.09 ± 0.01 , the Ca/N and P/N apical ratios were 0.17 ± 0.04 and 0.13 ± 0.03 respectively. (**Tables 2,4**). No differences were observed between coronal and apical side of the thread in terms of Ca/P. (**Tables 6,7**).

One deep thread was also performed. OM analysis revealed trabecular bone tissue which was present on both coronal and apical sides of the thread.

ESEM investigation revealed a more electron dense bone on the coronal side of the thread, with some osteocytes lacunae and some osteon close to the peri-implant interface, suggesting active bone remodelling.

This bone remodelling also occurred on remote bone with some osteons well visible and more electron dense bone structure.

EDX micro analysis revealed higher Ca/N and P/N values on the apical side, compared to the coronal side of the thread, the differences were statistically significant ($p<0.05$). (**Tables 3,5**)

Remote bone demonstrated similar Ca/N and P/N values to the apical side of the thread, however their high SD values suggest active bone remodelling. No differences were observed between coronal and apical side of the thread in terms of Ca/P. (**Tables 6,7**).

Bone architecture of retrieved samples

Analysis of bone architecture and remodelling activity/occurrence around the analysed threads is reported in **Table 1**. Loaded samples revealed the higher presence of cortical bone tissue, mostly evidenced on the upper threads: 7 out of 10 sites revealed a cortical bone morphology. Interestingly alveolar bone remodelling was observed on 7 sites, 4 of which on the upper thread and 3 on the lower threads.

Unloaded samples revealed trabecular bone morphology in 6 out of 10 investigated threads. Interestingly, alveolar bone remodelling was observed in 2 upper threads and just one apical thread.

Other threads showed few osteons close to the implant site and few osteocytes, suggesting limited bone remodelling on samples' deep threads.

Graphs of Ca/N P/N and Ca/P ratios, used to assess the degree of mineralization at the peri-implant thread are reported in **Figure 3**.

Loaded samples revealed higher Ca/N and P/N ratios on the upper thread when compared to the lower thread in 4 out of 5 cases. In these 4 cases, also signs of bone remodelling were observed (**Table 1**). Statistically significant differences were observed in 3 out of 5 cases (samples 6504, 6517 and 6518) ($p < 0.05$). Ca/P ratio at the thread interface of **loaded samples** were higher at the upper thread when compared in the deep thread in all the loaded samples, 4 of these showed statistically significant differences ($p < 0.05$).

Unloaded samples revealed higher Ca/N and P/N ratios on the upper thread in all the 5 cases, 1 of these was statistically significant (sample 6519) however, the other were not statistically significant ($p > 0.05$). interestingly 3 investigated upper threads showed were nearly equal values to the deep threads (samples 6507, 6516 and 6521). Differently from loaded samples, Ca/P ratios at the thread interface follows a not linear trend, with no differences between the upper and deep thread. All these trends were also observed on **remote bone**, which may indicate that remote bone tissues (300-500 microns) from the implant site is equally affected by initial loading forces.

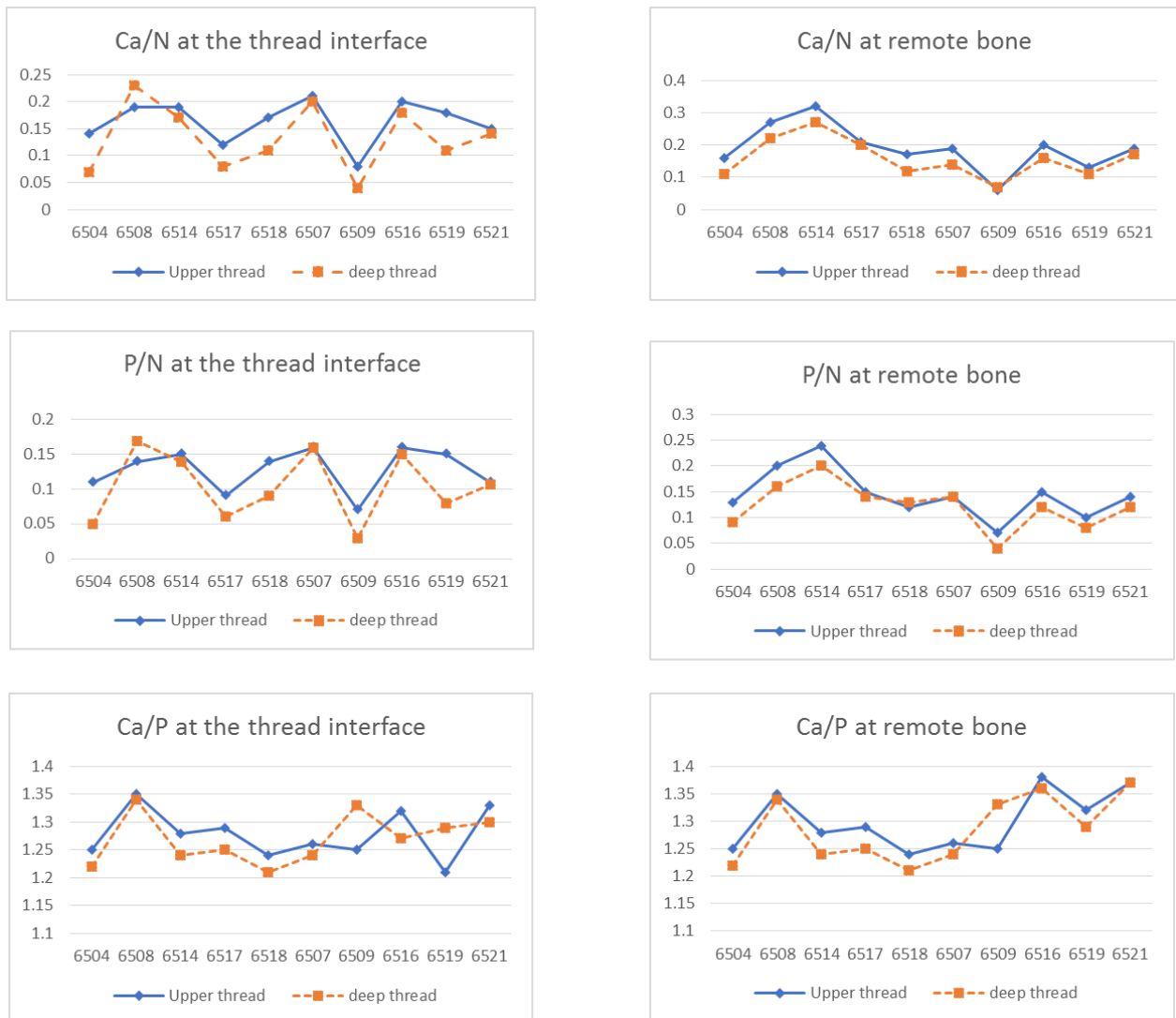


Figure 3- Ca/N, P/N and Ca/P atomic ratios calculated at the thread interface (apical and coronal sites values combined) and on remote bone (300 and 500 microns sites values combined)

DISCUSSION

The analysis of human retrieved dental implants is a very useful tool in the evaluation of the peri-implant bone interface (Coelho *et al.* 2009, Shah *et al.* 2014, Mangano *et al.* 2015). Variations observed at this interface were observed and described in several animal studies (Palmquist 2009, 2010). However, human retrieved implants analyses should be used when possible to validate the obtained results (Sakakura *et al.* 2005, Mangano *et al.* 2015).

In the present study, a microchemical analysis of the peri-implant bone interface of loaded and non-loaded retrieved dental implants was performed. All implants were submitted to the same placement protocol, and retrieval time was standardized at 4 months (unloaded group) or 6 months (loaded group) from placement.

In several loaded samples increased number of osteocytes lacunae and osteons were detected close to the implant interface, as well as the detection of different electron dense bone areas, which revealed signs of physiological bone remodelling (Mangano *et al.* 2015, Zhou *et al.* 2017, Shah *et al.* 2019).

Osteocytes, residing in the bone lacunae, were defined as the master orchestrators of skeletal activity (Schaffer *et al.* 2014) for their role in new bone formation through the SOST/Sclerostin mechanism (Robling *et al.* 2008) and remodelling through the signalling mechanism involving RANK, RANK Ligand and osteoprotegerin (Nakashima *et al.* 2011).

Our results demonstrate that 2 months of loading induces significant changes on peri-implant bone, which was evident not only on the upper threads, but also on the deepest threads. These may be attributable to the loading forces which are transmitted not only on the implant neck/emergence, but also more apically.

A finite element analysis study on 4 different implant configurations revealed that under dynamic conditions, loading forces are mainly distributed on the coronal portions of the threads, but also in some apical portion of the implant body (Chen *et al.* 2012), which is in line with the deep thread bone remodelling areas encountered in some of the loaded specimens.

In the present studies, 3 different atomic ratios were used to assess the peri implant bone microchemistry and the degree of mineralization. Ca/P ratios found were lower than values reported in literature (Ca/P range 1.32-1.67) (Shah *et al.* 2014).

It is known that biological hydroxyapatite, defined as carbonated hydroxyapatite, contains a number of impurities derived from the substitution of Ca^{++} ions with other mineral components including, HPO_4^- , CO_3^- , Mg^{++} , Na^+ , F^- and OH^- ions (Kourkoumelis *et al.* 2012). Indeed, EDX microanalyses revealed most of these elements in the evaluated samples.

Alterations of Ca/P ratios may be related to Ca ions substitution with inorganic minerals, which may affect bone strength and quality (Kourkoumelis *et al.* 2012), which may occur in physiological and pathological conditions (osteoporosis) (Fei *et al.* 2007).

Another possible explanation of lowered Ca/P values may be that EDX was performed on histological samples, thus an additional influence of the resin content may be expected in the analysis.

Considering Ca/P atomic ratios, an interesting trend was observed: whether on loaded samples almost similar and non-significant differences were observed between the upper and deep threads on both interface bone and on remote bone (**Figure 3**), unloaded samples followed a heterogeneous trend. In our study, the Ca/P ratios heterogeneous trend may be explained by the fact that without loading stimulation, mineralization of the bone implant interface and surrounding bone resulted irregular, possibly corroborating the concept that loading is a significant factor which influences peri-implant bone remodelling processes.

Ca/N and P/N values were used to analyse changes in the mineralization degree on upper and deep threads. N was used instead of C to evaluate the bone organic content because of the resin used for sample fixation, according to a previously published protocol (Gandolfi *et al.* 2018).

Again, 2-month period demonstrated to induce significant changes, with a general increase of mineralization of the upper thread compared to the deep threads.

Ca/N and P/N were also used to assess whether the coronal on the apical side of the thread revealed any significant differences in mineralization. However, even though apical side of the thread demonstrated higher Ca/N and P/N values in a higher number of the cases of the loaded group, high standard deviations and the presence of bone remodelling processes may deter to achieve definitive conclusions. We may speculate that samples with a longer follow-up, will demonstrate areas with low remodelling processes. Indeed, a previous investigation found that samples retrieved after 14-17 years of load demonstrated a more uniform thread (Gandolfi *et al.* 2018).

CONCLUSION

Conclusions may be summarized as follows:

- In absence of peri-implant inflammatory events, loading significantly affects bone architecture. Even after only 2-month loading period, significative peri-implant bone remodeling processes were identified.
- The majority of loaded samples showed cortical bone architecture with signs of bone remodeling on upper threads, in some cases bone remodeling was observed also on deep threads.
- Most of the unloaded samples revealed low signs of bone remodeling on deepest thread and irregular/low mineralized tissues.

REFERENCES

- Albrektsson T, Brånemark PI, Hansson HA, Lindström J. Osseointegrated titanium implants. Requirements for ensuring a long-lasting, direct bone-to-implant anchorage in man. *Acta Orthop Scand* 1981;52:155–170.
- Albrektsson T, Johansson C. Osteoinduction, osteoconduction and osseointegration. *Eur Spine J* 2001;10: 96–101.
- Araujo MG, Lindhe J. Peri-implant health. *Journal of Clinical Periodontology* 2018;45:S230-S236.
- Barros RR, Degidi M, Novaes AB, Piattelli A, Shibli JA, Iezzi, G. Osteocyte density in the peri-implant bone of immediately loaded and submerged dental implants. *J Periodontol* 2009;80:499-504.
- Bigi A, Cojazzi G, Panzavolta S, Ripamonti A, Roveri N, Romanello M, Noris Suarez K, Moro L. Chemical and structural Characterization of the Mineral Phase from Cortical and Trabecular Bone. *J Inorg Biochem* 1997;68:45-51.
- Bolind P, Johansson CB, Balshi TJ, Langer B, Albrektsson T. A study of 275 retrieved Brånemark oral implants. *Int J Periodontics Restorative Dent* 2005; 25:425–437.
- Chen LJ, He H, Li YM, Li T, Guo XP, RF Wang. Finite element analysis of stress at implant–bone interface of dental implants with different structures. *Transactions of Nonferrous Metals Society of China* 2011;21: 1602-1610.
- Chrcanovic BR, Albrektsson T, Wennerberg A. Dental implants inserted in fresh extraction sockets versus healed sites: A systematic review and meta-analysis. *J Dent* 2015;43:16-41.
- Davies JE, Mendes VC, Ko JC, Ajami E. Topographic scale-range synergy at the functional bone/implant interface. *Bio materials* 2014;35:25–35.
- Davies JE. Understanding peri-implant endosseous healing. *J Dent Educ.* 2003;67:932-49.
- De Bruyn H, Atashkadeh M, Cosyn J, van de Velde T. Clinical outcome and bone preservation of single TiUnite™ implants installed with flapless or flap surgery. *Clin Implant Dent Relat Res* 2011; 13:175–183.
- Eliades G, Mantzourani M, Labella R, Mutti B, Sharma D. Interactions of dentine desensitisers with human dentine: morphology and composition. *J Dent* 2013;41:S28-S39.
- Engfeldt B, Hjerpe A. Density gradient fractionation of dentine and bone powder. *Calcif Tissue Res* 1974;16:261-275.

Fei YR, Zhang M, Li M, Huang YY, He W, Ding WJ, Yang JH. Element analysis in femur of diabetic osteoporosis model by SRXRF microprobe. *Micron*. 2007;38:637–642. doi: 10.1016/j.micron.2006.09.003

Gandolfi MG, Iezzi G, Piattelli A, Prati C, Scarano A. Osteoinductive potential and bone-bonding ability of ProRoot MTA, MTA Plus and Biodentine in rabbit intramedullary model: Microchemical characterization and histological analysis. *Dent Mater* 2017;33:221-238.

Gandolfi MG, Taddei P, Pondrelli A, Zamparini F, Prati C, Spagnuolo G. Demineralization, collagen modification and remineralization degree of human dentin after EDTA and citric acid treatments. *Mater* 2019;12. doi: 10.3390/ma12010025.

Gandolfi MG, Zamparini F, Iezzi G, Degidi M, Botticelli D, Piattelli A, et al. Microchemical and micromorphologic ESEM-EDX analysis of bone mineralization at the thread interface in human dental implants retrieved for mechanical complications after 2 months to 17 years. *Int J Periodontics Restorative Dent* 2018;38:431-441.

Halldin A, Jimbo R, Johansson CB, Wennerberg A, Jacobsson M, Albrektsson T, Hansson S. Implant stability and bone remodeling after 3 and 13 days of implantation with an initial static strain. *Clin Implant Dent Relat Res*. 2014;16:383-93.

Hermann JS, Cochran DL, Nummikoski PV, Buser D. Crestal bone changes around titanium implants. A radiographic evaluation of unloaded nonsubmerged and submerged implants in the canine mandible. *J Periodontol*. 1997;68:1117–1130.

Iezzi G, Piattelli A, Mangano C, Degidi M, Testori T, Vantaggiato G, Fiera E, Frosecchi M, Floris P, Perroni R, Ravera L, Moreno GG, De Martinis E, Perrotti V. Periimplant bone response in human-retrieved, clinically stable, successful, and functioning dental implants after a long-term loading period: A report of 17 cases from 4 to 20 years. *Implant Dent* 2016;25:380-386.

Kourkoumelis N, Balatsoukas I, Tzaphlidou M. Ca/P concentration ratio at different sites of normal and osteoporotic rabbit bones evaluated by Auger and energy dispersive X-ray spectroscopy. *J Biol Phys* 2012;38:279-291.

Lang NP, Pun L, Lau KY, Li KY, Wong MC. A systematic review on survival and success rates of implants placed immediately into fresh extraction sockets after at least 1 year. *Clin Oral Implants Res* 2012;23:39-66.

Mangano C, Piattelli A, Mortellaro C, Mangano F, Perrotti V, Iezzi G. Evaluation of Peri-Implant Bone Response in Implants Retrieved for Fracture After More Than 20 Years of Loading: A Case Series. *J Oral Implantol.* 2015 ;41:414-418.

Oh TJ, Yoon J, Misch CE, Wang HL. The causes of early implant bone loss: myth or science? *J Periodontol* 2002;73:322–333.

Terheyden H, Lang NP, Bierbaum S, Stadlinger B. Osseointegration – communication of cells. *Clin. Oral Impl. Res.* 23, 2012, 1127–1135 doi: 10.1111/j.1600-0501.2011.02327.x

Palmquist A, Lindberg F, Emanuelsson L, Branemark R, Engqvist H, Thomsen P. Biomechanical, histological, and ultrastructural analyses of laser micro and nano-structured titanium alloy implants: a study in rabbit. *J Biomed Mater Res A* 2010;92:1476–1486. doi:10.1002/jbm.a.32439

Palmquist, A, Lindberg F, Emanuelsson, L, Branemark, R, Engqvist H, Thomsen P. Morphological studies on machined implants of commercially pure titanium and titanium alloy (Ti6Al4V) in the rabbit. *J Biomed Mater Res B* 2009 91B, 309 –319. (doi:10.1002/jbm.b.31404)

Prati C, Zamparini F, Scialabba VS, Gatto MR, Piattelli A, Montebugnoli L, et al. A 3-year prospective cohort study on 132 calcium phosphate-blasted implants: Flap vs flapless technique. *Int J Oral Maxillofac Implants* 2016;31:413-423.

Qian J, Wennerberg A, Albrektsson T. Reasons for Marginal Bone Loss around Oral Implants. *Clin Implant Dent Relat Res* 2012;14:792-807.

Robling AG, Niziolek PJ, Baldridge LA, Condon KW, Allen MR, Alam I, Mantila SM, Gluhak-Heinrich J, Bellido TM, Harris SE, Turner CH. Mechanical stimulation of bone in vivo reduces osteocyte expression of Sost/sclerostin. *J Biol Chem* 2008;283:5866–5875.

Sanz M, Ivanoff C, Weingart D, Wiltfang J, Gahlert M, Cordaro L, et al. Clinical and radiologic outcomes after submerged and transmucosal implant placement with two-piece implants in the anterior maxilla and mandible: 3-year results of a randomized controlled clinical trial. *Clin Implant Dent Relat Res* 2015;17:234-246.

Schaffler MB, Cheung WY, Majeska R, Kennedy O. Osteocytes: master orchestrators of bone. *Calcif Tissue Int* 2014; 94:5–24.

Shah FA, Nilson B, Brånemark R, Thomsen P, Palmquist A. The bone-implant interface nanoscale analysis of clinically retrieved dental implants. *Nanomedicine* 2014;10:1729-1737.

Shah FA, Thomsen P, Palmquist A. Osseointegration and current interpretations of the bone-implant interface. *Acta Biomater.* 2019;84:1-15.

Nakashima T, Hayashi M, Fukunaga T, Kurata K, Oh-Hora M, Feng JQ, Bonewald LF, Kodama T, Wutz A, Wagner EF, Penninger JM, Takayanagi H. Evidence for osteocyte regulation of bone homeostasis through RANKL expression, *Nat Med* 2011;17:1231-1234.

Zhao D, Wu Y, Xu C, Zhang F. Immediate dental implant placement into infected vs. non-infected sockets: a meta-analysis. *Clin Oral Implants Res* 2016;27:1290-1296.

Zhou W, Kuderer S, Liu Z, Ulm C, Rausch-Fan X, Tangl S. Peri-implant bone remodeling at the interface of three different implant types: a histomorphometric study in mini-pigs. *Clinical Oral Implants Research* 2017;28:1443–1449.

1.2 Clinical strategies to achieve (alveolar peri-implant) bone stability

Hard and soft tissue stability of peri-implant sites is a prerequisite for long term function and aesthetic outcome in implant dentistry. (Berglundh et al. 2002, Qian et al. 2012)

Different factors should be considered, the first months from implant placement and after loading procedures, including type of post-extractive socket (implant placement timing), bone quality (Hämmerle et al. 2004, Chrcanovic et al. 2014), surgery procedures (implant insertion depth, surgical and re-exposure trauma) (Sanz et al. 2015, Guarnieri et al. 2018) complications during the healing phases (implant superinfection, implant micromovements, occlusal loads). (Berglundh & Lindhe 1996, Jung et al. 2012) and cleansability of the implant restorations. (Pontoriero et al. 1994, Heitz-Mayfield & Salvi 2018)

Implant placement timing is an important factor which should be considered before surgical procedures. Placement of implants in long term healed ridges demonstrated higher bone loss when compared to healing ridges (2-3 months from extractions) according to a recent study (Prati et al. 2017), which was also supported by several histological studies (Mainetti et al. 2015, 2016, Baffone 2011, 2013)

Surgery procedures also play a critical role on alveolar bone remodeling procedures.

According to literature, nonsubmerged and flapless (Prati et al. 2016) techniques offer optimal performances in terms of marginal bone preservation (Paul et al. 2017). Moreover, these less invasive techniques are more preferred by patients, in particular when dealing with elderly populations (Sato et al. 2018).

Implant abutment connection is a critical factor for post-loading marginal bone remodeling. (Hermann et al. 2000, Brogini et al. 2006) Bacteria infiltration of the micro gap, (Barone et al. 2016) stress at the implant-abutment neck and abutment micromovements add risks for soft tissue inflammation, bone loss and early failures. In this context, **several neck morphologies** have been designed and tested recently, including a long hyperbolic neck which is claimed to support soft tissue adaptation on both provisional and definitive crown, shifting the implant-abutment connection over the tissue levels and far from bone margin. Some case series have been recently published (Canullo et al. 2017, Sola Ruiz et al. 2017, Zamparini et al. 2019).

In the present chapter, several clinical studies are reported, which are focused on the evaluation of different clinical strategies to achieve soft and hard tissues stability.

1.2.1 Factors affecting soft and hard tissues around over tissue level hyperbolic neck implants. A three-year prospective cohort study

AIM

The aim of this study was to evaluate soft and hard tissues modifications of two-piece implants with the hyperbolic neck placed “over tissue level” in a cohort of patients followed for a period of at least 3 years. Implant were placed in different post-extractive timing such as immediate, early and delayed.

MATERIALS AND METHODS

Study setting and patient selection

The study design was a single-blind human longitudinal prospective cohort study evaluating clinical and radiologic parameters after 3 years for the treatment of patients who had been lost at least one single tooth. The study was conducted in one University Endodontic Clinical Department and in two private dental offices. Patient recruitment was performed from September 2014 to February 2016.

Patients were followed-up between October 2014 and March 2019 by the same clinical team. All patients included in this investigation were treated according to the principles established by the Declaration of Helsinki as modified in 2013. (World Medical Association Declaration of Helsinki 2013) Before enrolment, written and verbal information were given by the clinical staff and each patient gave a written consent according to the above-mentioned principles. An additional signed informed consent was obtained from all patients stating that they accepted the treatment plan and agreed to cover the costs and follow the maintenance hygiene program. This report was written according to the Consolidated Standards of Reporting trials guidelines for reporting clinical trials (Vandenbroucke et al. 2007) and respecting the guidelines published by Dodson in 2007. (Dodson 2007)

The patients were considered eligible for inclusion in the clinical protocol based on the inclusion criteria reported in **Table 1**. Exclusion criteria are reported in **Table 2**.

Table 1	Inclusion criteria
	- age 18-75
	- presence of a single failing tooth or a single tooth gap with both neighbouring teeth present
	- possibility to be included in a hygiene recall program and implant control for at least 3 years
	- smoking less than 10 cigarettes by day

Table 2	Exclusion criteria
---------	--------------------

- Medical and/or general contraindications for the surgical procedures (ASA score ≥ 3)
- poor oral hygiene and lack of motivation
- active clinical periodontal disease in the natural dentition expressed by probing pocket depth >4 mm and bleeding on probing
- smoking more than 10 cigarettes by day
- uncontrolled diabetes mellitus
- systemic or local diseases that could compromise post-operative healing and osseointegration
- alcohol and/or drug abuse
- pregnancy or lactating
- malocclusion and other occlusal disorder (bruxism)
- bisphosphonate therapy

Patients allocation

The type of implant placement (immediate, early or delayed according to the Third ITI Consensus Conference) was specifically determined by an experienced university clinician following rigorous criteria aiming to get the best clinical practice (judgmental allocation). (Taxel et al. 2014)

The following groups were defined:

- Immediate post-extraction implant group (Type 1 for ITI): when the implant was placed into fresh extraction socket immediately after extraction of root affected by chronic periapical disease and/or seriously damaged hopeless teeth were assigned to this group. Only chronic periapical lesions were present and identified by periapical radiolucency.
- Early implant group (Type 2 for ITI): when the implant was placed in healed bone after 8-12 weeks after extraction of root affected by acute periapical lesion and/or abscess, pus and clinical symptoms.
- Delayed implant group (Type 4 for ITI): when the implant was placed in edentulous mature bone 10-12 months after the tooth extraction.

Pre-surgical protocol

The day before surgery, all patients were submitted to a preventive pharmacological treatment consisting of 1gr amoxicillin/clavulanic acid (Augmentin, GlaxoSmithKline, Brentford, UK) a tablet at 24 and 12 hours before the surgery and chlorhexidine digluconate 0.12% gel (Corsodyl Gel, GlaxoSmithKline, Brentford, UK) 3 applications per day. Antibiotic administration continued for 5 post-operative days.

Implant surgery

Implant surgeries were conducted by the same operator under local anaesthesia with mepivacaine chlorhydrate 30mg/ml (Carboplyina, Dentsply Italia srl, Roma, USA) in sterile conditions.

All implants were placed with one-stage surgical procedures. No surgical guides were used.

Immediate implant placement

For immediate insertion an atraumatic root extraction was performed and a careful inspection of the socket site was made. All granulation tissue was gently debrided from the apical portion of the socket. Then a 1.2 mm drill was used to prepare the intra-socket place, following the palatal bony walls as a guide. Twist and calibrated drills at 225 rpm were then used and irrigated with sterile saline solution. Primary implant stability was obtained by anchoring the implant in the remaining apical portion of the socket at least 3 mm beyond the root apex area.

When necessary, (4 cases) a porcine corticocancellous bone substitute (Osteobiol MP3, Tecknoss Dental, Coazze, Italy) was applied into the surgical site to fill the socket and to reduce any gaps between the implant and the residual bone.

Zirconium oxide-blasted acid-etched titanium (ZirTi) implant (Prima, Sweden & Martina, Due Carrare, Padova, Italy) characterized by a 2.8 mm hyperbolic long neck were inserted to keep the blasted surface at cortical bone level and the smooth machined neck surface 1-1.5 mm over the gingival level, to achieve a transmucosal insertion. 1.0 mm cover screw was then positioned and maintained for all the healing phases.

Early and delayed implant placement

The surgical procedures were similar for the Early and Delayed placements. No flaps were reflected. An initial 1.2 mm diameter drill was used to mark the position, angle and depth. The drill passed through the mucosa (transmucosal), cortical bone and cancellous bone under copious saline irrigation. A twist and calibrated drill at 225 rpm was used and a site of the adequate depth and diameter was created whilst irrigating with sterile saline solution. The entire rough surface region of implants was positioned to keep the blasted surface at cortical bone level and the smooth machined neck surface 1-1.5 mm over the gingival level, to achieve a transmucosal insertion. A cover screw of 1 mm was then positioned and maintained for all the healing phases. No sutures were performed. A surgical dressing (Coe Pack, America Inc., Alsip, IL, USA) was applied on the implant site and kept in position for 5-7 days.

Maryland bridge placement

During the healing phase period, Maryland bridge restoration was used as "interim" prosthesis in 46 cases. Briefly, the enamel palatal/lingual surfaces of adjacent teeth were etched with H3PO4 gel (3M ESPE, St Paul, MN, USA) and gently washed for 20 seconds with tap water. Scotchbond Universal bonding system (3M ESPE, St Paul, MN, USA) was applied on the enamel surface with a small brush.

Relyx Ultimate (3M ESPE, St Paul, MN, USA) was applied to fix a customized Maryland bridge to the palatal tooth surface for 2-3 months.

Post-operative procedures

Patients were instructed to follow a soft diet regime for one week, to rinse 3 times/day with 0.12% chlorhexidine mouthwash for 3 weeks and to perform oral hygiene on the Coe-Pak using a normal medium toothbrush for the first week and for 2 weeks after surgical pack removal. Thereafter, conventional brushing and flossing were permitted.

Prosthetic rehabilitation

Three months after implant insertion, impressions with polyether materials (Permadyne and Garant, 3M ESPE, St Paul, MN, USA) were taken in customized resin trays (pick-up impression technique). Provisional resin crowns were carefully designed to keep the crown margins with the finishing line at gingival level contour, which resulted partially compressed. Customized titanium abutments were screwed after 5-7 days. All resin crowns were positioned with temporary cement (Temp Bond, Kerr, Scafati, Italy) for initial prosthetic rehabilitation. In this way, the implant-abutment connection resulted internal to the crowns. Abutment were intended to increase the retention of cement-crown monoblock. Three-four weeks later definitive prosthetic metal-ceramic rehabilitations were positioned and fixed with a polycarboxylate cement (Heraeus Kulzer GmbH, Hanau, Germany). Great attention was made to prevent any cement excess around the restorations. Definitive crowns were also prepared so that all metal and ceramic finishing lines were in correspondence of implant hyperbolic neck. Fitting of metal was gently and carefully detected to create a mechanical metal-to-metal friction. Two experienced prosthodontists made all prosthetic procedures. Crown gingival level resulted in correspondence of hyperbolic neck portion.

Follow-up implant evaluation

Active periodontal therapy consisting of motivation, instruction in oral hygiene practice, scaling and root planning was performed until no/modest periodontal disease was present.

Hard and soft tissues evaluation

Marginal Bone Level (MBL): Intraoral periapical radiographs of all implants were taken using a paralleling technique with Rinn-holders and analog films (Kodak Ektaspeed Plus, Eastman Kodak Co., Rochester, NY, USA) after implant placement (baseline) and at 1 (T1), 3 (T3), 6 (T6), 12 (T12), 24 (T24) and 36 months after implant insertion (T36).

All X-rays were scanned with a slide scanner with a resolution of 968 dpi and a magnification factor of x20. The known length and diameter of implants were used to calibrate the measurement. The crestal marginal bone and the bone-implant interface were examined to evaluate the marginal bone morphology. MBL was assessed at the mesial and distal implant surfaces by measuring the distance between the reference point of the implant platform to the most coronal bone-to-implant contact level using a scale divided into 0.1 mm steps according to previous studies (Sanz *et al.* 2014, Thoma *et al.* 2014) and corrected according to the known height and width of each implant. (Galindo-Moreno *et al.* 2014) Radiographic evaluation was performed in single-blind by one additional examiner. Before evaluating the

radiographs, the examiner was calibrated by using well-defined instructions and reference radiographs with different marginal bone level measures.

Pink Esthetic Score (PES): PES was assessed following Fürhauser et al. (Fürhauser *et al.* 2005) at 6, 12 and 36 months after implant insertion. Briefly, one trained examiner blindly evaluated patients photographs. The examiner performed two assessments for each photograph at an interval of 4 weeks; at the second assessment, the photographs were scored in the reverse order. Seven variables were evaluated vs. a natural reference tooth using a 0-1-2 scoring system (0 being the lowest and 2 being the highest value): mesial papilla, distal papilla, soft-tissue level, soft-tissue contour, alveolar process deficiency, soft-tissue colour and texture. The maximum achievable PES was 14.

Peri-implant soft tissue thickness/gingival biotype: the soft tissue thickness around implants and their corresponding mesial/distal neighboring teeth was determined. The soft tissue was pierced midfacially at three millimeters apical to the gingival margin with an endodontic file (K-file Nr. 20; Dentsply-Maillefer, Switzerland). Gingival biotype was defined thick (soft tissue thickness > 2mm) or thin (soft tissue thickness ≤ 2mm). (Cosgarea *et al.* 2015, Zembic *et al.* 2009, Ferrari *et al.* 2017)

Plaque score: Plaque score (Cosyn *et al.* 2016) was assessed at four sites (mesial, distal, vestibular and palatal) around the implant restorations at T12 and T36. A dichotomous score was given (0= no visible plaque score at the soft margin; 1= visible plaque at the soft margin). **Bleeding on probing (BoP):** BoP was measured at four sites (mesial, distal, vestibular and palatal) around the implant restorations at T12 and T36. A dichotomous score was given (0= no bleeding; 1= bleeding).

Statistical analysis of the MBL

Statistical analyses were performed using Stata 13.1 (StataCorp, College Station, TX).

Linear regression models were fitted to evaluate the existence of any significant difference the operative parameters, times (one month, 3 months, 6 months, 1 year, 2 years and 3 years), and the interactions between each parameter and time. To take into account the correlation in the data due to the presence of multiple implants per subject, the abovementioned regression models were estimated following a generalized estimating equation (GEE) approach. We adjusted the estimates of coefficients' standard errors and confidence intervals by using a robust variance-covariance estimator. (Rogers 1993)

A multiple linear regression with stepwise selection was fitted to evaluate the relationship between MBL at 36 months and the following variables: gender (male/female), location (mandible/maxilla), position (anterior/posterior), endodontic adjacent teeth (yes/no), implant placement (immediate/ early/ delayed), implant diameter (3.8/4.25/5.0), implant length (10/11.5) and gingival biotype (thin/thick).

Box plots were created by using Sigma plot 12 software (Systat, Usa) to show the range and distribution of MBL (mm) as a function of implant placement timing (immediate/early/delayed) and gingival biotype (thin/thick) at 1, 3, 6, 12,24 and 36 months from implant insertion.

RESULTS

A total of 56 patients (66 implants) with a mean age of 55 ± 9 years (27 men and 29 women) were included. One patient failed to comply with the follow-up visits (total drop out was 1.79%). The survival rate was 100%. No wound infection, osteitis, bone graft sequestration occurred during the follow-up period. Two screw loosening had been reported after 20 and 24 months, respectively. No other complications occurred. **Table 3** depicts implant distribution and MBL (mean \pm SD) according to the pre-, intra- and postoperative evaluated parameters.

Table 3. MBL (Mean \pm SD) of the placed implants according to the operative parameters

		n	T ₁	T ₃	T ₆	T ₁₂	T ₂₄	T ₃₆
<i>Pre-operative parameters</i>								
Implant location	Maxilla	52	0.01 \pm 0.24 ^{Aa}	0.16 \pm 0.39 ^{Ba}	0.24 \pm 0.32 ^{Ba}	0.40 \pm 0.43 ^{Ca}	0.60 \pm 0.46 ^{Ca}	0.53 \pm 0.49 ^{Ca}
	Mandible	14	0.08 \pm 0.22 ^{Aa}	0.26 \pm 0.35 ^{Ba}	0.39 \pm 0.25 ^{Ba}	0.54 \pm 0.41 ^{Ca}	0.82 \pm 0.48 ^{Da}	0.85 \pm 0.47 ^{Da}
Implant position	Anterior	17	-0.02 \pm 0.18 ^{Aa}	0.11 \pm 0.33 ^{Ba}	0.19 \pm 0.29 ^{Ba}	0.26 \pm 0.36 ^{Ba}	0.57 \pm 0.39 ^{Ca}	0.46 \pm 0.35 ^{Ca}
	Posterior	49	0.06 \pm 0.23 ^{Aa}	0.21 \pm 0.36 ^{Ba}	0.32 \pm 0.33 ^{Ba}	0.51 \pm 0.41 ^{Cb}	0.69 \pm 0.48 ^{Ca}	0.71 \pm 0.43 ^{Ca}
Gender	Male	29	0.05 \pm 0.23 ^{Aa}	0.23 \pm 0.35 ^{Ba}	0.29 \pm 0.33 ^{Ba}	0.41 \pm 0.41 ^{Ca}	0.62 \pm 0.48 ^{Ca}	0.64 \pm 0.47 ^{Ca}
	Female	37	0.03 \pm 0.23 ^{Aa}	0.15 \pm 0.36 ^{Ba}	0.26 \pm 0.32 ^{Ba}	0.47 \pm 0.42 ^{Ba}	0.70 \pm 0.49 ^{Ca}	0.68 \pm 0.48 ^{Ca}
Endodontic adjacent teeth	No	30	0.03 \pm 0.22 ^{Aa}	0.24 \pm 0.37 ^{Ba}	0.31 \pm 0.33 ^{Ba}	0.46 \pm 0.42 ^{BCa}	0.68 \pm 0.48 ^{Ca}	0.65 \pm 0.48 ^{Ca}
	Yes	36	0.04 \pm 0.23 ^{Aa}	0.15 \pm 0.36 ^{Ba}	0.26 \pm 0.32 ^{Ba}	0.43 \pm 0.41 ^{BCa}	0.64 \pm 0.48 ^{Ca}	0.68 \pm 0.47 ^{Ca}
Implant placement	Immediate	16	0.06 \pm 0.13 ^{Aa}	0.15 \pm 0.34 ^{Ba}	0.19 \pm 0.23 ^{Ba}	0.24 \pm 0.30 ^{Ba}	0.63 \pm 0.32 ^{Ca}	0.55 \pm 0.42 ^{Ca}
	Early	20	0.01 \pm 0.23 ^{Aa}	0.13 \pm 0.41 ^{Ba}	0.16 \pm 0.33 ^{Ba}	0.27 \pm 0.40 ^{BCa}	0.40 \pm 0.45 ^{Ca}	0.43 \pm 0.44 ^{Ca}
	Delayed	30	0.05 \pm 0.25 ^{Aa}	0.26 \pm 0.33 ^{Ba}	0.42 \pm 0.26 ^{Cb}	0.63 \pm 0.38 ^{DB}	0.84 \pm 0.47 ^{EB}	0.81 \pm 0.43 ^{EB}
<i>Intra-operative parameter</i>								
Implant	3.8	23	0.11 \pm 0.23 ^{Aa}	0.29 \pm 0.36 ^{Aa}	0.38 \pm 0.32 ^{ABa}	0.57 \pm 0.41 ^{Ba}	0.78 \pm 0.49 ^{BCa}	0.87 \pm 0.49 ^{Ca}
Diameter	4.25	34	0.01 \pm 0.22 ^{Aa}	0.13 \pm 0.36 ^{Aa}	0.24 \pm 0.32 ^{Ba}	0.42 \pm 0.41 ^{BCa}	0.65 \pm 0.48 ^{Ca}	0.60 \pm 0.47 ^{Ca}
	5.0	9	-0.05 \pm 0.20 ^{Aa}	0.10 \pm 0.33 ^{Aa}	0.16 \pm 0.30 ^{Aa}	0.25 \pm 0.38 ^{ABa}	0.37 \pm 0.42 ^{Ba}	0.48 \pm 0.38 ^{Ba}
Implant	10.0	43	0.06 \pm 0.54 ^{Aa}	0.15 \pm 0.54 ^{Aa}	0.26 \pm 0.54 ^{Ba}	0.45 \pm 0.54 ^{BCa}	0.68 \pm 0.54 ^{Ca}	0.72 \pm 0.54 ^{Ca}
Length	11.5	23	0.02 \pm 0.23 ^{Aa}	0.25 \pm 0.23 ^{Ba}	0.31 \pm 0.23 ^{Ba}	0.43 \pm 0.23 ^{Ba}	0.56 \pm 0.23 ^{Ca}	0.51 \pm 0.23 ^{Ca}
<i>Post-operative parameter</i>								
Gingival thickness	Thin	40	0.08 \pm 0.21 ^{Aa}	0.26 \pm 0.29 ^{Ba}	0.38 \pm 0.25 ^{Ca}	0.60 \pm 0.37 ^{Da}	0.82 \pm 0.48 ^{Ea}	0.78 \pm 0.46 ^{Ea}
	Thick	26	-0.02 \pm 0.23 ^{Aa}	0.08 \pm 0.43 ^{Ba}	0.14 \pm 0.37 ^{Bb}	0.24 \pm 0.39 ^{Ba}	0.46 \pm 0.44 ^{Cb}	0.51 \pm 0.41 ^{Cb}
Total		66	0.04 \pm 0.22 ^A	0.19 \pm 0.35 ^B	0.24 \pm 0.32 ^B	0.44 \pm 0.36 ^C	0.66 \pm 0.46 ^D	0.69 \pm 0.49 ^D

At T6, early and immediate implants showed mean MBL of 0.13 ± 0.41 , 0.15 ± 0.41 , statistically different ($p < 0.05$) to MBL values of delayed group, which showed greater bone loss (mean MBL was 0.26 ± 0.33).

At T36, the difference is reduced, being that only early implants showed statistically different values from delayed group ($p = 0.005$). Differently, immediate implants showed no differences from both early ($p = 0.28$) and delayed groups ($p = 0.16$). Mean MBL values were 0.81 ± 0.43 for delayed group, 0.43 ± 0.44 for early group and 0.55 ± 0.42 for

immediate group. Thick biotype implants showed a stable MBL during the healing phases (T3), initial loading phases (T6) and at 12 months from insertion (T12) ($p>0.05$). This data revealed an early phase crestal bone stability which lead to reduced bone loss values at T24 and T36. Differently, Thin biotype implants showed an evident MBL variation at the first 3 months (T3), which further increased up to T24 and stabilized at T36.

BOX plot representations taking account implant placement timing and gingival biotype are reported in **Figures 1 and 2**.

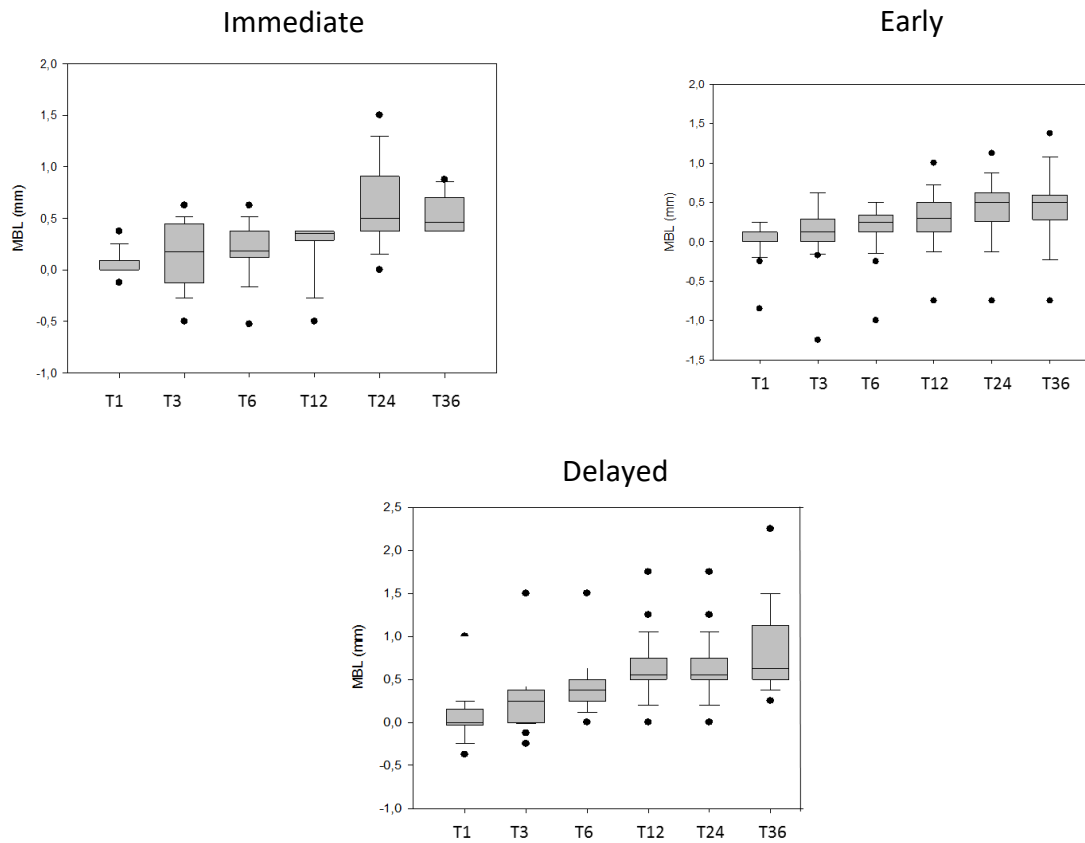


Figure 1: Box plot depicting MBL of immediate, early and delayed implants of this study.

Delayed implants showed the widest distribution of values at T24 and T36, with the higher presence of positive outlier. Interestingly, immediate implants reveal a wide distribution of values at T3, likely attributable to alveolar bone remodeling values of post-extraction sockets.

Interestingly, only immediate implants reveal a wide distribution of values at the 3 months from insertion (T3) (**Figure 1a**), likely attributable to alveolar bone remodeling values of post-extraction sockets.

Early implants show reduced MBL values at all the evaluation times (**Figure 1b**). Delayed implants showed the widest distribution of values at T36, with the higher presence of positive outlier (**Figure 1c**).

Figure 2a evidences a wider distribution and a more consistent decrease of MBL values for implants surrounded by thin biotype. Differently, implants with a thick biotype showed a more stable MBL at T1 and at T36 (**Figure 2b**). Multiple-mixed logistic regression which explores factors associated to MBL at T36 is reported in **Table 4a**. The analysis confirmed that only gingival biotype statistically affected MBL at T36 ($p=0.031$). After stepwise selection, gingival biotype remained the only variable significantly associated to MBL at T36 ($p=0.025$) (**Table 4b**). Graphs representing PES scores at T6, T12 and T36 are reported in **Figure 3**. Mean PES value at T6 was 10.76 ± 1.19 (range 8-13; median 11; IQR 10-12). These values slight increased at T12 and T36, where mean values were 11.76 ± 1.10 (range 9-13; median 12; IQR 11-12) and 11.83 ± 1.03 (range 9-14; median 12; IQR 11-13) respectively.

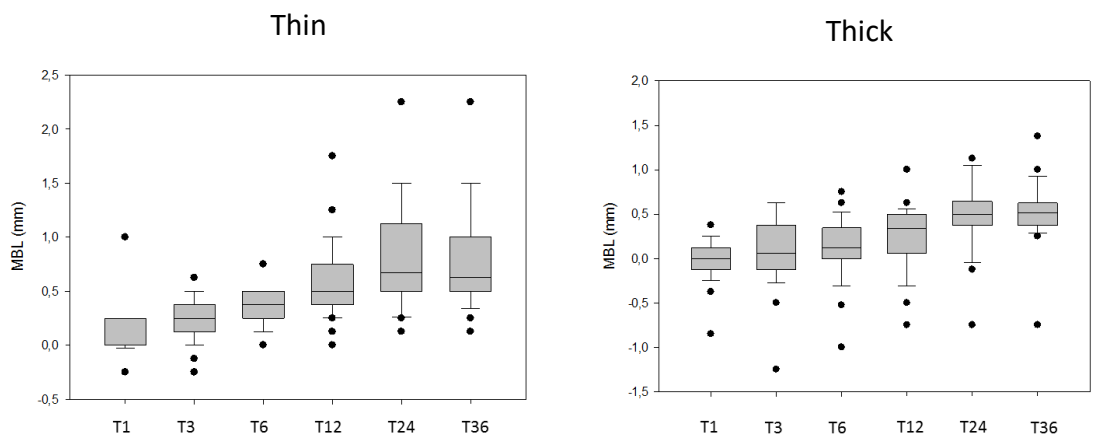
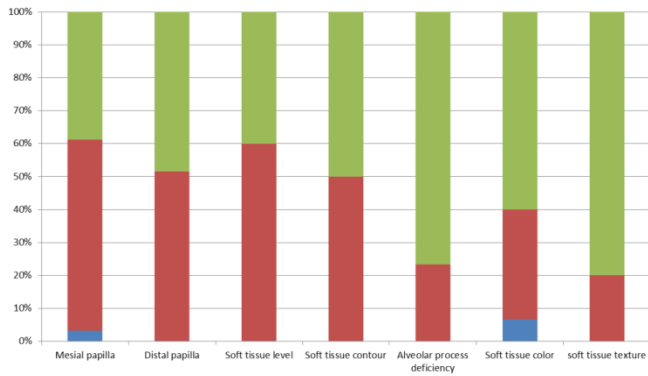


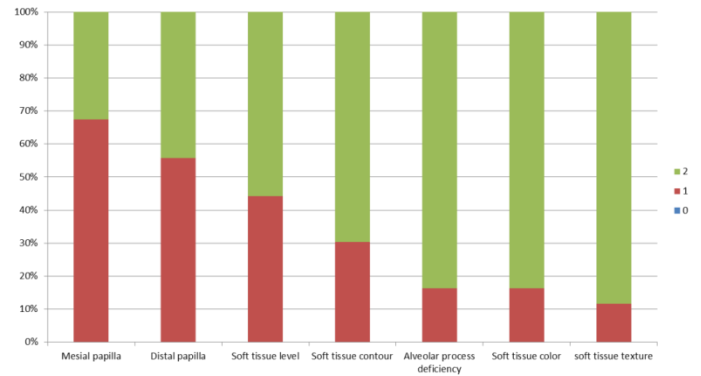
Figure 2. Box plot representing MBL of implants with thin and thick: a wider distribution and a more consistent MBL variation is present in thin group. Differently, implants with a thick biotype showed a more stable MBL, in particular at T₁ and at T₂₄ and T₃₆.

a



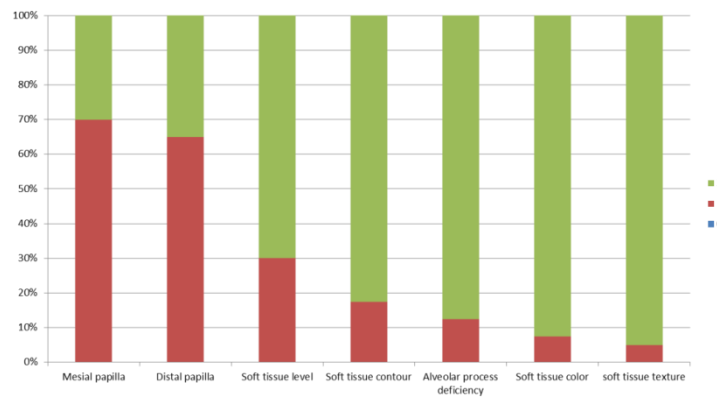
6 months

b



12 months

c



36 months

Figure 3. Graphs representing PES at 6,12 and 36 months. No 0 scores have been reported at 12 and 36 months evaluation.

PES evidenced mesial and distal papilla parameter improvement at 12 months, with slight modifications at 36 months. No 0 scores have been reported at 12 and 36 months evaluation. All the other parameters generally increased to the maximum scores: in particular, soft tissues color and textures showed the maximum score in 92-95% of the cases at 36 months, indicating a healthy tissue with no inflammation and no gingival discoloration attributable to soft tissue recession. Plaque score and BoP evaluated at T12 and T36 are reported in Table 5. A small percentage of BoP positive sites has been reported at T36, mainly at mesial site (6.2%). Plaque score was positive in a larger sample, mainly at mesial site (23.3%). Interestingly, both of these values were lower than that reported at T12 (9.6% and 36.2%, respectively).

DISCUSSION

The placement of implant designed with a long hyperbolic smooth neck positioned over tissue level may be considered an innovative strategy and a suggestive clinical approach, as the neck resulted exposed to the oral environment during the pre-loading time before prosthetic application. This study demonstrated that the strategy is free from any complications such as gingivitis and soft tissue mucositis. Moreover, no plaque accumulation was observed (evidenced by negative BoP and low Plaque score values) on the surface of exposed neck. Finally, MBL observed resulted stable both in pre-loading and post-loading period (up to 3 years) after abutment application and crown cementation in all the three implant placement groups (immediate, early and delayed implant placement) fulfilling the traditional accepted criteria. (Albrektsson *et al.* 1986)

The technique presents some advantages and obviously some limitations. The diameter of neck was lower than implant diameter and part of the hyperbolic configuration usually resulted into the thickness of gingival tissue. From a clinical point of view gingival tissue adapted itself to the smooth surface during healing phases. In the present study no complications were detected during transfer application and impression procedure, as the neck resulted well detectable and free from blood or fluids. Again, no technical critical problems were observed during the abutment application. The use of the strategy to apply implant with a “long” hyperbolic neck exposed allowed several advantages. The implant-abutment connection is far from the hard tissues and so avoided any periimplant soft tissue manipulation after the first surgery. This concept is in accordance with Romanos *et al.* (Romanos *et al.* 2015), which reported the insertion of definitive abutment immediately after implant insertion (“Onetime abutment concept”) without further disconnections as a useful strategy to avoid bone loss in submerged or crestal level implants. In the present study, all provisional crown were cemented. The crown was designed to keep the gingival margin at gingival tissue level or just 0.1-0.2 mm under the level with a modest gingival tissue compression as in natural tooth preparation. The configuration of neck-abutment resulted similar to the natural tooth abutment. After some preliminary evaluation, polycarboxylate cement was selected as adhesive sealer as resulted easy to be removed during setting time (if excess was present). (Prati *et al.* 2017) The present protocol also allowed us to manage cemented restorations without soft tissue inflammations and peri-implantitis, which are some of the most criticized aspects of cement retained crown. (Sailer *et al.* 2012) Deep subcrestal placement of the implant abutment junction may also increase the risk for cement excess. (Sancho-Puchades *et al.* 2017) This technique allowed the growth and maturation of the soft tissues on the abutment, helping papilla to remain stable and health with adequate esthetic results up to 12 months that were stable at the 3- year follow-up. Hahn in 2005 reported the use of a one piece transmucosal implant characterized by a smooth neck in a cohort of patients. (Hahn 2005) Further studies evaluated this implant in different clinical conditions, finding contradictory results. Östman *et al.* found increased bone loss, soft tissue recessions and implant failures when these implants were placed using an immediate loading protocol and in situ abutment customization. (Östman *et al.* 2007) Froum & Khouly found no implant failure and stable bone crest level after 8.5 years either using flapless or a flap technique. (Froum & Khouly 2017) In this study, selected operative parameters which are related as significant factors affecting MBL were analysed.

(Chrcanovic *et al.* 2014, Prati *et al.* 2016, Prati *et al.* 2017) This was performed as reduced information is present in literature regarding Prama implant. Likewise, soft tissues modifications and esthetic outcome were also investigated as no information are present up to 3 years. In this study, gingival biotype was found to be the most significant factor associated to MBL. Implant surrounded by thick biotype showed a more stable MBL when compared to that placed in a thin biotype. Gingival thickness has been reported as one of the most important factors affecting MBL during the initial bone remodeling processes historical animal models⁷ and in several clinical studies. (Puisys & Linkevicius 2015) This fact has been attributed to the formation of a biological barrier between the implant and the oral environment. Recently, significantly less bone loss has been observed on triangularshaped implants placed at crestal level with flapped approach. (Linkevicius *et al.* 2018) This means that, when possible, the use of hyperbolic neck implant requires a thick biotype. Thick biotype may create a solid/strong connective tissue around this neck.

MBL variation of implant placed immediately and during the first months from extraction is related to the events of the alveolar socket bone remodeling. It was found that bone remodeling naturally occurs during the first weeks from tooth extraction. (Araújo & Lindhe 2005) In our study immediate and early implants followed a similar pattern up to 12 months. Delayed implants showed a consistent MBL variation in the first 3 months, statistically significant from both early and immediate implant groups. Mature long-time edentulous bone offers a modest new bone formation, as well explained in different histological studies. (Mainetti *et al.* 2015, Mainetti *et al.* 2016) Bone density may probably be different in healing alveolar sockets, when compared to long time edentulous bone. A mature cortical bone may be severely damaged by surgery procedures and requires more osteoclast to remove the high amount of bone debris. PES was used in this study to monitor soft tissues variation during the follow-up. (Fürhauser *et al.* 2005) Most of the studies used PES in the anterior maxilla. (Hämmerle *et al.* 2004, Cosyn *et al.* 2016, Raes *et al.* 2013, Cosyn *et al.* 2012) One study used PES in the posterior mandible and maxilla to evaluate any differences between two different abutment restorations. (Weinlander *et al.* 2010)

In the present study, PES scores revealed soft tissues improvement from 6 to 12 months, with an overall tissue stability at 36 months. The hyperbolic neck helped to support a rapid healing and soft tissue adaptation. Peri-implant mucosa resulted sound and stable in all implants. In particular, a high % of implants showed the highest score value for the alveolar process deficiency, soft tissue colour and soft tissue texture at the end of the follow-up. This good outcome could be related to both the implant neck characteristics and the minimally invasive surgical protocol. One of the main limitations to remark is that the implant angulation cannot be modified after implant insertion, for the absolute necessity to place implant in the right position perpendicularly to the margin and parallel to the other roots. Indeed, transmucosal emergence profile of the neck cannot be modified after placement. Maryland bridge provisional restorations were positioned in a high number of cases and maintained until impression procedures was performed. The use of Maryland was suggested to prevent any aesthetic disadvantage of implant neck exposure.

CONCLUSION

The present two-piece implants placed with the hyperbolic neck over tissue level demonstrated hard and soft tissues stability up to 3 years with low complications. In addition:

-The over tissue level neck supports peri-implant soft tissues and allows a fast healing in immediate and early placement groups.

-This protocol offered a simplified approach for cement-retained single implant rehabilitations without complex or invasive surgical procedures.

This 3-year study demonstrated that biotype and delayed implant placement parameters were the factors mostly related to marginal bone loss.

REFERENCES

Albrektsson T, Zarb G, Worthington P, Eriksson AR. The long-term efficacy of currently used dental implants: a review and proposed criteria of success. *Int J Oral Maxillofac Implants.* 1986;1:11-25.

Araújo MG, Lindhe J. Dimensional ridge alterations following tooth extraction. An experimental study in the dog. *J Clin Periodontol* 2005;32:212-218.

Baffone GM, Botticelli D, Pantani F, et al. Influence of various implant platform configurations on peri-implant tissue dimensions: An experimental study in dog. *Clin Oral Implants Res.* 2011;22:438–444.

Baffone GM, Botticelli D, Pereira FP, et al. Influence of buccal bony crest width on marginal dimensions of periimplant hard and soft tissues after implant installation an experimental study in dogs. *Clin Oral Implants Res.* 2013;24:250–254.

Barone A, Alfonsi F, Derchi G, Tonelli P, Toti P, Marchionni S, Covani U. The Effect of Insertion Torque on the Clinical Outcome of Single Implants: A Randomized Clinical Trial. *Clin Implant Dent Relat Res* 2016;18:588-600.

Berglundh T, Lindhe J. Dimension of the Periimplant mucosa. Biological width revisited. *J Clin Periodontol* 1996; 23:971-973.

Berglundh T, Persson L, & Klinge B. A systematic review of the incidence of biological and technical complications in implant dentistry reported in prospective longitudinal studies of at least 5 years. *J Clin Periodontol* 2002, 29, 197-212.

Broggini N, McManus LM, Hermann JS, Medina R, Schenk RK, Buser D, et al. Peri-implant inflammation defined by the implant-abutment interface. *J Dent Res* 2006;85:473-478.

Buser D, Mericske-Stern R, Dula K, Lang NP. Clinical experience with one-stage, non-submerged dental implants. *Adv Dent Res* 1999;13:153-161.

Canullo L, Tallarico M, Pradies G, Marinotti F, Loi I, Cocchetto R. Soft and hard tissue response to an implant with a convergent collar in the esthetic area: preliminary report at 18 months. *Int J Esthet Dent* 2017;12:306-323.

Chan D, Pelekos G, Ho D, Cortellini P, Tonetti MS. The depth of the implant mucosal tunnel modifies the development and resolution of experimental peri-implant mucositis: A case-control study. *J Clin Periodontol* 2019.

Chrcanovic BR, Albrektsson T, Wennerberg A. Flapless versus conventional flapped dental implant surgery: a meta-Analysis. *PLOS ONE* 2014;9:1-14.

Cosgarea R, Gasparik C, Ducea D, Culic B, Dannewitz B, Sculean A. Peri-implant soft tissue colour around titanium and zirconia abutments: a prospective randomized controlled clinical study. *Clin Oral Implants Res* 2015;26:537-544.

Cosyn J, Eghbali A, De Bruyn H, Dierens M, De Rouck T. Single Implant Treatment in Healing Versus Healed Sites of the Anterior Maxilla: An Esthetic Evaluation. *Clin Implant Dent Relat Res* 2012;14:517-526.

Cosyn J, Eghbali A, Hermans A, Vervaeke S, De Bruyn H, Cleymaet R. A 5-year prospective study on single immediate implants in the aesthetic zone. *J Clin Periodontol* 2016;43: 702-709.

Crespi R, Cappare P, Polizzi E, Gherlone E. Fresh-Socket Implants of Different Collar Length: Clinical Evaluation in the Aesthetic Zone. *Clin Implant Dent Relat Res* 2015;17:871-878.

Dodson TB. A guide for preparing a patient-oriented research manuscript. *Oral Surg Oral Med Oral Pathol Radiol Endod* 2007;104:307-315.

Ferrari M, Carrabba M, Vichi A, Goracci C, Cagidiaco MC. Influence of abutment color and mucosal thickness on soft tissue color. *Int J Oral Maxillofac Implants* 2017;32:393-399.

Flores-Guillen J, Álvarez-Novoa C, Barbieri G, Martín C, Sanz M. Five-year outcomes of a randomized clinical trial comparing bone-level implants with either submerged or transmucosal healing. *J Clin Periodontol* 2018;45:125-135.

French D, Cochran DL, Ofec R. Retrospective Cohort Study of 4,591 Straumann Implants Placed in 2,060 Patients in Private Practice with up to 10-Year Follow-up: The Relationship Between Crestal Bone Level and Soft Tissue Condition. *Int J Oral Maxillofac Implants* 2016;31:168-178.

Froum S, Khouly I. Survival Rates and Bone and Soft Tissue Level Changes Around One-Piece Dental Implants Placed with a Flapless or Flap Protocol: 8.5-Year Results. *The Int J Period Rest* 2017;37:327–337.

Fürhauser R, Florescu D, Benesch T, Haas R, Mailath G, Watzek G. Evaluation of soft tissue around single-tooth implant crowns: the pink esthetic score. *Clin Oral Implants Res* 2005;16:639-644.1.

Galindo-Moreno P, León-Cano A, Ortega-Oller I, Monje A, Suárez F, ÓValle F, Spinato S, Catena A. Prosthetic abutment height is a key factor in peri-implant marginal bone loss. *J Dent Res* 2014;93:80s-85s.

Guarnieri R, Ceccarelli R, Ricci JL, Testori T. Implants With and Without Laser-Microtextured Collar: A 10-Year Clinical and Radiographic Comparative Evaluation. *Implant Dent* 2018;27:81-88.

Hahn, J. One-piece root-form implants: a return to simplicity. *Journal of Oral Implantology* 2005;31: 77–84.

Hämmerle CH, Chen ST, Wilson TG Jr. Consensus statements and recommended clinical procedures regarding the placement of implants in extraction sockets. *Int J Oral Maxillofac Implant* 2004 19:26-28.

Heitz-Mayfield LJA, Salvi GE. Peri-implant mucositis. *J Clin Periodontol* 2018;45:S237-S245.

Hermann JS, Buser D, Schenk RK, Cochran DL. Crestal bone changes around titanium implants. A histometric evaluation of unloaded non-submerged and submerged implants in the canine mandible. *J Periodontol* 2000;71:1412-24.

Jung RE, Zembic A, Pjetursson BE, Zwahlen M, Thoma DS. Systematic review of the survival rate and the incidence of biological, technical, and aesthetic complications of single crowns on implants reported in longitudinal studies with a mean follow-up of 5 years. *Clin Oral Implants Res* 2012;23:2-21.

Linkevicius T, Linkevicius R, Alkimavicius J, Linkeviciene L, Andrijauskas P, Puisys A. Influence of titanium base, lithium disilicate restoration and vertical soft tissue thickness on bone stability around triangular-shaped implants: A prospective clinical trial. *Clin Oral Implants Res* 2018;29:716-724.

Loi I, Di Felice A. Biologically oriented preparation technique (BOPT): a new approach for prosthetic restoration of periodontically healthy teeth. *Eur J Esthet Dent* 2013;8:10-23.

Mainetti T, Lang NP, Bengazi F et al. Immediate loading of implants installed in a healed alveolar bony ridge or immediately after tooth extraction: an experimental study in dogs. *Clin Oral Implants Res* 2015;26:435-441.

Mainetti T, Lang NP, Bengazi F et al. Sequential healing at implants installed immediately into extraction sockets. An experimental study in dogs. *Clin Oral Implants Res* 2016; 27:130-138.

Östman PO, Hellman M, Albrektsson T and Sennerby L. Direct loading of Nobel Direct® and Nobel Perfect® onepiece implants: a 1-year prospective clinical and radiographic study. *Clin Oral Implants Res* 2007,18:409-418.

Paul S, Petsch M, Held U. Modeling of Crestal Bone After Submerged vs Transmucosal Implant Placement: A Systematic Review with Meta-Analysis. *Int J Oral Maxillofac Implants* 2017;32:1039-1050.

Pontoriero R, Tonelli MP, Carnevale G, Mombelli A, Nyman SR, Lang NP. Experimentally induced periimplant mucositis. A clinical study in humans. *Clin Oral Implants Res* 1994;5:254-259.

Prati C, Zamparini F, Pirani C, Gatto MR, Piattelli A, Gandolfi MG. Immediate Early and Delayed Implants: A 2- Year Prospective Cohort Study of 131 Transmucosal Flapless Implants Placed in Sites With Different Pre-extractive Endodontic Infections. *Impl Dent* 2017; 26:654-663

Prati C, Zamparini F, Pirani C, Montebugnoli L, Gandolfi MG. Multifactorial statistical analysis toward evaluation of MBL, PES and PI of a novel nonsubmerged implant to restore a single tooth: A 1-year prospective cohort study. *J Oral Sci Rehab* 2017;3:32-41.

Prati C, Zamparini F, Scialabba VS Gatto MR, Piattelli A, Montebugnoli L, Gandolfi MG. A 3-year prospective cohort study on 132 calcium phosphate blasted implants: flap vs flapless technique. *Int J Oral Maxillofac Implants*. 2016;31:413-423.

Puisys A, Linkevicius T. The influence of mucosal tissue thickening on crestal bone stability around bone-level implants. A prospective controlled clinical trial. *Clin Oral Implants Res* 2015;26:123-129

Qian J, Wennerberg A, Albrektsson T. Reason for marginal bone loss around oral implants. *Clin Implant Dent Relat Res* 2012;14:792-807.

Raes F, Cosyn J, De Bruyn H. Clinical, esthetic and patient-related outcome of immediately loaded single implants in the anterior maxilla: a prospective study in extraction sockets, healed ridges and grafted sites. *Clin Implant Dent Relat Res* 2013;15:819-835.

Rogers WH. Regression standard errors in clustered samples. *Stata Technical Bulletin* 1993;13:19-23.

Romanos GE, Aydin E, Gaertner K, Nentwig G-. Long-term results after subcrestal or crestal placement of delayed loaded implants. *Clin Implant Dent Relat Res* 2015;17:133-141.

Sailer I, Mühlemann S, Zwahlen M, Hämmerle CHF, Schneider D. Cemented and screw-retained implant reconstructions: A systematic review of the survival and complication rates. *Clin Oral Implants Res* 2012;23:163-201.

Sancho-Puchades M, Cramer D, Özcan M, Sailer I, Jung RE, Hämmerle CHF, Thoma DS. The influence of the emergence profile on the amount of undetected cement excess after delivery of cement-retained implant reconstructions. *Clin Oral Implants Res* 2017;28:1515-1522.

Sanz M, Cecchinato D, Ferrus J, Salvi GE, Ramseier C, Lang NP, Lindhe J. Implants placed in fresh extraction sockets in the maxilla: clinical and radiographic outcomes from a 3-year follow-up examination. *Clin Oral Implants Res* 2014;25:321-327.

Sanz M, Ivanoff CJ, Weingart D, Wiltfang J, Gahlert M, Cordaro L et al. Clinical and Radiologic Outcomes after Submerged and Transmucosal Implant Placement with Two-Piece Implants in the Anterior Maxilla and Mandible: 3-Year Results of a Randomized Controlled Clinical Trial. *Clin Implant Dent Relat Res* 2015;17:234-246.

Sato Y, Kitagawa N, Isobe A. Implant treatment in ultra-aged society. *Jpn Dent Sci Rev* 2018;54:45-51.

Schwarz F, Messias A, Sanz-Sánchez I, Carrillo de Albornoz A, Nicolau P, Taylor T, Beuer F, Schär A, Sader R, Guerra F, Sanz M. Influence of implant neck and abutment characteristics on peri-implant tissue health and stability. Oral reconstruction foundation consensus report. *Clin Oral Implants Res*. 2019 in press.

Solá-Ruiz MF, Highsmith JR, Labaig-Rueda C, Agustín-Panadero R. Biologically oriented preparation technique (BOPT) for implant-supported fixed prostheses. *J Clin Exp Dent* 2017;9:603-607

Taxel P, Ortiz D, Shafer D, Pendrys D, Reisine S, Rengasamy K, Freilich M. The relationship between implant stability and bone health markers in post-menopausal women with bisphosphonate exposure. *Clin Oral Invest* 2014;18:49- 57.

Thoma DS, Sanz Martin I, Benic GI, Roos M, Hämmerle CH. Prospective randomized controlled study comparing two dental implant systems: demographic and radiographic results at one year of loading. *Clin Oral Implants Res* 2014;25:142-149.

Vandenbroucke JP, von Elm E, Altman DG et al. Strengthening the reporting of observational studies in epidemiology (STROBE): explanation and elaboration PLoS Med 2007;4:1628-1654.

Weinlander M, Lekovic V, Spadijer-Gostovic S, Milicic B, Wegscheider WA, Piehslinger E. Soft tissue development around abutments with a circular macro-groove in healed sites of partially edentulous posterior maxillae and mandibles: a clinical pilot study. Clin.Oral Impl Res 2010; 22:743–752

World Medical Association Declaration of Helsinki: Ethical principles for medical research involving human subjects. JAMA. 2013;310:2191-2194.

Zembic A, Sailer I, Jung RE, Hammerle CHF. Randomized-controlled clinical trial of customized zirconia and titanium implant abutments for single tooth implants in canine and posterior regions: 3-year results. Clin Oral Implants Res 2009;20:802-808.

1.2.2 A multi-level analysis of platform-switching flapless implants placed tissue-level: 4-year prospective cohort study

AIM

The aim of the present study was to assess the survival and success, as well as the factors affecting MBL around nonsubmerged implants placed with a flapless technique up to 48 months from insertion.

MATERIALS AND METHODS

Study setting and patient selection

The study design was a single-blind human longitudinal prospective cohort with a minimum follow-up of 4 years.

The study was conducted in one University Endodontic Clinical Department and in two private dental offices between January 2011 and January June 2018 by the same clinical team.

Recruitment of patients was performed from October 2009 to June 2014.

Once included in the study, patients were treated from January 2010 to July 2014.

All patients included in this investigation were treated according to the principles established by the Declaration of Helsinki as modified in 2013. (World Medical Association Declaration of Helsinki 2013)

Before enrolment, written and verbal information were given by the clinical staff and each patient gave a written consent according to the above-mentioned principles. An additional signed informed consent was obtained from all patients stating that they accepted the treatment plan and agreed to cover the costs and follow the maintenance hygiene program. This report was written according to the Consolidated Standards of Reporting trials guidelines for reporting clinical trials (STROBE) (Vandenbroucke *et al.* 2007) and respecting the guidelines published by Dodson in 2007. (Dodson 2007)

The patients were considered eligible or non-eligible for inclusion in the clinical protocol based on the following criteria:

Inclusion criteria

- 18-75 years of age at the time of implant placement
- partially dentate requiring dental implants
- possibility to be included in a hygiene recall program and implant control for at least 4 years

Exclusion criteria

- Medical and/or general contraindications for the surgical procedures (ASA score ≥ 3)
- poor oral hygiene and lack of motivation
- active clinical periodontal disease in the dentition expressed by probing pocket depth >4 mm and bleeding on probing
- smoking more than 20 cigarettes by day
- uncontrolled diabetes mellitus
- systemic or local diseases that could compromise post-operative healing and osseointegration

- alcohol and/or drug abuse
- pregnancy or lactating
- malocclusion and other occlusal disorder (bruxism)
- bisphosphonate therapy

Clinical evaluations of periapical status were made by three experienced operators included as Authors.

Treatment procedures

Choice of the surgical approach and timing of implant placement, (immediate, early, delayed according to the timing classification proposed by the Third ITI Consensus Conference) (Hämmerle *et al.* 2004) was not determined randomly as the purpose of the study was to use well-defined clinical parameters for the “best clinical practice”. (Taxel *et al.* 2014)

Therefore, the choice of the different surgical approach and the consequent clinical decision and implant placement timing (immediate, early and delayed) was made on the basis of the following clinical criteria: presence of acute endodontic periapical lesion (with pain, fistula, exudate/pus, tenderness and radiographic apical translucency or all of them) and/or the presence of chronic periapical disease (Periapical Index or PAI 3-4). (Ørstavik *et al.* 1986)

The three surgical timings were defined as follow:

- Immediate post-extraction implant (Type 1 for ITI) (Hämmerle *et al.* 2004): when the implant was placed into fresh extraction socket immediately after extraction of root affected by chronic periapical disease and/or seriously damaged hopeless (or fractured) teeth were assigned to this group. Only chronic periapical lesions were present and identified by periapical radiolucency.
- Early implant (Type 2 for ITI) (Hämmerle *et al.* 2004): when the implant was placed in healed bone after 8-12 weeks after extraction of root affected by acute periapical lesion and/or abscess, pus and clinical symptoms.
- Delayed implant (Type 4 for ITI) (Hämmerle *et al.* 2004): when the implant was placed in edentulous mature bone 10-12 months after the tooth extraction for different reasons,

Surgical procedures

Cylindrical implants (SP Premium, Sweden & Martina, Padova, Italy) with zirconium-oxide blasted (ZirTi) surface, smooth machined collar 0.5 mm, tulip-shape profile switching platform emergence profile 0.3 mm, hexagonal internal connection and 3.8 or 4.25 or 5.0 mm diameter (10.0 mm or 11.5 mm length) were used.

One single experienced surgeon performed all surgeries.

A careful occlusal and periodontal examination was performed on each patient, including presence of plaque, gingivitis, pocket depth and radiographic bone loss of all remaining teeth. Oral hygiene instruction and periodontal therapy were performed when and where indicated.

Two days prior to the intervention, all patients were asked to comply with a pharmacological regime that included amoxicillin/clavulanic acid 1 gr tablet and application of chlorhexidine digluconate 0.20% gel (Corsodyl Gel, GlaxoSmithKline UK, Brentford, UK) twice a day, according with a previous study. (Anitua *et al.* 2014)

Antibiotic administration continued during 5-6 days after surgery.

All surgical procedures were conducted under local anesthesia with mepivacaine chlorhydrate 30mg/ml (Carboplyina, Dentsply Italia srl, Roma, Italy). No computer-aided guide was used.

Implants were placed in order to obtain transmucosal nonsubmerged tissue level position healing. The smooth machined collar of the implant platform was placed in the thickness of gingival tissue while the divergent rough implant portion was lean/nested at the bony crest (using standard protocol). In all implants an adequate primary stability was obtained. The final insertion torque value ranged between 20-70 N/cm² and was recorded. Considering the thickness of the mucosa, a 1 mm or 2-3 mm high cover-healing screw, that emerged just over the gingival level, was applied.

Immediate implant placement

For immediate post-extractive insertion an atraumatic flapless root extraction was performed and a careful inspection of the socket site was made. All granulation tissue was gently debrided from the apical portion of the socket.

Then a 1.2 mm drill was used to prepare the intra-socket place, following the palatal bony walls as a guide. Twist and calibrated drills at 225 rpm were then used and irrigated with sterile saline solution.

Primary implant stability was obtained by anchoring the implant in the remaining apical portion of the socket at least 3 mm beyond the root apex area.

When necessary, (4 cases) a porcine corticocancellous bone substitute (Osteobiol MP3, Tecknoss Dental, Coazze, Italy) was applied into the surgical site to fill the socket and to reduce any gaps between the implant and the residual bone.

Considering the thickness of the mucosa, a 1 mm or 2-3 mm high cover-healing screw, that emerged just over the gingival level, was applied, following a nonsubmerged healing approach (as above mentioned).

Early and delayed implant placement

The surgical procedures were similar for the Early and Delayed placements. No flaps were reflected.

An initial 1.2 mm diameter drill was used to mark the position, angle and depth. The drill passed through the mucosa (transmucosal), cortical bone and cancellous bone under copious saline irrigation. A twist and calibrated drill at 225 rpm was used and a site of the adequate depth and diameter was created whilst irrigating with sterile saline solution.

The entire rough surface region of implants was positioned approx. 1 mm under the cortical bone level and smooth machined collars of the implant platform were placed in the thickness of gingival tissue. The cover screw was at tissue level exposed.

Considering the thickness of the mucosa, a 1 mm or 2-3 mm high cover-healing screw, that emerged just over the gingival level, was applied, following a nonsubmerged healing approach (as above mentioned). No computer-aided surgical guides were used.

Post-operative procedures

A surgical dressing (Coe-Pak, GC, Tokyo, Japan) was placed on the wound in all patients and removed at the first clinical control after one week

Patients were instructed to follow a soft diet regime for one week, to rinse 3 time/day with 0.12% chlorhexidine gel for 3 weeks and to perform oral hygiene on the Coe-Pak using a normal-medium toothbrush for the first week and for 2 weeks after surgical pack removal. Thereafter, conventional brushing and flossing were permitted.

Prosthetic rehabilitation

Prosthetic phases started after 3 months from implant insertion. No second surgeries to expose the implant neck were performed. Briefly, cover screws were removed, impression posts were placed and impressions made with polyether materials (Permadyne™ and Garand™, 3M ESPE, St Paul, MN, USA) in customized trays for pick up technique.

Customized definitive abutments were screwed on the implants after approx. 15 days and provisional resin crowns cemented with temporary zinc-oxide eugenol cement (Temp Bond, Kerr, Scafati, Italy).

Definitive prosthetic metal-ceramic rehabilitation, made by two equally experienced prosthodontists, were positioned on definitive abutments and fixed with polycarboxylate cement (Heraeus Kulzer GmbH, Hanau, Germany) 12-15 days later. (Prati *et al.* 2017)

The quantity of the extruded cement was reduced by filling the occlusal half of the crown and maintaining an occlusal space of the abutment screw channel as internal venting to minimize the hydraulic pressure through slowing cement escape. Patients were instructed to continuously bite on a cotton roll for 5 minutes. Subsequently dental floss was used to remove the cement flow.

Follow-up implant evaluation

Active periodontal therapy consisting of motivation, instruction in oral hygiene practice, scaling and root planning was performed during the entire time of observation, no bleeding on probing and pocket probing depth ≥ 3 mm were detected during the follow-up procedures. Routinary follow-up visits were performed every 6 months from implant loading. Occurrence of endodontic treatments on implant adjacent teeth was also recorded.

Gingival thickness evaluation

The soft tissue thickness around implants and their corresponding mesial neighboring teeth was determined at 4 year follow-up. The soft tissue was pierced mid-facially at three millimeters apical to the gingival margin with an endodontic file. (K-file Nr. 20; Dentsply-Maillefer, Switzerland). Gingival biotype was defined thick (soft tissue thickness > 2 mm) or thin (soft tissue thickness ≤ 2 mm). (Cosgarea *et al.* 2015, Zembic *et al.* 2009, Ferrari *et al.* 2017)

Radiographic assessment

Intraoral periapical radiographs of all implants were taken using a paralleling technique with Rinn-holders and analog films (Kodak Ektaspeed Plus, Eastman Kodak Co., Rochester, NY, USA) after implant placement (baseline) and at 1, 3, 6, 12 and 24 months after implant insertion.

All X-rays were scanned with a slide scanner with a resolution of 968 dpi and a magnification factor of x20. Length and diameter of implants were used to calibrate the measurement.

The crestal marginal bone and the bone-implant interface were examined to evaluate the marginal bone morphology. MBL was assessed at the mesial and distal implant surfaces by measuring the distance between the reference point of the implant platform to the most coronal bone-to-implant contact level using a scale divided into 0.1 mm steps according to previous studies (Sanz *et al.* 2014, Thoma *et al.* 2014) and corrected according to the known height and width of each implant. (Galindo-Moreno *et al.* 2015)

Radiographic evaluation was performed in single-blind by one additional examiner. Before evaluating the radiographs, the examiner was calibrated by using well-defined instructions and reference radiographs with different marginal bone level measures.

Evaluated Variables

MBL was measured and evaluated according to the following variables:

- 1) Preoperative parameters: Implant location (maxilla/mandible), Implant position (anterior/posterior) Gender (male/female), Endodontically treated adjacent teeth (yes/no), Smoke (yes/no), Implant placement timing (immediate/early/delayed)
- 2) Intra operative parameters: Implant diameter (3.8/4.25/5.0)
- 3) Post-operative parameters: Gingival thickness (yes/no)

Statistical analysis

Statistical analyses were performed using Stata 13.1 (StataCorp, College Station, TX).

Linear regression models were fitted to evaluate the existence of any significant difference regarding endodontically treated adjacent teeth (yes/no), times (one month, 3 months, 6 months, 12, 24, 36 and 48 months), and the interactions between endodontically treated adjacent teeth and time. To take into account the correlation in the data due to the presence of multiple implants per subject, the abovementioned regression models were estimated following a generalized estimating equation (GEE) approach. The estimates of coefficients' standard errors and confidence intervals were adjusted by using a robust variance-covariance estimator. (Rogers 1993) The same analysis was performed for all the operative variables.

A multiple linear regression with stepwise selection was fitted to evaluate the relationship between MBL at 36, 48 months and the following variables: gender (male/female), smoke (yes/no), location (mandible/maxilla), implant position (anterior/posterior), endodontic adjacent teeth (yes/no), adjacent teeth coronal restoration (direct/indirect/no restoration), implant placement timing (immediate/early/delayed), implant diameter (3.8/4.25/5.0), gingival thickness" (thin/thick).

Box plots were created by using Sigma plot 12 software (Systat, Usa) to show the range and distribution of MBL (mm) as a function of implant placement timing (immediate, early delayed) at at 1, 3, 6, 12, 24, 36 and 48 months from implant insertion.

RESULTS

Study population and demographic data

According to the inclusion/exclusion criteria, 76 patients (128 implants) were studied with a mean age of 55.6 ± 10.7 years (42 women and 34 men). Eight patients (17 implants) were identified as smokers, consuming between 10 to 20 cigarettes/day and included in the study; these patients were distributed evenly across the three groups (3 in immediate, 2 in early and 3 in delayed group).

The survival rate was 98.4% as 2 delayed implants failed during the observational time.

Two non-smoker patients dropped out after 6 and 36 months, respectively. Total drop out was 2.58%.

No wound infection, osteitis and bone graft sequestration occurred during follow-up period.

Mucositis was observed in one patient after 3 months caused by a recurrent unscrewing of the implant abutment. The abutment was removed and the area was carefully treated with chlorhexidine 0.12%. After 1 month, a new abutment was screwed and a new metal-ceramic crown was cemented.

Radiographic and clinical assessment

Mean MBL did not significantly change from T_{24} to T_{36} and T_{48} ($p > 0.05$). The values were 0.89 0.95 and 0.99 mm, respectively.

MBL of implants placed according to all the evaluated parameters is reported in **Table 1**.

Regarding pre-operative parameters, no statistical differences were observed for **implant position, gender and smoke** at T_{36} . Differently, **implant location, presence of endodontic adjacent teeth and implant placement timing significantly affected MBL**, revealing the most considerable variations at T_{36} .

Concerning **implant diameter** as intra-operative and **gingival thickness** as post operative parameter, no MBL significant differences were present at both T_{36} and T_{48} ($p > 0.05$).

Significant differences were present considering **implant location** at T_{36} (maxilla/mandible) ($p = 0.004$). Implant placed in the maxilla showed reduced bone loss when compared to that placed in the mandible.

Implants placed in sites with no **adjacent endodontically treated teeth** shows a more stable MBL at T_{36} (mean MBL was 0.70mm vs 1.16mm, respectively), the differences were statistically significant ($p < 0.001$).

Considering **implant placement timing**, MBL increased significantly with time (from 1 month and 3-month pre-loading evaluation to the 24-36 month post-loading evaluation) in all the three groups (immediate, early and delayed). Early implants showed the lowest bone loss at all the evaluation times. Immediate implants demonstrated a similar behavior up to T_6 .

Table 1.		MBL (Mean ± SD) of the placed implants according to the operative parameters							
		n	T ₁	T ₃	T ₆	T ₁₂	T ₂₄	T ₃₆	T ₄₈
<i>Pre-operative parameters</i>									
Implant location	Maxilla	70	0.15 ± 0.38 ^{Aa}	0.23 ± 0.65 ^{Aa}	0.32 ± 0.51 ^{ABb}	0.50 ± 0.61 ^{Bb}	0.72 ± 0.76 ^{Ca}	0.75 ± 0.75 ^{Cb}	0.86 ± 0.69 ^{Ca}
	Mandible	58	0.29 ± 0.44 ^A	0.36 ± 0.49 ^{Aa}	0.63 ± 0.67 ^{Ba}	0.90 ± 0.75 ^{Ca}	1.05 ± 0.80 ^{Ca}	1.20 ± 0.87 ^{Ca}	1.19 ± 0.71 ^{Ca}
Implant position	Anterior	16	0.20 ± 0.39 ^{Aa}	0.22 ± 0.60 ^{Aa}	0.39 ± 0.57 ^{Ba}	0.50 ± 0.69 ^{Ba}	1.18 ± 0.77 ^{Ca}	0.91 ± 0.89 ^{Ca}	0.80 ± 0.64 ^{Ca}
	Posterior	112	0.22 ± 0.40 ^{Aa}	0.29 ± 0.57 ^{Aa}	0.48 ± 0.52 ^{Ba}	0.65 ± 0.70 ^{Ca}	0.87 ± 0.76 ^{Da}	0.95 ± 0.81 ^{Da}	1.03 ± 0.68 ^{Da}
Gender	Male	57	0.12 ± 0.36 ^{Aa}	0.15 ± 0.41 ^{Aa}	0.29 ± 0.54 ^{Ba}	0.52 ± 0.68 ^{Ca}	0.74 ± 0.66 ^{Da}	0.83 ± 0.71 ^{Da}	0.85 ± 0.64 ^{Da}
	Female	71	0.27 ± 0.49 ^{Aa}	0.39 ± 0.65 ^{Ab}	0.59 ± 0.61 ^{Bb}	0.82 ± 0.69 ^{Cb}	1.05 ± 0.82 ^{Da}	1.08 ± 0.91 ^{Da}	1.21 ± 0.68 ^{Da}
Endodontic adjacent teeth	No	59	0.19 ± 0.38 ^{Aa}	0.25 ± 0.56 ^{Aa}	0.42 ± 0.61 ^{Ba}	0.56 ± 0.69 ^{Ba}	0.82 ± 0.73 ^{Ca}	0.70 ± 0.68 ^{BCa}	0.88 ± 0.68 ^{Ba}
	Yes	69	0.23 ± 0.39 ^{Aa}	0.28 ± 0.51 ^{Aa}	0.49 ± 0.56 ^{Ba}	0.76 ± 0.68 ^{Ca}	0.95 ± 0.65 ^{Da}	1.16 ± 0.69 ^{Eb}	1.17 ± 0.68 ^{Ea}
Smoke	Smokers	17	0.11 ± 0.42 ^{Aa}	0.12 ± 0.52 ^{Aa}	0.19 ± 0.56 ^{Aa}	0.57 ± 0.75 ^{Ba}	0.81 ± 0.86 ^{Ca}	0.82 ± 0.96 ^{Ca}	0.84 ± 0.67 ^{Ca}
	Non smokers	111	0.22 ± 0.41 ^{Aa}	0.27 ± 0.53 ^{Aa}	0.46 ± 0.52 ^{Ba}	0.69 ± 0.35 ^{Ba}	0.88 ± 0.75 ^{Ca}	0.97 ± 0.89 ^{Ca}	1.07 ± 0.65 ^{Ca}
Implant placement	Immediate	24	0.09 ± 0.30 ^{Aa}	0.14 ± 0.35 ^{Aa}	0.23 ± 0.27 ^{Ba}	0.61 ± 0.59 ^{Ca}	0.80 ± 0.62 ^{Ca}	0.73 ± 1.07 ^{Ca}	0.76 ± 0.58 ^{Ca}
	Early	21	0.01 ± 0.18 ^{Aa}	0.03 ± 0.29 ^{Aa}	0.10 ± 0.47 ^{Aa}	0.22 ± 0.66 ^{Bb}	0.53 ± 0.67 ^{Ba}	0.66 ± 0.71 ^{Bab}	0.73 ± 0.57 ^{Ba}
	Delayed	83	0.29 ± 0.45 ^{Ab}	0.39 ± 0.62 ^{Ab}	0.62 ± 0.66 ^{Bb}	0.82 ± 0.68 ^{Ca}	1.02 ± 0.76 ^{Da}	1.16 ± 0.81 ^{Db}	1.22 ± 0.69 ^{Db}
<i>Intra-operative parameter</i>									
Implant Diameter	3.8	53	0.27 ± 0.30 ^{Aa}	0.34 ± 0.33 ^{Aa}	0.43 ± 0.27 ^{ABa}	0.60 ± 0.69 ^{Ba}	0.76 ± 0.70 ^{Ba}	0.99 ± 0.70 ^{Ca}	0.95 ± 0.67 ^{Ca}
	4.25	56	0.22 ± 0.19 ^{Aa}	0.33 ± 0.29 ^{Aa}	0.56 ± 0.47 ^{Ba}	0.76 ± 0.64 ^{Ba}	1.07 ± 0.72 ^{Ca}	0.96 ± 0.72 ^{Ca}	1.08 ± 0.67 ^{Ca}
	5.0	19	0.11 ± 0.41 ^{Aa}	0.08 ± 0.62 ^{Aa}	0.24 ± 0.64 ^{Ba}	0.57 ± 0.84 ^{Ca}	0.75 ± 1.01 ^{Da}	0.83 ± 1.01 ^{Da}	0.91 ± 0.65 ^{Da}
<i>Post-operative parameter</i>									
Gingival thickness	Thin	73	0.19 ± 0.34 ^{Aa}	0.27 ± 0.39 ^{Aa}	0.53 ± 0.58 ^{Ba}	0.75 ± 0.66 ^{Ba}	0.97 ± 0.77 ^{BCa}	1.06 ± 0.82 ^{Ca}	1.16 ± 0.72 ^{Ca}
	Thick	55	0.25 ± 0.48 ^{Aa}	0.31 ± 0.75 ^{Aa}	0.38 ± 0.64 ^{ABa}	0.53 ± 0.75 ^{Ba}	0.78 ± 0.79 ^{BCa}	0.81 ± 0.81 ^{Ba}	0.80 ± 0.65 ^{Ba}
Total		128	0.21 ± 0.38 ^A	0.28 ± 0.56 ^A	0.47 ± 0.57 ^B	0.67 ± 0.78 ^C	0.89 ± 0.81 ^D	0.95 ± 0.85 ^D	0.99 ± 0.68 ^D

Interestingly, when considering MBL at T₄₈, only **implant placement timing** shows statistically significant differences. Delayed implants shows a higher MBL variation (mean value was 1.22± 0.69) mm when compared to both immediate and early implants (values were 0.76± 0.58 and 0.73±0.57, respectively).

Multilevel mixed logistic regression analysis at T₃₆ is reported in **Table 2a**.

The analysis confirms the significant influence of **endodontically treated adjacent teeth** (p<0.0001), **implant placement timing** (p=0.044) and **implant location** (maxilla/mandible) (p=0.019). No statistical differences were observed for the other parameters (p<0.05), Multiple linear regression after stepwise selection (**Table 2b**) additionally confirms that all the 3 variables statistically affected MBL at T₃₆ (p value was 0.001 for endodontic treated adjacent teeth, 0.031 for implant location and 0.044 for implant placement timing).

Table 2a. Multilevel-mixed logistic regression exploring factor associated to MBL at 36 months				
Groups	Coefficient	Robust SE	95% CI	p-value
<i>Pre-operative parameters</i>				
Gender	0.204	0.144	(-0.079; 0.487)	0.158
Location	0.373	0.159	(0.061; 0.685)	0.019
Smoke	0.252	0.146	(-0.034; 0.137)	0.084
Position	-0.276	0.169	(-0.609; 0.056)	0.104
Endodontically treated adjacent teeth	0.501	0.143	(0.219; 0.780)	<0.0001
Implant placement group	0.181	0.089	(0.005; 0.357)	0.044
<i>Intra-operative parameters</i>				
Implant Diameter	0.052	0.118	(-0.179; 0.283)	0.659
<i>Post-operative parameters</i>				
Gingival biotype	-0.128	0.135	(-0.394; 0.137)	0.343

Table 2b Multiple linear regression after stepwise selection				
Groups	Coefficient	Robust SE	95% CI	p-value
Implant placement group	0.168	0.083	(0.003; 0.337)	0.045
Location	0.335	0.155	(0.031; 0.639)	0.031
Endodontically treated adjacent teeth	-0.57	0.335	(-1.228; 0.859)	0.001

Multilevel mixed logistic regression analysis at T₄₈ is reported in **Table 3a**. Interestingly, none of the evaluated parameters appears to significantly affect MBL at this time. Implant placement group appears to be a factor which significantly affects implant MBL only after stepwise logistic regression, confirming data shown in Table 1 (p=0.020). (**Table 3b**)

Table 3a. Multilevel-mixed logistic regression exploring factor associated to MBL at 48 months

Groups	Coefficient	Robust SE	95% CI	p-value
<i>Pre-operative parameters</i>				
Gender	0.226	0.190	(-0.146; 0.598)	0.234
Location	0.138	0.237	(-0.326; 0.604)	0.559
Smoke	0.252	0.146	(-0.034; 0.137)	0.084
Position	-0.186	0.308	(-0.792; 0.419)	0.546
Endodontically treated adjacent teeth	0.329	0.172	(-0.009; 0.668)	0.056
Implant placement group	0.180	0.150	(-0.113; 0.475)	0.229
<i>Intra-operative parameters</i>				
Implant Diameter	0.075	0.121	(-0.161; 0.31)	0.532
<i>Post-operative parameters</i>				
Gingival biotype	-0.224	0.186	(-0.254; 0.432)	0.227

Table 3b Multiple linear regression after stepwise selection

Groups	Coefficient	Robust SE	95% CI	p-value
Implant placement group	0.231	0.998	(0.362; 0.427)	0.020
Thickness	-0.291	0.280	(0.334; 1.432)	0.076

Box plots representations concerning implant placement timing are showed in **Figure 3**. Delayed group showed the highest presence of outliers, in particular after T_6 from insertion (post loading period). Early group showed the most stable MBL values (less wide distributions) up to T_6 (preloading time) and at T_{48} .

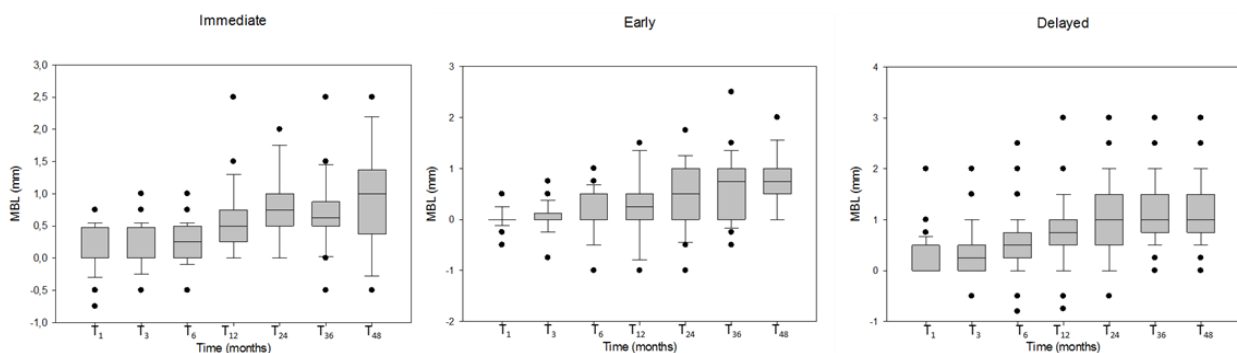


Figure 1: Boxplot representation of placed implants at different evaluation times. Outliers are represented by circle points.

DISCUSSION

This is the first 4-year study where platform-switch implants were used with an enlarged implant neck positioned following a nonsubmerged healing. The results obtained confirms previously reported 2-year prospective study. (Prati *et al.* 2017)

The enlarged neck resulted partially immersed along the soft tissues thickness, the entire 0.50 mm smooth machined neck surface close to the most superficial gingiva and the rough surface close to the deeper gingival tissues.

Several benefits may be provided following this protocol. As cover screws (or healing screws, depending on the soft tissue thickness) resulted exposed at soft tissue levels, additional surgeries before the prosthetic phases could be avoided. The **implant-abutment connection**, as well as the crown margins, resulted more distant from bone tissues, allowing a better control of cement flowing from the restoration and avoiding the risks for **cement overflow** and cement retention in proximity with the bone tissues. (Buser *et al.* 1999)

This risk was reported in studies where subcrestal or equicrestal implants have been performed, conditions where cement excess cannot be adequately controlled (Linkevicius *et al.* 2013, Linkevicius *et al.* 2011, Canullo *et al.* 2016) or when methacrylate based cements are used. (Korsch *et al.* 2014) A recent study evaluated clinical radiographic and immunologic parameters around platform switch dental implants with cement retained or screw retained restorations. (Al Amri *et al.* 2017) Conclusions were that the type of crown retention does not affect BoP, Pocket depth, MBL and levels of IL-1B. In the present study a polycarboxylate cement was used as luting agent.

MBL values follow a similar trend when compared to previously reported with other implant brands (Lago *et al.* 2018), neck (Romanos *et al.* 2015), insertion depth (Sanz *et al.* 2016), and surgical interventions. (Prati *et al.* 2016) A previous randomized clinical trial evaluating bone level implants placed submerged or with a transmucosal approach found similar MBL values at 36 months. (Sanz *et al.* 2016) Likewise, MBL remained stable after the first 12 months from insertion, where the greater bone level changes occurred. (Sanz *et al.* 2016) A recently published randomized clinical trial comparing flared tissue level versus platform-switch bone level implants found lower MBL values at 5

years (mean MBL of tissue level implant was 0.61 ± 0.75) (Lago *et al.* 2018) than that reported in our study (0.99 ± 0.68). However, pre-loading MBL changes were not considered in that study as the MBL evaluation started from the delivery of the definitive crown.

Significant bone level changes/remodeling during the **pre load period occurs**. This concept has been also reported with other implants and surgical approaches. (Nickenig *et al.* 2010, Prati *et al.* 2016)

Indeed, in the present study, mean MBL at 3 months (pre-load) was statistically different to 6 months MBL (post load) ($p=0.001$), the values being 0.28 ± 0.56 and 0.47 ± 0.57 respectively, thus corroborating this hypothesis.

Data on implant depth insertion, are mostly from histological studies (Romanos *et al.* 2015). Implants with a tulip-shaped (flared) neck placed in a most apical position revealed more bone loss when compared to the same implants placed supracrestally. This was attributed to the removal of a great portion of the coronal bone, thus potentially compromising blood supply of the remaining cortical bone. (Valles *et al.* 2017, Alomrani *et al.* 2015)

In accordance with these histological findings, a recent randomized clinical trial concluded that the preparation of the implant site following a subcrestal approach may induce more stress on marginal bone, which can turn into greater bone resorption after implant placement. (Gatti *et al.* 2018)

Different operative variables have been analyzed in this study, which found to be important in on bone level changes. Some of them revealed to greatly affect MBL.

Implant location, presence of endodontic adjacent teeth and implant placement timing were significantly related to MBL at T₃₆.

Delayed group (implant placement timing) revealed significant differences from T₃ to T₄₈, showing greater bone loss compared to both immediate and early implants. Indeed, box plots (**Figure 3**) clearly evidences that delayed implants presented a wider distribution of implant with MBL values > 1.0 mm at T₄₈.

Implant position parameter did not significantly influence MBL at T₃₆ and at T₄₈($p>0.05$). The group discrepancies may have influenced this result.

Presence of endodontically treated adjacent teeth close to peri-implant site are rarely reported even though among all causes of implant failures, retrograde peri-implantitis or endodontic peri-implantitis may have a central role. (Quirynen *et al.* 2005, López-Martínez *et al.* 2015)

In the present study, the presence of one or more **endodontic treated teeth** adjacent to the implant site (**Endodontic adjacent teeth** parameter) appears to affect MBL only at T₃₆ ($p=0.042$): mean MBL of implants with no adjacent endodontic treated teeth varied from $0.82\text{mm} \pm 0.73$ at T₂₄ to $0.72\text{mm} \pm 0.68$ at T₃₆ (**$p>0.05$**).

Retrograde peri-implantitis may be an important cause of implant failures, the infection triggered by bacteria present in an adjacent (generally) active periapical lesion. (Quirynen *et al.* 2005)

In some cases, dormant bacteria may remain silent around asymptomatic endodontic treated teeth. (Nair 2006, Siqueira

et al. 2014, Zhou *et al.* 2009)

A radiological follow-up of endodontic treated teeth might be important to identify this critical condition.

Considering **gender**, female patients showed an increased MBL after 3 years, compared to males (mean MBL was 1.08mm vs 0.83mm respectively). These differences, however, were not statistically significant ($p=0.157$). From literature, male patients seem to have higher risks of implant failure however these data are controversial as it is difficult to correlate peri-implant bone loss and patient gender. (Chrcanovic *et al.* 2015)

In the present study **smoke** was found to not significantly affect MBL in the medium-term. The small sample size of smoking patients and the groups discrepancies (17 implants in 8 patients vs 92 implants in 57 patients) may justify this finding.

Gingival thickness was evaluated in all patients at 48-month follow-up. Interestingly, even though thin biotype showed higher values of MBL this parameter appears not to influence MBL at 36 and 48 months($p>0.05$).

Implants placement timing was found to be the most significant factors affecting MBL on nonsubmerged platform-switch tulip-shaped implants. In particular delayed implant groups showed the greatest bone loss. Differences were statistically significant at all the evaluation times. Drilling procedures at the implant site may be responsible for bone necrosis and bone smear layer formation, inducing the activation of osteoclasts and vascularization damage. Both these conditions may be responsible for higher bone resorption of the mature cortical bone. (Baffone *et al.* 2011 and 2013)

It should be underlined that the reduced bone loss values reported in this study may be influenced by the operator expertise who performed the surgeries and the possibility of patients to be included in a hygienic recall programme. This protocol should be further validated with long term follow-up.

Conclusions

Conclusion may be summarized as follows:

- Tulip-shaped neck platform switch implants may be placed at tissue level (nonsubmerged) with a minimally invasive flapless technique.
- The present protocol demonstrated a reduced bone loss in the early phases from implant placement and a MBL stability at 36 and 48 months.
- Among all the evaluated parameters, only implant placement timing appears to significantly affect MBL before loading and during the entire period of observation.
- Delayed implant placement was responsible for higher bone loss when compared to early and immediate

REFERENCES

Al Amri MD, Al-Rasheed AS, Al-Kheraif AA, Alfadda SA. Comparison of Clinical, Radiographic, and Immunologic Inflammatory Parameters Around Dental Implants with Cement-Retained and Screw-Retained Restorations: A 5-Year Prospective Cohort Study in Men. *Int J Prosthodont* 2017;30:384-389.

Alomrani AN, Hermann JS, Jones AA, Buser D, Schoolfield J, Cochran DL. The effect of a machined collar on coronal hard tissue around titanium implants: a radiographic study in the canine mandible. *Int J Oral Maxillofac Implants* 2005;20:677-686.

Anitua E, Piñas L, Begoña L, Orive G. Long-term retrospective evaluation of short implants in the posterior areas: clinical results after 10–12 years. *J Clin Periodontol* 2014;41:404-411.

Baffone GM, Botticelli D, Pantani F, Cardoso LC, Schweikert MT, Lang NP. Influence of various implant platform configurations on peri-implant tissue dimensions: An experimental study in dog. *Clin Oral Implants Res* 2011;22:438-444.

Baffone GM, Botticelli D, Pereira FP, Favero G, Schweikert M, Lang NP. Influence of buccal bony crest width on marginal dimensions of periimplant hard and soft tissues after implant installation an experimental study in dogs. *Clin Oral Implants Res* 2013;24:250-254.

Buser D, Janner SFM, Wittneben J-, Brägger U, Ramseier CA, Salvi GE. 10-Year Survival and Success Rates of 511 Titanium Implants with a Sandblasted and Acid-Etched Surface: A Retrospective Study in 303 Partially Edentulous Patients. *Clin Implant Dent Relat Res* 2012;14:839-851.

Buser D, Mericske-Stern R, Dula K, Lang NP. Clinical experience with one-stage, non-submerged dental implants. *Adv Dent Res* 1999;13:153-161.

Cairo F, Carnevale G, Buti J, Nieri M, Mervelt J, Tonelli P et al. Soft-tissue re-growth following fibre retention osseous resective surgery or osseous resective surgery: a multilevel analysis. *J Clin Periodontol* 2015;42:373-9.

Canullo L, Cocchetto R, Marinotti F, Oltra DP, Diago MP, Loi I. Clinical evaluation of an improved cementation technique for implant-supported restorations: a randomized controlled trial. *Clin Oral Implants Res* 2016;27:1492-1499.

Canullo L, Fedele GR, Iannello G, Jepsen S. Platform switching and marginal bone-level alterations: The results of a randomized-controlled trial. *Clin Oral Implants Res* 2010;21:115-121.

Chrcanovic BR, Albrektsson T, Wennerberg A. Dental implants inserted in male versus female patients: a systematic review and meta-analysis. *J Oral Rehabil* 2015;42:709-722.

Cordaro L, Torsello F, Chen S, Ganeles J, Brägger U, Hämmerle C. Implant-supported single tooth restoration in the esthetic zone: Transmucosal and submerged healing provide similar outcome when simultaneous bone augmentation is needed. *Clin Oral Implants Res* 2013;24:1130-1136.

Cosgarea R, Gasparik C, Dudea D, Culic B, Dannewitz B, Sculean A. Peri-implant soft tissue colour around titanium and zirconia abutments: a prospective randomized controlled clinical study. *Clin Oral Implants Res* 2015;26:537-544.

Dodson TB. A guide for preparing a patient-oriented research manuscript. *Oral Surg Oral Med Oral Pathol Radiol Endod* 2007;104:307-315.

Ferrari M, Carrabba M, Vichi A, Goracci C, Cagidiaco MC. Influence of abutment color and mucosal thickness on soft tissue color. *Int J Oral Maxillofac Implants* 2017;32:393-399.

Flores-Guillen J, Álvarez-Novoa C, Barbieri G, Martín C, Sanz M. Five-year outcomes of a randomized clinical trial comparing bone-level implants with either submerged or transmucosal healing. *J Clin Periodontol* 2018;45:125-135.

French D, Cochran DL, Ofec R. Retrospective Cohort Study of 4,591 Straumann Implants Placed in 2,060 Patients in Private Practice with up to 10-Year Follow-up: The Relationship Between Crestal Bone Level and Soft Tissue Condition. *Int J Oral Maxillofac Implants* 2016;31:168-178.

Galindo-Moreno P, León-Cano A, Ortega-Oller I, Monje A, O Valle F, Catena A. Marginal bone loss as success criterion in implant dentistry: beyond 2 mm. *Clin Oral Implants Res* 2015;26:28-34.

Gatti C, Gatti F, Silvestri M, Mintrone F, Rossi R, Tridondani G et al. A Prospective Multicenter Study on Radiographic Crestal Bone Changes Around Dental Implants Placed at Crestal or Subcrestal Level: One-Year Findings. *Int J Oral Maxillofac Implants* 2018;33:913-918.

Giacomel MC, Camati P, Souza J, Deliberador T. Comparison of Marginal Bone Level Changes of Immediately Loaded Implants, Delayed Loaded Nonsubmerged Implants, and Delayed Loaded Submerged Implants: A Randomized Clinical Trial. *Int J Oral Maxillofac Implants* 2017;32:661-666.

Hämmerle CH, Chen ST, Wilson TG Jr. Consensus statements and recommended clinical procedures regarding the placement of implants in extraction sockets. *Int J Oral Maxillofac Implants* 2004 19:26-28.

Hermann JS, Buser D, Schenk RK, Schoolfield JD, Cochran DL. Biologic Width around one- and two-piece titanium implants. *Clin Oral Implants Res* 2001;12:559-571.

Ibañez C, Catena A, Galindo-Moreno P, Noguerol B, Magán-Fernández A, Mesa F. Relationship Between Long-Term Marginal Bone Loss and Bone Quality, Implant Width, and Surface. *Int J Oral Maxillofac Implants* 2016;31:398-405.

Jung RE, Zembic A, Pjetursson BE, Zwahlen M, Thoma DS. Systematic review of the survival rate and the incidence of biological, technical, and aesthetic complications of single crowns on implants reported in longitudinal studies with a mean follow-up of 5 years. *Clin Oral Implants Res* 2012;23:2-21.

Klinge B. Peri-implant marginal bone loss: An academic controversy or a clinical challenge? *Eur J Oral Implantol* 2012;5:13-19.

Korsch M, Obst U, Walther W. Cement-associated peri-implantitis: a retrospective clinical observational study of fixed implant-supported restorations using a methacrylate cement. *Clin Oral Implants Res* 2014;25:797-802.

Lago L, da Silva L, Martinez-Silva I, Rilo B. Radiographic Assessment Of Crestal Bone Loss In Tissue-Level Implants Restored By Platform Matching Compared With Bone-Level Implants Restored By Platform Switching: A Randomized, Controlled, Split-Mouth Trial With 3-Year Follow-Up. *Int J Oral Maxillofac Implants* 2018 in press.

Lazzara RJ, Porter SS. Platform switching: A new concept in implant dentistry for controlling post-restorative crestal bone levels. *Int J Periodontics Restorative Dent* 2006;26:9-17.

Linkevicius T, Puisys A, Vindasiute E, Linkeviciene L, Apse P. Does residual cement around implant-supported restorations cause peri-implant disease? A retrospective case analysis. *Clinical Oral Implant Research* 2013; 24:1179-1184.

Linkevicius T, Vindasiute E, Puisys A, Peculiene V. The influence of margin location on the amount of undetected cement excess after delivery of cement-retained implant restorations. *Clinical Oral Implant Research* 2011;22:1379-1384.

López-Martínez F, Gómez Moreno G, Olivares-Ponce P, Eduardo Jaramillo D, Eduardo Maté Sánchez de Val J, Calvo-Guirado JL. Implants failures related to endodontic treatment. An observational retrospective study. *Clin Oral Implants Res* 2015;26:992-995.

Nair PN. On the causes of persistent apical periodontitis: A review. *Int Endod J* 2006;39:249-281.

Nickenig HJ, Wichmann M, Schlegel KA, Nkenke E, Eitner S. Radiographic evaluation of marginal bone levels during healing period, adjacent to parallel-screw cylinder implants inserted in the posterior zone of the jaws, placed with flapless surgery. *Clin Oral Implants Res* 2010;21:1386-1393.

Ørstavik D, Kerekes K, Eriksen HM. The periapical index: a scoring system for radiographic assessment of apical periodontitis. *Endod Dent Traumatol* 1986;2:20-34.

Paul S, Petsch M, Held U. Modeling of Crestal Bone After Submerged vs Transmucosal Implant Placement: A Systematic Review with Meta-Analysis. *Int J Oral Maxillofac Implants* 2017;32:1039-1050.

Pjetursson BE, Thoma D, Jung R, Zwahlen M, Zembic A. A systematic review of the survival and complication rates of implant-supported fixed dental prostheses (FDPs) after a mean observation period of at least 5 years. *Clin Oral Implants Res* 2012;23:22-38.

Prati C, Zamparini F, Pirani C, Gatto MR, Piattelli A, Gandolfi MG. Immediate early and delayed implants: A 2-year prospective cohort study of 131 transmucosal flapless implants placed in sites with different pre-extractive endodontic infections. *Implant Dent* 2017;26:654-663.

Prati C, Zamparini F, Scialabba VS, Gatto MR, Piattelli A, Montebugnoli L et al. A 3-year prospective cohort study on 132 calcium phosphate blasted implants: flap vs flapless technique. *Int J Oral Maxillofac Implants* 2016;31:413-423.

Quirynen M, Vogels R, Alsaadi R, Naert I, Jacobs R, van Steenberghe D. Predisposing conditions for retrograde peri-implantitis and treatment suggestions. *Clin Oral Implants Res* 2005;16:599-608.

Rogers WH. Regression standard errors in clustered samples. *Stata Technical Bulletin* 1993;13:19-23.

Romanos GE, Aydin E, Gaertner K, Nentwig G. Long-term results after subcrestal or crestal placement of delayed loaded implants. *Clin Implant Dent Relat Res* 2015;17:133-141.

Sanz M, Cecchinato D, Ferrus J, Salvi GE, Ramseier C, Lang NP et al. Implants placed in fresh extraction sockets in the maxilla: clinical and radiographic outcomes from a 3-year follow-up examination. *Clin Oral Implants Res* 2014;25:321-327.

Sanz M, Ivanoff CJ, Weingart D, Wiltfang J, Gahlert M, Cordaro L et al. Clinical and Radiologic Outcomes after Submerged and Transmucosal Implant Placement with Two-Piece Implants in the Anterior Maxilla and Mandible: 3-Year Results of a Randomized Controlled Clinical Trial. *Clin Implant Dent Relat Res* 2015;17:234-246.

Sanz Martin I, Benic GI, Hammerle CH, Thoma DS. Prospective randomized controlled clinical study comparing two dental implant types: Volumetric soft tissue changes at 1 year of loading. *Clin Oral Implants Res* 2016;27:406-411.

Schwarz F, Mihatovic I, Golubovich V, Schär A, Sager M, Becker J. Impact of abutment microstructure and insertion depth on crestal bone changes at nonsubmerged titanium implants with platform switch. *Clin Oral Implants Res*. 2015;26:287-92.

Siqueira Jr. JF, Rôças IN, Ricucci D, Hülsmann M. Causes and management of post-treatment apical periodontitis. *Br Dent J* 2014; 216:305-312.

Taxel P, Ortiz D, Shafer D, Pendrys D, Reisine S, Rengasamy K et al. The relationship between implant stability and bone health markers in post-menopausal women with bisphosphonate exposure. *Clin Oral Invest* 2014;18:49-57.

Thoma DS, Sanz Martin I, Benic GI, Roos M, Hämmerle CH. Prospective randomized controlled study comparing two dental implant systems: demographic and radiographic results at one year of loading. *Clin Oral Implants Res* 2014;25:142-149.

Valles C, Rodríguez-Ciurana X, Nart J, Santos A, Galofre M, Tarnow D. Influence of Implant Neck Surface and Placement Depth on Crestal Bone Changes Around Platform-Switched Implants: A Clinical and Radiographic Study in Dogs. *J Periodontol* 2017;88:1200-1210.

Vandenbroucke JP, von Elm E, Altman DG, Gøtzsche PC, Mulrow CD, Pocock SJ et al. Strengthening the reporting of observational studies in epidemiology (STROBE): explanation and elaboration *PLoS Med* 2007;4:1628-1654.

World Medical Association Declaration of Helsinki: Ethical principles for medical research involving human subjects. *JAMA* 2013;310:2191-2194.

Zembic A, Sailer I, Jung RE, Hammerle CH. Randomized-controlled clinical trial of customized zirconia and titanium implant abutments for single tooth implants in canine and posterior regions: 3-year results. *Clin Oral Implants Res* 2009;20:802-808.

Zhou W, Han C, Li D, Li Y, Song Y, Zhao Y. Endodontic treatment of teeth induces retrograde peri-implantitis. *Clin Oral Implants Res* 2009;20:1326-1332.

Zucchelli G, Mounssif I, Mazzotti C, Stefanini M, Marzadori M, Petracci E, et al. Coronally advanced flap with and without connective tissue graft for the treatment of multiple gingival recessions: A comparative short- and long-term controlled randomized clinical trial. *J Clin Periodontol* 2014;41:396-403.

2. Endodontic-related periapical bone defects and new biomaterials for periapical bone regeneration

2.1 Endodontic-related periapical bone defects

Endodontic-related periapical lesions (known as apical periodontitis) are inflammatory disorder of periradicular tissues caused by persistent microbial infection within the endodontic space, where necrotic tissues offer a suitable niche to proliferate and grow without disturbances from the immune system, if no adequate root canal treatment is performed (Nair 2006). Unlike the oral cavity, the root canal system has no commensal microbiota, and any microorganism detected here can be regarded as a potential pathogen.

These lesions are very common and widespread in the world population. (Pak *et al.* 2012). Prevalence of periapical radiolucencies is high and increases with age: 5% of all teeth without root canal treatment and 25% with a root canal treatment have a periapical radiolucent lesion (Pak *et al.* 2012).

Several highly virulent bacteria were detected into infected root canals. These bacteria can be identified not only into the root canal lumen, but also into dentinal tubules (Foschi *et al.* 2005) and over the periapical space (Ricucci *et al.* 2015). In these spaces, bacteria do not grow in a planktonic state, but instead in a proper complex symbiotic population, organized in a biofilm system, which offers high resistance to antibacterial molecules than the same organisms in planktonic state (Wilson 1996, Costerton & Stewart 2000).

Treponema denticola and *Enterococcus faecalis* has been significantly associated with acute periapical lesion and root canal treatment failures, respectively (Foschi *et al.* 2005). Interestingly, detection of *Treponema Denticola* was also positive in other distant organs, such as the heart (Cavrini *et al.* 2005), at sites of esophageal cancer (Narikiyo *et al.* 2004) and to the brain in Alzheimer affected patients (Riviere *et al.* 2002).

Several local and systemic complications are described due to untreated apical periodontitis, including alveolar nerve paresthesia (Ricucci *et al.* 2018), re-exacerbation of the lesion which in rare cases can be life-threatening (Li *et al.* 1999, Pappa & Jones 2005), coronary heart disease, infective endocarditis and low-birth preterm births (Siqueira *et al.* 2011, Fouad *et al.* 2009, Zhang *et al.* 2016).

Moreover, the presence of large and infected bone defects may hinder bone graft procedures and immediate implant installation when the affected tooth needs to be extracted (Crhcanovich *et al.* 2014).

Root canal treatment main aim is to completely remove the infected tissues into the affected through an adequate shaping disinfection and filling of the root canals. Traditional techniques with Nickel Titanium (NiTi) rotary instrumentation and bioinert root canal sealers allow to manage endodontic affected tooth and to preserve the tooth in function. Survival rate of root treated teeth demonstrated high percentage of survival rates (Ng *et al.* 2010,2011, Ricucci *et al.* 2011, Pirani *et al.* 2015 and 2017) . However, root canal treatment success, namely the complete resolution of the periapical lesions does not follow a similar trend, with a variable range reported in literature, in particular in tooth with

a pre-existing periapical lesion (Kirkevang *et al.* 2007, 2011, Landis boren *et al.* 2015, Fristad *et al.* 2004, Prezl *et al.* 2016).

The following papers report the success and survival rates in the long term (10 and 20 years) of some of the most used traditional endodontic procedures. In particular, the first study focusses on secondary root canal treatments with carrier based technique (Thermafill and Ah Plus), and the second report the treatment of a large cohort of patients with a single cone technique and CRCS.

REFERENCES

Cavrini F, Pirani C, Foschi F, Montebugnoli L, Sambri V, Prati C. Detection of *Treponema denticola* in root canal systems in primary and secondary endodontic infections. A correlation with clinical symptoms. *New Microbiol.* 2008;31:67-73.

Cavrini F, Sambri V, Moter A, Servidio D, Marangoni A, Montebugnoli L, Foschi F, Prati C, Di Bartolomeo R, Cevenini R. Molecular detection of *Treponema denticola* and *Porphyromonas gingivalis* in carotid and aortic atheromatous plaques by FISH: report of two cases. *J Med Microbiol.* 2005;54:93-6.

Chrcanovic BR, Martins MD, Wennerberg A. Immediate placement of implants into infected sites: a systematic review. *Clin Implant Dent Relat Res.* 2015;17 Suppl 1:e1-e16.

Costerton JW, Stewart PS. Biofilms and device-related infections. In: Nataro PJ, Balser MJ, Cunningham-Rundels S, eds. *Persistent Bacterial Infections.* Washington, DC: ASM Press, 2000, pp. 423–39.

Fouad AF. Endodontic infections and systemic disease. In: Fouad AF, ed. *Endodontic microbiology.* Hoboken, NJ: Wiley, 2017, pp. 385-402.

Fristad I, Molven O, Halse A. Nonsurgically retreated root-filled teeth - Radiographic findings after 20-27 years. *Int Endod J* 2004;37,12-18.

Kirkevang LL, Væth M, Horsted-Bindslev P, Bahrami G, Wenzel A. Risk factors for developing apical periodontitis in a general population. *Int Endod J* 2007;40,290-299.

Kirkevang LL, Væth M, Wenzel A. 10-year follow-up observations of periapical and endodontic status in a Danish population. *Int Endod J* 2012;45, 829–839,

Landys Borén D, Jonasson P, Kvist T. Long-term survival of endodontically treated teeth at a public dental specialist clinic. *J Endod* 2015;41,176-181.

Li X, Tronstad L, Olsen I. Brain abscesses caused by oral infection. *Endod Dent Traumatol* 1999; 15: 95–101.

Nair PN. On the causes of persistent apical periodontitis: A review. *International Endodontic Journal* 2006;39, 249-281.

Narikiyo M, Tanabe C, Yamada Y, Igaki H, Tachimori Y, Kato H, Muto M, Montesano R, Sakamoto H, Nakajima Y, Sasaki H. Frequent and preferential infection of *Treponema denticola*, *Streptococcus mitis*, and *Streptococcus anginosus* in esophageal cancers. *Cancer Sci.* 2004;95:569-74.

Ng YL, Mann V, Gulabivala K. Tooth survival following non-surgical root canal treatment: a systematic review of the literature. *International Endodontic Journal* 2010;43,171-189.

- Ng YL, Mann V, Gulabivala K. A prospective study of the factors affecting outcomes of non-surgical root canal treatment: Part 2: Tooth survival. *Int Endod J* 2011;44,610-625.
- Pak JG, Fayazi S, White SN. Prevalence of periapical radiolucency and root canal treatment: a systematic review of cross-sectional studies. *J Endod*. 2012;38:1170-6.
- Pappa H, Jones DC. Mediastinitis from odontogenic infection. A case report. *Brit Dent J* 2005; 198: 547–8.
- Petersson K, Fransson H, Wolf E, Håkansson J. Twenty-year follow-up of root filled teeth in a Swedish population receiving high-cost dental care. *Int Endod J* 2016;49,636-645.
- Pirani C, Chersoni S, Montebugnoli L, Prati C. Long-term outcome of non-surgical root canal treatment: a retrospective analysis. *Odontology* 2015;103,185-193.
- Pirani C, Friedman S, Gatto MR, Iacono F, Tinarelli V, Gandolfi MG, Prati C. Survival and periapical health after root canal treatment with carrier-based root fillings: Five-year retrospective assessment. *Int Endod J* 2017 in press.
- Pretzl B, Eickholz P, Saure D, Pfefferle T, Zeidler A, Dannewitz B. Endodontic status and retention of molars in periodontally treated patients: results after 10 or more years of supportive periodontal therapy. *J Clin Periodontol* 2016;43, 1116-1123.
- Ricucci D, Loghin S, Siqueira JF Jr. Complicated untreated apical periodontitis causing paraesthesia: A case report. *Aust Endod J*. 2018;44:281-285.
- Ricucci D, Russo J, Rutberg M, Burleson JA, Spångberg LS. A prospective cohort study of endodontic treatments of 1369 root canals: results after 5 years. *Oral Surg Oral Med Oral Pathol Oral Radiol Endod* 2011;112, 825-842.
- Ricucci D, Siqueira JF, Lopes WSP, Vieira AR, Rôças IN. Extraradicular infection as the cause of persistent symptoms: A case series. *J Endod* 2015; 41, 265-273.
- Riviere GR, Riviere KH, Smith KS. Molecular and immunological evidence of oral *Treponema* in the human brain and their association with Alzheimer's disease. *Oral Microbiol Immunol*. 2002;17:113-8.
- Siqueira JF Jr. Treatment of endodontic infections. London: Quintessence Publishing; 2011. Wiley-Blackwell; 2009. pp. 320–38.
- Wilson M. Susceptibility of oral bacterial biofilms to antimicrobial agents. *J. Med. Microbiol*. 1996; 44, 79–87.
- Zhang J, Huang X, Lu B, Zhang C, Cai Z. Can apical periodontitis affect serum levels of CRP, IL-2, and IL-6 as well as induce pathological changes in remote organs? *Clin Oral Investig* 2016; 20: 1617–24.



The fate of root canals obturated with Thermafil: 10-year data for patients treated in a master's program

Chiara Pirani¹ · Fausto Zamparini¹ · Ove A. Peters² · Francesco Iacono¹ · Maria Rosaria Gatto¹ · Luigi Generali³ · Maria Giovanna Gandolfi¹ · Carlo Prati¹

Received: 29 March 2018 / Accepted: 22 November 2018 / Published online: 5 December 2018
© Springer-Verlag GmbH Germany, part of Springer Nature 2018, corrected publication 2019

Abstract

Objectives Retrospective description of the 10-year success rate of endodontic treatments with Thermafil (TF).

Materials and methods Patients treated by postgraduate students in an Endodontics Master's Program (2006–2008) were enrolled. All treated root canals were filled with TF and AH Plus. Teeth satisfying the inclusion criteria (206 teeth in 89 patients) were reexamined clinically and radiographically to estimate a 10-year survival and periapical health. Demographic and medical data were registered; collected information included pre-, intra-, and postoperative variables. Teeth were classified as “healthy” (PAI ≤ 2 in absence of signs/symptoms), “endodontically diseased” (presenting at least one of the following: PAI ≥ 3, signs/symptoms, retreated in the course of the follow-up, or extracted for endodontic reasons), or “non-endodontically diseased” (extracted for non-restorable fractures or periodontal disease). For teeth lost during the 10-year follow-up, details and reason of extraction were analyzed. Two PAI-calibrated examiners assessed outcomes blinded to preoperative status. Bivariate and multilevel analyses were performed (α level set at 0.05).

Results At 10 years, 179 (87%) teeth survived and 27 were extracted: 20 for non-endodontic reasons (excluded from success analysis) and 7 for endodontic reasons (considered “endodontically diseased”). Multilevel analysis revealed that the probability of extraction was increased by the presence of preoperative pain (odds ratio = 6.720; 95% confidence interval, 1.483–30.448) and by maxillary location (odds ratio = 2.950; 95% confidence interval, 1.043–8.347). Concerning periapical status, 159/186 teeth (85%) were assessed as “healthy.” Multilevel analysis confirmed that maxillary location (odds ratio = 3.908; 95% confidence interval, 1.370–11.146), presence of flare up (odds ratio = 9.914; 95% confidence interval, 2.388–41.163), and fracture occurrence (odds ratio = 35.412; 95% confidence interval, 3.366–372.555) decreased the odds of healing, respectively.

Conclusions After 10 years, teeth filled with Thermafil in a specialist master's program presented a survival and a periapical health comparable to cohorts where root canals were filled with other obturation techniques.

Clinical relevance Carrier-based techniques provide time savings for clinicians while satisfying clinical quality criteria for the root filling and consequently the clinical outcome.

Keywords Carrier-based system · Clinical outcome · Long term · Retrospective study · Survival

✉ Chiara Pirani
chiara.pirani4@unibo.it

¹ Endodontic Clinical Section, School of Dentistry, Department of Biomedical and Neuromotor Sciences (DIBINEM), Alma Mater Studiorum University of Bologna, Via San Vitale 59, 40125 Bologna, Italy

² Arthur A. Dugoni School of Dentistry, University of the Pacific, San Francisco, CA, USA

³ Department of Surgery, Medicine, Dentistry and Morphological Sciences with Transplant Surgery, Oncology and Regenerative Medicine Relevance, School of Dentistry, Endodontic Section, University of Modena and Reggio Emilia, Modena, Italy

Introduction

Filling the root canal system is a crucial step in a root canal treatment (RCT), aiming to prevent the passage of microorganisms and fluid along the root canal [1]. In 1978, Johnson devised a new method to thermo-plasticize gutta-percha and densely fill root canals [2]. Over time, a carrier-based obturation has become popular owing to the ease of use and the possibility to obtain consistently adequate technical results [3]. Even though more advanced versions of core carrier systems are present in the market, still, Thermafil (TF) remains as a very well-known and proven obturation technique [4–6]. Unfortunately, to date, available data on clinical outcomes of

teeth filled with the TF system stems from widely varying research designs [4–11]. Moreover, information is lacking comparing carrier-based systems to warm vertical compaction. Conversely, a number of clinical studies analyzing the outcomes of root canal treatments filled with carrier-based and lateral condensation have been published [4, 6–10].

Despite the fact that warm vertical condensation provides an excellent three-dimensional seal *in vitro* [12, 13], with an increased density of gutta-percha in the apical region [14, 15], there is no consensus in the literature concerning the superiority of warm techniques over cold lateral techniques regarding clinical outcomes.

Finally, while several clinical studies have evaluated RCT outcomes over short/medium observation times [5, 6, 10, 16–18], long-term assessments of teeth treated by specialists are rare.

Therefore, the primary aim of this 10-year retrospective study was to describe the survival and success of RCT when canals were obturated with TF; secondarily, factors influencing success and survival rate were identified.

Materials and methods

Sample size estimation

The sample size concerning the healing rate was based on results from a previous study [11]. Hypothesizing that teeth without periapical lesions healed 15% more than teeth with lesions, in the range between 90 and 75% of healing rate [19], with 80% power and 5% significance in a one-tailed test, a minimum of 77 teeth is needed in each of the two groups. Seventy-four teeth with periapical lesions were encountered in this retrospective study.

Study design

A total of 420 patients attended the Endodontic Clinical Section, Dental Clinical School of DIBINEM—University of Bologna from January 2006 to January 2008, for evaluation and treatment of endodontic pathosis. Of these, 230 subjects received RCT and were enrolled in full compliance with the Declaration of Helsinki [20]. Every subject signed an informed consent form accepting the treatment plan, to cover costs of treatment and maintenance, including participation in the follow-up program and inclusion in an eventual study. Records of treated patients were accessed from April 2016 to January 2018, and only subjects fulfilling all inclusion criteria were enrolled: local residents; age range between 18 and 70 at the time of treatment; ASA I and II; adequate oral hygiene, with Plaque Index of $\leq 20\%$ [21]; and preoperative probing depth of ≤ 5 mm. From these, only subjects that had a definitive restoration placed within 2 weeks after a root canal treatment and presented with full clinical and radiographic

data [11] with a minimum of 10-year follow-up were included in the present study.

Clinical protocol

The initial study protocol was approved by the University of Bologna, Department of Oral Sciences ethical committee. All treatments were performed by postgraduate students attending a Master's Program in Endodontics, supervised by trained tutors.

A standardized protocol was followed, involving anesthesia with mepivacaine (Carboplyina, Molteni, Scandicci, Italy) and rubber dam isolation (Hygienic Dental Dam, Coltène Whaledent, Cuyahoga Falls, USA) before creating a straight-line access. Inadequate coronal restorations and decay were removed before instrumenting root canals. Primary treatment was performed in the following manner: a step-down procedure with Gates-Glidden burs #2-3-4 (Dentsply Maillefer, Ballaigues, Switzerland) was followed by subsequent use of manual K-files (Dentsply Maillefer) or nickel-titanium instruments (ProTaper Universal, Dentsply Maillefer) following the manufacturer's instructions. Canals were irrigated by alternating 5% NaOCl (Nicolor, Ogna, Muggiò, Italy) and 10% EDTA (Tubuliclean, Ogna) solutions throughout instrumentation. Final irrigation was performed with 3 min NaOCl, 3 min EDTA, and 3 min NaOCl.

In the case of endodontic retreatment, ultrasonic tips (StartX, Dentsply Maillefer) were used to remove any existing metal and fiber posts under magnification. Pre-existing root filling material was removed with K-files and Gates-Glidden aided by solvents (Endosolv E or Endosolv R, Septodont, Saint-Maur-des-Fossés, France). If it was not possible to reach the entire working length (WL), files were used to the point of the canal that hand files had penetrated to. Working length was in all cases established with the aid of an electronic apex locator (Root ZX, Morita, Tokyo, Japan) and radiographically confirmed. TF Size verifiers were used to select TF obturators that fitted passively at WL. Obturators were disinfected in a 5% NaOCl solution for 1 min. Canal walls were then coated with a thin layer of AH Plus sealer (Dentsply-DeTrey, Konstanz, Germany) using a K-file. The selected obturator was heated in the Thermaprep Plus oven (Dentsply Maillefer) and slowly introduced into the canal until its final position. After 8–10 s, the obturator was sectioned with a Thermancut bur, keeping it in position with light pressure. A radiograph was then taken to reveal the quality of the filling. Between appointments, access cavities were temporized with Coltosol (Coltène Whaledent, Altstätten, Switzerland).

Teeth were definitively restored under rubber dam isolation within 2 weeks after root filling. After applying a self-etching dentin-bonding agent (Clearfil SE BOND, Kuraray, Osaka, Japan), flowable (Gradia Flow, GC Corporation, Tokyo, Japan) and high-filled composite resins (Gradia, GC Corporation) were applied incrementally in 1.5 mm layers

and light-cured (Elipar 3 M ESPE, St. Paul, USA). Cavities that encompassed more than one marginal ridge (both ridges, one ridge, and one or more cusps) were restored using fiber posts. Post space was prepared with #4-3-2 Gates-Glidden drills; dentin was etched with 35% phosphoric acid for 15 s, rinsed with water for 10 s, and dried with paper points. Carbon posts (Tech 2000 XOP, Isasan, Rovello Porro, Italy) were luted with Scotchbond 1/RelyX Arch (3 M ESPE). Severely compromised teeth with more than one missing marginal ridge and one or more missing cusps were restored with provisional resin crowns cemented with Temp Bond (Kerr Dental, Scafati, Italy) temporary cement. In these cases, porcelain fused to metal crowns were placed 3 to 6 months after endodontic treatment and cemented with a polycarboxylate cement (Heraeus Kulzer, Hanau, Germany).

Outcome evaluation

Data were collected from both clinical assessment and radiographic evaluation. The final outcome evaluation was performed by two previously calibrated examiners, with equivalent experience who were blinded to both preoperative data and patients’ names. Another examiner was consulted in case of disagreement. A Periapical Index (PAI) [22] score was determined for each root in the study. Multi-rooted teeth were assigned a PAI score based on the root with the highest score.

Twenty-eight variables were considered in the initial univariate model, out of which five were demographic/medical conditions (Table 1) and 23 were pre-, intra-, and postoperative factors (see Tables 2, 3 and 4). Root filling quality was assessed in terms of length as follows: adequate, short fill (>

2 mm from the radiographic apex), overfilling (sealer/gutta-percha extruded from the radiographic apex), and in terms of density of the filling material (radiographic absence/presence of voids). Post-endodontic coronal restorations were described as having crown coverage or composite restoration and post placement.

At the end-point evaluation, teeth presenting a PAI score of ≤ 2 in addition to no symptoms and no clinical signs of apical periodontitis represented the healthy group [22, 23] and were accounted as a success. The remaining teeth were split into two groups: non-endodontic disease and endodontic disease. The former group was composed of teeth extracted for non-endodontic reasons (root fractures or periodontal disease), the latter group presented either a PAI score of ≥ 3, symptoms, clinical signs of disease or undergone further treatment before the end-point (orthograde or surgical s, hemisection, or extraction due to endodontic pathosis) (Fig. 1). The reasons for extraction were derived from the treatment records and the most recent radiograph was used to extract information concerning the treatment data.

Statistical analysis

Univariate and bivariate distributions were used, aiming to retrospectively describe survival and periapical health and their association with clinical parameters (pre-, intra-, and postoperative variables). Multilevel analysis (mixed effects model) was performed at the patient and tooth level aiming to identify clinical parameters significantly affecting survival and periapical health. Kaplan-Meier (KM) survival analysis described the cumulative survival of the teeth examined and analyzed the influence of the causes of extraction. The significance level was a priori set at $\alpha = 0.05$.

Results

A total of 206 teeth in 89 patients fulfilled all the inclusion criteria and were available for review after 10 years (Table 1). No significant effect on survival was observed in grouping teeth according to demographic, behavioral, and medical parameters of patients. Teeth of female patients presented a significantly higher healing rate than males (93 vs 79%, $p = 0.006$).

Descriptive analysis of pre-, intra-, and postoperative parameters of the study cohort and bivariate results for both survival and periapical health are reported in Tables 2, 3 and 4.

The average survival time was 8.5 ± 3.2 years (for teeth that were extracted, follow-up ended on the extraction date). The average extraction time was 5.4 ± 3.2 years after treatment. In total, 27 teeth were lost during the 10-year follow-up period: 20 for non-endodontic reasons (excluded from the analysis of periapical health) of which 15 for crown/root fracture and five

Table 1 Descriptive analysis of demographic, behavioral, and medical parameters of patients included in the study cohort

Variables	Patients treated (N)
Gender	
Female	49
Male	40
Age group	
< 30	7
30–50	27
> 50	55
Smoke	
Yes	14
No	75
Bisphosphonate treatment	
Yes	10
No	79
ASA	
1	50
≥ 2	39
Total	89

Table 2 Descriptive analysis of preoperative parameters of the study cohort. Significant associations are set in *italics*

Variables	Teeth treated (<i>N</i>)	<i>N</i>	Survive % <i>N</i>	<i>P</i> value	Teeth assessed (<i>Na</i>)*	<i>N</i>	Healthy % <i>Na</i>	<i>P</i> value
Preoperative parameters								
Group of teeth				0.352				0.108
Anterior	41	38	93%		39	32	82%	
Premolar	59	52	88%		52	49	94%	
Molar	106	89	84%		95	78	82%	
Number of canals				0.199				0.181
≤ 2	100	90	90%		91	81	89%	
> 2	106	89	84%		95	78	82%	
Tooth location				0.467				0.013
Maxilla	101	86	85%		90	71	79%	
Mandible	105	93	89%		96	88	92%	
Previous restoration				0.333				0.148
None	59	55	93%		55	51	93%	
Amalgam	43	37	86%		39	31	80%	
Composite	55	45	82%		48	38	79%	
Crown	49	42	86%		44	39	89%	
Previous pain				0.038				0.847
Present	131	109	83%		114	97	85%	
Absent	75	70	93%		72	62	86%	
Initial diagnosis				0.703				0.086
Pulpitis (reversible/irreversible)	85	72	85%		75	64	85%	
Periapical lesion	42	38	90%		38	33	87%	
Previously treated without lesion	21	19	90%		19	19	100%	
Previously treated with lesion	39	32	82%		36	26	72%	
Endo-perio	3	3	100%		3	3	100%	
Prosthetic reason (Vital)	16	15	94%		15	14	93%	
Percussion test				0.432				0.385
Negative	131	112	85%		117	98	84%	
Positive	75	67	89%		69	61	88%	
Pulp vitality				0.393				0.887
Yes	92	82	89%		85	73	86%	
No	114	97	85%		101	86	85%	
Type of treatment				0.606				0.846
First treatment	146	128	88%		131	114	87%	
Retreatment	60	51	85%		55	45	82%	
PAI initial				0.764				0.186
PAI ≤ 2	132	114	86%		118	104	88%	
PAI ≥ 3	74	65	88%		68	55	81%	
Occlusal contact				0.120				0.152
Yes	204	178	87%		184	158	86%	
No	2	1	50%		2	1	50%	
Total	206	179	87%		186	159	85%	

Significant associations are highlighted with Bold typeface

Na* Total of 186 teeth include seven teeth extracted for endodontic reasons, assessed as ‘endodontically diseased’

for periodontal disease. Seven teeth were extracted for endodontic reasons (considered “endodontically diseased”).

Figure 2 shows a Kaplan-Meier survival distribution for the examined teeth; two peak times of extraction were observed:

Table 3 Descriptive analysis of intra-operative parameters of the study cohort. Significant associations are set in italics

Variables	Teeth treated (N)	N	Survived % N	P value	Teeth assessed (Na)*	N	Healthy % Na	P value
Intra-operative parameters								
N of appointments				0.070				0.904
Single	52	49	94%		50	43	86%	
Multiple	154	130	84%		136	116	85%	
Instrument type				0.108				0.845
Hand files	168	149	89%		154	132	86%	
Ni-Ti	38	30	79%		32	27	84%	
Curvature radius				0.228				0.611
Straight	98	89	91%		90	79	88%	
Moderate	98	81	83%		87	73	84%	
Severe	10	9	90%		9	7	78%	
Root filling quality				0.450				0.202
Underfilled	50	43	86%		44	34	77%	
Adequate	105	94	90%		96	85	89%	
Overfilled	51	42	82%		46	40	87%	
Voids				0.019				0.012
Yes	31	31	100%		31	22	71%	
No	175	148	85%		155	137	88%	
Localization voids				/				0.408
Coronal	6	6	100%		6	5	83%	
Middle third	19	19	100%		19	14	74%	
Apical	6	6	100%		6	3	50%	
Apical diameter				0.194				0.055
< 35	130	116	89%		120	107	89%	
35	76	63	83%		66	52	79%	
Instrument separation				0.581				0.558
Yes	2	2	100%		2	2	100%	
No	204	177	87%		184	157	85%	
Flare-up				0.411				0.011
Yes	15	12	80%		13	8	62%	
No	191	167	87%		173	151	87%	
Total	206	179	87%		186	159	85%	

Significant associations are highlighted with Bold typeface

Na* Total of 186 teeth include seven teeth extracted for endodontic reasons, assessed as ‘endodontically diseased’

within 46 months (early extractions) and over 120 months (delayed extractions). Out of the seven extracted teeth for endodontic disease, four were lost within the early peak-time period (early extractions). Concerning the extraction cause, a chi-square analysis did not identify significant differences ($p = 0.657$) between early and delayed extractions. The estimated mean survival time was shorter for extractions due to endodontic disease (45 months mean life, 95% CI 11–80 months) in comparison with fracture (74 months mean life, 95% CI 57–92 months) and periodontal disease (63 months, 95% CI 36–91 months) (Fig. 3). The lower boundary of the 95% confidence interval was 11 months for a diagnosis of endodontic pathosis, 57 for fracture, and 36 for periodontal disease.

The presence of preoperative pain, the presence of voids in the root filling material, and the occurrence of intra/postoperative complications had a significant effect on survival in a bivariate analysis (Tables. 2, 3 and 4).

Multilevel analysis revealed that the presence of preoperative pain increases the probability of extraction by more than six times in comparison with asymptomatic cases (odds ratio = 6.720; 95% confidence interval, 1.483–30.448); similarly, a maxillary location increases the probability of extraction by three times compared to a mandibular location (odds ratio = 2.950; 95% confidence interval, 1.043–8.347) (Table 5). The risk ratio was equal to 95% for maxilla/mandible and 89% for previous pain (presence/absence) denoting how survival was 5% less in the maxilla

Table 4 Descriptive analysis of postoperative parameters of the study cohort. Significant associations are set in italics

Variables	Teeth treated (<i>N</i>)	<i>N</i>	Survived % <i>N</i>	<i>P</i> value	Teeth assessed (<i>Na</i>)*	<i>N</i>	Healthy % <i>Na</i>	<i>P</i> value
Postoperative parameters								
Final restoration				0.220				0.949
Direct	67	61	91%		63	54	86%	
Crown	139	118	85%		123	105	85%	
Post placement				0.903				0.749
Yes	59	51	86%		53	46	87%	
No	147	128	87%		133	113	85%	
Complication				0.0001				0.0001
Perforation	6	6	100%		6	6	100%	
Root fracture	14	2	14%		5	1	20%	
Absent	186	171	92%		175	152	87%	
Total	206	179	87%		186	159	85%	

Significant associations are highlighted with Bold typeface

*Na** Total of 186 teeth include seven teeth extracted for endodontic reasons, assessed as ‘endodontically diseased’

and 11% less in the presence of previous pain. Deeping the type of pain, stratified analysis according to the type of pain (pulpal/periapical origin), demonstrated no significant association neither with survival ($p = 0.386$) nor with healing ($p = 0.071$ for PAI fin and $p = 0.189$ for PAI fin without extractions).

Out of the 186 surviving teeth, 159 (85%) were classified as healthy (endodontic success) at the 10-year follow-up. Tooth location, the presence of voids in the filling material, the occurrence of flare-up, and non-restorable fractures were significantly associated with a reduced success rate in the bivariate analysis (Tables. 2, 3 and 4). A multilevel analysis confirmed the following clinical variables that increase the odds of developing endodontic disease: maxillary location (odds ratio = 3.908; 95% confidence interval: 1.370–11.146), a flare-up presence (odds ratio = 9.914; 95% confidence interval, 2.388–41.163) and fracture occurrence (odds ratio = 35.412; 95% confidence interval, 3.366–372.555). Clinical relevance of tooth location, specifically, a maxillary location, reduces the healing of 14% respect mandible location (risk ratio = 0.86) as the presence of flare-up (risk ratio = 0.71) reduces the healing of 29% in comparison with its absence and fracture occurrence (risk ratio = 0.23) reduces the healing of 73% in comparison with the absence of such complications (Table 6).

Nonsignificant value using Hosmer-Lemeshow Goodness of fit test were obtained both for survival ($p = 0.674$) and healing ($p = 0.731$) indicating that the models predict the true estimate of the population.

Discussion

This cohort study described 10-year clinical outcomes of teeth after root canal treatment filled with Thermafil and evaluated,

by means of retrospective analysis, whether the success rate was comparable with the currently considered gold-standard technique in the literature. Retrospective investigations have been frequently used as the basis for further prospective and cohort studies since they allow the evaluation of a large number of variables that can affect the RCT outcome [24].

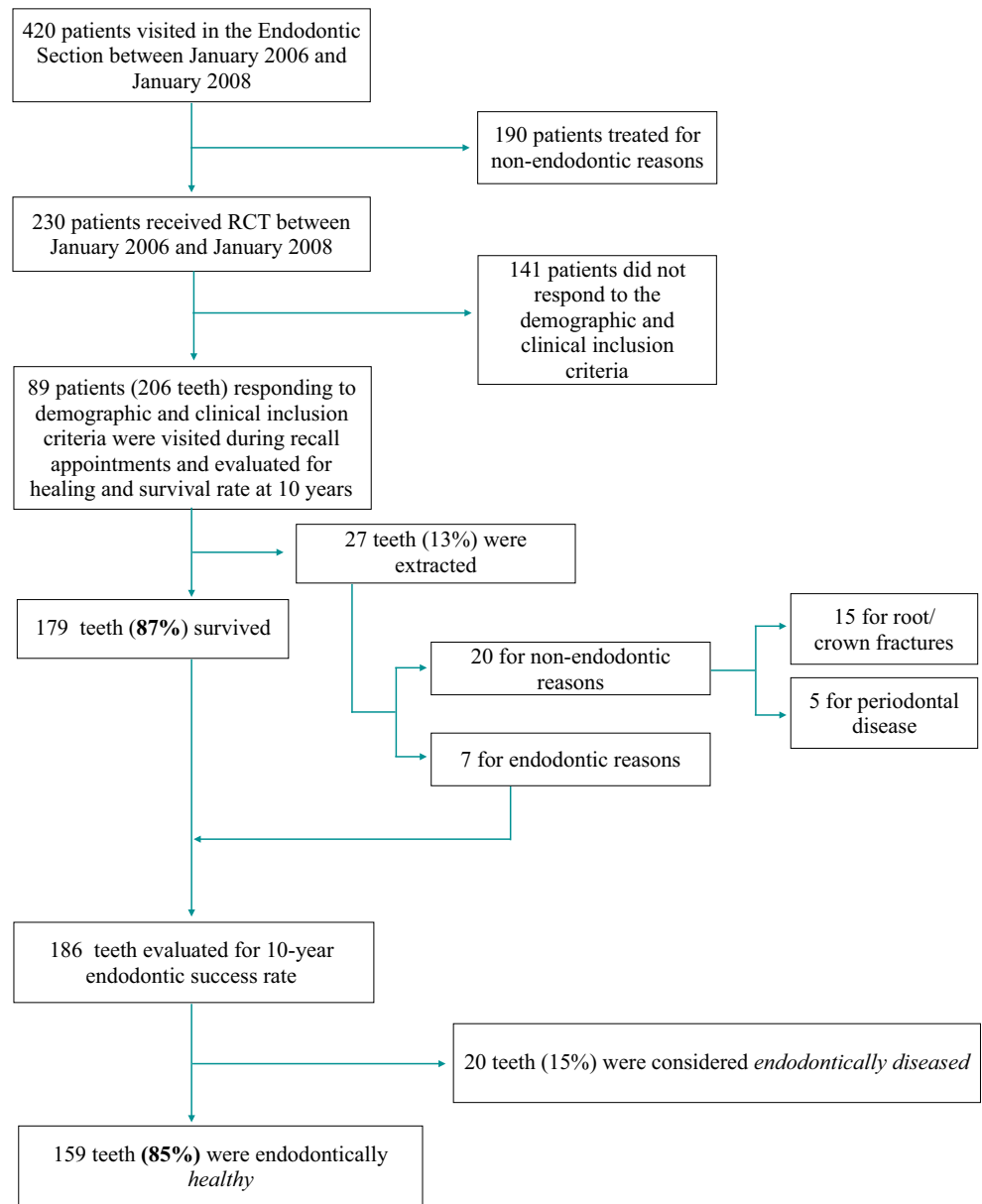
The major advantage of this kind of study is related to the availability of data, resulting in an easier and faster collection of information. Pre-, intra-, and postoperative conditions can be easily analyzed to explain the distribution of the disease during an extended observation time.

A strength of this observational investigation is the high degree of standardization of the clinical protocol of RCT and conservative restorations, performed during a postgraduate training course by operators with likely similar skills and degrees of experience. Different from most clinical studies, in order to statistically analyze the present data, a multilevel model was used to assume teeth as correlated within patients, and not as an independent entity [25, 26].

Clinical long-term follow-up studies on RCT performed with modern endodontic techniques are rare and often have an observation time of 1 or 2 years [27] while, to the best of our knowledge, this is the first clinical study aiming to evaluate the outcome of TF at 10 years. Only limited in vivo studies [4–6, 8, 10, 11] are available concerning the clinical use of TF. Moreover, the majority of these clinical studies evaluated a short/medium observation time [6–10].

In one phase of the Toronto Study project [16], the obturation technique emerged as a significant factor affecting the outcome, with a higher success rate for vertical compaction compared to lateral compaction. Another clinical study [28] suggested a significantly higher success rate for vertical compaction when compared to lateral condensation.

Fig. 1 Flowchart of the study

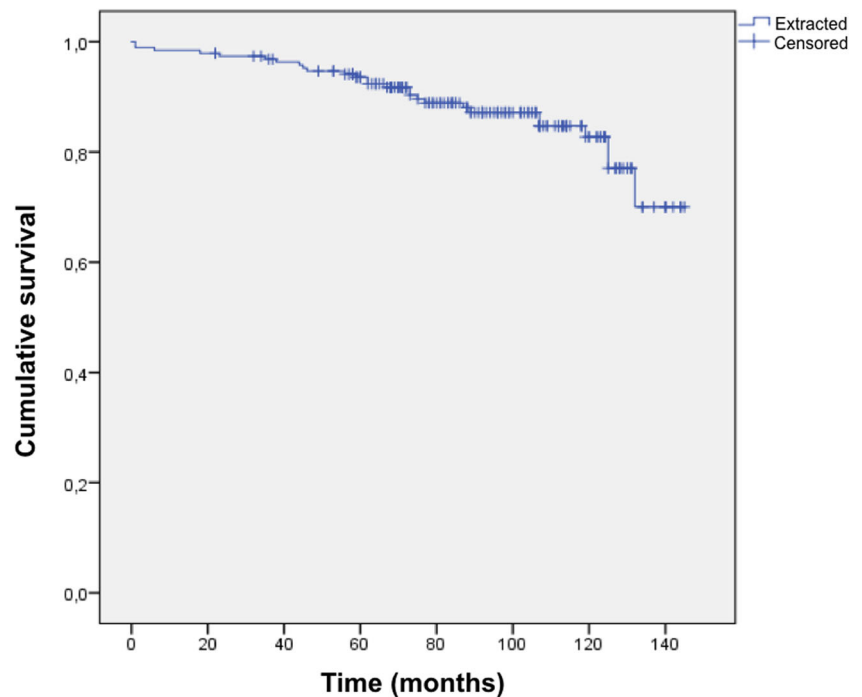


Survival

The current view in endodontic literature is to include tooth survival as an outcome descriptor. The high survival rate reported in the present dataset can be explained considering that carrier-based systems do not require load forces due to compaction of the gutta-percha and for this reason, there are no wedging effects [29]. In the present clinical study, the reported 87% long-term survival rate for teeth treated by postgraduate students is well within in the range reported by other studies with a similar follow-up period. The reported proportion surviving 10 years following treatment ranged from 75 [30] to 89% [31], with an estimated pooled proportion based on a meta-analysis of 86.7% [32].

Dammaschke et al. [33] showed that RCT conducted by students had a survival rate of 85.1% after 10 years. Mindiola et al. [34], in a retrospective epidemiological study at 10 years, reported a survival rate greater than 95%. Lumley et al. [19], in an observation time of up to 10 years, estimated a survival rate of 74% with no re-intervention. Fonzar et al. [35] reported that 93% of the root canal treated teeth survived 10-years. Burry et al. [36], in a retrospective study performed on patients with dental insurance, reported a survival rate for molars at the 10-year interval of 86%, with a significant relationship between providers and tooth type. Landys Borén [37], in a clinical study, reported that 81.5% of the teeth treated in a specialist clinic in endodontics survived at least 10 years. Moreover, they also found that only 7% of extracted teeth were related to endodontic pathosis.

Fig. 2 Kaplan-Meier survival function curve of 206 teeth treated with TF root fillings. A total of 27 teeth (13%) were extracted during the study period



Consistent with these results, we found that tooth loss is most frequently due to non-endodontic reasons, for reasons such as non-restorable fractures [30, 38]. In fact, 55% of extracted teeth (15/27) were lost for fractures, similarly to data reported previously [37, 39]. Most of the extracted teeth were lost either within 4 years after completion of root canal

treatment or over the 10-year period of the present study, highlighting the existence of two critical periods: early and delayed tooth loss. Moreover, from a Kaplan-Meier survival analysis, it emerged that more than half of extractions for the endodontic disease were performed within 46 months after the root canal treatment. This demonstrated a non-homogeneous

Fig. 3 Kaplan-Meier survival function curve of 27 teeth extracted during the study period, according to the cause loss: endodontic disease (seven teeth), non-restorable fracture (15 teeth), and periodontal disease five teeth

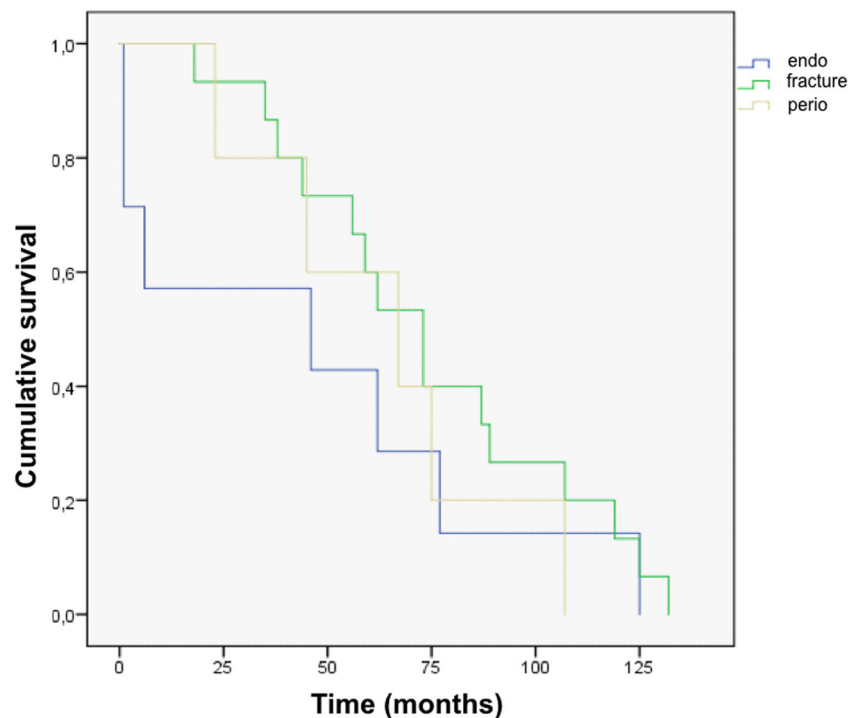


Table 5 Multilevel analysis exploring factors related to outcome “survival”

Parameter	Odds ratio	<i>P</i>	95% CI
Intercept	0.177	0.536	0.001–43.962
Maxilla (reference: mandible)	2.950	0.042	1.043–8.347
Previous pain (reference: no)	6.720	0.014	1.483–30.448

distribution of tooth loss for endodontic reasons and confirmed that extractions due to endodontic disease occur early [40, 41] even if their frequency is lower compared to other causes.

In particular, we can speculate that in order to increase the survival rate, the endodontic time margin is before 46 months. This time frame is the higher limit of the interval of the accidental events responsible for the extractions. A similar number of extractions were noticed after 120 months, the 10-year period of the present study. However, this phenomenon can be related to the physiologic aging of the tooth structure, inducing changes in tooth microstructure and chemical composition [42].

The presence of preoperative pain was found to be related to a reduction of tooth survival at 10 years; this may be explained considering that patients who have experienced preoperative pain are more inclined towards tooth extraction when symptoms reappear. This observation is consistent with a previous report [43] stating that teeth with preoperative symptomatology have a higher chance of being extracted after treatment. However, no differences were noticed concerning the cause of pain: pulpal or periapical.

Among examined preoperative conditions, pulp vitality was found to have a crucial impact on tooth survival. Teeth with preoperative non-vital pulp were associated with a lower survival chance at 10 years, probably due to a greater tooth destruction and consequently presenting larger restorations and structural weakness. Similar conclusions have been reported by Stoll et al. [31].

In contrast to other studies, present findings suggested a lower survival rate for maxillary teeth when compared to mandibular. In particular, upper premolars were found to have a reduced survival.

Table 6 Multilevel analysis exploring factors related to outcome “periapical health”

Parameter	Odds ratio	<i>P</i>	95% CI
Intercept	0.055	0.001	0.022–0.141
Maxilla (reference: mandible)	3.908	0.011	1.370–11.146
Flare-up (reference: no)	9.914	0.002	2.388–41.163
Perforation	0.232	0.524	0.003–21.191
Root fracture (reference: absence)	35.412	0.003	3.366–372.555

It was interesting to note that the variable “instrument type” (manual instrumentation versus different nickel-titanium rotary instruments) did not produce a statistically significant difference on neither success nor survival [44]. Similarly, the final restoration type (presence/absence of crown placement) and post placement did not have a significant effect on either outcome descriptor.

Success

Overall, apical health at the end of the observation period was high, with 85%. However, root canal treatments were provided in a University dental school setting and for this reason, present findings should be generalized with caution. Root canal-treated patients at dental schools may have higher success rates and better quality of root fillings [36].

A recent clinical retrospective study [45] described a similar cohort and reported a corresponding long-term survival rate but differed in the success rate (79% compared to 85% obtained with TF in the present study). However, the clinical protocols in these two studies varied concerning providers (trained specialists vs postgraduates students).

Reportedly, the Therafil method simplifies the skill of gutta-percha insertion/compaction [3] providing a long-term sealing ability when used in association with AH Plus cement [46], enabling operators with a different level of experience to produce consistently adequate results. This significant difference between two obturation methods could suggest that less-experienced operators can provide effective long-term endodontic outcomes when a carrier-based obturation technique is used.

Reference to root filling voids was not substantial in our evaluation because of the high number of false positives reported by Liang et al. [47] when a two-dimensional radiographic model was used to assess the density of root fillings.

In this study, the success rate was negatively influenced by three factors, one of which was the occurrence of inter-appointment flare-ups that occurred in 15 of the analyzed cases. This finding is consistent with Ng et al. [43] who, at 2–4 years in 750 teeth treated by endodontic postgraduate students, reported a success rate of 80%, with a less favorable prognosis in the presence of a flare-up. A possible explanation is that flare-ups may be caused by extrusion of contaminated material during canal preparation, which could stimulate a foreign body reaction, an extra-radicular infection, or can express an incomplete chemo-mechanical debridement, leading to treatment failure [43], thus resulting in a higher probability of tooth extraction.

In the present retrospective study, several prognostic factors were associated with a reduced periapical healing, such as the occurrence of complications. Complications were divided between perforations and non-restorable fractures: however, the low number of teeth with complications (20 teeth) needs to be very careful in the interpretation of the results. Perforations

were found not to significantly affect the long-term success whereas non-restorable crown/root fractures were found to have an important negative effect on the healing rate. It should be emphasized that fracture occurrence, even in the long-term analysis, is confirmed as the most important factor-inducing treatment failure [39, 48]. Our results suggested a lower success rate for maxillary teeth than for mandibular, and this could be explained by the complex anatomy of the upper teeth [49].

Conclusions

The significant clinical impact of this paper lies in the high success rate (85%) of RCT obturated with TF/AH Plus when assessed in the long term. The use of carrier-based techniques entails timesaving for clinicians while satisfying the quality of the root filling and consequently the clinical outcome as demonstrated in this study, intended as periapical healing and survival.

Funding The work was supported by the Master of Clinical Endodontology, School of Dentistry, Department of Biomedical and Neuromotor Sciences (DIBINEM), Alma Mater Studiorum University of Bologna, Bologna, Italy.

Compliance with ethical standards

Conflict of interest Chiara Pirani declares that she has no conflict of interest. Fausto Zamparini declares that he has no conflict of interest. Ove Peters serves as a consultant to Dentsply Sirona. Francesco Iacono declares that he has no conflict of interest. Maria Rosaria Gatto declares that she has no conflict of interest. Luigi Generali declares that he has no conflict of interest. Maria Giovanna Gandolfi declares that she has no conflict of interest. Carlo Prati declares that he has no conflict of interest.

Ethical approval All procedures performed in the present study were in accordance with the ethical standards of the institutional and/or national research committee and with the 1964 Helsinki declaration and its later amendments or comparable ethical standards.

Informed consent Informed consent was obtained from all individual participants included in the study.

Disclaimer Although a variety of Dentsply products have been provided to the University of Bologna as part of Dentsply's global "School Grant Program," Dentsply was neither aware of this study nor informed of the results prior to publication. Dr. Ove Peters serves as a consultant to Dentsply Sirona.

References

- European Society of Endodontology (2006) Quality guidelines for endodontic treatment: consensus report of the European Society of Endodontology. *Int Endod J* 39:921–930
- Johnson WB (1978) A new gutta-percha technique. *J Endod* 4:184–188
- Mirfendereski M, Roth K, Bing F, Dubrowski A, Carnahan H, Azarpazhooh A, Basrani B, Torneck CD, Friedman S (2009) Technique acquisition in the use of two thermoplasticized root filling methods by inexperienced dental students: a micro-CT analysis. *J Endod* 35:1512–1517
- Lipski M (2000) Comparative study on the efficacy of root canal filling with gutta-percha by lateral condensation and Thermafil obturators. *Ann Acad Med Stetin* 46:317–330
- Gagliani MA, Cerutti A, Bondesan A, Colombo M, Godio E, Giacomelli G (2004) A 24-month survey on root canal treatment performed by NiTi engine driven files and warm gutta-percha filling associated system. *Minerva Stomatol* 53:543–554
- Chu CH, Lo ECM, Cheung GSP (2005) Outcome of root canal treatment using Thermafil and cold lateral condensation filling techniques. *Int Endod J* 38:179–185
- Özer SY, Aktener BO (2009) Outcome of root canal treatment using soft-core and cold lateral compaction filling techniques: a randomized clinical trial. *J Contemp Dent Pract* 10:74–81
- Hale R, Gatti R, Glickman GN, Opperman LA (2012) Comparative analysis of carrier-based obturation and lateral compaction: a retrospective clinical outcomes study. *Int J Dent*. <https://doi.org/10.1155/2012/954675>
- Qureshi B, Munir B, Akbar I (2012) A comparison of Thermafil and lateral condensation techniques in obturation of root canal system. *Pak Oral Dental J* 32:531–534
- Demirci GK, Çalişkan MK (2016) A prospective randomized comparative study of cold lateral condensation versus core/gutta-percha in teeth with periapical lesions. *J Endod* 42:206–210
- Pirani C, Friedman S, Gatto MR, Iacono F, Tinarelli V, Gandolfi MG, Prati C (2017) Survival and periapical health after root canal treatment with carrier-based root fillings: five-year retrospective assessment. *Int Endod J* 51:e178–e188. <https://doi.org/10.1111/iej.12757>
- Brothman P (1980) A comparative study of vertical and lateral compaction of gutta-percha. *J Endod* 7:27–30
- Venturi M, Di Lenarda R, Prati C, Breschi L (2005) An in vitro model to investigate filling of lateral canals. *J Endod* 31:877–881
- Clinton K, Van Himel T (2001) Comparison of a warm gutta-percha obturation technique and lateral condensation. *J Endod* 27:692–695
- Collins J, Walker MP, Kulild J, Lee C (2006) A comparison of three gutta-percha obturation techniques to replicate canal irregularities. *J Endod* 32:762–765
- Farzaneh M, Abitbol S, Friedman S (2004) Treatment outcome in endodontics: the Toronto study. Phase I and II: orthograde retreatment. *J Endod* 30:627–633
- Ricucci D, Russo J, Rutberg M, Burleson JA, Spångberg LS (2011) A prospective cohort study of endodontic treatments of 1369 root canals: results after 5 years. *Oral Surg Oral Med Oral Pathol Oral Radiol Endod* 112:825–842
- Fransson H, Dawson VS, Frisk F, Bjørndal L, Kvist T (2016) Survival of root-filled teeth in the Swedish adult population. *J Endod* 42:216–220
- Lumley PJ, Lucarotti PSK, Burke FJT (2008) Ten-year outcome of root fillings in the general dental service in England and Wales. *Int Endod J* 41:577–585
- World Medical Association: Declaration of Helsinki (2000) Ethical principles for medical research involving human subjects. *JAMA* 284:3043–3045
- Löe H (1967) The gingival index, the plaque index and the retention index systems. *J Periodontol* 38(Suppl):610–616
- Ørstavik D, Kerekes K, Eriksen HM (1986) The periapical index: a scoring system for radiographic assessment of apical periodontitis. *Endod Dent Traumatol* 2:20–34
- Kirkevang LL, Væth M, Hörsted-Bindslev P, Bahrami G, Wenzel A (2007) Risk factors for developing apical periodontitis in a general population. *Int Endod J* 40:290–299
- Bergenholtz G, Kvist T (2013) Call for improved research efforts on clinical procedures in endodontics. *Int Endod J* 46:697–699

25. Hussein FE, Liew AKC, Ramlee RA, Abdullah D, Chong BS (2016) Factors associated with apical periodontitis: a multilevel analysis. *J Endod* 42(10):1441–1445
26. Prati C, Pirani C, Zampani F, Gatto MR, Gandolfi MG (2018) A 20-year historical prospective cohort study of root canal treatments. A Multilevel analysis. *Int Endod J* 51:955–968. <https://doi.org/10.1111/iej.12908>
27. Bergholtz G (2016) Assessment of treatment failure in endodontic therapy. *J Oral Rehabil* 43:753–758
28. Aqrabawi JA (2006) Outcome of endodontic treatment of teeth filled using lateral condensation versus vertical compaction (Schilder's technique). *J Contemp Dent Pract* 7:17–24
29. Tang W, Wu Y, Smales RJ (2010) Identifying and reducing risks for potential fractures in endodontically treated teeth. *J Endod* 36:609–617
30. Caplan DJ, Kolker J, Rivera EM, Walton RE (2002) Relationship between number of proximal contacts and survival of root canal treated teeth. *Int Endod J* 35:193–199
31. Stoll R, Betke K, Stachniss V (2005) The influence of different factors on the survival of root canal fillings: a 10-year retrospective study. *J Endod* 31:783–790
32. Ng YL, Mann V, Gulabivala K (2010) Tooth survival following non-surgical root canal treatment: a systematic review of the literature. *Int Endod J* 43:171–189
33. Dammaschke T, Steven D, Kaup M, Reiner KH (2003) Long-term survival of root-canal-treated teeth: a retrospective study over 10 years. *J Endod* 29:638–643
34. Mindiola MJ, Mickel AK, Sami C, Jones JJ, Lalumandier JA, Nelson SS (2006) Endodontic treatment in an American Indian population: a 10-year retrospective study. *J Endod* 32:828–832
35. Fonzar F, Fonzar A, Buttolo P, Worthington HW, Esposito M (2009) The prognosis of root canal therapy: a 10-year retrospective cohort study on 411 patients with 1175 endodontically treated teeth. *Eur J Oral Implantol* 2:201–208
36. Burry JC, Stover S, Eichmiller F, Bhagavatula P (2016) Outcomes of primary endodontic therapy provided by endodontic specialists compared with other providers. *J Endod* 42:702–705
37. Landys Borén D, Jonasson P, Kvist T (2015) Long-term survival of endodontically treated teeth at a public dental specialist clinic. *J Endod* 41:176–181
38. Pratt I, Aminoshariae A, Montagnese TA, Williams KA, Khalighinejad N, Mickel A (2016) Eight-year retrospective study of the critical time lapse between root canal completion and crown placement: its influence on the survival of endodontically treated teeth. *J Endod* 42:1598–1603
39. Pirani C, Iacono F, Gatto MR, Fitzgibbon RM, Chersoni S, Shemesh H, Prati C (2017) Outcome of secondary root canal treatment filled with Thermafil: a 5-year follow-up of retrospective cohort study. *Clin Oral Invest* 22:1363–1373. <https://doi.org/10.1007/s00784-017-2229-5>
40. Vire DE (1991) Failure of endodontically treated teeth: classification and evaluation. *J Endod* 17:338–342
41. Salehrabi R, Rotstein I (2004) Endodontic treatment outcomes in a large patient population in the USA: an epidemiological study. *J Endod* 30:846–850
42. Yan W, Montoya C, Øilo M, Ossa A, Paranjpe A, Zhang H, Arola D (2017) Reduction in fracture resistance of the root with aging. *J Endod* 43:1494–1498
43. Ng YL, Mann V, Gulabivala K (2011) A prospective study of the factors affecting outcomes of nonsurgical root canal treatment: part 2: tooth survival. *Int Endod J* 44:610–625
44. Peters OA, Barbakow F, Peters CI (2004) An analysis of endodontic treatment with three nickel-titanium rotary root canal preparation techniques. *Int Endod J* 37:849–859
45. Pirani C, Chersoni S, Montebugnoli L, Prati C (2015) Long-term outcome of non-surgical root canal treatment: a retrospective analysis. *Odontology* 103:185–193
46. Gandolfi MG, Parrilli AP, Fini M, Prati C, Dummer PM (2013) 3D micro-CT analysis of the interface voids associated with Thermafil root fillings used with AH Plus or a flowable MTA sealer. *Int Endod J* 46:253–263
47. Liang YH, Li G, Wesselink PR, Wu MK (2011) Endodontic outcome predictors identified with periapical radiographs and cone-beam computed tomography scans. *J Endod* 37:326–331
48. Touré B, Faye B, Kane AW, Lo CM, Niang B, Boucher Y (2011) Analysis of reasons for extraction of endodontically treated teeth: a prospective study. *J Endod* 37:1512–1515
49. Lupi-Pegurier L, Bertrand MF, Muller-Bolla M, Rocca JP, Bolla M (2002) Periapical status, prevalence and quality of endodontic treatment in an adult French population. *Int Endod J* 35:690–697

Publisher's note Springer Nature remains neutral with regard to jurisdictional claims in published maps and institutional affiliations.

A 20-year historical prospective cohort study of root canal treatments. A Multilevel analysis

C. Prati¹ , C. Pirani¹ , F. Zamparini¹ , M. R. Gatto²  & M. G. Gandolfi² 

¹Endodontic Clinical Section; and ²Laboratory of Biomaterials and Oral Pathology, Dental School, Department of Biomedical and Neuromotor Sciences, University of Bologna, Bologna, Italy

Abstract

Prati C, Pirani C, Zamparini F, Gatto MR, Gandolfi MG. A 20-year historical prospective cohort study of root canal treatments. A Multilevel analysis. *International Endodontic Journal*, 51, 955–968, 2018.

Aim To evaluate the number of healthy and functional root filled teeth of patients included in a recall programme for at least 20 years.

Methodology Teeth were root filled by a single specialist following manual canal instrumentation, lateral/vertical compaction of gutta-percha and restored with glass-ionomer cements and bonding system/composite resin. In a large percentage of teeth, a metal-ceramic crown was placed during follow-up. Patients included in the recall programme ($n = 130$) were blindly assessed both clinically and radiographically (every 2 years) to evaluate clinical symptoms and periapical status (PAI). The following variables were analysed: age, tooth location, tooth type, initial diagnosis, PAI, root filling length and coronal restoration type. Chi-square test and multilevel analysis were performed to detect variables associated with treatment functionality and disease/lesions ($P < 0.05$). A cumulative teeth survival curve was constructed by means of Kaplan–Meier using extractions as the end-point.

Results At the 20-year recall, 72 patients (31 M, 41 F; mean age 57.7 ± 8.29 years; 196 teeth)

completed the follow-up. Thirty-six patients were excluded for medical complications or died before the end of the study. Drop-outs consisted of 22 patients (17%) who did not complete the follow-up. Single metal-ceramic crowns were positioned after 4–6 months in 40% of teeth. Composite restorations were replaced with single metal-ceramic crowns during the follow-up in 53% of teeth after 8–19 years. Of 196 teeth, 155 were classified as *Survived* (79%), 128 of which (65%) were *Healthy* ($PAI \leq 2$). Thirty-nine teeth (20%) were extracted for nonendodontic reasons. Twenty-nine teeth (15%) were classified as: re-exacerbation (11 teeth; 5.6%) or persistent asymptomatic lesions (18 teeth; 9%). Only two re-exacerbated teeth were extracted. Multilevel analysis confirmed the clinical relevance of tooth type ($P = 0.001$) on *Survived* and *healthy* teeth ($P = 0.007$). Tooth location ($P = 0.0045$) and initial diagnosis ($P = 0.019$) significantly affected only *Healthy* teeth.

Conclusions Root filled teeth were more frequently extracted for non-endodontic reasons rather than for endodontic disease. The majority of teeth with adequate root fillings, adequate restorations and included in a recall programme remained functional and healthy for more than 20 years.

Keywords: long-term cohort study, periapical lesion, root canal treatment.

Received 13 July 2017; accepted 6 February 2018

Introduction

The need for long-term clinical studies on teeth following root canal treatment is essential (Tickle *et al.*

2008, Fonzar *et al.* 2009, Ng *et al.* 2011a,b, Bergenholtz & Kvist 2013, Dammaschke *et al.* 2013, Skupien *et al.* 2013, Landys Borén *et al.* 2015, Bergenholtz 2016). Such studies overcome gaps in knowledge and increase the evidence on tooth survival and health of periapical tissues. The vast majority of clinical studies on root filled teeth are based on 5–10 follow-up periods (Tickle *et al.* 2008, Fonzar *et al.* 2009, Ng *et al.* 2011a,b, Dammaschke *et al.*

Correspondence: Carlo Prati, Dental School, University of Bologna, Via San Vitale 59, 40125 Bologna, Italy (e-mail: carlo.prati@unibo.it).

2013, Skupien *et al.* 2013, Landys Borén *et al.* 2015, Pirani *et al.* 2015, 2018), revealing that root filling quality and preoperative periapical status are the most important factors related to the final outcome (Chugal *et al.* 2001, Cheung 2002, Alley *et al.* 2004, Stoll *et al.* 2005, Kirkevang *et al.* 2007, Lumley *et al.* 2008, Ng *et al.* 2011a,b, Ricucci *et al.* 2011).

Post-treatment disease associated with root filled teeth at 1–5 years have been reported in a range between 10–50% and the main causes were suggested to be the incomplete removal of debris and bacteria (Kirkevang *et al.* 2007, Tickle *et al.* 2008, Fonzar *et al.* 2009, Ng *et al.* 2011a,b, Dammaschke *et al.* 2013, Skupien *et al.* 2013, Landys Borén *et al.* 2015, Pirani *et al.* 2015, 2018). On the contrary, in long-term studies (10–20 years) it is possible that other condition may be responsible for re-exacerbation of endodontic disease and the late appearance of pathosis (Ricucci *et al.* 2011) or for tooth loss (Pirani *et al.* 2015, Bergenholtz 2016, Barborika *et al.* 2017). At long-term follow-up/evaluation (i.e. after 10–20 years) root filled teeth may be affected by many other clinical complications not directly related to the initial endodontic disease, or the development of a periapical lesion. The reasons for retreatment of previously treated canals are usually the development of a periapical lesion due to recontamination of the root canal (Molven *et al.* 2002, Fristad *et al.* 2004) and persistent periapical lesions (Nair 2006). The percentage of secondary root canal treatments after 10 years is not reported frequently (Petersson *et al.* 1991, Eckerbom *et al.* 2007, Kirkevang *et al.* 2012, Pirani *et al.* 2015). Again, the analysis of root filled teeth that survive 20 years or more may offer various clinical and technical indications to improve treatment protocols.

The aim of this historical prospective cohort study was to evaluate the long-term clinical outcome of root canal treatments performed between 1989 and 1996 on 130 patients included in a hygiene recall programme.

Material and methods

Participants and study design

A total of 404 consecutive patients (inception cohort) received one or more root canal treatment between January 1989 and January 1996. Patients were treated in three different private dental offices and in a University Department by a single operator experienced in Endodontics and Restorative Dentistry.

This report was written according to Consolidated Standards of Reporting trials guidelines for reporting clinical trials (Vandenbroucke *et al.* 2007) and following Dodson's guidelines (Dodson 2007).

The study was conducted in full accordance with ethical principles, including the Declaration of Helsinki (World Medical Association Declaration of Helsinki 2013). At the time of root canal treatment, an informed consent was signed by each participant accepting the treatment plan and associated costs and their agreement to follow the maintenance programme. Patients were considered eligible for the clinical protocol and recall programme if they fulfilled the following inclusion criteria:

1. At least one single tooth requiring a root canal treatment
2. Aged 18–65 years
3. Local geographic resident
4. Similar socio-economic condition (medium-high education and economic level) (Oakes & Rossi 2003)
5. Absence of fixed and/or removable prostheses designed to include root filled teeth.

Patients older than 65 years at the time of root canal treatment as well as affected by severe systemic disease (diabetes, Parkinson disease, cardiovascular disease etc.) were excluded from the recall programme and included in a different follow-up protocol. Moreover, all patients with multiple prosthetic restorations were excluded; these patients were followed up by the Prosthetic Clinical Section.

For these reasons, a total of 274 patients were excluded from the recall programme for the following reasons: 89 for geographical location, 40 for socio-economic issues and 75 where the root filled teeth were used as abutments for fixed/mobile prostheses and were therefore followed by the Prosthetic Clinical Section (Fig. 1).

A total of 130 patients responded to the criteria and were included in a hygienic recall programme and attended at least every 2 years. The final evaluation was performed between February 2015 and December 2016 in two private dental offices (one dental office closed and patients were recalled in the other two) and in one University Department. The study evaluated preoperative parameters (age, gender, tooth type, tooth location, initial diagnosis and initial Periapical Index (PAI) (Ørstavik *et al.* 1986), an intra-operative parameter (root filling length) and a postoperative parameter (coronal restoration type).

Preoperative diagnosis

Reasons for root canal treatment were classified into three categories on the basis of clinical and radiographic findings: pulpal disease (vital pulps underwent root canal treatment due to deep carious lesions or for prosthetic reasons), acute/chronic periapical lesions with apical radiolucency in teeth with untreated roots (periapical lesion), acute or chronic periapical lesion in previously root filled teeth (re-exacerbated endodontic lesion).

Root canal treatment protocol

Each root canal treatment was performed under rubber dam isolation, with straight-line access prepared using a diamond burs mounted on high-speed water-cooled handpieces (W&H, Bürmoos Austria). A modified step-back manual instrumentation technique was used as a routine procedure in which the coronal third was enlarged with Gates Glidden burs no. 3 and 4 at low speed. Working length (WL) was determined 0.5 mm from the radiographic apex. The apical third was prepared using stainless steel K-files (FKG, La Chaux-de-Fonds, Switzerland) with step-back increments of 1 mm. Five millilitres of 5% NaOCl (Nicolor 5; OGNA, Muggiò, Italy) and 5 mL hydrogen peroxide (OGNA), were used as root canal irrigants. Warm compacted gutta-percha points (Hygenic/Whaledent Inc., Cuyahoga Falls, OH, USA) and CRCS sealer (Hygenic/Whaledent Inc.) were used to fill the root canals. Intraoral periapical radiographs were used to evaluate WL during root canal instrumentation and filling.

Root fillings were defined as 'underfilled' if shorter than 2 mm from the radiographic apex, 'adequate' if within 2 mm from the radiographic apex, 'overfilling' if material protruded over 2 mm from the radiographic apex.

One visit root canal treatment was usually performed when treating a tooth with vital pulp. When not possible, teeth were temporarily restored with a non-eugenol provisional dressing (Cavit 3M/ESPE, Seefeld, Germany or Coltosol, Coltene AG, Altstätten, Switzerland) without the placement of intracanal medicament between appointments, in accordance with a previous study (Chong & Pitt Ford 1992).

Coronal restoration

All teeth were restored within 2–3 weeks following root filling with an adhesive permanent 2-mm thick

build-up using a light-cured glass-ionomer cement (Vitrebond, 3M, St.Paul, MN, USA) followed by the application of phosphoric acid etchant solution for 20–30 s and a bonding system (Clearfil New Bond or Clearfil Photo Bond, Kuraray Co., Ltd, Osaka, Japan) applied according to manufacturer's directions and total-etch technique. Photo-curable composite materials (Clearfil Photo Posterior, Kuraray Co., Ltd, Kyoto, Japan; Z100, 3M) were applied and photo-cured using a multilayering technique to complete the restoration. Information related to the date and type of restoration was recorded in the clinical chart of each patient. No amalgam restorations were performed at the time of the endodontic procedures. All teeth were occlusally loaded. When appropriate, approx. 4–6 months after endodontic procedures a metal-ceramic crown was prepared and cemented with a polycarboxylate cement (Heraeus Kulzer, Hanau, Germany).

A total of 11 teeth required a customized metal post following root filling, which was prepared and cemented with polycarboxylate cement before placement of the crown.

Postoperative evaluation

Periapical radiographs and clinical criteria were used to classify the final outcome. Each patient was checked during the routine recall visit and inspected by one of two examiners for coronal/crown and periapical radiographic status.

Radiographs were taken using the paralleling technique and dental intraoral films were used (Kodak, Rochester, NY, USA). Exposure time of each filling was standardized and a film holder was used (Rinn Corp., Elgin, IL, USA). Radiographic evaluation was performed pre-and post-operatively, every 2 years, when the clinical symptoms or coronal status required a further radiographic inspection and at the end-point (≥ 20 years) by one additional examiner blinded to the study. Prior to radiographic evaluation, the examiner was calibrated using well-defined instructions and reference radiographs with various types of periapical lesions. At the end-point, periapical tissues were classified on the basis of the Periapical Index score (PAI) (Ørstavik *et al.* 1986) as follows:

1. *Healthy*: absence of radiographic signs of periapical lesions (PAI score ≤ 2), and absence of clinical signs and symptoms including no tenderness to

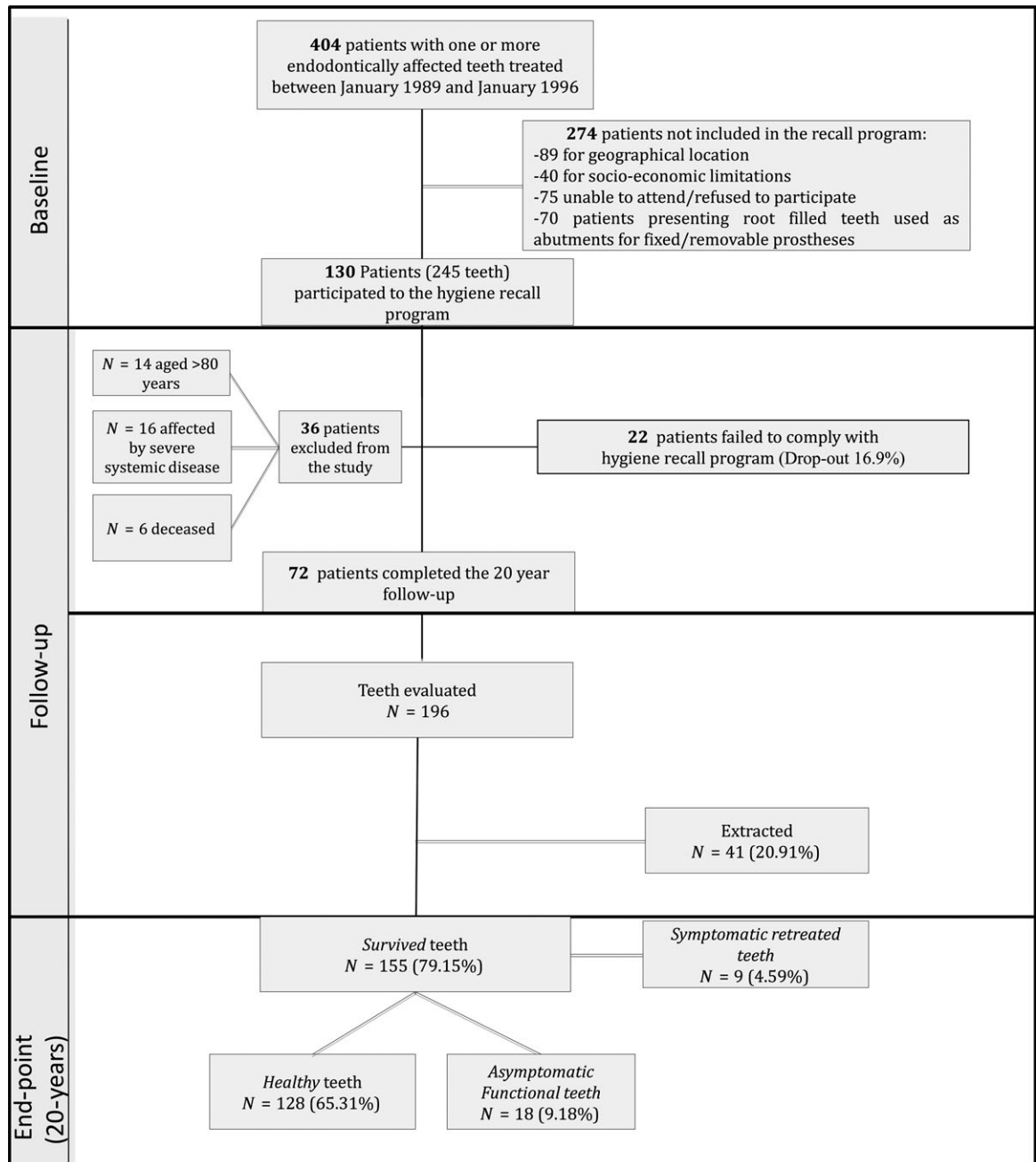


Figure 1 Flow chart of the study cohort representing the trend of root canal treatments.

percussion. *Healthy* teeth determined the success rate of the study.

2. *Endodontic lesion*: radiological signs of endodontic disease (PAI score ≥ 3) during follow-up.

Causes and time of tooth extraction were recorded and dichotomized between *non-endodontically diseased* (tooth mobility caused by deep periodontal bone pockets,

periodontal abscess, root fracture, non-restorability or external root resorption that required tooth extraction) and *symptomatic non-retreatable endodontically diseased* (recurrent symptoms, periapical abscess and fistula).

Irrespective of the number of treated roots, the tooth was always considered as the unit of evaluation and classified according to the worst value/highest

score for each root. According to the inclusion criteria, radiographs were accepted only if they possessed proper angulation and were properly processed with adequate bone tissue included below or above root apices.

Teeth were classified according to their location (maxilla/mandible) and type (anterior/posterior). The anterior group included incisors and canines, while the posterior group included premolars and molars.

Restoration quality was assessed through clinical inspection and periapical radiographs during the recall programme. Presence of fractures in the composite restoration, secondary caries around the margins of the restoration, marginal discrepancies and discoloration were indicators for a new crown placed and cemented with a polycarboxylate cement.

Crowns positioned 4–6 months after root canal treatment were defined as 'initial crowns' ($n = 78$).

A number of teeth required the preparation of a metal-ceramic crown during the recall evaluation period to reinforce teeth, for aesthetic reasons or for fracture prevention. These crowns were identified as 'Initinere crowns' ($n = 103$). At the end-point, 181/196 teeth had a metal-ceramic crown (92%).

After 20 years, teeth restored entirely with composite resins (without metal-ceramic crowns) were defined as 'GIC + Composite' ($n = 15$).

Statistical analysis

Descriptive analysis using subject and tooth as unit of analysis was performed; means (standard deviation) or proportion and bivariate tables according to the type of parameters (quantitative or qualitative) were computed. The χ^2 test was used aiming to evaluate the association between anatomical, clinical and radiographic parameters with the final status (survival and lesion).

Cox proportional hazards analysis was used to compare the distributions of time-to-event among teeth having the event for extracted teeth and for teeth that developed an endodontic lesion (evidenced by PAI ≥ 3). These two distributions were compared without the inclusion of censored values.

Bootstrapping technique was used to obtain confidence intervals and a P -value aiming to obtain a more accurate estimate, given the skewed distribution of time-to-event data. Creating a large number of datasets and computing the statistics on each of these datasets fits better to the definition of confidence interval. Bias-corrected and accelerated (BCa) 95%

confidence intervals were computed (Zelterman & Thomas 1996).

A survival curve was constructed by means of Kaplan–Meier evaluation using extraction as the end-point. Multilevel analysis was carried out at patient and tooth level. A logistic binary regression was applied as the outcome was dichotomous (survival and lesion), using as a reference category, respectively, extraction and not *Healthy*. Age and gender were set as person specific fixed effects whereas clinical parameters (tooth location, tooth type, initial diagnosis, initial PAI, root filling length and coronal restoration) as tooth specific fixed effects. α -level was a priori set at 0.05.

Results

A total of 130 patients participated in the recall programme. Of these patients, 36 were excluded due to severe medical disease that occurred during the 20-year follow-up (i.e. neurological diseases such as Parkinson, cardiovascular disease, cancer etc.) or decease. Total drop-out included 22 patients (17%) that missed one or more hygiene recall visits and were unable to participate in the 20-year follow-up (discontinuers) (Fig. 1). The final study population consisted of 72 patients (31 F, 41 M; mean age 57.7 ± 8.29 years). A total of 196 root filled teeth were clinically and radiographically evaluated as described in Fig. 1.

Teeth classified as *Survived* were 79% ($n = 155$). Including all teeth functional after 20 years, that is healthy teeth free from disease, asymptomatic teeth with a periapical lesion and teeth that required a re-intervention for endodontic reasons. Teeth classified as *Healthy* were 65% ($n = 128$) (Table 1) as illustrated in Figs 1 and 2. No instrument fractures nor canal transportation occurred.

No significant differences were observed for tooth location (maxilla versus mandible) on both *Survived* and *healthy* teeth. On the contrary, statistical differences were observed for tooth type (anterior and posterior) in both *Survived* ($P = 0.001$) and *Healthy* ($P = 0.003$) teeth. Initial (preoperative) diagnosis and initial (preoperative) PAI significantly affected the percentage of *Healthy* teeth ($P = 0.001$ and $P = 0.019$, respectively) but not *Survived* teeth.

No differences were observed in root filling length, likely due to the fact that the sample size included only a small percentage of underfilling (4%) and no overfilling. Coronal restoration type did not have a significant impact on *Survived* and *healthy* teeth, although crowns

initially placed ('initial crown' group) had the highest value of both *Survived* and *healthy* teeth.

Figure 2 describes complications/events that occurred during the 20-year follow-up: 29 teeth (15% of total teeth) had a periapical radiolucency and constituted the *endodontic lesion* group, nine (4%) were retreated due to clinical symptomatology and only two were extracted because of endodontic disease where retreatment was not feasible (1%). Eighteen teeth (9.2%) were asymptomatic and did not require further intervention (see also Tables 2 and 3).

Figure 3 shows the Kaplan–Meier cumulative survival curve of teeth followed for 20 years. The percentage of extractions was 21%, namely 41 teeth. Table 2 depicts the reasons for tooth extraction, revealing that 39 teeth were extracted for nonendodontic reasons (periodontal disease-abscess, destructive caries, root fracture) (20%). The remaining two constituted teeth extracted for endodontic reasons (endodontic abscess).

The initial crown group had the lowest percentage of extractions (14%). The *In-itinere* crown group and GIC + composite group had a similar percentage of

extracted teeth (26% and 20%, respectively) (Table 3). Apical radiolucencies usually healed after 1–2 years for small periapical lesions (PAI 3), while for larger lesions a longer period was required (2–3 years).

Initial vs final PAI scores of the entire 196 teeth are provided in Table 4. A great number of teeth with an initial periapical lesion (PAI \geq 3) had no periapical radiolucency at 20-year follow-up (PAI 1–2). Overall 73% of teeth with initial PAI 4 demonstrated a PAI 1 or 2, and in 10% of the cases an improved lesion. Teeth with an initial PAI 3 were associated with an absence of periapical lesions in 58% of cases and a stable lesion in 23%. Only one tooth had a worse PAI score (that remained asymptomatic for the entire follow-up). Interestingly, two teeth with preoperative PAI five were lost during the follow-up.

Cox proportional hazards report the time-to-event of extracted teeth, which resulted in a lower than time-to-event of teeth which developed an endodontic lesion (HR: 1.691, BCa 95%CI: 0.056–1.018, $P = 0.024$) (Fig. 4). Multilevel analysis confirmed the clinical relevance of tooth type ($P = 0.001$) on tooth survival. Anterior tooth type had greater

Table 1 Descriptive analysis of considered variables: end-point survival and periapical health are showed

	<i>n</i>	Survived teeth			Healthy teeth		
		<i>n</i>	%	<i>P</i> -value	<i>n</i>	%	<i>P</i> -value
Preoperative variables							
Tooth location							
Maxilla	116	97	83.62	0.06	82	70.61	0.122
Mandible	80	58	72.52		46	57.52	
Tooth type							
Anterior	63	59	93.63	0.001	49	77.77	0.003
Posterior	133	96	72.18		79	59.39	
Initial diagnosis							
Pulpal disease	133	103	77.44		92	69.2	
Periapical lesion	40	32	80.00	0.58	26	65.0	0.001
Re-exacerbated	23	20	86.69		10	43.5	
Initial PAI							
PAI \leq 2	133	103	77.44	0.41	91	68.42	0.019
PAI \geq 3	63	52	82.53		37	58.73	
Intra-operative variable							
Root filling length							
Adequate	187	146	78.04		121	64.71	
Overfilling	0	0	–	0.11	0	–	0.261
Underfilling	9	9	100.00		7	77.7	
Postoperative variable							
Coronal restoration type							
GIC + composite	15	12	80.0		8	53.3	
Initial crowns	78	67	85.8	0.12	62	79.8	0.139
<i>In-itinere</i> crowns	103	76	73.7		58	56.3	
Total	196	155	79.13		128	65.3	

Significant associations are expressed in bold type ($P < 0.05$).

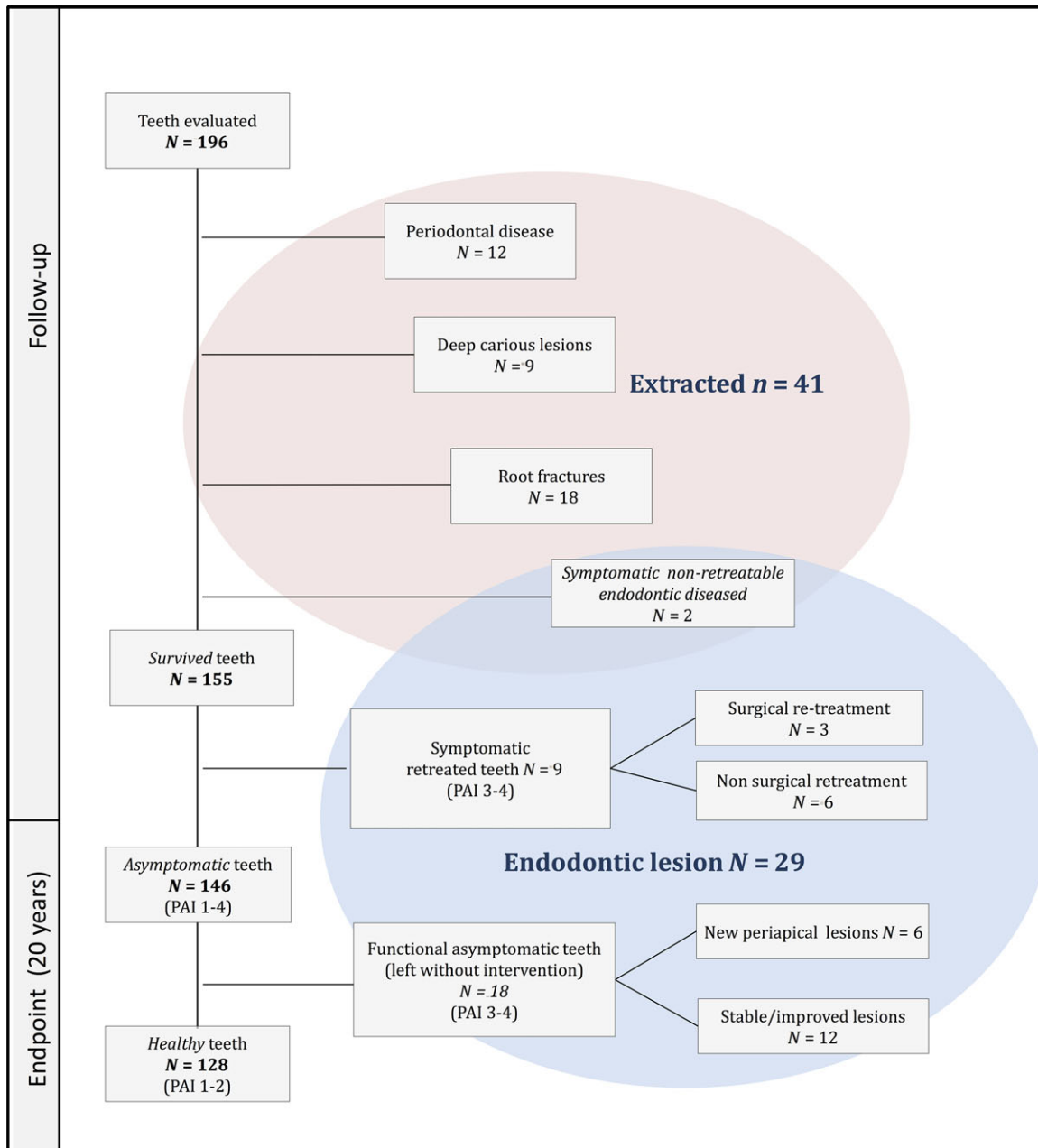


Figure 2 Flow chart of complications/events occurred during the 20-year follow-up: *Symptomatic non-retreatable endodontic diseased* teeth were included in both groups as they developed an endodontic disease and were extracted due to the impossibility of them being retained. *Functional asymptomatic teeth* left without intervention included teeth with persistent periapical lesions or a new endodontic lesion, but remained silent during the follow-up.

survival rates than posterior teeth (odds ratio = 2.54). Also, tooth location was significant ($P = 0.029$), maxillary teeth having greater survival in contrast with mandibular teeth (odds ratio = 1.568) (Table 5).

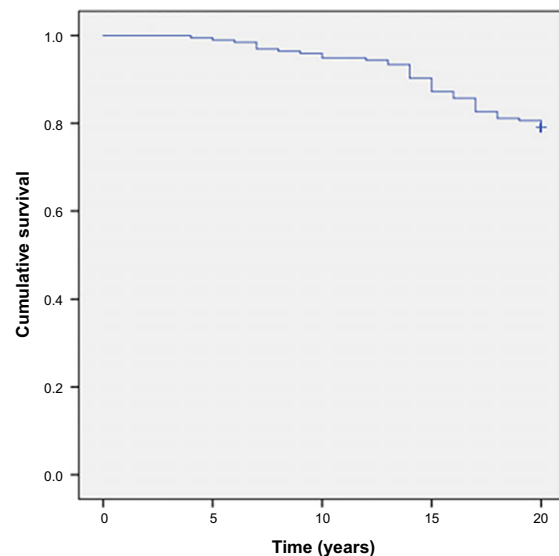
Multilevel analysis concerning the outcome *Healthy* versus endodontic lesion group (Table 6), confirmed the clinical relevance of tooth type ($P = 0.007$) and location ($P = 0.045$), with anterior type being associated with more healing in comparison with posterior

Table 2 Reasons for tooth extractions during the 20-year recall programme (n %)

Reason for extraction	n	Periodontal disease		Destructive coronal/radicular caries		Root fractures		Endodontic reasons	
		n	%	n	%	n	%	n	%
Initial diagnosis									
Pulpal disease	30	10	33.33	3	10.00	15	50.00	2	6.67
Periapical lesion	8	2	25.00	3	37.50	3	37.50	0	0
Re-exacerbated	3	0	0	3	100.00	0	0	0	0
Total	41	12	29.62	9	21.95	18	43.91	2	4.52

Table 3 Coronal restoration at the end of 20-year follow-up and final diagnosis. Presence of initial crowns, crowns application during the observational period (*In-itinere* crowns) and without crowns (GIC + composite)

Final diagnosis	n	Healthy		Endodontic lesion				Extracted	
		n	%	n	%	n	%	n	%
Coronal restoration									
GIC + composite	15	8	53.3	0	–	4	26.7	3	20.0
Initial crowns	78	62	79.5	3	3.8	2	2.6	11	14.1
<i>In-itinere</i> crowns	103	58	56.3	15	14.6	3	2.9	27	26.2
Total	196	128	65.3	18	9.2	9	4.6	41	20.9

**Figure 3** Cumulative teeth survival (Kaplan–Meier curve). At the 20-year recall, 20.92% of teeth (n = 41) had been extracted.

teeth (odds ratio = 2.983). Maxillary location improved healing (odds ratio = 1.994) in comparison with the mandible. Furthermore, an initial diagnosis of pulpal disease increased healing status in comparison with re-exacerbated diagnosis (odds ratio = 3.536) (Table 6). No significant effect was

Table 4 Cross-table of final PAI against initial PAI. EX, extractions were added as an ultimate sixth stage

Initial PAI	Final PAI (n)					
	Healthy		Endodontic lesion			Extractions
	1	2	3	4	5	
1 (n = 81)	52	13	3	2	0	11
2 (n = 52)	20	11	2	0	0	19
3 (n = 31)	14	4	7	1	0	5
4 (n = 30)	20	2	3	1	0	4
5 (n = 2)	0	0	0	0	0	2

Grey shade indicates survived teeth that developed endodontic lesion (PAI \geq 3).

Black shade indicates teeth that had been extracted.

observed for age and gender. A representative series of periapical radiographs of treated teeth included in the study are shown in Figs 5–7.

Discussion

This historical prospective cohort study describes the survival and outcome of root canal treatments performed on patients included in a hygiene recall programme after 20 years. Currently, there is a lack of evidence regarding endodontic complications/failures that may occur after such a long time span (i.e. 20 years).

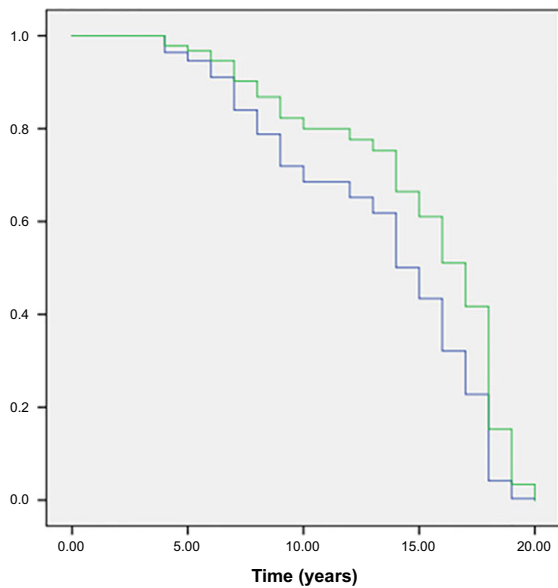


Figure 4 Cox proportional hazards analysis time-to-event curves of extractions (blue line) and endodontic lesion development (green line) during the 20-year follow-up. Teeth that first developed an endodontic lesion and that were later extracted ($n = 2$) were excluded from the analysis. The time-to-event of extracted teeth were lower than teeth which developed an endodontic lesion (HR: 1.691, BCa 95% CI: 0.056–1.018, $P = 0.024$).

Table 5 Multilevel analysis exploring factors related to *survived* teeth

Parameter	Odds ratio	<i>P</i>	95% CI
Intercept	3.618	0.078	0.866; 15.120
Tooth type (reference: posterior)			
Anterior	2.540	0.001	1.598; 4.035
Tooth location (reference: mandible)			
Maxilla	1.568	0.029	1.047; 2.349

Significant associations are expressed in bold type ($P < 0.05$).

The study demonstrated that approximately 80% of root filled teeth (and classified as *Survived*) were preserved and functional for more than 20 years. On the contrary, approximately 20% of teeth were extracted for nonendodontic reasons, such as periodontal disease (bone pocket with periodontal abscess) or caries, which resulted in root and coronal fractures.

Previous long-term studies conducted for 20 years have reported survival rates of approximately 71% (Eckerbom *et al.* 2007) and 65% (Petersson *et al.* 2016). Another study evaluated the survival of root filled molars in periodontally treated patients after

Table 6 Multilevel analysis exploring factors related to *Healthy* teeth

Parameter	Odds ratio	<i>P</i>	95% CI
Intercept	0.649	0.667	0.090; 4.683
Tooth type (reference: posterior)			
Anterior	2.983	0.007	1.355; 6.560
Tooth location (reference: mandible)			
Maxilla	1.994	0.045	1.017; 3.912
Initial diagnosis (reference: re-exacerbated)			
Pulpal disease	3.536	0.019	1.237; 10.115
Periapical lesion	2.680	0.104	0.815; 8.820

Significant associations are expressed in bold type ($P < 0.05$).

13.2 years and observed a survival rate of 71.2% and a healing rate of 65.8% (Pretzl *et al.* 2016). In a previous 10-year study (Pirani *et al.* 2015), the survival rate of root filled teeth was 87.1%. A number of studies (Tavares *et al.* 2009) report a higher risk of periodontal disease associated with root filled teeth than teeth with vital pulps (Timmerman & Van der Weijden 2006).

The Cox proportional hazard analysis revealed that extractions and endodontic disease development during the 20-year follow-up did not demonstrate a similar trend (Fig. 4). In the present study, preoperative initial diagnosis did not influence the results of *Survived* teeth ($P > 0.05$). However, it affected *Healthy* teeth ($P = 0.001$) (see Table 1). In fact, almost 86% of samples with an initial diagnosis of re-exacerbated teeth were functional and free from pain or clinical symptomatology but had the lowest percentage of *Healthy* teeth (44%).

As values reported in Table 1 were not independent (more than one tooth was treated in some patients) a multilevel analysis was also performed to confirm these results. Initial diagnosis did not have a significant influence on tooth survival ($P > 0.05$) (Table 5). Multilevel analysis demonstrated that an initial diagnosis of pulpal disease (pulpal disease group) had greater healing rates in the long-term (odds ratio = 3.536), compared to teeth that had undergone retreatment (re-exacerbated group) (Table 6). Age and gender did not have a significant influence on both tooth outcome/survival ($P > 0.05$).

The study found a number of reasons for extraction (i.e. periodontal disease/lesion, destructive caries). These reasons affected tooth survival greatly and were not correlated with the presence of an endodontic periapical lesion. Extraction due to root fracture was the most frequent; 18 of 41 teeth were extracted for these reasons (9% of the total). These data are close



Figure 5 (a) Patient treated in 1992 for pulpitis of maxillary first molar (PAI 2) and second premolar (PAI 1); preoperatively, premolar had an infiltrated resin restoration; molar had an amalgam restoration with acute sensibility and distal caries lesion. (b) 10-year follow-up (2002): premolar was restored with composite resin (GIC + Composite group) and molar with metal-ceramic crown (Initial crowns group). Root filled teeth were stable with no apical re-exacerbation. (c) 23-year follow-up (2015): both teeth are categorized as endodontically *healthy* (PAI = 1). An initial distal carious lesion was observed on the second premolar (no apical radiolucency was observed).

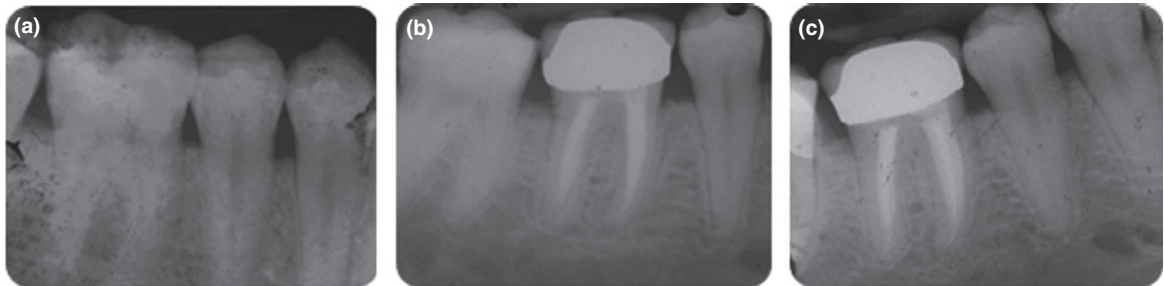


Figure 6 (a) Patient treated (1993) for pulpitis of mandibular first molar (PAI = 1). (b) One-year follow-up (1994): tooth was restored with a metal-ceramic crown (Initial crowns group) and classified as *Healthy* (PAI = 1). (c) Twenty-two-year follow-up (2015): tooth remained *healthy* with no periapical re-exacerbation.



Figure 7 (a) Patient treated in 1994 for acute periapical lesion due to infiltration of amalgam restoration of mandibular first molar (PAI = 4). (b) Eight-year follow-up (2002). No periapical lesion was present (PAI = 1). A definitive metal-ceramic crown was scheduled on this tooth (*In-itinere* crowns group) as a deterioration of composite restoration was observed clinically. (c) Twenty-two-year follow-up. Tooth was considered healthy (PAI = 1). The adjacent tooth was root filled with Thermafil and Ah Plus sealer following pulpitis.

to that of a previous 10-year study (approx. 6%) (Landys Borén *et al.* 2015). In the literature, non-restorable carious lesions are reported as the main cause of extraction of teeth after root canal treatment

(Zadik *et al.* 2008), as these teeth are more caries susceptible than nonendodontically treated teeth (Merdad *et al.* 2011) and may harbour a higher percentage of pathogenic bacteria on the surface of their larger

restorations (Merdad *et al.* 2011). Two systematic reviews (Ng *et al.* 2007, 2010) on tooth survival after root canal treatment highlighted the role of four parameters on the longevity of treated teeth: crown restoration, proximal contacts, abutment for prosthesis and tooth type, confirming the quality of coronal restoration as one of the most important factors influencing the outcome of root canal treatment. Similar findings are reported in a 20-year follow-up clinical study (Eckerbom *et al.* 2007), corroborating the importance of the maintenance of a long-term coronal seal. In the present study the coronal seal parameter did not affect the final outcome. The positioning of crowns 4–6 months after root canal treatment or during the follow-up period probably reduced the risk of leakage/root fracture/extraction. The possibility to recall patients routinely allowed the replacement of most of these restorations after 8–12 years and in some cases, a metal-ceramic crown partially substituted the composite resin restoration. Crowns were applied during the observation period (*In-itinere*) in restorations which had marginal deterioration, enamel chipping and/or secondary caries. Thus, an accurate control of coronal leakage risk was possible. A meta-analysis has stressed the role of a stable adequate restoration (Gillen *et al.* 2011).

The high survival and success rates may be accounted for by the experience of the operator who performed treatments using traditional manual canal instrumentation available at that time, and to the restorative materials used for tooth reconstruction.

No instrument fractures and other endodontic complications occurred. The use of new manual instruments and their frequent replacement probably prevented a number of (serious) problems. The adhesive materials and technique used in the present study were similar to the materials currently in use today.

Obviously, this study is influenced by the operative techniques and materials used approximately 20–25 year ago and by the understanding of adhesion at that time. The choice of the materials and techniques used to perform root canal treatments and restorations was supported by many studies (Kemp-Scholte & Davidson 1990, Prati *et al.* 1991, Van Meerbeek *et al.* 1992). The use of adhesive techniques to restore the crown of root filled teeth, such as glass-ionomer cements/base (Kemp-Scholte & Davidson 1990), total-etch dentine-enamel bonding systems and composite resins may have positively influenced the long-term survival rate, as these materials have a stable hybrid

layer morphology and bond strength–dentine adhesion (Van Meerbeek *et al.* 1992, 1993, 1994, De Munck *et al.* 2005). No amalgam restorations were used to restore root filled teeth and thus were not included in this study. Vitrebond was selected as it demonstrated the best sealing ability in Class I and II restorations *in vitro* and the highest release of fluoride compared to bonding systems (Prati & Pashley 1992). The presence of an adequate and stable coronal seal, probably provided by adhesive techniques in addition to GICs/composite restoration and metal-ceramic crown prevented the recontamination/infection of the root canal (Gillen *et al.* 2011, Ricucci & Siqueira 2011) or of the periapical bone (Ricucci *et al.* 2015).

Later development of periapical lesions on root filled teeth may often indicate either re-establishment of bacteria through coronal leakage, or reactivation of dormant bacteria within the root canal, due to ineffective irrigation/disinfection protocols (Molven *et al.* 2002) or due to the bacteria still present inside dentinal tubules and lateral canals (Vieira *et al.* 2012).

A small number of teeth (9%) had a periapical radiolucency but were asymptomatic. This condition may further consolidate the hypothesis that in some cases (i.e. retreatment) a periapical radiolucency may remain clinically silent on root filled teeth (if an adequate coronal and apical seal is present), probably as consequence of incomplete bone remineralization and persistence of fibrous tissues around the periapical sites (Nair 2006, Siqueira *et al.* 2014, Ricucci *et al.* 2016). As no cases of overfilling were present, the possibility of long-standing irritation of the root canal sealer used can be excluded.

The use of a sealer (CRCS) mainly composed of calcium-hydroxide, radiopacifier and eucalyptol may have contributed to the good biological outcome. This sealer was selected at the baseline due to its sealing properties and lower eugenol content with respect to the other available sealers (Barnett *et al.* 1989). CRCS has antimicrobial properties (Shakya *et al.* 2016) and good clinical outcomes in the short/medium-term (Waltimo *et al.* 2001), compared to traditional zinc-oxide eugenol sealers (ZOE).

One of the limits of this study is the relatively high number of patients lost due to death or medical complications. However, considering the long-term nature of the study this should be considered acceptable and inevitable. Some patients (>60–65 years) were excluded from the study as after 20 years, most of them had severe systemic diseases (i.e. cancer, uncontrolled diabetes, hypertension, Parkinson etc.) that

altered their quality of life, oral environment and saliva buffering capacity and thus increased the risk for cervical caries, periodontal disease and fractures.

Patients with multiple prosthetic restorations, as well as removable dentures were *a priori* excluded from the study follow-up as these rehabilitations may induce additional stress on root and induce/create the conditions for a higher percentage of root fractures (Sorensen & Martinoff 1985). A final limitation is that only one operator performed all the root canal treatments. Operator skills (as above mentioned) may have contributed to the high success and survival of this long-term study.

Conclusions

A high rate (80%) and *healthy* teeth (65%) was achieved for root filled more than 20 years ago. This outcome was achieved using no NiTi files, no ultrasonic activation of irrigants and no 3D radiological devices (such as CBCT), as all of the treatments were performed before their introduction. At 20 years, approx 20% of root filled teeth were lost for non-endodontic reasons, such as periodontal abscess, root fracture and deep caries lesion frequently involving subgingival root region.

The presence of a recall programme (comprising hygiene and endo-restorative control) helped to maintain a high percentage of teeth. Indeed, the percentage of late failure or re-exacerbation that required a further root canal treatment was limited and the cases where the treatment was not feasible and required tooth extraction were rare.

Acknowledgements

A special thanks to Prof. Carel Davidson (Acta University Amsterdam, The Netherlands) and Prof. Paul Lambrecht (KU Leuven University, Belgium), respectively, promotor and co-promotor of PhD thesis 'Factors affecting marginal integrity of composite restorations in human teeth' discussed by Carlo Prati at Academisch Centrum Tandheelkunde Amsterdam (Acta University) in 1992. The protocol of this study was submitted to ClinicalTrials.gov (ClinicalTrials.gov Identifier: NCT03215225).

Conflict of interest

The authors have stated explicitly that there are no conflict of interests in connection with this article.

References

- Alley BS, Kitchens GG, Alley LW, Eleazer PD (2004) A comparison of survival of teeth following treatment performed by general dentists or by specialists. *Oral Medicine Oral Pathology Oral Radiology and Endodontics* **98**, 115–8.
- Barborka BJ, Woodmansey KE, Glickman GN, Schneiderman ES, He J (2017) Long-term clinical outcome of teeth obturated with Resilon. *Journal of Endodontics* **43**, 556–60.
- Barnett F, Trope M, Rooney J, Tronstad L (1989) *In vivo* sealing ability of calcium hydroxide-containing root canal sealers. *Endodontic Dental Traumatology* **5**, 23–6.
- Bergenholtz G (2016) Assessment of treatment failure in endodontic therapy. *Journal of Oral Rehabilitation* **43**, 753–8.
- Bergenholtz G, Kvist T (2013) Call for improved research efforts on clinical procedures in endodontics. *International Endodontic Journal* **46**, 697–9.
- Cheung GSP (2002) Survival of first time nonsurgical root canal treatment performed in a dental teaching hospital. *Oral Medicine Oral Pathology Oral Radiology and Endodontics* **93**, 596–604.
- Chong BS, Pitt Ford TR (1992) The role of intracanal medication in root canal treatment. *International Endodontic Journal* **25**, 97–106.
- Chugal NM, Clive JM, Spangberg LS (2001) A prognostic model for assessment of the outcome of endodontic treatment: effect of biologic and diagnostic variables. *Oral Medicine Oral Pathology Oral Radiology and Endodontics* **91**, 342–52.
- Dammaschke T, Nykiel K, Sagheri D, Schäfer E (2013) Influence of coronal restorations on the fracture resistance of root canal-treated premolar and molar teeth: a retrospective study. *Australian Endodontic Journal* **39**, 48–56.
- De Munck J, Vargas M, Iracki J *et al.* (2005) One-day bonding effectiveness of new self-etch adhesives to bur-cut enamel and dentin. *Operative Dentistry* **30**, 39–49.
- Dodson TB (2007) A guide for preparing a patient-oriented research manuscript. *Oral Medicine Oral Pathology Oral Radiology and Endodontics* **104**, 307–15.
- Eckerbom M, Flygare L, Magnusson T (2007) A 20-year follow-up study of endodontic variables and apical status in a Swedish population. *International Endodontic Journal* **40**, 940–8.
- Fonzar F, Fonzar A, Buttolo P, Worthington HV, Esposito M (2009) The prognosis of root canal therapy: a 10-year retrospective cohort study on 411 patients with 1175 endodontically treated teeth. *European Journal of Oral Implantology* **2**, 201–8.
- Fristad I, Molven O, Halse A (2004) Nonsurgically retreated root-filled teeth – radiographic findings after 20-27 years. *International Endodontic Journal* **37**, 12–8.
- Gillen BM, Looney SW, Gu LS *et al.* (2011) Impact of the quality of coronal restoration versus the quality of root canal filling on success of root canal treatment: a

- systematic review and meta-analysis. *Journal of Endodontics* **37**, 895–902.
- Kemp-Scholte CM, Davidson CL (1990) Complete marginal seal of Class V resin composite restorations effected by increased flexibility. *Journal of Dental Research* **69**, 1240–3.
- Kirkevang LL, Væth M, Horsted-Bindslev P, Bahrami G, Wenzel A (2007) Risk factors for developing apical periodontitis in a general population. *International Endodontic Journal* **40**, 290–9.
- Kirkevang LL, Væth M, Wenzel A (2012) 10-year follow-up observations of periapical and endodontic status in a Danish population. *International Endodontic Journal* **45**, 829–39.
- Landys Borén D, Jonasson P, Kvist T (2015) Long-term survival of endodontically treated teeth at a public dental specialist clinic. *Journal of Endodontics* **41**, 176–81.
- Lumley PJ, Lucarotti PSK, Burke FJT (2008) Ten-year outcome of root fillings in the General Dental Service in England and Wales. *International Endodontic Journal* **41**, 577–85.
- Merdad K, Soonbul H, Bukhary S, Reit C, Birkhed D (2011) Caries susceptibility of endodontically treated versus non-endodontically treated teeth. *Journal of Endodontics* **37**, 139–42.
- Molven O, Halse A, Fristad I, MacDonald-Jankowski D (2002) Periapical changes following root-canal treatment observed 20–27 years postoperatively. *International Endodontic Journal* **35**, 784–90.
- Nair PNR (2006) On the causes of persistent apical periodontitis: a review. *International Endodontic Journal* **39**, 249–81.
- Ng YL, Mann V, Rahbaran S, Lewsey J, Gulabivala K (2007) Outcome of primary root canal treatment: systematic review of the literature—Part 1. Effects of study characteristics on probability of success. *International Endodontic Journal* **40**, 921–39.
- Ng YL, Mann V, Gulabivala K (2010) Tooth survival following non-surgical root canal treatment: a systematic review of the literature. *International Endodontic Journal* **43**, 171–89.
- Ng YL, Mann V, Gulabivala K (2011a) A prospective study of the factors affecting outcomes of nonsurgical root canal treatment: Part 1: Periapical health. *International Endodontic Journal* **44**, 583–609.
- Ng YL, Mann V, Gulabivala K (2011b) A prospective study of the factors affecting outcomes of non-surgical root canal treatment: Part 2: Tooth survival. *International Endodontic Journal* **44**, 610–25.
- Oakes JM, Rossi PH (2003) The measurement of SES in health research: current practice and steps toward a new approach. *Social Science & Medicine* **56**, 769–84.
- Ørstavik D, Kerekes K, Eriksen HM (1986) The periapical index: a scoring system for radiographic assessment of apical periodontitis. *Endodontic Dental Traumatology* **2**, 20–34.
- Petersson K, Håkansson R, Håkansson J, Olsson B, Wennberg A (1991) Follow-up study of endodontic status in an adult Swedish population. *Dental Traumatology* **7**, 221–5.
- Petersson K, Fransson H, Wolf E, Håkansson J (2016) Twenty-year follow-up of root filled teeth in a Swedish population receiving high-cost dental care. *International Endodontic Journal* **49**, 636–45.
- Pirani C, Chersoni S, Montebugnoli L, Prati C (2015) Long-term outcome of non-surgical root canal treatment: a retrospective analysis. *Odontology* **103**, 185–93.
- Pirani C, Friedman S, Gatto MR et al. (2018) Survival and periapical health after root canal treatment with carrier-based root fillings: five-year retrospective assessment. *International Endodontic Journal* **51**, e178–88.
- Prati C, Pashley DH (1992) Dentin wetness, permeability and thickness and bond strength of adhesive systems. *American Journal of Dentistry* **5**, 33–8.
- Prati C, Pashley DH, Montanari G (1991) Hydrostatic intrapulpal pressure and bond strength of bonding systems. *Dental Materials* **7**, 54–8.
- Pretzl B, Eickholz P, Saure D, Pfefferle T, Zeidler A, Dannewitz B (2016) Endodontic status and retention of molars in periodontally treated patients: results after 10 or more years of supportive periodontal therapy. *Journal of Clinical Periodontology* **43**, 1116–23.
- Ricucci D, Siqueira JF Jr (2011) Recurrent apical periodontitis and late endodontic treatment failure related to coronal leakage: a case report. *Journal of Endodontics* **37**, 1171–5.
- Ricucci D, Russo J, Rutberg M, Burleson JA, Spångberg LSW (2011) A prospective cohort study of endodontic treatments of 1369 root canals: results after 5 years. *Oral Medicine Oral Pathology Oral Radiology and Endodontics* **112**, 825–42.
- Ricucci D, Siqueira JF, Lopes WSP, Vieira AR, Rôças IN (2015) Extraradicular infection as the cause of persistent symptoms: a case series. *Journal of Endodontics* **41**, 265–73.
- Ricucci D, Rôças IN, Alves FRF, Loghin S, Siqueira JF Jr (2016) Apically extruded sealers: fate and influence on treatment outcome. *Journal of Endodontics* **42**, 243–9.
- Shakya VK, Gupta P, Tikku AP et al. (2016) An *in-vitro* evaluation of antimicrobial efficacy and flow characteristics for AH plus, MTA fillapex, CRCS and gutta flow 2 root canal sealer. *Journal of Clinical Diagnostic Research* **10**, 104–8.
- Siqueira JF Jr, Rôças IN, Ricucci D, Hülsmann M (2014) Causes and management of post-treatment apical periodontitis. *British Dental Journal* **216**, 305–12.
- Skupien JA, Opdam N, Winnen R et al. (2013) A practice-based study on the survival of restored endodontically treated teeth. *Journal of Endodontics* **39**, 1335–40.
- Sorensen JA, Martinoff JT (1985) Endodontically treated teeth as abutments. *Journal of Prosthetic Dentistry* **53**, 631–6.
- Stoll R, Betke K, Stachniss V (2005) The influence of different factors on the survival of root canal fillings: a 10-year retrospective study. *Journal of Endodontics* **31**, 783–90.

- Tavares PBL, Bonte E, Boukpepsi T, Siqueira JF, Lasfargues JJ (2009) Prevalence of apical periodontitis in root canal-treated teeth from an urban French population: influence of the quality of root canal fillings and coronal restorations. *Journal of Endodontics* **35**, 810–3.
- Tickle M, Milsom K, Qualtrough A, Blinkhorn F, Aggarwal VR (2008) The failure rate of NHS funded molar endodontic treatment delivered in general dental practice. *British Dental Journal* **204**, 1–6.
- Timmerman MF, Van der Weijden GA (2006) Bone level around endodontically treated teeth in periodontitis patients. *Journal of Clinical Periodontology* **33**, 620–5.
- Van Meerbeek B, Inokoshi S, Braem M, Lambrechts P, Vanherle G (1992) Morphological aspects of the resin-dentin interdiffusion zone with different dentin adhesive systems. *Journal of Dental Research* **71**, 1530–40.
- Van Meerbeek B, Willems G, Lambrechts P *et al.* (1993) Assessment by nano-indentation of the hardness and elasticity of the resin-dentin bonding area. *Journal of Dental Research* **72**, 1434–42.
- Van Meerbeek B, Peumans M, Verschuere M *et al.* (1994) Clinical status of ten dentin adhesive systems. *Journal of Dental Research* **73**, 1690–702.
- Vandenbroucke JP, von Elm E, Altman DG *et al.* (2007) Strengthening the reporting of observational studies in epidemiology (STROBE): explanation and elaboration. *PLoS Medicine* **4**, 1628–54.
- Vieira AR, Siqueira JF Jr, Ricucci D, Lopes WSP (2012) Dentinal tubule infection as the cause of recurrent disease and late endodontic treatment failure: a case report. *Journal of Endodontics* **38**, 250–4.
- Waltimo TM, Boiesen J, Eriksen HM, Ørstavik D (2001) Clinical performance of 3 endodontic sealers. *Oral Medicine Oral Pathology Oral Radiology and Endodontics* **92**, 89–92.
- World Medical Association Declaration of Helsinki (2013) Ethical principles for medical research involving human subjects. *Journal of the American Medical Association* **310**, 2191–4.
- Zadik Y, Sandler V, Bechor R, Salehrabi R (2008) Analysis of factor related to extraction of endodontically treated teeth. *Oral Medicine Oral Pathology Oral Radiology and Endodontics* **106**, 31–5.
- Zelterman D, Le CT, Louis TA (1996) Bootstrap techniques for proportional hazards models with censored observations. *Statistics and Computing* **6**, 191–9.

2.2 New biomaterials for periapical bone regeneration

After a proper root canal shaping and disinfection, root canal filling must be performed to fill and seal the canal.

Common ISO specifications (ISO 6876/2012) report that a root canal sealer must be:

- 1) Biocompatible
- 2) Bioinert
- 3) Easy to use
- 4) Non porous and insoluble
- 5) Radiopaque (> 3mm Al)
- 6) Low cost

These properties allow a proper seal at the root canal apex, in order to entomb bacteria and to prevent root canal reinfection (Peak *et al.* 2001). Conventional root canal sealers materials are bioinert, namely they do not exert a positive or negative reaction when in contact with the living tissues (ISO 6876/2012). However, cytotoxic effect and an irritating activity at the periapical bone have been described in literature. (Jung *et al.* 2011). Similarly, unhealing periapical lesions which may be attributable to residual bacterial infection at the periapical bone cannot be avoided with traditional bioinert root canal sealers (Ricucci *et al.* 2011).

Hydraulic Calcium silicates cements (CaSi), also known as MTA-based (mineral trioxide aggregate) materials (Prati & Gandolfi 2015) are a class of biomaterials which are currently revolutionizing endodontics in terms root preservation and tooth vitality. Main use of these materials was root perforation repair, root end surgery and pulp capping procedures (Prati & Gandolfi 2015, Primus *et al.* 2019). These hydraulic materials are biocompatible, bioactive (apatite forming ability) and are able to positively interact with periapical bone tissues (Gandolfi *et al.* 2013, Prati & Gandolfi 2015).

A material can be considered bioactive if it evokes a positive response from the host (BSI 2007) and a bioactive material must be able to elicit a biological response at the interface and induce the formation of a bond between tissue and the material (Hench & West 1996). The concept of bioactivity is closely correlated with biointeractivity, i.e. the ability to exchange information within a biological system (BSI 2007). This means that a bioactive material reacts chemically with body fluids in a manner compatible with the repair processes of the tissue. An artificial material can bind to living bone by the formation of a bone-like apatite layer on its surface in the body environment or by biofunctionalization (i.e. chemical and/or physical modifications of the surface of a non-biological material to make it biointeractive) (BSI 2007, Gandolfi *et al.* 2010).

Upon exposure to body fluids, CaSi forms a hydrated silica-rich layer, able to release calcium ions and increase local pH (Gandolfi *et al.* 2011). This microenvironment is particularly favorable for apatite nucleation and also provides biologically active ions for bone mineralizing cells. Ca ions are strong mineralizing cell signaling molecules, which specifically modulate osteopontin, bone morphogenetic protein-2 and alkaline phosphatase (Rashid *et al.* 2003, Ma *et al.* 2005, Sun *et al.* 2009). Si ions may provide an additional stimulus as the presence of Si is directly related to neoangiogenesis processes during early bone formation. (Wu & Chang, 2013; Zhai *et al.* 2012). Moreover, a bone bonding ability, through the formation of a bone like tissue of CaSi materials have been demonstrated in an animal model. (Gandolfi *et al.* 2017)

For these properties, CaSi materials are now used to design innovative root canal sealers and to modify their properties for the most suitable clinical use in complex endodontic cases (Prati & Gandolfi 2015, Camilleri *et al.* 2011).

In the present chapter, different recently introduced endodontic sealing materials have been characterized following a standardized protocol to assess their chemical physical and micromorphological properties and to compare these materials to traditional root canal sealing materials.

REFERENCES

BSI. Terminology for the bio-nano interface. PAS 132, 2007.

Camilleri J. Characterization of hydration products of mineral trioxide aggregate. *Int Endod J* 2008;41, 408–17.

Gandolfi MG, Iacono F, Agee K, Siboni F, Tay F, Pashley DH, Prati C. Setting time and expansion in different soaking media of experimental accelerated calcium-silicate cements and ProRoot MTA. *Oral Surg Oral Med Oral Pathol Oral Radiol Endod* 2009;108, e39–45.

Gandolfi MG, Iezzi G, Piattelli A, Prati C, Scarano A. Osteoinductive potential and bone-bonding ability of ProRoot MTA, MTA Plus and Biodentine in rabbit intramedullary model: Microchemical characterization and histological analysis. *Dent Mater.* 2017;33:e221-e238.

Gandolfi MG, Iezzi G, Piattelli A, Prati C, Scarano A. Osteoinductive potential and bone-bonding ability of ProRoot MTA, MTA Plus and Biodentine in rabbit intramedullary model: Microchemical characterization and histological analysis. *Dent Mater* 2017;33:e221-e238.

Gandolfi MG, Taddei P, Modena E, Siboni F, Prati C. Biointeractivity-related versus chemi/physisorption-related apatite precursor-forming ability of current root end filling materials. *J Biomed Mater Res B Appl Biomater.* 2013;101:1107-23.

Gandolfi MG, Taddei P, Tinti A, De Stefano Dorigo E, Rossi PL, Prati C. Kinetics of apatite formation on a calcium-silicate cement for root-end filling during ageing in physiological-like phosphate solutions. *Clin Oral Investig.* 2010;14:659-68.

Gandolfi MG, Taddei P, Tinti A, Prati C. Apatite-forming ability (bioactivity) of ProRoot MTA. *Int Endod J.* 2010;43:917-29.

Gandolfi MG, Taddei P, Tinti A, Prati C. Apatite-forming ability (bioactivity) of ProRoot MTA. *Int Endod J* 2010; 43:917-929.

- Gandolfi MG, Shah SN, Feng R, Prati C, Akintoye SO. Biomimetic Calcium- Silicate Cements Support Differentiation of Human Orofacial Mesenchymal Stem Cells. *J Endod* 2011;37, 1102–1108.
- Hench LL & West JK. Biological applications of bioactive glasses. *Life Chemistry Reports* 1996;13, 187-241.
- Jung S, Sielker S, Hanisch MR, Libricht V, Schäfer E, Dammaschke T. Cytotoxic effects of four different root canal sealers on human osteoblasts. *PLoS One* 2018;26,13.
- Ma S, Yang Y, Carnes DL, Kim K, Park S, Oh SH, Ong JL. Effects of dissolved calcium and phosphorous on osteoblast responses. *J Oral Implantol* 2005;31,61–67.
- Peak JD, Hayes SJ, Bryant ST, Dummer PM. The outcome of root canal treatment. A retrospective study within the armed forces (Royal Air Force). *Br Dent J* 2001;10;190:140-4.
- Prati C, Gandolfi MG. Calcium silicate bioactive cements: Biological perspectives and clinical applications. *Dent Mater* 2015;31:351-370.
- Primus CM, Tay FR, Niu LN. Bioactive tri/dicalcium silicate cements for treatment of pulpal and periapical tissues. *Acta Biomater* 2019;27.
- Rashid F, Shiba H, Mizuno N, Mouri Y, Fujita T, Shinohara H, Ogawa T, Kawaguchi H, Kurihara H. The effect of extracellular calcium ion on gene expression of bone-related proteins in human pulp cells. *J Endod* 2003;29 104–107.
- Ricucci D, Russo J, Rutberg M, Burleson JA, Spångberg LS. A prospective cohort study of endodontic treatments of 1369 root canals: results after 5 years. *Oral Surg Oral Med Oral Pathol Oral Radiol Endod* 2011;112, 825-842.
- Sun J, Wei L, Liu X, Li J, Li B, Wang G, Meng F. Influences of ionic dissolution products of dicalcium silicate coating on osteoblastic proliferation, differentiation and gene expression. *Acta Biomater* 2009;5:1284–1293.
- Taddei P, Tinti A, Gandolfi MG, Rossi PL, Prati C. Ageing of calcium silicate cements for endodontic use in simulated body fluids: a micro-Raman study. *J Raman Spectrosc* 2009;40:1858-1866.
- Zhai W, Lu H, Chen L, Lin X, Huang Y, Dai K, Naoki K, Chen G, Chang J. Silicate bioceramics induce angiogenesis during bone regeneration. *Acta Biomater* 2012;8:341–349.
- Wu C, Chang J. A review of bioactive silicate ceramics. *Biomed Mater* 2013;8:03200.



Available online at www.sciencedirect.com

ScienceDirect

journal homepage: www.elsevier.com/locate/gie



ORIGINAL ARTICLE/ARTICOLO ORIGINALE

CONGRESSO INTERNAZIONALE ROMA 2016 – VINCITORE PREMIO RICCARDO GARBEROGLIO

Properties of a novel polydimethylsiloxane endodontic sealer[☆]



Proprietà di un nuovo cemento endodontico a base di polidimetilsilossano

Maria Giovanna Gandolfi^{a,*}, Ashkan Karami Shabankare^a,
Fausto Zamparini^{a,b}, Carlo Prati^b

^aLaboratory of Biomaterials and Oral Pathology, School of Dentistry, Department of Biomedical and Neuromotor Sciences, University of Bologna, Bologna, Italy

^bEndodontic Clinical Section, School of Dentistry, Department of Biomedical and Neuromotor Sciences, University of Bologna, Bologna, Italy

Received 1 March 2017; accepted 13 March 2017

Available online 6 May 2017

KEYWORDS

Ion release;
Polydimethylsiloxane;
Sealing ability;
Wide apex;
Wet apex;
Guttaflow Bioseal.

Abstract

Aim: The study aims to assess sealing ability of a novel polydimethylsiloxane-based sealer in simulated wet root canals with wide apex, ion release (calcium and pH) and examine samples using ESEM.

Materials and methods: GuttaFlow bioseal, GuttaFlow2, and RoekoSeal Automix (Coltène/Whaledent Inc.) were tested.

Roots were prepared to obtain an apical diameter #40 using nickel–titanium rotary files (HyFlex CM, Coltène/Whaledent Inc.), each root was filled with single cone technique and immediately inserted into a simulated socket (filled with 0.02 mL of simulated body fluid) to reproduce the clinical conditions of a wet apical environment. Sealing ability was evaluated as fluid filtration rate at 1, 14, 28 days, and 10 months.

After 28 days in simulated body fluid, apices were examined using an Environmental Scanning Electron Microscope (ESEM).

[☆] Congresso Internazionale Roma 2016 Vincitore Premio Riccardo Garberoglio.

* Corresponding author at: Laboratory of Biomaterials and Oral Pathology, School of Dentistry, Department of Biomedical and Neuromotor Sciences, University of Bologna, Via San Vitale, 59, 40125 Bologna, BO, Italy.

E-mail: mgiovanna.gandolfi@unibo.it (M.G. Gandolfi).

Peer review under responsibility of Società Italiana di Endodonzia.



Production and hosting by Elsevier

<http://dx.doi.org/10.1016/j.gien.2017.03.002>

1121-4171/© 2017 Società Italiana di Endodonzia. Production and hosting by Elsevier B.V. This is an open access article under the CC BY-NC-ND license (<http://creativecommons.org/licenses/by-nc-nd/4.0/>).

PAROLE CHIAVE

Rilascio ionico;
 Polidimetilsilossano;
 Capacità di sigillo;
 Apici beanti;
 Guttaflow Bioseal.

Alkalinizing activity and calcium release was evaluated after 3 h and 1, 7, 14, and 28 days.

Data were analysed using Kolmogorov–Smirnov test ($p < 0.05$).

Results: Fluid filtration analysis showed no significant difference within materials. Significant difference was observed between 10 months observation and other time frames ($p < 0.05$) of the same group.

GuttaFlow bioseal showed a significantly higher alkalinising activity ($p < 0.05$). Calcium release ability showed no significant difference through time, however significant differences were observed among materials ($p < 0.05$).

Observation using ESEM at 28 days after root obturation showed the presence of the materials sealing the wide apical foramen.

Conclusions: All materials showed satisfying sealing ability. However due to low calcium release, their use is not suggested when apical barrier formation and periapical bone regeneration are needed.

© 2017 Società Italiana di Endodonzia. Production and hosting by Elsevier B.V. This is an open access article under the CC BY-NC-ND license (<http://creativecommons.org/licenses/by-nc-nd/4.0/>).

Riassunto

Obiettivi: Valutare il sigillo di un nuovo cemento endodontico a base di polidimetilsilossano in apici beanti-umidi tramite il metodo fluid-filtration, l'osservazione microscopica (ESEM), ed il rilascio ionico (calcio-pH).

Materiali e metodi: Sono stati testati i seguenti materiali: GuttaFlow bioseal, GuttaFlow2, e RoekoSeal Automix.

I campioni radicolari sono stati preparati con strumenti al nickel–titanio (HyFlexCM) fino ad un diametro apicale #40. Al fine di riprodurre le condizioni cliniche di umidità, a seguito dell'otturazione canalare con tecnica del cono singolo, i campioni sono stati inseriti in un alveolo artificiale (riempito con 0.02 mL di soluzione salina). La capacità di sigillo è stata valutata tramite fluid filtration analysis a 1, 14, 28 giorni e 10 mesi.

Dopo 28 giorni in soluzione salina, l'apice dei campioni è stato esaminato avvalendosi del Microscopio a Scansione Elettronica (ESEM).

Rilascio di calcio e pH sono stati valutati dopo 3 ore e 1, 7, 14, 28 giorni.

I dati sono stati analizzati usando il test Kolmogorov–Smirnov ($p < 0.05$).

Risultati: L'analisi del sigillo apicale ha mostrato differenze significative tra 10 mesi ed il restante dei tempi d'analisi ($p < 0.05$), mentre non ci sono state differenze tra i materiali.

GuttaFlow bioseal ha mostrato attività alcalinizzante significativamente più alta ($p < 0.05$). Ci sono state differenze statisticamente significative nel rilascio di calcio tra i materiali ($p < 0.05$), ma non tra i tempi.

L'analisi microscopica a 28 giorni dall'otturazione canalare ha confermato l'otturazione apicale da parte dei materiali.

Conclusioni: Tutti i materiali testati hanno mostrato capacità di sigillo soddisfacenti. Tuttavia a causa del ridotto rilascio di calcio riscontratosi, il loro utilizzo non è consigliato nei casi dove sia richiesta la formazione di una barriera apicale e rigenerazione ossea periapicale.

© 2017 Società Italiana di Endodonzia. Production and hosting by Elsevier B.V. Cet article est publié en Open Access sous licence CC BY-NC-ND (<http://creativecommons.org/licenses/by-nc-nd/4.0/>)

Introduction

A wide apex is a frequent manifestation of treatment failures or incomplete root development caused by traumatic events or carious lesions. In such cases, moisture management and sealing ability becomes challenging and no endodontic sealers is able to ensure a satisfying apical seal. This leads to an increasing interest of clinicians in materials able to seal in moist environment (water, blood or other fluids) and induce apical barrier formation when needed.

In treating teeth with wide and wet apices, polydimethylsiloxane (silicon)-based sealers may represent a viable alternative to calcium silicate-based sealer. They appear to have clinical benefits in terms of homogeneity and adaptation,¹ and absorb stress generated by mastication during root

flexure due to their viscosity and elasticity.² Such materials are currently being marketed by Coltene Whaledent, as: RoekoSeal Automix, GuttaFlow 2, and GuttaFlow bioseal. RoekoSeal[®] Automix is one of the first silicon-based sealer productions of Coltene Whaledent, showing satisfying in vitro sealing ability up to 1 year in wide and straight canals.³ GuttaFlow[®] 2 is an advancement of the existing GuttaFlow[®] (Coltene Whaledent) material in capsules; appearing to show a slight expansion during setting⁴ and guaranteeing a tight seal.⁵ According to in vitro studies, apical seal is either significantly improved⁶ or similar when compared to AH Plus.⁷ GuttaFlow[®] bioseal is Coltene's latest hydrophilic sealer containing gutta-percha powder, polydimethylsiloxane, and bioactive glass ceramic. GuttaFlow bioseal showed alkalinizing activity together with negligible solubility and slight

calcium release when compared to GuttaFlow 2 and RoekoSeal Automix.⁸ According to Gandolfi et al.,⁸ the incorporation of a calcium silicate component may represent an attractive strategy to obtain a bioactive biointeractive flowable guttapercha sealer for moist/bleeding apices with bone defects.

The aim of the present study was to assess the sealing ability in simulated wide wet apices and ion release activity (pH of soaking water and calcium release) of polydimethylsiloxane-based sealers. Also examining root apex using environmental scanning electron microscopy.

Materials and methods

Materials

A comparison between the following endodontic sealers was undergone: polydimethylsiloxane-based sealers (Coltène/Whaledent Inc., USA) GuttaFlow bioseal, GuttaFlow 2, and RoekoSeal Automix (Table 1).

Sealing ability

Root preparation

Human caries free single-rooted extracted teeth ($N = 36$) with oval root canals were cleaned before preservation in a distilled water solution at 4 °C for less than a month. All teeth were sectioned at 12 ± 1 mm from the apex with a water-cooled diamond bur (FG Intensive n.D2 Lugano-Grancia, Switzerland), followed by thorough examination under an operating microscope (OPMI pico Zeiss microscope, Carl Zeiss S.p.A. Milano MI, Italy) in order to confirm the presence of a single oval-shaped canal. After working length establishment at the anatomic apex, canal shaping and debridement was performed with 0.02 taper stainless steel K-files and 0.04 taper nickel–titanium rotary instrument (HyFlex CM 40/04, Coltène/Whaledent GmbH + Co. KG, Langenau, Germany) using a micro-motor (X-SMART plus, Dentsply, Maillefer Instruments Holding S.à.r.l., Switzerland). A step-down technique was performed until a size 40 apical sit was established

(Fig 1). The canals were irrigated between each instrument with 0.5 mL of ethylenediaminetetraacetic acid (EDTA, Ogna, Muggiò, Italy) and 1 mL of 5% NaOCl (Nicolor, Ogna, Muggiò, Italy). Both solution were delivered from a 30-G side-vented syringes inserted to 1 mm short of the working length, afterwards rinsed with deionized water for 1 min and dried with sterile paper points (Mynol, Milwaukee, WI, USA).

1.1.1. Root obturation and simulation of humid environment “Artificial alveolar chamber”

In order to reproduce the clinical conditions of a wet environment and apical stop, a customised wet chamber device was designed. A silicon-made support (Optosil; Heraeus Kulzer, Hanau, Germany) was specifically designed in order to create an artificial alveolus (Fig 2).⁹ A simulated body fluid solution (0.02 mL of Hank’s Balanced Salt Solution [HBSS]; Lonza, Verviers, Belgium) was added to 1/3 of the bottom of the support to simulate the presence of periapical fluid; the composition of the HBSS was (g/L) 0.4 KCl, 0.06 KH₂PO₄ anhydrous, 0.35 NaHCO₃, 8.0 NaCl, 0.05 Na₂HPO₄ anhydrous and 1.0 D-glucose.

Each root was placed inside the chamber so the periapical space and the entire root canal were filled by HBSS. The presence of fluid solution inside the root canal was assessed using paper points. The apical stop (i.e., silicon support) was 1 mm after apical foramen.

The six aforementioned endodontic sealers ($n = 6$ per group) were used for obturation. In all cases the obturation was followed by the insertion of a 40/0.06 taper gutta-percha point (Hygienic, Coltène/Whaledent Inc.) using single cone technique, after apical sit establishment (Figs. 3).

1.1.2. Fluid filtration analysis

A 18-gauge needle inserted across a plexiglass support was introduced into the coronal third of the filled root (5 mm) and the coronal side of the root was fixed to the plexiglass support with cyanoacrylate (Rocket, Corona, CA, USA) (Fig. 4). The external surface of root was coated with nail varnish to seal the root surface except for the apical orifice (2 mm apical free from varnish).¹⁰

Table 1 Tested materials and components.

Materials	Manufacturer	Lot n° and expiration date (year–month)	Ingredients
RoekoSeal Automix	Coltène/Whaledent Inc., OH, USA	6211034 (2015–12)	Polydimethylsiloxane, silicone oil, paraffin-base oil, platinum catalyst, zirconium dioxide
GuttaFlow 2	Coltène/Whaledent Inc., OH, USA	G07095 (2016–12) F51370 (2015–11)	Gutta-percha powder, polydimethylsiloxane, platinum catalyst, zirconium dioxide, cro-silver (preservative), colouring.
GuttaFlow bioseal	Coltène/Whaledent Inc., OH, USA	140814P3EZB (2016–08)	Gutta-percha powder, polydimethylsiloxane, platinum catalyst, zirconium dioxide, silver (preservative), colouring, bioactive glass ceramic

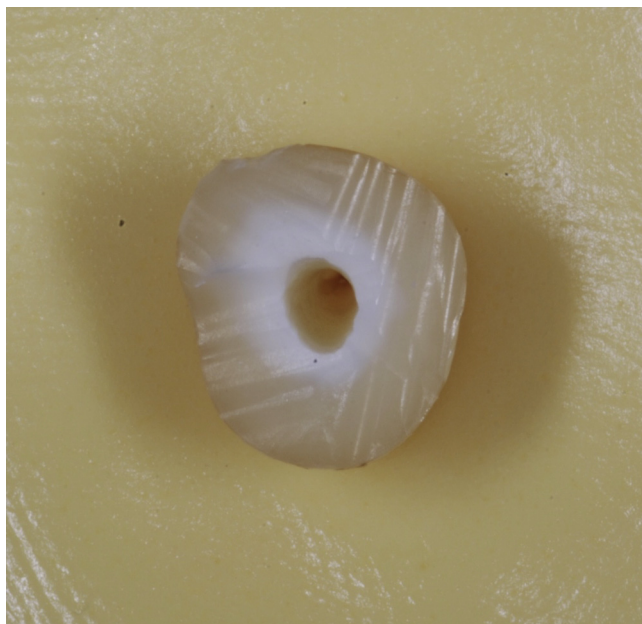


Figure 1 Sample preparation: before root obturation of samples.

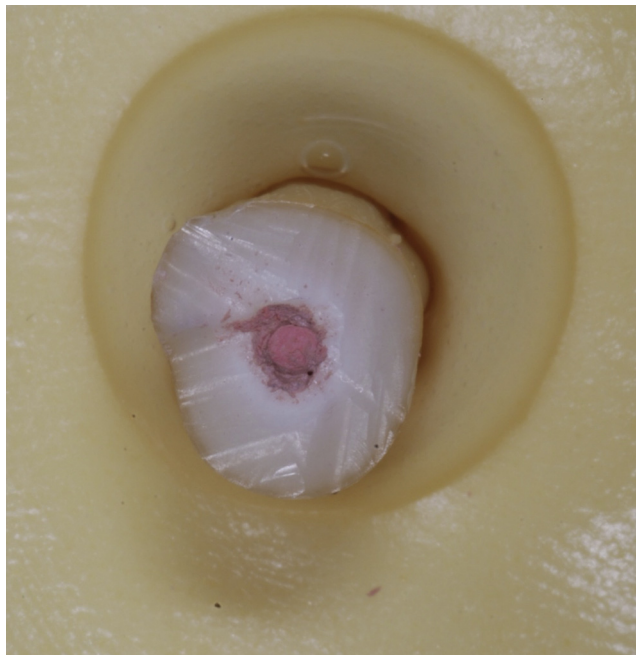


Figure 3 Sample preparation: after root obturation of samples.

A high-precision device (digital fluid flow meter) able to detect micrometric fluid movements through the apical system designed by Gandolfi was used for fluid flow rate measurements (Fig. 5). The micrometric forward movement of an air bubble inside the micro capillary was converted into a fluid flow measurement (microinfiltration) through the filled root. Each sample was connected to the device (through the 18-gauge needle) working at a hydraulic pressure of 6.9 kPa (1 psi) and contained deionised water with chlorhexidine 0.03% to prevent bacterial contamination inside the system.

The fluid filtration rate was measured (Fig. 6) after different storage of the sample in HBSS at 37 °C after 1, 14 and 28 days. Three measurements, of 4 min each, were made for individual samples, and the mean was calculated. The results

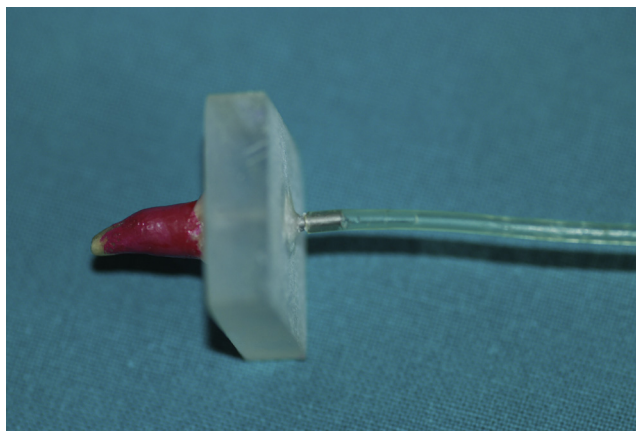


Figure 4 Before fluid filtration analysis: coronal side of root fixed to plexiglass support with cyanoacrylate.



Figure 2 Wet chamber: sample are positioned in a customised silicon wet chamber.



Figure 5 Digital fluid flow meter.

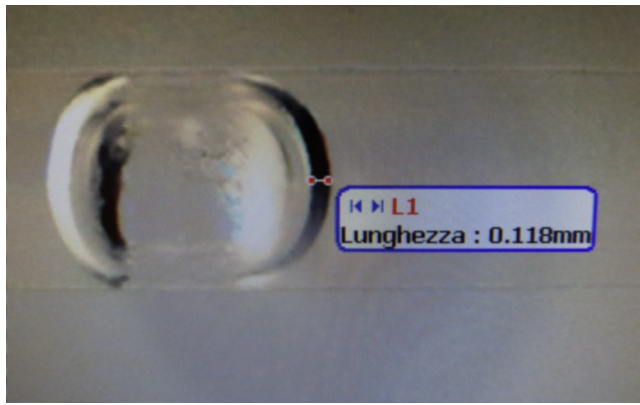


Figure 6 Measurements: Micrometric forward movement of the air bubble have been converted into micrometric fluid flow to evaluate the sealing ability.

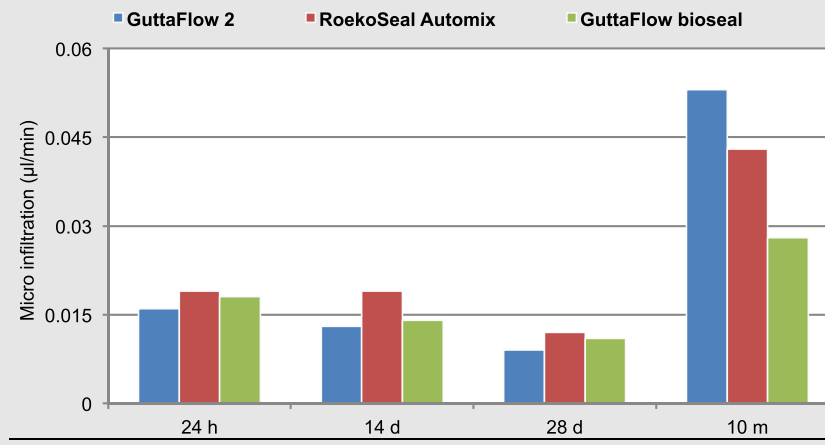
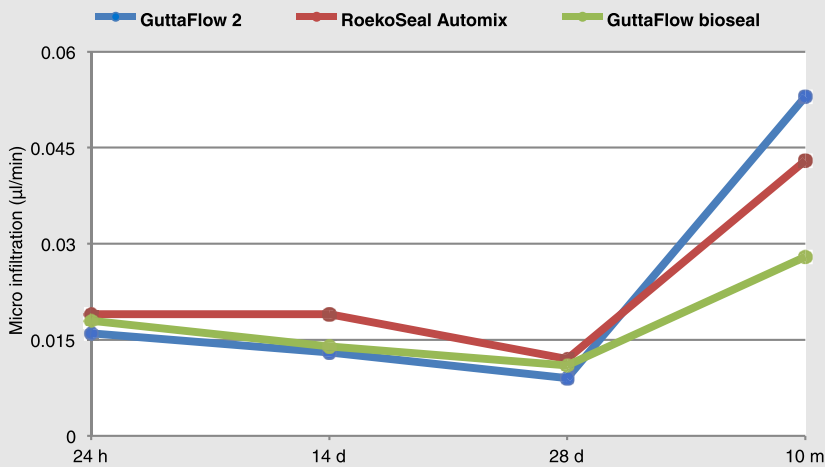
obtained as micrometers per minute were converted to $\mu\text{L}/\text{min}$.

Calcium release and alkalinising activity (pH of soaking water)

Measurements were made starting from the compaction of freshly mixed sealers into PVC (polyvinyl chloride) moulds (8.0 ± 0.1 mm diameter and 1.6 ± 0.1 mm thickness), to prepare material disks ($n = 10$ for each material). The excess was removed leaving an exposed surface area on each sample of 50.24 ± 0.01 mm². Each mould was afterwards positioned inside a cylindric polypropylene container with 3 cm height and 4 cm diameter, filled with 10 mL deionised water (pH 6.8), sealed with its appropriate stopple, and stored at 37 °C. After 3 h, 1, 7, 14, and 28 days, deionised water was collected for analysis and replaced. The collected water was analysed for pH and Ca release using a potentiometric method under

Table 2 Micro infiltration ($\mu\text{L}/\text{min}$, $n = 6$ per group) of filled root canals. Data with different superscript small letters in column (among materials) and superscript capital letters in row (within materials) are statistically different.

	24 hours	14 days	28 days	10 months
GuttaFlow 2	0.016 ± 0.010^{Aa}	0.013 ± 0.006^{Aa}	0.009 ± 0.002^{Aa}	0.053 ± 0.050^{Ba}
RoekoSeal Automix	0.019 ± 0.016^{Aa}	0.019 ± 0.008^{Aa}	0.012 ± 0.006^{Aa}	0.043 ± 0.030^{Ba}
GuttaFlow bioseal	0.018 ± 0.008^{Aa}	0.014 ± 0.010^{Aa}	0.011 ± 0.003^{Aa}	0.028 ± 0.025^{Ba}



magnetic stirring at room temperature (24 °C). Calculation was performed until the measurement stabilised.^{11,12}

The pH was measured using a selective temperature-compensated electrode (Sen Tix Sur WTW, Weilheim, Germany) connected to a multi-parameter laboratory meter (inoLab 750 WTW, Weilheim, Germany) previously calibrated with standard solutions. The amount of calcium ions was measured using a calcium probe (Calcium ion electrode, Eutech instruments Pte Ltd, Singapore) after addition of 0.200 mL (2%) of ionic strength adjuster (ISA, 4 mol/L KCl, WTW, Weilheim, Germany). Then the mean and standard deviations were calculated.

Environmental Scanning Electron Microscope (ESEM) analysis

Root samples were prepared and obturated using sealing ability’s methodology. In order to simulate a humid environment, samples were then completely immersed in simulated body fluid (HBSS) and stored at 37 °C for 28 days. Afterwards, apices were examined using an Environmental Scanning Electron Microscope (ESEM).¹³

All samples were examined uncoated at low vacuum (100 Pa), accelerating voltage of 20 kV, 8.5 mm working distance, 0.5 wt% detection level, 133 eV resolution, 100 μs amplification time. Sample apices were observed by ESEM at different magnifications ranging from 92× to 3000×.

Statistical analysis

The results were statistically analyzed. Kolmogorov–Smirnov test (*p* < 0.05) for fluid filtration, alkalinising activity and calcium release was performed.

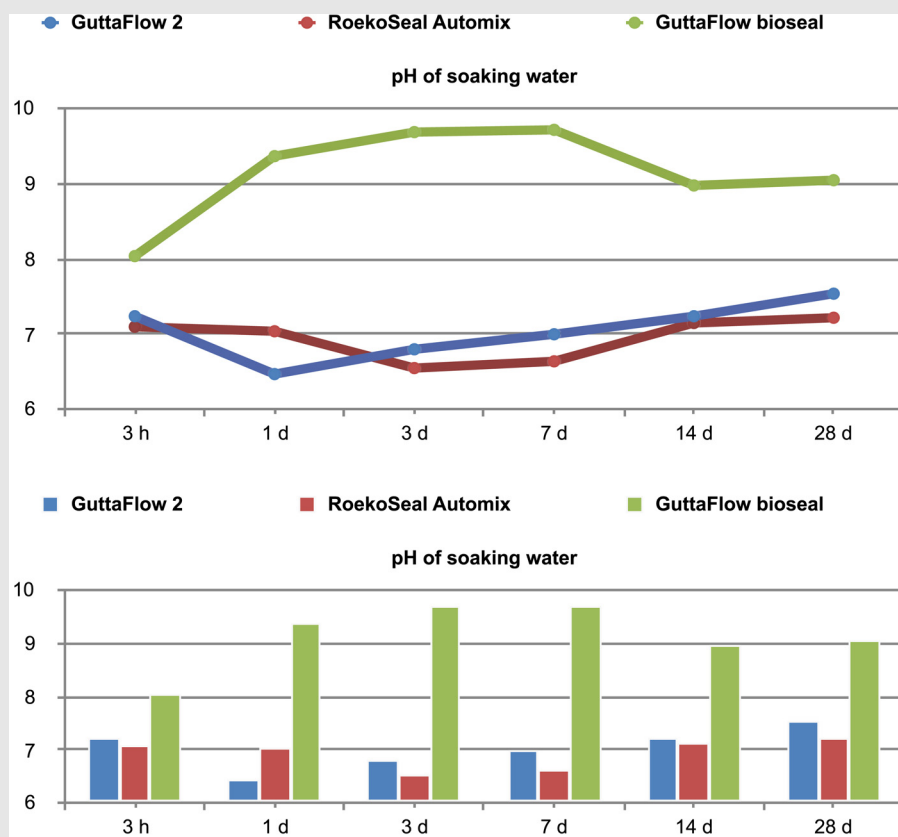
Results

Sealing ability

Table 2 reports the mean values of the fluid filtration rate (μl/min) of all groups at different storage times (1, 14, 28 days, and 10 months). No statistically significant difference was observed among the materials, while significant differences were observed when comparing 10 months observation with other time frames (*p* < 0.05). Even though at 10 months

Table 3 pH of soaking water (*n* = 10 for each material). Data followed by different superscript small letters in column (among materials) and superscript capital letters in row (within materials) are statistically different. Equal capital letters denote no statistical differences.

	3 h	1 day	3 days	7 days	14 days	28 days
GuttaFlow 2	7.24 ± 0.05 ^{Aa}	6.47 ± 0.08 ^{Aa}	6.80 ± 0.06 ^{Aa}	7.00 ± 0.09 ^{Aa}	7.24 ± 0.05 ^{Aa}	7.54 ± 0.08 ^{Aa}
RoekoSeal Automix	7.10 ± 0.09 ^{Aa}	7.04 ± 0.09 ^{Aa}	6.55 ± 0.08 ^{Aa}	6.64 ± 0.07 ^{Aa}	7.15 ± 0.10 ^{Aa}	7.22 ± 0.08 ^{Aa}
GuttaFlow bioseal	8.04 ± 0.15 ^{Ab}	9.37 ± 0.10 ^{Ab}	9.69 ± 0.07 ^{Ab}	9.72 ± 0.16 ^{Ab}	8.98 ± 0.02 ^{Ab}	9.05 ± 0.10 ^{Ab}



minimum flow of 0.028 ± 0.025 (GuttaFlow bioseal) and maximum of 0.053 ± 0.050 (GuttaFlow 2) were recorded, no significant difference was observed.

Calcium release and alkalinising activity (pH of soaking water)

Statistically significant differences were observed among materials. GuttaFlow bioseal showed a significantly higher alkalinising activity ($p < 0.05$). While no significant differences were observed among materials through time (Table 3).

Calcium release ability showed no significant difference through time, however significant differences were observed among all three materials ($p < 0.05$) (Table 4).

Environmental scanning electron microscope (ESEM) analysis

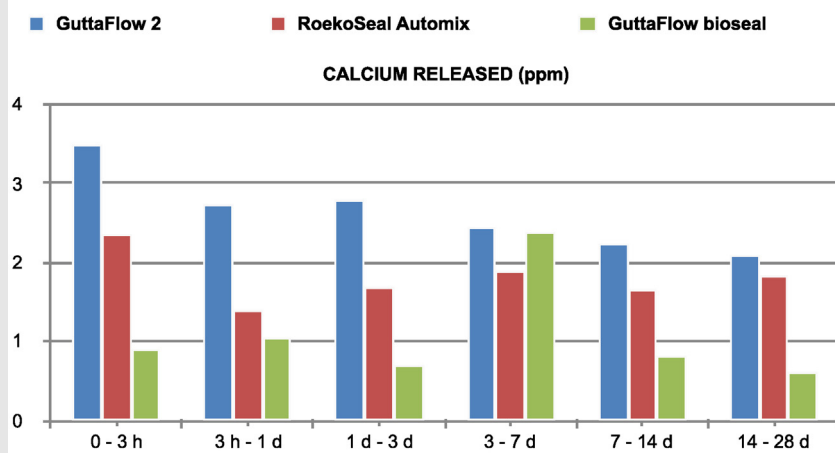
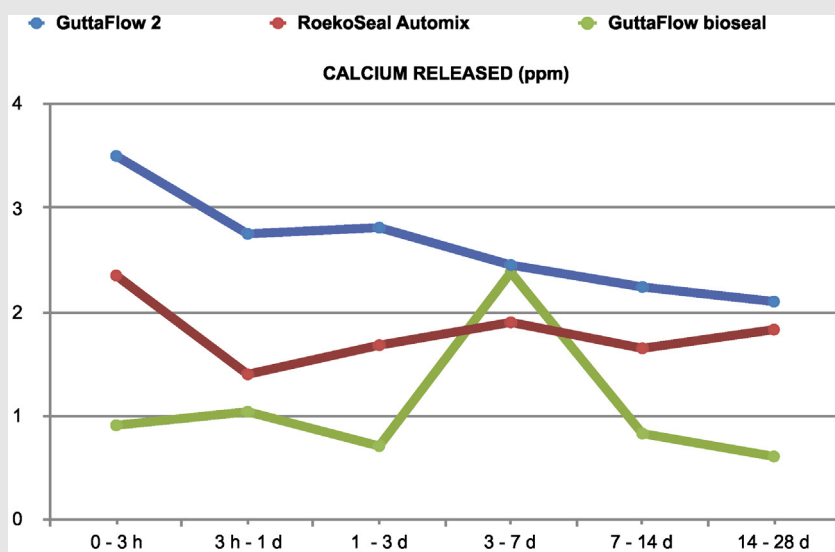
Fig. 7 reports ESEM observations of the apical region after 28 days of root obturation and immersion in simulated body fluid (HBSS). All images show the presence of the materials sealing the wide apical foramen. Higher magnification indicates morphological differences.

Discussion

Being able to estimate the material's sealing ability degradation process overtime gives the opportunity to have an insight on the severity of microbial apical leakage. Most studies conducted on sealing ability are unable to provide such

Table 4 Calcium released in ppm ($n = 10$ for each material) in 10 mL of deionized soaking water at 37 °C. Data followed by different superscript small letters in column (among materials) and superscript capital letters in row (within materials) are statistically different.

	0–3 hours	3 hours–1 day	1–3 days	3–7 days	7–14 days	14–28 days	Cumulative
GuttaFlow 2	3.50 ± 0.25^{Aa}	2.75 ± 0.41^{Aa}	2.81 ± 0.28^{Aa}	2.45 ± 0.29^{Aa}	2.24 ± 0.28^{Aa}	2.10 ± 0.29^{Aa}	$15,86 \pm 1.89^a$
RoekoSeal Automix	2.35 ± 0.11^{Ab}	1.40 ± 0.11^{Ab}	1.68 ± 0.13^{Ab}	1.90 ± 0.19^{Ab}	1.65 ± 0.17^{Ab}	1.83 ± 0.17^{Ab}	$19,81 \pm 1.11^b$
GuttaFlow bioseal	0.91 ± 0.09^{Ac}	1.04 ± 0.10^{Ac}	0.71 ± 0.04^{Ac}	2.38 ± 0.44^{Ac}	0.83 ± 0.09^{Ac}	0.61 ± 0.09^{Ac}	$6,46 \pm 1.57^c$



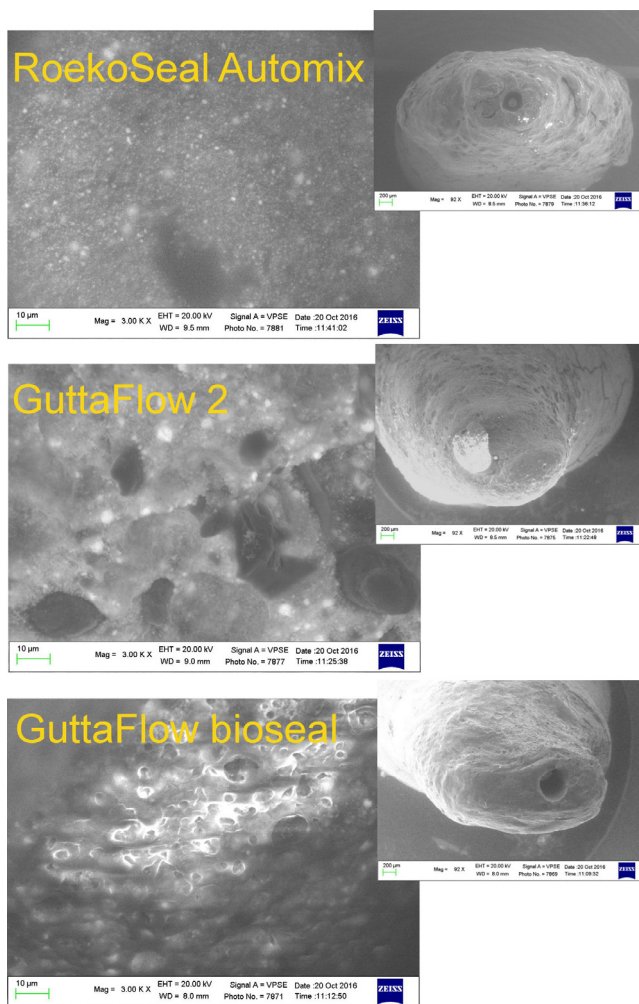


Figure 7 ESEM images showing wide apices of the roots filled with the tested materials at magnification ranging from 92 \times to 3000 \times .

information due to the fact that observations are generally restricted to 3 months. A 10-month follow-up is needed to presumably collect reliable data.

Even though fluid filtration test in wide and wet apices at 10-month follow-up showed no statistically significant difference among materials, bioglass-based GuttaFlow bioseal recorded the lowest values of apical leakage and GuttaFlow 2 the highest. Significant differences were observed at 10 months observation, possibly due to the sealer's degradation process overtime.

GuttaFlow bioseal showed satisfying alkalizing activity, being in accordance with recent findings.⁸ In this study the highest pH value ranging from 8 to 9 of GuttaFlow bioseal, suggests antibacterial activity which could be related to its bioactive glass composition. Increase in hydroxyl ions leads to low concentrations of bacteria such as the *Enterococcus faecalis*, a major responsible for root canal treatment failures.¹⁴

According to a study¹⁵ on the effect of pH and ionic strength on the reactivity of bioglass, only at pH 8 a total reconstruction of glass occurs, comprising silica and calcium phosphate rich layers formation. At higher pH (pH > 9),

selective dissolution is impeded by an immediate precipitation of a calcium phosphate layer, meanwhile at lower pH a total breakdown of glass is observed. Calcium release is observed to be slower in water, probably because of the faster formation of calcium containing salts, which are less soluble at higher pH.

When immersed in a simulated body fluid, the calcium ions released with phosphate promote the formation of a superficial layer of calcium phosphate (CaP) able to fill the open voids. On a clinical standpoint, the combination of the apatite (CaP) forming ability^{16,17} and gutta-percha could result in an improvement of the sealer's sealing ability¹⁸ due to CaP deposition.¹³

The sealing ability evaluated showed a stable behaviour up to 28 days. However, at 10 months evaluation a reduction was observed. Such significant difference might be due to the intrinsic degradation process of the materials. Even though, no statistical difference was observed at 10-month follow-up among materials, GuttaFlow bioseal's lower flow values may indicate calcium phosphate deposition,⁸ and therefore better sealing ability.

ESEM analysis at 28 days after root obturation gave insights on the wide apical sealing quality in wet environment.

Conclusions

All sealers showed adequate sealing abilities with no statistically significant difference among materials. Significant differences were observed when fluid filtration test was prolonged for 10 months, suggesting that a higher apical leakage could be related to the sealer's degradation process overtime.

Clinical relevance

GuttaFlow bioseal demonstrated to be a promising endodontic material used in teeth with wide (apical diameter 40) and wet apices. Nonetheless, low calcium release evaluated limits its adoption in conditions where an apical barrier formation is required.

Conflict of interest

The authors deny any conflict of interest related to this study.

Acknowledgments

Funds for the research were provided by the institutional research funds RFO 2015–2016 UNIBO of Prof. C Prati and Prof. MG Gandolfi.

References

1. Elayouti A, Achleithner C, Löst C, Weiger R. Homogeneity and adaptation of a new gutta-percha paste to root canal walls. *J Endod* 2005;**31**:687–90.
2. Ørstavik D, Nordahl I, Tibballs JE. Dimensional change following setting of root canal sealer materials. *Dent Mater* 2001;**17**: 512–9.

3. Wu MK, van der Sluis LW, Wesselink PR. A 1-year follow-up study on leakage of single-cone fillings with RoekoRSA sealer. *Oral Surg Oral Med Oral Pathol Oral Radiol Endod* 2006;**101**:662–7.
4. Brackett MG, Martin R, Sword J, Oxford C, Rueggeberg FA, Tay FR. Comparison of seal after obturation techniques using a polydimethylsiloxane-based root canal sealer. *J Endod* 2006;**32**:1188–90.
5. Hammad M, Qualtrough A, Silikas N. Extended setting shrinkage behavior of endodontic sealers. *J Endod* 2008;**34**:90–3.
6. Savariz A, González-Rodríguez MP, Ferrer-Luque CM. Long-term sealing ability of GuttaFlow versus Ah Plus using different obturation techniques. *Med Oral Patol Oral Cir Bucal* 2010;**15**:e936.
7. Elias I, Guimarães GO, Caldeira CL, Gavini G, Cai S, Akisue E. Apical sealing ability comparison between GuttaFlow and AH Plus: in vitro bacterial and dye leakage. *J Health Sci Inst* 2010;**28**:77–9.
8. Gandolfi MG, Siboni F, Prati C. Properties of a novel polysiloxane-guttapercha calcium silicate-bioglass-containing root canal sealer. *Dent Mater* 2016;**32**:e113–26.
9. Prati C, Siboni F, Polimeni A, Bossu M, Gandolfi MG. Use of calcium-containing endodontic sealers as apical barrier in fluid-contaminated wide-open apices. *J Appl Biomater Function Mater* 2014;**12**:263–70.
10. Gandolfi MG, Prati C. MTA and F-doped MTA cements used as sealers with warm gutta-percha. Long-term study of sealing ability. *Int Endod J* 2010;**43**:889–901.
11. Gandolfi MG, Taddei P, Modena E, Siboni F, Prati C. Biointeractivity-related versus chemi/physorption-related apatite precursor-forming ability of current root end filling materials. *J Biomed Mater Res B Appl Biomater* 2013;**101**:1107–23.
12. Gandolfi MG, Taddei P, Tinti A, De Stefano Dorigo E, Prati C. Alpha-TCP improves the apatite-formation ability of calcium-silicate hydraulic cement soaked in phosphate solutions. *Mater Sci Eng C* 2011;**31**:1412–22.
13. Gandolfi MG, Parrilli AP, Fini M, Prati C, Dummer PMH. 3D micro-CT analysis of the interface voids associated with Thermafil root fillings used with AH Plus or a flowable MTA sealer. *Int Endod J* 2013;**46**:253–63.
14. Stuart CH, Schwartz SA, Beeson TJ, Owatz CB. *Enterococcus faecalis*: its role in root canal treatment failure and current concepts in retreatment. *J Endod* 2006;**32**:93–8.
15. Cerruti M, Greenspan D, Powers K. Effect of pH and ionic strength on the reactivity of Bioglass 45S5. *Biomaterials* 2005;**26**:1665–74.
16. Parirokh M, Torabinejad M. Mineral trioxide aggregate: a comprehensive literature review. Part III. Clinical applications, drawbacks, and mechanism of action. *J Endod* 2010;**36**:400–13.
17. Prati C, Gandolfi MG. Calcium silicate bioactive cements: biological perspectives and clinical applications. *Dent Mater* 2015;**31**:351–70.
18. Iacono F, Pedulla E, Rapisarda E, Prati C, Gandolfi MG. Long-term sealing ability of 3 endodontic obturation techniques. *Gen Dent* 2014;**62**:20–3.

Properties of BioRoot RCS, a tricalcium silicate endodontic sealer modified with povidone and polycarboxylate

F. Siboni¹ , P. Taddei², F. Zamparini^{1,3}, C. Prati³ & M. G. Gandolfi¹

¹Laboratory of Biomaterials and Oral Pathology; ²Unit of Biochemistry; and ³Endodontic Clinical Section, Department of Biomedical and NeuroMotor Sciences, University of Bologna, Bologna, Italy

Abstract

Siboni F, Taddei P, Zamparini F, Prati C, Gandolfi MG. Properties of BioRoot RCS, a tricalcium silicate endodontic sealer modified with povidone and polycarboxylate. *International Endodontic Journal*, 50, e120–e136, 2017.

Aim To evaluate the chemical and physical properties of a tricalcium silicate root canal sealer containing povidone and polycarboxylate (BioRoot RCS), a calcium silicate MTA-based sealer containing a salicylate resin (MTA Fillapex), a traditional eugenol-containing sealer (Pulp Canal Sealer) and an epoxy resin-based root canal sealer (AH Plus).

Methodology Calcium release, pH, setting time, water sorption, volume of open pores, volume of impervious portion, apparent porosity and weight loss were measured. The ability to nucleate calcium phosphates (CaP) after ageing 28 days in a simulated body fluid was evaluated using ESEM-EDX and micro-Raman spectroscopy. Data were statistically analysed ($P = 0.05$) using one-way ANOVA (setting time, radiopacity, solubility, water sorption, porosity) or two-way ANOVA (ion release tests).

Results BioRoot RCS had a final setting time of 300 min and adequate radiopacity (5.2 mm Al). It

demonstrated the highest ($P < 0.05$) and more prolonged ability to release calcium ions (721 ppm at 3 h) and to increase the pH (11–12) ($P < 0.05$); B-type carbonated apatite deposits were found on aged BioRoot RCS (biointeractivity-related CaP-forming ability). A final setting time of 270 min and good calcium release (17.4 ppm at 3 h) were measured for MTA Fillapex; apatite deposits were present on aged samples. No calcium release and no alkalizing activity were measured for Pulp Canal Sealer and AH Plus; no CaP nucleation was detected on aged Pulp Canal Sealer, and some apatite deposits were found on aged AH Plus (chemi/physisorption-related CaP-deposition). Higher and significantly different ($P < 0.05$) porosity, water sorption and solubility were measured for the two calcium silicate sealers, especially for BioRoot RCS.

Conclusions BioRoot RCS had bioactivity with calcium release, strong alkalizing activity and apatite-forming ability, and adequate radiopacity.

Keywords: BioRoot RCS, calcium phosphate (apatite) nucleation, calcium release, endodontic sealer, MTA Fillapex, tricalcium silicate.

Received 27 February 2017; accepted 2 September 2017

Introduction

Endodontic therapies have benefited greatly from tricalcium silicate endodontic cements, commonly

known as MTA-based (mineral trioxide aggregate) cements. These materials are hydrophilic, require water to set and have good biocompatibility and apatite-forming ability (Gandolfi *et al.* 2013b, Prati & Gandolfi 2015).

For these reasons, several forms of tricalcium silicate cements have been developed for use as endodontic sealers (Gandolfi & Prati 2010, Camilleri 2011, Gandolfi *et al.* 2013a, Vitti *et al.* 2013a) in order to modify and tailor the properties (Camilleri

Correspondence: Maria Giovanna Gandolfi, Laboratory of Biomaterials and Oral Pathology, Department of Biomedical and NeuroMotor Sciences, Dental School, University of Bologna, Via San Vitale 59, 40125 Bologna, Italy (Tel.: +390512088176; fax: +39051225208; e-mail: mgiovanna.gandolfi@unibo.it).

2008, Gandolfi *et al.* 2009a, 2013a,b, 2014, 2015). For example, bismuth oxide, a radiopacifying agent used in most MTA-based cements, may participate in the hydration processes of tricalcium silicates particles (Camilleri 2008) as well as in tooth discoloration (Vallés *et al.* 2013), especially when in contact with sodium hypochlorite (Camilleri 2014). In the same way, organic agents improve the physical characteristics of the cement but may change its chemical and biological properties.

BioRoot RCS (Septodont, Saint-Maur-des Fosses, France) is a powder/liquid hydraulic tricalcium silicate-based cement (Gilles & Oliver 2012) marketed since February 2015 and recommended for single-cone technique or cold lateral condensation root filling. The powder contains tricalcium silicate, povidone and zirconium oxide; the liquid is an aqueous solution of calcium chloride and polycarboxylate. BioRoot RCS has been reported to induce *in vitro* the production of angiogenic and osteogenic growth factors by human periodontal ligament cells (Camps *et al.* 2015); moreover, it has a lower cytotoxicity than other conventional root canal sealers, may induce hard tissue deposition (Dimitrova-Nakov *et al.* 2015, Prüllage *et al.* 2016) and has antimicrobial activity (Arias-Moliz & Camilleri 2016).

MTA Fillapex (Angelus, Londrina, Brazil) is a salicylate resin-based sealer containing tricalcium silicate particles (MTA), silicon dioxide and bismuth oxide (Flores *et al.* 2011). It has suitable flow, good sealing and low solubility (Vitti *et al.* 2013b, Gandolfi *et al.* 2016) and is indicated for use in cold and warm root filling techniques (Viapiana *et al.* 2014). The organic component of salicylate resin reduced cell survival rates (da Silva *et al.* 2017, Rodríguez-Lozano *et al.* 2017) and increased cytotoxicity (Collado-González *et al.* 2017).

This study assessed the chemical and physical properties (i.e. calcium release, alkalizing activity, setting times, radiopacity solubility and porosity) of a tricalcium silicate-based sealer (BioRoot RCS) in comparison with a salicylate resin-based sealer (MTA Fillapex) and two other popular sealers (AH Plus, Dentsply DeTrey GmbH, Konstanz, Germany and Pulp Canal Sealer, Kerr, Scafati, Italy); moreover, the ability to nucleate calcium phosphates (CaPs) on their surface upon immersion in a simulated body fluid was evaluated using ESEM-EDX and micro-Raman analyses.

Materials and methods

Materials

The materials tested are reported in Table 1. The sealers were prepared in accordance with the manufacturers' instructions and tested immediately.

Alkalizing activity (pH) and calcium release

The freshly prepared pastes were compacted with a spatula into polyvinyl chloride moulds (8 ± 0.1 mm diameter; 1.6 ± 0.1 mm height), and the excess was removed. The filled moulds ($n = 10$ for each material) were immediately immersed in 10 mL of deionized water (pH 6.8), sealed and stored at 37 °C. The water was replaced at each end-point (3 h and 1, 3, 7, 14, 28 days), and the collected water was analysed for pH at room temperature (24 °C) by a potentiometric method under magnetic stirring using a selective electrode (Sen Tix Sur; WTW, Weilheim, Germany) connected to a multiparameter laboratory meter (inoLab 750; WTW) previously calibrated with standard solutions. The number of calcium ions released was measured using a calcium probe (calcium ion electrode; Eutech Instruments Pte Ltd, Singapore) after addition of 0.200 mL (2%) of ionic strength adjuster (ISA; 4 mol L⁻¹ KCl; WTW).

Setting times

The initial and final setting times were measured by evaluating the absence of indentation caused by Gillmore needles (ASTM C 226-07 Standard Specification for Air-Entraining Additions for Use in the Manufacture of Air-Entraining Hydraulic Cement).

The initial Gillmore tip (113.4 g weight and 2.12 mm diameter) and the final Gillmore tip (453.6 g weight and 1.06 mm diameter) were used on the cement paste stored at 37 °C and $95 \pm 5\%$ relative humidity in a mould of 10 mm diameter and 2 mm thickness.

Radiopacity

The radiopacity tests were performed in accordance with ISO 6876:2012 (dental root canal sealing materials). Completely set samples (10 ± 0.1 mm diameter; 1.0 ± 0.1 mm height) were radiographed using a radiographic unit (Myray Cefla, Imola, Italy) with a

Table 1 Materials, manufacturers and composition of the tested sealers

	Manufacturer	Lot, Exp	Composition
BioRoot RCS	Septodont, Saint Maur-des-Fosses, France	B15847, 06-17	Powder: tricalcium silicate, zirconium oxide and povidone Liquid: aqueous solution of calcium chloride and polycarboxylate
MTA Fillapex	Angelus, Londrina, Brazil	39410, 04-18	Base paste (yellow): salicylate resin, natural resin, calcium tungstate, nanoparticulated silica, pigments Catalyst paste (white): diluting resin, mineral trioxide aggregate (MTA), nanoparticulated silica, pigments
AH Plus	Dentsply DeTrey GmbH, Konstanz, Germany	1504000319, 03-17	Paste A: diepoxide, calcium tungstate, zirconium oxide, aerosil, pigment (Fe oxide) Paste B: 1-adamantane amine, <i>N,N</i> -dibenzyl-5-oxa-nonandiamine-1,9, TCD-Diamine, calcium tungstate, zirconium oxide, aerosil, silicone oil
Pulp Canal Sealer	Kerr Italia S.r.l., Salerno, Italy	5155329, 03-16	Powder: zinc oxide, silver powder, thymol iodide, dimeric acid resin Liquid: 4-allyl-2-methoxyphenol, balsam resin and water

reference aluminium step-wedge (60 mm long, 10 mm wide, thickness varying from 2 to 6 mm in 1-mm increments). The radiographic unit was set at 3 cm distance, 0.13 s exposure at 70 KVp and 8 mA. The film (Kodak dental film, Eastman Kodak Company, Carestream Health Inc., Rochester, New York, NY, USA) was processed (automatic developer, 4 min at 30 °C) and scanned (Epson Perfection V750 PRO, Jakarta, Indonesia). The radiographic density (colour intensity) data were converted (software ImageJ, Wayne Rasband, National Institutes of Health (NIH), Bethesda, MD, USA) into aluminium step-wedge equivalent thickness (mm Al). A radiopacity equal or higher than 3 mm Al is required by the ISO 6876.

Solubility, water sorption, porosity

The freshly prepared pastes were compacted into polyvinyl chloride moulds (8 ± 0.1 mm diameter; 1.6 ± 0.1 mm height), and the excess was removed. The filled moulds ($n = 10$ for each material) were placed at 37 °C and 95% relative humidity for a period of 50% longer than the setting time, that is 450 min for BioRoot RCS, 405 min for MTA Fillapex, 1860 min for AH Plus, 90 min for PCS (Siboni *et al.* 2017).

Each un moulded sample was weighed to determine the initial mass (I) and immediately immersed vertically in 20 mL of distilled water and placed at 37 °C for 24 h. The mass whilst suspended in water (S) was determined. The specimens were then removed from water, and the excess water from the surface of each sample was removed using a moistened filter paper (20 mL of distilled water dropped on a 9 cm wide 12.5-cm-long glass plate covered by a filter paper), and the saturated mass (M) was

recorded. Finally, the samples were dried at 37 °C until the weight was stable, and the final dry mass (D) was recorded. Each weight measurement was repeated three times using an analytical balance (Bel Engineering series M, Monza, Italy) and determined to the nearest 0.001 g. Mean values of the measures were reported.

The *water sorption* A ($A = [(M - D)/D] \times 100$) and the *solubility* S ($S = [(I - D)/D] \times 100$) were calculated as percentage of the original weight. ISO 4049 (polymer-based restorative materials) guidelines were applied, instead of ISO 9917 (water-based cements) or ADA specification 8 (zinc oxide eugenol cements) recommendations, as some materials (AH Plus and MTA Fillapex) are not water-based and as the residual method for the solubility of calcium silicate cements is inadequate because it only evaluates the dissolution of water-soluble components and the dispersed/disintegrated portions.

The sample volume V ($V = M - S$) was calculated in cm^3 .

Then, the *apparent porosity* P ($P = [(M - D)/V] \times 100$), that is the relation between the volume of the item and the volume of water absorbed on immersion, was calculated in percentages (following Archimedes' principle as volume of fluid displaced by the immersed sample), as previous papers on endodontic sealers (Barros *et al.* 2014, Gandolfi *et al.* 2016), pulp capping and root-end filling materials (Gandolfi *et al.* 2012, 2015, Siboni *et al.* 2017), and porous bio-ceramics (Unosson *et al.* 2015, He *et al.* 2016) proposed.

The porosity, water sorption and solubility were also measured after a period of 7 days at 37 °C and 99% RH to test the sealers after a longer setting and further hydration of the cement.

Statistical analysis

The results were analysed statistically. A two-way ANOVA followed by RM Student–Newman–Keuls test ($P < 0.05$) was performed for the ions release tests. A one-way ANOVA followed by Student–Newman–Keuls test ($P < 0.05$) was performed for setting time, radiopacity, solubility, water sorption and porosity.

Surface characterization and calcium phosphate nucleation in simulated body fluid

The freshly prepared materials were promptly immersed upright in 20 mL of HBSS (Hank's balanced salt solution, Lonza Walkersville, Inc., Walkersville, MD, USA) (Gandolfi *et al.* 2011b) and stored at 37 °C for 28 days, according to ISO 23317 (implants for surgery – *In vitro* evaluation for apatite-forming ability of implant materials) useful for predicting the *in vivo* bone-bonding ability. The HBSS was replaced weekly.

The surfaces of dry powders, freshly mixed materials and samples soaked in HBSS were examined using an environmental scanning electron microscope (ESEM, Zeiss EVO 50; Carl Zeiss, Oberkochen, Germany) connected to a secondary electron detector for elemental dispersive X-ray microanalysis (EDX; Oxford Instruments, Abingdon, UK). The freshly mixed samples and those soaked in HBSS were examined by ESEM in wet conditions without any other preparation. Operative conditions were low vacuum (100 Pascal), accelerating voltage of 20 kV, working distance 8.5 mm, 0.5 wt% detection level, 133 eV resolution, amplification time 100 μ s, and measuring time of 60 s for spectra. EDX provided microchemical spectra and semiquantitative compositional data (weight % and atomic % of the elemental composition).

Micro-Raman spectra were measured on the surface of the fresh samples as well as on the single components (i.e. before mixing) and after ageing in HBSS for 28 days (Gandolfi *et al.* 2011b). The spectra were obtained using a Jasco NRS-2000C instrument in back-scattering conditions with 4 cm^{-1} spectral resolution, using the 532-nm Green Diode Pumped Solid State (DPSS) Laser Driver (RgBLase LLC, USA) with a power of ca. 25 mW, properly filtered. A 160 K cooled digital CCD (Spec-10: 100B, Roper Scientific Inc.). A microscope of 100 \times magnification with a confocal pinhole with an aperture

diameter of 3000 μ m was used. The spectra of the aged samples were measured also using a confocal pinhole with an aperture diameter of 200 μ m, to obtain signals from a limited in-depth region. All the Raman measurements were made in a fully nondestructive way, without any sample manipulation. All the reported spectra are an average of at least five measurements.

Results

Alkalinizing activity (pH) and calcium release

BioRoot RCS raised the pH of the immersion water significantly more ($P < 0.05$) than the other materials for the first 14 days of immersion (Table 2). Its pH was approx. 11–12 for the first 14 days, then after 28 days the pH decreased to 8.7, but alkalinization was still present; in particular, the alkalinizing activity was significantly higher ($P < 0.05$) than MTA Fillapex for the first 14 days of immersion. AH Plus had a pH of 7.1–7.8, whereas Pulp Canal Sealer demonstrated a weak acidification of the soaking water, especially in the first 3 days of immersion.

For BioRoot RCS, the release of calcium ions started immediately after sample immersion (Table 2), decreased during the testing time, but remained significantly high until 28 days, demonstrating long-term activity. For MTA Fillapex, the maximum calcium release was observed between 1 and 3 days. Nevertheless, BioRoot RCS had a significantly greater amount of leaked calcium during the testing period. No calcium release was recorded for Pulp Canal Sealer at any time of immersion, whilst AH Plus had a negligible leakage of 1–2 ppm. However, no significant differences were found between Pulp Canal Sealer and AH Plus.

Physical properties

The final setting time of Bioroot RCS was 300 ± 5 min (Table 3), longer than the manufacturer's information (<240 min).

The final setting times of AH Plus, Pulp Canal Sealer and MTA Fillapex were 1240, 60 and 270 min, respectively.

All the materials demonstrated radiopacity values greater than 3 mm Al (Table 3), as named by ISO 6876, although BioRoot RCS had a radiopacity of 5.18 mm Al. The materials had different apparent porosity values (Table 4), being significantly higher

Table 2 Alkalisizing activity and calcium ions released in distilled water

Alkalisizing activity (pH) and Calcium released (ppm) in soaking water						
	3 h	1 day	3 days	7 days	14 days	28 days
pH						
BioRoot RCS	11.7 ± 0.2 ^{A a}	12.1 ± 0.1 ^{A a}	10.6 ± 0.9 ^{B a}	11.1 ± 0.9 ^{B a}	11.3 ± 0.9 ^{B a}	8.7 ± 0.9 ^{C a}
MTA Fillapex	9.5 ± 0.1 ^{A b}	9.5 ± 0.2 ^{A b}	9.1 ± 0.2 ^{A b}	9.2 ± 0.1 ^{A b}	7.7 ± 0.1 ^{B b}	8.4 ± 0.1 ^{C a}
AH Plus	7.6 ± 0.2 ^{A c}	7.3 ± 0.1 ^{A c}	7.4 ± 0.1 ^{A c}	7.3 ± 0.2 ^{A c}	7.1 ± 0.2 ^{A c}	7.1 ± 0.3 ^{A b}
Pulp Canal Sealer	6.0 ± 0.7 ^{A d}	6.1 ± 0.6 ^{A d}	6.2 ± 0.5 ^{A d}	6.6 ± 0.3 ^{B d}	7.0 ± 0.2 ^{BC c}	7.2 ± 0.3 ^{C b}
	0–3 h	3 h–1 day	1–3 days	3–7 days	7–14 days	14–28 days
Calcium released						
BioRoot RCS	721.4 ± 81.3 ^{A a}	177.2 ± 36.7 ^{B a}	87.0 ± 37.9 ^{C a}	90.3 ± 35.8 ^{C a}	94.5 ± 32.0 ^{C a}	40.4 ± 12.8 ^{C a}
MTA Fillapex	17.4 ± 3.1 ^{A b}	31.1 ± 3.4 ^{B b}	31.0 ± 3.7 ^{B b}	23.6 ± 4.0 ^{A b}	21.3 ± 2.2 ^{A b}	15.9 ± 3.2 ^{A b}
AH Plus	2.0 ± 0.7 ^{A c}	1.8 ± 0.8 ^{A c}	1.2 ± 0.7 ^{A c}	1.2 ± 1.3 ^{A c}	1.4 ± 1.14 ^{A c}	1.1 ± 0.7 ^{A c}
Pulp Canal Sealer	0.8 ± 0.1 ^{A c}	0.8 ± 0.1 ^{A c}	0.8 ± 0.5 ^{A c}	0.9 ± 0.5 ^{A c}	0.7 ± 0.2 ^{A c}	0.9 ± 0.2 ^{A c}

Different capital letters represent significant differences ($P < 0.05$) in the same line, whilst different small letters represent differences in the same column (two-way ANOVA followed by RM Student–Newman–Keuls with $P < 0.05$, $n = 10$ per group).

Table 3 Radiopacity (mm Al) and setting times (min, determined after storage at 37 °C and 95 ± 5% relative humidity using Gilmore needles for initial and final setting times)

	Initial setting time (min)	Final setting time (min)	Radiopacity (mm Al; ISO>3)
BioRoot RCS	55 ± 5 ^a	300 ± 5 ^a	5.2 ± 0.3 ^a
MTA Fillapex	130 ± 5 ^b	270 ± 5 ^b	7.1 ± 0.6 ^b
AH Plus	480 ± 5 ^c	1240 ± 5 ^c	11.8 ± 0.3 ^c
Pulp Canal Sealer	40 ± 5 ^d	60 ± 5 ^d	10.5 ± 0.5 ^d

Different letters represent significant differences ($P < 0.05$) in the same column (one-way ANOVA followed by Student–Newman–Keuls with $P < 0.05$, $n = 3$ per group).

for BioRoot RCS ($P < 0.05$) and MTA Fillapex ($P < 0.05$) than Pulp Canal Sealer and AH Plus after both pre-setting times (setting time plus 50% and after 7 days at 37 °C 99% RH). No significant difference was recorded between the apparent porosity values of each material measured under the two test conditions. On the other hand, BioRoot RCS and MTA Fillapex had values of water sorption and solubility significantly lower after 7 days of pre-setting ($P < 0.05$). No differences were recorded for Pulp Canal Sealer and AH Plus.

Surface characterization and calcium phosphate nucleation in simulated body fluid

BioRoot RCS

Dry BioRoot RCS powder in the ESEM analysis (Fig. 1) displayed granules varying widely in size (2–10 µm); EDX detected carbon (C), nitrogen (N),

oxygen (O), silicon (Si), calcium (Ca) and zirconium (Zr). The Ca/Si atomic ratio calculated by EDX data was 3.74.

The freshly mixed paste had a homogeneous surface and displayed a strong increase of C and the appearance of chlorine (Cl), derived from the liquid. The Ca/Si atomic ratio was 3.20.

After soaking in HBSS, a uniform coating of small spherulites and thick deposits of aggregated spherulites were observed on the surface; EDX detected sodium (Na), high magnesium (Mg), Cl (attributable to HBSS medium), phosphorous (P) and the marked decrease in Si and Zr. The Ca/P atomic ratio at 28 day was 5.21. Figure 2 shows the average micro-Raman spectra of fresh BioRoot RCS as well as after ageing in HBSS for 28 days. The spectrum of the fresh material shows the bands of triclinic alite (Conjeaud & Boyer 1980) and zirconia monoclinic polymorph (Witke *et al.* 2001). At wavenumbers higher than 1000 cm⁻¹, the bands assignable to the organic component were detected.

Upon ageing in HBSS, the bands ascribable to a B-type carbonated apatite (carbonate substituting for phosphate) (Nelson & Featherstone 1982) and calcite (Martinez-Ramirez *et al.* 2003) appeared; the bands of the underlying cement were still detectable, although with a lower relative intensity than in the fresh material.

Pulp Canal Sealer

ESEM images of Pulp Canal Sealer revealed (Fig. 3) a fine powder; EDX detected C, O, zinc (Zn), silver (Ag) and iodine (I). The freshly mixed paste had a flat and

Table 4 Porosity, water sorption and solubility calculated after 24 h of immersion

	Apparent porosity (%)	Water sorption (%)	Solubility (%)
Setting + 50% 37 °C 99% RH before test			
BioRoot RCS	53.9 ± 4.8 ^a	43.5 ± 3.8 ^a	37.6 ± 3.2 ^a
MTA Fillapex	21.4 ± 2.3 ^b	13.3 ± 0.9 ^b	13.6 ± 1.2 ^b
AH Plus	3.4 ± 0.9 ^c	1.3 ± 0.7 ^c	1.2 ± 0.3 ^c
Pulp Canal Sealer	8.8 ± 1.6 ^d	3.5 ± 0.8 ^d	2.6 ± 0.5 ^c
7 days at 37 °C 99% RH before test			
BioRoot RCS	51.6 ± 1.4 ^a	36.1 ± 2.2 ^e	14.2 ± 2.0 ^b
MTA Fillapex	19.3 ± 2.2 ^b	12.1 ± 1.5 ^b	11.1 ± 1.3 ^d
AH Plus	2.8 ± 0.7 ^c	1.4 ± 0.4 ^c	0.8 ± 0.3 ^c
Pulp Canal Sealer	8.4 ± 1.4 ^d	3.3 ± 0.6 ^d	2.1 ± 0.3 ^c

Different letters represent significant differences ($P < 0.05$) in the same column (one-way ANOVA followed by Student-Newman-Keuls with $P < 0.05$, $n = 10$ per group).

homogeneous surface and displayed an increase of C and appearance of N, derived from the liquid. After soaking in HBSS, no significant changes in surface morphology and no deposits were observed; EDX detected the appearance of Na, P, Cl and Ca derived from the HBSS.

Figure 4 shows the average micro-Raman spectra recorded on the liquid phase and the powder of Pulp Canal Sealer, as well as on the freshly mixed cement and after ageing in HBSS for 28 days. The spectrum of the liquid component shows the bands due to eugenol (Chowdhry *et al.* 2015), whilst that of the powder is dominated by the bands of zinc oxide (Zhang *et al.* 2009) and the organic component (thymol iodide). The quality of the latter spectrum as well as of the fresh material and after ageing in HBSS was degraded by fluorescence, which may be due to the thymol iodide component or to trace impurities present in the powder. In fact, it must be recalled that photoluminescence has a much higher probability of occurring than Raman scattering so that traces of impurities (i.e. not deliberately added to the sample) may have enough fluorescence to mask the Raman signal.

The spectrum of the fresh sample is dominated by the bands of zinc oxide; the broadening around 490 cm^{-1} and the band at 150 cm^{-1} indicate the presence of zinc hydroxide; mixing the ZnO powder with eugenol-based liquid triggers the setting reaction and allows the formation of $\text{Zn}(\text{OH})_2$ and zinc eugenolate, in the presence of humidity. The bands of the latter component (Gandolfi *et al.* 2013b) were only partially detected due to the high fluorescence of the sample. For the same reason, the spectrum of the

Pulp Canal Sealer cement aged in HBSS revealed only the main bands of the organic component and zinc oxide. No apatite/calcite deposit was detected, in agreement with ESEM-EDX analyses.

AH Plus

AH Plus (Fig. 5) had inorganic granules immersed in an organic matrix in the ESEM. EDX had these elements in the two pastes: C, N, O, Si, Ca, Zr and tungsten (W) for paste A and C, N, O, Ca, Zr and W for paste B. The freshly mixed paste had an irregular surface.

After soaking in HBSS, significant changes in surface morphology were observed as follows: the organic matrix was not visible and a homogeneous deposit appeared. EDX detected Na, P, Cl and Ca from the HBSS; Si, Zr and W were no longer detected. Ca/P atomic ratio was 1.57 at 28 days, indicating the deposition of Ca-poor apatite.

Figure 6 shows the average micro-Raman spectra recorded on the pastes A and B of AH Plus as well as on the freshly mixed cement and after ageing in HBSS for 28 days.

In the micro-Raman spectrum of paste A, the strongest bands belonged to calcium tungstate (Nyquist *et al.* 1997), zirconia monoclinic polymorph (Witke *et al.* 2001) and bisphenol A and F epoxide resins (van Overbeke *et al.* 2000, Merad *et al.* 2009, Hardis *et al.* 2013), in agreement with the composition declared by the producer. The FeO and aerosil components could contribute to the bands at 642 cm^{-1} (de Faria *et al.* 1997) and 509 cm^{-1} (Chlosta *et al.* 2011), respectively; the former is also attributable to zirconia and bisphenol A epoxide resin, the latter to zirconia.

The micro-Raman spectrum of paste B revealed the bands of monoclinic zirconia and calcium tungstate, all with higher relative intensities than in paste A, in agreement with the EDX data. The bands above 1000 cm^{-1} are ascribable to the organic component, some of them (indicated) specifically to the aromatic diamine (i.e. *N,N'*-dibenzyl-5-oxa-nonandiamine-1,9). The freshly mixed cement showed the bands of both pastes A and B.

Upon ageing in HBSS, a B-type carbonated apatite was detected but the bands of the underlying cement were still detectable. Note that the relative intensity of the band at 1258 cm^{-1} decreased, due to the epoxide group consumption occurring during cement hardening, in agreement with the results reported in the literature (Merad *et al.* 2009).

MTA Fillapex

The yellow base paste and white catalyst paste of MTA Fillapex observed with the ESEM (Fig. 7) had different surface morphologies. In the yellow paste, it was easier to recognize the inorganic granules, whilst the white paste had a homogenous surface with only a few granules immersed in an organic matrix. The EDX analysis detected the elements present in the two pastes: C, N, O, Si, Ca, W, aluminium (Al) and titanium (Ti) in the yellow paste and C, O, Al, Si, Ti, sulphur (S) and bismuth (Bi) in the white paste. The freshly mixed paste had a homogenous and flat surface; the inorganic granules were visible, immersed in an organic matrix. After soaking in HBSS, a deposit

appeared; EDX detected the appearance of Na, P and Cl and Ca from the HBSS. Most elements constituting the cement were no longer detected. The Ca/P atomic ratio was 1.41 at 28 days, indicating a deposition of Ca/poor non-Apatitic CaPs.

Figure 8 shows the average micro-Raman spectra recorded on the white and yellow pastes of MTA Fillapex, as well as on the freshly mixed cement and after ageing in HBSS for 28 days.

The spectrum of the yellow paste shows the bands assignable to the salicylate resin, calcium tungstate and titanium oxide (as anatase (Nyquist *et al.* 1997)). The white paste contained an organic resin, belite and alite, anatase and bismuth oxide. These

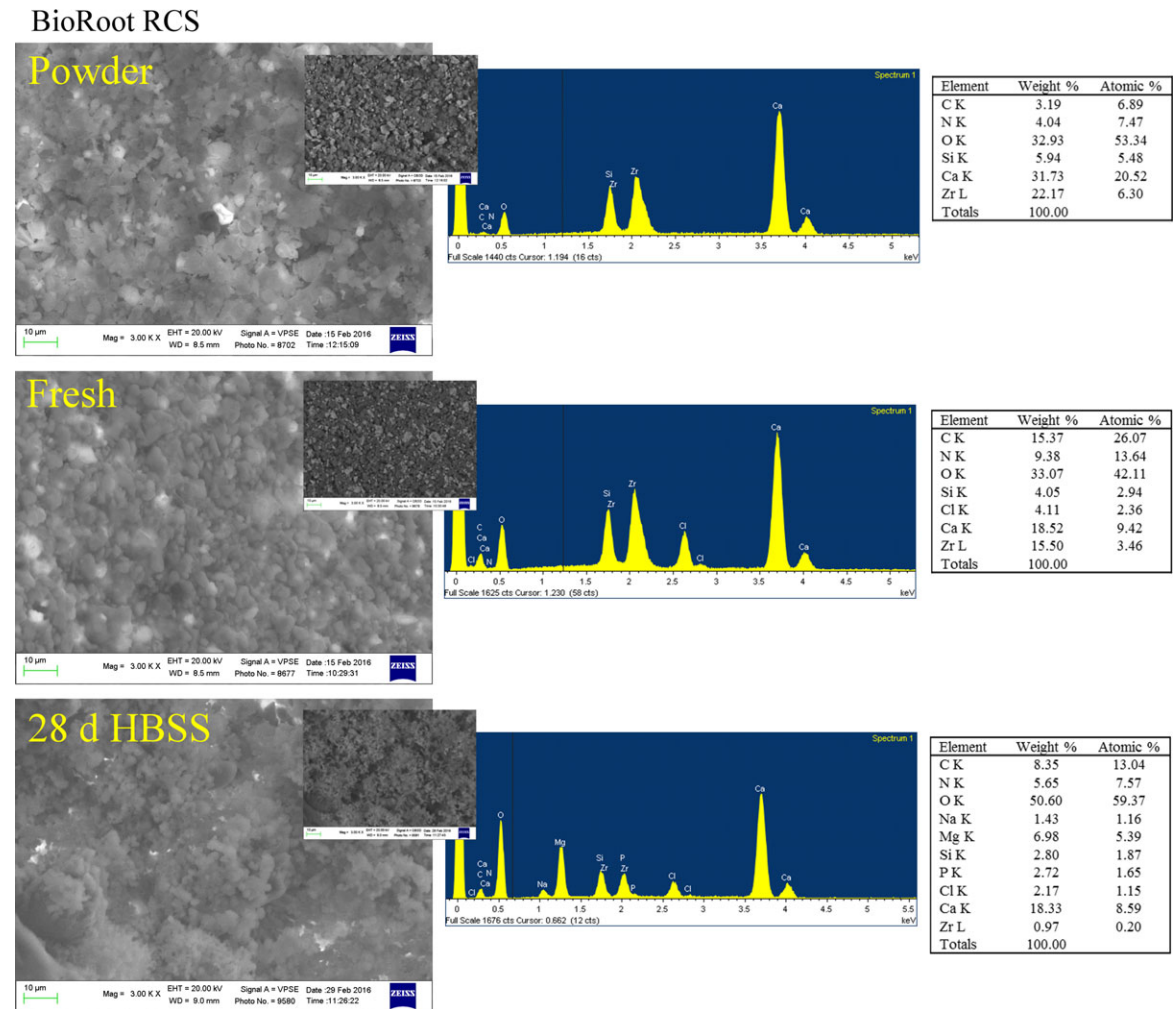


Figure 1 ESEM images and EDX microanalysis of BioRoot RCS powder, freshly mixed and after 28 days in HBSS. The image shows the surface morphology and the composition of the powder and freshly mixed cement. After immersion in HBSS, a coating of small spherulites containing Ca and P appears on the sample surface.

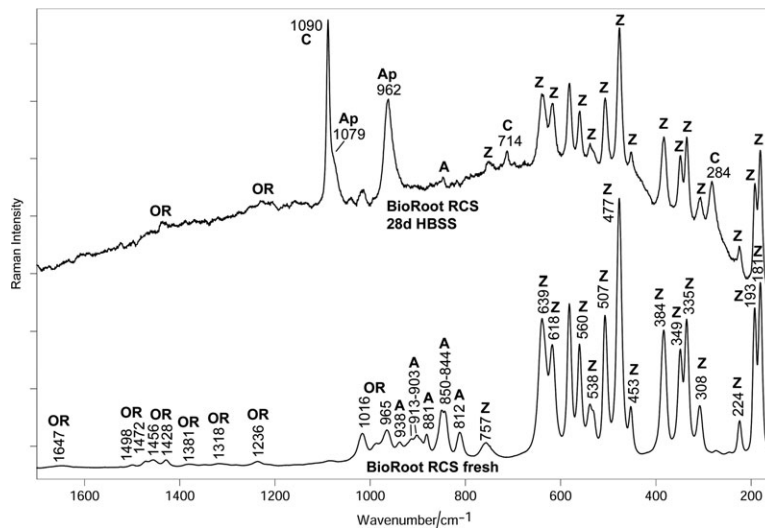


Figure 2 Average micro-Raman spectra of fresh BioRoot RCS as well as after ageing in HBSS for 28 days. The spectra were recorded by using a 3000- μm confocal pinhole. The bands ascribable to the organic component (OR), monoclinic zirconia (Z), triclinic alite (A), apatite (Ap) and calcite (C) are indicated.

components were also detected in the spectrum of the fresh cement. The tricalcium silicate bands had significantly lower relative intensities than in BioRoot RCS; no tricalcium aluminate and calcium sulphate were detected in any material.

Upon ageing in HBSS, an apatite deposit was observed; the bands of the underlying cement were still observable (in particular, those assignable to calcium tungstate and anatase).

Discussion

The ESEM and micro-Raman analyses confirmed that BioRoot RCS consisted of a fine powder of tricalcium silicate and zirconium oxide mixed with an aqueous solution of calcium chloride and polycarboxylate. BioRoot RCS demonstrated lower radiopacity values than reported in the literature (Khalil *et al.* 2016).

Zirconium oxide is present to increase the radiopacity (see Table 3, as required by ISO 6876). Thirty per cent of ZrO_2 does not affect the hydration reaction of tricalcium silicate cements (Camilleri *et al.* 2011, Li *et al.* 2013, Guerreiro Tanomaru *et al.* 2014), improves physical properties such as compressive strength and triggers a better biological response than hydraulic tricalcium silicate cements containing bismuth oxide (Li *et al.* 2013, Silva *et al.* 2014). Bismuth oxide in tricalcium silicate cements has been demonstrated to produce a deleterious effect on

in vitro human marrow stromal cells growth (Gandolfi *et al.* 2009b, 2010). Furthermore, ZrO_2 has been reported to allow a greater and longer release of calcium ions and to make the tricalcium silicate cements more biocompatible (Li *et al.* 2017).

Interestingly, EDX detected traces of W (as a radiopacifier agent) in the yellow paste of MTA Fillapex, not reported in the technical data sheet. Raman confirmed the presence of calcium tungstate.

The amount of Ca^{2+} ions released by BioRoot RCS was higher and more prolonged than the other materials tested. The amount of calcium released by AH Plus and Pulp Canal Sealer was absent or negligible.

Both BioRoot RCS and MTA Fillapex raised the pH of the surrounding environment (Table 2). Alkaline pH promotes antibacterial activity (Siqueira & Lopes 1999, Al-Hezaimi *et al.* 2006, Reston & Souza Costa 2009, Poggio *et al.* 2015) and favours apatite nucleation (Prati & Gandolfi 2015, Gandolfi *et al.* 2013b). AH Plus did not change significantly the pH of the soaking water, and values remained near neutral (7.1–7.6); on the contrary, Pulp Canal Sealer had a low acidification tendency (pH was 6.0–6.2) in the early testing time due to the leaking of eugenol into the surrounding environment (Zhou *et al.* 2013).

After soaking for 28 days in HBSS, both BioRoot RCS and MTA Fillapex had a CaPs layer covering the cement surface. The high Ca/P values of BioRoot RCS were likely correlated to the great Ca of tricalcium

Pulp Canal Sealer

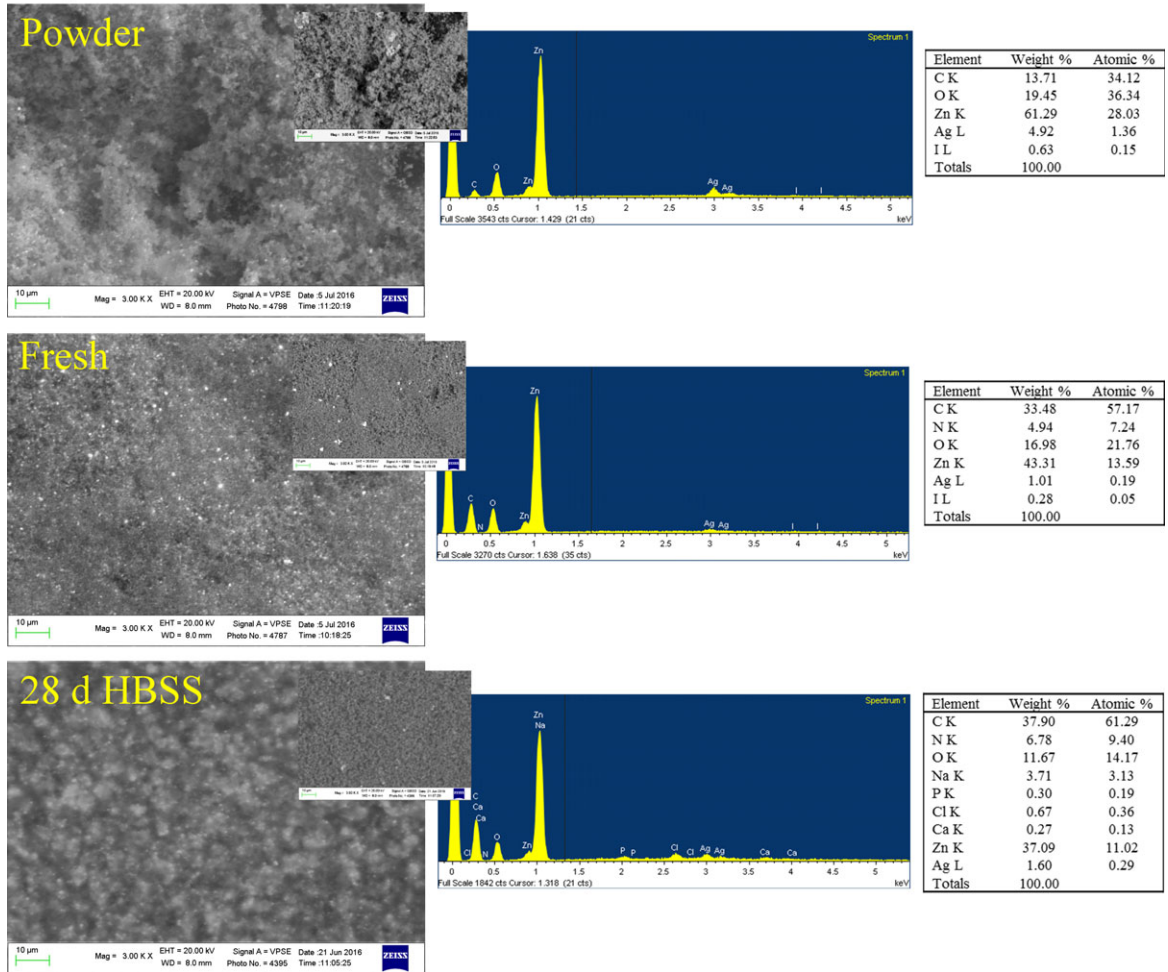


Figure 3 ESEM images and EDX microanalysis of Pulp Canal Sealer powder, freshly mixed and after 28 days in HBSS. The image shows the surface morphology and the composition of the powder and freshly mixed cement. No deposit was detected on the sample surface after immersion in HBSS.

silicate composition and the contribution of calcium carbonates (Gandolfi *et al.* 2013a).

No CaPs deposits were detected on the Pulp Canal Sealer surface. AH Plus had a thin CaPs deposit despite the low/negligible amount of calcium ions released. This result was in agreement with a previous study (Gandolfi *et al.* 2013a), where sparse calcium phosphate deposits were detected on AH Plus after immersion in HBSS.

To evaluate the relative thickness of the deposit, micro-Raman spectra on the surface of the aged samples were measured also using a 200 µm pinhole, that is under optical conditions more sensitive to the surface of the samples. The average spectra are

shown in Fig. 9. No apatite deposit was detected on Pulp Canal Sealer. If compared with the spectra recorded with a 3000-µm pinhole (Figs 2, 6 and 8), the relative intensity of the apatite bands was higher when using a 200-µm pinhole, which is more sensitive to the superficial deposit. The spectra still show the marker bands of the respective underlying cements with the exception of BioRoot RCS, which thus formed the thickest deposit.

For AH Plus and MTA Fillapex, the spectra of Fig. 9 showed a thicker layer on MTA Fillapex since the $I_{965(Ap)}/I_{916(CaWO_4)}$ intensity ratio was higher for the latter than for the former. Therefore, the thickness of the apatite deposit decreased along the series

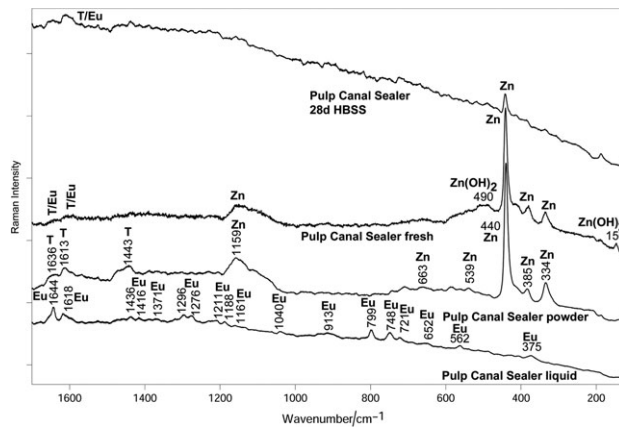


Figure 4 Average micro-Raman spectra recorded on the liquid phase and the powder of Pulp Canal Sealer, as well as on the mixed cement just prepared (i.e. fresh) and after ageing in HBSS for 28 days. The spectra were recorded by using a 3000- μm confocal pinhole. The bands ascribable to eugenol (Eu), zinc oxide (ZnO), thymol iodide (T) and zinc hydroxide ($\text{Zn}(\text{OH})_2$) are indicated.

AH Plus

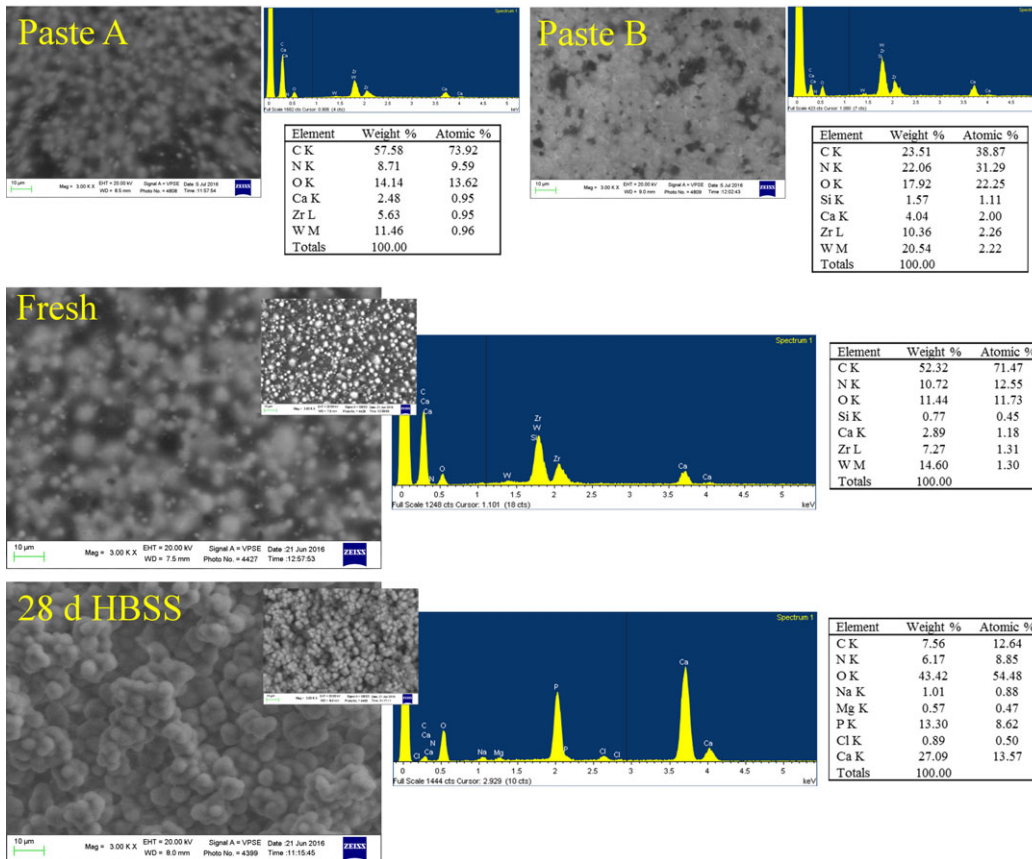


Figure 5 ESEM images and EDX microanalysis of AH Plus paste A, paste B, freshly mixed and after 28 days in HBSS. The image shows the surface morphology and the composition of the pastes and freshly mixed cement. After immersion in HBSS, a coating of spherulites containing Ca and P appears on the sample surface.

BioRoot RCS > MTA Fillapex > AH Plus > Pulp Canal Sealer (no deposit). This trend is in agreement with the cumulative calcium release data after 28 days of immersion (BioRoot RCS 1210.8 ppm; MTA Fillapex 140.3 ppm; AH Plus 8.7 ppm; Pulp Canal Sealer 5.7 ppm). The 965 cm^{-1} apatite band had a different full-width at half maximum (FWHM₉₆₅) in the different samples: under both optical conditions, that is 3000 μm (Figs 2, 6 and 8) and 200 μm (Fig. 9) pinholes, it decreased along the series MTA Fillapex > BioRoot RCS > AH Plus, suggesting that apatite crystallinity increased from MTA Fillapex to AH Plus.

The prolonged release of calcium ions has been demonstrated to be a key factor to promote endodontic and periodontal tissue regeneration (Hakki *et al.* 2009, Matsumoto *et al.* 2013) enhancing the bioactivity and biocompatibility of the material. In fact, modern endodontic protocols require the use of materials able not only to perform a good and stable seal and prevent recurrent infections, but also to promote periapical tissue regeneration and contribute to the

recruitment of osteo-odontogenic stem cells within the apical environment (da Silva *et al.* 2008, Gandolfi *et al.* 2009, 2011a, Bryan *et al.* 2010, Gandolfi & Prati 2010, Silva *et al.* 2012).

The ion releasing ability and the formation of a CaPs layer could also explain the good *in vitro* biocompatibility reported for BioRoot RCS (Dimitrova-Nakov *et al.* 2015): when in contact with mouse pulpal stem cells, BioRoot RCS did not alter cell viability or cell morphology, whilst Pulp Canal Sealer induced cell death even in the presence of a small amount of material.

Both tricalcium silicate-containing materials were associated with ion release, porosity, water sorption and solubility higher than AH Plus and Pulp Canal Sealer.

The solubility was calculated as weight loss for samples set for a period 50% longer than the final setting time before testing; the measurements was repeated by leaving the samples at 37 °C and 98–100% relative humidity for 7 days to permit a longer and more extensive hydration.

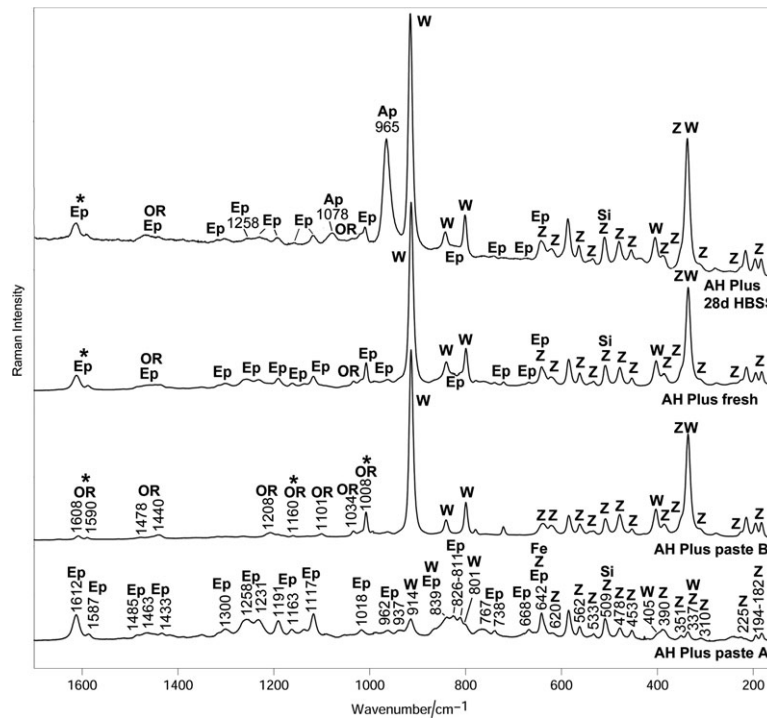


Figure 6 Average micro-Raman spectra recorded on the pastes A and B of AH Plus as well as on the mixed cement just prepared (i.e. fresh) and after ageing in HBSS for 28 days. The spectra were recorded using a 3000- μm confocal pinhole. The bands ascribable to the organic component (OR), bisphenols A and B epoxide resins (Ep), monoclinic zirconia (Z), calcium tungstate (W) silica (Si), ferrous oxide (Fe) and apatite (Ap) are indicated. The bands ascribable in paste B to the aromatic diamine (i.e. *N,N'*-dibenzyl-5oxa-nonandiamine-1,9) are marked with an asterisk.

As reported in Table 4, only AH Plus and Pulp Canal Sealer had solubility values lower than 3% as required by the ISO standard, and no significant differences were recorded between the two setting conditions (setting time +50% and 7 days) for these materials. BioRoot RCS and MTA Fillapex had high solubility (>3%); these materials are more hydrophilic, which produced greater porosity and solubility values. Pulp Canal Sealer and AH Plus are hydrophobic materials and did not adsorb water; consequently, the porosity and solubility values are significantly lower than for the tricalcium silicate-containing materials. The solubility values of BioRoot RCS and MTA Fillapex decreased significantly after 7 days; however,

no significant differences were recorded for porosity and water sorption between the two test conditions.

Setting times of AH Plus, Pulp Canal Sealer and MTA Fillapex were similar to those reported in literature (Camilleri & Mallia 2011, Baldi et al. 2012, Gandolfi et al. 2016).

For BioRoot RCS and MTA Fillapex, the hydration processes continued after the final setting time and permit the ion release and CaP nucleation for 28 days. The high values of solubility in distilled water of the early set BioRoot RCS are correlated with high Ca²⁺ and OH⁻ release, which dissolve leaving voids. When immersed in a simulated body fluid, the calcium ions combined with phosphate promoting the

MTA Fillapex

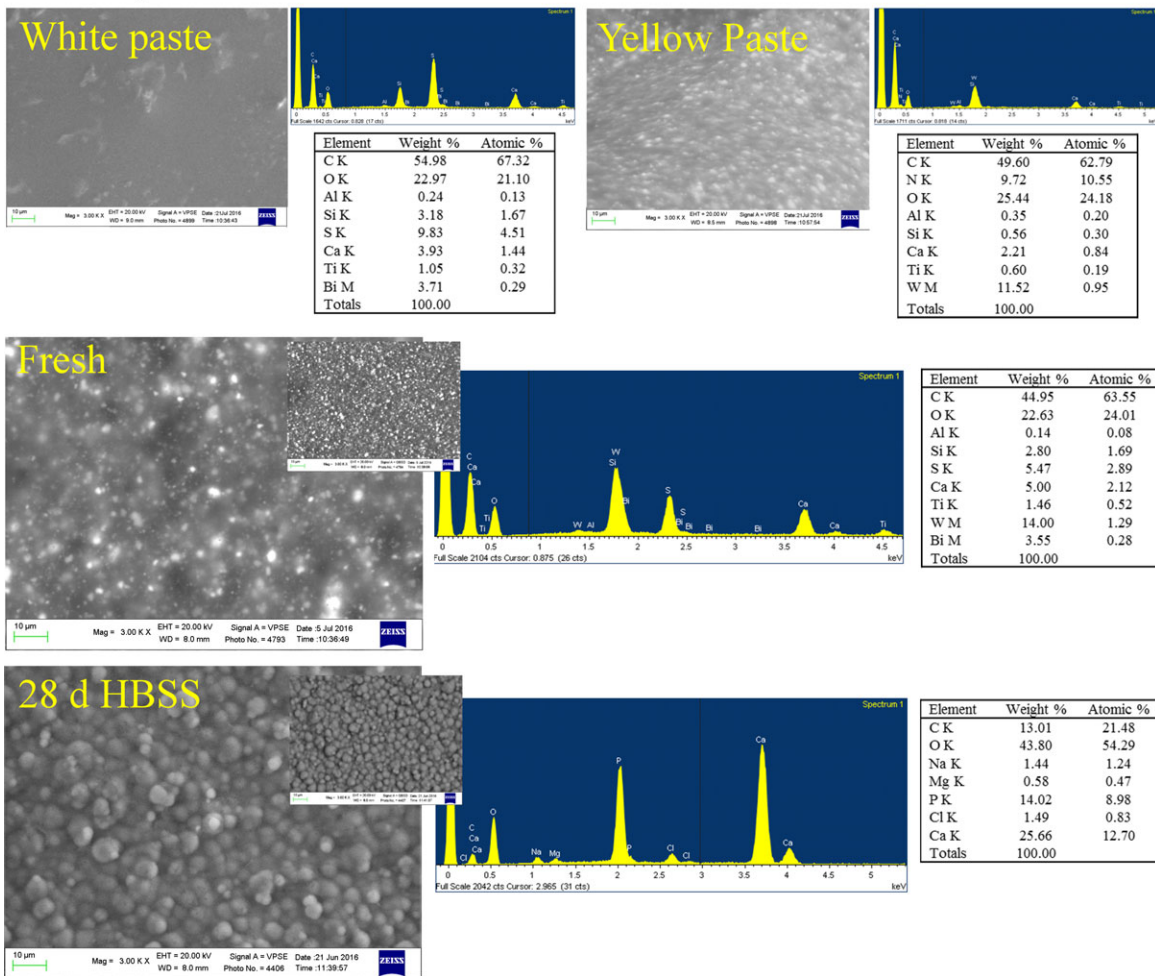


Figure 7 ESEM images and EDX microanalysis of MTA Fillapex white paste, yellow paste, freshly mixed and after 28 days in HBSS. The image shows the surface morphology and the composition of the pastes and freshly mixed cement. After immersion in HBSS, a coating of small spherulites containing Ca and P appears on the sample surface.

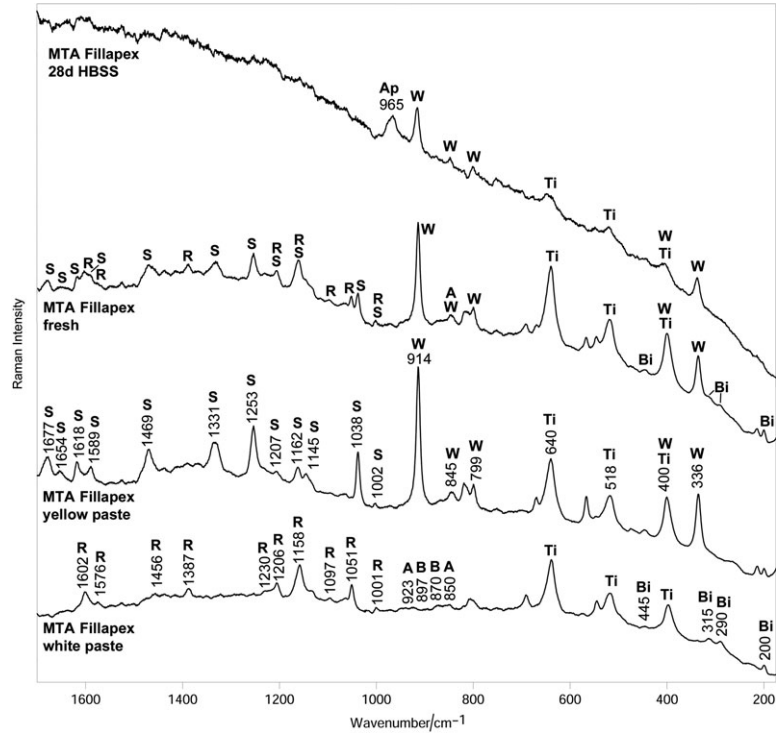


Figure 8 Average micro-Raman spectra recorded on the white and yellow pastes of MTA Fillapex as well as on the mixed cement just prepared (i.e. fresh) and after ageing in HBSS for 28 days. The spectra were recorded by using a 3000- μm confocal pinhole. The bands ascribable to the salicylate resin (S), calcium tungstate (W), anatase (Ti), diluent resin (R), bismuth oxide (Bi), alite (A), belite (B) and apatite (Ap) are indicated.

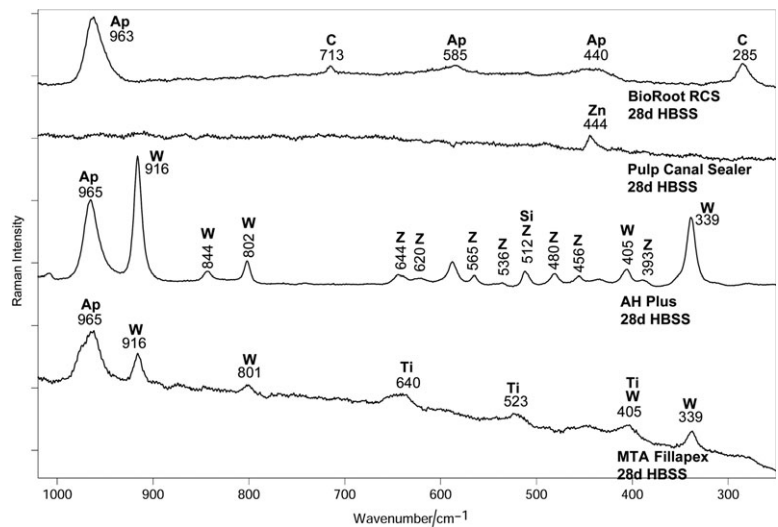


Figure 9 Average micro-Raman spectra recorded on the surface of BioRoot RCS, Pulp Canal Sealer, AH Plus and MTA Fillapex aged in HBSS for 28 days. The spectra were recorded by using a 200- μm confocal pinhole. The bands ascribable to calcite (C), apatite (Ap), zinc oxide (Zn), calcium tungstate (W), monoclinic zirconia (Zr), silica (Si) and anatase (Ti) are indicated.

formation of a superficial layer of CaP able to fill the open voids. Clinically, this apatite (Ap)-forming ability (Sarkar *et al.* 2005, Parirokh & Torabinejad 2010, Cornélio *et al.* 2015) with gutta-percha may improve sealing ability by the deposition of calcium phosphates (CaPs) at the interface (Gandolfi *et al.* 2013b, Iacono *et al.* 2014).

This study confirmed that BioRoot RCS and MTA Fillapex release mineralizing ions (Ca^{++}), bind biologically active ions and trigger the nucleation of apatite precursors on the material surface (bioactivity). On the other hand, AH Plus did not show the ability to release ions so the formation of calcium phosphate deposits was related to the presence of functional groups in the material that adsorb the ions involved in apatite nucleation (chemi/physisorption-related CaPs deposition).

Concerning solubility, water sorption and porosity tests, unfortunately, there is a lack of an international standard and test methods (ISO) for both conventional and resin-modified tricalcium silicate MTA-like cements (Gandolfi *et al.* 2012). This deficiency has been also mentioned by others (Nekoofar *et al.* 2007). There is a need for a standard requirement for the aforementioned materials in relationship to their specific clinical application (root-end filling materials, endodontic sealers, pulp capping materials, etc.). The tests suggested in the available specifications are often inappropriate/unfeasible and inapplicable to calcium silicate-based materials. The solubility and porosity of tricalcium silicate (MTA-type) materials in distilled water do not predict the real stability and integrity of such materials *in vivo*. It has been demonstrated that in the presence of serum proteins, the solubility is much lower than in water (Gandolfi *et al.* 2011c). It can be speculated that the same will occur under *in vivo* conditions. Moreover, as previously mentioned, apatite deposition on the sealer surface and within the internal porosities counterbalances these values.

Silva *et al.* (2017) proposed a different methodological set-up to test the solubility and dimensional changes of endodontic sealers using a micro-CT approach in order to simulate clinical condition.

Tricalcium silicate sealers present new and innovative properties compared to conventional sealers such as calcium release, apatite-forming ability and hydrophilicity. These characteristics are useful for teeth with wide and open apices, wet and blood-filled canals apical thirds and root perforations. They may accelerate the healing of apical bone defects by improving bone regeneration *in vitro* (da Silva *et al.*

2017) and *in vivo* (Margunato *et al.* 2015). BioRoot RCS sealer requires a cold condensation technique, and its composition may play a positive role in preventing demineralization of root dentine (Reyes-Carmona *et al.* 2010).

Conclusion

BioRoot RCS is a bioactive material able to nucleate carbonated apatite deposits in relationship to its prolonged ability to release calcium ions and to basify the environment.

MTA Fillapex had much lower calcium release and less apatite deposition after ageing in HBSS.

No calcium release, no alkalizing activity and no CaPs nucleation were detected for aged Pulp Canal Sealer.

Some apatite deposits were found on AH Plus despite the absence of calcium release and alkalizing activity.

All sealers fulfilled the standard requirements in terms of radiopacity. However, the significantly low radiopacity values of BioRoot RCS may not satisfy clinicians who usually utilize other more radiopaque sealers (i.e. AH Plus and Pulp Canal Sealer).

The data support the potential of bioactive tricalcium silicate sealers such as BioRoot RCS to promote periapical healing, bone regeneration and sealing by mineralization and apatite deposition at the root canal wall interface.

Conflict of interest

The authors have stated explicitly that there are no conflicts of interest in connection with this article.

References

- Al-Hezaimi K, Al-Shalan TA, Naghshbandi J, Oglesby S, Simon JH, Rotstein I (2006) Antibacterial effect of two mineral trioxide aggregate (MTA) preparations against *Enterococcus faecalis* and *Streptococcus sanguis* *in vitro*. *Journal of Endodontics* **32**, 1053–6.
- Arias-Moliz MT, Camilleri J (2016) The effect of the final irrigant on the antimicrobial activity of root canal sealers. *Journal of Dentistry* **52**, 30–6.
- Baldi JV, Bernardes RA, Duarte MA *et al.* (2012) Variability of physicochemical properties of an epoxy resin sealer taken from different parts of the same tube. *International Endodontic Journal* **45**, 915–20.
- Barros J, Silva MG, Rodrigues MA *et al.* (2014) Antibacterial, physicochemical and mechanical properties of endodontic

- sealers containing quaternary ammonium polyethyleneimine nanoparticles. *International Endodontic Journal* **47**, 725–34.
- Bryan TE, Khechen K, Brackett MG, Messer RL, El-Awady A, Primus CM, et al. (2010) *In vitro* osteogenic potential of an experimental calcium silicate-based root canal sealer. *Journal of Endodontics* **36**, 1163–9.
- Camilleri J (2008) Characterization of hydration products of mineral trioxide aggregate. *International Endodontic Journal* **41**, 408–17.
- Camilleri J (2011) Evaluation of the effect of intrinsic material properties and ambient conditions on the dimensional stability of white mineral trioxide aggregate and Portland cement. *Journal of Endodontics* **37**, 239–45.
- Camilleri J (2014) Color stability of white mineral trioxide aggregate in contact with hypochlorite solution. *Journal of Endodontics* **40**, 436–40.
- Camilleri J, Mallia B (2011) Evaluation of the dimensional changes of mineral trioxide aggregate sealer. *International Endodontic Journal* **44**, 416–24.
- Camilleri J, Cutajar A, Mallia B (2011) Hydration characteristics of zirconium oxide replaced Portland cement for use as a root end filling material. *Dental Materials* **27**, 845–54.
- Camps J, Jeanneau C, El Ayachi I, Laurent P, About I (2015) Bioactivity of a calcium silicate-based endodontic cement (BioRoot RCS): interactions with human periodontal ligament cells *in vitro*. *Journal of Endodontics* **41**, 1469–73.
- Chlosta R, Tzolova-Müller G, Schlögl R, Hess C (2011) Nature of dispersed vanadium oxide: influence of the silica support structure and synthesis methods. *Catalysis Science & Technology* **1**, 1175–81.
- Chowdhry BZ, Ryall JP, Dines TJ, Mendham AP (2015) Infrared and Raman spectroscopy of eugenol, isoeugenol, and methyl eugenol: conformational analysis and vibrational assignments from density functional theory calculations of the anharmonic fundamentals. *Journal of Physical Chemistry A* **119**, 11280–92.
- Collado-González M, Tomás-Catalá CJ, Oñate-Sánchez RE, Moraleda JM, Rodríguez-Lozano FJ (2017) Cytotoxicity of GuttaFlow Bioseal, GuttaFlow2, MTA Fillapex, and AH plus on human periodontal ligament stem cells. *Journal of Endodontics* **43**, 816–22.
- Conjeaud M, Boyer H (1980) Some possibilities of Raman microprobe in cement chemistry. *Cement and Concrete Research* **10**, 61–70.
- Cornélio AL, Rodrigues EM, Salles LP et al. (2015) Bioactivity of MTA Plus, Biodentine and experimental calcium silicate-based cements in human osteoblast-like cells. *International Endodontic Journal* **26**, 39–47.
- Dimitrova-Nakov S, Uzunoglu E, Ardila-Osorio H et al. (2015) *In vitro* bioactivity of Bioroot™ RCS, via A4 mouse pulpal stem cells. *Dental Materials* **31**, 1290–7.
- de Faria DLA, Venâncio Silva S, de Oliveira MT (1997) Raman microspectroscopy of some iron oxides and oxyhydroxides. *Journal of Raman Spectroscopy* **28**, 873–8.
- Flores DS, Rached FJ, Versiani MA, Guedes DF, Sousa-Neto MD, Pecora JD (2011) Evaluation of physicochemical properties of four root canal sealers. *International Endodontic Journal* **44**, 126–35.
- Gandolfi MG, Prati C (2010) MTA and F-doped MTA cements used as sealers with warm gutta-percha. Long-term study of sealing ability. *International Endodontic Journal* **43**, 889–901.
- Gandolfi MG, Iacono F, Agee K et al. (2009a) Setting time and expansion in different soaking media of experimental accelerated calcium-silicate cements and ProRoot MTA. *Oral Surgery, Oral Medicine, Oral Pathology, Oral Radiology, and Endodontology* **108**, e39–45.
- Gandolfi MG, Ciapetti G, Perut F et al. (2009b) Biomimetic calcium-silicate cements aged in simulated body solutions. Osteoblasts response and analyses of apatite coating. *Journal of Applied Biomaterials and Biomechanics* **7**, 160–70.
- Gandolfi MG, Ciapetti G, Taddei P et al. (2010) Apatite formation on bioactive calcium-silicate cements for dentistry affects surface topography and human marrow stromal cells proliferation. *Dental Materials* **10**, 974–92. <https://doi.org/10.1016/j.dental.2010.06.002>.
- Gandolfi MG, Shah SN, Feng R, Prati C, Akintoye SO (2011a) Biomimetic calcium-silicate cements support differentiation of human orofacial mesenchymal stem cells. *Journal of Endodontics* **37**, 1102–8.
- Gandolfi MG, Taddei P, Tinti A, Dorigo De Stefano E, Prati C (2011b) Alpha-TCP improves the apatite-formation ability of calcium-silicate hydraulic cement soaked in phosphate solutions. *Materials Science and Engineering C* **31**, 1412–22.
- Gandolfi MG, Taddei P, Siboni F, Modena E, Ciapetti G, Prati C (2011c) Development of the foremost light-curable calcium-silicate MTA cement as root-end in oral surgery. Chemical-physical properties, bioactivity and biological behavior. *Dental Materials* **27**, e134–57.
- Gandolfi MG, Siboni F, Prati C (2012) Chemical-physical properties of TheraCal, a novel light-curable MTA-like material for pulp capping. *International Endodontic Journal* **45**, 571–9.
- Gandolfi MG, Taddei P, Modena E, Siboni F, Prati C (2013a) Biointeractivity-related versus chemi/physorption-related apatite precursor-forming ability of current root end filling materials. *Journal of Biomedical Materials Research Part B: Applied Biomaterials* **101**, 1107–23.
- Gandolfi MG, Parrilli AP, Fini M, Prati C, Dummer PM (2013b) 3D micro-CT analysis of the interface voids associated with Therafil root fillings used with AH Plus or a flowable MTA sealer. *International Endodontic Journal* **46**, 253–63.
- Gandolfi MG, Siboni F, Primus CM, Prati C (2014) Ion release, porosity, solubility, and bioactivity of MTA plus tricalcium silicate. *Journal of Endodontics* **40**, 1632–7.
- Gandolfi MG, Siboni F, Botero T, Bossù M, Riccitiello F, Prati C (2015) Calcium silicate and calcium hydroxide materials for pulp capping: biointeractivity, porosity, solubility and

- bioactivity of current formulations. *Journal of Applied Biomaterials & Functional Materials* **13**, 43–60.
- Gandolfi MG, Siboni F, Prati C (2016) Properties of a novel polysiloxane-guttapercha calcium silicate-bioglass-containing root canal sealer. *Dental Materials* **32**, e113–26.
- Gilles R, Oliver M (2012) Dental material. Patent No. US 0270184 A1.
- Guerreiro Tanomaru JM, Storto I, Da Silva GF et al. (2014) Radiopacity, pH and antimicrobial activity of Portland cement associated with micro- and nanoparticles of zirconium oxide and niobium oxide. *Dental Materials* **33**, 466–70.
- Hakki SS, Bozkurt SB, Hakki EE, Belli S (2009) Effects of mineral trioxide aggregate on cell survival, gene expression associated with mineralized tissues, and biomineralization of cementoblasts. *Journal of Endodontics* **35**, 513–9.
- Hardis R, Jessop J, Peters FE, Kessler MR (2013) Cure kinetics characterization and monitoring of an epoxy resin using DSC, Raman spectroscopy, and DEA. *Composites Part A: Applied Science and Manufacturing* **49**, 100–8.
- He D, Zhuang C, Xu S et al. (2016) 3D printing of Mg-substituted wollastonite reinforcing diopside porous bioceramics with enhanced mechanical and biological performances. *Bioactive Materials* **1**, 85–92.
- Iacono F, Pedulla E, Rapisarda E, Prati C, Gandolfi MG (2014) Long-term sealing ability of 3 endodontic obturation techniques. *General Dentistry* **62**, 20–3.
- Khalil I, Naaman A, Camilleri J (2016) Properties of tricalcium silicate sealers. *Journal of Endodontics* **11**, 1529–35. <https://doi.org/10.1016/j.joen.2016.06.002>.
- Li Q, Deacon AD, Coleman NJ (2013) The impact of zirconium oxide nanoparticles on the hydration chemistry and biocompatibility of white Portland cement. *Dental Materials* **32**, 808–15.
- Li X, Yoshihara K, De Munck J et al. (2017) Modified tricalcium silicate cement formulations with added zirconium oxide. *Clinical Oral Investigations* **21**, 895–905.
- Margunato S, Taşlı PN, Aydın S, Karapınar Kazandağ M, Şahin F (2015) *In vitro* evaluation of ProRoot MTA, Biodentine, and MM-MTA on human alveolar bone marrow stem cells in terms of biocompatibility and mineralization. *Journal of Endodontics* **41**, 1646–52.
- Martinez-Ramirez S, Sanchez-Cortes S, Garcia Ramos JV, Domingo C, Fortes C, Blanco-Varela MT (2003) Micro-Raman spectroscopy applied to depth profiles of carbonates formed in lime mortar. *Cement and Concrete Research* **33**, 2063–8.
- Matsumoto S, Hayashi M, Suzuki Y, Suzuki N, Maeno M, Ogiso B (2013) Calcium ions released from mineral trioxide aggregate convert the differentiation pathway of C2C12 Cells into osteoblast lineage. *Journal of Endodontics* **39**, 68–75.
- Merad L, Cochez M, Margueron S et al. (2009) In-situ monitoring of the curing of epoxy resins by Raman spectroscopy. *Polymer Testing* **28**, 42–5.
- Nekoofar MH, Adusei G, Sheykhrezae MS, Hayes SJ, Bryant ST, Dummer PMH (2007) The effect of condensation pressure on selected physical properties of mineral trioxide aggregate. *International Endodontic Journal* **40**, 453–61.
- Nelson DG, Featherstone JD (1982) Preparation, analysis, and characterization of carbonated apatites. *Calcified Tissue International* **34**, S69–81.
- Nyquist RA, Putzig CL, Leugers MA (1997) *Handbook of Infrared and Raman Spectra of Inorganic Compounds and Organic Salts*. San Diego: Academic Press.
- van Overbeke E, Carlier V, Devaux J, Carter JT, McGrail PT, Legras R (2000) The use of Raman spectroscopy to study the reaction between an amine-terminated thermoplastic and epoxy resins. *Polymer* **41**, 8241–5.
- Parirokh M, Torabinejad M (2010) Mineral trioxide aggregate: a comprehensive literature review-part III: clinical applications, drawbacks, and mechanism of action. *Journal of Endodontics* **36**, 400–13.
- Poggio C, Beltrami R, Colombo M, Ceci M, Dagna A, Chiesa M (2015) *In vitro* antibacterial activity of different pulp capping materials. *Journal of Clinical and Experimental Dentistry* **7**, e584–8.
- Prati C, Gandolfi MG (2015) Calcium silicate bioactive cements: biological perspectives and clinical applications. *Dental Materials* **31**, 351–70. <https://doi.org/10.1016/j.dental.2015.01.004>.
- Prüllage RK, Urban K, Schäfer E, Dammaschke T (2016) Material properties of a tricalcium silicate-containing, a mineral trioxide aggregate-containing, and an epoxy resin-based root canal sealer. *Journal of Endodontics* **42**, 784–8.
- Reston EG, Souza Costa CA (2009) Scanning electron microscopy evaluation of the hard tissue barrier after pulp capping with calcium hydroxide, mineral trioxide aggregate (MTA) or ProRoot MTA. *Australian Endodontic Journal* **35**, 78–84.
- Reyes-Carmona JF, Felipe MS, Felipe WT (2010) The biomineralization ability of mineral trioxide aggregate and Portland cement on dentin enhances the push-out strength. *Journal of Endodontics* **36**, 286–91.
- Rodríguez-Lozano FJ, García-Bernal D, Oñate-Sánchez RE, et al. (2017) Evaluation of cytocompatibility of calcium silicate-based endodontic sealers and their effects on the biological responses of mesenchymal dental stem cells. *International Endodontic Journal* **50**, 67–76.
- Sarkar NK, Caicedo R, Ritwik P, Moiseyeva R, Kawashima I (2005) Physicochemical basis of the biologic properties of mineral trioxide aggregate. *Journal of Endodontics* **31**, 97–100.
- Siboni F, Taddei P, Prati C, Gandolfi MG (2017) Properties of NeoMTA Plus and MTA Plus cements for endodontics. *International Endodontic Journal* **50**, e83–94.
- Silva EJ, Accorsi-Mendonca T, Almeida JF, Ferraz CC, Gomes BP, Zaia AA (2012) Evaluation of cytotoxicity and up-regulation of gelatinases in human fibroblast cells by four

- root canal sealers. *International Endodontic Journal* **45**, 49–56.
- Silva GF, Bosso R, Ferino RV *et al.* (2014) Microparticulated and nanoparticulated zirconium oxide added to calcium silicate cement: evaluation of physicochemical and biological properties. *Journal of Biomedical Materials Research Part A* **102**, 4336–45.
- Silva EJ, Perez R, Valentim RM *et al.* (2017) Dissolution, dislocation and dimensional changes of endodontic sealers after a solubility challenge: a micro-CT approach. *International Endodontic Journal* **50**, 407–14.
- da Silva PT, Pappen FG, Souza EM, Dias JE, Bonetti Filho I, Carlos IZ, *et al.* (2008) Cytotoxicity evaluation of four endodontic sealers. *Brazilian Dental Journal* **19**, 228–31.
- da Silva EJ, Zaia AA, Peters OA (2017) Cytocompatibility of calcium silicate-based sealers in a three-dimensional cell culture model. *Clinical Oral Investigations* **21**, 1531–6.
- Siqueira JF, Lopes HP (1999) Mechanisms of antimicrobial activity of calcium hydroxide: a critical review. *International Endodontic Journal* **32**, 361–9.
- Unosson EJ, Persson C, Engqvist H (2015) An evaluation of methods to determine the porosity of calcium phosphate cements. *Journal of Biomedical Materials Research Part B: Applied Biomaterials* **103**, 62–71.
- Vallés M, Mercadé M, Duran-Sindreu F, Bourdelande JL, Roig M (2013) Influence of light and oxygen on the color stability of five calcium silicate-based materials. *Journal of Endodontics* **39**, 525–8.
- Viapiana R, Guerreiro-Tanomaru JM, Tanomaru-Filho M, Camilleri J (2014) Investigation of the effect of sealer use on the heat generated at the external root surface during root canal obturation using warm vertical compaction technique with System B heat source. *Journal of Endodontics* **40**, 555–61.
- Vitti RP, Prati C, Sinhoreti MA *et al.* (2013a) Chemical-physical properties of experimental root canal sealers based on butyl ethylene glycol disalicylate and MTA. *Dental Materials* **29**, 1287–94.
- Vitti RP, Prati C, Silva EJ *et al.* (2013b) Physical properties of MTA Fillapex sealer. *Journal of Endodontics* **39**, 915–8.
- Witke K, Österle W, Skopp A, Woydt M (2001) Raman microprobe spectroscopy and transmission electron microscopy of thermal sprayed ZrO₂ coatings before and after rub testing of outer air seals. *Journal of Raman Spectroscopy* **32**, 1008–14.
- Zhang R, Yin PG, Wang N, Guo L (2009) Photoluminescence and Raman scattering of ZnO nanorods. *Solid State Sciences* **11**, 865–9.
- Zhou HM, Shen Y, Zheng W, Li L, Zheng YF, Haapasalo M (2013) Physical properties of 5 root canal sealers. *Journal of Endodontics* **39**, 1281–6.



Properties of calcium silicate-monobasic calcium phosphate materials for endodontics containing tantalum pentoxide and zirconium oxide

Fausto Zamparini¹ · Francesco Siboni¹ · Carlo Prati¹ · Paola Taddei² · Maria Giovanna Gandolfi¹

Received: 30 October 2017 / Accepted: 16 April 2018 / Published online: 8 May 2018
© Springer-Verlag GmbH Germany, part of Springer Nature 2018

Abstract

Objective

The aim of the study was to evaluate chemical-physical properties and apatite-forming ability of three premixed calcium silicate materials containing monobasic calcium phosphate ($\text{CaH}_4\text{P}_2\text{O}_8$) bioceramic, tantalum pentoxide and zirconium oxide, recently marketed for endodontics (TotalFill BC-Sealer, BC-RRM-Paste, BC-RRM-Putty).

Materials and methods

Microchemical and micromorphological analyses, radiopacity, initial and final setting times, calcium release and alkalisating activity were tested. The nucleation of calcium phosphates (CaPs) and/or apatite after 28 days ageing was evaluated by ESEM-EDX and micro-Raman spectroscopy.

Results

BC-Sealer and BC-RRM-Paste showed similar initial (23 h), prolonged final (52 h) setting times and good radiopacity (> 7 mm Al); BC-RRM-Putty showed fast initial (2 h) and final setting times (27 h) and excellent radiopacity (> 9 mm Al). All materials induced a marked alkalisation (pH 11–12) up to 28 days and showed the release of calcium ions throughout the entire test period (cumulative calcium release 641–806 ppm). After 28 days ageing, a well-distributed mineral layer was present on all samples surface; EDX demonstrated relevant calcium and phosphorous peaks. B-type carbonated apatite and calcite deposits were identified by micro-Raman spectroscopy on all the 28-day-aged samples; the deposit thickness was higher on BC-RRM-Paste and BC-RRM-Putty, in agreement with calcium release data.

Conclusions

These materials met the required chemical and physical standards and released biologically relevant ions. The CaSi-CaH₄P₂O₈ system present in the materials provided Ca and OH ions release with marked abilities to nucleate a layer of B-type carbonated apatite favoured/accelerated by the bioceramic presence.

Clinical relevance

The ability to nucleate apatite may lead many clinical advantages: In orthograde endodontics, it may improve the sealing ability by the deposition of CaPs at the material-root dentine interface, and in endodontic surgery, it could promote bone and periodontal tissue regeneration. As premixed materials, their application in endodontics may result easier in several complex endodontic situations (apicoectomy, root perforation, presence of wide/wet apices).

Keywords TotalFill BC-Sealer · TotalFill BC-RRM-Paste · TotalFill BC-RRM-Putty · Calcium silicate · Monobasic calcium phosphate · Bioceramics

✉ Maria Giovanna Gandolfi
mgiovanna.gandolfi@unibo.it

¹ Laboratory of Biomaterials and Oral Pathology, Dental School, Department of Biomedical and Neuromotor Sciences, University of Bologna, Bologna, Italy

² Biochemistry Unit, Department of Biomedical and Neuromotor Sciences, University of Bologna, Bologna, Italy

Introduction

In the last two decades, several hydraulic calcium silicate (HCaSi) materials have been developed for different endodontic applications due to their chemical-physical properties (hydrophilicity and self-setting in fluid-contaminated environments) and good biological behaviour [1, 2].

Recently, calcium silicate-based materials containing monobasic calcium phosphate bioceramic (BC) (Lu D, Zhou S, Hydraulic cement compositions and methods of making and using the same patent US 2006/0213395 A1), known as EndoSequence by Brasseler in the USA or TotalFill by FKG in Europe, have been launched. TotalFill BC formulation has been modified for different endodontic applications, namely Sealer (BC-Sealer) for endodontic sealing, RRM-Paste (BC-RRM-Paste) for root perforations and reparation/resorption, and RRM-Putty (BC-RRM-Putty) for root-end filling, apexification and pulp capping. Their setting reaction is activated by the hydration induced by the moisture present in the peri-radicular area, into the root canal, or into dentinal tubules [3].

Calcium phosphates (CaPs) represent an attractive ingredient due to their contribution to the positive cell response and activation of matrix mineralisation genes [4, 5]. CaPs components in hydraulic calcium silicate cements showed to markedly modify the chemical-physical properties [6], improve cell response [7] and increase the apatite-forming ability [8].

Regarding these BC materials, some chemical-physical properties have been investigated, mainly for BC-Sealer [3, 9–12]. Only two studies have been published on BC-RRM-Putty [13, 14] and BC-RRM-Paste [15, 16]. No one of these materials have been submitted to the complete screening of many chemical-physical properties, and no studies analysed the apatite nucleation in Simulated Body Fluids through Raman analysis or the open/close porosity, solubility, ion release and water sorption.

Therefore, the present study aimed to screen many selected chemical-physical properties with potential clinical implications (ion release, initial and final setting times, radiopacity, solubility, water sorption and porosity) and the ability to nucleate apatite of these BC materials.

Materials and methods

Materials

The tested materials are listed in Table 1. All the materials are premixed, ready-to-use commercial materials proposed for different endodontic applications (root perforation, root canal sealer, root-end cavity filling).

Radiopacity

The radiopacity tests were performed in accordance with ISO 6876:2012 (Dental root canal sealing materials). Samples were prepared according to the manufacturer's instructions and compacted into moulds (10.0 mm diameter, 1.0 mm height; $n = 3$ per group). Completely set samples were demoulded and radiographed using a radiographic unit (Myray Cefla, Imola, Italy) with a reference aluminium step wedge (60 mm long, 10 mm wide thickness varying from 2 to 6 mm in 1-mm increments). The target-film distance was approx. 30 cm with the sample at 3 cm from the surface of the radiographic tube, 0.13 s exposure at 70 kVp and 8 mA [17].

The film (Kodak dental film, Eastman Kodak Company, Carestream Health Inc., Rochester, New York, NY, USA) was processed (automatic developer, 4 min at 30 °C) and scanned (Epson Perfection V750 PRO, Jakarta, Indonesia). The radiographic density (colour intensity) data were converted (software ImageJ, Wayne Rasband, National Institutes of Health (NIH), Bethesda, MD, USA) into aluminium step-wedge equivalent thickness (mm Al). A radiopacity equal or higher than 3 mm Al is required by the ISO 6876:2012.

Setting times

Samples were prepared following the manufacturer's instructions and compacted into a mould (10-mm diameter, 2 mm thickness; $n = 3$ per group). The initial and final setting times were measured by evaluating the absence of indentation caused by Gillmore needles (ASTM C 226-07 Standard Specification for Air-Entraining Additions for Use in the Manufacture of Air-Entraining Hydraulic Cement) with the following modifications. Ten grams of samples were used instead of 650 g and the physiological temperature of 37 °C instead of 25 °C [18]. The initial Gillmore tip (113.4 g weight and 2.12 mm diameter) and the final Gillmore tip (453.6 g weight and 1.06 mm diameter) were used on the cement paste stored at 37 °C and $95 \pm 5\%$ relative humidity [17, 18].

Alkalis activity, calcium release, porosity, solubility, water sorption

Materials compacted into polyvinylchloride moulds (8-mm diameter, 1.6 mm height; $n = 8$ per group) were immediately

Table 1 Composition and lot number of the tested materials; manufacturer BUSA, Brasseler U.S.A Dental, Savannah, GA, USA

	Composition	Lot. number
BC-Sealer	Zirconium oxide, calcium silicates, calcium phosphate monobasic, calcium hydroxide, filler and thickening agents	14003SP
BC-RRM-Paste	Zirconium oxide, calcium silicates, tantalum pentoxide, calcium phosphate monobasic, filler agents	BP 15002
BC-RRM-Putty	Zirconium oxide, calcium silicates, tantalum pentoxide, calcium phosphate monobasic, filler agents	1501BPP

immersed in 10 mL of deionised water (pH 6.8) into polypropylene sealed containers and stored at 37 °C. The soaking water was replaced at each endpoint (3 h and 1, 3, 7, 14, 28 days) and analysed for pH and calcium content under magnetic stirring at room temperature (24 °C) by potentiometric method by multiparameter laboratory meter (inoLab 750, WTW, Weilheim, Germany) connected to a selective electrode (Sen Tix Sur; WTW) for pH measurements or a calcium probe (Calcium ion electrode, Eutech Instruments Pte Ltd, Singapore) after addition of a ionic strength adjuster (ISA; 4 mol/L KCl; WTW) for released calcium measurements.

Other filled moulds ($n = 6$ samples for each material) were placed at 37 °C and 99% relative humidity for a period of 50% longer than the final setting time [19, 20]. Each demoulded sample was weighed to determine the initial mass (I) and immediately immersed vertically in 20 mL of distilled water and placed at 37 °C for 24 h. The mass whilst suspended in water (S) was determined. The specimens were then removed from water, and the excess water from the surface of each sample was removed using a moistened filter paper (20 mL of distilled water dropped on a 9 cm wide 12.5-cm-long glass plate covered by a filter paper), and the saturated mass (M) was recorded. Finally, the samples were dried at 37 °C until the weight was stable, and the final dry mass (D) was recorded. Open pores volume ($V_{OP} = M - D$, in cm^3), impervious portion volume ($V_{IP} = D - S$, in cm^3) and apparent porosity ($P = [(M - D)/V] \times 100$, in percentage) were calculated following Archimedes' principle [20–23]. Water sorption ($A = [(M - D)/D] \times 100$) and solubility ($S = [(I - D)/D] \times 100$) were calculated as percentage of the original weight [19, 20]. Each weight measurement was repeated three times using an analytical balance (Bel Engineering series M, Monza, Italy) and determined to the nearest 0.001 g. Mean values of the measures were reported.

Surface characterisation and CaPs nucleation

Fresh samples were compacted into a mould (8 mm diameter, 1.6 mm height) immediately immersed upright in 20 mL of HBSS (Hank's Balanced Salt Solution, Lonza, Verviers, Belgium) and stored at 37 °C for 28 days (ISO 23317:2014) weekly replaced [24, 25].

Surface of fresh and 28-day aged materials was examined ($n = 3$ per group) by environmental scanning electron microscopy (ESEM; Zeiss EVO 50) with elemental dispersive X-ray microanalysis (EDX; Oxford Instruments) and micro-Raman spectrometry. Operative ESEM-EDX conditions are reported elsewhere [20, 26]; reported images and elemental analyses are representative for each group.

Micro-Raman spectra were measured on the surface of the fresh samples as well as after ageing in HBSS for 28 days. They were obtained using a Jasco NRS-2000C instrument in back-scattering conditions with 4 cm^{-1} spectral resolution,

using the 532-nm Green Diode Pumped Solid State (DPSS) Laser Driver (RgBLase LLC, USA) with a power of ca. 25 mW, properly filtered. A 160-K cooled digital CCD (Spec-10: 100B, Roper Scientific Inc.) was used as detector. A microscope of $\times 100$ magnification with a confocal pinhole with an aperture diameter of $3000 \mu\text{m}$ was utilised. The spectra of the aged Total Fill BC Sealer were measured also using a confocal pinhole with an aperture diameter of $200 \mu\text{m}$, to obtain signals from a limited in-depth region.

All the Raman measurements were made in a fully non-destructive way, without any sample manipulation. All the reported spectra are average of five measurements at least.

The relative alite (tricalcium silicate) content of the fresh samples was evaluated with reference to zirconia, which was present in all the materials under study; to this purpose, the $I_{823(\text{alite})}/I_{480(\text{zirconia})}$ Raman intensity ratio was calculated as peak heights, where $I_{823(\text{alite})}$ and $I_{480(\text{zirconia})}$ were the intensity of the Raman bands at 823 and 480 cm^{-1} , respectively, i.e. the strongest bands assignable to alite and zirconia phases.

Statistical analysis

Results were analysed by two-way ANOVA with RM Student-Newman-Keuls test ($p < 0.05$) for ion release or one-way ANOVA with Student-Newman-Keuls test ($p < 0.05$) for setting times, radiopacity, solubility, water sorption and porosity.

Results

Radiopacity and setting times

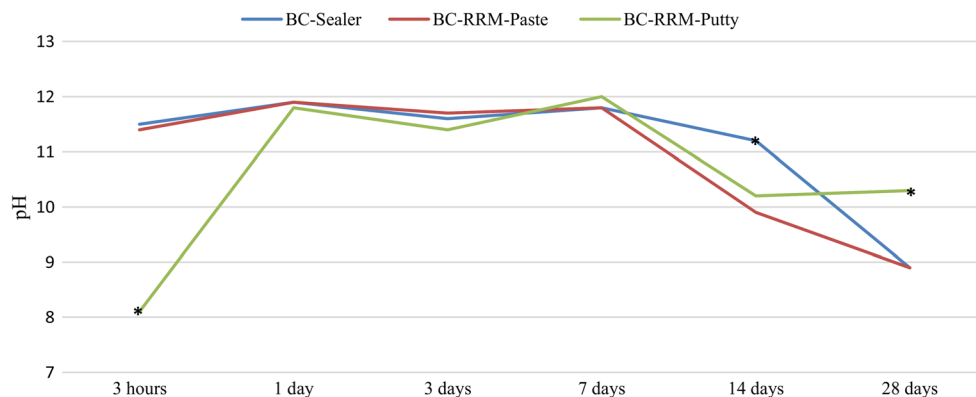
Materials showed high radiopacity values (Table 2). In particular, BC-RRM-Putty showed the highest radiopacity values, statistically different from the other two materials ($p < 0.05$). Initial and final setting times showed similar values for BC-Sealer and BC-RRM-Paste (Table 2). Differently, BC-RRM-Putty showed markedly lower values ($p < 0.05$) of both initial and final setting times.

Alkalisising activity and calcium release

All materials induced a marked alkalisisation of the soaking water (Fig. 1). BC-Sealer and BC-RRM-Paste showed higher pH values up to 3 h, compared to BC-RRM-Putty ($p < 0.05$) which demonstrated a higher long-term alkalisising ability. The pH was approx. 11–12 during the first 7 days for all the materials, and then it decreased; at 28 days, BC-RRM-Putty showed higher values than the other materials ($p < 0.05$). All materials showed a marked ability to immediately release calcium (ppm) (Table 3). After 14 days, BC-RRM-Putty showed statistically higher mean values (117.9 ppm) ($p < 0.05$). All

Table 2 Radiopacity and setting times of the examined materials. Different superscript small letters represent statistically significant differences among the materials (one-way repeated measures analysis of variance followed by Student-Newman-Keuls test ($p < 0.05$))

	Radiopacity (mm Al)	Initial setting time (h)	Final setting time (h)
BC-Sealer	7.45 ± 0.48 ^a	23.0 ± 0.1 ^a	52.0 ± 0.1 ^a
BC-RRM-Paste	7.24 ± 0.36 ^a	22.5 ± 0.1 ^a	51.0 ± 0.1 ^a
BC-RRM-Putty	9.17 ± 0.34 ^b	2.0 ± 0.1 ^b	27.0 ± 0.1 ^b

**Fig. 1** pH values of the soaking water of the tested materials: BC-Sealer and BC-RRM-Pasted showed high alkaline values (around 12) from 3 h; their values were similar up to 7 days. BC-RRM Putty reached a similar pH at 1 day and remained constant up to 7 days. At 14 days, pH of all the

materials decreased. BC-Sealer showed a higher pH than the other two materials. Differently, at 28 days, BC-RRM-Putty showed a higher pH value. Asterisks represent statistically significant differences among the materials ($p < 0.05$)

tested materials showed a decrease to similar values of calcium release at 28 days, demonstrating a long-time activity. BC-RRM-Paste showed the highest cumulative release, followed by BC-RRM-Putty and BC-Sealer ($p < 0.05$).

Porosity, solubility, water sorption

Materials showed different physical properties (Table 4): BC-Sealer showed the highest values of V_{OP} , P , A and S ($p < 0.05$). Interestingly, BC-RRM-Putty showed the lowest values in term of V_{IP} and, as consequence, the most reduced percentage of A , PS ($p < 0.05$).

Surface characterisation and CaPs nucleation

Fresh BC-Sealer

ESEM showed a quite regular surface with sparse granules (Fig. 2a, b); EDX spectra (Fig. 2c) displayed the constitutive elements (wt% range) carbon (C, 23.30–32.11), nitrogen (N, 5.83–12.48), oxygen (O, 27.14–31.54), silicon (Si, 0.90–1.75), phosphorus (P, 0–0.51), calcium (Ca, 5.48–11.58) and zirconium (Zr, 16.78–29.36).

Micro-Raman (Fig. 2g) detected monoclinic zirconia [27], monobasic calcium phosphate, triclinic alite, β -belite [28], anhydrite [29] and an organic component.

Table 3 Calcium released in soaking water: different superscript letters represent statistically significant differences (two-way repeated measures analysis of variance followed by Student-Newman-Keuls test ($p < 0.05$) in the same horizontal row (capital letters) or in the same column (small letters))

Calcium released (ppm)	0–3 h	3 h–1 day	1–3 days	3–7 days	7–14 days	14–28 days	Cumulative
BC-Sealer	173.1 ± 19.6 ^{aA}	135.7 ± 22.5 ^{aB}	107.1 ± 24.6 ^{aC}	134.6 ± 22.6 ^{bD}	74.6 ± 30.2 ^{aE}	11.1 ± 4.0 ^{aF}	641.9 ± 23.1 ^a
BC-RRM-Paste	173.2 ± 8.3 ^{aA}	168.6 ± 13.2 ^{bA}	185.7 ± 33.1 ^{bA}	197.4 ± 12.6 ^{aB}	68.0 ± 21.2 ^{aBC}	11.1 ± 4.5 ^{aD}	806.9 ± 45.2 ^b
BC-RRM-Putty	153.7 ± 14.7 ^{bA}	161.7 ± 24.1 ^{bA}	130.5 ± 26.4 ^{cAB}	188.3 ± 30.9 ^{aC}	117.9 ± 6.0 ^{bD}	13.5 ± 1.3 ^{aE}	768.3 ± 62.7 ^b

Table 4 Porosity (open porosity V_{OP} , impervious porosity V_{IP} and apparent porosity P), water sorption (A) and solubility (S) of the tested materials. Different superscript small letters represent statisticallysignificant differences among the materials (one-way analysis of variance followed by Student-Newman-Keuls test ($p < 0.05$))

Porosity, water sorption and solubility in soaking water

	V_{OP} (cm ³)	V_{IP} (cm ³)	P (%)	A (%)	S (%)
BC-Sealer	0.0719 ± 0.0060 ^a	0.0582 ± 0.0068 ^a	55.3 ± 3.4 ^a	39.8 ± 0.29 ^a	29.3 ± 3.1 ^a
BC-RRM-Paste	0.0390 ± 0.0017 ^b	0.0623 ± 0.0035 ^b	38.5 ± 0.7 ^b	20.5 ± 0.9 ^b	18.1 ± 0.3 ^b
BC-RRM-Putty	0.0033 ± 0.0061 ^c	0.0782 ± 0.0084 ^c	32.91 ± 1.5 ^c	14.9 ± 0.7 ^c	13.7 ± 1.7 ^c

Fresh BC-RRM-Paste

ESEM showed a regular surface with sparse granules (Fig. 3a, b); EDX (Fig. 3c) revealed C (21.28–35.58), N (5.83–10.65), O (33.92–34.32), Si (2.79–3.65), P (0.24–0.83), Ca (8.52–14.59), Zr (10.52–16.12), tantalum (Ta, 1.46–2.79) and traces of sulphur (S, 0.26–0.50). In addition to calcium silicates, zirconia, monobasic calcium phosphate, anhydrite and organic components, micro-Raman also detected tantalum pentoxide (Fig. 3g) [30].

Fresh BC-RRM-Putty

ESEM showed a higher amount of granules on surface (Fig. 4a, b). EDX (Fig. 4c) and micro-Raman (Fig. 4g) revealed the same components/phases of BC-RRM-Paste. C (11.17–15.62), N (3.81–7.92), O (35.15–36.90), Si (4.82–5.92), P (0.51–1.11), S (0.42–0.80), Ca (19.64–23.60), Zr (11.57–14.01) and Ta (1.30–3.85) were detected.

Twenty-eight-day aged BC-Sealer

ESEM showed a coating composed of small spherulites (Fig. 1d, e). EDX (Fig. 1f) detected the appearance of sodium (Na), magnesium (Mg) and chlorine (Cl), the increase of Ca and P and the decrease of Si. Zr became undetectable. Ca/P atomic ratio ranged from 2.87 to 3.40. Micro-Raman (Fig. 2g) showed B-type carbonated apatite deposition, as revealed by the strengthening of the 960 cm⁻¹ phosphate band and the appearance of the band at about 1075 cm⁻¹ [31]. Calcite [32] was also detected. Bands due to the underlying cement (particularly those due to zirconia) were still detectable also using 200 μm pinhole. To gain more insights into the formed phases and thus to confirm the assignments above, the deposit was removed from the surface of the sample and analysed through micro-Raman spectroscopy by focusing the laser onto single granules. The spectra reported in Fig. 2h are representative of the single detected phases: The top spectrum belongs to B-type carbonated apatite, the bottom one to calcite.

Twenty-eight-day aged BC-RRM-Paste

ESEM showed a well-distributed coating composed of small spherulites (Fig. 3d, e). EDX (Fig. 3f) detected the presence of Na, Mg, Cl and potassium (K), Ca and P increase, Si decrease; Ta and Zr were not detected. Ca/P was 1.96–2.26. Micro-Raman detected B-type carbonated apatite and calcite deposits (Fig. 3g); the bands ascribable to the underlying cement were very weak.

Twenty-eight-day aged BC-RRM-Putty

ESEM revealed the covering of a thick layer of nanospherulites (Fig. 4d, e). EDX revealed the presence of Na, Mg, Cl and potassium (K), a moderate Ca and a marked P increase and traces of Si (Fig. 4f). Ta and Zr were not detected. Ca/P was 1.84–1.98. Micro-Raman showed B-type carbonated apatite and calcite deposits (Fig. 4g); the bands ascribable to the underlying cement were extremely weak.

Discussion

The surface microchemical characterisation, the ability to nucleate CaPs and the screening of selected chemical-physical properties of new calcium silicate endodontic materials containing monobasic calcium phosphate CaH₄P₂O₈ are investigated in this study. A great number of these properties are poorly investigated and data published in literature are controversial, in particular if we consider the materials chemical composition, their modifications when immersed in simulated clinical conditions (apatite nucleation ability) and their radiopacity.

Compositional EDX and micro-Raman analyses showed the presence of calcium silicates (triclinic alite and β-belite), monobasic calcium phosphate, monoclinic zirconia and tantalum pentoxide in BC-RRM-Paste and BC-RRM-Putty, in agreement with the manufacturer declaration. On the basis of the trend of the $I_{823(\text{alite})}/I_{480(\text{zirconia})}$ Raman intensity ratio, it can be affirmed that alite increased along the series BC-Sealer ($I_{823(\text{alite})}/I_{480(\text{zirconia})} = 0.31 \pm 0.01$) < BC-RRM ($I_{823(\text{alite})}$

Fig. 2 ESEM images, EDX microanalyses and micro-Raman spectra (average of at least five measurements, measured under different optical conditions, i.e., using pinholes with 3000 and 200 μm diameters) of fresh and 28-day aged samples of BC-Sealer. **a, b** Fresh samples ($\times 3000$ magnification) showed a quite regular surface with sparse granules. **c** EDX displayed C, N, O, Si, P, Ca and Zr. In particular, approx. 30% in wt of Zr was detected by EDX of fresh samples. **d, e** Twenty-eight-day aged samples ($\times 3000$ magnification) revealed a regular surface with a well-distributed layer of small spherulites. **f** EDX spectra revealed the appearance of Na, Mg and Cl (attributable to the HBSS medium), the decrease of C, N and traces of Si, and the marked increase of O, P and Ca. No Zr was detected. **g** Micro-Raman analysis on fresh samples shows the bands ascribable to the organic component (OR), anhydrite (An), monobasic calcium phosphate (mCaP), monoclinic zirconia (Z), triclinic alite (A) and β -belite (B). Micro-Raman analysis on 28-day aged samples showed the formation of calcite (C) and B-type carbonated apatite (Ap) on the material surface. Zirconia (Z) bands were still detected also by using a 200 μm pinhole. **h** Micro-Raman spectra recorded on single granules of the deposit removed from the surface of the 28-day aged sample (* = laser emission lines).

$I_{480(\text{zirconia})} = 1.01 \pm 0.01 < \text{BC-RRM-Putty}$ ($I_{823(\text{alite})}$ / $I_{480(\text{zirconia})} = 1.26 \pm 0.09$), in agreement with the EDX data.

In our study, micro-Raman analyses on fresh samples showed higher anhydrite amounts in BC-RRM-Putty and BC-RRM-Paste than in BC-Sealer; accordingly, EDX revealed the presence of S (0.4–0.7 wt%) only in the first two materials. Calcium sulphate and $\text{Ca}(\text{OH})_2$ are setting regulators [33]. Other EDX studies showed traces of S in fresh BC-RRM-Putty [13], but not in fresh BC-Sealer [3]. No EDX studies have been performed on fresh BC-RRM-Paste.

Interestingly, compositional analyses showed only traces of P (range 0–1.11%), although the presence of calcium phosphate monobasic is declared among the BC-Sealer ingredients, whilst it is absent in the safety data sheet composition (strangely no ingredients are reported for both BC-RRM-Paste and BC-RRM-Putty). A previous study reported no traces of P in BC-RRM-Putty composition [13], which has been related to the overlapping of P and Zr peaks that may underestimate the P content [34].

The presence of Ta (2–3 wt%) is responsible for the high radiopacity of the BC-RRM-Paste and BC-RRM-Putty, despite the halved presence of Zr (10–15 wt%) compared to the BC-Sealer (≈ 30 wt%). Indeed, all materials showed excellent radiopacity (7.45–9.17 mm Al), especially BC-Sealer, with markedly higher values than that required by ISO 6876 specification (> 3 mm Al) providing potential advantages for clinicians.

Other HCaSi endodontic materials introduced zirconium oxide in their formulation for the provided advantages in comparison with other radiopacifying agents such as bismuth oxide. Some of the most important characteristics are that zirconium oxide is more bio-inert [35], less cytotoxic [18], and does not cause tooth discolouration when in contact with some endodontic irrigants, such as NaOCl. [36]

Radiopacity is an important property for endodontic materials in both orthograde and retrograde clinical application. A

low radiopaque material cannot be monitored during the endodontic procedures to evaluate the periradicular seal.

In our study, BC-Sealer showed consistently higher values (7.45 mm Al) than that required from ISO 6876/2012 (> 3 mm Al). Differently, other studies obtained higher (10.8 mm Al) [3] or lower (3.8 mm Al, 6.7 mm Al) [9, 10] values; this may be related to different reasons as 10-cm distance from the radiographic unit instead of 30 cm [10] or different radiological parameters (exposure times, tube voltages) [9], or a different X-ray device (digital phosphor plate) [3].

In recent studies [17, 19], calcium silicate-based root canal sealers showed radiopacity values markedly lower than that displayed by BC-Sealer, namely BioRoot 5.2 mm Al, Guttaflow Bioseal 5.65 mm Al and MTA Fillapex 7.17 mm Al; despite all these values that are higher than that specified by ISO 6876/2012, these sealers might not satisfy clinicians preferring more radiopaque easier detectable materials.

In our study, BC-RRM-Putty or BC-RRM-Paste showed high radiopacity results (9.17 and 7.24 mm Al). No other studies investigated radiopacity of these materials.

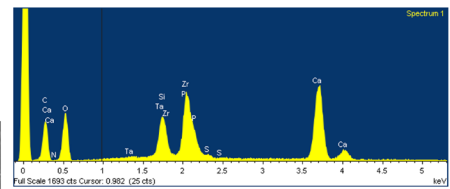
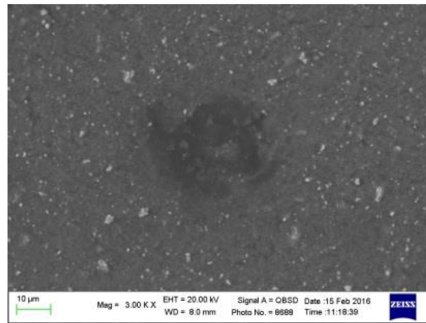
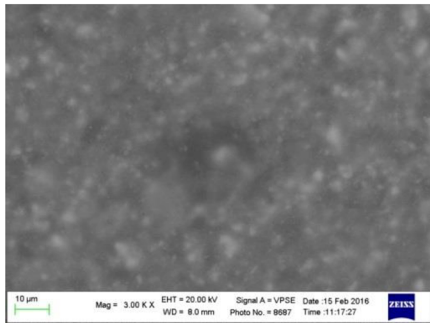
All materials showed marked Ca leaching and strong alkalisating activity, both higher (especially Ca release) than other commercial HCaSi materials previously tested in the same laboratory with the same methodology [2], including salicylate-based root canal sealers (MTA Fillapex) [19], tricalcium silicate powders modified with a polymer gel (MTA plus and Neo MTA plus) [20, 37] and calcium silicate sealers modified with povidone and polycarboxylate [17].

In particular, calcium release was high since 3-h immersion and showed a similar trend for the tested materials. Cumulative calcium release was extremely high for all the three sealers, revealing mean values comprised from 641.9 to 806.9 ppm. The ability to release Ca^{++} and OH^- may be important if we consider the biointeractive properties of these ions. Calcium ions are powerful signalling ions for mineralising cells [38], such as osteoblasts [39], orofacial bone mesenchymal stem cells [7], dental pulp stem cells [40] and cementoblasts [41]. OH^- release during the hydration processes increases the local pH, inducing an important antibacterial effect [3]. Moreover, alkaline pH favours apatite precipitation. These materials proved to strongly alkalisate the soaking medium in the first hours (up to 12), with decreasing values from 14 days. At 28 days, all the materials showed a pH > 8 , with one of them (BC-RRM-Putty) that maintained a pH value around 10. These values suggest that these materials may preserve their properties in the long-term, providing a support to peri-radicular healing processes.

The alkalisating activity of BC-Sealer, showing a pH > 11.7 after 1-day immersion, is in agreement with a previous study [9]. BC-RRM-Paste showed similar values than BC-Sealer, with the exception of the 14-day evaluation, that was significantly lower ($p < 0.05$). Differently, BC-RRM Putty showed a higher alkalisating activity in the long-term: pH mean value at

BC-RRM-Paste

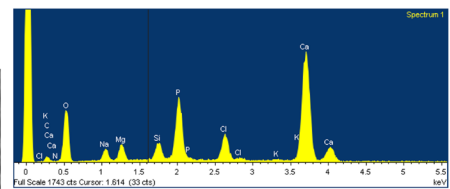
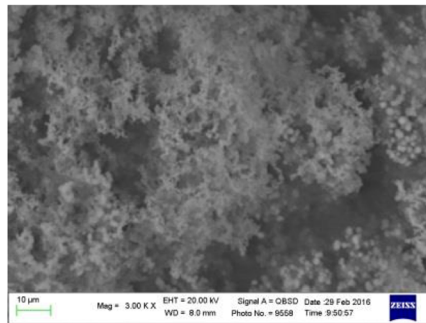
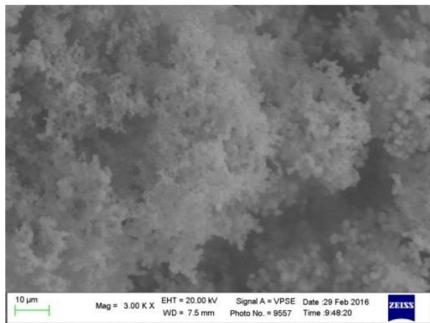
fresh



c

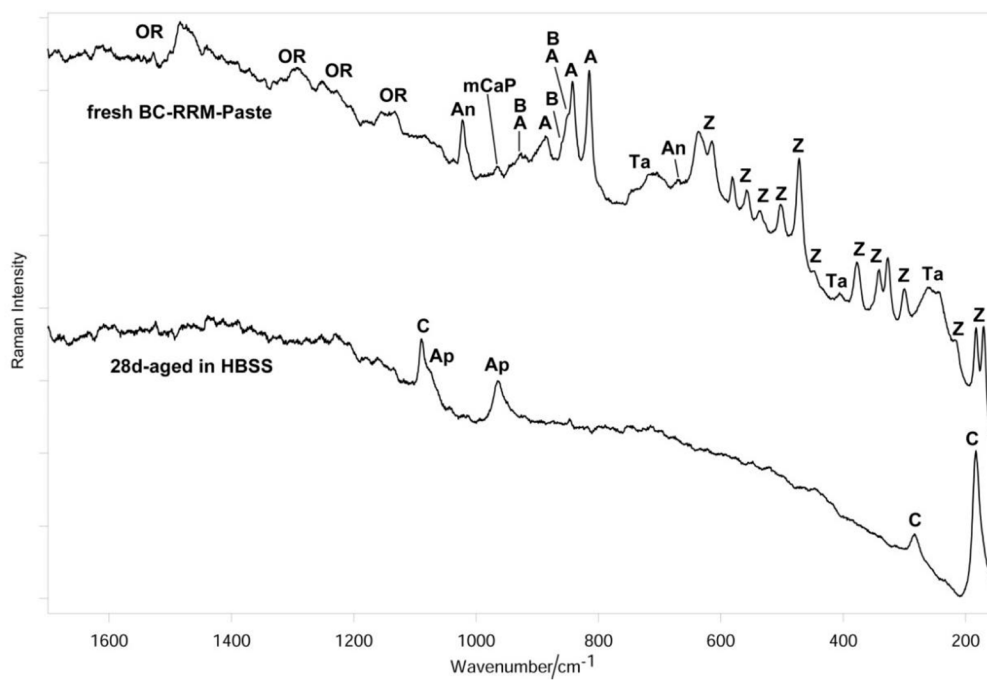
Element	Weight %	Atomic %
C K	28.04	42.79
N K	5.53	7.24
O K	34.02	38.98
Si K	2.79	1.82
P K	0.64	0.38
S K	0.35	0.20
Ca K	11.88	5.43
Zr L	14.73	2.96
Ta M	2.03	0.21
Totals	100.00	

28d-aged in HBSS



f

Element	Weight %	Atomic %
C K	6.77	11.34
N K	2.70	3.88
O K	46.99	59.06
Na K	2.67	2.34
Mg K	2.54	2.10
Si K	2.09	1.49
P K	8.97	5.82
Cl K	4.24	2.40
K K	0.18	0.09
Ca K	22.84	11.46
Totals	100.00	



g

Fig. 3 ESEM images, EDX microanalyses and micro-Raman spectra (average of at least five measurements) of fresh and 28-day aged samples of BC-RRM-Paste. **a, b** Fresh samples showed a regular surface with a large amount of small granules. **c** EDX on fresh samples revealed C, N, O, Si, P, Ca, Zr, Ta and S. **d, e** Twenty-eight-day aged samples revealed a regular surface with a well-distributed layer of small spherulites. **f** EDX spectra revealed the appearance of Na, Mg, Cl and K (attributable to the HBSS medium), the decrease of C, N and traces of Si, and the marked increase of O, P and Ca. Zr, Ta and S were not detected. **g** Micro-Raman analysis on fresh samples revealed bands ascribable to the organic component (OR), anhydrite (An), monobasic calcium phosphate (mCaP), monoclinic zirconia (Z), triclinic alite (A), β -belite (B) and tantalum pentoxide (Ta). A thick layer of B-type carbonated apatite (Ap) and calcite (C) deposition was detected on 28-day aged samples.

28-day evaluation was 10.3 ± 0.4 , significantly higher than the other two materials ($p < 0.05$).

No studies assessed the alkalising activity of BC-RRM-Putty or BC-RRM-Paste; only a study *ex vivo* on BC-RRM-Paste tested the pH of the material surface in root-filled sections [16].

The biointeractive properties provide different biological and clinical advantages. In addition to the abovementioned cytological effects related to calcium release, the early strong alkalisation may better counteract the early bacterial site contamination after endodontic procedures (after root end surgeries, root perforation and in the presence of infected periapical lesions). Moreover, apatite nucleates in alkaline pH [28] and the formation of an apatite layer may improve the biocompatibility (ISO 23317:2014), mineralising cell response and bone healing.

Differences in *open porosity* among the materials is related to water sorption, solubility, ion release and setting time. The lowest values of *open porosity* found for BC-RRM-Putty can be correlated to the lowest Ca release and alkalising activity at short times and to the fast-initial setting time. Differently, the highest open porosity of BC-Sealer is related to the high water sorption, high calcium release and solubility, and to the prolonged initial setting time. It should be underlined that the *in vivo* solubility of CaSi materials is lower than *in vitro* due to the presence of serum proteins and apatite nucleation [8] and that the open porosity, water sorption and solubility resulted markedly lower than other CaSi-based materials tested in the same laboratory with the same methodology [2, 19, 20].

No porosity studies have been previously published on BC-RRM-Paste or BC-Sealer, and only a study evaluated the apparent porosity of BC-RRM-Putty by a different method (gas saturation) showing lower values [14].

This study showed a very *fast initial setting time* for BC-RRM-Putty (2 h). This value was twice longer than that reported in a previous study [14], probably attributable to different materials storage (samples immersed in water bath at 37° instead of $99 \pm 5\%$ relative humidity). The final setting time of BC-Sealer was 23 h, in agreement with a previous study [3] and with the manufacturer statements. No studies on setting time have been performed on BC-RRM-Paste.

However, higher setting times may be expected in some endodontic situations such as in the presence of wet/wide apices where the environmental moisture and blood may adversely affect the setting time [11].

The study of the ability to nucleate apatite of these new materials is attractive, as the presence of CaPs component in HCasi cements should promote and accelerate the formation of a superficial CaPs layer [6].

In vitro investigation of materials apatite forming ability is an important analysis that needs to be evaluated when considering materials that need to be placed in contact with bone and periapical tissues. To the best of our knowledge, bioactivity was not adequately investigated regarding these materials. Indeed, no apatite forming ability studies have been previously published on BC-RRM-Paste. Only one study concerning BC-Sealer [42] and one study concerning BC-RRM-Putty [3] evaluated by XRD the apatite formation on fresh and aged samples. No microchemical surface studies of these materials have been performed by Raman in association with EDX. Two studies wrongly evaluated the apatite-forming ability after soaking in PBS using inadequate technique (EDX) [12, 15]. A study tested BC-RRM-Paste soaked in PBS for 7 days by SEM-EDX [15], showing well-distributed clusters of acicular-spherical CaP deposits, not different from our ESEM images.

Another study investigated BC-Sealer by SEM-EDX after immersion (in PBS for 1–90 days) [12]. However, no micro-Raman or XRD analyses were performed to ascertain the presence of apatite; therefore, the presence of apatite crystals on the mineral layer could not be assumed.

Conversely, in the present study, Raman analyses showed the nucleation of a B-type carbonated apatite on all the materials, whose thickness was higher on BC-RRM-Paste and BC-RRM-Putty than on BC-Sealer, in agreement with the calcium release cumulative data.

BC-RRM-Putty showed a Ca/P 1.84–1.96 typical of Ca-rich carbonated apatite [25] with contribution from calcium carbonate, BC-RRM-Paste showed Ca/P 1.96–2.26 resulting from Ca-rich carbonated apatite and calcium carbonate and BC-Sealer showed $Ca/P > 2.0$ due to high calcium carbonate formation.

At basic pHs (i.e. in the alkaline environment originated from the hydration of CaSi), monobasic calcium phosphate hydrolyses producing hydroxyapatite. In fact, this phase represents the least soluble calcium phosphate phase above pH 4.2; therefore, any other calcium phosphate above this pH will dissolve and reprecipitate as hydroxyapatite. In the presence of carbonate ions, carbonated apatite may form.

Raman spectroscopy has been widely applied, alone or in conjunction with other techniques, to the study of synthetic and biological carbonated apatites [43–46].

Several studies have proposed micro-Raman spectroscopy as technique of choice to detect B-type carbonated apatites in the study of physiological and pathological mineralisation processes thanks to its non-destructive and non-invasive

BC-RRM-Putty

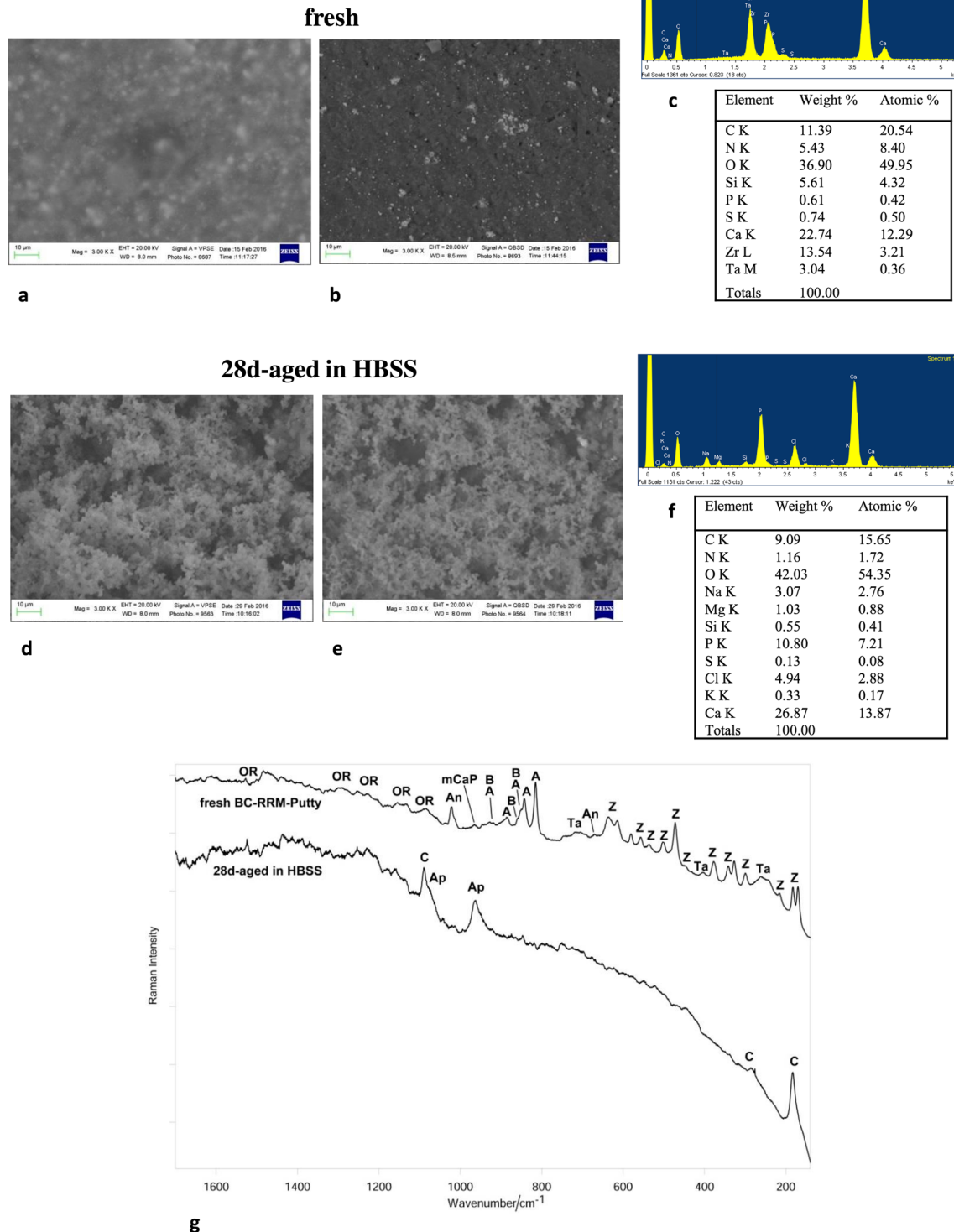


Fig. 4 ESEM images, EDX microanalyses and micro-Raman spectra (average of at least five measurements) of fresh and 28-day aged samples of BC-RRM-Putty. **a, b** Fresh samples showed a regular surface with a large amount of small granules. **c** EDX on fresh samples revealed C, N, O, Si, P, Ca, Zr, Ta and S. This material showed the highest percentages of Ca and Si. **d, e** Twenty-eight-day aged samples revealed a regular surface with a well-distributed layer of small spherulites. **f** EDX spectra revealed the appearance of Na, Mg, Cl and K (attributable to the

HBSS medium), the decrease of C, N and traces of Si and S, and the marked increase of O, P and Ca. Zr and Ta were not detected. **g** Micro-Raman analysis on fresh samples revealed bands assignable to the organic component (OR), anhydrite (An), monobasic calcium phosphate (mCaP), monoclinic zirconia (Z), triclinic alite (A), β -belite (B) and tantalum pentoxide (Ta). Twenty-eight-day aged samples showed a thick layer of B-type carbonated apatite (Ap) and calcite (C).

nature as well as its ability to probe small volumes in the cubic micrometer range [46–50].

In the present study, micro-Raman technique enabled to identify the single phases formed upon ageing, thanks to its micrometer-scale spatial resolution and thus to the possibility of recording spectra representative of single mineral granules (see Fig. 2h). This was not the case of the EDX spectra (and thus of the obtained Ca/P ratios), which were not representative of single phases, as reported above, due to the higher sampling volume of this technique.

The presence of B-type carbonate substitution in apatite has long been associated with a Raman feature at about 1070 cm^{-1} , although this band represents the envelope of two spectral components assignable to the ν_3 mode of the PO_4^{3-} group and to the ν_1 mode of the CO_3^{2-} group in apatite B-type substitution [44, 46].

With regard to the spectrum of B-type carbonated apatite reported in Fig. 2h, the relative intensity of the 1045 cm^{-1} (ν_3 mode of the PO_4^{3-} group) and 1072 cm^{-1} bands were reversed if compared to the hydroxyapatite spectrum, due to a strong contribution of the carbonate group to the 1072 cm^{-1} band [51].

Moreover, according to Awomusi et al., on the basis of the comparative analysis of the full width at half maximum of the bands at 1072 and 960 cm^{-1} as well as on their area ratio (Fig. 2h), it may be affirmed that the carbonate content in the deposited B-type carbonated apatite was about 10% and definitely higher than that reported for the bone (i.e. about 8%). [46]

According to Awonusi et al. [46] other weak spectral features assignable to B-type carbonated apatite were observed at about 695 and 720 cm^{-1} (ν_4 mode of the CO_3^{2-} group, Fig. 2h).

As previously described [29], when in the presence of biological fluids, (partial) dissolution and reprecipitation processes of CaP component occur inside CaSi-CaP cement mass leading to different reactions:

1. Calcium and phosphate ions released inside the calcium-silicate-hydrate mass can re-precipitate CaPs, mainly apatite, due to the high pH (i.e. high OH^- availability) in the cement.
2. CSH silanol groups (Si-OH) can bind Ca^{2+} or PO_4^{3-} and HPO_4^{2-} ions and trigger the nucleation of apatite [8].
3. Calcium-silicate-phosphate-hydrate (C-S-P-H) forms inside the CaP-containing CaSi cements [6, 29].
4. CaP in the cement formulation can react inside the hydrating cement mass by consuming $\text{Ca}(\text{OH})_2$ with the formation of C-S-P-H gel, with potential decrease of $\text{Ca}(\text{OH})_2$ content and alkalinity of the cement.

Apatite-forming (bioactive) material may provide important clinical advantages: In orthograde endodontics, it may improve the sealing ability through the deposition of CaPs at the interface [52]; in endodontic surgery (root end filling, perforation repair), it may promote bone and periodontal tissue regeneration [41, 53, 54] and enhance the material biocompatibility.

Furthermore, as premixed materials, their application may be easier in several complex endodontic situations (apicoectomy, root perforation, presence of wide/wet apices).

Conclusions

The investigated materials showed excellent radiopacity, adequate setting times and biointeractive properties with a marked ability to nucleate B-type carbonated apatite, favoured by the presence of $\text{CaH}_4\text{P}_2\text{O}_8$.

The CaSi-CaH₄P₂O₈ system of the BC premixed endodontic materials represents the latest result of the hydraulic calcium silicate technology, making them attractive materials for different endodontic applications.

Funding The study has been supported with the academic funds of Prof Gandolfi M.G. and Prof Taddei P.

Compliance with ethical standards

Conflict of interest The authors declare that they have no conflict of interest.

Ethical approval This article does not concern any studies with human participants or animals performed by any of the authors.

Informed consent For this type of study, formal consent is not required.

References

1. Niu LN, Jiao K, Wang TD, Zhang W, Camilleri J, Bergeron BE, Feng HL, Mao J, Chen JH, Pashley DH, Tay FR (2014) A review of the bioactivity of hydraulic calcium silicate cements. *J Dent* 42:517–533
2. Prati C, Gandolfi MG (2015) Calcium silicate bioactive cements: biological perspectives and clinical applications. *Dent Mater* 31:351–370
3. Xuereb M, Vella P, Damidot D, Sammut CV, Camilleri J (2015) In situ assessment of the setting of tricalcium silicate-based sealers using a dentin pressure model. *J Endod* 41:111–124
4. Ma S, Yang Y, Carnes DL, Kim K, Park S, Oh SH, Ong JL (2005) Effects of dissolved calcium and phosphorous on osteoblast responses. *J Oral Implantol* 31:61–67
5. Sun J, Wei L, Liu X, Li J, Li B, Wang G, Meng F (2009) Influences of ionic dissolution products of dicalcium silicate coating on osteoblastic proliferation, differentiation and gene expression. *Acta Biomater* 5:1284–1293
6. Gandolfi MG, Taddei P, Tinti A, Dorigo De Stefano E, Prati C (2011) Alpha-TCP improves the apatite-formation ability of calcium-silicate hydraulic cement soaked in phosphate solutions. *Mater Sci Eng C Mater Biol Appl* 31:1412–1422
7. Gandolfi MG, Shah SN, Feng R, Prati C, Akintoye SO (2011) Biomimetic calcium-silicate cements support differentiation of human orofacial mesenchymal stem cells. *J Endod* 37:1102–1108
8. Gandolfi MG, Taddei P, Siboni F, Modena E, Ciapetti G, Prati C (2011) Development of the foremost light-curable calcium-silicate MTA cement as root-end in oral surgery. Chemical-physical properties, bioactivity and biological behavior. *Dent Mater* 27:e134–e157

9. Candeiro GT, Correia FC, Duarte MA, Ribeiro-Siqueira DC, Gavini G (2012) Evaluation of radiopacity, pH, release of calcium ions, and flow of a bioceramic root canal sealer. *J Endod* 38:842–845
10. Lee JK, Kwak SW, Ha JH, Lee W, Kim HC (2017) Physicochemical properties of epoxy resin-based and bioceramic-based root canal sealers. *Bioinorg Chem Appl* 2017:2582849
11. Loushine BA, Bryan TE, Looney SW, Gillen BM, Loushine RJ, Weller RN, Pashley DH, Tay FR (2011) Setting properties and cytotoxicity evaluation of a premixed bioceramic root canal sealer. *J Endod* 37:673–677
12. Han L, Okiji T (2013) Bioactivity evaluation of three calcium silicate-based endodontic materials. *Int Endod J* 46:808–814
13. Moinzadeh AT, Aznar Portoles C, Schembri Wismayer P, Camilleri J (2016) Bioactivity potential of EndoSequence BC RRM putty. *J Endod* 42:615–621
14. Guo YJ, Du TF, Li HB, Shen Y, Mobuchon C, Hieawy A, Wang ZJ, Yang Y, Ma J, Haapasalo M (2016) Physical properties and hydration behavior of a fast-setting bioceramic endodontic material. *BMC Oral Health* 20:16–23
15. Shokouhinejad N, Nekoofar MH, Razmi H, Sajadi S, Davies TE, Saghiri MA, Gorjestani H, Dummer PMH (2012) Bioactivity of EndoSequence root repair material and bioaggregate. *Int Endod J* 45:1127–1134
16. Hansen SW, Marshall JG, Sedgley CM (2011) Comparison of intracanal EndoSequence root repair material and ProRoot MTA to induce pH changes in simulated root resorption defects over 4 weeks in matched pairs of human teeth. *J Endod* 37:502–506
17. Siboni F, Taddei P, Zamparini F, Prati C, Gandolfi MG (2017) Properties of bioroot RCS, a tricalcium silicate endodontic sealer modified with povidone and polycarboxylate. *Int Endod J* 50:e120–e136
18. Gandolfi MG, Ciapetti G, Taddei P, Perut F, Tinti A, Cardoso MV, Van Meerbeek B, Prati C (2010) Apatite formation on bioactive calcium-silicate cements for dentistry affects surface topography and human marrow stromal cells proliferation. *Dent Mater* 26:974–992
19. Gandolfi MG, Siboni F, Prati C (2016) Properties of a novel polysiloxane-guttapercha calcium silicate-bioglass-containing root canal sealer. *Dent Mater* 32:e113–e126
20. Siboni F, Taddei P, Prati C, Gandolfi MG (2017) Properties of NeoMTA plus and MTA plus cements for endodontics. *Int Endod J* 50:e83–e94
21. Barros J, Silva MG, Rodrigues MA, Alves FR, Lopes MA, Pina-Vaz I, Siqueira JF Jr (2014) Antibacterial, physicochemical and mechanical properties of endodontic sealers containing quaternary ammonium polyethylenimine nanoparticles. *Int Endod J* 47:725–734
22. Unosson EJ, Persson C, Engqvist H (2015) An evaluation of methods to determine the porosity of calcium phosphate cements. *J Biomed Mater Res B Appl Biomater* 103:62–71
23. He D, Zhuang C, Xu S, Ke X, Yang X, Zhang L, Yang G, Chen X, Mou X, Liu A, Gou Z (2016) 3D printing of Mg-substituted wollastonite reinforcing diopside porous bioceramics with enhanced mechanical and biological performances. *Bioactive Mater* 1:85–92
24. Gandolfi MG, Spagnuolo G, Siboni F, Procino A, Riveccio V, Pelliccioni GA, Prati C, Rengo S (2015) Calcium silicate/calcium phosphate biphasic cements for vital pulp therapy: chemical-physical properties and human pulp cells response. *Clin Oral Investig* 19:2075–2089
25. Gandolfi MG, Van Landuyt K, Taddei P, Modena E, Van Meerbeek B, Prati C (2010) Environmental scanning electron microscopy connected with energy dispersive x-ray analysis and raman techniques to study proRoot mineral trioxide aggregate and calcium silicate cements in wet conditions and in real time. *J Endod* 2010 36:851–857.
26. Gandolfi MG, Taddei P, Modena E, Siboni F, Prati C (2013) Biointeractivity-related versus chemi/physorption-related apatite precursor-forming ability of current root end filling materials. *J Biomed Mater Res B Appl Biomater* 101:1107–1123
27. Witke WÖ, Skopp A, Woydt M (2001) Raman microprobe spectroscopy and transmission electron microscopy of thermal sprayed ZrO₂ coatings before and after rub testing of outer air seals. *J Raman Spectrosc* 32:1008–1014
28. Conjeaud M, Boyer H (1980) Some possibilities of Raman microprobe in cement chemistry. *Cem Concr Res* 10:61–70
29. Sarma LP, Prasad PSR, Ravikumar N (1998) Raman spectroscopic study of phase transitions in natural gypsum. *J Raman Spectrosc* 29: 851–856
30. Dobal PS, Katiyar RS, Jiang Y, Guo R, Bhalla AS (2000) Raman scattering study of a phase transition in tantalum pentoxide. *J Raman Spectrosc* 31:1061–1065
31. Nelson DG, Featherstone JD (1982) Preparation, analysis, and characterization of carbonated apatites. *Calcif Tissue Int* 34:S69–S81
32. Martinez-Ramirez S, Sanchez-Cortes S, Garcia Ramos JV, Domingo C, Fortes C, Blanco-Varela MT (2003) Micro-Raman spectroscopy applied to depth profiles of carbonates formed in lime mortar. *Cem Concr Res* 33:2063–2068
33. Newbury DE (2009) Mistakes encountered during automatic peak identification of minor and trace constituents in electron-excited energy dispersive X-ray microanalysis. *Scanning* 31:91–101
34. Collepardi MM (2010) Water reducers/retarders, chapter 6 in concrete admixtures handbook. Properties, science and technology. Ed Ramachandran VS, pp 286–409
35. Camilleri J, Sorrentino F, Damidot D (2013) Investigation of the hydration and bioactivity of radiopacified tricalcium silicate cement, biodentine and MTA angelus. *Dent Mater* 29:580–593
36. Marciano MA, Duarte MA, Camilleri J (2015) Dental discoloration caused by bismuth oxide in MTA in the presence of sodium hypochlorite. *Clin Oral Investig* 19:2201–2209
37. Gandolfi MG, Siboni F, Primus CM, Prati C (2014) Ion release, porosity, solubility, and bioactivity of MTA plus tricalcium silicate. *J Endod* 40:1632–1637
38. Rashid F, Shiba H, Mizuno N, Mouri Y, Fujita T, Shinohara H, Ogawa T, Kawaguchi H, Kurihara H (2003) The effect of extracellular calcium ion on gene expression of bone-related proteins in human pulp cells. *J Endod* 29:104–107
39. Suzuki Y, Hayashi M, Tanabe N, Yasukawa T, Hirano Y, Takagi SC, Chow L, Suzuki N, Ogiso B (2015) Effect of a novel fluorapatite-forming calcium phosphate cement with calcium silicate on osteoblasts in comparison with mineral trioxide aggregate. *J Oral Sci* 57:25–30
40. Mizuno M, Banzai Y (2008) Calcium ion release from calcium hydroxide stimulated fibronectin gene expression in dental pulp cells and the differentiation of dental pulp cells to mineralized tissue forming cells by fibronectin. *Int Endod J* 41:933–938
41. Hakki SS, Bozkurt BS, Gandolfi MG, Prati C, Belli S (2013) The response of cementoblasts to calcium phosphate resin-based and calcium silicate-based commercial sealers. *Int Endod J* 46:242–252
42. Carvalho CN, Grazzotin-Soares R, de Miranda Candeiro GT, Gallego Martinez L, de Souza JP, Santos Oliveira P, Bauer J, Gavini G (2017) Micro push-out bond strength and bioactivity analysis of a bioceramic root canal sealer. *Iran Endod J* 12:343–348
43. Wang M, Qian R, Bao M, Gu C, Zhu P (2018) Raman, FT-IR and XRD study of bovine bone mineral and carbonated apatites with different carbonate levels. *Mater Lett* 210:203–206
44. Penel G, Leroy G, Rey C, Bres E (1998) MicroRaman spectral study of the PO₄ and CO₃ vibrational modes in synthetic and biological apatites. *Calcif Tissue Int* 63:475–481
45. Garskaite E, Gross KA, Yang SW, Yang TCK, Yang JC, Kareiva A (2014) Effect of processing conditions on the crystallinity and structure of carbonated calcium hydroxyapatite (CHAp). *CrystEngComm* 16:3950–3959
46. Awonusi A, Morris M, Tecklenburg M (2007) Carbonate assignment and calibration in the Raman spectrum of apatite. *Calcif Tissue Int* 81:46–52

47. Smith SJ, Emery R, Pitsillides A, Clarkin CE, Mahajan S (2017) Detection of early osteogenic commitment in primary cells using Raman spectroscopy. *Analyst* 142:1962–1973
48. Lloyd WR, Agarwal S, Nigwekar SU, Esmonde-White K, Loder S, Fagan S, Goverman D, Olsen BR, Jumlongras D, Morris MD, Levi B (2015) Raman spectroscopy for label-free identification of calciphylaxis. *J Biomed Opt* 20:080501/1–080501/3
49. Tamowski CP, Ignelzi MA Jr, Morris MD (2002) Mineralization of developing mouse calvaria as revealed by Raman microspectroscopy. *J Bone Miner Res* 17:1118–1126
50. Wopenka CB, Kent A, Pasteris JD, Yoon Y, Thomopoulos S (2008) The tendon-to-bone transition of the rotator cuff: a preliminary Raman spectroscopic study documenting the gradual mineralization across the insertion in rat tissue samples. *Appl Spectrosc* 62:1285–1294
51. Penel G, Delfosse C, Descamps M, Leroy G (2005) Composition of bone and apatitic biomaterials as revealed by intravital Raman microspectroscopy. *Bone* 36:893–901
52. Gandolfi MG, Parrilli AP, Fini M, Prati C, Dummer PMH (2013) 3D micro-CT analysis of the interface voids associated with Therafil root fillings used with AH plus or a flowable MTA sealer. *Int Endod J* 46:253–263
53. Al-Rabeah E, Perinpanayagam H, MacFarland D (2006) Human alveolar bone cells interact with ProRoot and tooth-colored MTA. *J Endod* 32:872–875
54. Matsumoto S, Hayashi M, Suzuki Y, Suzuki N, Maeno M, Ogiso B (2013) Calcium ions released from mineral trioxide aggregate convert the differentiation pathway of C2C12 cells into osteoblast lineage. *J Endod* 39:68–75

3. Tissue engineering approaches for experimental bone regeneration procedures

Occurrence of critical sized bone defects in the oral maxillofacial district due to trauma, infections and oncological reasons demands the design and development of new strategies for bone regeneration procedures.

Bone is one of the most transplanted tissues. Worldwide, over 2 million bone grafts procedures are annually performed with approx. 1 million surgeries performed in Europe, in particular in the oral district (Vallittu 2016).

The design and development of a new generation bioactive scaffolds, acting as bone mineralization platforms, stimulating bone regeneration processes and controlling local microbial colonization will be of predominant interest in future. Indeed “Gold standard” autologous bone graft demonstrated several drawbacks, including donor site morbidity, unpredictable regenerating bone volumes and grafts suprainfection. (Arvidson *et al.* 2010, Erbe *et al.* 2010). Similarly, allogenic and xenogenic bone grafts revealed drawback, such as lack of vascularization, immunogenicity, disease transmission and donor shortage (Sukumar & Drízhal 2008).

An ideal scaffold for bone regeneration purposes should be extremely porous, biocompatible, biointeractive (able to release biologically relevant ions), with tailored resorption and adequate mechanical properties.

One of the most useful strategy to obtain a multipurpose scaffold is to combine one or more materials, in order to get the best properties for each materials and limiting their weakness (Moussa & Aparicio 2019).

Several strategies/technologies have been developed and applied in the field of tissue engineering, including layer-by-layer assembly (Reddy *et al.* 2006), in-situ emulsion polymerization (Khan *et al.* 2016), and thermally induced phase separation technique (TIPS) (Fabbri *et al.* 2011).

Thermally Induced Phase Separation (TIPS) is an attractive experimental procedure for scaffold fabrication which allows obtaining a well-interconnected porous structure. This technique is based on the induction of a multiphase system through temperature changes by mixing of two or more solutions, having the possibility to obtain a wide range of structures with high porosity and interconnected pores without using complex and expensive techniques. (Fabbri *et al.* 2011). Moreover it is possible with this technique to combine several biomaterials.

Combining a polymeric matrix with one or more bioactive or biointeractive filler represents an interesting strategy in bone tissue engineering. Composite materials usually show an excellent balance between the strengths and weaknesses of their individual components.

Poly (α -hydroxy) acids such as polylactic acid (PLA), poly- ϵ -caprolactone (PCL) are synthetic biocompatible, biodegradable materials which may be used for biomedical applications. (Sheik *et al.* 2015, Tajbakhsh & Hajiali 2017). Their major drawback which limits their use may be hydrophobic behaviour and release of acidic products (A).

Calcium phosphates, are some of the most extensively fillers tested in bone tissue engineering (Mangano *et al.* 2011, Le Geros *et al.* 2003). These materials alone however, cannot provide the necessary biointeractive, bioactive, and mechanical properties for tissue engineering. Hydroxyapatite doped scaffolds demonstrated osteoconductive and long-term bone tissue stability, but revealed significant brittleness (Armentano *et al.* 2009).

Bioactive calcium silicate-based materials (CaSi) may provide interesting advantages in relationship to their chemistry as expose silanol groups and release silicon (Carlisle 1970, Day 2005, Zhai *et al.* 2012). CaSi demonstrated bioactive, (Gandolfi *et al.* 2010) biointeractive properties (Gandolfi *et al.* 2011a; Gandolfi *et al.* 2013; Prati & Gandolfi, 2015) and the ability to induce the differentiation of different population of cells, such as orofacial bone mesenchymal stem cells (Gandolfi *et al.* 2011b), cementoblasts (Von Arx 2016), pulp cells (Gandolfi *et al.* 2015).

In this chapter, Poly (α -hydroxyl) acids, Calcium phosphate and Calcium silicates were combined to produce highly porous scaffolds, which were later characterized for their chemical physical and micromorphological properties.

REFERENCES:

Armentano I, Dottori M, Fortunati E, Mattioli S, Kenny JM. Biodegradable polymer matrix Nanocomposites for tissue engineering: A review. *Polym Degradation Stab* 2010;95:2126-2146.

Arvidson K, Abdallah BM, Applegate LA, Baldini N, Cenni E, Gomez-Barrena E, Granchi D, Kassem M, Kontinen YT, Mustafa K, Pioletti DP, Sillat T, Finne-Wistrand A. Bone regeneration and stem cells. *J Cell Mol Med* 2011;15:718-746.

Carlisle EM. Silicon: A possible factor in bone calcification. *Science* 1970;167, 279–280.

Day RM. Bioactive glass stimulates the secretion of angiogenic growth factors and angiogenesis in vitro. *Tissue Engineering* 2005;11, 768–777.

Erbe EM, Marx JG, Clineff TD, Bellincampi LD. Potential of an ultraporous beta-tricalcium phosphate synthetic cancellous bone void filler and bone marrow aspirate composite graft. *Eur Spine J* 2001;10:S141-146.

Fabbri P, Cannillo V, Sola A, Dorigato A, Chiellini F. Highly porous polycaprolactone-45S5 Bioglass® scaffolds for bone tissue engineering. *Compos Sci Technol* 2010;70:1869-1878.

Gandolfi MG, Iezzi G, Piattelli A, Prati C, Scarano A. Osteoinductive potential and bone-bonding ability of ProRoot MTA, MTA Plus and Biodentine in rabbit intramedullary model: Microchemical characterization and histological analysis. *Dent Mater* 2017;33:e221-e238.

Gandolfi MG, Taddei P, Tinti A, Prati C. Apatite-forming ability (bioactivity) of ProRoot MTA. *Int Endod J* 2010;43:917-929.

Gandolfi MG, Taddei P, Siboni F, Modena E, Ciapetti G, Prati C. Development of the foremost light-curable calcium-silicate MTA cement as root-end in oral surgery. Chemical-physical properties, bioactivity and biological behavior. *Dent Mater* 2011;27:e134-57.

Gandolfi MG, Shah SN, Feng R, Prati C, Akintoye SO. Biomimetic calcium-silicate cements support differentiation of human orofacial mesenchymal stem cells. *J Endod.* 2011;37:1102-8.

Gandolfi MG, Taddei P, Modena E, Siboni F, Prati C. Biointeractivity-related versus chemi/physisorption-related apatite precursor-forming ability of current root end filling materials. *J Biomed Mater Res B Appl Biomater* 2013;101:1107-23.

- Gandolfi MG, Zamparini F, Degli Esposti M, Chiellini F, Fava F, Fabbri P, Taddei P, Prati C. Highly porous polycaprolactone scaffolds doped with calcium silicate and dicalcium phosphate dihydrate designed for bone regeneration. *Mater Sci Eng C Mater Biol Appl* 2019;102:341-361.
- Gandolfi MG, Zamparini F, Degli Esposti M, Chiellini F, Aparicio C, Fava F, Fabbri P, Taddei P, Prati C. Polylactic acid-based porous scaffolds doped with calcium silicate and dicalcium phosphate dihydrate designed for biomedical application. *Mater Sci Eng C Mater Biol Appl* 2018 1;82:163-181.
- Gandolfi MG, Siboni F, Botero T, Bossù M, Riccitiello F, Prati C. Calcium silicate and calcium hydroxide materials for pulp capping: biointeractivity, porosity, solubility and bioactivity of current formulations. *J Appl Biomater Funct Mater* 2015;13:43-60.
- Khan MU, Reddy KR, Snguanwongchai T, Haque E, Gomes VG. Polymer brush synthesis on surface modified carbon nanotubes via in situ emulsion polymerization *Colloid and Polymer Sci* 2016;294:1599-1610.
- LeGeros RZ, Lin S, Rohanizadeh R, Mijares D, LeGeros, JP. Biphasic calcium phosphate bioceramics: preparation, properties and applications. *Journal of Materials Science* 2003;14: 201-209.
- Mangano C, Paino F, d'Aquino R, de Rosa A, Iezzi G, Piattelli A, Laino L, Mitsiadis T, Desiderio V, Mangano F, Papaccio G, Tirino V. Human Dental Pulp Stem Cells hook into Biocoral scaffold forming an engineered biocomplex. *PLoS ONE* 2011;6:e18721.
- Prati C, Gandolfi MG. Calcium silicate bioactive cements: Biological perspectives and clinical applications. *Dent Mater* 2015;31:351-370.
- Reddy KR, Lee K, Gopalan AI, Kang H. Organosilane modified magnetite nanoparticles/poly(aniline-co-o/m-aminobenzenesulfonic acid) composites: Synthesis and characterization. *React Funct Polym* 2007;67:943-954.
- Reddy KR, Lee K, Gopalan AI, Showkat AM. Facile synthesis of hollow spheres of sulfonated polyanilines. *Polym J* 2006;38:349-354.
- Sheikh Z, Najeeb S, Khurshid Z, Verma V, Rashid H, Glogauer M. Biodegradable Materials for Bone Repair and Tissue Engineering Applications. *Materials* 2015;8: 5744–5794.
- Sukumar S, Držhal I. Bone grafts in periodontal therapy. *Acta Medica (Hradec Kralove)* 2008;51:203-207.
- Taddei P, Tinti A, Gandolfi MG, Rossi PL, Prati C. Ageing of calcium silicate cements for endodontic use in simulated body fluids: a micro-Raman study. *J Raman Spectrosc* 2009;40:1858-1866.
- Tajbakhsh S & Hajjali F. A comprehensive study on the fabrication and properties of biocomposites of poly(lactic acid)/ceramics for bone tissue engineering. *Mat Sci Eng C-Mater* 2017;70:897–912.
- Vallittu PK. Bioactive glass-containing cranial implants: an overview. *J Mater Sci* 2017;52: 8772.
- Von Arx T. Mineral trioxide aggregate (MTA) a success story in apical surgery. *Swiss Dent J* 2016;126, 573–595



Polylactic acid-based porous scaffolds doped with calcium silicate and dicalcium phosphate dihydrate designed for biomedical application



Maria Giovanna Gandolfi^{a,*}, Fausto Zamparini^{a,b}, Micaela Degli Esposti^c, Federica Chiellini^d, Conrado Aparicio^e, Fabio Fava^c, Paola Fabbri^c, Paola Taddei^f, Carlo Prati^b

^a Laboratory of Biomaterials and Oral Pathology, School of Dentistry, Department of Biomedical and Neuromotor Sciences, University of Bologna, Bologna, Italy

^b Endodontic Clinical Section, School of Dentistry, Department of Biomedical and Neuromotor Sciences, University of Bologna, Bologna, Italy

^c Department of Civil, Chemical, Environmental and Materials Engineering, University of Bologna, Bologna, Italy

^d BIOLab Research Group, Department of Chemistry and Industrial Chemistry, University of Pisa, Pisa, Italy

^e Minnesota Dental Research Center, Biomaterials and Biomechanics, School of Dentistry, University of Minnesota, Minneapolis, ME, United States

^f Biochemistry Unit, Department of Biomedical and Neuromotor Sciences, University of Bologna, Bologna, Italy

ARTICLE INFO

Keywords:

Porous scaffold
Polylactic acid
Calcium silicate
Calcium phosphate
Bone regeneration
Thermally induced phase separation

ABSTRACT

Poly(lactic acid) (PLA), dicalcium phosphate dihydrate (DCPD) and/or hydraulic calcium silicate (CaSi) have been used to prepare highly-porous scaffolds by thermally induced phase separation technique (TIPS). Three experimental mineral-doped formulations were prepared (PLA-10CaSi, PLA-5CaSi-5DCPD, PLA-10CaSi-10DCPD). Pure PLA scaffolds constituted the control group.

Scaffolds were tested for their chemical-physical and biological properties, namely calcium release, alkalinizing activity, surface microchemistry and micromorphology by ESEM, apatite-forming ability by EDX, micro-Raman and IR spectroscopy, thermal properties by differential scanning calorimetry, mechanical properties by quasi-static parallel-plates compression testing, porosity by a standard water-absorption method and direct-contact cytotoxicity.

All mineral-doped scaffolds released biologically relevant ions (biointeractive). A B-type carbonated apatite layer (thickness decreasing along the series PLA-10CaSi-10DCPD > PLA-10CaSi > PLA-5CaSi-5DCPD > PLA) was detected on the surface of all the 28d-aged scaffolds.

Surface pores of fresh scaffolds ranged from 10 to 20 μm in pure PLA to 10–100 μm in PLA-10CaSi. An increase in porosity was detected in 28d-aged pure PLA scaffolds (approx. 30% of material loss with decrease of the PLA chain length); differently, in mineral-doped scaffolds, the PLA degradation was balanced by deposition/nucleation of apatite. All scaffolds showed absence of toxicity, in particular PLA-10CaSi-10DCPD.

The designed scaffolds are biointeractive (release biologically relevant ions), nucleate apatite, possess high surface and internal open porosity and can be colonized by cells, appearing interesting materials for bone regeneration.

1. Introduction

Bone regeneration processes are extremely important in surgical disciplines, such as oral-maxillofacial surgery or dental implant surgery. While small bone defects or fractures can self-repair, bone graft materials are essential to restore large bone volumes lost for periapical endodontic lesions, cysts, tumours, bone trauma or bone atrophies for long-time edentulism [1,2].

An ideal bone substitute should possess many important properties such as biointeractivity, bioactivity, biocompatibility, osteoconductivity/osteoinductivity, high porosity, adequate mechanical

properties, the possibility to be shaped to the surgical size and antibacterial activity [1–3]. Currently biomaterial science spent a lot of efforts to design synthetic biomaterials fulfilling many of these properties [4].

Hybrid biomaterials composed of biodegradable synthetic polymers and inorganic materials showed suitable properties to be used for biomedical applications, including drug delivery [5] nanoscaffolds/carriers for gene therapy/delivery [6,7], in-vivo drug release tracking/monitoring [8], and antibacterial activity [9]. In particular, hybrid bi-phasic biomaterials composed of biodegradable synthetic polymers and synthetic calcium phosphates (CaP) showed interesting properties for

* Corresponding author at: Laboratory of Biomaterials and Oral Pathology, Dental School, University of Bologna, Via San Vitale 59, 40125 Bologna, Italy.
E-mail address: mgiovanna.gandolfi@unibo.it (M.G. Gandolfi).

bone tissue engineering [4,10–12].

Synthetic calcium phosphates such as hydroxyapatite (HA), alpha-tricalcium phosphate (α-TCP), beta-tricalcium phosphate (β-TCP), dicalcium phosphate dihydrate (DCPD) are used as bone substitutes for their biological properties, i.e. biocompatibility, osteoconductivity and non-immunogenicity [13,14]. However, in presence of critical size defects, these materials should be combined with polymers or other CaP to overcome their drawbacks [13,15]. For example, HA is highly osteoconductive and able to provide long-term bone tissue stability, but fails in mechanical properties at high loadings [10,15], while β-TCP is highly-interactive but fast-resorbing and unable to provide a long-term template to support cells migration from the periphery of the grafted area [13].

Hydraulic calcium silicate (CaSi) cements are biocompatible and biointeractive materials [16,17] able to release biologically active ions (Ca^{2+} and OH^-) acting on human mineralizing cells, such as osteoblasts [18,19], orofacial bone mesenchymal stem cells [20], cementoblasts [21] and pulp cells [22]. Their $\text{SiO}^-/\text{Si-OH}$ groups nucleate B-type carbonated apatite by absorption of Ca^{2+} and PO_4^{3-} ions [18,23,24], providing an excellent connection with bone tissue. In vivo, CaSi showed the ability to stimulate the formation of new bone when inserted in human periapical bone defects [25–28]. For these reasons, these materials are widely used in dentistry in direct contact with bone and mineralized tissues and represent the gold standard to seal resected root apices, to fill root canals and to favour the healing and protection of the dental pulp.

The incorporation of reactive degradable calcium phosphates, such as α-TCP or DCPD, into CaSi cements was found to enhance their biological properties and apatite-forming ability [24,29–31].

Biodegradable synthetic polymers such as polylactic acid (PLA) [32], polyglycolic acid (PGA), poly(lactide-co-glycolide) (PLGA) and poly-ε-caprolactone (PCL) have been recently used for scaffold design [33–36] due to their biocompatibility, degradation into non-toxic components, long shelf-life [37], easy processability, low cost and possibility to be customized/adapted to the surgical site. PLA is an aliphatic thermoplastic polyester obtained by polymerizing lactide monomers derived from lactic acid coming from the bacterial fermentation of corn dextrose. Poly D- and L-lactic acid isomers can be produced [38,39]. PLA degrades into carbon dioxide, lactic acid and water [35] and shows intermediate degradation times, if compared to other polymers with fast degradation such as PLGA (3–4 months), or delayed degradation such as PCL (≥ 2 years) [10,35,36,40]. PLA is widely used in orthopedic surgery to manufacture devices for fracture fixation or screws and represents an interesting matrix for composite scaffold production for different bone applications [10,39].

The combination of PLA biopolymer with reactive inorganic biomaterials such as CaSi or CaP could be an attractive method to produce biointeractive scaffolds with tailorable chemical-physical and adequate biological characteristics. Some experimental PLA-based scaffolds have been recently prepared incorporating inorganic components such as Bioglass [41], β-TCP [42] and HA [43].

Various functional polymers intended for biomedical use have been synthesized through different strategies/technologies, including layer-by-layer assembly [44], in-situ emulsion polymerization [45], copolymerization followed by self-assembly [46], and thermally induced phase separation technique (TIPS), which can produce homogeneous and highly porous structures by means of a simple experimental procedure [33].

In this study, PLA-based porous scaffolds doped with different percentages of CaSi and DCPD mineral powders were designed and produced by TIPS for bone regeneration purposes. Ion release and alkalinizing activity, apatite-forming ability, surface microchemistry and micromorphology, porosity, thermo-mechanical properties and cytotoxicity were investigated. To the best of our knowledge, no PLA scaffolds doped with DCPD and/or hydraulic CaSi have been previously fabricated using TIPS.

2. Material and methods

2.1. Materials

Poly(L-lactic acid) (MW = 65,000 g/mol, Ingeo™ biopolymer PLA 4060D, Natureworks LLC, Blair, NE, USA) was used.

The high molecular weight, which is a necessary prerequisite for the fabrication of highly porous scaffolds allowing proper handling (i.e. limited brittleness), was determined by gel permeation chromatography (GPC) ($M_n = 103,100$; $M_w = 232,900$; $M_p = 189,400$; $M_z = 406,600$; Polydispersity = 2.26) with an Agilent 1260 Infinity instrument equipped with a PLgel MiniMIX-A column (20 μm particle size, 4.6 × 250 mm) coupled with a Tosoh TSKgel SuperMultipore HZ-M column (4 μm particle size, 4.6 × 150 mm), with CHCl_3 as mobile phase, toluene as internal standard (1 μL/10 mL) and monodisperse polystyrene standards (EasiCal-PS1 Agilent kit) for obtaining the calibration curve.

Methanol (MeOH), ethanol (EtOH, 99.8%), 1,4-dioxane (DIOX) and chloroform (CHCl_3 , HPLC grade) all from Sigma Aldrich (Milan, Italy) were used as received without further purification.

PLA was received in pellet form and purified via dissolution in CHCl_3 (10% wt/vol) and reprecipitation in a large excess of cold MeOH, in order to eliminate residual polymerization catalysts.

Dicalcium phosphate dihydrate (DCPD; $\text{CaHPO}_4 \cdot 2\text{H}_2\text{O}$) powder (Sigma-Aldrich, Steinheim, Germany) and/or calcium silicate (CaSi) powders (Aalborg, Denmark), prepared by melt-quenching technique and milling procedures, as previously reported [30], and composed of dicalcium silicate, tricalcium silicate, tricalcium aluminate, and calcium sulfate, were added to PLA.

2.2. TIPS scaffolds preparation

The porous polymer scaffolds were prepared by TIPS starting from PLA solutions in DIOX (3.5% wt/vol). CaSi and DCPD were added to the PLA solution in powder form in amounts 5% or 10% by weight with respect to PLA.

Homogeneous dispersions were obtained by sonicating the mixtures for 3 h using the ultrasonic processor UP50H (Hielscher, 50 watts, 30 kHz), equipped with the sonotrode MS2 (made of titanium, tip diameter 2 mm). After mixing, solutions were placed inside disposable aluminum dishes of 60 mm in diameter, and cooled at -18°C . After 18 h, the frozen samples were extracted from the holders and fully immersed in EtOH bath precooled at -18°C , where they were kept for 48 h, with solvent refresh every 3 h. At the end of the extraction procedure, the porous scaffolds were taken out of the freezer and completely dried under vacuum [33] (Figs. 1, 2). Six disks (diameter 60 ± 1 mm, thickness 10 ± 0.1 mm) per composition were prepared.

The prepared scaffolds were:

- PLA-10CaSi
- PLA-5CaSi-5DCPD
- PLA-10CaSi-10DCPD
- PLA (control)

2.3. Calcium release and alkalinizing activity (pH of soaking water)

The samples (10 ± 0.1 mm long × 10 ± 0.1 mm high × 10 ± 0.1 mm thick; $n = 5$ for each composition) were immersed in 10 mL of deionized water inside polypropylene sealed containers and stored at 37°C . The soaking water was collected and replaced at six time points (3 h and 1, 3, 7, 14 and 28 days). The collected water was analyzed for pH and Ca^{2+} using a potentiometric method under magnetic stirring at room temperature (24°C).

The pH was measured using a selective temperature-compensated electrode (Sen Tix Sur WTW, Weilheim, Germany) connected to a multi-parameter laboratory meter (inoLab 750 WTW, Weilheim, Germany)

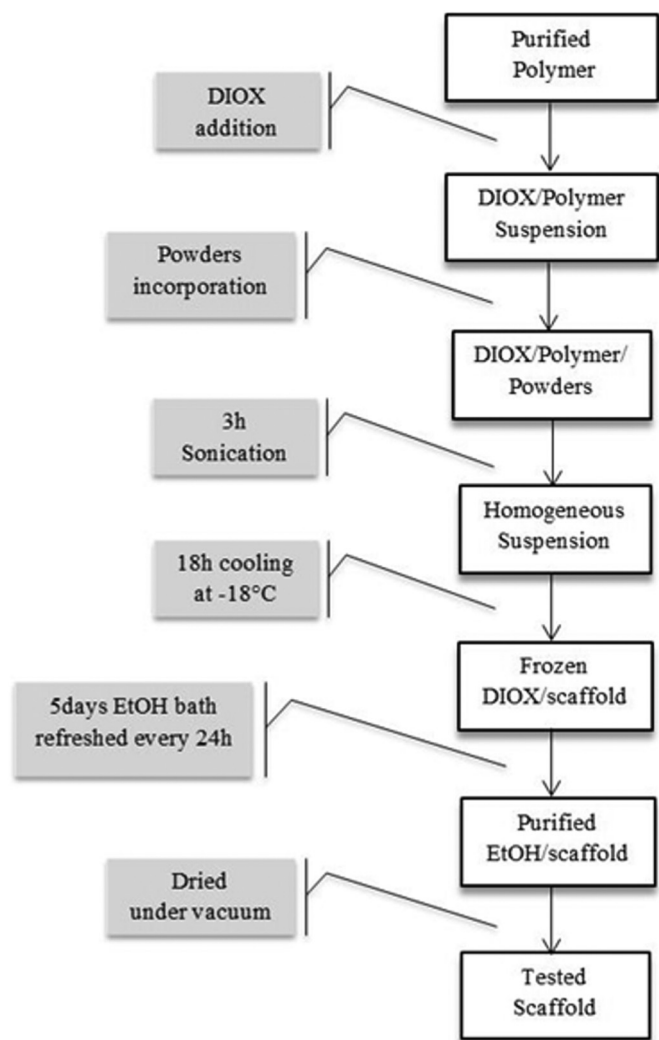


Fig. 1. Preparation steps and time-line of the experimental scaffolds.

previously calibrated with standard solutions.

The amount of calcium ions was measured using a calcium probe (Calcium ion electrode, Eutech instruments Pte Ltd., Singapore) after addition of 0.200 mL (2%) of ionic strength adjuster ISA, 4 mol/L KCl (WTW, Weilheim, Germany).

Calcium release and pH data were analyzed using two-way ANOVA followed by RM Student–Newman–Keuls test ($p < 0.05$). Different letters represent statistically significant differences ($p < 0.05$) in the same line (capital letters) or in the same column (small letters).

2.4. Calcium phosphate nucleation

The International Standard ISO 23317 method was used to evaluate the formation of a layer rich in Ca and P (CaP covering) on the surface of the scaffolds soaked in Hank's balanced salt solution (HBSS, Lonza, Verviers, Belgium) used as simulated body fluid [17,20]. The HBSS composition was: Ca^{++} 1.27 mM, Cl^- 144.7 mM, K^+ 5.8 mM, Na^+ 141.6 mM, Mg^{++} 0.81 mM, HCO_3^- 4.17 mM, SO_4^- 0.81 mM, H_2PO_4^- 0.44 mM and HPO_4^- 0.336 mM. Each sample was placed in 20 mL of HBSS at 37 °C for 28 days, and tested for the apatite forming ability.

The scaffolds ($n = 3$ per composition) were examined using an environmental scanning electron microscope (ESEM, Zeiss EVO 50; Carl Zeiss, Oberkochen, Germany) connected to a secondary electron detector for energy dispersive X-ray analysis (EDX; Oxford INCA 350 EDS, Abingdon, UK) using computer-controlled software (Inca Energy Version 18). Specimens were placed directly onto the ESEM stub and examined in wet conditions without any previous preparation (the samples were not coated for this analysis) at low vacuum (100 Pascal) in Quadrant Back-Scattering Detector (QBSD) mode, using an accelerating voltage of 20 kV, working distance 8.5 mm, 0.5 wt% detection level, 133 eV resolution, amplification time 100 μs , measuring time 60 s. EDX microchemical analysis was carried out at random in areas of $\sim 50 \mu\text{m} \times 50 \mu\text{m}$ to evaluate the relative element content. Elemental microanalysis (weight % and atomic %) with ZAF correction method was performed in full frame to analyze entire areas.

The fresh and aged scaffolds were analyzed by FT-Raman, micro-Raman and attenuated Total Reflectance ATR/IR spectroscopy.

FT-Raman was used to gain insights into the bulk of the samples, while micro-Raman and ATR/IR were utilized to analyze their surface;

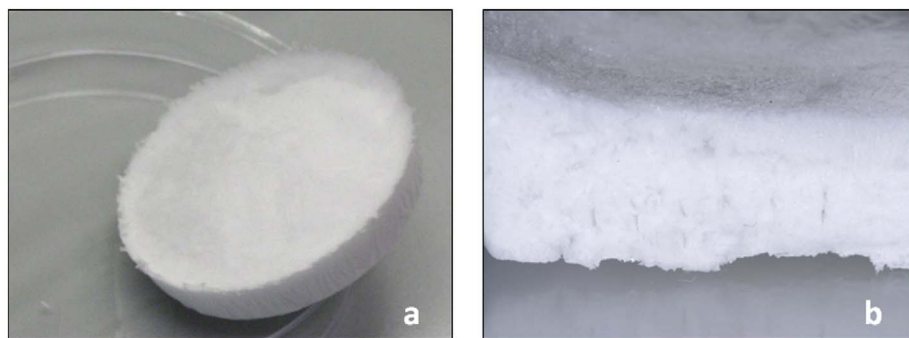
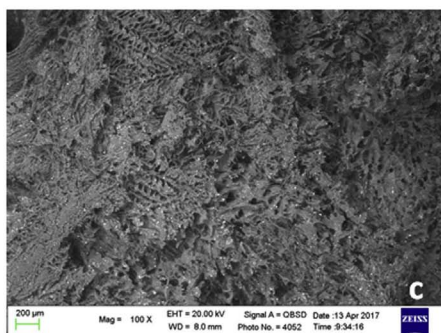


Fig. 2. PLA scaffold from TIPS (a) and its cross section (b,c). ESEM image of PLA-10CaSi-10DCPD cross section showing mineral granules embedded into a porous PLA matrix (c).



IR spectroscopy was also chosen to investigate the possible interactions between the PLA and inorganic phases. In fact, this technique is more sensitive to hydrogen bond interactions.

FT-Raman spectra were recorded on a Bruker MultiRam FT-Raman spectrometer equipped with a cooled Ge-diode detector. The excitation source was a Nd³⁺-YAG laser (1064 nm) in the backscattering (180°) configuration. The focused laser beam diameter was about 100 µm and the spectral resolution 4 cm⁻¹. Laser power at the sample was about 150 mW. Two spectra on each sample were recorded and averaged. Only the FT-Raman spectra of the pure PLA scaffolds will be reported and discussed, since the composites had a significant fluorescence signal under the used measurement conditions.

Micro-Raman spectra were obtained using a Jasco NRS-2000C instrument in back-scattering conditions with 4 cm⁻¹ spectral resolution, using the 532 nm Green Diode Pumped Solid State (DPSS) Laser Driver (RgBlase LLC, USA) with a power of ca. 25 mW. A 160 K cooled digital CCD (Spec-10: 100B, Roper Scientific Inc.) was used as detector. Microscope objectives with 10× and 100× magnifications were utilized. The former was used to analyze the fresh composite samples; in fact, under these conditions, the laser spot size, i.e. the excitation source was about 20 µm and enables to obtain more representative spectra of these intrinsically inhomogeneous samples. The 100× magnification (with a laser spot size of about 1 µm) was used to analyze the aged samples. Each reported micro-Raman spectrum is an average of at least five measurements.

ATR/IR spectra were recorded on a Bruker Alpha Fourier Transform FTIR spectrometer, equipped with a platinum ATR single reflection diamond module and a Deuterated Lanthanum α-Alanine doped TriGlycine Sulfate (DLαTGS) detector; the spectral resolution was 4 cm⁻¹, and the number of scans was 64 for each spectrum. Each reported IR spectrum is an average of two measurements.

The I₈₇₅/I₁₄₅₅ Raman intensity ratio was used for a relative quantitative evaluation of polymeric chain length [47–49]. The I_{960(AP)}/I_{875(PLA)} (Raman) and I_{1030(AP)}/I_{1750(PLA)} (IR) intensity ratios were calculated to gain information on the relative thickness of the apatite deposit formed on the aged scaffolds. All the ratios were calculated as peak heights from the single spectra recorded on each sample. Average values are reported and discussed.

2.5. Scaffolds bulk open porosity

Bulk open porosity was measured according to the standard procedure UNI EN 1936 “Natural Stone Test Methods - Determination of real density and apparent density, and of total and open porosity”. Briefly, dry and weighted specimens (m_d) were put into an evacuation vessel and the pressure was lowered gradually to 20 mbar. The pressure was maintained for 2 h to eliminate the air contained in the open pores of the specimens. Demineralized water at 20 ± 5 °C was slowly introduced into the vessel and the pressure was maintained at 20 mbar. After approximately 30 min and when all the specimens were completely immersed, the vessel was returned to atmospheric pressure and the specimens were left in water for 24 h at atmospheric pressure. Then, each specimen was weighted in water and the mass in water was recorded as m_h. Each specimen was quickly wiped with a dampened cloth and the mass m_s of the specimen saturated with water was determined.

The open porosity P₀ of the scaffold is expressed by the ratio (as a percentage) of the volume of open pores and the apparent volume of the specimen, by the equation $P_0 = (m_s - m_d) / (m_s - m_h) \times 100$.

The open porosity was determined in triplicate and expressed as mean ± standard deviation.

2.6. Surface porosity evaluated by the morphometric analysis on ESEM images

ESEM images were analyzed through Image J program (National Institutes of Health, Bethesda, USA) to evaluate the scaffolds porosity,

in terms of percentage [50]. Surface porosity was calculated as the ratio between the most black areas (micropores) and the total examined area. For each scaffold three measurements were performed in three different areas at 500× and 1000× magnification. For each magnification, the mean value was recorded.

2.7. Mechanical properties

Quasi-static compression tests were performed on cylinder specimens (40 mm diameter; 8 mm thickness) by using an Instron 4502 (Instron, MA, USA) electromechanical tensile testing machine, equipped with a 10 kN load cell. According to the standard method UNI EN ISO 604 “Plastics - Determination of compressive properties”, the measurements were performed at room temperature (25 °C) at a compression rate of 1 mm/min. At least three specimens were tested for each sample. Following the standard method UNI EN ISO 527 “Plastics - Determination of tensile properties”, a secant modulus (E) was evaluated between strains of 0.05% and 0.25%.

2.8. Thermal properties

Glass transition temperature (T_g) of the scaffolds was determined by means of a differential scanning calorimeter (DSC, Q10), fitted with a standard DSC cell, and equipped with a Discovery Refrigerated Cooling System (RCS90) (all TA Instruments, Delaware, USA). Samples of about 7 mg were placed into aluminum pans and subjected to two heating cycles from -90 °C to +110 °C with cooling and heating rates of 10 °C/min. The DSC cell was purged with dry nitrogen at 50 mL/min. The system was calibrated both in temperature and enthalpy with Indium standard. The real content of inorganic filler (CaSi or CaSi + DCPD) present in the composite scaffolds was determined by thermogravimetric analysis (TGA, Q50, TA Instruments, Delaware, USA), as residual weight after polymer decomposition and complete volatilization. Analyses were performed in triplicate under dry nitrogen flow (60 mL/min), on samples of about 20 mg, placed in platinum pans. Heating was performed from room temperature to +550 °C at a rate of 10 °C/min. Results are given as average value.

All data were processed with Thermal Analysis software (TA Instruments, Delaware, USA).

2.9. Analysis of the crystalline structures

Phase identification of the crystalline structure of CaSi and DCPD was performed through X-ray diffraction analysis (XRD), on the pure inorganic powders or PLA composite finely grounded under liquid nitrogen. The diffractometer (X'Pert PRO, Panalytical) used Cu Kα radiation at 40 mA and 40 kV. XRD patterns were collected at room temperature in 5–120° 2θ range, with a step size of 0.0167°, number of points 6882, counting time 59.690 s.

2.10. Cell toxicity test

2.10.1. Cell culture

Cell viability and proliferation experiments were carried out using the mouse embryo fibroblasts balb/3 T3 clone A31 cell line (CCL-163). Cells were purchased from American Type Culture Collection (ATCC) and propagated using Dulbecco's Modified Eagle Medium (DMEM), supplemented with 4 mM of L-glutamine, 1% of penicillin: streptomycin solution (10,000 U/mL: 10 mg/mL), 10% of calf serum and antimycotic (complete DMEM).

The scaffolds were mounted in CellCrownTM24 disposable inserts (Scaffdex, Tampere, Finland), placed in 24-wells plate and sterilized with an Ethanol:H₂O (70:30 v/v) solution for 30 min. Afterwards, samples were extensively washed with Dulbecco's Phosphate Buffer Saline (DPBS) containing 1% penicillin: streptomycin solution and pre-incubated for additional 3 h with complete DMEM before cell seeding.

2.10.2. Cell viability and proliferation by mitochondrial activity test

Samples were seeded with mouse embryo fibroblast balb/3T3 clone A31 cells (passage 73) by directly adding on to the scaffold surface 500 μ L of DMEM containing 1×10^4 cells/per well and incubated at 37 °C in a 5% CO₂ enriched atmosphere.

Cell tests were performed at days 7 and 14 after seeding. Cell proliferation was investigated by mean of WST-1 tetrazolium salt reagent (Roche Applied Science, Indianapolis, IN, USA). Briefly, cells were incubated for 4 h with WST-1 reagent diluted 1:10, at 37 °C and 5% CO₂. Measurements of formazan dye absorbance were carried out with a microplate reader (Biorad, Milan, Italy) at 450 nm, using 655 nm as reference wavelength. Cells at day 7 of culture cultured on tissue culture polystyrene (TCPS) were used as growth control.

The tests were performed in triplicate on the whole scaffold/cell construct and the data are reported as mean \pm standard deviation. Statistical differences were analyzed using one-way analysis of variance (ANOVA) and a p value < 0.05 was considered significant.

2.10.3. Cell morphological and cytoskeleton organization by confocal laser scanning microscopy (CLSM)

Cells morphology cultured on the experimental PLA-based scaffolds was investigated by CLSM at day 14 after seeding. Cells were fixed with 3.8% paraformaldehyde for 1 h in Phosphate Buffer Saline 0.01 M (PBS 1 \times) at room temperature and permeabilized with a PBS 1 \times /Triton X-100 solution (0.2%) for 10 min. After blocking with 1% (w/v) bovine serum albumin (BSA) in PBS 1 \times for 30 min, cells were incubated with phalloidin-Alexa Fluor 488 at room temperature in the dark for 1 h and then with 4'-6-diamidino-2-phenylindole (DAPI) solution for 30 min, to stain cells nuclei and F-Actin. Following each dyeing incubation, samples were extensively washed with PBS 1 \times and finally stored at 4 °C in the dark until observation by confocal laser scanning microscopy was performed. A Nikon Eclipse TE2000 inverted microscope equipped with EZ-C1 confocal laser (Nikon, Japan) with 10 \times and 20 \times objectives was used to analyze the samples. A 405 nm laser diode (405 nm emission) and an Argon ion laser (488 nm emission) were used to excite DAPI and Alexa-Fluor 488 fluorophores, respectively. Images were captured with Nikon EZ-C1 software with identical settings for each sample.

3. Results

3.1. Calcium release and alkalizing activity (pH)

The mineral-doped scaffolds had good values in terms of ion release. Cumulative release of calcium ions (mean \pm SD, expressed in ppm) ranged from 169.05 \pm 42.93 for PLA-5CaSi-5DCPD to 301.15 \pm 47.32 of PLA-10CaSi-10DCPD.

As expected, pure PLA scaffolds showed negligible calcium release (4.30 \pm 2.20 ppm). Ion release values evaluated at different time endpoints are showed in Table 1.

The highest values for Ca⁺⁺ release were detected in the first 2 endpoints. At times longer than 1 day, a general decrease was detected in all formulations. Calcium release decreased during the testing time,

Table 1

Ca⁺⁺ release (mean \pm SD, expressed in ppm) evaluated at 3, 24 h, 3, 7, 14 and 28 days. Calcium released from pure PLA samples was negligible. The highest cumulative Ca⁺⁺ release was observed for PLA-10CaSi-10DCPD, which was significantly higher than for all other experimental samples.

Scaffolds	Calcium released (ppm) (mean \pm SD)						
	0–3 h	3 h–1 day	1–3 days	3–7 days	7–14 days	14–28 days	Cumulative
PLA	0.59 \pm 0.39 ^{Aa}	1.24 \pm 0.22 ^{Aa}	0.95 \pm 0.70 ^{Aa}	0.77 \pm 0.38 ^{Aa}	0.81 \pm 0.42 ^{Aa}	0.73 \pm 0.63 ^{Aa}	4.30 \pm 2.20 ^a
PLA-10CaSi	65.13 \pm 37.42 ^{Ab}	66.02 \pm 12.41 ^{ABb}	23.63 \pm 5.60 ^{Cb}	22.90 \pm 5.99 ^{Cb}	19.18 \pm 3.19 ^{Cb}	10.68 \pm 5.84 ^{Cb}	208.15 \pm 33.46 ^b
PLA-5CaSi-5DCPD	34.27 \pm 12.79 ^{Ac}	50.81 \pm 33.77 ^{Bb}	39.12 \pm 9.17 ^{ABb}	20.42 \pm 8.41 ^{Bb}	12.25 \pm 2.15 ^{Cb}	8.17 \pm 2.58 ^{Cb}	169.05 \pm 42.93 ^b
PLA-10CaSi-10DCPD	68.41 \pm 37.76 ^{Ab}	122.32 \pm 33.21 ^{Bc}	42.59 \pm 3.39 ^{Cb}	33.35 \pm 4.75 ^{Cc}	15.66 \pm 2.91 ^{Db}	15.13 \pm 6.76 ^{Db}	301.15 \pm 47.32 ^c

In the vertical column, equal small superscript letter indicates no statistical differences among tested materials (p \geq 0.05).

In the horizontal row, equal capital superscript letter indicates no statistical differences among evaluation times (p \geq 0.05).

but remained significantly higher than for PLA for all 28 days, which demonstrated potential for long-term activity for all the mineral-doped samples.

PLA-10CaSi-10DCPD and PLA-10CaSi showed the highest calcium release values (68.41 \pm 37.76 and 65.13 \pm 37.42 ppm, respectively) at 3 h in deionized water; the former released the most significant calcium amount after 1 day (122.32 \pm 33.21 ppm).

Concerning the alkalizing activity, pH values showed a marked increase in the first 3 h (Table 2), ranging from 9.38 \pm 0.46 to 10.02 \pm 0.24 for the mineral-doped scaffolds. pH decreased after 1 and 3 days, but for all experimental scaffolds remained significantly higher than for control PLA. Until 3 days, PLA-10CaSi-10DCPD showed the most significant alkalizing activity compared to the other scaffolds. Interestingly, PLA-5CaSi-5DCPD doped scaffold had a statistically significant higher pH (alkalizing activity) at 1 day, comparable to PLA-10CaSi, but lower than PLA-10CaSi-10DCPD. For pure PLA scaffolds, pH remained around 7 at all testing times.

3.2. ESEM and surface porosity, EDX, Raman analyses

3.2.1. PLA scaffolds

ESEM analysis at 500 and 1000 \times magnifications revealed a micro-rough surface with irregular pits distributed on the scaffold surface (Fig. 3a,b). Micropores were well distributed on the whole surface, ranging from approx. 20 to 60 μ m. The average surface porosity, evaluated on three random areas at 500 \times and 1000 \times magnification, was 50.44% (range 41.23–56.41%) and 50.60% (range 42.02–63.51%), respectively (Fig. 4a).

EDX spectra of the examined area and of one random site (Fig. 3c,d) revealed constitutional peaks (C and O).

The FT-Raman and micro-Raman analysis of the PLA scaffold (Fig. 5a,b) showed that the sample was prevalently amorphous (see Table S1, Supplementary material, for bands wavenumber values and assignments), which was in agreement with previously reported data [48,51] and was confirmed by the DSC analysis performed on the samples. In fact, bands near 1770 and 400 cm⁻¹ are poorly structured, while in crystalline poly(L-lactic acid) (PLA100) they are split [52,53]. Moreover, the band at 923 cm⁻¹ observable in crystalline PLA100, due to 10₃ helical conformation [52], was not detected. The bands at about 1340 and 520 cm⁻¹ may be assigned to the D-lactic acid unit [53]. IR spectroscopy confirmed the prevalently amorphous character of the scaffold: the marker bands of crystallinity were observed with weak intensities and the 925 cm⁻¹ band due to 10₃ helical conformation was absent [54] (Fig. S1 and Table S2, for band wavenumber values and assignments [52,53,55], Supplementary material).

After 28 days of ageing in HBSS the degradation of PLA leads to the formation of larger pores (approx. 50–200 μ m), well visible by ESEM at 500 \times and 1000 \times magnifications (Fig. 3e,f). The larger pores exposed the internal structure of the scaffold. The average surface porosity of the HBSS aged scaffolds at 500 \times and 1000 \times magnifications was 65.74% (range 55.79–77.93%) and 68.94% (range 65.74–74.67%), respectively (Fig. 4a). The increase of the surface porosity from approx

Table 2

pH values (mean \pm SD) evaluated at 3, 24 h, 3, 7, 14 and 28 days. pH values were statistically higher for mineral doped scaffolds with respect to PLA traditional scaffold. Alkalinizing activity on deionized water was marked at the first day endpoints (3 and 24 h).

Scaffolds	pH of soaking water (mean \pm SD)					
	3 h	1 day	3 days	7 days	14 days	28 days
PLA	7.13 \pm 0.15 ^{Aa}	7.51 \pm 0.21 ^{Ba}	7.40 \pm 0.25 ^{Aa}	7.47 \pm 0.54 ^{Aa}	7.44 \pm 0.43 ^{Aa}	7.29 \pm 0.25 ^{Aa}
PLA-10CaSi	9.38 \pm 0.46 ^{Ab}	8.35 \pm 0.58 ^{Bbc}	7.23 \pm 0.41 ^{Ca}	7.27 \pm 0.14 ^{Ca}	7.24 \pm 0.28 ^{Ca}	7.09 \pm 0.29 ^{Ca}
PLA-5CaSi-5DCPD	9.82 \pm 0.12 ^{Ab}	8.52 \pm 0.64 ^{Bbc}	7.57 \pm 0.76 ^{Ca}	7.31 \pm 0.12 ^{Ca}	7.27 \pm 0.26 ^{Ca}	7.32 \pm 0.26 ^{Ca}
PLA-10CaSi-10DCPD	10.02 \pm 0.24 ^{Ab}	9.28 \pm 0.30 ^{Bc}	8.01 \pm 0.57 ^{Cb}	7.48 \pm 0.20 ^{Da}	7.23 \pm 0.16 ^{Da}	7.30 \pm 0.28 ^{Ea}
Deionized water	7.02 \pm 0.17 ^{Aa}	7.28 \pm 0.32 ^{Aa}	7.12 \pm 0.32 ^{Aa}	7.05 \pm 0.35 ^{Aa}	6.98 \pm 0.25 ^{Aa}	6.87 \pm 0.22 ^{Aa}

In the vertical column, equal small superscript letter indicates no statistical differences among tested materials ($p \geq 0.05$).

In the horizontal row, equal capital superscript letter indicates no statistical differences among evaluation times ($p \geq 0.05$).

50% of the fresh samples to approx 65% of the aged scaffolds indicates that approx. 30% of the PLA scaffold was degraded.

Punctual EDX spectra as well as those of the entire area (Fig. 3 g,h) showed small amounts of Ca, P, Na and Cl for PLA scaffold after 38 days HBSS.

The average micro-Raman spectrum recorded on the surface of the PLA scaffold after ageing in HBSS (Fig. 5) showed a 960 cm^{-1} band ascribable to an apatite deposit [55] rather than to HBSS; in fact, the spectrum recorded on the dried medium showed a band at 982 cm^{-1} (spectrum not shown), i.e. the wavenumber was shifted. A very weak spectral feature at nearly the same wavenumber value was detected also in the FT-Raman spectrum; however, its relative intensity was significantly lower due to the higher sensitivity of this technique to the

sample bulk. For the same reason, FT-Raman spectroscopy did not reveal any significant I_{875}/I_{1455} intensity ratio upon ageing, while micro-Raman spectroscopy revealed a decrease of this ratio (from 2.73 ± 0.17 to 2.45 ± 0.28 with values from single measurements as low as 2.1), suggesting a chain length decrease on the surface of the sample upon ageing in HBSS. IR spectroscopy confirmed the apatite forming ability of PLA, shown by the appearance of the bands at 1036, 600 and 560 cm^{-1} [55] in the spectrum of the sample aged in HBSS (Fig. S1 and Table S2, Supplementary material).

3.2.2. PLA-10CaSi scaffolds

ESEM analysis at $500\times$ and $1000\times$ magnifications (Fig. 6a,b) carried out on the fresh sample showed a micro-rough area with small

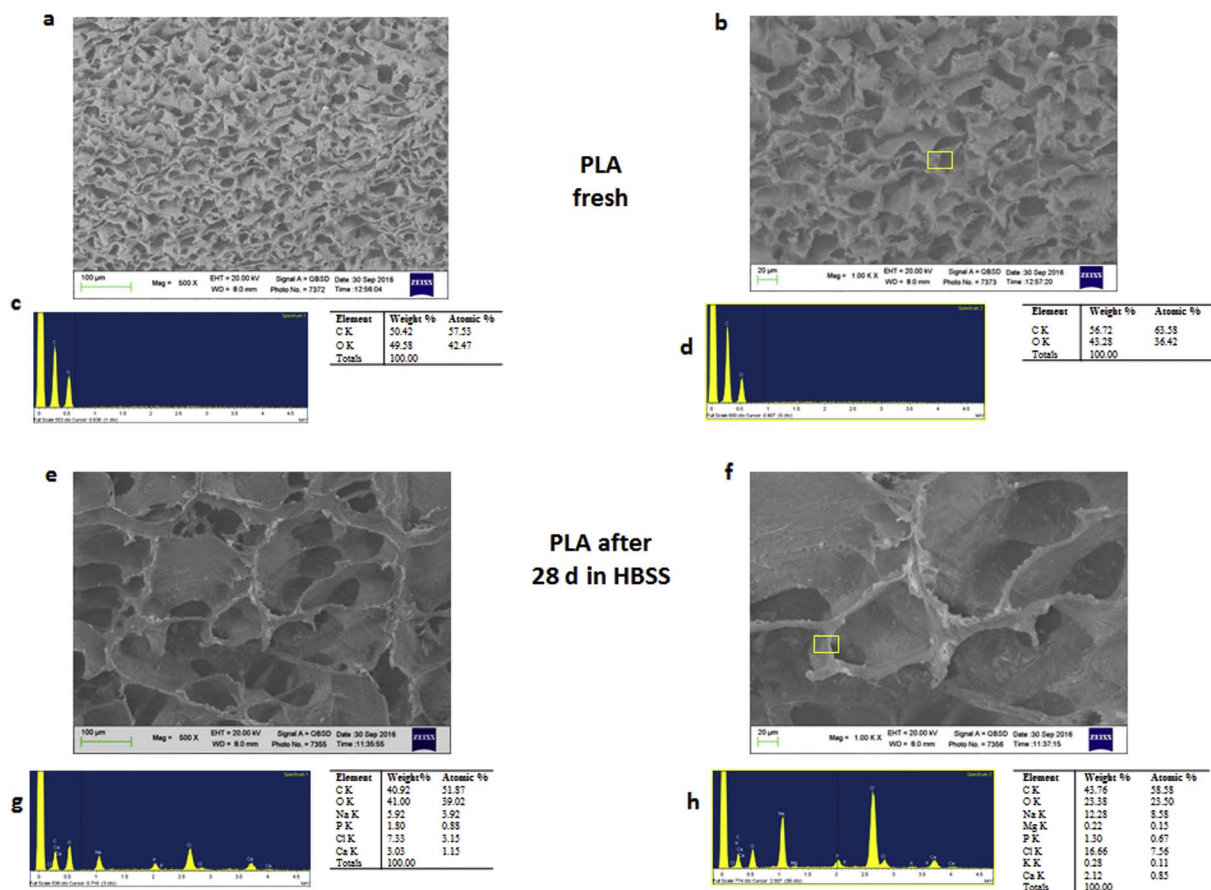


Fig. 3. ESEM surface micromorphology and EDX spectra of the PLA scaffold before (i.e. fresh) and after 28 days in HBSS ($500\times$ and $1000\times$ magnifications). A homogeneous surface with small circular and irregular-shaped porosities (ranging from $10\text{ }\mu\text{m}$ to $20\text{ }\mu\text{m}$) was revealed by ESEM in PLA scaffolds before ageing in HBSS. Irregular pits were distributed on the scaffold surface. After 28 days immersion in HBSS, the degradation of PLA leads to the formation of larger irregular-shaped pores (ranging from $50\text{ }\mu\text{m}$ to $200\text{ }\mu\text{m}$). The larger pores expose the internal structure of the scaffold. Small deposits were embedded on the edge of the pores. EDX spectrum of fresh PLA sample showed constitutional peaks (C and O); EDX spectra after 28 days in HBSS showed small amounts of Ca, P, Na and Cl.

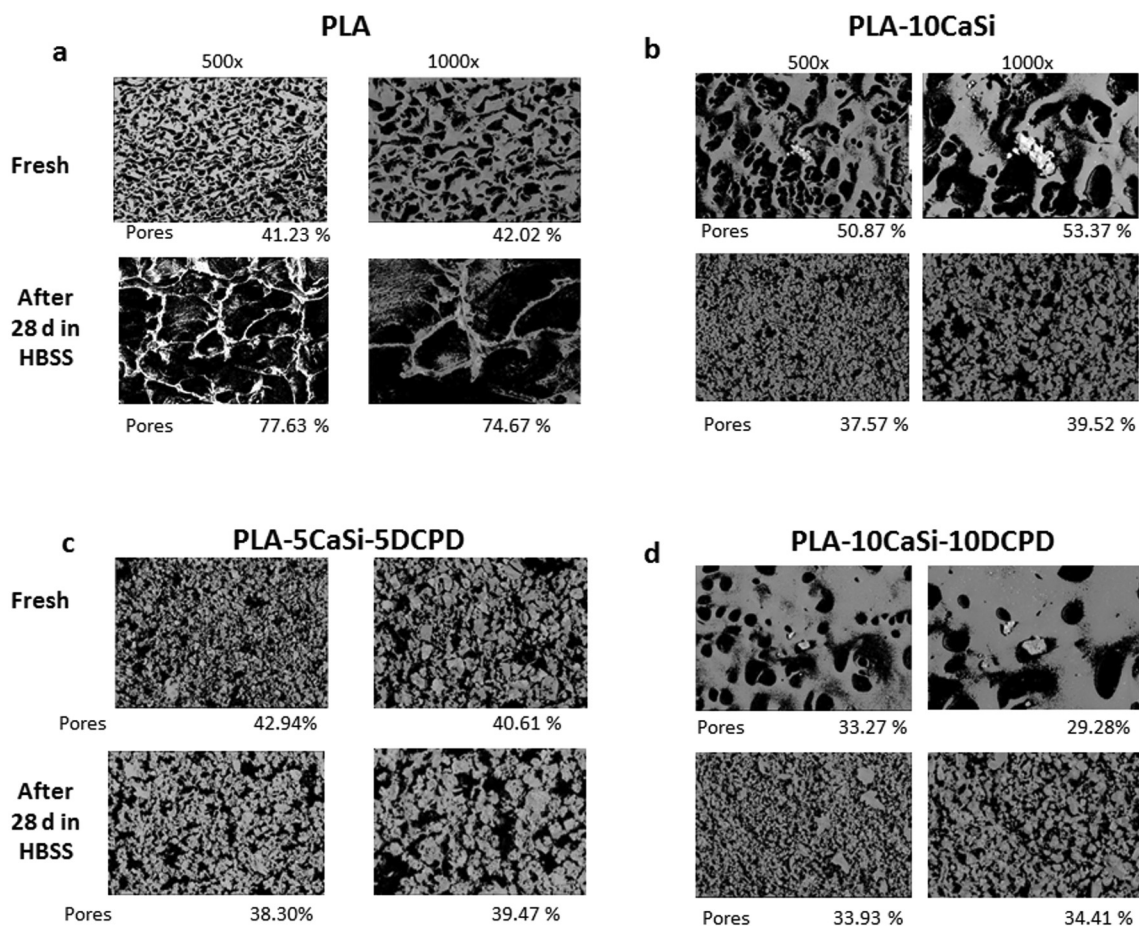


Fig. 4. Evaluation of the surface porosity in a random area (examined at 500 × and 1000 × magnification) of the experimental scaffolds before and after 28d-soaking in simulated body fluid. The surface porosity of the fresh scaffolds resulted different among the scaffolds and ranged from approx. 50% for PLA-10CaSi (b) to approx. 30% for PLA-10CaSi-10DCPD (d). PLA scaffold showed a marked increase of surface porosity after 28 days in HBSS (from approx 50% to approx 70%) (a). Differently, the surface porosity appears to decrease when the mineral phase is incorporated in the PLA matrix, in particular for PLA-10CaSi showing a reduction of the mean surface porosity from approx. 50% to approx. 37% (b).

circular pores (approx. 10–30 μm diameter) and larger elliptic pores (approx. 50–100 μm diameter). CaSi granules appeared spread into the scaffold structure (Fig. 6b). The mean value of the surface porosity, evaluated on three random areas at 500 × and 1000 × magnifications, were 59.2% (range 50.87–74.26%) and 54.28% (range 52.32–57.17%), respectively (Fig. 4b).

EDX on fresh samples (Fig. 6c) showed the peaks of the constitutional elements carbon (C) and oxygen (O), and traces of Ca and Si and Al from the incorporated CaSi granules.

Punctual EDX analysis of the granules (Fig. 6d) revealed the constitutional elements of the powder incorporated, mostly Ca, Si and traces of Al and S. Ca/Si ratio was 3.02.

Micro-Raman spectroscopy confirmed the incorporation of CaSi; actually, in the spectrum of fresh PLA-10CaSi, the bands due to monoclinic alite and belite (β-polymorph) [56], gypsum [57] appeared superimposed to those assignable to the polymer (Fig. 7 and Table S3, Supplementary material for bands wavenumber values and assignments). The presence of the calcite band at 1083 cm⁻¹ [58] was probably due to hydration in storage that leads to the formation of calcium hydroxide; which, exposed to air, formed calcium carbonate, as previously observed [59]. I₈₇₅/I₁₄₅₅ intensity ratio was 2.6 ± 0.2, i.e. similar to that observed in pure PLA scaffolds. The IR spectrum of the PLA-10CaSi scaffold showed the bands of the calcium silicate (weak) and calcium carbonate components superimposed to those of the polymer (Fig. S2 and Table S4 for bands wavenumber values and assignments [52,53,60–65], Supplementary material).

After 28 days of immersion in HBSS, ESEM revealed the appearance

of a mineral layer of calcium phosphate (CaP) on the surface of the scaffolds. This layer was distributed on the entire surface but not uniformly, as showed at 500 × and 1000 × magnifications (Fig. 6e,f). In less-covered areas, a less dense, degraded structure with medium-sized irregular pores (diameter 35–50 μm) was identified.

The mean values of the surface porosity, evaluated on three random areas at 500 × and 1000 ×, were 45.58% (range 37.57–56.01%) and 38.57% (range 32.12–44.08%), respectively (Fig. 4b). This surface porosity of the aged samples, which was lower than the one for fresh scaffolds, can be attributed to the nucleation of calcium phosphate deposits that likely replaced the degraded PLA.

EDX analyses of the entire area (Fig. 6g) showed appearance of P, Na, Cl, Mg and K peaks from the HBSS; decrease of intensity of the constitutional peaks C and O and increase of Ca and Si were observed, likely due to the progressive dissolution of the PLA structure that exposed more CaSi granules. The Ca/P atomic ratio calculated on the entire area was 4.2.

Punctual EDX spectra randomly recorded on the formed layer (Fig. 6h) revealed peaks similar to those detected in the spectrum of the entire area. Interestingly, increase of P and concurrent decrease of Si peak were observed at this point. Ca/P atomic ratio was 2.35.

The average micro-Raman spectrum recorded on the surface of PLA-10CaSi after ageing in HBSS (Fig. 7 and Table S3, Supplementary material) showed the presence of apatite (bands at 1039 and 959 cm⁻¹ [55]) and calcite (bands at 1083, 714 and 288 cm⁻¹ [58]) deposits. The bands of the polymer were still detectable. Upon ageing I₈₇₅/I₁₄₅₅ intensity ratio decreased from 2.6 ± 0.2 to 1.59 ± 0.14 and some

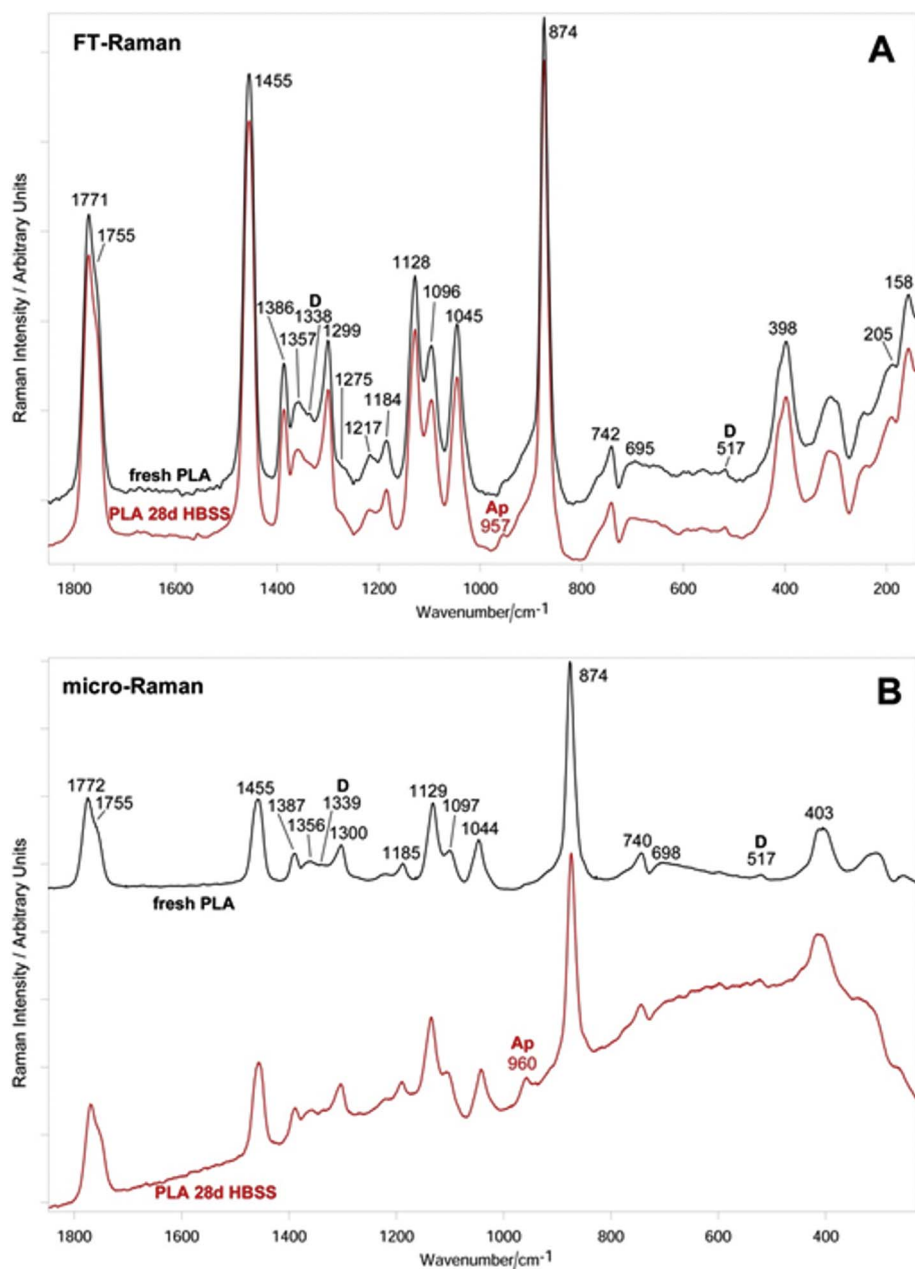


Fig. 5. FT-Raman (A) and micro-Raman (B) average spectra recorded on the surface of the PLA scaffold before (i.e. fresh, black line) and after ageing in HBSS for 28 days (red line). The bands prevalently assignable to the D-lactic acid unit (D) and apatite (Ap) are indicated. (For interpretation of the references to color in this figure legend, the reader is referred to the web version of this article.)

changes in the C=O stretching band profile were also observed. IR spectra confirmed the deposition of apatite and calcite phases; the bands of the polymer were detected with a very weak intensity (Fig. S3 and Table S4, Supplementary material). The band at 445 cm^{-1} is assignable to the CSH phase (hydrated silicate gel), produced upon hydration and polymerization of the calcium silicate component [65]. According to previous studies [59,65], the latter phenomenon is revealed by the increase in intensity of the band at 445 cm^{-1} with respect to the band at 510 cm^{-1} , which was no longer detected in the spectrum of the aged scaffold.

3.2.3. PLA-5CaSi-5DCPD scaffolds

ESEM images at $500\times$ and $1000\times$ magnifications on the fresh sample (Fig. 8a,b) showed a regular micro-rough surface with regular-shaped circular pores (diameter approx. $10\text{--}30\text{ }\mu\text{m}$). The mineral components of the CaSi cement and DCPD were evident and well distributed on the examined area.

The mean surface porosity, evaluated on three random areas at

$500\times$ and $1000\times$ was 45.49% (range 42.94–50.01%) and 40.08% (range 39.42–40.61%), respectively (Fig. 4c).

EDX analysis of the entire area of the fresh sample (Fig. 8c) showed C and O (constitutional PLA peaks), and Ca, Si and P peaks (from the incorporated CaSi and DCPD powders). The punctual spectrum (Fig. 8d) revealed the composition of the granules incorporated: the signal was mostly from Ca and Si (besides constitutional C and O peaks), with traces of P, Al and S. Ca/P atomic ratio on a CaP granule was 3.41, while that of the entire area was 3.34.

The micro-Raman spectrum recorded on the surface of fresh PLA-5CaSi-5DCPD (Fig. 9) confirmed the incorporation of both the doping agents. In fact, the bands of monoclinic alite and belite (β -polymorph), gypsum, calcite and DCPD [66] were observed together with those from the polymer (see Table S5, Supplementary material for bands wavenumber values and assignments). The I_{875}/I_{1455} intensity ratio was 2.8 ± 0.2 , i.e. it was not significantly different with respect to pure PLA scaffolds. The IR spectrum of fresh PLA-5CaSi-5DCPD was dominated by the bands of the polymer and weak spectral features

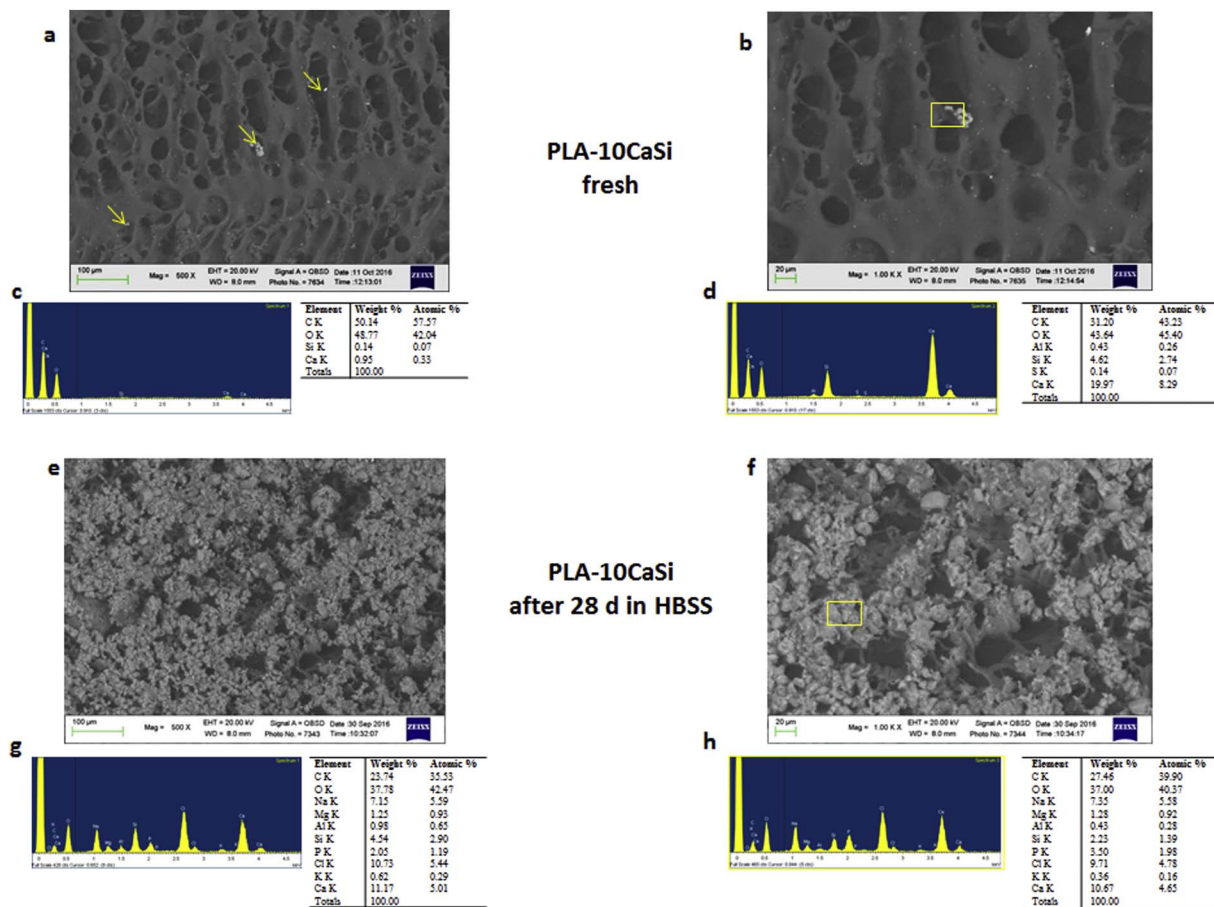


Fig. 6. ESEM surface micromorphology and EDX spectra of the PLA-10CaSi scaffold before (i.e. fresh) and after 28 days in HBSS (500 × and 1000 × magnifications). Small circular pores (ranging from 10 μm to 30 μm) as well as elliptic large pores (ranging from 50 μm to 100 μm) were present: small granules of CaSi were spread into all the scaffold structure; arrows show some calcium silicate granules incorporated in the scaffold. After 28 days immersion in HBSS a vast layer of CaP is formed in the surface; large irregular-shaped pores (approx 100 μm), as a result of PLA degradation, are evident beneath the mineral layer; EDX spectrum of fresh material shows C, O, (constititional peaks) and traces of Ca and Si; EDX spectrum of the sample immersed in HBSS for 28 days shows C and O (constititional peaks), Na, Cl, Mg and K peaks (attributable to HBSS), the appearance of Al and P and the increase of Ca and Si. The appearance of Al and Si peaks represents the progressive dissolution of the PLA structure that exposes more CaSi granules. The increase of Ca and appearance of P represents the apatite forming ability of the scaffold.

assignable to DCPD were detected (Fig. S4 and Table S6 for bands wavenumber values and assignments [52,53,60–64,67], Supplementary material); the calcium silicate component contributed to the band at 518 cm⁻¹.

After 28 days of HBSS immersion, a well evident layer of deposits covering the porous surface of the scaffold was present, as showed in Fig. 8e,f. The degradation of the PLA structure led to the formation of larger pores (approx. 20–100 μm), which were identified under the mineral layer and many deposits were nucleated into the micropores.

Surface porosity, evaluated on three random areas at 500 × and 1000 ×, displayed mean values of 42.90% (range 37.61–52.81%) and 43.82% (range 39.47–48.12%), respectively (Fig. 4c). The deposition of the mineral layer compensates for the porosity increase from the degradation of PLA.

EDX microanalysis of the entire area (Fig. 8g) showed moderate increase of Ca and P due to CaP deposits formation, a slight increase of Si and Al (attributable to the exposure of the CaSi granules due to PLA degradation) and the appearance of Na, Cl and K reflexes (from HBSS solution).

Punctual EDX spectrum of the underneath surface (Fig. 8h) revealed, besides the PLA constititional peaks (C,O), increase of Si and Al, which can be attributed to the exposure of more granules due to the polymer degradation.

The micro-Raman spectrum recorded on the surface of PLA-5CaSi-5DCPD after ageing in HBSS (Fig. 9 and Table S5, Supplementary

material) showed the appearance of a weak 964 cm⁻¹ band superimposed to the bands of the polymer. The I₈₇₅/I₁₄₅₅ intensity ratio decreased from 2.8 ± 0.2 to 2.5 ± 0.16 upon ageing, i.e. not significantly. No changes in the C=O stretching band profile were observed. Analogous results were obtained from the IR spectra: upon ageing in HBSS, the bands assignable to an apatite phase were detected together with those (intense) of the polymeric component (Fig. S3 and Table S6, Supplementary material).

3.2.4. PLA-10CaSi-10DCPD scaffolds

The fresh surface of the sample at 500 × and 1000 × magnifications (Fig. 10a,b) showed a compact, less porous surface compared to the other scaffolds, with spherical connected pores of different sizes (range 20–100 μm diameter). Small granules of CaSi and DCPD powders were present on the scaffold surface. In addition, the whole surface seemed to be embedded by these granules.

The mean porosity, evaluated on three random areas at 500 × and 1000 × magnifications was 31.51% (range 29.69–33.27%) and 26.94% (range 15.67–35.88%), respectively (Fig. 4d).

EDX spectrum (Fig. 10c) recorded in the entire area of the fresh scaffold showed C and O (constititional peaks) and traces of Ca, Si, Al, S and P (attributable to the incorporated CaSi and DCPD powders). Punctual EDX analysis of the granules (Fig. 10d) confirms the scaffold composition, revealing (besides C and O peaks) Ca, Si and reflexes of Al, P and S.

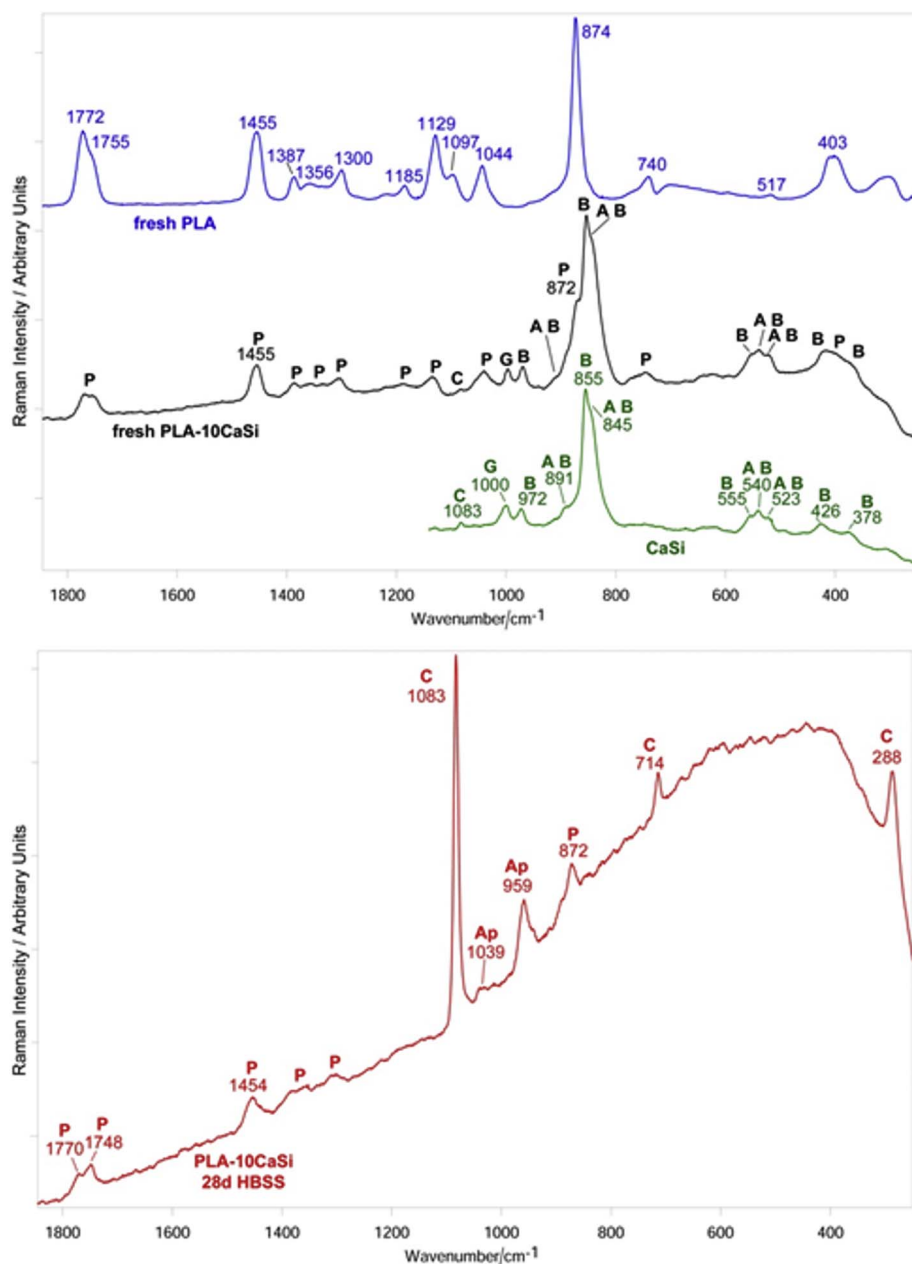


Fig. 7. Micro-Raman average spectra recorded on the surface of the PLA-10CaSi scaffold before (i.e. fresh, black line) and after ageing in HBSS for 28 days (red line). The bands prevalently assignable to the PLA polymer (P), gypsum (G), alite (A), belite (B), calcite (C), apatite (Ap) are indicated. (For interpretation of the references to color in this figure legend, the reader is referred to the web version of this article.)

The micro-Raman spectrum of the fresh PLA-10CaSi-10DCPD (Fig. 11) showed the bands of the CaSi cement components, DCPD and PLA (see Table S7, Supplementary material for bands wavenumber values and assignments). As expected, bands from the inorganic phases were detected with higher relative intensities than in PLA-5CaSi-5DCPD (Fig. 9). The I_{875}/I_{1455} intensity ratio was 2.5 ± 0.2 , i.e. not significantly different with respect to pure PLA scaffolds. The IR spectrum of fresh PLA-10CaSi-10DCPD was dominated by the bands of the polymer and spectral features assignable to DCPD were detected (Fig. S5 and Table S8 for bands wavenumber values and assignments, Supplementary material); the calcium silicate component contributed to the band at 520 cm^{-1} . It is interesting to note that in the composite, the C=O stretching band of PLA was shifted to lower wavenumber values with respect to pure polymer and sharpened: going from the latter to the former, its full-width at half maximum (FWHM) decreased from 33.6 to 32.5 cm^{-1} .

After 28 days of immersion in HBSS a uniform distributed layer of deposits was formed on the surface. This layer was more compact in comparison to the other experimental scaffolds, as showed in Fig. 10e,f.

Medium-sized pores (approx. $10\text{--}50 \mu\text{m}$ diameter) were present under the deposit, which formed also into the micropores.

The mean porosity, evaluated on three random areas at $500\times$ and $1000\times$ magnifications, was 32.28% (range 23.06–39.85%) and 28.89% (range 16.95–35.32%), respectively (Fig. 4d).

EDX analysis of the area (Fig. 10g) revealed C and O elements from PLA structure and appearance of Na, Cl and K reflexes (attributable to HBSS). A strong increase of the signal of Ca and P due to the calcium phosphate minerals was observed; the strengthening of the Si peak and the appearance of Al were due to CaSi granules exposed by PLA degradation.

Punctual EDX analysis on a random point of the mineral layer (Fig. 10h) showed, besides C and O constitutional peaks, strong peaks of Ca and P, presence of Si and Al (remnants of the material incorporated) and traces of Na, Cl, K attributable to the medium. Punctual Ca/P atomic ratio of one CaP deposit was 1.96, while that of the entire area was 4.05.

The average micro-Raman spectrum recorded on the surface of PLA-10CaSi-10DCPD after ageing in HBSS (Fig. 11) showed the bands

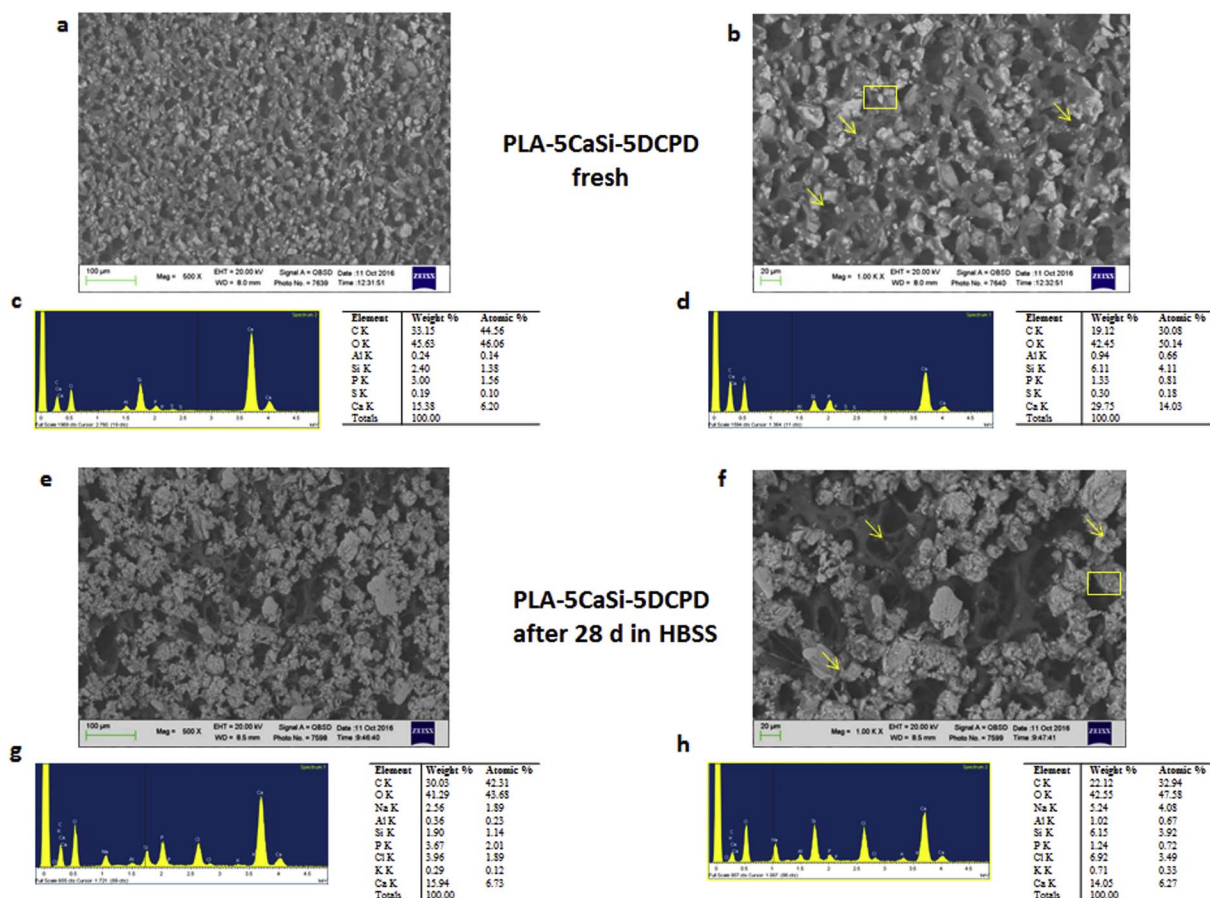


Fig. 8. ESEM surface micromorphology and EDX spectra of the PLA-5CaSi-5DCPD scaffold before (i.e. fresh) and after 28 days in HBSS (500 × and 1000 × magnifications). Fresh material surface appeared compact with a non-homogeneous distribution of the CaSi and DCPD powders. Small circular/elliptical pores (ranging from 10 μm to 20 μm) were homogeneously distributed on the surface (arrows). After 28 days of HBSS immersion, a well-distributed layer of CaP was present on the surface of the scaffold. Large irregular-shaped pores (ranging from 20 μm to 100 μm), as a result of matrix degradation, were identified under the mineral layer. Arrows show apatite formation into the micropores. Fresh sample spectrum shows C, O (constitutional peaks), and the Ca, Si, P peaks (attributed to CaSi and DCPD materials incorporated). Twenty-eight days HBSS spectrum shows the moderate increase of Ca and P (apatite formation), a slight decrease of Si, appearance of Al (attributed to the CaSi granules) and Na, Cl and K (attributed to HBSS solution).

typical of B-type carbonated apatite at 1070, 1039, 959, 613–595 and 437 cm^{-1} [55], and calcite, which were superimposed to those (weak) of the polymer (see Table S7, Supplementary material for assignments). For this reason, the estimated I_{875}/I_{1455} intensity ratio (2.2 ± 0.3) may be less reliable than for the other samples. In some single spectra bands of the polymer were not detected and only apatite was revealed (Fig. 11, bottom spectrum). The latter result was found also by IR spectroscopy: the average spectrum recorded on the surface of the scaffold aged in HBSS showed only the bands of the apatite and calcite phases (Fig. S3 and Table S8, Supplementary material) and the bands of the polymer were no longer detected.

3.3. Bulk open porosity, thermal and mechanical properties

TIPS procedure allowed to obtain all samples with bulk open porosity higher than 90%; data of porosity for all the produced samples are reported in Table 3, along with real contents of inorganic fillers present in the composite scaffolds as determined through TGA. Notwithstanding the extremely high level of open porosity reached during the fabrication of the scaffolds, elastic modulus and compression resistance remained at appropriate levels to ensure a proper handling and use of the scaffolds (Table 4). The introduction of ceramic fillers causes a noticeable increase of the materials stiffness just in the case of the highest filler content (PLA-10CaSi-10DCPD). If stress values at 30% and 60% deformation levels are considered, it can be concluded that the reinforcing action provided by CaSi and DCPD is more evident at higher

deformations, when the influence of the porosity on the mechanical behaviour plays a minor role and the compressive properties of the bulk scaffold become more relevant.

3.4. Analysis of the crystalline structures

XRD patterns of CaSi and DCPD pure powders, pristine PLA and the composite samples are reported in Fig. 12. For all the prepared compositions containing DCPD and/or CaSi, it is possible to observe the signals from inorganic fillers at their typical 2θ values.

3.5. Cell response

Cell viability and proliferation, employing WST-1 cell proliferation reagent was quantitatively investigated. The test is based on the mitochondrial enzymatic conversion of the tetrazolium salt WST-1 into soluble formazan, occurring only in metabolically active cells. The amount of formazan dye directly correlates with the number of viable cells present in the sample.

Cell proliferation was monitored at days 7 and 14 after seeding and results are reported in Fig. 13a. Cell grown onto TCPS were used as control up to 7 days of culture. After this time point cells reached the maximum confluence and could not be kept in culture for longer period.

Cell proliferation and viability was higher at 14 days than at 7 days for all the samples. A higher cell growth on mineral doped scaffold, compared to control group was observed, in particular at 7 days.

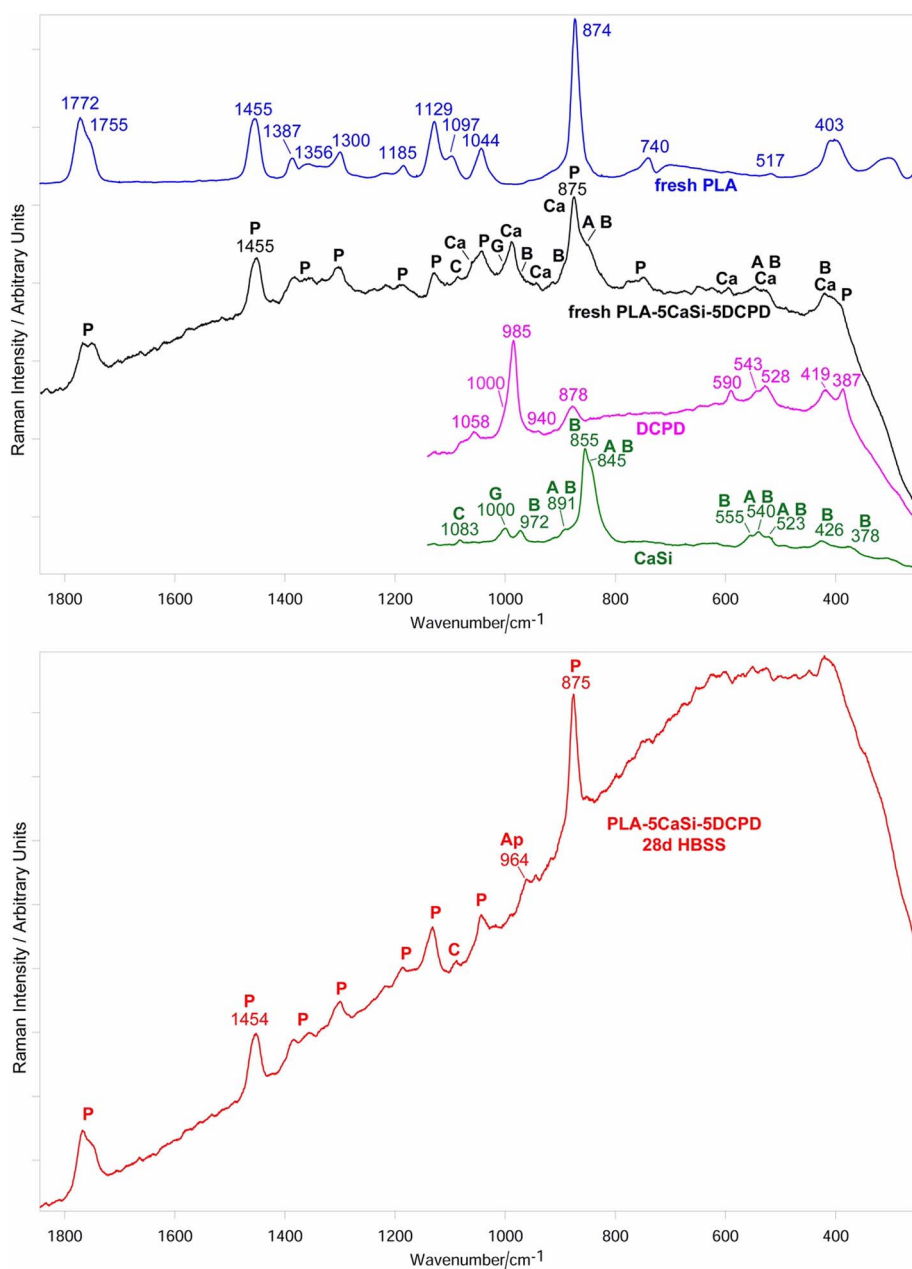


Fig. 9. Micro-Raman average spectra recorded on the surface of the PLA-5CaSi-5DCPD scaffold before (i.e. fresh, black line) and after ageing in HBSS for 28 days (red line). The bands prevalently assigned to the PLA polymer (P), gypsum (G), alite (A), belite (B), calcite (C), dicalcium phosphate dihydrate (Ca), apatite (Ap) are indicated. (For interpretation of the references to color in this figure legend, the reader is referred to the web version of this article.)

Results confirmed the lack of toxicity for all the investigated samples. All mineral doped scaffolds were colonized by more fibroblasts within the first 7 days of culture than control PLA. A slight increase in proliferation during the second week of culture was also assessed.

Cells grown on the experimental scaffolds were stained for F-actin and nuclei with phalloidin-Alexa Fluor 488 and DAPI, and the morphology and cytoskeleton organization were carried out by CLSM analysis.

After 14 days of culture, microscopic observations confirmed the quantitative data and revealed the presence of cells on all the scaffolds. A good degree of cell colonization of the scaffolds was confirmed by the visualization and distribution of cell nuclei, stained with DAPI (Fig. 13b).

The staining of the cells with phalloidin-Alexa Fluor 488 to visualize cell cytoskeleton resulted less effective, probably due to the thickness of the samples. Nevertheless, representative images of cells grown onto PLA-10CaSi-10DCPD displayed a consistent F-actin organization with stress fibers well stretched along the cytoplasm, thus corroborating the

possibility of the developed scaffolds to act as synthetic extracellular matrix for cell adhesion and proliferation (Fig. 13c).

4. Discussion

In this study, experimental PLA-based scaffolds were produced incorporating different percentages of hydraulic CaSi cement and DCPD mineral powders by means of TIPS.

TIPS is a simple experimental procedure to produce homogeneous and highly porous structures: the phase separation is induced by lowering the temperature under the freeze point of the solvent used to dissolve the polymer (1,4-dioxan in this case, DIOX) and disperse the bioactive filler (DCPD and/or CaSi), in order to solidify the composite into its interstitial spaces. The frozen solvent is then chemically extracted by contact with another solvent (liquid–solid separation), miscible with the former and having lower freeze point (MeOH in this case); the extracting solvent progressively removes the frozen solvent and pores and cavities remain in place of it. Main advantages connected

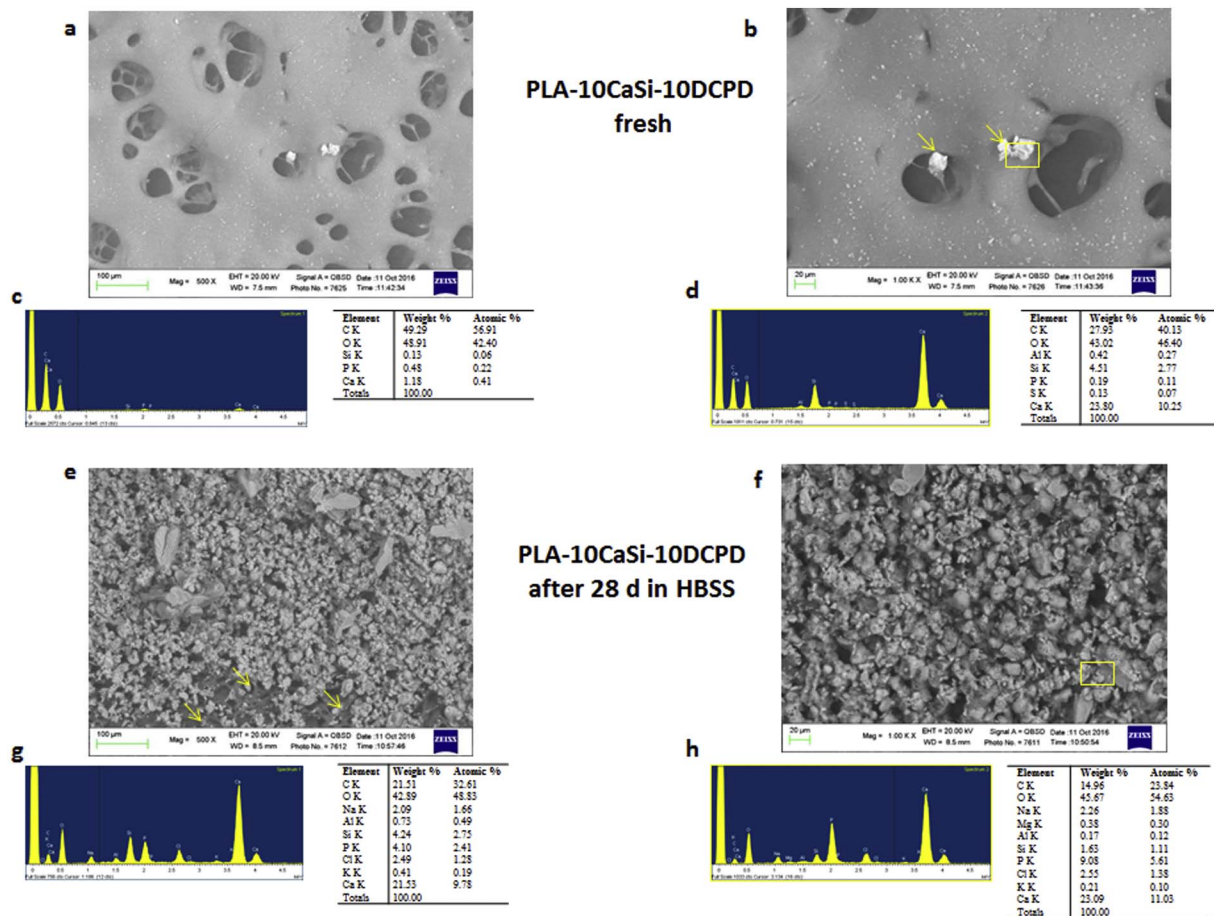


Fig. 10. ESEM surface micromorphology and EDX spectra of the PLA-10CaSi-10DCPD scaffold before (i.e. fresh) and after 28 days in HBSS (500 × and 1000 × magnifications). Small circular pores (ranging from 10 μm to 40 μm) were distributed in a solid surface. Arrows show some granules of CaSi and DCPD powders incorporated in the structure. After 28 days immersion in HBSS, a homogeneous and well distributed layer of CaP was formed on the surface. Irregular-shaped pores (ranging from 10 μm to 50 μm) were well identified under the calcium-phosphate layer. Arrows show apatite formation into the micropores. EDX spectrum of fresh scaffold shows C, O (constitutional peaks), and traces of Ca, Si and P peaks (attributed to CaSi and DCPD powders). Spectrum of the 28 day HBSS-aged sample shows C, O (constitutional peaks), Na, Cl, K (attributed to HBSS), a marked increase of Ca and P (apatite formation), Si increase and appearance of Al (CaSi granules exposure following PLA degradation).

with TIPS are related to very high level of porosity that can be obtained (> 90%). The full control on the final composite composition that TIPS procedure allows [33], has been confirmed for the samples object of this study by checking the real content in inorganic filler(s) present in the porous PLA-based scaffolds through TGA analysis. The residual weight recorded after the decomposition and volatilization of the polymer phase (occurring at ca. 355 °C) corresponding to the real content in CaSi and DCPD in the composite scaffolds, resulted almost identical to the nominal filler content.

TIPS resulted very convenient to produce highly porous composite structures made of PLA filled with amounts of CaSi and DCPD arriving at 20 wt% in the case of PLA-10CaSi-10DCPD. Due to the different density between the polymer matrix and the inorganic fillers, different techniques would not have been able to deliver homogeneously dispersed samples. Fig. 2 shows a PLA scaffold obtained by TIPS (a), its cross section (thickness 8 mm), (b) and one section acquired at high magnification through ESEM (c).

Being a process that requires low temperatures, TIPS also does not induce any modification in the morphological structure of the crystalline fillers upon mixing with the polymer phase; this was confirmed by XRD analysis (Fig. 12). From these XRD patterns, however, it is not possible to compare the intensities of the peaks for the purpose of quantitative evaluations, as pure powders and composite samples with the PLA matrix have different diffraction powers.

Different tests have been performed to evaluate their chemical reactivity (ion release, alkalizing activity, and apatite-forming ability),

surface microchemistry and micromorphology, porosity, thermo-mechanical properties and cytotoxicity.

The designed scaffolds were biointeractive (ion-releasing ability) and bioactive (apatite-nucleation ability) as well as suitable to be colonized by cells. These results suggest a potential role of these materials in osteoblasts (and other mineralizing cells or precursors) activation and their use as attractive materials for bone defects regeneration.

Bone regeneration, especially in a bone defect, is a complex and dynamic process where different cells, chemical and immunological mediators are deployed, performing different tasks with the results of a continuous site modification.

In this study, CaSi materials have been introduced owing to their positive bio-interaction with mineralizing cells [30,40], mainly due to the calcium release and apatite-forming ability. This is the reason why they are widely used in dentistry (mainly in endodontics) for the application in contact with bone tissue (i.e. periapical bone) and healing mineralized tissues (dentin repair, periapical bone lesions regeneration, apicogenesis/apexification).

Extracellular Ca⁺⁺ ions are necessary for bone cells mineralization signaling. During mineralization processes, they specifically modulate osteopontin, bone morphogenetic protein-2 and alkaline phosphatase [68–70]. In particular, the high amount of ion release in the first 24 h may represent a stimulatory signal for bone marrow cells migration to the site of ion release [71].

In this study, all the experimental mineral-doped samples showed remarkable Ca⁺⁺ release and alkalization of the media, especially

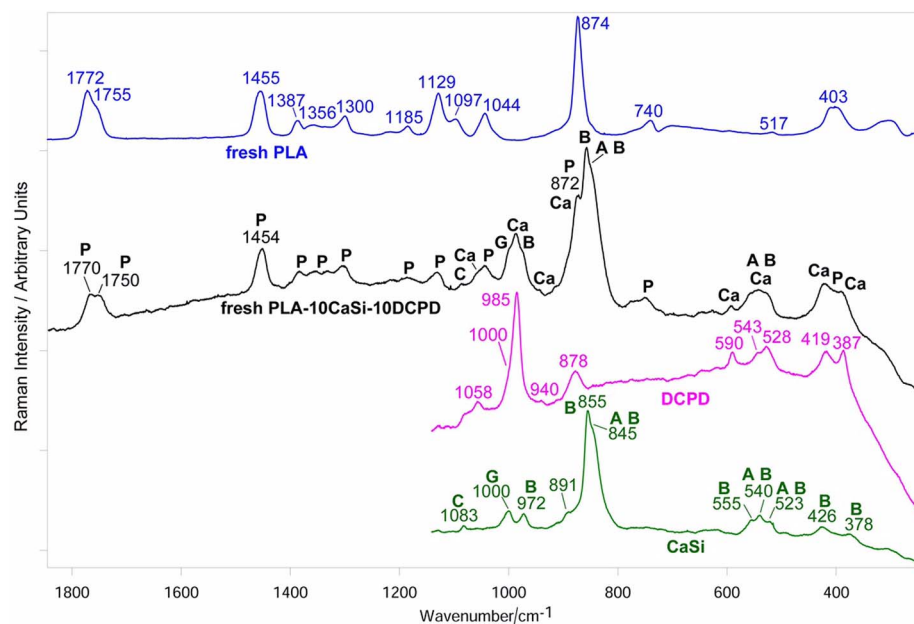


Fig. 11. Micro-Raman average spectra recorded on the surface of the PLA-10CaSi-10DCPD scaffold before (i.e. fresh) and after ageing in HBSS for 28 days. The bands prevalently assigned to the PLA polymer (P), gypsum (G), alite (A), belite (B), calcite (C), dicalcium phosphate dihydrate (Ca), apatite (Ap) are indicated.

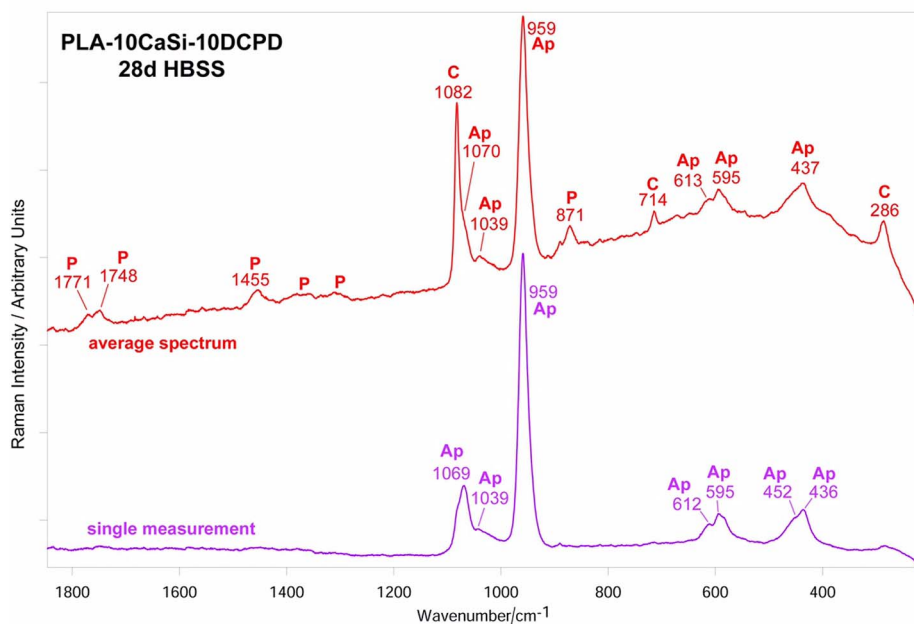


Table 3

Real content of inorganic filler (wt%) determined by TGA and open porosity of PLA-based scaffolds obtained by TIPS calculated by standard procedure (UNI EN 1936:2007) (mean ± SD).

Scaffold	Real content of inorganic filler (wt%)	open porosity (%)
PLA	–	93.8 ± 0.1
PLA-10CaSi	9.7 ± 0.4	92.6 ± 0.1
PLA-5CaSi-5DCPD	9.2 ± 0.6	91.8 ± 0.1
PLA-10CaSi-10DCPD	18.8 ± 1.3	92.4 ± 0.2

during the first days. Thus, mineral CaSi and DCPD components of the scaffolds reacted and release Ca⁺⁺ and OH⁻ ions.

The release of OH⁻ ions leads to a marked increase of pH in deionized water. This activity is important [72,73] for bone remodeling and regeneration processes and appeared evident in the first days of ageing of the mineral doped scaffolds. Osteoblasts activity increases with alkaline pH and is reduced in acid environment. In particular, collagen

Table 4

Glass transition temperature determined by DSC and compression mechanical properties of PLA-based scaffolds obtained by TIPS (mean ± SD).

Scaffold	Tg (°C)	E (MPa)	σ _{30%} (MPa)	σ _{60%} (MPa)
PLA	57.4	0.226 ± 0.085	0.094 ± 0.009	0.217 ± 0.032
PLA-10CaSi	57.5	0.239 ± 0.071	0.115 ± 0.062	0.324 ± 0.034
PLA-5CaSi-5DCPD	57.3	0.255 ± 0.002	0.136 ± 0.002	0.351 ± 0.001
PLA-10CaSi-10DCPD	59.0	0.312 ± 0.084	0.133 ± 0.005	0.373 ± 0.008

E (MPa) elastic modulus.

σ_{30%} and σ_{60%} (MPa) are the stress values at 30% and 60% elongation, respectively.

synthesis, alkaline phosphatase activity, and thymidine incorporation are stimulated in alkaline conditions (above 7.4) [74,75]. An alkaline environment also stimulates the expression of BMP-2 [76], the solubilization of bioactive components from the organic matrix [77] and the deposition of apatite [78,79].

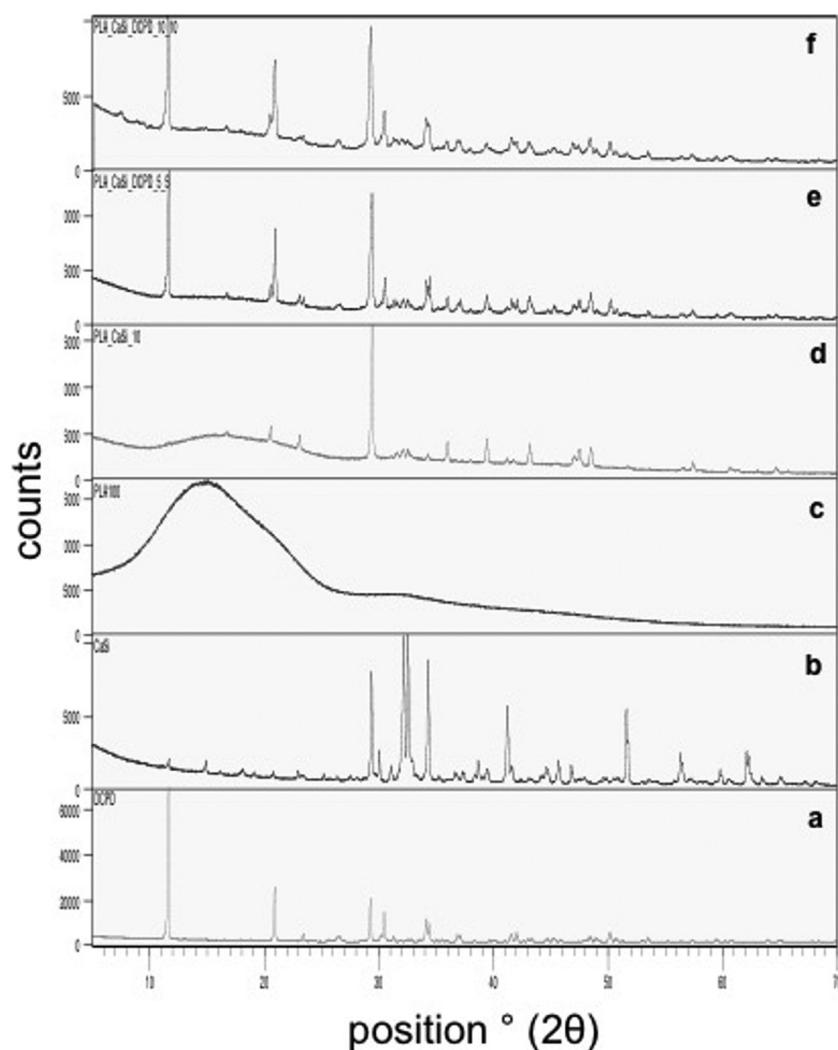


Fig. 12. XRD patterns of pure DCPD (a) and CaSi (b) powders, pristine PLA (c), PLA-10CaSi (d), PLA-5CaSi-5DCPD (e) and PLA-10CaSi-10DCPD (f).

Silicon plays an important role in mineralization and bone formation. Silicon induces *in vitro* BMP-2 gene expression [80] and bone signaling pathways of bone marrow stem cells [81]. Silicon-containing materials may induce angiogenesis through increasing gene expression of pro-angiogenic cytokine receptors and up-regulate downstream signaling of nitric oxide synthesis, genes and activity [81,82]. Moreover, SiO_4^{4-} groups of CaSi and the Si-OH groups of the CSH phase, which at alkaline pH are prevalently deprotonated, have been correlated to the nucleation of a bone-like carbonated apatite layer [83–85], which may bond to the living bone.

In the present study, DCPD has been inserted in the formulation as it can lead to the formation of calcium deficient apatite by reacting with $\text{Ca}(\text{OH})_2$ from the hydration of CaSi, following the reaction [30]: $6\text{CaHPO}_4 \cdot 2\text{H}_2\text{O} + 3\text{Ca}(\text{OH})_2 \rightarrow \text{Ca}_9(\text{HPO}_4)(\text{PO}_4)_5(\text{OH}) + 17\text{H}_2\text{O}$. Calcium deficient apatite may transform into bone-like carbonated apatite, as detected by micro-Raman and IR spectroscopy.

To investigate the possible interactions between the PLA and inorganic phases, IR spectroscopic analyses were carried out. The IR spectra of the composites were compared with those of the reference spectra, i.e. PLA and CaSi for the PLA-10CaSi scaffold, and PLA, CaSi and DCPD for PLA-5CaSi-5DCPD and PLA-10CaSi-10DCPD. The spectra reported in Figs. S2 and S4, Supplementary material, for fresh PLA-10CaSi and PLA-5CaSi-5DCPD showed no significant differences either in band wavenumber values or in band width with respect to the reference spectra. On the contrary, in the spectrum of fresh PLA-10CaSi-10DCPD (Fig. S5, Supplementary material), detectable decreases in the

C=O stretching band wavenumber value and FWHM were observed with respect to pure PLA. This result may be interpreted as a sign of the C=O involvement in $\text{C}=\text{O} \cdots \text{H}-\text{OPO}_3^{2-}$ hydrogen bond interactions between the polymer and the HPO_4^{2-} ion of DCPD. In fact, such an interaction results in a weakening of the C=O bond and thus in a decrease of its absorbance wavenumber value. Moreover, it must be stressed that in all the composites, the IR I_{1080}/I_{1128} intensity ratio was lower than in pure PLA (Fig. S6(A), Supplementary material). On the basis of the assignments of these bands (Table S1, Supplementary material) and in agreement with Zhang et al. [55], this trend suggests that the presence of the inorganic DCPD and/or CaSi phases should induce conformational polymer rearrangements which involved the COC backbone and determined changes in interchain interactions between CH_3 groups.

The *in vitro* evaluation of apatite forming ability is a highly predictable technique, used to evaluate materials bioactivity before *in vivo* testing, in order to focus the efforts on the best suitable material [86]. Thus, we may expect a similar activity *in vivo*.

The micro-Raman and IR analyses showed that all the scaffolds under study nucleated apatite after 28 days of immersion in HBSS. In the average spectra recorded on the samples, the bands of PLA were detected, although with different relative intensities. The $I_{960(\text{Ap})}/I_{875(\text{PLA})}$ (Raman) and $I_{1030(\text{Ap})}/I_{1750(\text{PLA})}$ (IR) intensity ratios were used as markers of the thickness of the apatite deposit. It may be observed that both these ratios (Fig. S6(B) and (C), Supplementary material), and thus the apatite thickness, increased along the series $\text{PLA} < \text{PLA-10CaSi} < \text{PLA-5CaSi-5DCPD} < \text{PLA-10CaSi-10DCPD}$.

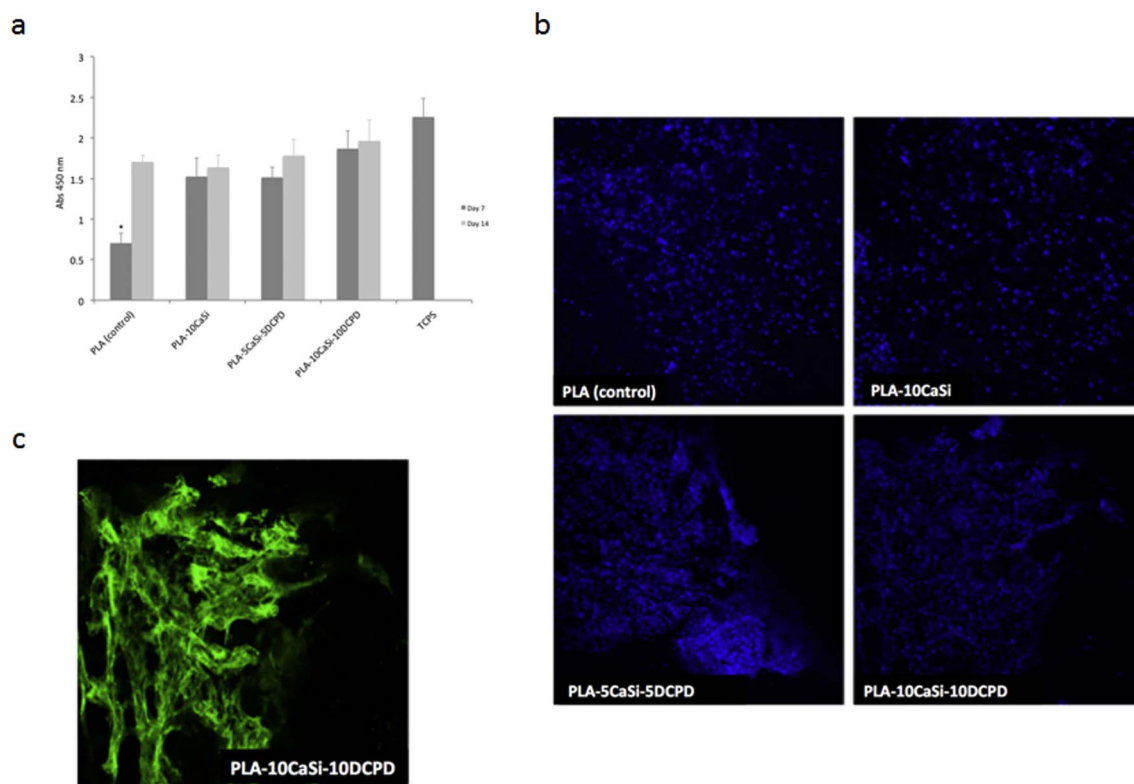


Fig. 13. (a) Quantitative results of cell proliferation on the experimental scaffolds and TCPS. Cell proliferation and viability was higher at 14 days than at 7 days for all the samples. A higher cell growth on mineral doped scaffold, compared to control group (PLA control) was observed, in particular at 7 days. Value marked by asterisk is significantly different ($p < 0.05$).

(b) CLSM micrograph of cell colonization of mineral doped scaffolds. Cells nuclei were stained with DAPI. Images were captured using $10\times$ magnification objective. After 14 days of culture, microscopic observations confirmed the quantitative data and revealed the presence of cells on all the investigated samples.

(c) CLSM visualization of F-actin cytoskeleton of cells stained with phalloidin-Alexa Fluor 488 recorded at $20\times$ magnification, representative images of cells grown onto PLA-10CaSi-10DCPD displayed a consistent F-actin organization with stress fibers well stretched along the cytoplasm.

5CaSi-5DCPD < PLA-10CaSi < PLA-10CaSi-10DCPD, in agreement with the cumulative calcium release data (Table 1).

Micro-Raman and IR analyses showed that also the pure PLA scaffolds nucleated apatite on their surface, although to the lowest extent among the samples under study. This result could be surprising since the bioactivity of PLA appears to be still under debate. Some studies have reported that the polymer has no apatite forming ability [87,88], while others have found an opposite behaviour [89–91]. These contradicting results suggest that the chemical and physical properties of the sample (i.e. the physical form and porosity) play a crucial role in mineralization experiments.

The PLA-10CaSi-10DCPD scaffold formed the thickest apatite deposit; actually, in the average micro-Raman spectrum recorded on its surface after ageing in HBSS, all the bands characteristic of B-type carbonated apatite were observed. On the other hand, in several single micro-Raman spectra recorded on this sample, the bands of PLA were not detected (Fig. 12, bottom spectrum), since the thick deposit masked the signal of the polymer underneath. This behaviour was observed only for this scaffold and correlates with the highest amount of calcium ions (Table 1) and the highest alkalizing activity (Table 2). On the other hand, this is the only sample whose IR spectrum after ageing did not show any PLA band (Fig. S3, Supplementary material), and thus the $I_{1030(\text{Ap})}/I_{1750(\text{PLA})}$ IR intensity ratio tended towards ∞ (Fig. S6(B), Supplementary material).

An alkaline environment has been reported to accelerate the PLA degradation [48,92], which occurs through the hydrolysis of the ester bonds and leads to the formation of lower molecular weight degradation products. The biodegradation mechanism and kinetics of the polymer depend on a series of factors which control water accessibility to ester linkages: composition, molecular weight, configurational

structure, morphology, crystallinity, presence of residual monomer and low molecular weight compounds, processing, annealing and sterilization [93,94]. The degradation of semi-crystalline polymers has been reported to proceed with a progressive increase in crystallinity since the amorphous domains are more prone to degradation; thus, if the amorphous parts of the polymer leave its crystalline domains, crystallinity increases.

Raman spectroscopy proved to be suitable to investigate the degradation mechanism of the scaffolds under study. The FT-Raman spectra of the PLA scaffold agreed with the data previously reported on a PLA-based periodontal membrane [47,48] in which the chain length in the sample bulk did not change upon ageing and no increases in crystallinity were observed since the starting material was prevalently amorphous. Micro-Raman spectroscopy showed that upon immersion in HBSS a certain chain length decrease occurred on the surface of the sample. An analogous behaviour was observed also for the composite scaffolds; the changes observed in the C=O stretching region may be ascribed to the formation of shortened polymeric chains [95].

The range of micropores size is crucial for different biological functions. A pore size in the 1–20 μm range is important for cell-matrix interactions, such as type of cells attracted, cells orientation and in-growth, nutrients or metabolites transportation. Pores between 100 and 1000 μm are necessary for neo angiogenesis, fluids and nutrients transportation, new bone ingrowth and formation. In particular, a pore size between 100 and 400 μm is required for osteoblast proliferation and fibro-vascular endothelial growth [96]. TIPS resulted a proper fabrication technique for the preparation of highly porous PLA scaffolds doped with considerable amounts (up to 20 wt%) of mineral fillers. The combination of bulk porosity higher than 90% and high inorganic particles loading would have generated very brittle samples if different

preparation techniques (i.e. salt leaching) were used.

Interestingly, the mineral-doped scaffolds showed lower or stable surface porosity values after 28 days in simulated body fluid, likely due to the CaP nucleation into the PLA structure: PLA 10-CaSi showed the highest decrease of surface porosity (Fig. 5b), while PLA-10CaSi-10DCPD and PLA-5CaSi-5DCPD showed small variations, as reported in Fig. 5c and d. This surface porosity difference may be explained by the irregularities of the CaP layer on the scaffolds surface, well evident in Figs. 7, 9 and 11. It is likely that CaSi and DCPD powders, which are well distributed inside the entire thickness of the scaffolds and not only on the surface (Fig. 2c), may act as apatite nucleation cores into the PLA matrix. Thus, we may expect that after the complete degradation of the PLA matrix, the mineral-doped scaffolds would result in a fully-constituted apatite porous body.

Differently, pure PLA scaffolds showed no ions release, poor apatite formation, a wide range of pores (from a minimum of 10 μm to a maximum of 200 μm), and an approx 30% degradation after 28 days (Fig. 5a) (similar degradation time reported in literature [35]).

Our study confirms that the morphology and the structure of the experimental mineral-doped scaffolds during ageing in body fluids is a dynamic combination of PLA degradation and concurrent bioactive ion release and apatite formation, as observed in previous studies [97–99]. These concurrent events may contribute to drive the integration of the scaffold into the bone defect and likely support/favour bone regeneration. This study does not report comparative information with benchmark reference materials, since similar kind of scaffolds are not commercially available at present. In vivo tests have been scheduled and results will be published in a forthcoming paper.

5. Conclusions

Key findings of this article may summarized as follows:

- TIPS fabrication technique allowed to produce highly porous (i.e. > 90%) scaffolds;
- PLA found to be a proper matrix for the production of mineral doped scaffolds which slowly degrades and allows the precipitation of CaP on its structure;
- The incorporation of reactive CaSi and DCPD mineral powders overcomes PLA disadvantages (hydrophobicity, release of acid degradation products and reduced cell adhesion and growth) and allows to create biointeractive (Ca^{++} and OH^- ion release), bioactive (apatite forming) and biocompatible scaffolds.

These properties suggest the potential role of the designed scaffolds in mineralizing cells activation and make them attractive materials for bone regeneration.

Appendix A. Supplementary data

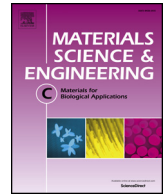
Supplementary data to this article can be found online at <http://dx.doi.org/10.1016/j.msec.2017.08.040>.

References

- [1] Bone grafting materials for dental applications: a practical guide, *Compend. Contin. Educ. Dent.* 18 (1997) 1013–1018.
- [2] S.N. Papageorgiou, P.N. Papageorgiou, J. Deschner, W. Götz, Comparative effectiveness of natural and synthetic bone grafts in oral and maxillofacial surgery prior to insertion of dental implants: systematic review and network meta-analysis of parallel and cluster randomized controlled trials, *J. Dent.* 48 (2016) 1–8.
- [3] T. Traini, A. Piattelli, S. Caputi, M. Degidi, C. Mangano, A. Scarano, V. Perrotti, G. Iezzi, Regeneration of human bone using different bone substitute biomaterials, *Clin. Implant. Dent. Relat. Res.* 17 (2015) 150–162.
- [4] X.J. Loh, D. Kai, Special issue: biomedical applications editorial, *Mater. Sci. Eng. C* 70 (2017) 933–934.
- [5] Z. Li, E. Ye, Lakshminarayanan R. David, X.J. Loh, Recent advances of using hybrid nanocarriers in remotely controlled therapeutic delivery, *Small* 12 (2016) 4782–4806.
- [6] X.J. Loh, T. Lee, Q. Dou, G.R. Deen, Utilising inorganic nanocarriers for gene delivery, *Biomater. Sci.* 4 (2016) 70–86.
- [7] C. Zheng, H. Gao, D. Yang, M. Liu, H. Cheng, Y. Wu, et al., PCL-based thermogelling polymers for in vivo delivery of chemotherapeutics to tumors, *Mater. Sci. Eng. C* 74 (2017) 110–116.
- [8] S.S. Liow, Q. Dou, D. Kai, Z. Li, S. Sugianto, C.Y.Y. Yu, R.T.K. Kwok, X. Chen, Y.-L. Wu, S.T. Ong, A. Kizhakeyil, N.K. Verma, B.Z. Tang, X.J. Loh, Long-term real-time in vivo drug release monitoring with AIE thermogelling polymer, *Small* 13 (2017) 1603404.
- [9] H.C. Guo, E. Ye, Z. Li, M.Y. Han, X.J. Loh, Recent progress of atomic layer deposition on polymeric materials, *Mater Sci Eng C Mater Biol Appl* 70 (2017) 1182–1191.
- [10] I. Armentano, M. Dottori, E. Fortunati, S. Mattioli, J.M. Kenny, Biodegradable polymer matrix nanocomposites for tissue engineering: a review, *Polym. Degrad. Stab.* 95 (2010) 2126–2146.
- [11] D.P. Forrester, T.J. Klein, M.A. Woodruff, Challenges in engineering large customized bone constructs, *Biotechnol. Bioeng.* 114 (2016) 1129–1139.
- [12] C. Mangano, F. Paino, R. d'Aquino, A. de Rosa, G. Iezzi, A. Piattelli, L. Laino, T. Mitsiadis, V. Desiderio, F. Mangano, G. Papaccio, V. Tirino, Human dental pulp stem cells hook into bioceramic scaffold forming an engineered biocomplex, *PLoS One* 6 (2011) e18721.
- [13] R.Z. LeGeros, S. Lin, R. Rohanizadeh, D. Mijares, J.P. LeGeros, Biphasic calcium phosphate bioceramics: preparation, properties and applications, *J. Mater. Sci.* 14 (2003) 201–209.
- [14] I. Yip, L. Ma, N. Mattheos, M. Dard, N.P. Lang, Defect healing with various bone substitutes, *Clin. Oral Implants Res.* 26 (2015) 606–614.
- [15] V.L. Zizzari, S. Zara, G. Tetè, R. Vinci, E. Gherlone, A. Cataldi, Biologic and clinical aspects of integration of different bone substitutes in oral surgery: a literature review, *Oral Surg. Oral Med. Oral Pathol. Oral Radiol.* 122 (2016) 392–402.
- [16] C. Prati, M.G. Gandolfi, Calcium silicate bioactive cements: biological perspectives and clinical applications, *Dent. Mater.* 31 (2015) 351–370.
- [17] M.G. Gandolfi, P. Taddei, E. Modena, F. Siboni, C. Prati, Biointeractivity-related versus chemi/physorption-related apatite precursor-forming ability of current root end filling materials, *J. Biomed. Mater. Res. Part B Appl. Biomater.* 101 (2013) 1107–1123.
- [18] Y. Suzuki, M. Hayashi, N. Tanabe, T. Yasukawa, Y. Hirano, S.C. Takagi, L. Chow, N. Suzuki, B. Ogiso, Effect of a novel fluorapatite-forming calcium phosphate cement with calcium silicate on osteoblasts in comparison with mineral trioxide aggregate, *J. Oral Sci.* 57 (2015) 25–30.
- [19] M.G. Gandolfi, G. Iezzi, A. Piattelli, C. Prati, A. Scarano, Osteoinductive potential and bone-bonding ability of ProRoot MTA, MTA plus and biodentine in rabbit intramedullary model: microchemical characterization and histological analysis, *Dent. Mater.* 33 (2017) e221–e238.
- [20] M.G. Gandolfi, S.N. Shah, R. Feng, C. Prati, S.O. Akintoye, Biomimetic calcium-silicate cements support differentiation of human orofacial mesenchymal stem cells, *J. Endod.* 37 (2011) 1102–1108.
- [21] S.S. Hakki, B.S. Bozkurt, B. Ozcopur, M.G. Gandolfi, C. Prati, S. Belli, The response of cementoblasts to calcium phosphate resin-based and calcium silicate-based commercial sealers, *Int. Endod. J.* 46 (2013) 242–252.
- [22] M.G. Gandolfi, F. Siboni, T. Botero, M. Bossù, F. Riccitello, C. Prati, Calcium silicate and calcium hydroxide materials for pulp capping: biointeractivity, porosity, solubility and bioactivity of current formulations, *J. Appl. Biomater. Funct. Mater.* 13 (2015) 43–60.
- [23] M.G. Gandolfi, P. Taddei, A. Tinti, C. Prati, Apatite-forming ability (bioactivity) of ProRoot MTA, *Int. Endod. J.* 43 (2010) 917–929.
- [24] P. Taddei, A. Tinti, M.G. Gandolfi, P.L. Rossi, C. Prati, Ageing of calcium silicate cements for endodontic use in simulated body fluids: a micro-Raman study, *J. Raman Spectrosc.* 40 (2009) 1858–1866.
- [25] M. Torabinejad, N. Chiaviani, Clinical application of mineral trioxide aggregate, *J. Endod.* 25 (1993) 197–205.
- [26] E. Tahan, D. Celik, K. Er, T. Taşdemir, Effect of unintentionally extruded mineral trioxide aggregate in treatment of tooth with periradicular lesion: a case report, *J. Endod.* 36 (2010) 760–763.
- [27] M.K. Çalıřkan, U. Tekin, M.E. Kaval, M.C. Solmaz, The outcome of apical microsurgery using MTA as the root-end filling material: 2- to 6-year follow-up study, *Int. Endod. J.* 49 (2016) 245–254.
- [28] T. von Arx, Mineral trioxide aggregate (MTA) a success story in apical surgery, *Swiss Dent. J.* 126 (2016) 573–595.
- [29] M.G. Gandolfi, P. Taddei, A. Tinti, Dorigo E. De Stefano, C. Prati, Alpha-TCP improves the apatite-formation ability of calcium-silicate hydraulic cement soaked in phosphate solutions, *Mater. Sci. Eng. C* 31 (2011) 1412–1422.
- [30] M.G. Gandolfi, G. Spagnuolo, F. Siboni, A. Procino, V. Rivieccio, G.A. Pelliccioni, C. Prati, S. Rengo, Calcium silicate/calcium phosphate biphasic cements for vital pulp therapy: chemical-physical properties and human pulp cells response, *Clin Oral Investig* 19 (2015) 2075–2089.
- [31] D. Correa, A. Almirall, R.G. Carrodegua, L.A. dos Santos, A.H. De Aza, J. Parra, L. Morejón, J.A. Delgado, α -Tricalcium phosphate cements modified with β -dicalcium silicate and tricalcium aluminate: physicochemical characterization, in vitro bioactivity and cytotoxicity, *J. Biomed. Mater. Res. Part B* 103 (2015) 72–83.
- [32] S. Tajbaksh, F. Hajiali, A comprehensive study on the fabrication and properties of biocomposites of poly(lactic acid)/ceramics for bone tissue engineering, *Mater. Sci. Eng. C* 70 (2017) 897–912.
- [33] P. Fabbri, V. Cannillo, A. Sola, A. Dorigato, F. Chiellini, Highly porous polycaprolactone-45S5 Bioglass® scaffolds for bone tissue engineering, *Compos. Sci. Technol.* 70 (2010) 1869–1878.

- [34] A. Asti, L. Gioglio, Natural and synthetic biodegradable polymers: different scaffolds for cell expansion and tissue formation, *Inst. J. Artif. Organs*. 37 (2014) 187–205.
- [35] Z. Sheikh, S. Najeib, Z. Khurshid, V. Verma, H. Rashid, M. Glogauer, Biodegradable materials for bone repair and tissue engineering applications, *Materials* 8 (2015) 5744–5794.
- [36] M.A. Woodruff, D.W. Hutmacher, The return of a forgotten polymer—polycaprolactone in the 21st century, *Prog. Polym. Sci.* 35 (2010) 1217–1256.
- [37] F. Asa'ad, G. Pagni, S.P. Pilipchuk, A.B. Gianni, W.V. Giannobile, G. Rasperini, 3D-printed scaffolds and biomaterials: review of alveolar bone augmentation and periodontal regeneration applications, *Int. J. Dent.* 2016 (2016) 1239842, <http://dx.doi.org/10.1155/2016/1239842>.
- [38] R.A. Auras, B. Harte, S. Selke, R. Hernandez, Mechanical, physical, and barrier properties of poly(lactide) films, *Journal of Plastic Film & Sheeting* 19 (2003) 123–135.
- [39] B. Tyler, D. Gullotti, A. Mangraviti, T. Utsuki, H. Brem, Poly(lactide) (PLA) controlled delivery carriers for biomedical applications, *Adv. Drug Deliv. Rev.* 107 (2016) 163–175.
- [40] C.X. Lam, D.W. Hutmacher, J.T. Schantz, M.A. Woodruff, S.H. Teoh, Evaluation of polycaprolactone scaffold degradation for 6 months in vitro and in vivo, *J. Biomed. Mater. Res.* A 90 (2009) 906–919.
- [41] S. Haimi, N. Suuriniemi, A.M. Haaparanta, V. Ellä, B. Lindroos, H. Huhtala, S. Rätty, H. Kuokkanen, G.K. Sándor, M. Kellomäki, S. Miettinen, R. Suuronen, Growth and osteogenic differentiation of adipose stem cells on PLA/bioactive glass and PLA/ β -TCP scaffolds, *Tissue Eng. Part A* 15 (2009) 1473–1480.
- [42] L. Siqueira, F.R. Passador, M.M. Costa, A.O. Lobo, E. Sousa, Influence of the addition of β -TCP on the morphology, thermal properties and cell viability of poly(lactide) fibers obtained by electrospinning, *Mater Sci Eng C Mater Biol Appl* 52 (2015) 135–143.
- [43] J. Huang, J. Xiong, J. Liu, W. Zhu, J. Chen, L. Duan, J. Zhang, D. Wang, Evaluation of the novel three-dimensional porous poly(L-lactide acid)/nano-hydroxyapatite composite scaffold, *Biomed. Mater. Eng.* 26 (Suppl. 1) (2015) S197–205.
- [44] K.R. Reddy, K. Lee, A.I. Gopalan, A.M. Showkat, Facile synthesis of hollow spheres of sulfonated polyanilines, *Polym. J.* 38 (2006) 349–354.
- [45] M.U. Khan, K.R. Reddy, T. Ngunwongchai, E. Haque, V.G. Gomes, Polymer brush synthesis on surface modified carbon nanotubes via in situ emulsion polymerization, *Colloid Polym. Sci.* 294 (2016) 1599–1610.
- [46] K.R. Reddy, K. Lee, A.I. Gopalan, H. Kang, Organosilane modified magnetite nanoparticles/poly(aniline-co-o/m-aminobenzenesulfonic acid) composites: synthesis and characterization, *React. Funct. Polym.* 67 (2007) 943–954.
- [47] P. Taddei, A. Tinti, G. Fini, Vibrational spectroscopy of polymeric biomaterials, *J. Raman Spectrosc.* 32 (2001) 619–629.
- [48] P. Taddei, P. Monti, R. Simoni, Vibrational and thermal study on the in vitro and in vivo degradation of a poly(lactide acid)-based bioabsorbable periodontal membrane, *J. Mater. Sci. Mater. Med.* 13 (2002) 469–475.
- [49] V. Guarino, F. Causa, P. Taddei, M. Di Foggia, C. Ciapetti, D. Martini, C. Fagnano, N. Baldini, L. Ambrosio, Poly(lactide acid) fibre reinforced polycaprolactone scaffolds for bone tissue engineering, *Biomaterials* 29 (2008) 3662–3670.
- [50] M.A. Castilla Bolaños, J. Buttigieg, J.C. Briceño Triana, Development and characterization of a novel porous small intestine submucosa-hydroxyapatite scaffold for bone regeneration, *Mater. Sci. Eng. C* 72 (2017) 519–525.
- [51] P. Taddei, S. Tozzi, G. Zuccheri, S. Martinotti, E. Ranzato, V. Chiono, L. Carmagnola, M. Tsukada, Intermolecular interactions between *B. mori* silk fibroin and poly(L-lactide acid) in electrospun composite nanofibrous scaffolds, *Mater Sci Eng C Mater Biol Appl* 70 (2017) 777–787.
- [52] G. Kister, G. Cassanas, M. Vert, B. Pauvert, A. Téral, Vibrational analysis of poly(L-lactide acid), *J. Raman Spectrosc.* 26 (1995) 307–311.
- [53] G. Kister, G. Cassanas, M. Vert, Effects of morphology, conformation and configuration on the IR and Raman spectra of various poly(lactide acids), *Polymer* 39 (1998) 267–273.
- [54] J. Zhang, H. Tsuji, I. Noda, Y. Ozaki, Weak intermolecular interactions during the melt crystallization of poly(L-lactide) investigated by two-dimensional infrared correlation spectroscopy, *J. Phys. Chem. B* 108 (2004) 11514–11520.
- [55] D.G. Nelson, J.D. Featherstone, Preparation, analysis, and characterization of carbonated apatites, *Calcif. Tissue Int.* 34 (1982) S69–81.
- [56] M. Conjeaud, H. Boyer, Some possibilities of Raman microprobe in cement chemistry, *Cem. Concr. Res.* 10 (1980) 61–70.
- [57] L.P. Sarma, P.S.R. Prasad, N. Ravikumar, Raman spectroscopic study of phase transitions in natural gypsum, *J. Raman Spectrosc.* 29 (1998) 851–856.
- [58] S. Martínez-Ramírez, S. Sánchez-Cortés, J.V. García Ramos, C. Domingo, C. Fortes, M.T. Blanco-Varela, Micro-Raman spectroscopy applied to depth profiles of carbonates formed in lime mortar, *Cem. Concr. Res.* 33 (2003) 2063–2068.
- [59] P. Taddei, E. Modena, A. Tinti, F. Siboni, C. Prati, M.G. Gandolfi, Vibrational investigation of calcium silicate cements for endodontics in simulated body fluids, *J. Mol. Struct.* 993 (2011) 367–375.
- [60] I. Lecompte, C. Henrist, M. Liegeois, A. Rulmont, R. Cloots, (Micro)-structural comparison between geopolymers, alkali-activated slag cement and Portland cement, *J. Eur. Ceram. Soc.* 26 (2006) 3789–3797.
- [61] T.L. Hughes, C.M. Methven, T.G.J. Jones, S.E. Pelham, P. Fletcher, C. Hall, Determining cement composition by Fourier transform infrared spectroscopy, *Adv. Cem. Based Mater.* 2 (1995) 91–104.
- [62] M.I. Domínguez, J. Carpena, D. Borschnek, M.A. Centeno, J.A. Odriozola, J. Rose, Apatite and Portland/apatite composite cements obtained using a hydrothermal method for retaining heavy metals, *J. Hazard. Mater.* 150 (2008) 99–108.
- [63] M.D. Lane, Mid-infrared emission spectroscopy of sulfate and sulfate-bearing minerals, *Am. Mineral.* 92 (2007) 1–18.
- [64] F.A. Andersen, L. Brecevic, Infrared spectra of amorphous and crystalline calcium carbonate, *Acta Chem. Scand.* 45 (1991) 1018–1024.
- [65] M.Y.A. Mollah, W. Yu, R. Schennach, D.L. Cocke, A Fourier transform infrared spectroscopic investigation of the early hydration of Portland cement and the influence of sodium lignosulfonate, *Cem. Concr. Res.* 30 (2000) 267–273.
- [66] R.L. Frost, Y. Xi, R.E. Pogson, G.J. Millar, K. Tan, S.J. Palmer, Raman spectroscopy of synthetic $\text{CaHPO}_4 \cdot 2\text{H}_2\text{O}$ and in comparison with the cave mineral brushite, *J. Raman Spectrosc.* 43 (2012) 571–576.
- [67] J. Xu, I.S. Butler, D.F.R. Gilson, FT-Raman and high-pressure infrared spectroscopic studies of dicalcium phosphate dihydrate ($\text{CaHPO}_4 \cdot 2\text{H}_2\text{O}$) and anhydrous dicalcium phosphate (CaHPO_4), *Spectrochim. Acta Part A* 55 (1999) 2801–2809.
- [68] F. Rashid, H. Shiba, N. Mizuno, et al., The effect of extracellular calcium ion on gene expression of bone-related proteins in human pulp cells, *J. Endod.* 29 (2003) 104–107.
- [69] S. Ma, Y. Yang, D.L. Carnes, K. Kim, S.H. Park, S.H. Oh, J.L. Ong, Effects of dissolved calcium and phosphorus on osteoblast responses, *J. Oral Implantol.* 31 (2005) 61–67.
- [70] J. Sun, L. Wei, X. Liu, J. Li, B. Li, G. Wang, F. Meng, Influences of ionic dissolution products of dicalcium silicate coating on osteoblastic proliferation, differentiation and gene expression, *Acta Biomater.* 5 (2009) 1284–1293.
- [71] S.M. Moe, Calcium homeostasis in health and in kidney disease, *Compr. Physiol.* 15 (6) (2016) 1781–1800.
- [72] D.H. Kohn, M. Sarmadi, J.I. Helman, P.H. Krebsbach, Effects of pH on human bone marrow stromal cells in vitro: implications for tissue engineering of bone, *J. Biomed. Mater. Res.* 60 (2002) 292–299.
- [73] F.H. Moghadam, T. Tayebi, M. Dehghan, G. Esлами, H. Nadri, A. Moradi, H. Vahedian-Ardakani, K. Barzegar, Differentiation of bone marrow mesenchymal stem cells into chondrocytes after short term culture in alkaline medium, *Int. J. Hematol. Oncol. Stem Cell Res.* 8 (2014) 12–19.
- [74] K.K. Kaysinger, W.K. Ramp, Extracellular pH modulates the activity of cultured human osteoblasts, *J. Cell. Biochem.* 68 (1998) 83–89.
- [75] T.R. Arnett, Extracellular pH regulates bone cell function, *J. Nutr.* 138 (2008) 415–418.
- [76] J. Camps, C. Jeanneau, I.E. Ayachi, P. Laurent, I. About, Bioactivity of a calcium silicate-based endodontic cement (BioRoot RCS): interactions with human periodontal ligament cells in vitro, *J. Endod.* 41 (2015) 1469–1473.
- [77] L. Graham, P.R. Cooper, N. Cassidy, J.E. Nor, A.J. Sloan, A.J. Smith, The effect of calcium hydroxide on solubilization of bio-active dentine matrix components, *Biomaterials* 27 (2006) 2865–2873.
- [78] C. Liu, Y. Huang, W. Shen, J. Cui, Kinetics of hydroxyapatite precipitation at pH 10 to 11, *Biomaterials* 22 (2001) 301–306.
- [79] H.R. Le, K.Y. Chen, C.A. Wang, Effect of pH and temperature on the morphology and phases of co-precipitated hydroxyapatite, *J. Sol-Gel Sci. Technol.* 61 (2012) 592–599.
- [80] M.Y. Shie, S.J. Ding, H.C. Chang, The role of silicon in osteoblast-like cell proliferation and apoptosis, *Acta Biomater.* 7 (2011) 2604–2614.
- [81] S. Wang, X. Wang, F.G. Draenert, O. Albert, H.C. Schröder, V. Mailänder, G. Mitrov, W.E. Müller, Bioactive and biodegradable silica biomaterial for bone regeneration, *Bone* 67 (2014) 292–304.
- [82] W. Zhai, H. Lu, L. Chen, X. Lin, Y. Huang, K. Dai, K. Naoki, G. Chen, J. Chang, Silicate bioceramics induce angiogenesis during bone regeneration, *Acta Biomater.* 8 (2012) 341–349.
- [83] M.G. Gandolfi, P. Taddei, F. Siboni, E. Modena, G. Ciapetti, C. Prati, Development of the foremost light-curable calcium-silicate cement as root-end in oral surgery. Chemical-physical properties, bioactivity and biological behaviour, *Dent. Mater.* 27 (2011) e134–e157.
- [84] M.G. Gandolfi, G. Ciapetti, P. Taddei, F. Perut, A. Tinti, M.V. Cardoso, B. Van Meerbeek, C. Prati, Apatite formation on bioactive calcium-silicate cements for dentistry affects surface topography and human marrow stromal cells proliferation, *Dent. Mater.* 26 (2010) 974–992.
- [85] P. Velasquez, Z.B. Luklinska, L. Meseguer-Olmo, J.E. Mate-Sanchez de Val, R.A. Delgado-Ruiz, J.L. Calvo-Guirado, M.P. Ramirez-Fernandez, P.N. de Aza, α TCPC ceramic doped with dicalcium silicate for bone regeneration applications prepared by powder metallurgy method: in vitro and in vivo studies, *J. Biomed. Mater. Res. A* 101 (2013) 1943–1954.
- [86] A.A. Zadpoor, Relationship between in vitro apatite-forming ability measured using simulated body fluid and in vivo bioactivity of biomaterials, *Mater Sci Eng C Mater Biol Appl* 35 (2014) 134–143.
- [87] J.Y. Bae, J.E. Won, J.S. Park, H.H. Lee, H.W. Kim, Improvement of surface bioactivity of poly(lactide acid) biopolymer by sandblasting with hydroxyapatite bioceramic, *Mater. Lett.* 65 (2011) 2951–2955.
- [88] S.A. Oh, J.E. Won, H.W. Kim, Composite membranes of poly(lactide acid) with zinc-added bioactive glass as a guiding matrix for osteogenic differentiation of bone marrow mesenchymal stem cells, *J. Biomater. Appl.* 27 (2012) 413–422.
- [89] R. Zhicheng, W. Zeng, Y. Kuang, J. Zhang, X. Liu, Y. Lu, X. Cheng, Enhanced bioactivity of osteoblast-like cells on poly(lactide acid)/poly(methyl methacrylate)/nano-hydroxyapatite scaffolds for bone tissue engineering, *Fibers and Polymers* 16 (2015) 245–253.
- [90] C.B. Danoux, D. Barbieri, H. Yuan, J.D. Bruijn, C.A. van Blitterswijk, P. Habibovic, In vitro and in vivo bioactivity assessment of a poly(lactide acid)/hydroxyapatite composite for bone regeneration, *Biomaterials* 4 (2014) e27664.
- [91] H. Shi, Q. Gan, L. Liu, Y. Ma, J. Hu, Y. Yuan, C. Liu, Poly(glycerol sebacate)-modified poly(lactide acid) scaffolds with improved hydrophilicity, mechanical strength and bioactivity for bone tissue regeneration, *RSC Adv.* 5 (2015) 79703–79714.

- [92] D. Cam, S.H. Hyon, Y. Ikada, Degradation of high molecular weight poly(L-lactide) in alkaline medium, *Biomaterials* 16 (1995) 833–843.
- [93] R. Langer, J. Kahn, B.D. Ratner, A.S. Hoffmann, F.J. Schoen, J.E. Lemons (Eds.), *Biomaterials Science. An Introduction to Materials in Medicine*, Academic Press, San Diego, 1996, p. 64.
- [94] M. Vert, S.M. Li, G. Splenlehauer, P. Guerin, Bioresorbability and biocompatibility of aliphatic polyesters, *J. Mater. Sci. Mater. Med.* 3 (1992) 432–446.
- [95] G. Cassanas, G. Kister, E. Fabrègue, M. Morssli, L. Bardet, Raman spectra of glycolic acid, L-lactic acid and D,L-lactic acid oligomers, *Spectrochim. Acta* 49A (1993) 271–279.
- [96] R.A. Perez, G. Mestres, Role of pore size and morphology in musculo-skeletal tissue regeneration, *Mater. Sci. Eng. C* 61 (2016) 922–939.
- [97] P. Taddei, A. Tinti, M. Reggiani, C. Fagnano, In vitro mineralization of bioresorbable poly(ϵ -caprolactone)/apatite composites for bone tissue engineering: a vibrational and thermal investigation, *J. Mol. Struct.* 744-747 (2005) 135–143.
- [98] P. Taddei, M. Di Foggia, F. Causa, L. Ambrosio, C. Fagnano, In vitro bioactivity of poly(ϵ -caprolactone)-apatite (PCL-AP) scaffolds for bone tissue engineering: the influence of the PCL/AP ratio, *Int. J. Artif. Org.* 29 (2006) 719–725.
- [99] V. Guarino, P. Taddei, M. Di Foggia, C. Fagnano, G. Ciapetti, L. Ambrosio, The influence of hydroxyapatite particles on “in vitro” degradation behavior of PCL based composite scaffolds, *Tissue Eng. Part A* 15 (2009) 3655–3668.



Highly porous polycaprolactone scaffolds doped with calcium silicate and dicalcium phosphate dihydrate designed for bone regeneration

Maria Giovanna Gandolfi^{a,*}, Fausto Zamparini^{a,b}, Micaela Degli Esposti^c, Federica Chiellini^d, Fabio Fava^c, Paola Fabbri^c, Paola Taddei^e, Carlo Prati^b

^a Laboratory of Biomaterials and Oral Pathology, School of Dentistry, Department of Biomedical and Neuromotor Sciences, University of Bologna, Bologna, Italy

^b Endodontic Clinical Section, School of Dentistry, Department of Biomedical and Neuromotor Sciences, University of Bologna, Bologna, Italy

^c Department of Civil, Chemical, Environmental and Materials Engineering, University of Bologna, Bologna, Italy

^d BIOLab Research Group, Department of Chemistry and Industrial Chemistry, University of Pisa, Pisa, Italy

^e Biochemistry Unit, Department of Biomedical and Neuromotor Sciences, University of Bologna, Bologna, Italy

ARTICLE INFO

Keywords:

Porous scaffold
Polycaprolactone
Calcium silicate
Calcium phosphate
Bone regeneration
Thermally induced phase separation

ABSTRACT

Polycaprolactone (PCL), dicalcium phosphate dihydrate (DCPD) and/or calcium silicates (CaSi) have been used to prepare highly porous scaffolds by thermally induced phase separation technique (TIPS). Three experimental mineral-doped formulations were prepared (PCL-10CaSi, PCL-5CaSi-5DCPD, PCL-10CaSi-10DCPD); pure PCL scaffolds constituted the control group.

Scaffolds were tested for their chemical-physical and biological properties, namely thermal properties by differential scanning calorimetry (DSC), mechanical properties by quasi-static parallel-plates compression testing, porosity by a standard water-absorption method calcium release, alkalizing activity, surface micro-chemistry and micromorphology by Environmental Scanning electronic Microscopy (ESEM), apatite-forming ability in Hank Balanced Saline Solution (HBSS) by Energy Dispersive X-ray Spectroscopy (EDX) and micro-Raman, and direct contact cytotoxicity.

All mineral-doped scaffolds released calcium and alkalized the soaking medium, which may favor a good biological (osteogenic) response.

ESEM surface micromorphology analyses after soaking in HBSS revealed: pure PCL, PCL-10CaSi and PCL-10CaSi-10DCPD kept similar surface porosity percentages but different pore shape modifications. PCL-5CaSi-5DCPD revealed a significant surface porosity increase despite calcium phosphates nucleation ($p < 0.05$).

Micro-Raman spectroscopy detected the formation of a B-type carbonated apatite (Ap) layer on the surface of PCL-10CaSi-10DCPD aged for 28 days in HBSS; a similar phase (but of lower thickness) formed also on PCL-5CaSi-5DCPD and PCL; the deposit formed on PCL-10CaSi was mainly composed of calcite.

All PCL showed bulk open porosity higher than 94%; however, no relevant brittleness was observed in the materials, which retained the possibility to be handled without collapsing.

The thermo-mechanical properties showed that the reinforcing and nucleating action of the inorganic fillers CaSi and DCPD improved viscoelastic properties of the scaffolds, as confirmed by the increased value of storage modulus and the slight increase in the crystallization temperature for all the biomaterials.

A detrimental effect on the mechanical properties was observed in samples with the highest amount of inorganic particles (PCL-10CaSi-10DCPD).

All the scaffolds showed absence of toxicity, in particular PCL-10CaSi-10DCPD.

The designed scaffolds are biointeractive (release biologically relevant ions), nucleate apatite, possess high surface and internal open porosity and can be colonized by cells, creating a bone forming osteoblastic micro-environment and appearing interesting materials for bone regeneration purposes.

* Corresponding author at: Laboratory of Biomaterials and Oral Pathology, Dental School, University of Bologna, Via San Vitale 59, 40125 Bologna, Italy.
E-mail address: mgiovanna.gandolfi@unibo.it (M.G. Gandolfi).

<https://doi.org/10.1016/j.msec.2019.04.040>

Received 28 May 2018; Received in revised form 31 January 2019; Accepted 12 April 2019

Available online 17 April 2019

0928-4931/© 2019 Published by Elsevier B.V.

1. Introduction

Trauma, tumor resection, infections and disease frequently result in critical sized bone defects (unable to heal spontaneously) or fractures in cranio-maxillo-facial, oral and orthopaedic districts [1]. Management of these worldwide diseases necessitates predictable bone grafting or major surgical reconstruction.

Gold standard autologous bone graft for oral and maxillofacial surgery has not a predictable outcome, particularly when the host possesses a compromised immune response and lowered/decreased bone healing [2]. Furthermore, autologous bone graft does not ensure a predictable regenerating bone volume and requires further autograft bone harvesting with additional co-morbidities and higher costs [2].

A great number of materials currently marketed as bone substitutes are not bioactive, not osteoinductive and with high risks for bacterial suprainfections. There is an increasing trend to utilize non-metallic materials such as polymers, ceramics and composites rather than metals [3].

The use of biocompatible slow-resorbing porous scaffolds where stem cells can migrate, grow and differentiate into bone mineralizing cells, represent an interesting approach for tissue engineering.

Polycaprolactone (PCL) is a semicrystalline linear aliphatic polyester widely used for biomedical application, such as orthopaedic screws, drug delivery devices [4] and scaffolds for bone tissue engineering [5]. PCL may be obtained by either ring opening polymerization of ϵ -caprolactone using a variety of anionic, cationic and coordination catalysts or via free radical ring-opening polymerization of 2-methylene-1,3-dioxepane [6]. Re-emergence of this polymer in the biomedical field is related to the good processability, compatibility with different polymers, broad molecular weight range, solubility in common organic solvents and the possibility to tailor its mechanical properties [7]. Moreover its long bioresorption time (2 years) may be useful in tissue engineering procedures [8]. On the other hand, PCL suffers from drawbacks due to its intrinsic hydrophobic chemical nature, its poor surface wettability and interaction with biological fluids, limiting/hampering cells adhesion and proliferation [6]. To overcome its drawbacks, PCL composites were produced by adding inorganic phases, such as hydroxyapatite [9,10].

Biointeractivity with the local environment - i.e. capability to exchange of information between a biological system and capability of sending and/or receiving information from a living organism [11] - is another interesting requisite for a scaffold providing biological advantages.

Hydraulic Calcium Silicate Cements (HCSC) are attractive materials for their release of biologically relevant ions (biointeractivity) [12], antibacterial activity and capability to nucleate apatite (bioactivity) [13] and support the growth and differentiation of human orofacial mesenchymal stem cells [14], human marrow stromal cells [15] and pulp cells [16]. These properties justified their wide application in dentistry as materials to be placed in close vicinity to pulp or bone tissue [13,17]. Nowadays, HCSC are used in several dental applications: in endodontics as root canal sealers [18], as root-end filling materials [19], for direct pulp capping [16] and as mineral filler in scaffolds for bone regeneration [20]. The incorporation of **Calcium phosphates**, such as dicalcium phosphate dihydrate (DCPD) further improves apatite-forming ability of HCSC, as previously demonstrated [21].

Several techniques have been developed to produce scaffolds for tissue engineering, including electrospinning technique [5], 3D printing [22], salt leaching [23] and thermally induced phase separation (TIPS) [20,24]. TIPS procedure allows the preparation of highly porous (> 90%) scaffolds without the need of high temperatures that may alter the properties of the polymer matrix or those of the mineral filler [20].

Porosity is a key factor to be considered when approaching tissue regeneration. Numerous attempts to produce highly porous scaffolds by several techniques and different materials are reported in literature. Poly(lactic)-based scaffolds enriched with 20% beta tricalcium

phosphates produced by salt leaching technique reaching a porosity of 87%, were tested for cranial defects in rabbits showing optimal bone ingrowth [25]. Composite sponges made of poly(lactic co glycolic), collagen and apatite particulates were produced by sintering, reaching porosity values of 87% [26]. Despite there is no consensus regarding the optimal pore sizes, porosity values and percentage of interconnected pores in literature [27], however high porosity values (over 90%) are beneficial for bone tissue engineering [24–26,28], with the result of higher cell proliferation, enhanced bone ingrowth and osteogenesis processes [27], which is attributable to the greater transport of oxygen and nutrients [29].

Considering the potentiality of TIPS to produce highly porous PCL scaffolds [24] together with the biological properties of HCSC [13–15,17,18] it should be interesting to produce by TIPS highly porous PCL-based scaffolds doped with HCSC with/without DCPD for maxillofacial bone regeneration. To date, no similar scaffolds have been proposed.

Therefore, the aim of this study was to fabricate bioactive biointeractive highly porous PCL-based scaffolds doped with different amounts of HCSC and/or DCPD mineral powders at low temperature by using TIPS technique. The experimental scaffolds were tested for physical-mechanical properties, surface microchemistry and micro-morphology, ion release and alkalizing activity, calcium phosphate nucleation, and direct-contact cytotoxicity.

2. Material and methods

2.1. Materials

Methanol (MeOH), ethanol (EtOH, 99.8%), 1,4-dioxan (DIOX) and chloroform (CHCl₃, HPLC grade) all from Sigma Aldrich (Milan, Italy) were used as received without further purification. Polycaprolactone (PCL, average Mn 45,000 g/mol, Sigma-Aldrich, Milan, Italy) was received in pellet form and purified via dissolution in CHCl₃ (15% wt/vol) and reprecipitation in a large excess of cold MeOH, in order to eliminate residual polymerization catalysts.

Dicalcium phosphate dihydrate (DCPD; CaHPO₄·2H₂O) powder (Sigma-Aldrich, Steinheim, Germany) and/or calcium silicate (CaSi) powders (Aalborg, Denmark), prepared by melt-quenching technique and milling procedures [16], and composed of dicalcium silicate, tricalcium silicate, tricalcium aluminate, and calcium sulfate, were added to PCL.

2.2. Scaffolds preparation by TIPS

The porous polymer scaffolds were prepared by TIPS starting from PCL solutions in DIOX (3.5% wt/vol). CaSi and DCPD were added to the PCL solution in powder form in amounts 5% or 10% by weight with respect to PCL. Homogeneous dispersions were obtained by sonicating the mixtures for 3 h using the ultrasonic processor UP50H (Hielscher, 50 watts, 30 kHz), equipped with the sonotrode MS2 (made of titanium, tip diameter 2 mm). After mixing, solutions were placed inside disposable aluminum dishes of 60 mm in diameter, and cooled at -18°C . After 18 h, the frozen samples were extracted from the holders and fully immersed in EtOH bath precooled at -18°C , where they were kept for 72 h, with solvent refresh every 24 h. At the end of the extraction procedure, the porous scaffolds were taken out of the freezer, immersed in deionized water under ultrasounds treatment for at least 1 h, then completely dried in forced-air circulating oven at 35°C [20,24] (Fig. 1).

Six disks (diameter 60 ± 1 mm, thickness 10 ± 0.1 mm) per composition were prepared, to cover all characterization needs (Fig. 2).

The prepared scaffolds were:

- PCL-10CaSi
- PCL-5CaSi-5DCPD
- PCL-10CaSi-10DCPD

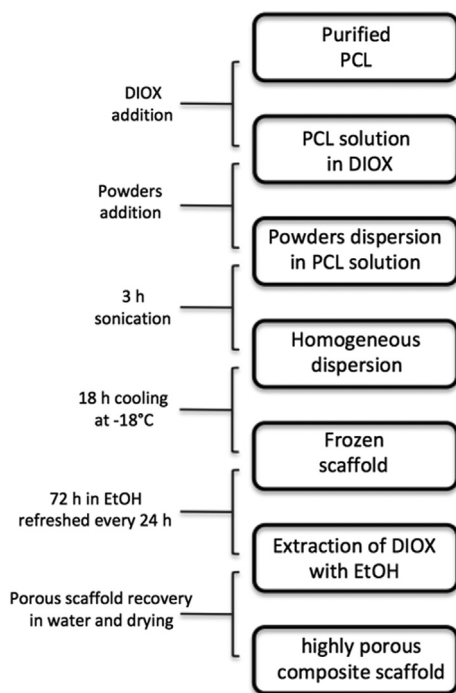


Fig. 1. Time line protocol of Thermally-Induced phase separation (TIPS) technique used in this study.



Fig. 2. PCL mineral-doped scaffold produced by using TIPS.

- PCL (control)

2.3. Bulk open porosity

Bulk open porosity was measured according to the standard procedure UNI EN 1936 “Natural Stone Test Methods - Determination of real density and apparent density, and of total and open porosity”. Briefly, dry and weighted specimens (m_d) were put into an evacuation vessel and the pressure was lowered gradually to 20 mbar. The pressure was maintained for 2 h to eliminate the air contained in the open pores of the specimens. Demineralized water at $20 \pm 5^\circ\text{C}$ was slowly introduced into the vessel and the pressure was maintained at 20 mbar. After approximately 30 min and when all the specimens were completely immersed, the vessel was returned to atmospheric pressure and the specimens were left in water for 24 h at atmospheric pressure. Then, each specimen was weighted in water and the mass in water was recorded as m_h . Each specimen was quickly wiped with a dampened cloth and the mass m_s of the specimen saturated with water was determined.

The open porosity P_o of the scaffold is expressed by the ratio (as a percentage) of the volume of open pores and the apparent volume of the specimen, by the equation $P_o = (m_s - m_d) / (m_s - m_h) \times 100$.

The open porosity was determined in triplicate and expressed as mean \pm standard deviation.

Data collected on porosity were used to calculate an approximate value of the porous composite scaffolds from the equation $P = (1 - \rho_{\text{foam}} / \rho_{\text{matrix}}) \times 100$, assuming PCL density to be 1.14 g cm^{-3} and fillers density to be 2.5 g cm^{-3} .

2.4. Surface porosity, cross-section morphology and internal porous architecture by morphometric analysis on ESEM images

Cross-section morphology and internal porous architecture of the scaffolds before and after 28 days soaking in Hank's balanced salt solution were investigated using an environmental scanning electron microscope Quanta-200 Fei instrument (Oxford Instruments, ESEM) connected to a secondary (SE) or backscattered electron detector (BS), at low vacuum (75 Torr) applying 20 keV. Samples were analyzed without conductive coating.

ESEM images were analyzed through Image J software (National Institutes of Health, Bethesda, USA) to evaluate the scaffolds' surface porosity (%) [20], and to estimate the average pore size. Surface porosity was calculated as the ratio between dark areas (micropores) and the total examined area. Mean values were calculated from measures taken in three different areas of the samples, at magnification ranging from $200\times$ to $1000\times$. Surface porosity among the fresh scaffolds and 28d aged scaffold was analyzed using Two-Way ANOVA followed by RM Student–Newman–Keuls test ($p < 0.05$).

2.5. Dynamic mechanical thermal properties

Glass transition temperature (T_g), elastic modulus (E'), loss modulus (E'') and loss factor ($\tan\delta$) were determined through dynamic mechanical thermal analysis (DMTA) using a Q800 DMA equipment by TA Instruments (Delaware, USA). Cylindrical specimens (diameter $37 \pm 1 \text{ mm}$, thickness $8 \pm 0.1 \text{ mm}$) were tested in compression mode at a constant frequency of 1 Hz, under strain control fixed at 1% while heated from -55 to 40°C at a rate of $3^\circ\text{C}/\text{min}$ under nitrogen gas flow. The specific storage modulus was calculated from the determined E' values divided by porous scaffold density.

Melting and crystallization temperatures and the respective enthalpies of transition (T_m , T_c , ΔH_m , ΔH_c) of the scaffolds were determined by means of a differential scanning calorimeter (DSC, Q10), fitted with a standard DSC cell, and equipped with a Discovery Refrigerated Cooling System (RCS90) (all TA Instruments, Delaware, USA). Samples of about 7 mg were placed into aluminum pans and subjected to two heating cycles from -50°C to $+100^\circ\text{C}$ with cooling and heating rates of $10^\circ\text{C}/\text{min}$. The DSC cell was purged with dry nitrogen at 50 mL/min. The system was calibrated both in temperature and enthalpy with Indium standard.

The real content of inorganic filler (CaSi or CaSi + DCPD) present in the composite scaffolds was determined by thermogravimetric analysis (TGA, Q50, TA Instruments, Delaware, USA), as residual weight after polymer decomposition and complete volatilization. Analyses were performed in triplicate under dry nitrogen flow (60 mL/min), on samples of about 20 mg, placed in platinum pans. Heating was performed from room temperature to $+600^\circ\text{C}$ at a rate of $10^\circ\text{C}/\text{min}$. Results are given as average value calculated over three samples.

All DMTA and DSC data were processed with Thermal Analysis software (TA Instruments, Delaware, USA).

2.6. Calcium release and alkalinizing activity (pH of soaking water)

The samples ($10 \pm 0.1 \text{ mm}$ long \times $10 \pm 0.1 \text{ mm}$ high \times $10 \pm 0.1 \text{ mm}$ thick; $n = 6$ for each composition) were immersed in

10 mL of deionized water inside polypropylene sealed containers and stored at 37 °C. The soaking water was collected and replaced at six time points (3 h and 1, 3, 7, 14 and 28 days). The collected water was analyzed for pH and Ca²⁺ using a potentiometric method under magnetic stirring at room temperature (24 °C).

The pH was measured using a selective temperature-compensated electrode (Sen Tix Sur WTW, Weilheim, Germany) connected to a multi-parameter laboratory meter (inoLab 750 WTW, Weilheim, Germany) previously calibrated with standard solutions.

The amount of calcium ions was measured using a calcium probe (Calcium ion electrode, Eutech instruments Pte Ltd., Singapore) after addition of 0.200 mL (2%) of ionic strength adjuster ISA, 4 mol/L KCl (WTW, Weilheim, Germany).

Calcium release and pH data were analyzed using two-way ANOVA followed by RM Student–Newman–Keuls test ($p < 0.05$). Different letters represent statistically significant differences ($p < 0.05$) in the same line (capital letters) or in the same column (small letters).

2.7. Calcium phosphate nucleation by ESEM-EDX, FT-Raman, micro-Raman and ATR/IR spectroscopy and XRD analysis

The apatite forming ability i.e. formation of a calcium phosphates (CaPs) on the scaffolds surface after soaking in Hank's balanced salt solution (HBSS, Lonza, Verviers, Belgium) was evaluated [16,20]. Each sample was placed in 20 mL of HBSS at 37 °C for 28 days.

The fresh and aged scaffolds were analyzed by ESEM-EDX, FT-Raman, micro-Raman and ATR/IR spectroscopy and by XRD.

An environmental scanning electron microscope (ESEM, Zeiss EVO 50; Carl Zeiss, Oberkochen, Germany) connected to a secondary electron detector for energy dispersive X-ray analysis (EDX; Oxford INCA 350 EDS, Abingdon, UK) using computer-controlled software (Inca Energy Version 18) was used. Specimens were placed directly onto the ESEM stub and examined in wet conditions without any previous preparation (the samples were not coated for this analysis) at low vacuum (100 Pascal). EDX microchemical analysis was carried out at random in areas of $\sim 50 \mu\text{m} \times 50 \mu\text{m}$ to evaluate the relative element content. Elemental microanalysis (weight % and atomic %) with ZAF correction method was performed in full frame to analyze entire areas.

Fourier Transform Raman (FT-Raman) spectroscopy was used to gain insights into the bulk of the samples, while the micro-Raman technique was utilized to analyze their surface.

FT-Raman spectra were recorded on a Bruker MultiRam FT-Raman spectrometer equipped with a cooled Ge-diode detector. The excitation source was a Nd³⁺-YAG laser (1064 nm) in the backscattering (180°) configuration. The focused laser beam diameter was about 100 μm and the spectral resolution 4 cm^{-1} . Laser power at the sample was about 150 mW. Three spectra on each sample were recorded and averaged.

Micro-Raman spectra were obtained using a Jasco NRS-2000C instrument in back-scattering conditions with 4 cm^{-1} spectral resolution, using the 532 nm Green Diode Pumped Solid State (DPSS) Laser Driver (RgBlase LLC, USA) with a power of ca. 20 mW. A 160 K cooled digital CCD (Spec-10: 100B, Roper Scientific Inc.) was used as detector. Microscope objectives with 10 \times and 100 \times magnifications were utilized. The former was used to detect the doping agents in fresh PCL-5CaSi-5DCPD, i.e. the composite sample containing the lowest amount of each of them; in fact, under these conditions, the laser spot size, i.e. the excitation source was about 20 μm and enables to obtain more representative spectra of these intrinsically inhomogeneous samples. The 100 \times magnification (with a laser spot size of about 1 μm) was used to analyze all the other samples. Each reported micro-Raman spectrum is an average of at least five measurements.

The $I_{959(\text{Ap}+\text{PCL})}/I_{1443(\text{PCL})}$ and $I_{959(\text{Ap}+\text{PCL})}/I_{1306(\text{PCL})}$ Raman ratios (where $I_{959(\text{Ap}+\text{PCL})}$, $I_{1443(\text{PCL})}$ and $I_{1306(\text{PCL})}$ were the intensities of the bands at 959, 1443 and 1306 cm^{-1} , respectively) were used to assess the relative thickness of the apatite phase enucleated on the different scaffolds. In fact, the band at 959 cm^{-1} is assignable to apatite [30]

besides PCL [31], while PCL bands at 1443 and 1306 cm^{-1} were used as internal standards, due to their assignments to both amorphous and crystalline phases of the polymer [31] (and thus their intensity does not depend on possible changes in polymer crystallinity induced by ageing). Although these ratios do not represent a measurement of the absolute thickness of the apatite phase, they allow a comparative evaluation between samples. In fact, at increasing apatite thickness, the contribution of the PCL bands to the Raman spectrum of the aged scaffolds progressively decreases, determining a progressive increase in the $I_{959(\text{Ap}+\text{PCL})}/I_{1443(\text{PCL})}$ and $I_{959(\text{Ap}+\text{PCL})}/I_{1306(\text{PCL})}$ Raman ratios.

Raman spectroscopy is a powerful technique for characterizing chain conformation and crystallinity in semicrystalline polymers; in contrast to diffraction methods, it can also test short-range ordering. Several studies have used Raman spectroscopy to quantitatively determine PCL crystallinity [32–36].

In agreement with previous investigations [35,37–40] the PCL crystallinity was relatively evaluated through the Raman $I_{1419(\text{PCL C})}/I_{1443(\text{PCL C+A})}$ and $I_{1285(\text{PCL C})}/I_{1306(\text{PCL C+A})}$ intensity ratios, where $I_{1419(\text{PCL C})}$ and $I_{1285(\text{PCL C})}$ were the intensity of the bands at 1419 and 1285 cm^{-1} , assignable to the crystalline phase [31], while $I_{1443(\text{PCL C+A})}$ and $I_{1306(\text{PCL C+A})}$ were the intensities of the already mentioned internal standard bands at 1443 and 1306 cm^{-1} . All the ratios were calculated as peak heights from the single spectra recorded on each sample. Average values are reported and discussed. Although these ratios do not represent a direct measurement of the PCL crystallinity, they allow one to follow its trend with time. To further support the results obtained through these ratios, the PCL C=O stretching region (1750–1710 cm^{-1}) has been analyzed by band fitting according to previous studies [32–35].

The curve-fitting analysis was performed using the OPUS/IR version 2.0 program, which uses the Levenberg–Marquardt algorithm. After baseline correction, the band fitting procedure allowed to decompose the C=O stretching spectral profile into its three components at about 1736, 1728 and 1724 cm^{-1} , assigned to a random coil PCL chain conformation (“amorphous 1”), an otherwise structureless coil with C=O bonds on neighboring chains oriented antiparallel to each other due to dipole-dipole interactions (“amorphous 2”) and ordered chains packed into the crystal lattice (“crystalline”), respectively [36].

The Raman component profiles were described as a linear combination of Lorentzian and Gaussian functions. The content of each structure was calculated from the area of the individually assigned bands and expressed as fraction of the total area.

X-ray diffraction (XRD) measurements were recorded by a Philips PW1830 diffractometer. The characterizations were performed in air and at room temperature (range 25°–50°2 θ , number of steps 1250, time per step 1 s, scan speed 0.02°2 θ /s and step size of 0.02°2 θ and range 30°–33°2 θ , number of steps 250, time per step 4 s, scan speed 0.005°2 θ /s and step size of 0.02°2 θ). PCL-10CaSi-10DCPD was selected as reference material in order to identify the crystalline phase precipitated on the surface of the scaffold after 28 days of soaking in HBSS.

2.8. Direct-contact cytotoxicity test

2.8.1. Cell culture

Cell viability and proliferation experiments were carried out using the mouse embryo fibroblasts balb/3T3 clone A31 cell line (CCL-163). Cells were purchased from American Type Culture Collection (ATCC) and propagated using Dulbecco's Modified Eagle Medium (DMEM), supplemented with 4 mM of L-glutamine, 1% of penicillin: streptomycin solution (10,000 U/mL: 10 mg/mL), 10% of calf serum and antimycotic (complete DMEM).

The scaffolds were mounted in CellCrownTM24 disposable inserts (Scaffdex, Tampere, Finland), placed in 24-wells plate and sterilized with an Ethanol:H₂O (70:30 v/v) solution for 30 min. Afterwards, samples were extensively washed with Dulbecco's Phosphate Buffer Saline (DPBS) containing 1% penicillin: streptomycin solution and pre-

incubated for additional 3 h with complete DMEM before cell seeding.

2.8.2. Cell viability and proliferation by mitochondrial activity test

Samples were seeded with mouse embryo fibroblast balb/3T3 clone A31 cells (passage 73) by directly adding on to the scaffold surface 500 μL of DMEM containing 1×10^4 cells/per well and incubated at 37 °C in a 5% CO_2 enriched atmosphere.

Cell tests were performed at days 7 and 14 after seeding. Cell proliferation was investigated by mean of WST-1 tetrazolium salt reagent (Roche Applied Science, Indianapolis, IN, USA). Briefly, cells were incubated for 4 h with WST-1 reagent diluted 1:10, at 37 °C and 5% CO_2 . Measurements of formazan dye absorbance were carried out with a microplate reader (Biorad, Milan, Italy) at 450 nm, using 655 nm as reference wavelength. Cells at day 7 of culture cultured on tissue culture polystyrene (TCPS) were used as growth control.

The tests were performed in triplicate on the whole scaffold/cell construct and the data are reported as mean \pm standard deviation. Statistical differences were analyzed using one-way analysis of variance (ANOVA) and a p value < 0.05 was considered significant.

2.8.3. Cell morphological and cytoskeleton organization by Confocal Laser Scanning Microscopy (CLSM)

Cells morphology cultured on the experimental PCL-based scaffolds was investigated by CLSM at day 14 after seeding. Cells were fixed with 3.8% paraformaldehyde for 1 h in Phosphate Buffer Saline 0.01 M (PBS 1 \times) at room temperature and permeabilized with a PBS 1X/Triton X-100 solution (0.2%) for 10 min. After blocking with 1% (w/v) bovine serum albumin (BSA) in PBS 1 \times for 30 min, cells were incubated with phalloidin-Alexa Fluor 488 at room temperature in the dark for 1 h and then with 4'-6-diamidino-2-phenylindole (DAPI) solution for 30 min, to stain cells nuclei and F-Actin. Following each dyeing incubation, samples were extensively washed with PBS 1 \times and finally stored at 4 °C in the dark until observation by confocal laser scanning microscopy was performed. A Nikon Eclipse TE2000 inverted microscope equipped with EZ-C1 confocal laser (Nikon, Japan) with 10 \times and 20 \times objectives was used to analyze the samples. A 405 nm laser diode (405 nm emission) and an Argon ion laser (488 nm emission) were used to excite DAPI and Alexa-Fluor 488 fluorophores, respectively. Images were captured with Nikon EZ-C1 software with identical settings for each sample.

3. Results

3.1. Bulk open porosity, thermal and mechanical properties

TIPS procedure allowed to obtain all samples with bulk open porosity of about 95%; porosity values and weight contents of inorganic fillers as determined through TGA for all the composite scaffolds, are reported in Table 3. PCL melting temperature observed in the second heating scan and crystallization temperature observed during the cooling scan and their respective enthalpies of transition determined by DSC are reported in Table 4, along with the percentage of crystallinity.

TIPS procedure allowed to obtain all samples with bulk open porosity of about 95%; porosity values and weight contents of inorganic fillers as determined through TGA for all the composite scaffolds, are reported in Table 1.

PCL melting temperature observed in the second heating scan and crystallization temperature observed during the cooling scan and their respective enthalpies of transition determined by DSC are reported in Table 2, along with the percentage of crystallinity. The percentage of crystallinity was calculated as shown in the following equation $X_c = [(\Delta H_M) / (\Delta H_{OM} W)] \times 100$, where X_c is percentage of crystallinity, ΔH_M is the enthalpy of melting during the second heating scan, $\Delta H_{OM} = 136 \text{ J/g}$ (melting enthalpy for 100% of crystalline PCL) and W is the weight fraction of PCL in the blends [41].

Table 3 collects dynamic mechanical properties (glass transition temperature-Tg, elastic modulus-E', loss modulus-E'', loss factor-tan δ)

Table 1

Open porosity (%), porous scaffold density (g/cm^{-3}) and filler weight content (wt%) of PCL-based scaffolds (mean \pm SD).

Scaffolds	Open porosity (%)	Filler weight content (wt%)	ρ_{foam} (g cm^{-3})
PCL	94.9 \pm 0.1	–	0.058
PCL-10CaSi	94.9 \pm 0.1	8.6 \pm 1.2	0.065
PCL-5CaSi-5DCPD	94.7 \pm 0.1	8.6 \pm 1.7	0.067
PCL-10CaSi-10DCPD	94.3 \pm 0.1	21.9 \pm 3.5	0.082

Porous scaffold density (ρ_{foam}) calculated by porosity values from the equation $P = (1 - \rho_{\text{foam}} / \rho_{\text{matrix}}) \times 100$, assuming PCL density to be 1.14 g cm^{-3} and fillers density to be 2.5 g cm^{-3} .

Table 2

Melting temperatures, enthalpy of melting, crystallization temperature, enthalpy of crystallization, and crystallinity percentage of PCL-based scaffolds.

Scaffolds	Tm (°C)	ΔH_M (J/g)	Tc (°C)	ΔH_c (J/g)	χ_c (%)
PCL	56	57	27	52	42
PCL-10CaSi	57	54	29	48	43
PCL-5CaSi-5DCPD	57	52	30	49	42
PCL-10CaSi-10DCPD	56	49	28	46	46

Tm = melting temperature, Tc = crystallization temperature. From DSC analysis.

determined by DMTA [42].

3.2. Calcium release and alkalizing activity (pH)

Ion release values evaluated at different time endpoints are showed in Table 4.

Pure PCL scaffolds showed no/negligible ability to release calcium (4.77 ± 2.20 ppm). The mineral-doped scaffolds showed a moderate ability to release Calcium ions. Cumulative release of calcium ions (mean \pm SD, expressed in ppm) ranged from 67.91 ± 27.34 for PCL-5CaSi-5DCPD to 101.78 ± 15.83 of PCL-10CaSi-10DCPD.

Calcium release decreased during the testing time, but remained markedly higher than PCL for all 28 days ($p < 0.05$), demonstrating a potential long-term activity for all the mineral-doped samples (except for PCL-5CaSi-5DCPD, which showed a non-linear trend).

PCL-10CaSi-10DCPD showed the highest calcium release values from 3 h to 7 days, differences were statistically significant compared to the other samples from 3 h to 3 days ($p < 0.05$).

PCL-10CaSi and PCL5CaSi-5DCPD showed the highest initial calcium release values.

Alkalinizing activity showed a marked increase in the first three hours (Table 5), ranging from 9.29 ± 0.50 to 8.92 ± 0.45 for the mineral-doped scaffolds.

The pH increase remained relevant until 1 day for PCL-10CaSi-10DCPD and PCL-5CaSi-5DCPD. In particular, PCL-10CaSi-10DCPD showed the highest alkalinizing ability at 3 h and 1 day (mean values were 9.29 and 9.11), statistically different from all the mineral doped scaffolds ($p < 0.001$). Then, after 3 days, pH decreased and remained not statistically different from both pure PCL and deionized water ($p > 0.05$).

3.3. Cross-section and internal porous architecture investigated by ESEM

ESEM analysis (200 \times) performed on the scaffolds' cross-section after 28 days soaking in HBSS (Figs. 3 and 4), revealed a more compact structure with respect to the pristine samples. The pore size before soaking is in the range between 40 and 100 μm for neat PCL, PCL-10CaSi and PCL-5CaSi-5DCPD, and in the range between 30 and 60 μm for PCL-10CaSi-10DCPD. After soaking, all samples showed pore size

Table 3
Dynamic mechanical thermal properties of PCL-based scaffolds.

Dynamic mechanical thermal properties					
Scaffolds	Tg (°C)	E' (MPa)	E'' (MPa)	tanδ	Specific E' (MPa cm ³ g ⁻¹)
PCL	-21.1 ± 0.8	0.21 ± 0.03	0.03 ± 0.01	0.12 ± 0.01	3.62
PCL-10CaSi	-26.6 ± 3.1	0.32 ± 0.01	0.03 ± 0.01	0.09 ± 0.02	4.93
PCL-5CaSi-5DCPD	-17.4 ± 1.9	0.26 ± 0.11	0.03 ± 0.01	0.13 ± 0.02	3.88
PCL-10CaSi-10DCPD	-20.8 ± 4.2	0.17 ± 0.06	0.01 ± 0.01	0.13 ± 0.01	2.07

Tg = mechanical glass transition temperature obtained as peak of tanδ, E' = storage modulus, E'' = loss modulus, tanδ = loss factor, specific E' = storage modulus divided by porous scaffold density. From DMTA analysis.

Table 4
The release of Ca release (mean ± SD, expressed in ppm) evaluated at six endpoints. Calcium released from PCL samples was irrelevant. The highest cumulative calcium release was observed for PCL-10CaSi-10DCPD.

Calcium release (ppm) (mean ± SD)							
Scaffolds	0–3 h	3 h–1 day	1–3 days	3–7 days	7–14 days	14–28 days	Cumulative
PCL	0.98 ± 0.29 ^{aA}	0.52 ± 0.48 ^{aA}	0.76 ± 0.66 ^{aA}	0.83 ± 0.34 ^{aA}	0.91 ± 0.41 ^{aA}	0.70 ± 0.30 ^{aA}	4.77 ± 2.20 ^a
PCL-10CaSi	18.80 ± 2.81 ^{bA}	12.60 ± 2.41 ^{bA}	12.70 ± 5.07 ^{bA}	13.65 ± 4.61 ^{bA}	8.45 ± 2.71 ^{bB}	11.08 ± 4.61 ^{bAB}	75.06 ± 17.08 ^b
PCL-5CaSi-5DCPD	18.17 ± 6.67 ^{bA}	14.02 ± 4.41 ^{bA}	12.68 ± 6.68 ^{bA}	7.37 ± 2.71 ^{cB}	3.93 ± 0.91 ^{cB}	11.71 ± 6.91 ^{bA}	67.91 ± 27.34 ^b
PCL-10CaSi-10DCPD	15.41 ± 3.33 ^{bA}	26.03 ± 7.91 ^{cB}	22.43 ± 4.60 ^{cB}	16.45 ± 3.47 ^{bAB}	8.52 ± 2.13 ^{bC}	12.92 ± 2.17 ^{bC}	101.78 ± 15.83 ^c

Different superscript letters represent statistically significant differences (2-way repeated measures analysis of variance followed by Student-Newman-Keuls test (p < 0.05) in the same horizontal row (capital letters) or in the same column (small letters).

lower than 50 μm.

ESEM micrographs of the fresh scaffolds recorded by backscattered electron detector (Fig. 4a–d) revealed a good filler dispersion and no aggregation up to high filler content. After 28 days soaking, a good filler dispersion can still be observed but some aggregation occurred (Fig. 4e–h). In particular, calcium phosphates (CaPs) particles partially fill the pores and therefore reduce the initial porosity as clearly shown in Fig. 4f (PCL-10CaSi after soaking) and in its 500× magnification (Fig. 5).

3.4. ESEM and surface porosity, EDX, Raman and XRD analyses

3.4.1. PCL scaffolds

ESEM analysis at 500 and 1000× magnifications (Fig. 6a and b) revealed an irregular porous structure on the entire surface with large pores, ranging from 20 to 200 μm. The shape of these pores was mostly elliptic or circular.

The mean surface porosity, evaluated on three random areas at 500× and 1000× magnification, was 51.58% (range 49.25–54.16%) and 52.22% (range 47.18–59.11%), respectively.

EDX on spectra on one random area, as well as on the entire area (Fig. 6c and d) showed PCL constitutional peaks, namely Carbon (C) and Oxygen (O).

The FT-Raman and micro-Raman average spectra of the fresh PCL scaffold showed the bands characteristic of both crystalline and

amorphous phases [31], as indicated in the Fig. 7a and b; this result reveals the semi-crystalline character of the polymer.

After 28 days soaking in HBSS, ESEM at 500× and 1000× magnification (Fig. 6e and f) showed a uniform rough surface with small circular pores, ranging from 10 to 20 μm (smaller than that of fresh samples). Mean surface porosity, calculated on 3 random areas at 500× and 1000× magnification was 48.67% (range 45.78–51.17%) and 49.89% (46.54–55.19%). No statistically significant differences were present between porosity of fresh and 28d aged samples (p = 0.233).

Punctual EDX spectra, as well as those of the entire area, (Fig. 6g and h) revealed scaffold constitutional peaks (C, O) and small amounts of sodium (Na) and Chlorine (Cl) (attributable to HBSS medium).

After ageing in HBSS, micro-Raman spectroscopy showed an increase in the relative intensity of the band at 959 cm⁻¹ (Fig. 7b); it must be observed that this band is present also in the spectrum of the PCL polymer [31] and its strengthening upon HBSS is ascribable to the superposition of the PO₄³⁻ symmetric stretching mode of an apatite phase [30] deposited on the surface of the scaffold. The trend of the Raman I_{959(Ap+PCL)}/I_{1443(PCL)} and I_{959(Ap+PCL)}/I_{1306(PCL)} intensity ratios confirmed apatite deposition (Fig. 7c); in fact, both these ratios increased upon ageing in HBSS, although the high standard deviation associated to the measurements suggest that the deposit was not uniformly distributed to the scaffold surface. Moreover, it must be observed that the FT-Raman technique did not detect any strengthening of the 959 cm⁻¹ (Fig. 7b); this result showed that apatite deposition

Table 5

The pH of soaking water (mean ± SD) evaluated at 3, 24 h, 3, 7, 14 and 28 days. pH values were statistically higher for mineral doped scaffolds with respect to PCL traditional scaffold up to 1 day (p < 0.05). After that pH values were similar to pure PCL and deionized water.

pH of soaking water (mean ± SD)							
Scaffolds	3 h	1 day	3 days	7 days	14 days	28 days	
PCL	7.46 ± 0.23 ^{aA}	7.43 ± 0.21 ^{aA}	7.49 ± 0.26 ^{aA}	7.58 ± 0.15 ^{aA}	7.48 ± 0.27 ^{aA}	7.30 ± 0.13 ^{aA}	
PCL-10CaSi	9.20 ± 0.62 ^{bA}	8.09 ± 0.79 ^{bB}	7.66 ± 0.24 ^{aC}	7.37 ± 0.16 ^{aC}	7.54 ± 0.08 ^{aC}	7.50 ± 0.09 ^{aC}	
PCL-5CaSi-5DCPD	8.92 ± 0.45 ^{bA}	8.62 ± 0.36 ^{aC}	7.96 ± 0.42 ^{aB}	7.31 ± 0.09 ^{aC}	7.43 ± 0.20 ^{aC}	7.52 ± 0.14 ^{aC}	
PCL-10CaSi-10DCPD	9.29 ± 0.50 ^{bA}	9.11 ± 0.42 ^{dA}	8.09 ± 0.53 ^{aB}	7.41 ± 0.11 ^{aC}	7.42 ± 0.13 ^{aC}	7.45 ± 0.14 ^{aC}	
deionized water	7.32 ± 0.17 ^{aA}	7.48 ± 0.32 ^{aA}	7.42 ± 0.32 ^{aA}	7.05 ± 0.35 ^{aA}	7.06 ± 0.25 ^{aA}	6.87 ± 0.22 ^{aA}	

Different superscript letters represent statistically significant differences (2-way repeated measures analysis of variance followed by Student-Newman-Keuls test (p < 0.05) in the same horizontal row (capital letters) or in the same column (small letters).

ESEM-SE analysis

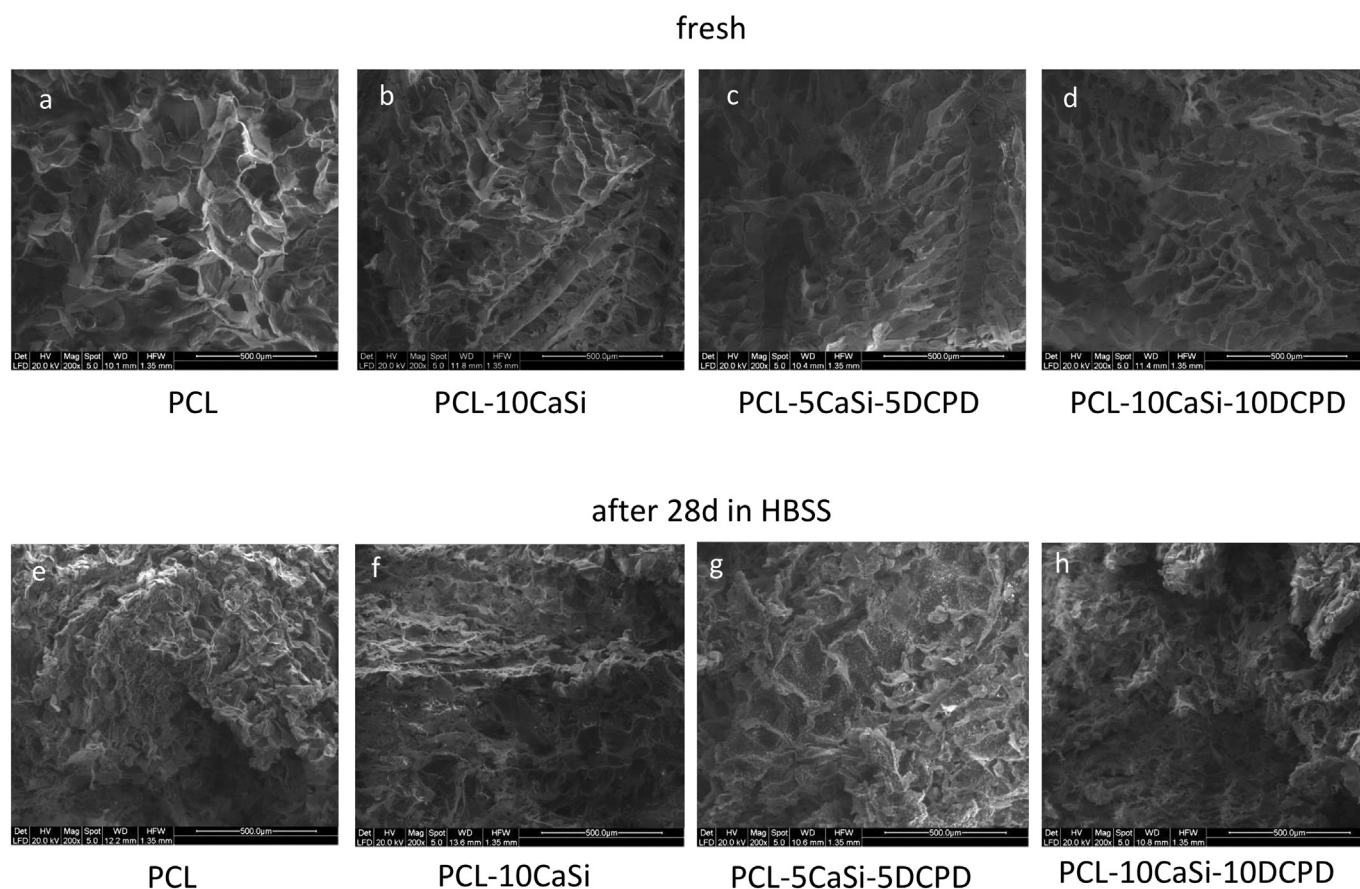


Fig. 3. Micrographs recorded by secondary electrons (ESEM-SE) on the cross sections at $200\times$ magnification of the scaffolds before (a) PCL, (b) PCL-10CaSi, (c) PCL-5CaSi-5DCPD, (d) PCL-10CaSi-10DCPD and after 28 days soaking in HBSS, (e) PCL, (f) PCL-10CaSi, (g) PCL-5CaSi-5DCPD, (h) PCL-10CaSi-10DCPD.

prevalently involved the sample surface (to which the micro-Raman technique is sensitive) rather than the bulk (of which the FT-Raman spectrum is representative). Nevertheless, it must be stressed that the micro-Raman spectrum of the HBSS-aged scaffold still showed the bands of the polymer, suggesting that the thickness of the apatite deposit was not enough to mask the scaffold underneath.

With regards to the polymeric component, both FT-Raman and micro-Raman average spectra (Fig. 7a and b) showed that upon ageing in HBSS, the bands characteristic of the crystalline phase decreased in intensity, while those assignable to the amorphous phase strengthened. To follow the trend of PCL crystallinity, the Raman $I_{1419(\text{PCL C})}/I_{1443(\text{PCL C+A})}$ and $I_{1285(\text{PCL C})}/I_{1306(\text{PCL C+A})}$ intensity ratios were calculated from both FT-Raman and micro-Raman spectra and their trend is reported in Fig. S1, Supplementary Material; as can be seen from the histograms, both ratios generally decreased upon ageing, suggesting a certain increase in the amorphous character of the scaffold upon ageing. To further support this trend, the C=O stretching band has been analyzed by curve fitting, and Fig. S2, Supplementary Material reports as an example the FT-Raman spectra of fresh and HBSS-aged scaffolds fitted into their “crystalline”, “amorphous 1” and “amorphous 2” components. The percentages of each structure obtained by this procedure are reported in Fig. S3, Supplementary Material; as can be easily seen, both FT-Raman and micro-Raman fitting data confirmed a certain decrease in PCL crystallinity.

3.4.2. PCL-10CaSi scaffolds

ESEM micro-analysis at $500\times$ and $1000\times$ magnifications (Fig. 8a

and b) was carried out on the fresh sample surface, revealing a honeycomb-like regular structure. Pores were mostly circular, their diameter ranged from 15 to $30\mu\text{m}$. Small dense granules were uniformly spread on all the surface.

The mean surface porosity, evaluated on three random areas at $500\times$ and $1000\times$ magnification, was 55.16% (range 52.32–60.21%) and 56.43% (range 54.15–58.71%), respectively.

EDX on fresh samples (Fig. 8c) revealed, besides the constitutional peaks (C, O), also presence of Ca and traces of Si (from CaSi powder). Punctual EDX (Fig. 8d) on one granule revealed the presence of Ca and Si, but also traces of Aluminum (Al) and Sulphur (S). Atomic Ca/Si ratio was 2.98.

The FT-Raman average spectrum of the fresh PCL-10CaSi scaffold was of bad quality because of the high fluorescence background [44] due to the calcium silicate cement (Fig. 9a); most of the bands of PCL were observed although with low intensity. For this reason, the $I_{1419(\text{PCL C})}/I_{1443(\text{PCL C+A})}$ and $I_{1285(\text{PCL C})}/I_{1306(\text{PCL C+A})}$ intensity ratios appeared unreliable and thus were not calculated. The PCL bands below 1000 cm^{-1} were hardly detectable due to the strong fluorescence bands at about 805 and 730 cm^{-1} assignable to belite [43]. Therefore, it was not possible calculate the I_{959}/I_{1443} and I_{959}/I_{1306} ratios.

The micro-Raman average spectrum of the same scaffold (Fig. 9b) showed the bands of both PCL and CaSi component (in particular, alite and belite phases [43,44]). The above mentioned marker ratios of PCL crystallinity, i.e. $I_{1419(\text{PCL C})}/I_{1443(\text{PCL C+A})}$ and $I_{1285(\text{PCL C})}/I_{1306(\text{PCL C+A})}$, were not significantly different with respect to pure PCL scaffolds.

After 28 days of immersion in HBSS, ESEM showed (Fig. 8e) a

ESEM-BS analysis

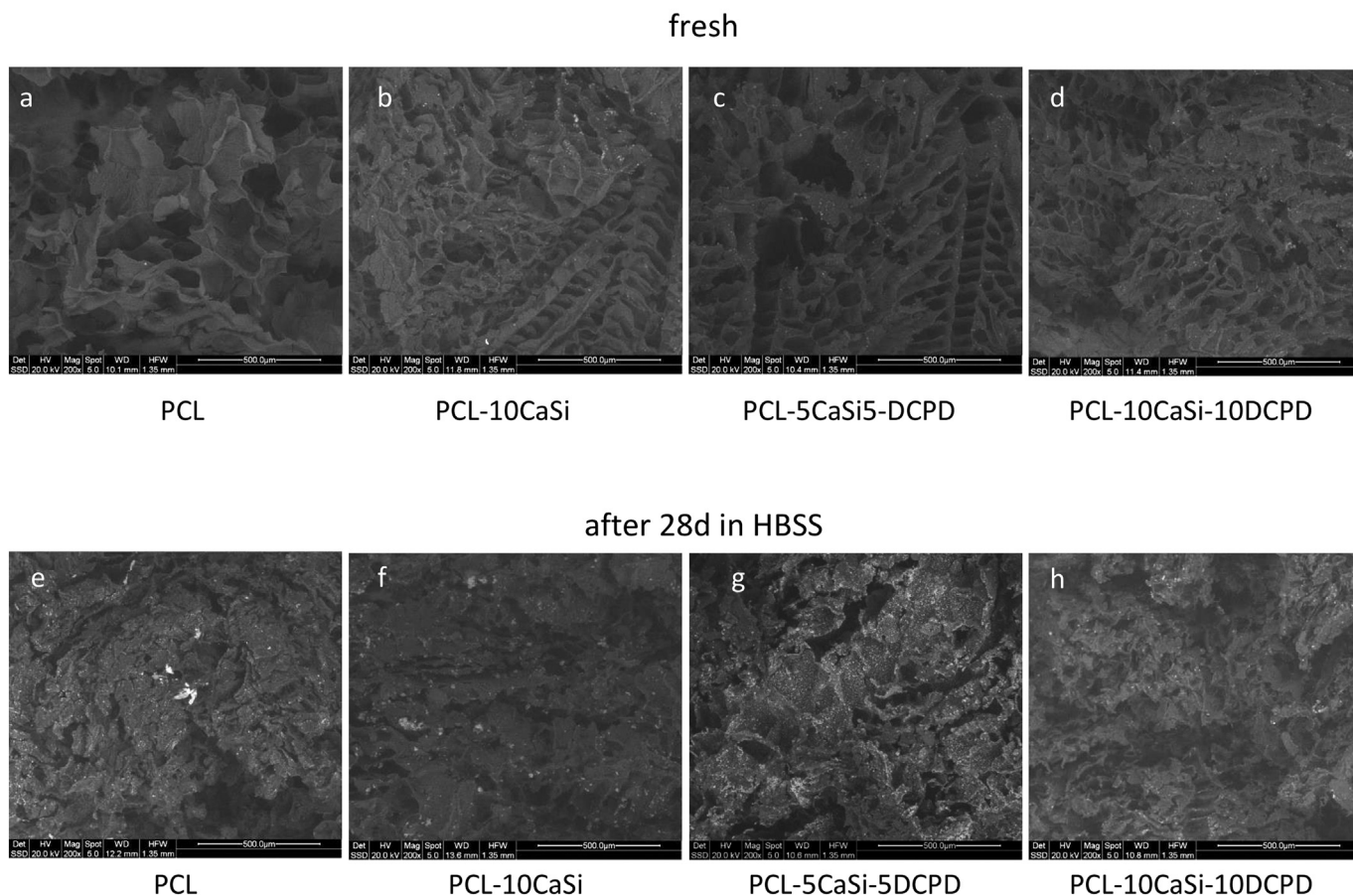


Fig. 4. Micrographs recorded by backscattered electron (ESEM-BS) on the cross sections at $200\times$ magnification of the scaffolds before (a) PCL, (b) PCL-10CaSi, (c) PCL-5CaSi-5DCPD, (d) PCL-10CaSi-10DCPD and after 28 days soaking in HBSS, (e) PCL, (f) PCL-10CaSi, (g) PCL-5CaSi-5DCPD, (h) PCL-10CaSi-10DCPD.

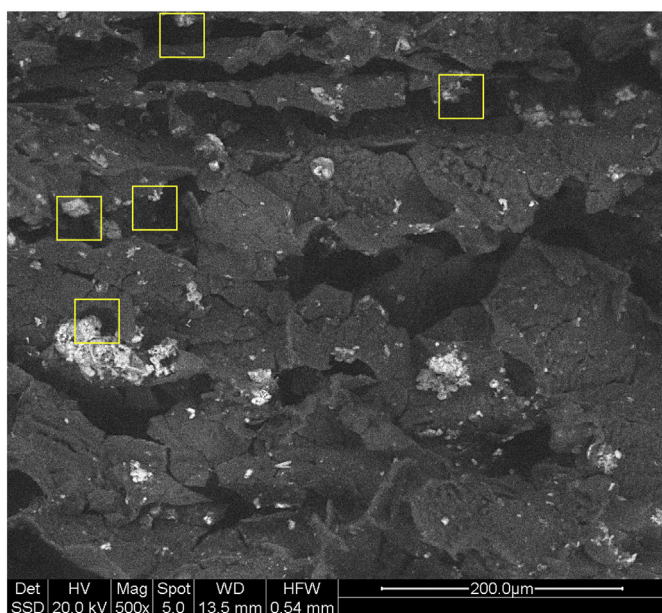


Fig. 5. Micrograph recorded by backscattered electron (ESEM-BS) on the PCL-10CaSi scaffold cross-section at $500\times$ magnification after 28 days soaking in HBSS. Yellow rectangles highlight the calcium phosphates (CaPs) particles that partially fill the pores. (For interpretation of the references to colour in this figure legend, the reader is referred to the web version of this article.)

similar structure with the deposition of a small mineral layer on the scaffold surface. This layer was not uniformly distributed on all the scaffold surface.

The mean surface porosity, evaluated on three random areas at $500\times$ and $1000\times$ magnification, was 57.35% (range 56.58–57.78%) and 56.96% (range 51.66–63.14%), respectively. No statistically significant differences were present between porosity of fresh samples and that of 28d aged samples ($p = 0.555$).

ESEM images of one area at high magnification (Fig. 8f) revealed irregularities on the honeycomb-like structure with the presence of aggregated mineral deposits.

EDX on the entire area (Fig. 8g), as well as punctual EDX (Fig. 8h) revealed the constitutional elements (C, O), the appearance of Na, Cl and P, and a moderate increase of Ca. Traces of Si and Al were also detected.

Atomic Ca/P ratio calculated on the entire area was 1.67, while on the punctual spectrum was 2.35.

After ageing in HBSS, the FT-Raman average spectrum of PCL-10CaSi (Fig. 9a) showed a marked decrease in the fluorescence bands of belite and the spectrum background significantly improved. Some PCL bands that were not detected in the spectrum of the fresh sample became observable. Both the FT-Raman and micro-Raman average spectra of the aged scaffold showed a band at about 1085 cm^{-1} assignable to calcite. No significant changes in the $I_{959(\text{Ap}+\text{PCL})}/I_{1443(\text{PCL})}$ and $I_{959(\text{Ap}+\text{PCL})}/I_{1306(\text{PCL})}$ intensity ratios were observed in the micro-Raman spectra; thus, no significant CaP deposition was detected.

As shown in Fig. 10, from the comparison between the XRD patterns

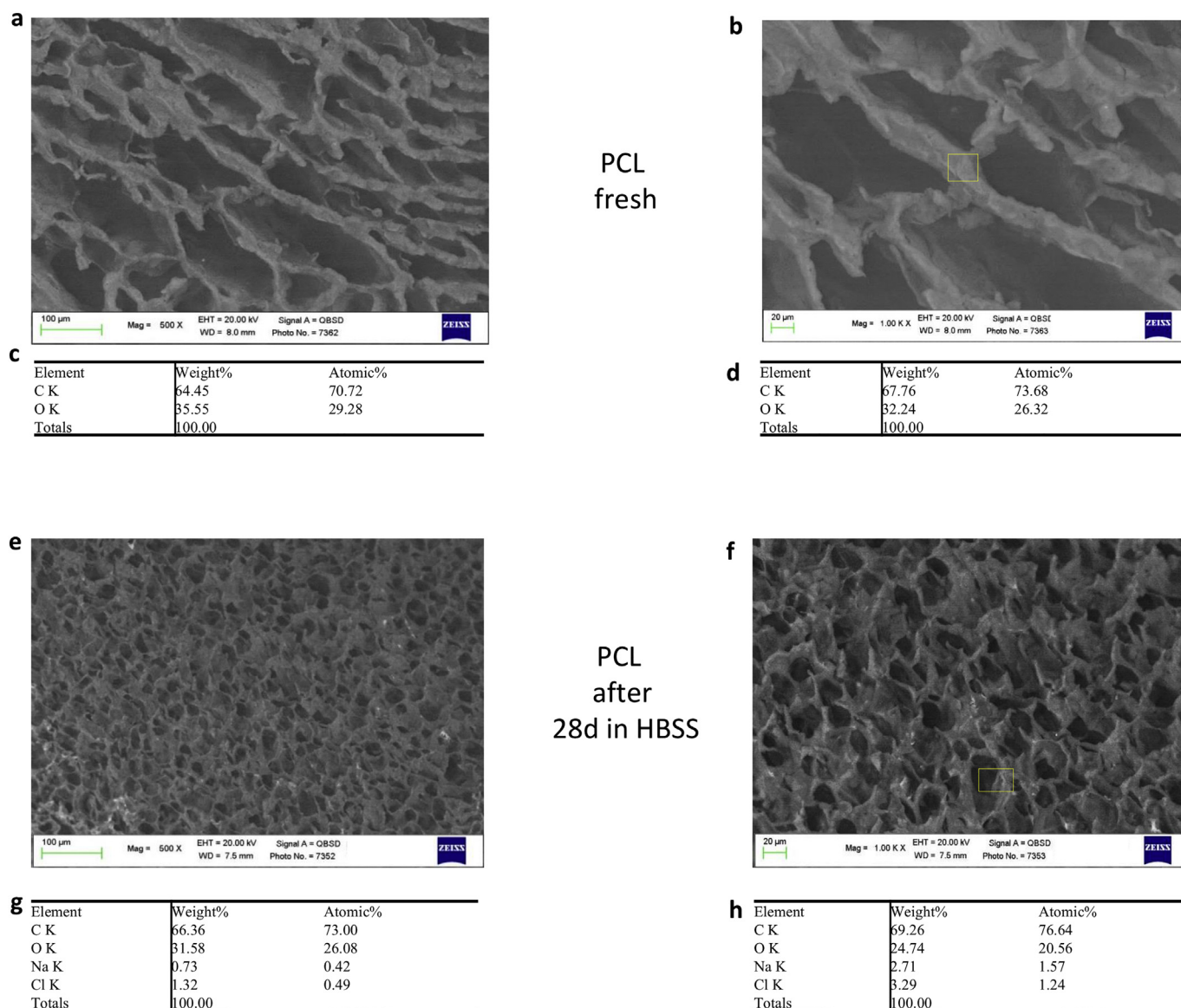


Fig. 6. ESEM-BS surface micromorphology and EDX spectra of the PCL scaffold before (i.e. fresh) and after 28 days in HBSS (500 \times and 1000 \times magnifications). An irregular porous structure was present with large pores, ranging from 20 to 200 μm . After 28 days immersion in HBSS, a uniform rough surface with small circular pores, ranging from 10 to 20 μm (smaller than that of fresh samples) was present. EDX on fresh samples revealed PCL constitutional peaks (C, O). After 28 days in HBSS, EDX showed besides constitutional peaks (C, O) also the presence of Na and Cl (from HBSS).

of the crystalline phases on PCL-10CaSi-10DCPD scaffolds before (a) and after (b) 28 days of immersion in simulated body fluids, it was possible to detect precipitated hydroxyapatite on the surface of the soaked scaffold. In particular, the observed reflections were consistent with the main reflection at $31.7^\circ 2\theta$ of hydroxyapatite and B-type apatite standard JCPDS card file number 3410 [45,46].

3.4.3. PCL-5CaSi-5DCPD scaffolds

ESEM images at 500 \times magnification on fresh sample (Fig. 11a) showed an irregular structure, less porous than the previous investigated samples. Large but sparse irregular pores, ranging from 30 to 200 μm , were present on the surface. Some granules can be appreciated at higher magnification (1000 \times) (Fig. 11b).

The mean surface porosity, evaluated on three random areas at 500 \times and 1000 \times magnification, was 38.27% (range 35.59–39.62%) and 40.42% (range 33.69–44.28%), respectively.

EDX on the entire area (Fig. 11c) revealed constitutional elements (C, O) and traces of Ca and P. EDX on one granule (Fig. 11d) revealed

the presence of Ca, Si, Al (from CaSi), C and O. Ca/Si ratio was 3.12.

The FT-Raman average spectrum of the fresh PCL-5CaSi-5DCPD was similar to that of fresh PCL-10CaSi, although of a better quality, in agreement with the lower CaSi content of the former (Fig. 12a). The average micro-Raman spectrum of fresh PCL-5CaSi-5DCPD recorded at a 100 \times magnification did not show the bands of CaSi and DCPD doping agents (Fig. 12b). However, these components were detected by using a 10 \times magnification (Fig. S4, Supplementary Material).

As observed also for the PCL-10CaSi scaffold, the spectral features assignable to the PCL polymer did not show significant changes in relative intensity with respect to the pure PCL scaffold (compare Figs. 7 and 12), and no significant changes in the $I_{1419(\text{PCL C})}/I_{1443(\text{PCL C+A})}$ and $I_{1285(\text{PCL C})}/I_{1306(\text{PCL C+A})}$ intensity ratios were observed.

After 28 days of immersion in HBSS, ESEM showed (Fig. 11e) a honeycomb-like structure, with more regular and numerous circular pores, their diameter ranged from 20 to 50 μm . At higher magnification (Fig. 11f) a heterogeneous, yet constant, mineral layer can be observed on the scaffold surface also present into some pores.

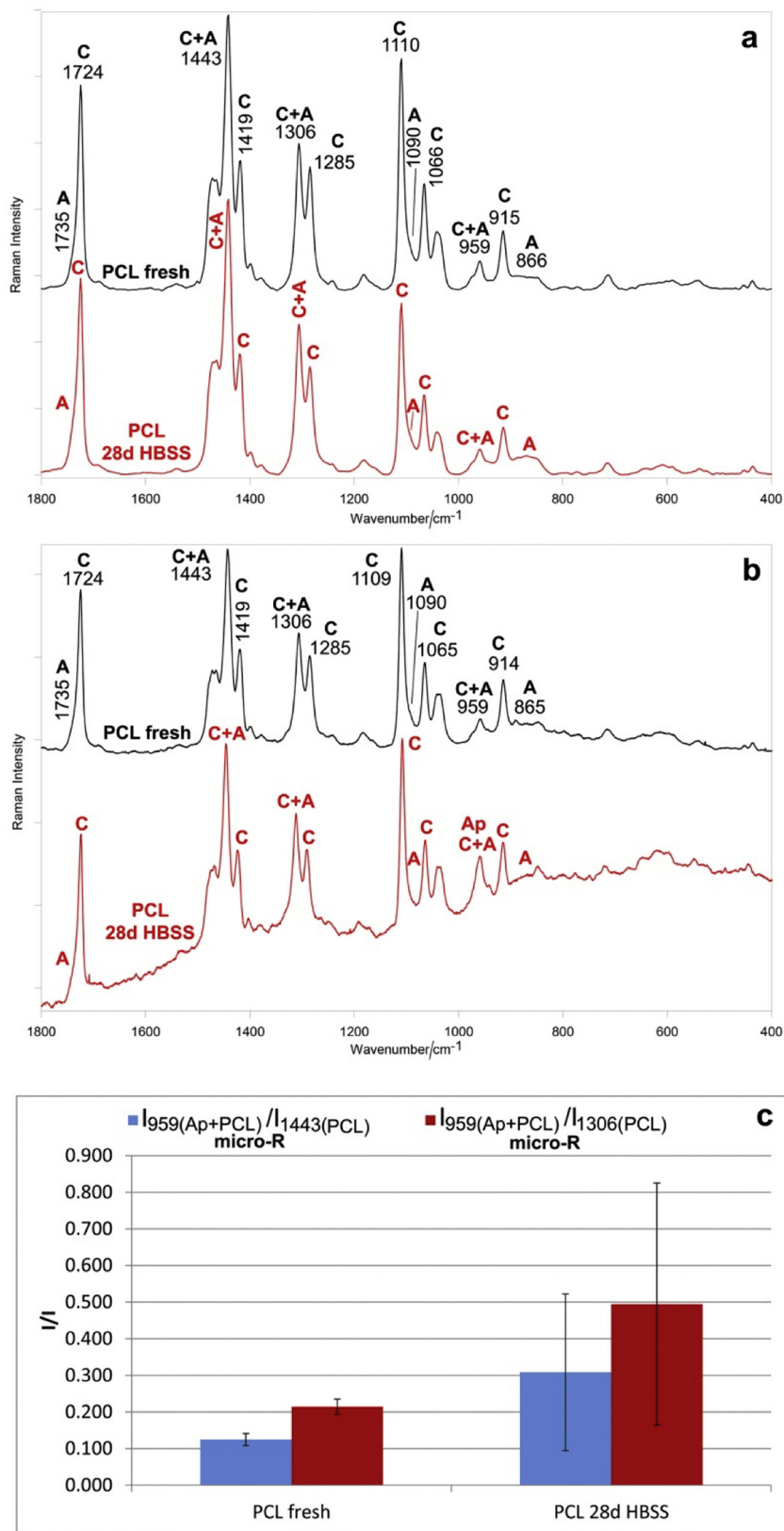


Fig. 7. FT-Raman (a) and micro-Raman (b) average spectra recorded at a 100× magnification on the surface of the PCL scaffold before (i.e. fresh, black line) and after ageing in HBSS for 28 days (red line). The bands prevalently assignable to crystalline (C) and amorphous (A) PCL polymer as well as apatite (Ap) are indicated. (c) Trend of the $I_{959(Ap+PCL)}/I_{1443(PCL)}$ and $I_{959(Ap+PCL)}/I_{1306(PCL)}$ intensity ratios (average ± standard deviation) as calculated from the micro-Raman spectra of the PCL scaffolds. (For interpretation of the references to colour in this figure legend, the reader is referred to the web version of this article.)

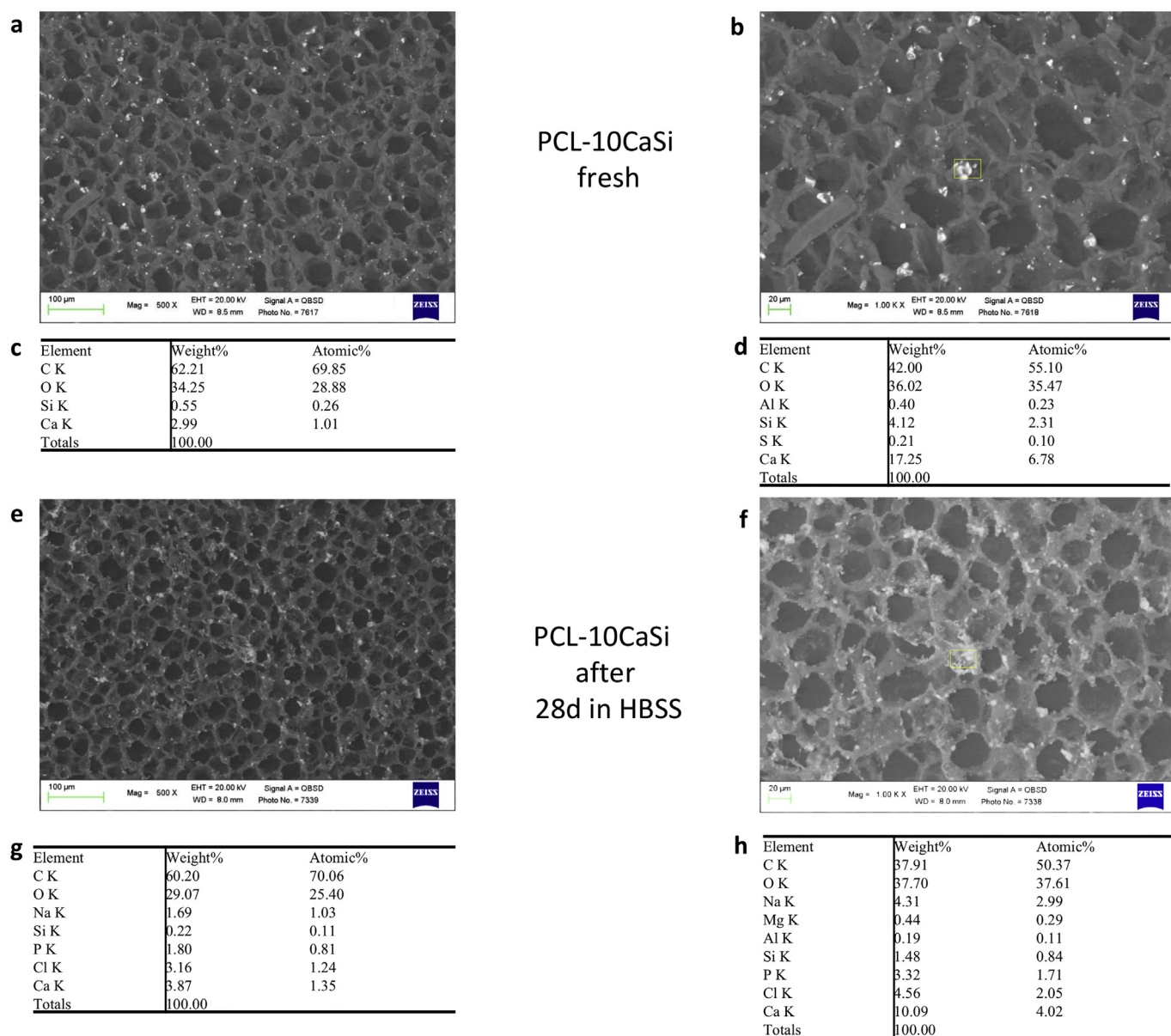


Fig. 8. ESEM-BS surface micromorphology and EDX spectra of the PCL-10CaSi scaffold before (i.e. fresh) and after 28 days in HBSS (500 \times and 1000 \times magnifications). A honeycomb-like structure mostly composed of small circular pores (range 15–30 μm) was observed. Small dense granules were also well-distributed on the scaffold surface. After 28 days in HBSS a layer of CaP was present on the scaffold structure that appeared unaltered. EDX on one granule revealed the presence of C and Ca, but also traces of Aluminum (Al) and Sulphur (S). EDX after immersion in HBSS taken on the entire area revealed the constitutional elements (C, O), the appearance of Na, Cl and P, and a moderate increase of Ca. Traces of Si and Al were also detected.

The mean surface porosity, evaluated on three random areas at 500 \times and 1000 \times magnifications, was 51.13% (range 48.11–53.06%) and 50.98% (range 48.70–52.50%), respectively. Statistically significant differences were present between porosity of fresh and 28d aged samples ($p < 0.001$).

EDX on the entire area (Fig. 11g) of the 28d aged sample revealed, besides the constitutional peaks (C, O) and the elements from the HBSS medium (Na, Cl and Potassium (K)), the increase of Ca, the appearance of P. Punctual EDX on one mineral deposit (Fig. 11h) revealed the appearance of the same elements from the medium (Na, Cl, K and traces of Magnesium (Mg)), constitutional elements (C, O), the marked decrease of Si and the marked appearance of P. Atomic Ca/P ratio was 1.68 on the punctual spectrum, while on the entire area was 1.53.

Upon ageing in HBSS, the FT-Raman spectrum of the PCL-5CaSi-5DCPD scaffold improved (Fig. 12a), suggesting the formation of a deposit masking the fluorescence of the CaSi component underneath.

The average micro-Raman spectrum recorded on this aged scaffold (Fig. 12b) showed a certain increase in the relative intensity of the 959 cm^{-1} band and thus in the $I_{959(\text{AP} + \text{PCL})}/I_{1443(\text{PCL})}$ and $I_{959(\text{AP} + \text{PCL})}/I_{1306(\text{PCL})}$ intensity ratios (Fig. 12c). These results suggest that the deposit was mainly composed of apatite.

No significant changes in the $I_{1419(\text{PCL C})}/I_{1443(\text{PCL C} + \text{A})}$ and $I_{1285(\text{PCL C})}/I_{1306(\text{PCL C} + \text{A})}$ intensity ratios were observed upon ageing.

3.4.4. PCL-10CaSi-10DCPD scaffolds

ESEM on fresh samples at 500 \times magnification (Fig. 13a) showed a porous honeycomb-like regular structure with well distributed mineral granules. At higher magnification (Fig. 13b) small circular pores were observed; their diameter ranged from 15 to 30 μm .

The mean surface porosity, evaluated on three random areas at 500 \times and 1000 \times magnifications, was 41.42% (range 35.61–45.99%) and 41.65% (range 37.97–45.93%), respectively.

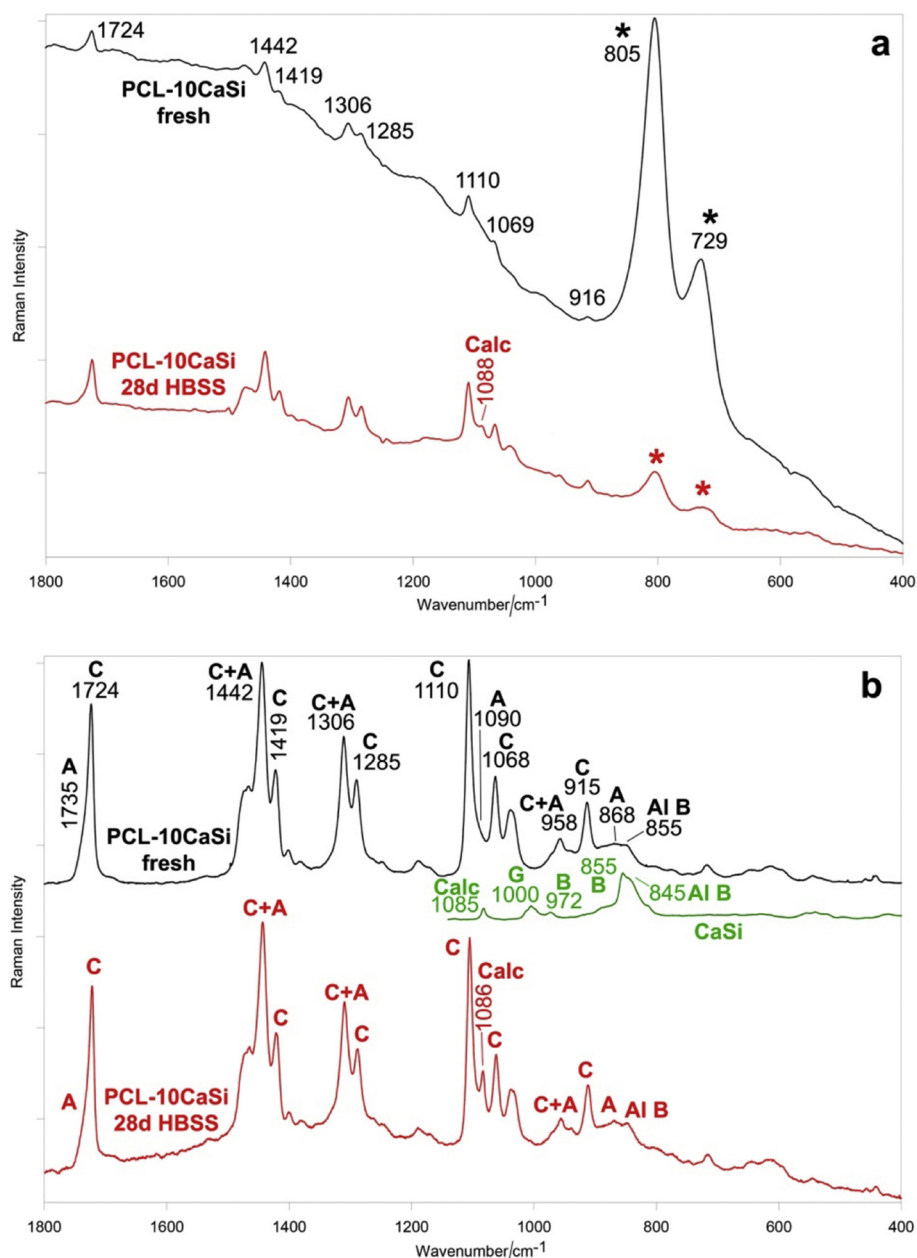


Fig. 9. FT-Raman (a) and micro-Raman (b) average spectra recorded at a $100\times$ magnification on the surface of the PCL-10CaSi scaffold before (i.e. fresh, black line) and after ageing in HBSS for 28 days (red line). The spectrum of the CaSi cement is reported for comparison. The bands prevalently assignable to crystalline (C) and amorphous (A) PCL polymer, gypsum (G), alite (Al), belite (B), calcite (Calc) are indicated. Asterisks indicate the fluorescence bands due to the belite phase. (For interpretation of the references to colour in this figure legend, the reader is referred to the web version of this article.)

EDX on the entire area (Fig. 13c), as well as on one granule (Fig. 13d), showed C, O (attributable to PCL structure), Ca, Si, P and Al (from CaSi and DCPD granules). Ca/Si ratio calculated on one granule was 3.75.

The FT-Raman average spectrum of the fresh PCL-10CaSi-10DCPD scaffold (Fig. 14a) was similar to that of PCL-10CaSi (Fig. 9a), as expected on the basis of the similar CaSi contents of these samples.

The micro-Raman average spectrum of fresh PCL-10CaSi-10DCPD (Fig. 14b) did not display the bands of the DCPD and CaSi components, which were detected in a single spectrum (Fig. S5, Supplementary Material). The presence of the doping agents was found not to alter the $I_{1419}(\text{PCL C})/I_{1443}(\text{PCL C+A})$ and $I_{1285}(\text{PCL C})/I_{1306}(\text{PCL C+A})$ intensity ratios if compared with the pure PCL scaffold.

After 28d immersion in HBSS, the surface appeared markedly different. ESEM showed (Figs. 13e and f) a mineral layer partially covering

a more porous structure. Pores ranged from 20 to $50\mu\text{m}$, a great number of them were obstructed by the mineral deposits.

The mean surface porosity, evaluated on three random areas at $500\times$ and $1000\times$ magnification, was 42.01% (range 38.14–44.17%) and 36.89% (range 35.94–37.51%), respectively. No statistically significant differences were present between porosity of fresh and 28d aged samples ($p = 0.924$).

EDX on the entire area revealed (Fig. 13g), besides the elements attributable to the scaffold constitution (C,O) and the HBSS, the marked increase of P and the decrease of Si. Ca slightly decreased. Interestingly, punctual EDX on the deposit (Fig. 13h) revealed the marked increase of P and the disappearance of Si. Atomic Ca/P ratio, calculated on the entire area, was 1.78, while on punctual spectrum was 2.68.

Upon ageing in HBSS, the FT-Raman average spectrum significantly improved and the fluorescence bands of belite component were

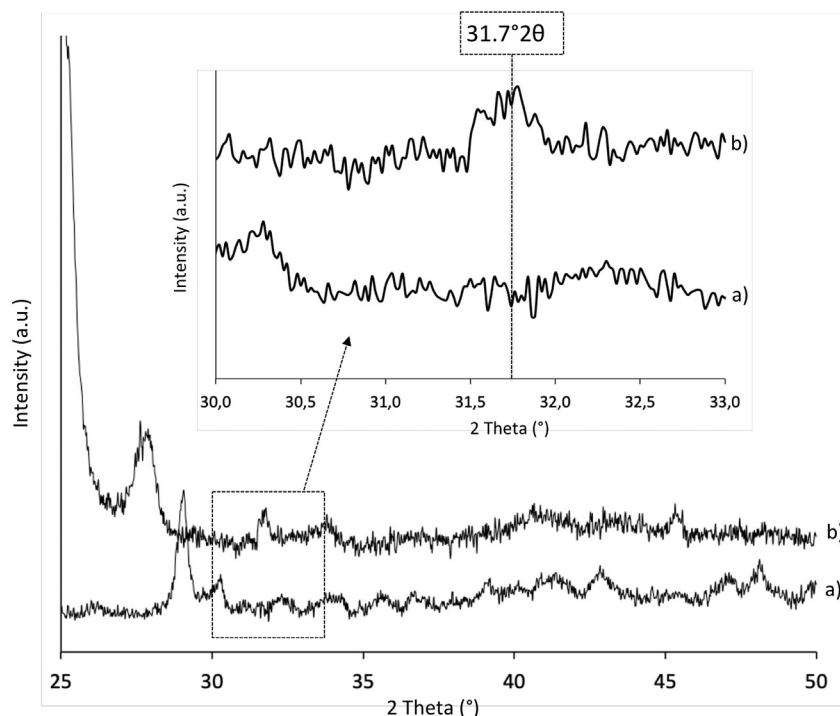


Fig. 10. XRD patterns of PCL-10CaSi-10DCPD before (a) and after (b) 28 days of soaking in HBSS. In the highlight the main reflection of HA and Ap at $31.7^\circ 2\theta$ can be clearly observed for PCL-10CaSi-10DCPD after soaking.

observable only with a very low intensity (Fig. 14a). In the micro-Raman average spectrum significant strengthening of the 959 cm^{-1} band was observed (Fig. 14b) and correspondingly the $I_{959(\text{Ap}+\text{PCL})}/I_{1443(\text{PCL})}$ and $I_{959(\text{Ap}+\text{PCL})}/I_{1306(\text{PCL})}$ intensity ratios noticeably increased (Fig. 14c). On the contrary, the $I_{1419(\text{PCL C})}/I_{1443(\text{PCL C+A})}$ and $I_{1285(\text{PCL C})}/I_{1306(\text{PCL C+A})}$ intensity ratios did not change upon ageing. To gain more insights into the formed deposit, Fig. S6, Supplementary Material shows a single micro-Raman spectrum (i.e. recorded on a single point) of PCL10CaSi-10DCPD aged for 28d in HBSS; the micro-Raman spectrum of a B-type carbonated apatite has been reported for reference as well as that of the fresh scaffold. As can be easily seen, in this single spectrum, the 959 cm^{-1} band appears much stronger than in the average one. Figure Fig. S7, Supplementary Material reports the results of the C=O band fitting analysis performed on the micro-Raman spectra of the fresh and HBSS-aged PCL10CaSi-10DCPD scaffolds (average and single spectra). As can be seen from these data, upon ageing, the PCL crystallinity did not significantly change. Therefore, the increase in the relative intensity of the band at 1067 cm^{-1} (Figs. 14b and S6, Supplementary Material), which has a contribution from crystalline PCL, may be interpreted as only due to the contribution of the CO_3^{2-} mode stretching mode of a B-type carbonated apatite [30]. Other bands of this phase (assignable to PO_4^{3-} bending modes) were detected around 600 and 400 cm^{-1} in both average and single spectra (Figs. 14b and S6, Supplementary Material). In the single spectrum, these bands appeared evidently stronger, due to the higher thickness of the deposit in the position where it was recorded.

3.5. Cell response

The *in vitro* biocompatibility of the investigated PCL-based composite scaffolds was assessed quantitatively by measuring cell viability and proliferation, employing WST-1 cell proliferation reagent. The test is based on the mitochondrial enzymatic conversion of the tetrazolium salt WST-1 into soluble formazan, occurring only in metabolically active cells. The amount of formazan dye directly correlates with the number of viable cells present in the sample. Balb/3T3 clone A31 cell

proliferation was monitored at days 7 and 14 after seeding (Fig. 15).

Investigations of cell morphology and cytoskeleton organization of Balb/3T3 cultured on the composites scaffolds were carried out by CLSM analysis. Cells were stained for F-actin and nuclei with phalloidin-Alexa Fluor 488 and DAPI respectively. After 14 days of culture microscopic observations confirmed the quantitative data and revealed the presence of Balb/3T3 cells on all the investigated samples. The occurring of a good degree of cell colonization of the developed scaffolds is confirmed by the visualization and distribution of cell nuclei, stained with DAPI (Fig. 16).

4. Discussion

The production of porous bioactive and biodegradable scaffolds is important in a great number of medical fields, such as oncological and orthopaedic surgery, maxillo-facial and oral surgery, periodontal and endodontic surgery.

In the present study biocompatible, bioactive (apatite forming) and biointeractive (able to release biologically relevant ions) mineral-doped PCL-based porous scaffolds were fabricated.

Following previously investigations on PLA matrices [20], CaSi and DCDP were included into PCL matrix to improve the polymer properties for tissue engineering, by reducing its hydrophobicity and enhancing its biological activity, to promote cells adhesion, growth and proliferation.

Previously, hybrid PCL-polyglycolic acid solution was used to produce biodegradable scaffolds by a 3D mold for human tooth-ligament in dental applications [47]. Then, PCL composites containing biphasic calcium phosphate (80:20 wt%) prepared by hot melt extrusion (100°C) for 3D printing were able to support the differentiation of human dental pulp stem cells into osteogenic lineage in calvarial defects [48]. PCL composites doped with 10–50 wt% of β -tricalcium phosphate produced by a foaming agent and heating at 90°C demonstrated to promote proliferation of human bone marrow mesenchymal stem cells also supporting the differentiation to reparative hard tissue [49].

Recently, PCL composites doped with 10–50 wt% of calcium

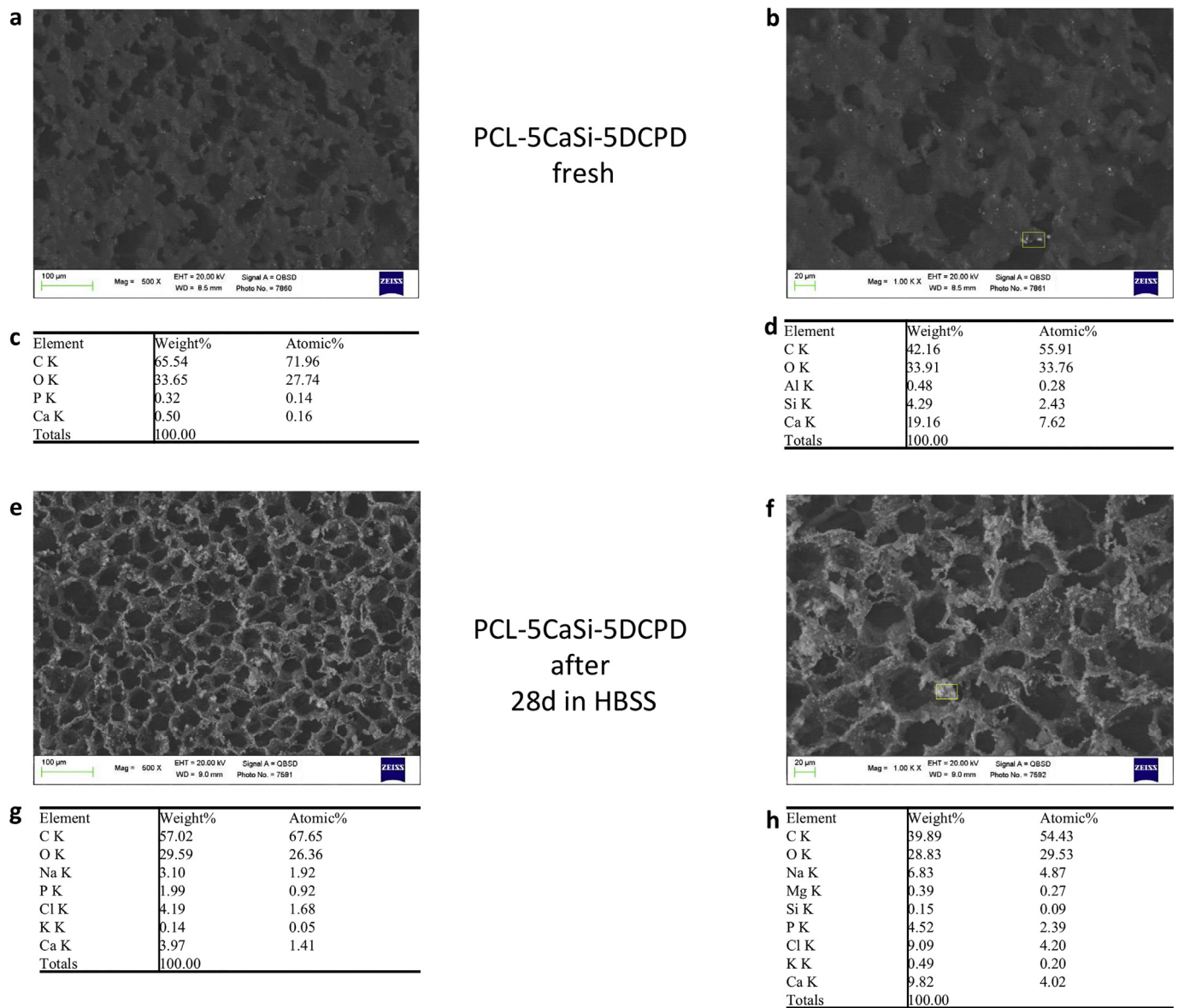


Fig. 11. ESEM-BS surface micromorphology and EDX spectra of the PCL-5CaSi-5DCPD scaffold before (i.e. fresh) and after 28 days in HBSS (500× and 1000× magnifications). Fresh sample showed an irregular structure, less porous than the previous investigated samples. Some granules can be appreciated at higher magnification (arrows). After 28 days of immersion in HBSS, a honeycomb-like structure, with more regular and numerous circular pores was observed. A heterogeneous, yet constant, mineral layer can be observed on the scaffold surface also present into some pores (arrows).

EDX of fresh samples on the entire area revealed constitutional elements (C, O) and traces of Ca and P. EDX on one granule revealed the presence of Ca, Si, Al (from CaSi), C and O. After 28d immersion in HBSS, EDX on the entire area revealed, besides the constitutional peaks (C, O) and the elements from the HBSS medium (Na, Cl and Potassium (K)), the increase of Ca and the appearance of P. Punctual EDX on one mineral deposit revealed the marked decrease of Si and the marked appearance of P (CaP formation).

silicate-based powders stirred at high temperatures (200 °C) were used to fabricate scaffolds for bone tissue engineering applications through 3D printing [50].

An opposite approach has been followed in two recent studies where commercial HCSC powders (ProRoot MTA or Biodentine) were added with PCL (60:40 wt%) used as linker to produce scaffolds for pulp regeneration by 3D printing [24,51]. These scaffolds showed homogeneous macroporosity (approx. 500 μm) and bulk open porosity approx. 70% [24,51].

For its simplicity and no need of highly technical tools, TIPS represents an attractive strategy to tailor the structure of highly porous polymer scaffolds filled with great amounts of inorganic powders, which would negatively affect the melt rheology of PCL, making its processability very difficult through using solution and melt-based

additive manufacturing techniques.

In our study, PCL scaffolds doped with CaSi and CaP produced by TIPS allowed the preparation of highly porous structures (Fig. 3) containing considerable amounts of mineral fillers (up to 20% wt). The **high porosity values** obtained (approaching 95%, Table 1) did not induce relevant brittleness in the materials, that retained the possibility to be easily handled during characterization tests, without risk of collapse. Moreover, a good filler dispersion and no aggregation is observed up to high filler content (Fig. 4).

The viscoelastic properties analyzed in compression mode using DMTA (Table 3) were consistent with the values previously reported in literature for analogous PCL-based porous systems [42]. The reinforcing and nucleating action of the inorganic fillers CaSi and DCPD on PCL matrix were confirmed by the increased value of storage modulus for all

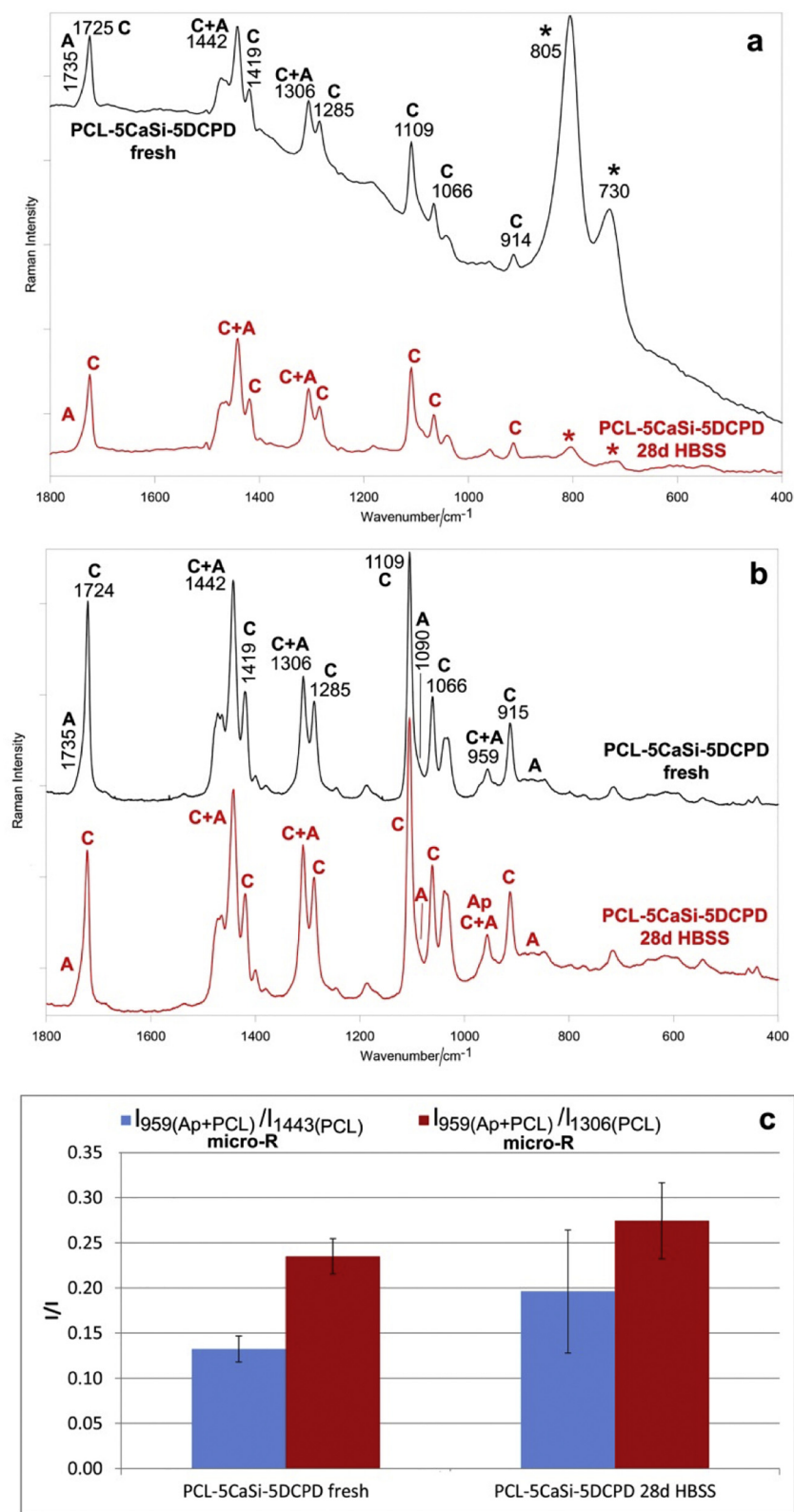


Fig. 12. FT-Raman (a) and micro-Raman (b) average spectra recorded at a 100× magnification on the surface of the PCL-5CaSi-5DCPD scaffold before (i.e. fresh, black line) and after ageing in HBSS for 28 days (red line). The bands prevalently assignable to crystalline (C) and amorphous (A) PCL polymer and apatite (Ap) are indicated. Asterisks indicate the fluorescence bands due to the belite phase. (c) Trend of the $I_{959(Ap+PCL)}/I_{1443(PCL)}$ and $I_{959(Ap+PCL)}/I_{1306(PCL)}$ intensity ratios (average \pm standard deviation) as calculated from the micro-Raman spectra of the PCL-5CaSi-5DCPD scaffolds. (For interpretation of the references to colour in this figure legend, the reader is referred to the web version of this article.)

the composites, and from the slight increase in the crystallization temperature. When the inorganic particles were loaded at the highest amount in PCL-10CaSi-10DCPD scaffold, a detrimental effect on the **mechanical properties** was observed (Table 5).

However, both vibrational and DSC results showed that the presence of the doping agents in the different scaffold formulations did not substantially affect the polymer structure, which remained semi-

crystalline. Actually, by comparing the pure PCL and composite scaffolds, the DSC and Raman techniques did not detect significantly different χ_c (%) (Table 2), $I_{1419(PCL\ C)}/I_{1443(PCL\ C+A)}$ and $I_{1285(PCL\ C)}/I_{1306(PCL\ C+A)}$, % “crystalline” phase values (Figs. S1 and S3, Supplementary Material), respectively. In other words, the presence of the mineral doping agents neither favors PCL crystallization (acting as nucleating sites [52,53] nor hinders polymer crystallization

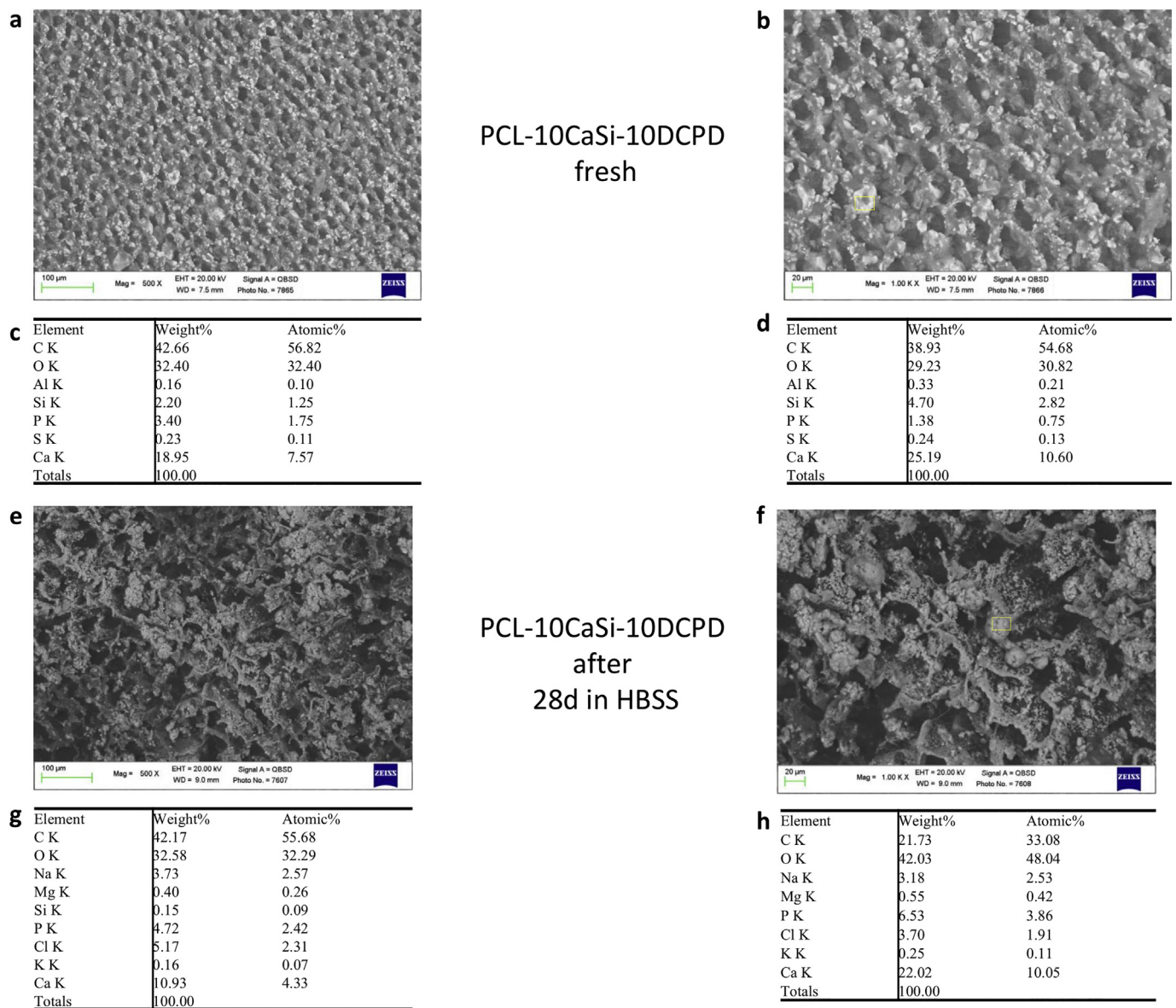


Fig. 13. ESEM-BS surface micromorphology and EDX spectra of the PCL-10CaSi-10DCPD scaffold before (i.e. fresh) and after 28 days in HBSS (500 \times and 1000 \times magnifications). A porous honeycomb-like regular structure with well distributed mineral granules was observed on fresh samples. After 28d immersion in HBSS, a mineral layer partially covered a more porous structure was observed. A great number of pores were obstructed by the mineral deposits (arrows).

EDX of fresh samples on the entire area, as well as on one granule, showed C, O (attributable to PCL structure), Ca, Si, P and Al (from CaSi and DCPD granules). After 28 days immersion in HBSS revealed, besides the elements attributable to the scaffold constitution (C, O) and the HBSS, the marked increase of P and the decrease of Si. Interestingly, punctual EDX on the deposit and revealed the marked increase of P and the disappearance of Si.

[48,54–57].

Limits of the designed mineral-doped scaffolds may be the low **mechanical properties**. However, in maxillofacial surgery, scaffolds may be positioned in non-load-bearing sites or in temporarily unloaded sites during healing, allowing the bone tissue regeneration through the scaffold which will be slowly replaced by new bone tissue. Similarly, conventional oral rehabilitation protocols show that loading procedures should be post-poned for several months, waiting for new bone formation [58]. The needed mechanical strength is to maintain their integrity and avoid tissue collapse or filling with fibrous tissue until complete tissue regeneration [59].

The mineral-doped scaffolds were able to release biologically relevant ions (OH and Ca), creating the conditions of a bone forming osteoblastic microenvironment. The initial marked **alkalinizing ability** of the mineral-doped scaffolds (approx. pH 9) triggers/favors the early CaP nucleation on the scaffold surface [60]. Hydroxide ions stimulate

the release of alkaline phosphatase and BMP-2 which participates in the mineralization processes [61,62].

Moreover, the alkaline pH created in the first days may also confer a slight antibacterial activity (enzymatic inhibition of microorganisms), that may be useful early after the treatment. HCSC antimicrobial properties are well-known in literature [13,63].

Ca ions from CaSi and HCSC powders are soluble molecular signals which trigger the cascade of cells differentiation into osteoblastic cell lines [64,65]. In particular osteopontin, bone sialoprotein [65], bone morphogenic protein-2 (BMP-2) and alkaline phosphatase are modulated by increasing concentrations of extracellular Ca ions [66].

SiOH silanol groups form owing to the hydration of calcium silicates particles. At alkaline pH, the deprotonation of SiOH groups should predominate with the consequent formation of SiO⁻ groups that acts as nucleating sites for the formation of apatite crystals [17]. Neo angiogenesis processes are also stimulated by the presence of Si ions in HCSC

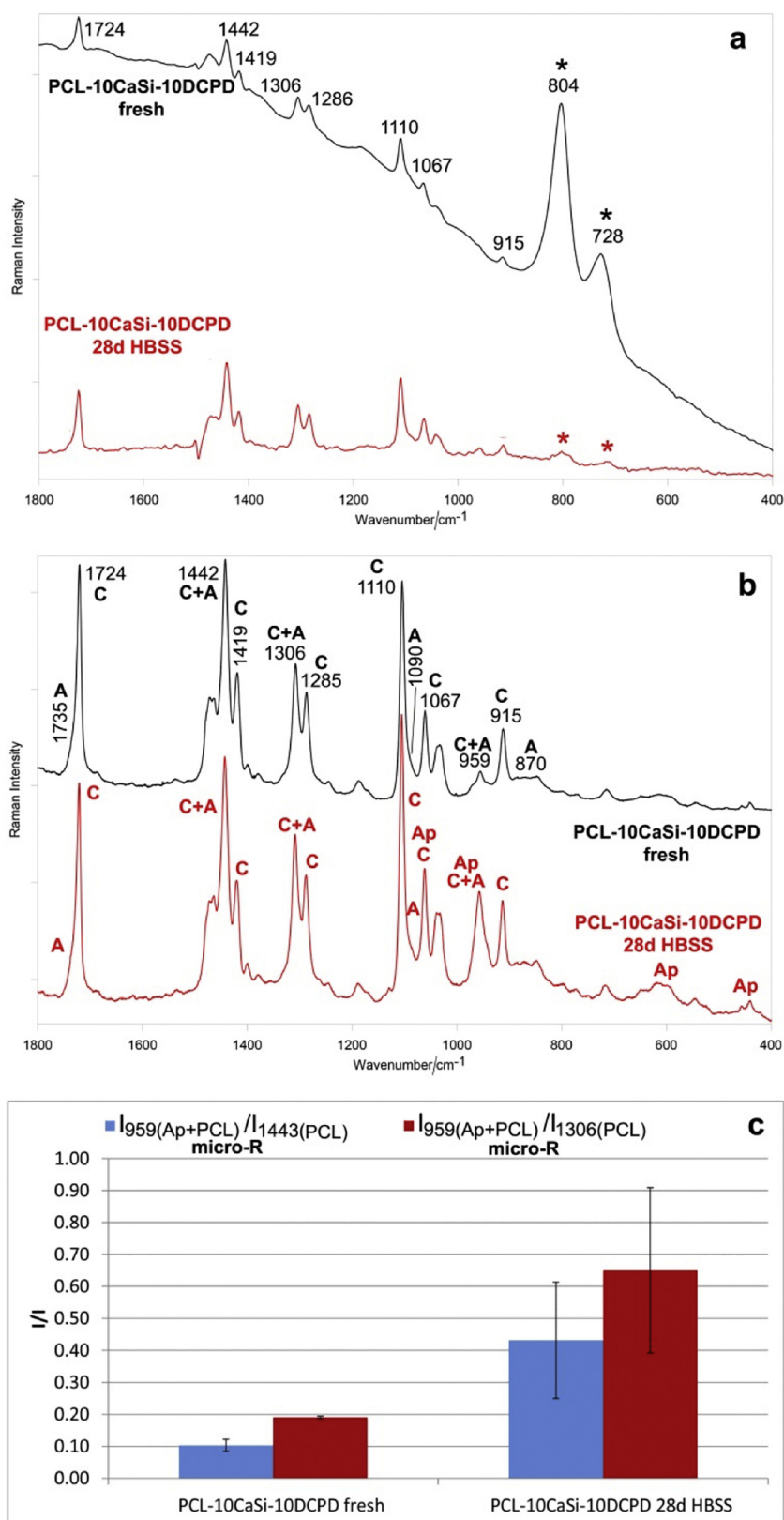


Fig. 14. FT-Raman (a) and micro-Raman (b) average spectra recorded at a 100× magnification on the surface of the PCL-10CaSi-10DCPD scaffold before (i.e. fresh, black line) and after ageing in HBSS for 28 days (red line). The bands prevalently assignable to crystalline (C) and amorphous (A) PCL polymer and B-type carbonated apatite (Ap) are indicated. Asterisks indicate the fluorescence bands due to the belite phase. (c) Trend of the $I_{959(Ap+PCL)}/I_{1443(PCL)}$ and $I_{959(Ap+PCL)}/I_{1306(PCL)}$ intensity ratios (average ± standard deviation) as calculated from the micro-Raman spectra of the PCL-10CaSi-10DCPD scaffolds. (For interpretation of the references to colour in this figure legend, the reader is referred to the web version of this article.)

through the increased gene expression of pro-angiogenic cytokines (such vascular endothelial growth factor) and nitric oxide synthesis [67–69].

A CaP layer was present on all the mineral doped scaffolds; FT-Raman and micro-Raman spectroscopy showed that, among the

analyzed scaffolds, the sample containing the highest amounts of CaSi and DCPD, i.e. PCL-10CaSi-10DCPD, formed the thickest deposit, as expectable on the basis of its highest release of calcium ions (Table 4) and its highest alkalinizing activity (Table 5), and as the presence of CaP in addition to CaSi, accelerates the apatite nucleation by calcium

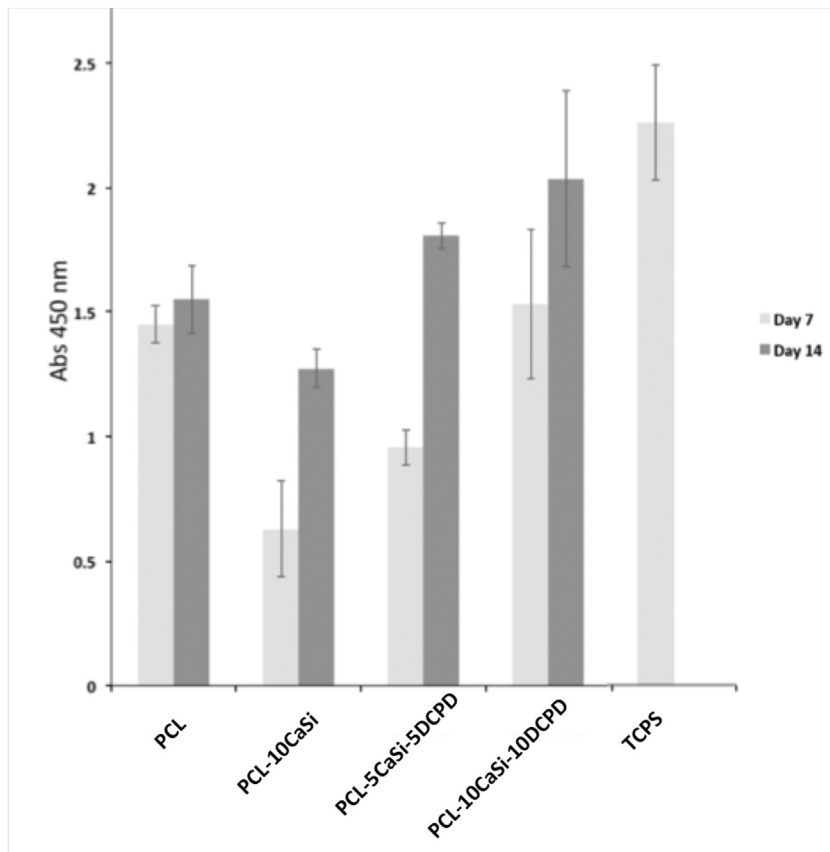


Fig. 15. Quantitative results of cell proliferation on the experimental scaffolds and TCPS. Cell proliferation and viability was higher at 14 days than at 7 days for all the samples. PCL-10CaSi-10DCPD resulted to be the most promising in sustaining a good cell proliferation during the first 7 days of culture, with a further increase at 14 days.

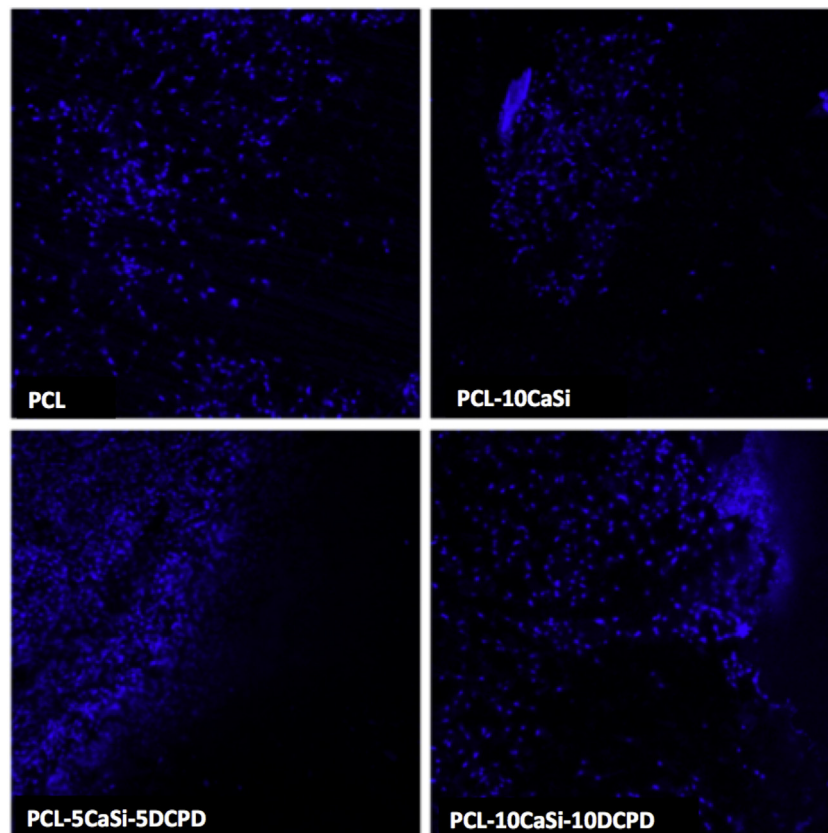


Fig. 16. CLSM micrograph of cell colonization of mineral doped scaffolds. Cells nuclei were stained with DAPI. Images were captured using 10× magnification objective. After 14 days of culture, microscopic observations confirmed the quantitative data and revealed the presence of cells on all the investigated samples.

silicates [21]. Actually, the FT-Raman spectra of this sample displayed the highest decrease in fluorescence upon soaking in HBSS (Fig. 14a); this spectral feature may be used to qualitatively estimate the thickness of the deposit. In fact, the thicker the deposit, the highest is the masking effect of the fluorescence produced by the cement underneath. At the same time, for the PCL-10CaSi-10DCPD scaffold, micro-Raman spectroscopy revealed the highest increases in the $I_{959(Ap+PCL)}/I_{1443(PCL)}$ and $I_{959(Ap+PCL)}/I_{1306(PCL)}$ intensity ratios (Fig. 14c). Surface porosity evaluation showed that CaP deposition counterbalanced the increase of porosity attributable to PCL degradation.

Concerning PCL-10CaSi-10DCPD, micro-Raman spectroscopy revealed that the deposit formed on this scaffold was mainly composed of B-type carbonated apatite (Figs. 14b and S6, Supplementary Material); the Ca/P value measured by EDX on the entire area was 1.78, consistently with the micro-Raman findings. At this purpose, it may be recalled that micro-Raman spectroscopy has been widely proposed as technique of choice to detect B-type carbonated apatites in the investigation of physiological and pathological mineralization processes [70–74].

It is interesting to note that the composite samples formed a relatively thin deposit; actually, the bands of the polymer underneath were still detectable, differently from the corresponding samples prepared using poly(L-lactic acid) (PLLA) as polymeric component [20]. The composite PCL-based samples formed a thinner deposit and released less calcium ions than the previously analyzed PLA-based scaffolds [20]; this result is not unexpected since it is well known that PCL is a more hydrophobic polymer than PLLA. For the scaffolds investigated in this study, the lower hydrophilicity of the polymeric matrix slowed down the hydration reaction of the cement and thus calcium release. Therefore, it is not surprising that they displayed a lower apatite forming ability than their PLLA analogues.

Micro-Raman analyses showed that also the pure PCL scaffolds nucleated apatite on their surface (Fig. 7); this result is in agreement with the ESEM observations (Fig. 3), which showed a noticeable decrease in pore sizes and porosity as a consequence of apatite deposition.

XRD analysis of PCL-10CaSi-10DCPD scaffold used as model composition revealed the presence of precipitated HA and Ap on the surface of the soaked scaffold (Fig. 10). HA and calcium phosphates particles observed on the surface and on the cross-sections of the scaffolds after soaking, partially fill the pores and therefore reduce the initial porosity leading to a more compact structure from a morphological point of view (Fig. 4).

An analogous apatite forming ability was observed for PLLA scaffolds [20]. Some studies have reported that PCL has no apatite forming ability [48,75–77], while others have found an opposite behavior, often by using more concentrated simulated body fluid solutions [78–81]. These contradicting results suggest, as previously reported [9] that the chemical and physical properties of the sample (i.e. the physical form and porosity) play a crucial role in mineralization experiments.

Whilst pure PCL scaffolds underwent a general decrease in porosity upon soaking in HBSS, the composite devices showed an opposite behaviour (see in particular the PCL-5CaSi-5DCPD), suggesting that polymer degradation and leaching of the mineral doping agents due to hydrolysis prevailed over apatite deposition. This different behaviour does not appear surprising. At this purpose, it must be recalled that the biodegradation rate of a polymer mainly depends on its intrinsic properties that control water accessibility to the ester linkages (i.e. those susceptible to hydrolysis): composition, hydrophilicity/hydrophobicity, surface area, morphology (crystalline/amorphous), glass transition temperatures, molecular weight [82,83]. The presence of the mineral doping agents should increase the degradation rate for several reasons. According to other studies [50,55,57,78], their hydrophilicity as well as the increase in the surface area they produce should allow the water molecules to penetrate more easily within the materials and to cause their hydrolytic degradation. Moreover, it must be stressed that the CaSi hydration reactions produce an alkaline pH (Table 5), which is

known to accelerate the hydrolysis of aliphatic polyesters such as PCL [38,57,84,85].

Upon ageing in HBSS, a certain crystallinity decrease (i.e. in the $I_{1419(PCL\ C)}/I_{1443(PCL\ C+A)}$ and $I_{1285(PCL\ C)}/I_{1306(PCL\ C+A)}$ intensity ratios and % “crystalline” phase) occurred in pure PCL scaffolds, as revealed by vibrational spectroscopy (Figs. S1 and S3, Supplementary Material). At this purpose, it must be recalled that in semicrystalline PCL polymers, an increase in crystallinity upon degradation has been often reported [84,86–89] and explained as a result of the fragmentation of the polymers into shorter chains which are more able to pack in a crystalline structure, or in terms of the preferential removal of the more easily degradable amorphous regions of the polymer, leading to an enrichment in crystalline domains. However, some studies have reported different trends and analogous decreases in crystallinity have been reported also by other authors for pure PCL [90,91] and composite calcium phosphate containing PCL-based devices [57,92]. For pure PCL samples, they have been explained by considering that degradation takes place not only in the amorphous phase, but also in the crystalline region, and the latter is converted to an imperfect crystal structure; for the composites, the mineral particles have been hypothesized to act as obstructions to the crystallization of the PCL chains. On the other hand, Raman spectroscopy showed that upon ageing in HBSS, no significant changes in polymer crystallinity (i.e. in the $I_{1419(PCL\ C)}/I_{1443(PCL\ C+A)}$ and $I_{1285(PCL\ C)}/I_{1306(PCL\ C+A)}$ intensity ratios) occurred. This result may be explained in relation to the findings by Žuckiene et al. [55], who have reported that the addition of montmorillonite to PCL-based polyurethanes, while allowing the water molecules to penetrate more easily within the materials, retards the rate of crystallinity change during degradation.

The *in vitro* **biocompatibility** of the designed scaffolds was assessed quantitatively by measuring cell viability and proliferation. The results confirmed the lack of toxicity for all the investigated samples (Fig. 15). PCL-10CaSi-10DCPD resulted to be the most promising in sustaining a good cell proliferation during the first 7 days of culture, with a further increase at 14 days (Fig. 15). Investigations of cell morphology and cytoskeleton organization of Balb/3T3 cultured on the scaffolds after 14 days confirmed the quantitative data and revealed the presence of Balb/3T3 cells on all the investigated samples (Fig. 16). The presence of a good degree of cell colonization of scaffolds is confirmed by the visualization and distribution of cell nuclei (Fig. 16). Representative images of cells grown onto PCL-10CaSi-10DCPD samples displayed a consistent F-actin organization with stress fibers well stretched along the cytoplasm, thus corroborating the possibility of the developed scaffolds to act as synthetic extracellular matrix for cell adhesion and proliferation (Fig. 17).

5. Conclusions

Key findings of this research may be summarized as follows:

- PCL is a suitable matrix for the production of mineral-doped scaffolds that allow the nucleation of CaP and apatite on their surface;
- TIPS fabrication technique allowed to produce highly porous PCL-based scaffolds (porosity approaching 95%), doped with considerable amounts of mineral fillers (up to 20 wt%);
- The incorporation of reactive hydrophilic CaSi and DCPD minerals allows to create biointeractive (Ca^{++} and OH^- ion release), bioactive (apatite nucleation) and biocompatible scaffolds, overcoming PCL disadvantages (hydrophobicity, release of acid degradation products and reduced cell adhesion and growth).
- The developed mineral-doped scaffolds may act synthetic extracellular matrices for cell adhesion and proliferation, and could have a potential role in the activation of mineralizing cells bone regeneration procedures.

Interestingly, by using TIPS technique the shape of the scaffolds may

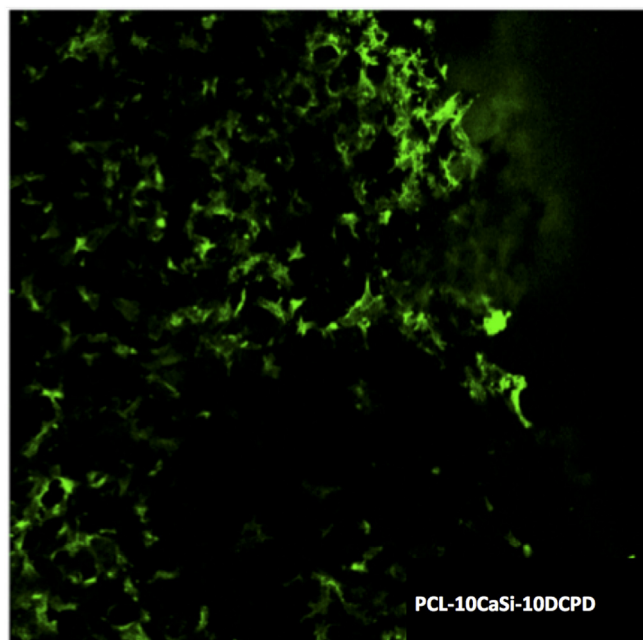


Fig. 17. CLSM visualization of F-actin cytoskeleton of cells stained with phalloidin-Alexa Fluor 488 recorded at 20 \times magnification, representative images of cells grown onto PCL-10CaSi-10DCPD displayed a consistent F-actin organization with stress fibers well stretched along the cytoplasm.

be designed according to the donor site shape, as the fabrication of the scaffold initiates from a liquid suspension that can be adapted to any desired mold.

Appendix A. Supplementary data

Supplementary data to this article can be found online at <https://doi.org/10.1016/j.msec.2019.04.040>.

References

- [1] K. Kriebel, C. Hieke, B. Müller-Hilke, M. Nakata, B. Kreikemeyer, Oral biofilms from symbiotic to pathogenic interactions and associated disease-connection of periodontitis and rheumatic arthritis by peptidylarginine deiminase, *Front. Microbiol.* 30 (9) (2018) 53.
- [2] A. Oryan, S. Alidadi, A. Moshiri, N. Maffulli, Bone regenerative medicine: classic options, novel strategies, and future directions, *J. Orthop. Surg. Res.* 17 (2014) 1–27.
- [3] P.K. Vallittu, Bioactive glass-containing cranial implants: an overview, *J. Mater. Sci.* 52 (2017) 8772–8784.
- [4] Zheng C, Gao H, Yang D-, Liu M, Cheng H, Wu Y-, et al. PCL-based thermo-gelling polymers for in vivo delivery of chemotherapeutics to tumors. *Mater Sci Eng C* 2017; 74: 110–116.
- [5] N.H. Marei, I.M. El-Sherbiny, A. Lotfy, A. El-Badawy, N. El-Badri, Mesenchymal stem cells growth and proliferation enhancement using PLA vs PCL based nanofibrous scaffolds, *Int. J. Biol. Macromol.* 93 (2016) 9–19.
- [6] M.A. Woodruff, D.W. Huttmacher, The return of a forgotten polymer—polycaprolactone in the 21st century, *Prog. Polym. Sci.* 35 (2010) 1217–1256.
- [7] A.H. Ambre, D.R. Katti, K.S. Katti, Biomaterialized hydroxyapatite nanoclay composite scaffolds with polycaprolactone for stem cell-based bone tissue engineering, *J. Biomed Mater Res Part A* 2015 (103A) (2015) 2077–2101.
- [8] H. Kwon, M. Yoo, I. Park, T. Kim, H. Lee, S. Lee, et al., A novel degradable polycaprolactone network for tissue engineering, *Biomaterials* 24 (2003) 801–808.
- [9] L. Shor, S. Güçeri, X. Wen, M. Gandhi, W. Sun, Fabrication of three-dimensional polycaprolactone/hydroxyapatite tissue scaffolds and osteoblast-scaffold interactions in vitro, *Biomaterials* 28 (2007) 5291–5297.
- [10] F. Causa, P.A. Netti, L. Ambrosio, G. Ciapetti, N. Baldini, S. Pagani, et al., Poly- ϵ -caprolactone/hydroxyapatite composites for bone regeneration: in vitro characterization and human osteoblast response, *J. Biomed. Mater. Res. A* 76A (2005) 151–162.
- [11] PAS 132, Terminology for the Bio-Nano Interface, (2007) (British Standards Institution).
- [12] M.G. Gandolfi, P. Taddei, E. Modena, F. Siboni, C. Prati, Biointeractivity-related versus chemi/physisorption-related apatite precursor-forming ability of current root end filling materials, *J. Biomed Mater Res B Appl Biomater* 101 (2013) 1107–1123.
- [13] C. Prati, M.G. Gandolfi, Calcium silicate bioactive cements: biological perspectives and clinical applications, *Dent. Mater.* 31 (2015) 351–370.
- [14] M.G. Gandolfi, S.N. Shah, R. Feng, C. Prati, S.O. Akintoye, Biomimetic calcium-silicate cements support differentiation of human orofacial mesenchymal stem cells, *J. Endod.* 37 (2011) 1102–1108.
- [15] M.G. Gandolfi, P. Taddei, A. Tinti, E.S. De Dorigo, P.L. Rossi, C. Prati, Kinetics of apatite formation on a calcium-silicate cement for root-end filling during ageing in physiological-like phosphate solutions, *Clin Oral Invest* 14 (2010) 659–668.
- [16] M.G. Gandolfi, G. Spagnuolo, F. Siboni, A. Procino, V. Riviaccio, G.A. Pelliccioni, C. Prati, S. Rengo, Calcium silicate/calcium phosphate biphasic cements for vital pulp therapy: chemical-physical properties and human pulp cells response, *Clin. Oral Invest.* 19 (2015) 2075–2089.
- [17] M.G. Gandolfi, F. Siboni, T. Botero, M. Bossù, F. Riccitiello, C. Prati, Calcium silicate and calcium hydroxide materials for pulp capping: biointeractivity, porosity, solubility and bioactivity of current formulations, *J. Appl. Biomater. Funct. Mater.* 13 (2015) 1–18.
- [18] F. Siboni, P. Taddei, F. Zamparini, C. Prati, M.G. Gandolfi, Properties of BioRoot RCS, a tricalcium silicate endodontic sealer modified with povidone and polycarboxylate, *Int. Endod. J.* 50 (2017) 120–136.
- [19] W. Zhou, Q. Zheng, X. Tan, D. Song, L. Zhang, D. Huang, Comparison of mineral trioxide aggregate and iRoot BP plus root repair material as root-end filling materials in endodontic microsurgery: a prospective randomized controlled study, *J. Endod.* 43 (2017) 1–6.
- [20] M.G. Gandolfi, F. Zamparini, M. Degli Esposti, F. Chiellini, C. Aparicio, F. Fava, C. Prati, Poly(lactic acid)-based porous scaffolds doped with calcium silicate and dicalcium phosphate dihydrate designed for biomedical application, *Mater Sci Eng C* 82 (2018) 163–181.
- [21] M.G. Gandolfi, P. Taddei, A. Tinti, E. De Stefano Dorigo, C. Prati, Alpha-TCP improves the apatite-formation ability of calcium-silicate hydraulic cement soaked in phosphate solutions, *Mater Sci Eng C* 31 (2011) 1412–1422.
- [22] Y.C. Chiu, H.Y. Fang, T.T. Hsu, C.Y. Lin, M.Y. Shie, The characteristics of mineral trioxide aggregate/polycaprolactone 3-dimensional scaffold with osteogenesis properties for tissue regeneration, *J. Endod.* 43 (2017) 923–929.
- [23] Y.S. Cho, M.W. Hong, M. Quan, S.Y. Kim, S.H. Lee, S.J. Lee, Y.Y. Kim, Y.S. Cho, Assessments for bone regeneration using the polycaprolactone SLUP (salt-leaching using powder) scaffold, *J. Biomed. Mater. Res. A* (12) (2017) 3432–3444.
- [24] P. Fabbri, V. Cannillo, A. Sola, A. Dorigato, F. Chiellini, Highly porous polycaprolactone-4585 Bioglass® scaffolds for bone tissue engineering, *Compos. Sci. Technol.* 70 (2010) 1869–1878.
- [25] T.D. Roy, J.L. Simon, J.L. Ricci, E.D. Rekow, V.P. Thompson, J.R. Parsons, Performance of degradable composite bone repair products made via three-dimensional fabrication techniques, *J. Biomed. Mater. Res. A* 66 (2003) 283–291.
- [26] G. Chen, T. Ushida, T. Tateishi, Poly(DL-lactic-co-glycolic acid) sponge hybridized with collagen microsponges and deposited apatite particulates, *J. Biomed. Mater. Res.* 57 (2001) 8–14.
- [27] V. Karageorgiou, D. Kaplan, Porosity of 3D biomaterial scaffolds and osteogenesis, *Biomaterials* 26 (2005) 5474–5491.
- [28] A.R. Amini, D.J. Adams, C.T. Laurencin, S.P. Nukavarapu, Optimally porous and biomechanically compatible scaffolds for large-area bone regeneration, *Tissue Eng Part A* 18 (2012) 1376–1388.
- [29] B. Feng, Z. Jinkang, W. Zhen, L. Jianxi, C. Jiang, L. Jian, M. Guolin, D. Xin, The effect of pore size on tissue ingrowth and neovascularization in porous bioceramics of controlled architecture in vivo, *Biomed. Mater.* 6 (2011) 015007.
- [30] D.G. Nelson, J.D. Featherstone, Preparation, analysis, and characterization of carbonated apatites, *Calcif. Tissue Int.* 34 (1982) 69–81.
- [31] G. Kister, G. Cassanas, M. Bergounhon, D. Hoarau, M. Vert, Structural characterization and hydrolytic degradation of solid copolymers of D,L-lactide-co- ϵ -caprolactone by Raman spectroscopy, *Polymer* 41 (2000) 925–932.
- [32] O. Hartman, C. Zhang, E.L. Adams, M.C. Farach-Carson, N.J. Petrelli, B.D. Chase, J.F. Rabolt, Biofunctionalization of electrospun PCL-based scaffolds with perlecan domain IV peptide to create a 3-D pharmacokinetic cancer model, *Biomaterials* 31 (2010) 5700–5718.
- [33] A. Baranowska-Korczyn, A. Warowicka, M. Jasiurkowska-Delaporte, B. Grzeskowiak, M. Jarek, B.M. Maciejewska, J. Jurga-Stopa, S. Jurga, Antimicrobial electrospun poly(ϵ -caprolactone) scaffolds for gingival fibroblast growth, *RSC Adv.* 6 (2016) 19647–19656.
- [34] Y. Yang, M. Chen, H. Li, H. Li, The degree of crystallinity exhibiting a spatial distribution in polymer films, *Eur. Polym. J.* 107 (2018) 303–307.
- [35] A. Weselucha-Birczyńska, M. Świętek, E. Sołtysiak, P. Galiński, L. Płachta, K. Piekara, M. Błażewicz, Raman spectroscopy and the material study of nano-composite membranes from poly(ϵ -caprolactone) with biocompatibility testing in osteoblast-like cells, *Analyst* 140 (2015) 2311–2320.
- [36] A.P. Kotula, C.R. Snyder, K.B. Migler, Determining conformational order and crystallinity in polycaprolactone via Raman spectroscopy, *Polymer* 117 (2017) 1–10.
- [37] P. Taddei, A. Tinti, M. Reggiani, C. Fagnano, In vitro mineralization of bioresorbable poly(ϵ -caprolactone)/apatite composites for bone tissue engineering: a vibrational and thermal investigation, *J. Mol. Struct.* 744–747 (2005) 135–143.
- [38] P. Taddei, M. Di Foggia, F. Causa, L. Ambrosio, C. Fagnano, In vitro bioactivity of poly(ϵ -caprolactone)-apatite (PCL-AP) scaffolds for bone tissue engineering: the influence of the PCL/AP ratio, *Int. J. Artif. Organs* 29 (2006) 719–725.
- [39] M. Di Foggia, U. Corda, E. Plescia, P. Taddei, A. Torreggiani, Effects of sterilisation by high-energy radiation on biomedical poly(ϵ -caprolactone)/hydroxyapatite (PCL/HA) composites, *J. Mater. Sci. Mater. Med.* 21 (2010) 1789–1797.

- [40] V. Guarino, V. Cirillo, P. Taddei, M.A. Alvarez-Perez, L. Ambrosio, Tuning size scale and crystallinity of PCL electrospun fibres via solvent permittivity to address hMSC response, *Macromol. Biosci.* 11 (2011) 1694–1705.
- [41] V. Crescenzi, G. Manzini, G. Calzolari, C. Borri, Thermodynamics of fusion of poly- β -propiolactone and poly- ϵ -caprolactone. Comparative analysis of the melting of aliphatic polylactone and polyester chains, *Eur. Polym. J.* 8 (1972) 449–463.
- [42] Tang M, Purcell M, Steele JAM Lee KY, McCullen S, Shakesheff KM, Bismark A, Stevens MM, Howdle SM, Williams CK. Porous copolymers of ϵ -PCL as scaffolds for tissue engineering, *Macromolecules* 2013; 46:8136–8143.
- [43] S.S. Potgieter-Vermaak, J.H. Potgieter, R. Van Grieken, The application of Raman spectrometry to investigate and characterize cement, part I: a review, *Cem. Concr. Res.* 36 (2006) 656–662.
- [44] M. Conjeaud, H. Boyer, Some possibilities of Raman microprobe in cement chemistry, *Cem. Concr. Res.* 10 (1980) 61–70.
- [45] H. Madupalli, B. Pavan, M.M.J. Tecklenburg, Carbonate substitution in the mineral component of bone: discriminating the structural changes, simultaneously imposed by carbonate in A and B sites of apatite, *J. Solid State Chem.* 255 (2017) 27–35.
- [46] N.F. Mohammad, R. Othman, F.Y. Yeoh, Controlling the pore characteristics of mesoporous apatite materials: hydroxyapatite and carbonate apatite, *Ceram. Int.* 41 (2014) 10624–10633.
- [47] C.H. Park, H.F. Rios, Q. Jin, M.E. Bland, C.L. Flanagan, S.J. Hollister, W.V. Giannobile, Biomimetic hybrid scaffolds for engineering human tooth-ligament interfaces, *Biomaterials* 31 (2010) 5945–5952.
- [48] N. Wongsupa, T. Nuntanarant, S. Kamolmattayakul, N. Thuaksuban, Assessment of bone regeneration of a tissue-engineered bone complex using human dental pulp stem cells/poly(ϵ -caprolactone)-biphase calcium phosphate scaffold constructs in rabbit calvarial defects, *J Mater Sci Mater Med* 28 (2017) 77, <https://doi.org/10.1007/s10856-017-5883-x>.
- [49] S.H. Huang, T.T. Hsu, T.H. Huang, C.Y. Lin, M.Y. Shie, Fabrication and characterization of polycaprolactone and tricalcium phosphate composites for tissue engineering applications, *J Dent Sci* 12 (2017) 33–43.
- [50] Y.H. Lin, Y.C. Chiu, Y.F. Shen, Y.H.A. Wu, M.Y. Shie, Bioactive calcium silicate/poly- ϵ -caprolactone composite scaffolds 3D printed under mild conditions for bone tissue engineering, *J. Mater. Sci. Mater. Med.* 29 (2018) 11, <https://doi.org/10.1007/s10856-017-6020-6>.
- [51] C.C. Ho, H.Y. Fang, B. Wang, T.H. Huang, M.Y. Shie, The effects of biodentine/polycaprolactone three-dimensional-scaffold with odontogenesis properties on human dental pulp cells, *Int. Endod. J.* 51 (2018) 291–300.
- [52] R. Neppalli, V. Causin, C. Marega, R. Saini, M. Mba, A. Marigo, Structure, morphology, and biodegradability of poly(ϵ -caprolactone)-based nanocomposites, *Polym. Eng. Sci.* 51 (2011) 1489–1496.
- [53] N. Koupaei, A. Karkhaneh, M. Daliri Joupri, Preparation and characterization of (PCL-crosslinked-PEG)/hydroxyapatite as bone tissue engineering scaffolds, *J Biomed Mater Res Part A* 103 (2015) 3919–3926.
- [54] M. Dziadek, J. Pawlik, E. Menaszek, E. Stodolak-Zych, K. Cholewa-Kowalska, Effect of the preparation methods on architecture, crystallinity, hydrolytic degradation, bioactivity, and biocompatibility of PCL/bioglass composite scaffolds, *J Biomed Mater Res Part B: Appl Biomater* 103B (2015) 1580–1593.
- [55] K. Žukienė, V. Jankauskaite, V. Betingyte, A. Baltusnikas, Properties of recycled polycaprolactone-based thermoplastic polyurethane filled with montmorillonites, *J. Appl. Polym. Sci.* 128 (2013) 2186–2196.
- [56] V. Romeo, G. Gorrasi, V. Vittoria, Encapsulation and exfoliation of inorganic lamellar fillers into polycaprolactone by electrospinning, *Biomacromolecules* 8 (2007) 3147–3152.
- [57] C.X.F. Lam, M.M. Savalani, S.H. Teoh, D.W. Hutmacher, Dynamics of in vitro polymer degradation of polycaprolactone-based scaffolds: accelerated versus simulated physiological conditions, *Biomed. Mater.* 3 (2008) 034108, <https://doi.org/10.1088/1748-6041/3/3/034108>.
- [58] G.O. Gallucci, A. Hamilton, W. Zhou, D. Buser, S. Chen, Implant placement and loading protocols in partially edentulous patients: a systematic review, *Clin. Oral Implants Res.* 29 (2018) 106–134.
- [59] Q.L. Loh, C. Choong, Three-dimensional scaffolds for tissue engineering applications: role of porosity and pore size, *Tissue Eng Part B Rev* 19 (2013) 485–502.
- [60] M.G. Gandolfi, G. Ciapetti, P. Taddei, F. Perut, A. Tinti, M.V. Cardoso, B. Van Meerbeek, C. Prati, Apatite formation on bioactive calcium-silicate cements for dentistry affects surface topography and human marrow stromal cells proliferation, *Dent. Mater.* 26 (2010) 974–992.
- [61] C. Estrela, G.B. Sydney, L.L. Bammann, Felipe Júnior O. Mechanism of action of calcium and hydroxyl ions of calcium hydroxide on tissue and bacteria, *Braz. Dent. J.* 6 (1995) 85–90.
- [62] T. Okabe, M. Sakamoto, H. Takeuchi, K. Matsushima, Effects of pH on mineralization ability of human dental pulp cells, *J Endod* 32 (3) (2006) 198–201.
- [63] K.F. Lovato, C.M. Sedgley, Antibacterial activity of endosseous root repair material and proroot MTA against clinical isolates of *Enterococcus faecalis*, *J Endod* 37 (2011) 1542–1546.
- [64] U. Ripamonti, Biomimetism, biomimetic matrices and the induction of bone formation, *J. Cell. Mol. Med.* 13 (2009) 2953–2972.
- [65] G.Y. Jung, Y.J. Park, J.S. Han, Effects of HA released calcium ion on osteoblast differentiation, *J Mater Sci Mat Med* 21 (2010) 1649–1654.
- [66] J. Sun, L. Wei, X. Liu, J. Li, B. Li, G. Wang, F. Meng, Influences of ionic dissolution products of dicalcium silicate coating on osteoblastic proliferation, differentiation and gene expression, *Acta Biomater.* 5 (2009) 1284–1293.
- [67] A. Paranjpe, H. Zhang, J.D. Johnson, Effects of mineral trioxide aggregate on human dental pulp cells after pulp-capping procedures, *J Endod* 36 (2010) 1042–1047.
- [68] S. Wang, X. Wang, F.G. Draenert, O. Albert, H.C. Schröder, V. Mailänder, G. Mitov, W.E. Müller, Bioactive and biodegradable silica biomaterial for bone regeneration, *Bone* 67 (2014) 292–304.
- [69] W. Zhai, H. Lu, L. Chen, X. Lin, Y. Huang, K. Dai, K. Naoki, G. Chen, J. Chang, Silicate bioceramics induce angiogenesis during bone regeneration, *Acta Biomater.* 8 (2012) 341–349.
- [70] S.J. Smith, R. Emery, A. Pitsillides, C.E. Clarkin, S. Mahajan, Detection of early osteogenic commitment in primary cells using Raman spectroscopy, *Analyst* 30 (142) (2017) 1962–1973.
- [71] W.R. Lloyd, S. Agarwal, S.U. Nigwekar, K. Esmonde-White, S. Loder, S. Fagan, J. Goverman, B.R. Olsen, D. Jumlongras, M.D. Morris, B. Levi, Raman spectroscopy for label-free identification of calciphylaxis, *J. Biomed. Opt.* 20 (2015) 80501.
- [72] C.P. Tarnowski, M.A. Igelzli Jr., M.D. Morris, Mineralization of developing mouse calvaria as revealed by Raman microspectroscopy, *J. Bone Miner. Res.* 17 (2002) 1118–1126.
- [73] B. Wopenka, A. Kent, J.D. Pasteris, Y. Yoon, S. Thomopoulos, The tendon-to-bone transition of the rotator cuff: a preliminary Raman spectroscopic study documenting the gradual mineralization across the insertion in rat tissue samples, *Appl. Spectrosc.* 62 (2008) 1285–1294.
- [74] G. Penel, C. Delfosse, M. Descamps, G. Leroy, Composition of bone and apatitic biomaterials as revealed by intravital Raman microspectroscopy, *Bone* 36 (2005) 893–901.
- [75] K.K. Gupta, A. Kundan, P.K. Mishra, P. Srivastava, S. Mohanty, N.K. Singh, A. Mishra, P. Maiti, Polycaprolactone composites with TiO₂ for potential nanobiomaterials: tunable properties using different phases, *Phys. Chem. Phys.* 14 (2012) 12844–12853.
- [76] Y.L. Cheng, Y.W. Chen, K. Wangde, M.Y. Shie, Enhanced adhesion and differentiation of human mesenchymal stem cell inside apatite mineralized/poly(dopamine)-coated poly(ϵ -caprolactone) scaffolds by stereolithography, *J. Mater. Chem. B* 4 (2016) 6307–6315.
- [77] Z. Heydari, D. Mohebbi-Kalhor, M.S. Afarani, Engineered electrospun polycaprolactone (PCL)/octacalcium phosphate (OCP) scaffold for bone tissue engineering, *Mater. Sci. Eng. C Mater. Biol. Appl.* 81 (2017) 127–132.
- [78] K. Khoshroo, T.S. Jafarzadeh Kashi, F. Moztarzadeh, M. Tahriri, H.E. Jazayeri, L. Tayebi, Development of 3D PCL microsphere/TiO₂ nanotube composite scaffolds for bone tissue engineering, *Mater Sci Eng C* 70 (2017) 586–598.
- [79] I. Gerçek Beşkardeş, M. Gümüşderelioglu, Biomimetic apatite-coated PCL scaffolds: effect of surface nanotopography on cellular functions, *J. Bioact. Compat. Polym.* 24 (2009) 507–524.
- [80] S.A. Park, J.B. Lee, Y.E. Kim, J.E. Kim, J.H. Lee, J.W. Shin, I.K. Kwon, W.D. Kim, Fabrication of biomimetic PCL scaffold using rapid prototyping for bone tissue engineering, *Macromol. Res.* 22 (2014) 882–887.
- [81] A. Suryavanshi, K. Khanna, K.R. Sindhu, J. Bellare, R. Srivastava, Magnesium oxide nanoparticle-loaded polycaprolactone composite electrospun fiber scaffolds for bone-soft tissue engineering applications: in-vitro and in-vivo evaluation, *Biomed. Mater.* 12 (2017) 055011, <https://doi.org/10.1088/1748-605X/aa792b>.
- [82] Langer R in: Kahn J, Ratner BD, Hoffmann AS, Schoen FJ, Lemons JE (Eds.), *Biomaterials Science. An Introduction to Materials in Medicine*, Academic Press, San Diego, 1996, p. 64.
- [83] M. Vert, S.M. Li, G. Splenlehauer, P. Guerin, Bioresorbability and biocompatibility of aliphatic polyesters, *J Mater Sci Mater Med* 3 (1992) 432–446.
- [84] P. Taddei, A. Tinti, G. Fini, Vibrational spectroscopy of polymeric biomaterials, *J. Raman Spectrosc.* 32 (2001) 619–629.
- [85] P. Taddei, R. Simoni, G. Fini, Spectroscopic study on the in vitro degradation of a biodegradable composite periodontal membrane, *J. Mol. Struct.* 565-566 (2011) 317–322.
- [86] M. Rutkowska, A. Dereszewska, M. Jastrzębska, H. Janik, Biodegradation of polycaprolactone in plant treatment active sludge, *Macromol Sympos* 130 (1998) 199–204.
- [87] C.H.F. Lam, D.W. Hutmacher, J.T. Schantz, M.A. Woodruff, S.H. Teoh, Evaluation of polycaprolactone scaffold degradation for 6 months in vitro and in vivo, *J. Biomed. Mater. Res.* 90 (2009) 906–919.
- [88] T. Yoshioka, F. Kamada, N. Kawazoe, T. Tateishi, G. Chen, Structural changes and biodegradation of PLLA, PCL, and PLGA sponges during in vitro incubation, *Polym. Eng. Sci.* 50 (2010) 1895–1903.
- [89] D.R. Chen, J.Z. Bei, G. Wang, Polycaprolactone microparticles and their biodegradation, *Polym. Degrad. Stab.* 67 (2000) 455–459.
- [90] Z. Gan, Q. Liang, J. Zhang, X. Jing, Enzymatic degradation of poly(ϵ -caprolactone) film in phosphate buffer solution containing lipases, *Polym. Degrad. Stab.* 56 (1997) 209–213.
- [91] S. Hermanova, R. Balkova, S. Voberkova, I. Chamradova, J. Omelkova, L. Richtera, L. Mravcova, J. Jancar, Biodegradation study on poly(ϵ -caprolactone) with bimodal molecular weight distribution, *J. Appl. Polym. Sci.* 127 (2013) 4726–4735.
- [92] Wang Y, Liu L, Guo. Characterization of biodegradable and cytocompatible nanohydroxyapatite/polycaprolactone porous scaffolds in degradation in vitro. *Polym. Degrad. Stab.* 2010; 95: 207–213.

Article

PLA-Based Mineral-Doped Scaffolds Seeded with Human Periapical Cyst-Derived MSCs: A Promising Tool for Regenerative Healing in Dentistry

Marco Tatullo ¹, Gianrico Spagnuolo ², Bruna Codispoti ¹, Fausto Zamparini ³, Anqi Zhang ⁴, Micaela Degli Esposti ⁵, Conrado Aparicio ⁴, Carlo Rengo ⁶, Manuel Nuzzolese ⁷, Lucia Manzoli ⁸, Fabio Fava ⁵, Carlo Prati ³, Paola Fabbri ⁵ and Maria Giovanna Gandolfi ^{3,*}

¹ Tecnologica Research Institute, Stem Cell Unit, 88900 Crotona, Italy;

marco.tatullo@tecnologicasrl.com (M.T.); bruna.codispoti@tecnologicasrl.com (B.C.)

² Department of Neurosciences, Reproductive and Odontostomatological Sciences, University of Naples “Federico II”, 80131 Napoli, Italy; gianrico.spagnuolo@gmail.com

³ Laboratory of Biomaterials and Oral Pathology, School of Dentistry, Department of Biomedical and Neuromotor Sciences, University of Bologna, 40125 Bologna, Italy; fausto.zamparini2@unibo.it (F.Z.); carlo.prati@unibo.it (C.P.)

⁴ MDRCBB-Minnesota Dental Research Center for Biomaterials and Biomechanics, School of Dentistry, University of Minnesota, Minneapolis, MN 55455, USA; azhang@umn.edu (A.Z.); apari003@umn.edu (C.A.)

⁵ Department of Civil, Chemical, Environmental and Materials Engineering, University of Bologna, 40131 Bologna, Italy; micaela.degliesposti@unibo.it (M.D.E.); fabio.fava@unibo.it (F.F.); p.fabbri@unibo.it (P.F.)

⁶ Department of Prosthodontics and Dental Materials, School of Dental Medicine, University of Siena, 53100 Siena, Italy; carlo.rengo@alice.it

⁷ University Hospitals Birmingham—NHS Foundation Trust, Birmingham B152GW, UK; manuelnuzzolese@libero.it

⁸ Cellular Signalling Laboratory, Institute of Human Anatomy, Department of Biomedical and Neuromotor Sciences, University of Bologna, 40126 Bologna, Italy; lucia.manzoli@unibo.it

* Correspondence: mgiovanna.gandolfi@unibo.it

Received: 22 January 2019; Accepted: 12 February 2019; Published: 16 February 2019



Abstract: Human periapical cyst mesenchymal stem cells (hPCy-MSCs) are a newly discovered cell population innovatively collected from inflammatory periapical cysts. The use of this biological waste guarantees a source of stem cells without any impact on the surrounding healthy tissues, presenting a valuable potential in tissue engineering and regenerative medicine applications. In the present study, hPCy-MSCs were collected, isolated, and seeded on three experimental mineral-doped porous scaffolds produced by the thermally-induced phase-separation (TIPS) technique. Mineral-doped scaffolds, composed of polylactic acid (PLA), dicalcium phosphate dihydrate (DCPD), and/or hydraulic calcium silicate (CaSi), were produced by TIPS (PLA-10CaSi, PLA-5CaSi-5DCPD, PLA-10CaSi-10DCPD). Micro-CT analysis evaluated scaffolds micromorphology. Collected hPCy-MSCs, characterized by cytofluorimetry, were seeded on the scaffolds and tested for cell proliferation, cells viability, and gene expression for osteogenic and odontogenic differentiation (DMP-1, OSC, RUNX-2, HPRT). Micro-CT revealed an interconnected highly porous structure for all the scaffolds, similar total porosity with 99% open pores. Pore wall thickness increased with the percentage of CaSi and DCPD. Cells seeded on mineral-doped scaffolds showed a superior proliferation compared to pure PLA scaffolds (control), particularly on PLA-10CaSi-10DCPD at day 12. A higher number of non-viable (red stained) cells was observable on PLA scaffolds at days 14 and 21. DMP-1 expression increased in hPCy-MSCs cultured on all mineral-doped scaffolds, in particular on PLA-5CaSi-5DCPD and PLA-10CaSi-10DCPD. In conclusion, the innovative combination of experimental scaffolds colonized with autologous stem cells from periapical cyst represent a promising strategy for regenerative healing of periapical and alveolar bone.

Keywords: polylactic acid (PLA)-based scaffolds; calcium silicate-containing scaffolds; bioactive scaffolds; porous scaffolds; human periapical cyst mesenchymal stem cells (hPCy-MSCs); regenerative dentistry; thermally induced phase separation technique (TIPS)

1. Introduction

The main stem cell ability to regenerate injured tissues confers them a central role in regenerative medicine. The first success obtained with hematopoietic stem cells encouraged studies on stem cell therapy for the treatment of several human diseases [1,2].

Mesenchymal stem cells (MSCs) retain both the proliferation ability and the capability to modulate inflammatory and immune response. These peculiar features strongly triggered the searching for novel sources of MSCs. The early MSCs were successfully isolated from bone marrow (hBM): surgical harvesting of hBM-MSCs is not a simple procedure, in fact, patients must undergo an invasive surgery to aspirate bone marrow from the iliac crests, and cells obtained from hBM are typically few [3]. The numerous issues related to MSCs collection have attracted the interest of researchers in discovering alternative sources of MSCs, in order to obtain them without any invasive or painful procedure.

Dental pulp infections and necrosis could lead to the formation of inflammatory tissues, richly infiltrated by macrophages, neutrophils, and lymphocytes, in the periapical region (periapical granuloma), with a consequent onset of apical periodontitis. The chronicization of such an inflammatory condition may evolve towards periapical cyst formation [4]. Endodontic inflammatory cysts have a high prevalence and they increase in elderly patients: 5% of teeth and 25% of teeth treated endodontically can have a periapical x-ray discovered lesion [5]. These data are probably highly under-estimated [6].

Recently, human periapical cyst-derived mesenchymal stem cells (hPCy-MSCs) were isolated by Italian researchers [7]. hPCy-MSCs population share the same phenotype with other types of oral derived MSCs, such as dental pulp stem cells. Such cells are characterized by high expression of stemness-related markers: CD13, CD29, CD44, CD73, CD90, CD105, and some hematopoietic markers, such as CD45 and CD34. [8,9] The high expression of CD146 on the surface of hPCy-MSCs is also linked to the multipotency of these cells [10]. hPCy-MSCs showed a great plasticity, showing a surprising odontogenic/osteogenic [11] and a neurogenic commitment [12] under specific conditions. The epithelial wall of inflammatory cysts represents an attractive source of mesenchymal stem cells to be used in regenerative medicine with special regards to orthopedic and dental applications [3]. Oral-derived stem cells associated with specific biomaterials are currently used in many tissue engineering procedures [13], with special regards to bone regeneration [14,15]. However, the right scaffold is still a challenging searching, in order to merge the best MSCs with the best scaffold.

When considering tissue engineering, a 3D porous scaffold is necessary for cells attachment, proliferation, differentiation, new blood vessels ingrowth, and, finally, new tissue formation [16]. An ideal scaffold for bone application should be extremely porous, biocompatible, biointeractive (able to release biologically relevant ions), with tailored resorption and adequate mechanical properties. Combining a polymeric matrix with one or more bioactive or biointeractive filler represents an interesting strategy in bone tissue engineering. Composite materials usually show an excellent balance between the strengths and weaknesses of their individual components. In this way, the fabrication of polymeric scaffolds is much easier and less time-consuming compared to ceramic scaffolds, which are also brittle and less versatile [17]. Calcium phosphate compounds such as hydroxyapatite and dicalcium and tricalcium phosphates are some of the most extensively fillers used in bone tissue engineering [18]. These materials alone however, cannot provide the necessary biointeractive, bioactive, and mechanical properties for dental tissue engineering. Hydroxyapatite doped scaffolds demonstrated osteoconductive and long-term bone tissue stability, but revealed significant brittleness

at high loadings [18,19], while b-TCP is highly-interactive but fast-resorbing and unable to provide a long-term template to support cells migration from the periphery of the grafted area [20,21].

Calcium silicates (CaSi) are hydraulic cements widely used in regenerative endodontics in close vicinity to pulp or bone tissue [22–24]. Nowadays, CaSi-based materials are used in several endodontic applications, such as root canal sealing [25,26], root-end filling materials [27], and for direct pulp capping [22]. CaSi biointeractivity and the property to nucleate calcium phosphates/apatite suggest their pivotal role in mineral tissue regeneration by activating the osteogenic potential and promoting the differentiation of mineralizing-cells [24]. The combination of reactive calcium phosphates (such as dicalcium phosphate dehydrate, DCPD) to CaSi materials demonstrated to enhance their biological properties and apatite-forming ability [28,29].

Several techniques have been developed to produce polymeric scaffolds for tissue engineering, including electrospinning technique [30], 3D printing [31], salt leaching [32], and thermally induced phase separation (TIPS) [33,34]. Hybrid Poly-ε-caprolactone-polyglycolic acid solution was used to produce biodegradable scaffolds by a 3D mold for human tooth-ligament in dental applications [35]. Then, polymeric composites containing biphasic calcium phosphate (80:20 wt %) prepared by hot melt extrusion (100 °C) for 3D printing were able to support the differentiation of human dental pulp stem cells into osteogenic lineage in calvarial defects [36]. Polymeric composites doped with 10–50 wt % of β-tricalcium phosphate produced by a foaming agent and heating at 90 °C demonstrated to promote proliferation of human bone marrow mesenchymal stem cells also supporting the differentiation to reparative hard tissue [37]. All these materials, however, failed to comply with porosity values over 90%.

TIPS is an experimental procedure to produce highly porous scaffolds without using high temperatures (which may alter the fillers properties). Our recent study found that a Polylactic Acid (PLA) polymeric scaffold doped with considerable amounts of bioactive and biointeractive fillers (up to 20%) and having a bulk porosity higher than 90% may be produced by TIPS [34].

The association of these promising scaffolds with hPCy-MSCs may result as an interesting regenerative approach in periapical regeneration and healing, where scaffolds with biointeractive bone-stimulating properties may be placed in the presence of large periapical bone defects.

Therefore, the aim of this study was to test the biological activity of mineral-doped CaSi-DCPD porous scaffolds by human periapical cyst-mesenchymal stem cells (hPCy-MSCs).

2. Materials and Methods

2.1. Materials

Poly(L-lactic acid MW = 65,000 g/mol) (Ingeo™ biopolymer PLA 4060D, Natureworks LLC, Blair, NE, USA) was used. Methanol (MeOH), ethanol (EtOH, 99.8%), 1,4-dioxan (DIOX), and chloroform (CHCl₃, HPLC grade) all from Sigma Aldrich (Milan, Italy) were used as received without further purification. PLA was received in pellet form and purified via dissolution in CHCl₃ (10% wt/vol) and reprecipitation in a large excess of cold MeOH, in order to eliminate residual polymerization catalysts [33]. Dicalcium phosphate dihydrate (DCPD; CaHPO₄·2H₂O) powders (Sigma-Aldrich, Steinheim, Germany) [22,29] and/or calcium silicate (CaSi) powders (Aalborg, Denmark) [23] composed of dicalcium silicate, tricalcium silicate, tricalcium aluminate, and calcium sulfate were prepared by melt-quenching technique and milling procedures [34].

2.2. TIPS Scaffolds Preparation

Porous mineral-doped scaffolds were prepared starting from PLA solutions in DIOX (3.5% wt/vol) as solvent and porogen agent; CaSi and DCPD powders were added to the PLA solution in amounts 5% or 10% by weight with respect to PLA. Homogeneous dispersions were obtained by sonicating the mixtures for 3 h using an ultrasonic processor (UP50H, Hielscher Ultrasonics, Teltow, Germany) working at 50 watts and 30 kHz, equipped with a sonotrode MS2 (made of titanium, tip diameter

2 mm). After mixing, solutions were placed inside disposable aluminium dishes of 60 mm in diameter, and cooled at $-18\text{ }^{\circ}\text{C}$. After 18 h, the frozen samples were removed from the dishes and fully immersed for 48 h in EtOH bath precooled at $-18\text{ }^{\circ}\text{C}$, with solvent refresh every 3 h for the DIOX extraction procedure. Then the porous samples were placed under vacuum and completely dried [33,34].

The prepared scaffolds were: PLA-10CaSi, PLA-5CaSi-5DCPD, PLA-10CaSi-10DCPD, and PLA as control.

2.3. Scaffold Characterization by Micro-CT

A coring/cylindrical section of each scaffold formulation has been used for micro-CT analysis (HMX-XT 225 X-tek system, Nikon, Minneapolis, MI, USA) (Figure 1). The scanning parameters used were 80 KV voltage, 69 μA Current, 35.3 magnification, 354 ms exposure time length, and 30,000 Shading correction white Target. The resolution of the scanned images was 5.66 μm . Two randomly selected cross-sectional slices of each scanned scaffold sample were shown here. All the images were adjusted to the same grey value range.

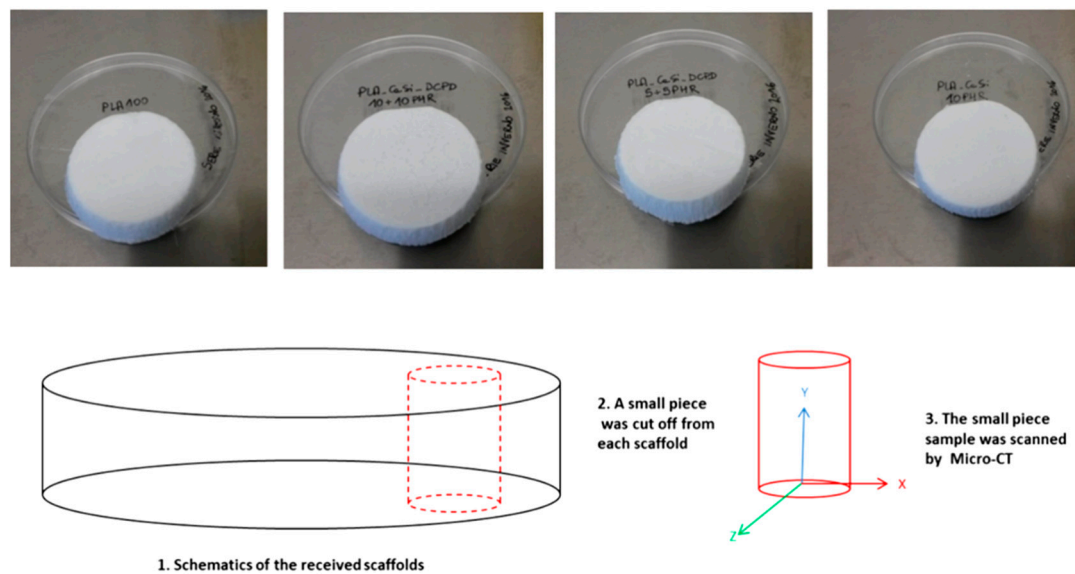


Figure 1. Highly-porous polylactic acid (PLA) scaffolds added with dicalcium phosphate dihydrate (DCPD) and/or hydraulic calcium silicate (CaSi) used in this study: Micro-CT scanning slices protocol.

The total porosity, open porosity, and the average wall thickness of each sample were analyzed based on the reconstructed 3D structure. After scanning, reconstruction of the original scanning pictures was performed using CT Pro 3D XT 3.1.11 (Nikon Metrology Brighton, MI, USA). VGSTUDIO MAX 3.1 (Volume Graphics Charlotte, NC, USA) was used to export slices of the reconstructed images to .dicom format, so that porosity and wall thickness analysis of the scaffolds could be quantified using CT Analyser 1.14.4.1+ (2012-14 Bruker microCT). For the porosity and wall thickness analysis, 16-bit .dicom slices were transferred to binary images. A proper threshold range was selected to show the scaffold structure in the binary version. After that, the binary images were transferred into the *Morphometry* version. The comparison between 16-bit .dicom version and the transferred *Morphometry* version was done for multiple slices of each sample to guarantee the selected threshold was reliable enough to show the scaffold structure as much as possible. With the images determined for optimal *Morphometry* the 3D total porosity, the 3D open porosity, and the average wall thickness were calculated for the whole 3D structure.

2.4. Cell Culture

Human third molars affected by massive caries were obtained after written informed consent from volunteers and collaborators requiring teeth extraction for severe pulp necrosis and local inflammation; after tooth extraction, inflammatory periapical cystic tissues were removed along with necrotic tooth. Surgical procedures were performed at Calabrodental Dental clinic in Crotona, Italy (ethical committee agreement code was: CBD-021/TRI/2016). All clinical investigations have been conducted according to the principles reported in the Declaration of Helsinki.

The isolation of human periapical cyst-derived mesenchymal stem cells (hPCy-MSCs) was obtained by the enzymatic digestion of cystic wall, with the aim to collect MSCs to further characterize in the following steps.

More in details, the cystic tissue was washed 5 times with phosphatase buffer saline (PBS, Corning, Manassas, VA, USA) added with 1% penicillin-streptomycin antibiotics (Invitrogen, 15140122, Carlsbad, CA, USA), and 2.5 µg/mL amphotericin B antimycotic (Invitrogen, 15290026, Carlsbad, CA, USA).

Then, the tissue was minced with a sterile scalpel and placed into a PBS solution, containing 3 mg/mL type I collagenase (Invitrogen, 17100-017, Carlsbad, CA, USA) with 4 mg/ml dispase (Sigma, D4818, Milan, Italy) for 2 h at 37 °C for a proper enzymatic digestion. The obtained solution was filtered, and the cells were collected after centrifugation at 1500RPM for 10 min: cells were plated in alpha-minimal essential medium (α-MEM) (Invitrogen, Carlsbad, CA, USA) added with 10% foetal bovine serum (FBS; Invitrogen, Carlsbad, CA, USA), 2mM glutamine, P/S (Invitrogen Carlsbad, CA, USA), and amphotericin-B (Invitrogen Carlsbad, CA, USA).

These cells were finally incubated at 37 °C and 5% CO₂, and the medium was replaced bi-weekly. Different batches of cells were used for this specific study.

2.5. Cytofluorimetric Analysis

Isolated cells were phenotypically investigated for the expression of mesenchymal stem cell-like markers using the following antibodies: anti-CD13 (PE, 560998, Becton Dickinson, San Jose, CA, USA), anti-CD90 (PE, 555596, Becton Dickinson, San Jose, CA, USA), anti-CD105 (APC, 562408, Becton Dickinson, San Jose, CA, USA), anti-CD73 (FITC, 561254, Becton Dickinson, San Jose, CA, USA), anti-CD146 (PE, sc-18837, Santa Cruz Biotechnology, Inc), anti-CD44 (FITC, 560977, Becton Dickinson, San Jose, CA, USA), and anti-CD29 (APC, 561794, Becton Dickinson, San Jose, CA, USA).

The absence of hematopoietic markers was assessed using anti-CD34 (FITC, 130-098-142, Miltenyi Biotec, Bergisch Gladbach, Germania), anti-CD45 (APC-H7, 560178, Becton Dickinson, EU), and anti-HLA-DR (PE, 130-104-873, Miltenyi Biotec, Bergisch Gladbach, Germania) antibodies. Cytofluorimetric measurements were performed using a NAVIOS instrument (Navios Flow Cytometer, Beckman Coulter, Life Sciences, Indianapolis, IN, USA) and the Kaluza 1.3 program (Kaluza Analysis Software, Beckman Coulter, Life Sciences, Indianapolis, IN, USA) was used for data analysis.

2.6. Proliferation Assay

The scaffolds were sized as 1 cm² squared pieces, with a sterile scalpel (0.5 cm thickness), and sterilized by UV-rays exposure for 2 h, and finally pre-incubated for 2 h with complete medium in 24-wells plates.

HPCy-MSCs were seeded in concentration of 7×10^5 on PLA-10CaSi, PLA-5CaSi-5DCPD and PLA-10CaSi-10DCPD scaffolds and incubated in α-MEM complete medium (see above) at 37 °C and 5% CO₂ enriched atmosphere; pure PLA scaffolds were used as control.

The same number of cells were plated on tissue culture treated 24-well plate as growth control.

Presto Blue reagent (Invitrogen, A13261, Carlsbad, CA, USA) has been used as metabolic assay for the evaluation of cell growth. Presto Blue reagent was diluted according to manufacturer's instructions and added to the wells containing the scaffolds seeded with hPCy-MSCs or the empty scaffolds (negative control).

After incubation for 2 h at 37 °C and 5% CO₂, the absorbance of resazurin dye was measured using a Multiskan GO (Thermo Fisher N10588, Waltham, MA, USA) spectrophotometer at 570–600 nm wavelength. Metabolic assays were performed at days 3, 7, 10, and 14.

2.7. Live/Dead Assay

The presence of viable and/or non-viable cells seeded on scaffolds was detected by staining samples with a solution of 2 µM Calcein AM (acetoxymethyl) and 4 µM EthDIII (Ethidium Homodimer III, Biotium, Hayward, 30002, CA, USA) in PBS. Calcein AM stains viable cells by emitting a green fluorescent signal (FITC) instead EthD-III stains only dead cells in red (rhodamine).

After 2 washings with PBS, samples were incubated with the staining-solution for 40 min at room temperature.

Fluorescent signal was revealed through a confocal laser scanning microscope (CLSM) (SP5, Leica, Wetzlar, Germany) and relative images were acquired by a microscope associated camera.

Live/dead assay has been performed at days 7, 14, and 21.

2.8. qPCR

After 21 days of cell culture, scaffolds seeded with hPCy-MSCs were washed with PBS and then cells have been harvested by using TRIzol reagent (Thermo Fisher, Carlsbad, CA, USA).

The Purelink™ RNA mini kit (Applied Biosystems, Vilnius, Lithuania) was used for RNA extraction, quantification of total RNA was performed by using a Multiskan Go spectrophotometer (Thermo scientific, Waltham, MA, USA). Total RNA samples (250 ng) were subjected to the reverse-transcription reaction using the High Capacity RNA-to-cDNA Kit (Applied Biosystems, Vilnius, Lithuania). cDNA samples were amplified by real-time PCR with the power SYBR green PCR Master Mix (Applied Biosystems, Vilnius, Lithuania) with 2 pmol of primers in a total volume of 10 µL.

Real-time PCR reactions were performed using a Pikoreal 96 (Thermo Fisher, Carlsbad, CA, USA) apparatus with the following conditions: initial denaturation step at 95 °C for 10 min, followed by 40 cycles of 10 s at 95 °C and 1 min at 60 °C. Relative expression levels were calculated using the $\Delta\Delta C_t$ method after normalization to the expression of the HRPT housekeeping gene.

Primer sequences for Runt-related transcription factor-2 (RUNX-2), dentin matrix protein-1 (DMP-1) and osteocalcin (OSC) genes are listed below:

RUNX-2

For: ATGTGTGTTTGTTCAGCAGCA

Rev: TCCCTAAAGTCACTCGGTATGTGTA

DMP-1

For: GTGAGTGAGTCCAGGGGAGATAA

Rev: TTTTGAGTGGGAGAGTGTGTGC

OSC

For: TGAGAGCCCTCACACTCCTC

Rev: ACCTTTGCTGGACTCTGCAC

2.9. Statistical Analysis

Results are expressed as the mean \pm standard deviation (SD) of three specific different experiments.

3. Results

3.1. Scaffolds Characterization by Micro-CT

In the PLA scaffold (control), micro-CT scan of 2 random slices revealed a heterogeneous highly porous structure (Figure 2). Pores appeared not to be uniform in size and shape with macro-pores ranging from 0.5 to 1.5 mm and large empty spaces in the central part of the structure. PLA-10CaSi

scaffolds had a highly porous, “honey-comb” like, and more regular structure (Figure 3) than the control scaffolds. Differently from the pure PLA sample, no empty areas were present in the central portion of the PLA-10CaSi scaffold. However, large pores (approx. 1 mm in radius) were evident in some parts of the scaffold. Smaller regular-shaped pores constituted most of the structure of these scaffolds. The small granules of the minerals conferred a higher radiopacity to these scaffolds compared to the control scaffolds, which allowed visualization of a more defined structure and indicated the mineral particles were well-distributed along the whole scaffold volume.

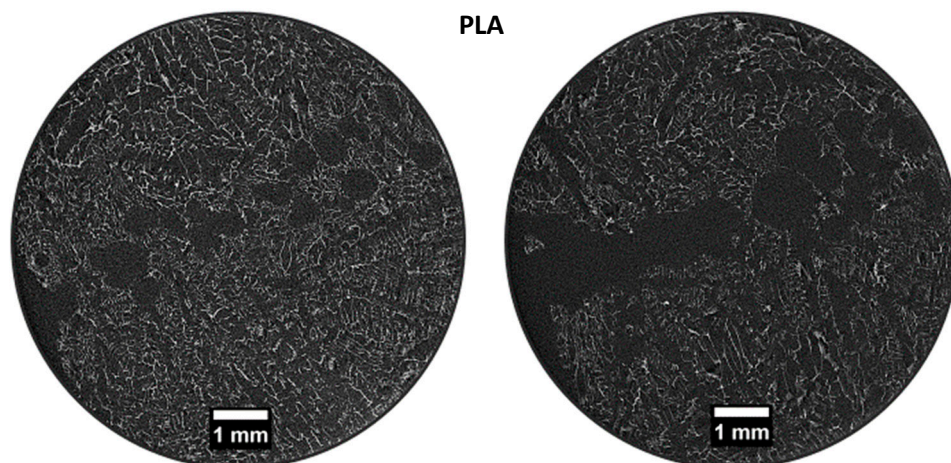


Figure 2. Micro-CT scan of 2 random slices of PLA scaffold, revealing a heterogeneous highly porous structure with a central empty area, attributable to sample brittleness.

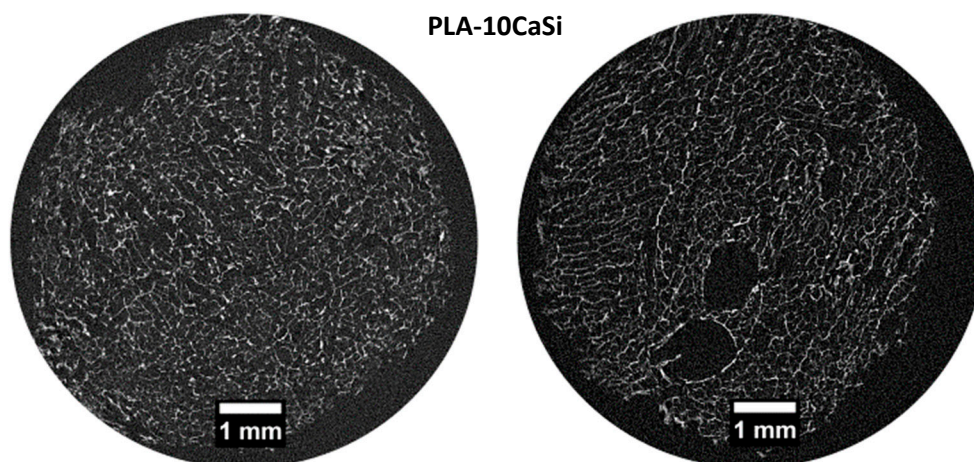


Figure 3. Micro-CT scan of 2 random slices of PLA-10CaSi shows highly porous, more regular “honey-comb” like structure. Small CaSi granules with higher radiopacity may be identified on all the scaffold structure.

PLA-5CaSi-5DCPD (Figure 4) and scaffold PLA-10CaSi-10DCPD (Figure 5) had very similar structures to the one of the PLA-10CaSi scaffold, including highly porous, regular “honey-comb” like structure with homogenous small pores and well distributed radiopaque mineral granules. However, at the edge of the scaffolds a higher concentration of CaSi and DCPD fillers can be identified. All tested scaffolds had a high, similar percentage of total porosity (86.4–89.4%) and open porosity (>99%), but the wall thickness of the pores increased with the amount of minerals used to load the scaffold (Figure 6). The open pore structure is an important feature for promoting colonization and degradation of the scaffolds. Also, the low standard deviation in the thickness of the pore walls corroborates the homogeneous distribution of the minerals in the structure of all the scaffolds.

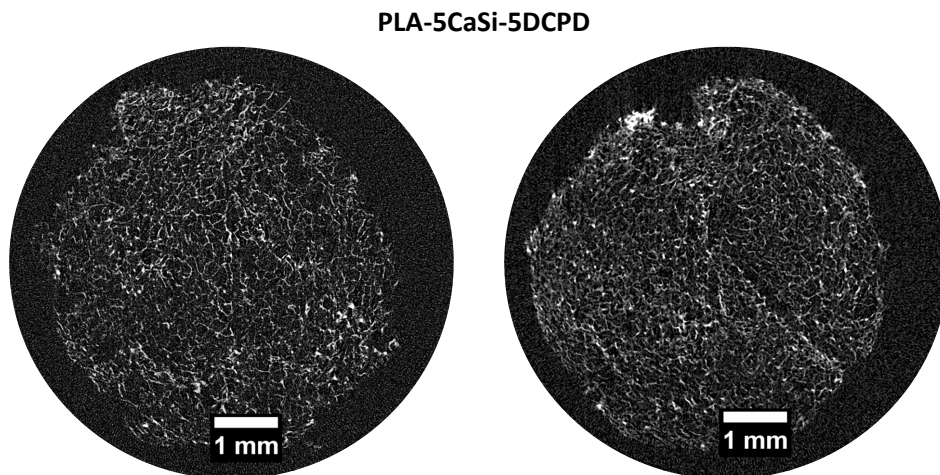


Figure 4. Micro-CT scan of 2 random slices of PLA-5CaSi-5DCPD reveals a highly porous regular “honey-comb” like structure, similar to the other mineral doped scaffolds. Some pores are occluded by radiopaque granules.

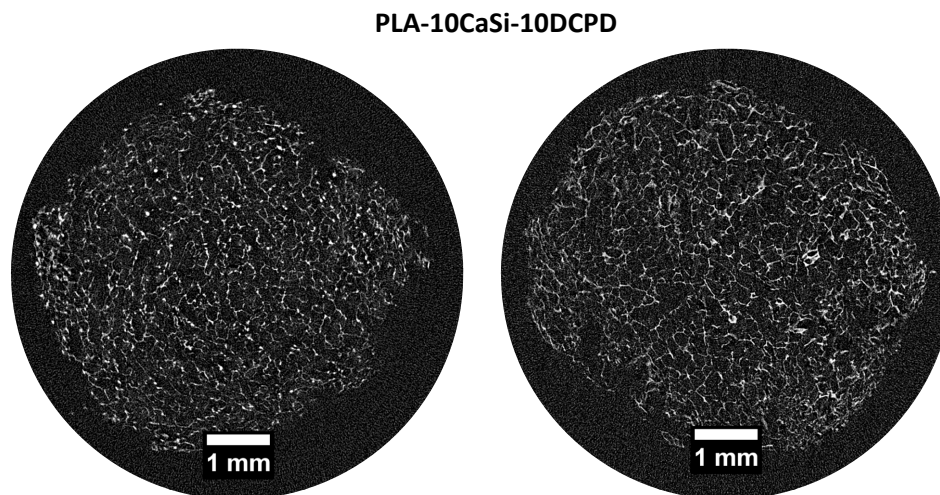
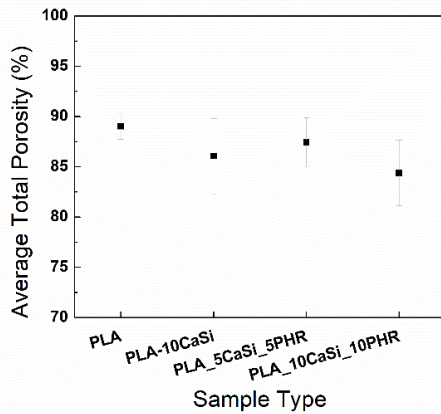


Figure 5. Micro-CT scan of 2 random slices of PLA-10CaSi-10DCPD reveals a highly porous regular “honey-comb like structure”, similar to the other mineral-doped scaffolds.

3.2. Biological Assays

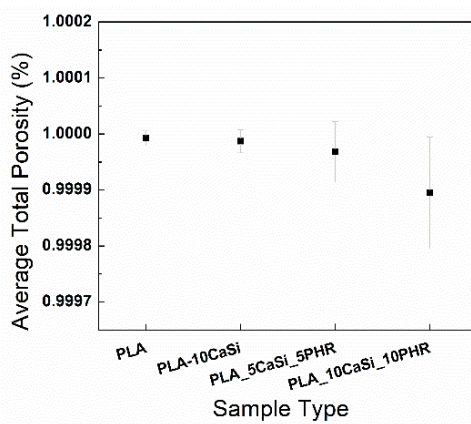
The cellular response of the recently described human periapical cyst-mesenchymal stem cells, seeded on highly-porous PLA-based scaffolds, mineral-doped with dicalcium phosphate dihydrate and/or hydraulic calcium silicate, has been investigated. Impressively high expression of mesenchymal stem cell-like markers was detected; in particular: CD90, CD105, CD73, CD44, CD29, and CD13 were highly expressed by cells isolated from human periapical cysts, so demonstrating their immature phenotype and the great regenerative potential of this MSC population meritoriously isolated from wasted biological tissues. The multipotent mesenchymal stromal nature of hPCy-MSCs was further confirmed by the lack of the expression of hematopoietic surface markers CD34, CD45, and HLA-DR (Figure 7).

(A) Total Porosity



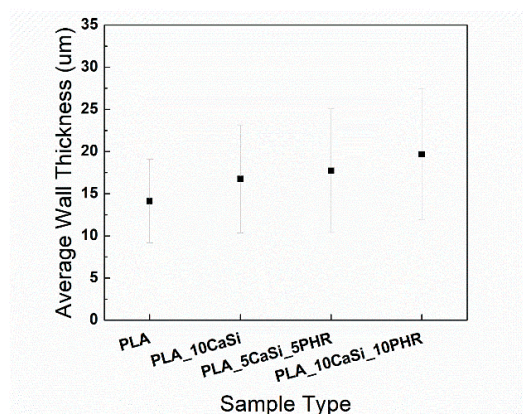
Sample Type	Total Porosity	
	Mean (%)	SD (%)
PLA	89.35291	1.293
PLA-10CaSi	88.26365	3.753
PLA-5CaSi-5DCPD	88.54365	2.460
PLA-10CaSi-10DCPD	86.41228	3.267

(B) Open Porosity



Sample Type	Open Porosity	
	Mean (%)	SD (%)
PLA	99.999782	1.312 × 10 ⁻⁵
PLA-10CaSi	99.999835	2.073 × 10 ⁻⁵
PLA-5CaSi-5DCPD	99.9998693	5.421 × 10 ⁻⁵
PLA-10CaSi-10DCPD	99.9999552	9.94 × 10 ⁻⁵

(C) Wall Thickness



Sample Type	Wall Thickness	
	Mean (mm)	SD (mm)
PLA	0.01413	0.00495
PLA-10CaSi	0.01676	0.0064
PLA-5CaSi-5DCPD	0.01773	0.00733
PLA-10CaSi-10DCPD	0.01968	0.0078

Figure 6. Quantification of % of total porosity (A), % of open porosity (B), and average wall thickness of the pores (C) from the micro-CT scanned samples of all different scaffolds.

3.3. Metabolic Assay

The proliferation rate of hPCy-MSCs has been quantified by using a resazurin-based metabolic assay (Presto Blue Invitrogen, A13261). The metabolic activity of live cells allows the conversion of resazurin into an optically-detectable component; the rate of resazurin conversion directly correlates with the number of viable cells present in the culture.

Cell proliferation was monitored at different time-points (3, 7, 10, and 14 days, after the seeding). Figure 8 shows the same hPCy-MSCs' growing trend, in all the experimental samples, with a maximum

peak reached at day 10, followed by a slightly decline at day 14. Interestingly, cells seeded on mineral-doped scaffolds showed a better proliferation ability, compared to the PLA-control group; this behavior was confirmed for those cells seeded on PLA-10CaSi-10DCPD scaffolds, particularly at day 10.

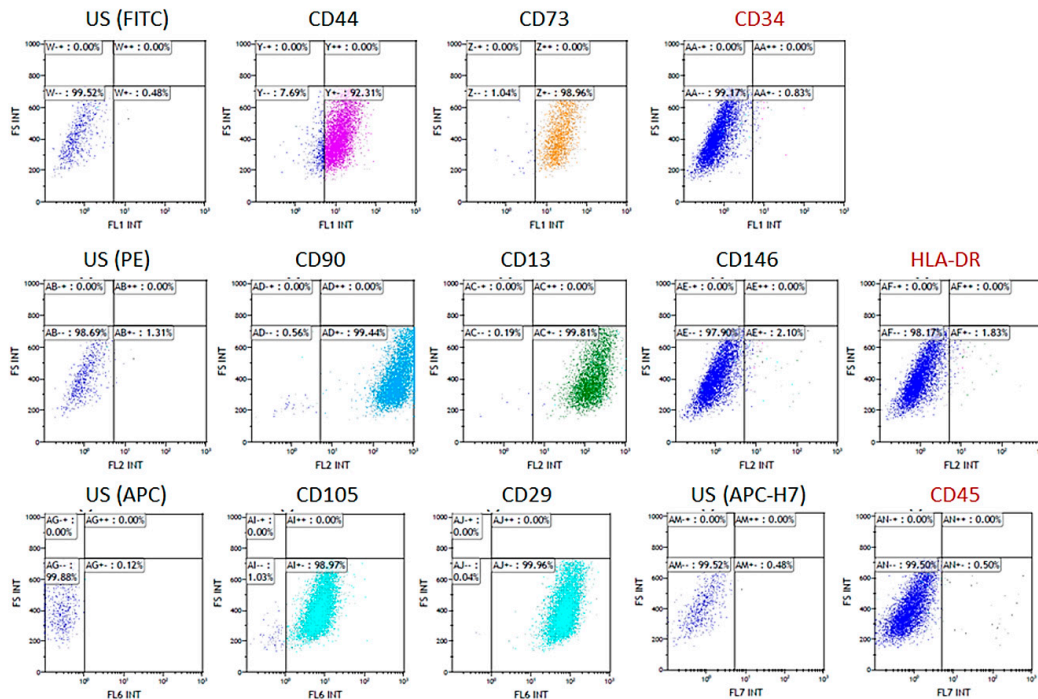


Figure 7. Cytofluorimetric analysis. Phenotypic expression pattern of primary cells isolated from human periapical cyst.

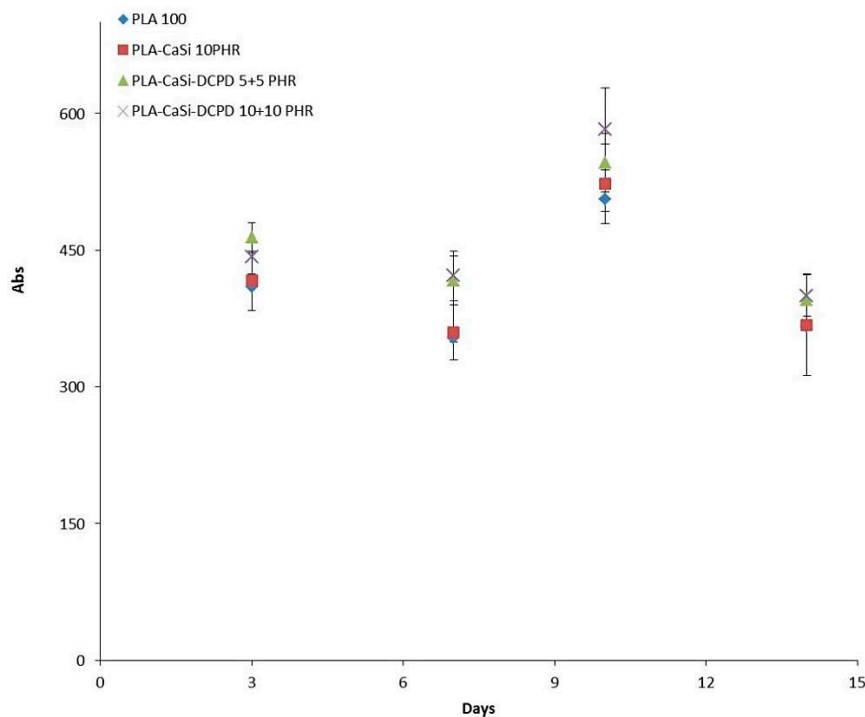


Figure 8. Proliferation curve. Quantitative results of hPCy-MSCs proliferation seeded on PLA scaffolds measured by the Prestoblue metabolic activity assay (absorbance (Abs) in the Y axis) at days 3, 7, 10, and 14 of culture (Time in the X axis). Error bars represent standard deviations.

3.4. Live/Dead Assay

The presence of live and dead cells after seeding on the experimental scaffolds at 7, 14, and 21 days of culture was examined by confocal analysis, by using specific Calcein AM-EthDIII live/dead fluorescent staining.

This assay provides green/red fluorescent staining of viable and non-viable cells, respectively; briefly, Calcein AM penetrates into live cells and is cleaved by the cytoplasmic esterases to yield the green fluorescent dye and is retained through membrane integrity of viable cells. EthD-III enters only dead cells with compromised plasma membranes and binds DNA, thus marks the nucleus with bright red fluorescence.

As evident in Figures 9–11, a good colonization of the scaffolds has been observed in all samples; but a higher number of non-viable cells (red-stained) is clearly observable in PLA-control scaffold at day 14 and at day 21. About hPCy-MSCs seeded on mineral doped scaffolds, PLA-10CaSi, PLA-5CaSi-5DCPD, and PLA-10CaSi-10DCPD, the green stained vital cells predominate at any time-point (day 7–14–21). Figure 12 describes the different microstructures of the analyzed scaffolds observed in Bright Field (B/F), by Confocal Laser Scanning Microscope (CLSM) at 10× magnification.

LIVE/DEAD Assay, day 7

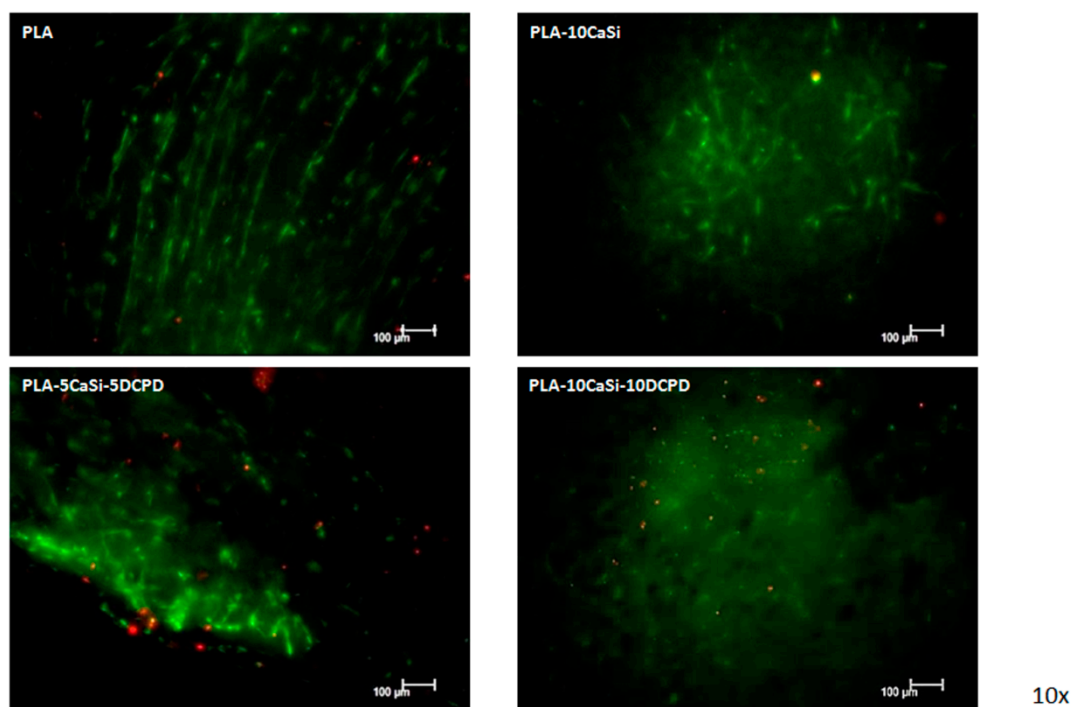


Figure 9. Live/dead assay. Live/dead staining, at day 7 of culture, in order to detect viable (green) and non-viable (red) hPCy-MSCs within the tested scaffolds (CLSM, 10× magnification).

3.5. Osteogenic Differentiation

In order to test the effects of different novel scaffolds made in our labs, we cultured the hPCy-MSCs on each of them, and we observed the variation of the genes expression closely related to osteogenesis and odontogenesis, by means of quantitative polymerase-chain-reaction. As reported in Figure 13, the expression of osteocalcin, a typical osteogenic marker, is homogeneous in cells seeded in the different experimental scaffolds. The mRNA levels of the early osteogenic marker RUNX-2 are increased in cells grown on PLA-10CaSi scaffold, and they are decreased in cells seeded on PLA-10CaSi-10DCPD. On the other hand, the expression of DMP-1, a well-known odontogenic and osteogenic marker, seems to be increased in hPCy-MSCs cultured on all mineral-doped scaffolds: interestingly, DMP-1 levels are

particularly increased in PLA-5CaSi-5DCPD and in PLA-10CaSi-10DCPD scaffolds, revealing the suitability of these two scaffolds in bone regeneration procedures.

LIVE/DEAD Assay, day 14

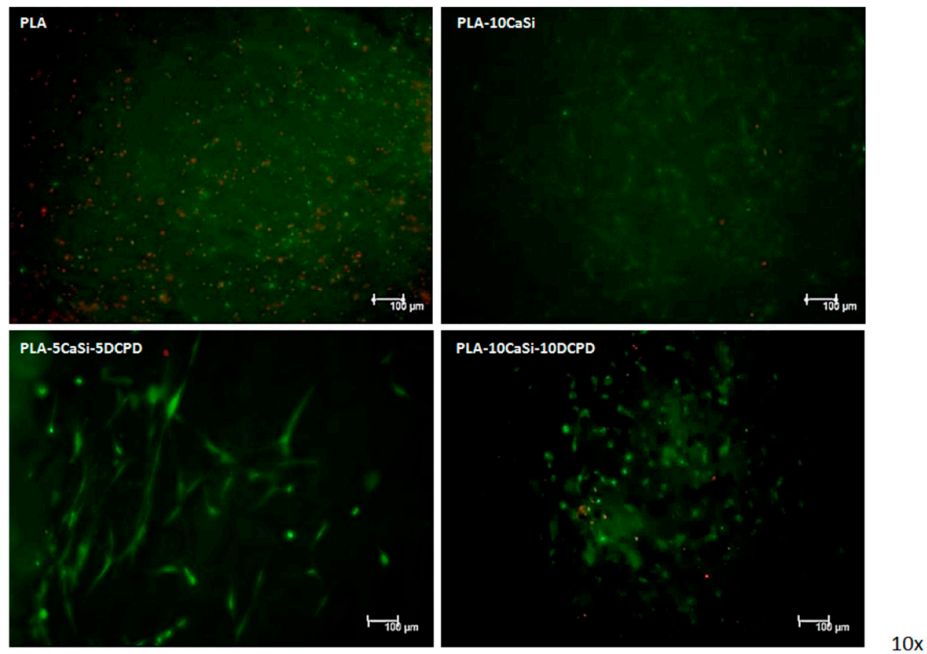


Figure 10. Live/dead assay. Live/dead staining, at day 14 of culture, in order to detect viable (green) and non-viable (red) hPCy-MSCs within the tested scaffolds (CLSM, 10× magnification).

LIVE/DEAD Assay, day 21

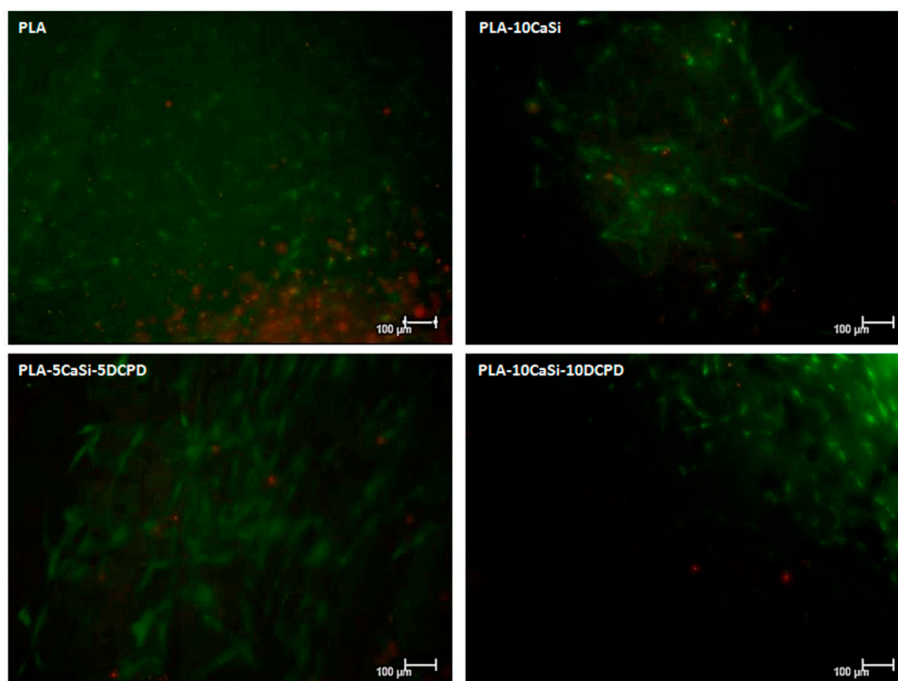


Figure 11. Live/dead assay. Live/dead staining, at day 21 of culture, in order to detect viable (green) and non-viable (red) hPCy-MSCs within the tested scaffolds (CLSM, 10× magnification).

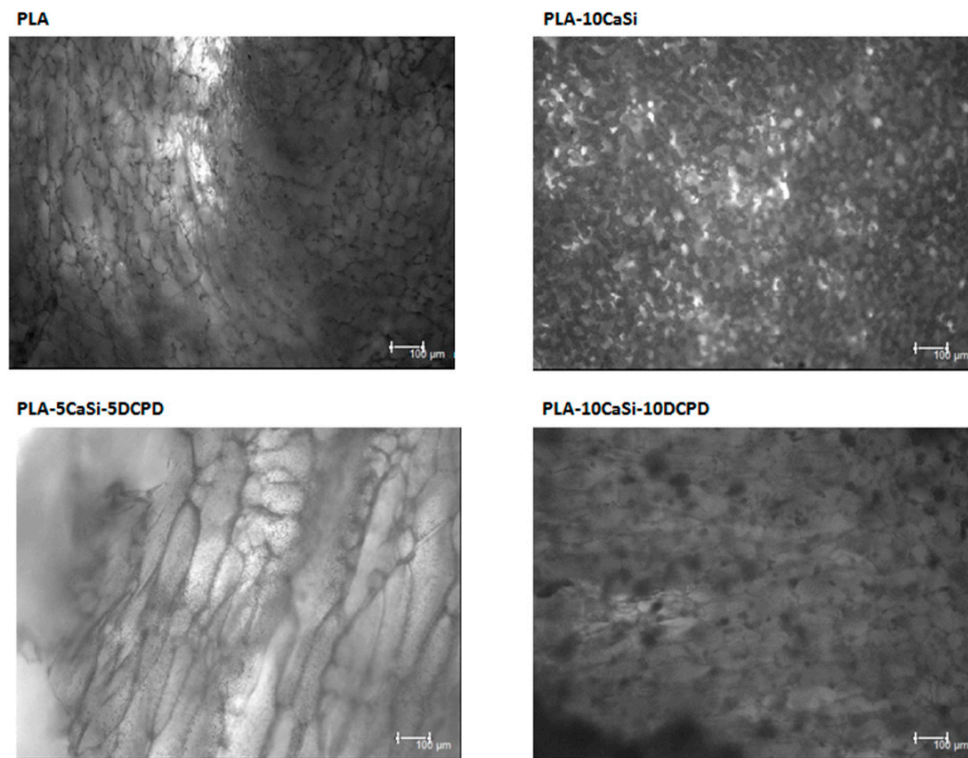


Figure 12. Comparison of different scaffolds microstructure in Bright Field (CLSM, 10× magnification).

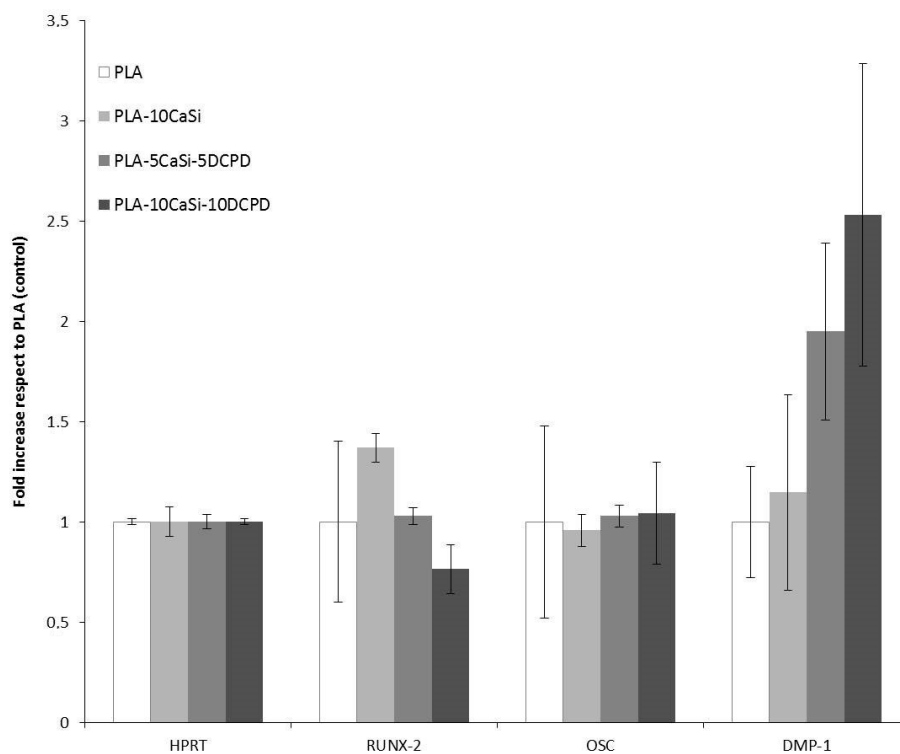


Figure 13. qPCR of hPCy-MSCs after 21 days of culture on mineral doped scaffolds. Histograms indicate fold increase in mRNA levels of hPCy-MSCs cells grown on PLA-10CaSi, PLA-5CaSi-5DCPD and PLA30 10CaSi-10DCPD, with respect to PLA control. Error bars indicate standard deviation of mean values.

4. Discussion

In the present study, hPCy-MSCs were isolated from periapical inflamed cystic tissues and seeded on bioactive mineral-doped novel scaffolds. It has been reported that hPCy-MSCs have key abilities, useful for bone and dental regeneration strategies: the association among these cells and specific osteogenic/odontogenic scaffolds is likely to trigger MSC differentiation towards specific lineages [3]. Clinical applications of such promising association of novel MSCs and novel scaffolds are particularly targeted on regenerative dentistry and biological-guided oral surgery.

TIPS allowed to produce highly porous composite structures, made of PLA filled with different amounts of CaSi and DCPD, up to 20 wt %. This technique did not induce any modification in the morphological structure of the crystalline fillers upon mixing with the polymer phase, as confirmed by an XRD analysis previously reported in literature [34].

TIPS allows to produce extremely highly porous structure with extensive pore interconnectivity [38] and to fabricate scaffolds with a great variation of micro and macropores, although it was difficult to produce pores over 200 μm [39] (structure with pore size 10–100 μm cells proliferation and migration, while 100–1000 μm allow bone ingrowth [40]). In the present study, the high standard deviation (over 30%) (Figure 6) of the wall thickness of the scaffolds, demonstrated a broad range of pore sizes, as reported in other studies on scaffolds production [34,40]. However, trabecular bone also shows a variability of trabecular thickness of approx. 30% [41,42].

PLA drawbacks (hydrophobicity, release of acid degradation products, and reduced cell adhesion and growth) are well-known in literature [18]: the addition of CaSi and DCPD mineral filler significantly improved the biointeractivity, biocompatibility, and apatite forming ability of the materials [34]. Indeed, hPCy-MSCs seeded on the mineral doped scaffolds showed a better colonization, growth, and proliferation on the mineral doped formulations when compared to pure PLA. This behavior is well evident in Figures 9–11, where a higher number of dead (red cells) may be observed on PLA scaffolds, in particular at 14 and 21 days.

In our study, a complex micro-CT characterization has been performed: scaffolds pores, their interconnectivity and size, the structural wall thickness, scaffolds anisotropy, and cross-sectional areas had been analyzed, showing a scaffold structure characterized by suitable interconnected pores, where cells were able to migrate, grow, and differentiate. Micro-CT analysis revealed no artefacts or empty areas in the middle part of the mineral-doped scaffold: the presence of mineral fillers was able to reinforce the polymer matrix. This behavior is also confirmed by previous mechanical tests, where pure PLA showed lower values of the elastic modulus, and PLA-10CaSi-10DCPD showed the highest values [34].

The highly porous structure is a key feature for the proper colonization of the mineral-doped scaffold by the cells. Importantly, the mineral compounds used to build the scaffolds were homogeneously distributed: this aspect is important to have a homogeneous bioactivation of the cells along the whole structure of the scaffold.

The evaluation of gene expression, after a long-term culture of oral-derived MSCs with the mineral-doped scaffolds, indicated that an increasing mineralization of scaffolds is closely correlated with the improved expression of the odontogenic/osteogenic marker DMP-1; strategically, we observed the levels of DMP-1 in each scaffold tested, but we would suggest to consider the PLA-10CaSi-10DCPD-based scaffolds as the gold standard, pushing the use of such scaffolds, added with autologous dental-derived MSCs, specifically in bone tissues and dental tissues repairing.

5. Conclusions

The most exciting challenge in regenerative dentistry is to find a scaffold able to ensure regenerative healing of periapical and alveolar bone, allowing tooth preservation. In this study, an innovative regenerative clinical approach was conceived through the combination of highly porous, biologically active (biointeractive) scaffolds with autologous hPCy-MSCs. These cells showed a good

growth rate and an interesting expression of the typical osteogenic/odontogenic marker DMP-1 on all the mineral-doped scaffolds compared to pure PLA scaffold.

In conclusion, the combination of a bioactive scaffolds colonized with autologous stem cells from periapical cysts may represent a promising strategy for regenerative healing of periapical and alveolar bone.

Author Contributions: Conceptualization, M.G.G.; Investigation, A.Z. and C.A.; Methodology, M.T., B.C., C.A., M.D.E. and P.F.; Software, A.Z.; Supervision, G.S., C.R., M.N., L.M., F.F., C.P. and M.G.G.; Visualization, F.Z.; Writing—original draft, M.T., F.Z. and M.G.G.; Writing—review & editing, M.T., F.Z. and M.G.G.

Funding: This research received no external funding.

Acknowledgments: Remembering Massimo Marrelli founder of the Technologica Research Institute of Crotona, died to the cloudburst of 27 October 2018.

Conflicts of Interest: The authors declare no conflict of interest.

References

1. Gyurkocza, B.; Rezvani, A.; Storb, R.F. Allogeneic hematopoietic cell transplantation: The state of the art. *Expert Rev. Hematol.* **2010**, *3*, 285–299. [[CrossRef](#)] [[PubMed](#)]
2. Codispoti, B.; Rinaldo, N.; Chiarella, E.; Lupia, M.; Spoleti, C.B.; Marafioti, M.G.; Aloisio, A.; Scicchitano, S.; Giordano, M.; Nappo, G.; et al. Recombinant TAT-BMI-1 fusion protein induces ex vivo expansion of human umbilical cord blood-derived hematopoietic stem cells. *Oncotarget* **2017**, *27*, 43782–43798. [[CrossRef](#)] [[PubMed](#)]
3. Tatullo, M.; Codispoti, B.; Pacifici, A.; Palmieri, F.; Marrelli, M.; Pacifici, L.; Paduano, F. Potential Use of Human Periapical Cyst-Mesenchymal Stem Cells (hPCy-MSCs) as a Novel Stem Cell Source for Regenerative Medicine Applications. *Front. Cell Dev. Biol.* **2017**, *5*, 103. [[CrossRef](#)] [[PubMed](#)]
4. Nair, P.N.R. On the causes of persistent apical periodontitis: A review. *Int. Endod. J.* **2016**, *39*, 249–281. [[CrossRef](#)] [[PubMed](#)]
5. Park, J.G.; Fayazi, S.; White, S.N. Prevalence of periapical radiolucency and root canal treatment: A systematic review of cross-sectional studies. *J. Endod.* **2012**, *38*, 1170–1176.
6. Berlin-Broner, Y.; Febbraio, M.; Levin, L. Association between apical periodontitis and cardiovascular diseases: A systematic review of the literature. *Int. Endod. J.* **2017**, *50*, 847–859. [[CrossRef](#)] [[PubMed](#)]
7. Marrelli, M.; Paduano, F.; Tatullo, M. Cells isolated from human periapical cysts express mesenchymal stem cell-like properties. *Int. J. Biol. Sci.* **2013**, *16*, 1070–1078. [[CrossRef](#)]
8. Kawashima, N. Characterisation of dental pulp stem cells: a new horizon fortissue regeneration? *Arch. Oral Biol.* **2012**, *57*, 1439–1458. [[CrossRef](#)]
9. Paduano, F.; Marrelli, M.; Palmieri, F.; Tatullo, M. CD146 Expression Influences Periapical Cyst Mesenchymal Stem Cell Properties. *Stem Cell Rev. Rep.* **2016**, *12*, 592–603. [[CrossRef](#)]
10. Covas, D.T.; Panepucci, R.A.; Fontes, A.M.; Silva, W.A.; Orellana, M.D.; Freitas, M.C.; Neder, L.; Santos, A.R.; Peres, L.C.; Jamur, M.C.; Zago, M.A. Multipotent mesenchymal stromal cells obtained from diverse human tissues share functional properties and gene-expression profile with CD146+ perivascular cells and fibroblasts. *Exp. Hematol.* **2008**, *36*, 642–654. [[CrossRef](#)]
11. Tatullo, M.; Falisi, G.; Amantea, M.; Rastelli, C.; Paduano, F.; Marrelli, M. Dental pulp stem cells and human periapical cyst mesenchymal stem cells in bone tissue regeneration: Comparison of basal and osteogenic differentiated gene expression of a newly discovered mesenchymal stem cell lineage. *J. Biol. Regul. Homeost. Agents* **2015**, *29*, 713–718. [[PubMed](#)]
12. Marrelli, M.; Paduano, F.; Tatullo, M. Human periapical cyst-mesenchymal stem cells differentiate into neuronal cells. *J. Dental Res.* **2015**, *94*, 843–852. [[CrossRef](#)] [[PubMed](#)]
13. Marrelli, M.; Falisi, G.; Apicella, A.; Apicella, D.; Amantea, M.; Cielo, A.; Bonanome, L.; Palmieri, F.; Santacroce, L.; Giannini, S.; et al. Behaviour of dental pulp stem cells on different types of innovative mesoporous and nanoporous silicon scaffolds with different functionalizations of the surfaces. *J. Biol. Regul. Homeost. Agents* **2015**, *29*, 991–997. [[PubMed](#)]

14. Paduano, F.; Marrelli, M.; White, L.J.; Shakesheff, K.M.; Tatullo, M. Odontogenic Differentiation of Human Dental Pulp Stem Cells on Hydrogel Scaffolds Derived from Decellularized Bone Extracellular Matrix and Collagen Type I. *PLoS ONE* **2016**, *11*, e0148225. [[CrossRef](#)] [[PubMed](#)]
15. Paduano, F.; Marrelli, M.; Alom, N.; Amer, M.; White, L.J.; Shakesheff, K.M.; Tatullo, M. Decellularized bone extracellular matrix and human dental pulp stem cells as a construct for bone regeneration. *J. Biomater. Sci. Polym. Edit.* **2017**, *28*, 730–748. [[CrossRef](#)] [[PubMed](#)]
16. Langer, R.; Vacanti, J.P. Tissue engineering. *Science* **1993**, *260*, 920–926. [[CrossRef](#)] [[PubMed](#)]
17. Moussa, D.G.; Aparicio, C. Present and future of tissue engineering scaffolds for dentin-pulp complex regeneration. *J. Tissue Eng. Regen. Med.* **2019**, *13*, 58–75. [[CrossRef](#)] [[PubMed](#)]
18. Armentano, I.; Dottori, M.; Fortunati, E.; Mattioli, S.; Kenny, J.M. Biodegradable polymer matrix nanocomposites for tissue engineering: A review. *Polym. Degrad. Stab.* **2010**, *95*, 2126–2146. [[CrossRef](#)]
19. Zizzari, V.L.; Zara, S.; Tetè, G.; Vinci, R.; Gherlone, E.; Cataldi, A. Biologic and clinical aspects of integration of different bone substitutes in oral surgery: A literature review. *Oral Surg. Oral Med. Oral Pathol. Oral Radiol.* **2016**, *122*, 392–402. [[CrossRef](#)]
20. LeGeros, R.Z.; Lin, S.; Rohanizadeh, R.; Mijares, D.; LeGeros, J.P. Biphasic calcium phosphate bioceramics: preparation, properties and applications. *J. Mater. Sci.* **2003**, *14*, 201–209.
21. Yip, I.; Ma, L.; Mattheos, N.; Dard, M.; Lang, N.P. Defect healing with various bone substitutes. *Clin. Oral Implant. Res.* **2015**, *26*, 606–614. [[CrossRef](#)] [[PubMed](#)]
22. Gandolfi, M.G.; Spagnuolo, G.; Siboni, F.; Procino, A.; Riviaccio, V.; Pelliccioni, G.A.; Prati, C.; Rengo, S. Calcium silicate/calcium phosphate biphasic cements for vital pulp therapy: chemical-physical properties and human pulp cells response. *Clin. Oral Investig.* **2015**, *19*, 2075–2089. [[CrossRef](#)] [[PubMed](#)]
23. Prati, C.; Gandolfi, M.G. Calcium silicate bioactive cements: biological perspectives and clinical applications. *Dental Mater.* **2015**, *31*, 351–370. [[CrossRef](#)] [[PubMed](#)]
24. Gandolfi, M.G.; Iezzi, G.; Piattelli, A.; Prati, C.; Scarano, A. Osteoinductive potential and bone-bonding ability of ProRoot MTA, MTA Plus and Biodentine in rabbit intramedullary model: Microchemical characterization and histological analysis. *Dental Mater.* **2017**, *33*, 221–238. [[CrossRef](#)] [[PubMed](#)]
25. Siboni, F.; Taddei, P.; Zamparini, F.; Prati, C.; Gandolfi, M.G. Properties of BioRoot RCS, a tricalcium silicate endodontic sealer modified with povidone and polycarboxylate. *Int. Endod. J.* **2018**, *50*, 120–136. [[CrossRef](#)] [[PubMed](#)]
26. Zamparini, F.; Siboni, F.; Prati, C.; Taddei, P.; Gandolfi, M.G. Properties of calcium silicate-monobasic calcium phosphate materials for endodontics containing tantalum pentoxide and zirconium oxide. *Clin. Oral Investig.* **2019**, *23*, 445–457. [[CrossRef](#)] [[PubMed](#)]
27. Zhou, W.; Zheng, Q.; Tan, X.; Song, D.; Zhang, L.; Huang, D. Comparison of Mineral Trioxide Aggregate and iRoot BP Plus Root Repair Material as Root-end Filling Materials in Endodontic Microsurgery: A Prospective Randomized Controlled Study. *J. Endod.* **2017**, *43*, 1–6. [[CrossRef](#)] [[PubMed](#)]
28. Gandolfi, M.G.; Taddei, P.; Modena, E.; Siboni, F.; Prati, C. Biointeractivity-related versus chemi/physisorption-related apatite precursor-forming ability of current root end filling materials. *J. Biomed. Mater. Res. B Appl. Biomater.* **2013**, *101*, 1107–1123. [[CrossRef](#)]
29. Gandolfi, M.G.; Taddei, P.; Tinti, A.; Dorigo, E.D.S.; Prati, C. Alpha-TCP improves the apatite-formation ability of calcium-silicate hydraulic cement soaked in phosphate solutions. *Mater. Sci. Eng. C Mater. Biol. Appl.* **2011**, *31*, 1412–1422. [[CrossRef](#)]
30. Marei, N.H.; El-Sherbiny, I.M.; Lotfy, A.; El-Badawy, A.; El-Badri, N. Mesenchymal stem cells growth and proliferation enhancement using PLA vs. PCL based nanofibrous scaffolds. *Int. J. Biol. Macromol.* **2016**, *93*, 9–19. [[CrossRef](#)]
31. Chiu, Y.C.; Fang, H.Y.; Hsu, T.T.; Lin, C.Y.; Shie, M.Y. The Characteristics of Mineral Trioxide Aggregate/Polycaprolactone 3-dimensional Scaffold with Osteogenesis Properties for Tissue Regeneration. *J. Endod.* **2017**, *43*, 923–929. [[CrossRef](#)] [[PubMed](#)]
32. Cho, Y.S.; Hong, M.W.; Quan, M.; Kim, S.Y.; Lee, S.H.; Lee, S.J.; Kim, Y.Y.; Cho, Y.S. Assessments for bone regeneration using the polycaprolactone SLUP (salt-leaching using powder) scaffold. *J. Biomed. Mater. Res. Part A* **2017**, *105*, 3432–3444. [[CrossRef](#)] [[PubMed](#)]
33. Fabbri, P.; Cannillo, V.; Sola, A.; Dorigato, A.; Chiellini, F. Highly porous polycaprolactone-45S5 Bioglass®scaffolds for bone tissue engineering. *Comp. Sci. Technol.* **2010**, *70*, 1869–1878. [[CrossRef](#)]

34. Gandolfi, M.G.; Zamparini, F.; Degli Esposti, M.; Chiellini, F.; Aparicio, C.; Fava, F.; Fabbri, P.; Taddei, P.; Prati, C. Polylactic acid-based porous scaffolds doped with calcium silicate and dicalcium phosphate dihydrate designed for biomedical application. *Mater. Sci. Eng. C Mater. Biological Appl.* **2018**, *82*, 163–181. [[CrossRef](#)] [[PubMed](#)]
35. Park, C.H.; Rios, H.F.; Jin, Q.; Bland, M.E.; Flanagan, C.L.; Hollister, S.J.; Giannobile, W.V. Biomimetic hybrid scaffolds for engineering human tooth-ligament interfaces. *Biomaterials* **2010**, *31*, 5945–5952. [[CrossRef](#)] [[PubMed](#)]
36. Wongsupa, N.; Nuntanarant, T.; Kamolmattayakul, S.; Thuaksuban, N. Assessment of bone regeneration of a tissue-engineered bone complex using human dental pulp stem cells/poly(ϵ -caprolactone)-biphasic calcium phosphate scaffold constructs in rabbit calvarial defects. *J. Mater. Sci. Mater. Med.* **2017**, *28*, 77. [[CrossRef](#)] [[PubMed](#)]
37. Huang, S.H.; Hsu, T.T.; Huang, T.H.; Lin, C.Y.; Shie, M.Y. Fabrication and characterization of polycaprolactone and tricalcium phosphate composites for tissue engineering applications. *J. Dental Sci.* **2017**, *12*, 33–43. [[CrossRef](#)]
38. Boccaccini, A.R.; Gough, J. *Tissue Engineering Using Ceramics and Polymers*; CRC Press: Boca Raton, FL, USA, 2007; Volume 15, pp. 320–327.
39. Janik, H.; Marzec, M. A review: fabrication of porous polyurethane scaffolds. *Mater. Sci. Eng. C Mater. Biological Appl.* **2015**, *48*, 586–591. [[CrossRef](#)]
40. Dutta, R.C.; Dutta, A.K. *3D Cell Culture: Fundamentals and Applications in Tissue Engineering and Regenerative Medicine*; CRC Press: Boca Raton, FL, USA, 2018; Volume 3, pp. 160–168.
41. Mullender, M.G.; Tan, S.D.; Vico, L.; Alexandre, C.; Klein-Nulend, J. Differences in osteocyte density and bone histomorphometry between men and women and between healthy and osteoporotic subjects. *Calcified Tissue Int.* **2005**, *77*, 291–296. [[CrossRef](#)]
42. Rehman, M.T.; Hoyland, J.A.; Denton, J.; Freemont, A.J. Age related histomorphometric changes in bone in normal British men and women. *J. Clin. Pathol.* **1994**, *47*, 529–534. [[CrossRef](#)]



© 2019 by the authors. Licensee MDPI, Basel, Switzerland. This article is an open access article distributed under the terms and conditions of the Creative Commons Attribution (CC BY) license (<http://creativecommons.org/licenses/by/4.0/>).

3.2.2 Culture Of Porcine Vascular Wall - Mesenchymal Stem Cells On 3d Biodegradable Highly Porous Mineral Doped Poly (A-Hydroxy) Acids Scaffolds

Monica Forni¹, Chiara Bernardini¹, Fausto Zamparini^{2,4}, Augusta Zannoni¹, Roberta Salaroli¹, Domenico Ventrella¹, Micaela Degli Esposti³, Paola Fabbri³, Fabio Fava³, Carlo Prati⁴, Maria Giovanna Gandolfi⁴

1- Department of Medical Veterinary Science DIMEVET

2- Laboratory of Biomaterials and Oral Pathology, School of Dentistry, Department of Biomedical and Neuromotor Sciences, University of Bologna, Bologna, Italy

3- Department of Civil, Chemical, Environmental and Materials Engineering, University of Bologna, Bologna, Italy

4- Endodontic Clinical Section, School of Dentistry, Department of Biomedical and Neuromotor Sciences, University of Bologna, Bologna, Italy

AIM

The aim of the present study was to evaluate the ability of pVW-MSCs to colonize experimental highly porous. Poly- α -hydroxyl based mineral doped scaffolds, and to express their angiogenic potential. PLA-and PCL-based scaffolds doped with CaSi and DCPD were tested in a 3D in vitro model and traditional 2D culture was used as control.

MATERIAL AND METHODS

Materials

Polycaprolactone (PCL) (average Mn 45000 g/mol, Sigma-Aldrich, Milan, Italy) was received in pellet form and purified via dissolution in CHCl_3 (15% wt/vol) and reprecipitation in a large excess of cold MeOH, in order to eliminate residual polymerization catalysts.

Poly(L-lactic acid) (PLA) (MW=65000 g/mol, IngeoTM biopolymer PLA 4060D, Natureworks LLC, Blair, NE, USA) was received in pellet form and purified via dissolution in CHCl_3 (10% wt/vol) and reprecipitation in a large excess of cold MeOH, in order to eliminate residual polymerization catalysts.

Methanol (MeOH), ethanol (EtOH, 99.8%), 1,4-dioxan (DIOX) and chloroform (CHCl_3 , HPLC grade) all from Sigma Aldrich (Milan, Italy) were used as received without further purification.

Dicalcium phosphate dihydrate (DCPD; $\text{CaHPO}_4 \cdot 2\text{H}_2\text{O}$) powder (Sigma-Aldrich, Steinheim, Germany) and/or calcium silicate (CaSi) powders (Aalborg, Denmark), prepared by melt-quenching technique and milling procedures, as previously reported, (Gandolfi *et al.* 2015) and composed of dicalcium silicate, tricalcium silicate, tricalcium aluminate, and calcium sulfate, were added to PLA or PCL.

All plastic used for standard culture condition were from BD-Falcon (Corning, NY USA). Antibiotic-antimycotic, Dulbecco's phosphate buffered saline (DPBS), DAPI staining solution were purchased from Gibco-Life Technologies (Carlsbad CA, USA). Trypsin-EDTA solution 1X, MTT based assay were purchased from Sigma-Aldrich (St. Louis, MO, USA). Pericyte Growth Medium was purchased from Promocell (Heidelberg, Germany). NucleoSpin RNA kit was purchased from Macherey-Nagel GmbH & Co. KG (Düren, Germany).

TIPS Scaffolds preparation

The porous polymer scaffolds were prepared by TIPS starting from PLA or PCL solutions in DIOX (3.5% wt/vol). CaSi

and DCPD were added to the polymer solution in powder form in 10% by weight with respect to PLA or PCL. (Gandolfi *et al.* 2018 and 2019).

Homogeneous dispersions were obtained by sonicating the mixtures for 3 hours using the ultrasonic processor UP50H (Hielscher, 50 watts, 30 kHz), equipped with the sonotrode MS2 (made of titanium, tip diameter 2 mm). After mixing, solutions were placed inside disposable aluminum dishes of 60 mm in diameter, and cooled at -18°C. After 18 h, the frozen samples were extracted from the holders and fully immersed in EtOH bath precooled at -18°C, where they were kept for 48 h, with solvent refresh every 3 h. At the end of the extraction procedure, the porous scaffolds were taken out of the freezer and completely dried under vacuum. Six disks (diameter 60 ± 1 mm, thickness 10 ± 0.1 mm) per composition were prepared. The prepared scaffolds were: PLA, PLA-10CaSi-10DCPD, PCL, PCL-10CaSi-10DCPD.

Surface porosity evaluated by the morphometric analysis on ESEM images

The scaffolds were examined using an environmental scanning electron microscope (ESEM, Zeiss EVO 50; Carl Zeiss, Oberkochen, Germany). Specimens were placed directly onto the ESEM stub and examined in wet conditions without any previous preparation (the samples were not coated for this analysis) at low vacuum (100 Pascal) in Quadrant Back-Scattering Detector (QBSD) mode, using an accelerating voltage of 20 kV, working distance 8.5 mm, 0.5 wt% detection level, 133 eV resolution, amplification time 100 μ s, measuring time 60 s. ESEM images were analyzed through Image J program (National Institutes of Health, Bethesda, USA) to evaluate the scaffolds porosity, in terms of percentage. Surface porosity was calculated as the ratio between the most black areas (micropores) and the total examined area (Gandolfi *et al.* 2018 and 2019, Castilla-Bolanos *et al.* 2016). For each scaffold three measurements were performed in three different areas at 500 \times and 1000 \times magnification. For each magnification, the mean value was recorded.

Isolation and culture of primary porcine Vascular Wall Mesenchymal Stem Cells

Primary porcine Vascular Wall Mesenchymal Stem Cells (pVW-MSCs) were isolated from the thoracic aorta of female 3-months-old pigs (Large White) euthanized for other experimental purposes, following the published methods previously described (Zaniboni *et al.* 2015), to generate three primary cell culture replicates. All procedures on pigs were reviewed and approved in advance by the Ethical Committee of the University of Bologna (Bologna, Italy) and were then approved by the Italian Ministry of Health (Protocol number n.43-IX/9 all.37; 20/11/2012). Cells were grown and expanded not beyond till passage (P) 6 in Pericyte Growth Medium (PGM – Promocell). All the experiments described in this paper were performed with cells at the third passage (P3), cultured in Pericyte Growth Medium (PGM).

Cell seeding efficiency assay

All the scaffolds were sterilized by the followed procedure: 30 min of incubation in absolute EtOH followed by three washes in DPBS (30 min each one), then cubic-shaped sections of about 1 mm on each side were produced with the help of scalpel blades. 30 sections were inserted into a microtube containing 500 μ l of culture medium (Pericyte Growth Medium) and incubated over night at 4°C. The day after, pVW-MSCs were seeded on different biomaterials (PLA-10CaSi-10DCPD and PCL-10CaSi-10DCPD) following a published method (Dozza *et al.* 2017) with some main adaptations. Microtubes with the biomaterials were incubated to reach a temperature of 38°C then the medium was removed and the biomaterials were drop-seeded with 100 μ l of a concentrated cell suspension containing 4×10^5 or 8×10^5 cells. The microcentrifuge tubes were placed on a rocker oscillating at 30 rpm for 2 hours to allow for initial cell attachment then 1ml of fresh cell culture medium was slowly added to each tube and cells were cultured for additional

24, 48, 72 hours in static condition at 38.5°C at 5% CO₂. Cell-free biomaterials were incubated under same conditions and used as control.

Cell seeding efficiency (CSE) was estimated using an indirect method (Dozza *et al.* 2016) after 24, 48 and 72 hours. Briefly the CSE was calculated based on the number of unattached cells that still present in the medium using the following equation $CSE (\%) = (1 - \text{cells}_u / \text{cells}_i) \times 100$, where cells_i is the number of cells initially seeded and cells_u is the number of unattached cells in the residual medium and in DPBS used for rinsing cell-seeded biomaterials. Unattached cells were counted by hemocytometer in three different aliquots of medium collected from each sample.

Metabolic cell activity assay

The metabolic pVW-MSCs activity was monitored at 24, 48 and 72 hours using MTT based assay, following the manufacturer's instruction, with some main adaptation. The culture medium was removed, scaffolds were washed twice with DPBS and then 20 µl of MTT substrate was added and recovered for 4 hours at 38,5 °C at 5% CO₂. After that, 200 µl of solubilisation solution was added and, after 30 min, the solution was vigorously mixed and the absorbance at a wavelength of 570 nm was measured spectrophotometrically, with the background subtraction at 690 nm.

RNA extraction and qPCR

RNA extraction was performed using TRI Reagent (Molecular Research Center) and NucleoSpin RNA II kit (Macherey-Nagel GmbH & Co. KG, Düren, Germany).

Briefly, culture medium was removed at 72 h and different scaffolds were washed with DPBS (twice); 500 µl of TRI Reagent (Molecular Research Center, Inc.) was added and the materials were lysed by using TH Tissue Homogenizer. Following, 100 µl of chloroform was added to the suspension and mixed well. After incubation at room temperature (10 min), samples were centrifuged (12000 g for 10 min) and the aqueous phase was recovered. An equal volume of absolute ethanol (99%) was added and the resulting solution was applied to the Nucleo spin RNA Column, RNA was finally purified according to the manufacturer's instructions. After spectrophotometric quantification (Denovix, Denovix Inc., Wilmington, NC) total RNA (500 ng) was reverse-transcribed to cDNA using the iScript cDNA Synthesis Kit (Bio-Rad Laboratories Inc., Hercules, CA, USA) in a final volume of 20 µl. Swine primers were designed using Beacon Designer 2.07 (Premier Biosoft International, Palo Alto, CA, USA). Primer sequences expected PCR product lengths and accession numbers in the NCBI database are shown in **Table 1**.

To evaluate gene expression profiles, quantitative real-time PCR (qPCR) was performed in CFX96 (Bio-Rad) thermal cycler using a multiplex real time reaction for reference genes (GAPDH, glyceraldehyde-3-phosphate dehydrogenase; HPRT, hypoxanthine guanine phosphoribosyl transferase; β-Actin), and using Taq-Man probes and SYBR green detection for target genes (CD90, α-SMA, NG2 and PDGFR-b). All amplification reactions were performed in 20 µL and analyzed in duplicates (10 µl/well). Multiplex PCR contained: 10 µl of iTaqMan Probes Supermix (Bio-RAD), 1 µL of forward and reverse primers (5 µM each) of each reference gene, 0.8 µl of iTaq-Man Probes (5 µM) of each reference gene, 2 µl cDNA and 2.6 µL of water. The following temperature profile was used: initial denaturation at 95°C for 30 seconds followed by 40 cycles of 95°C for 5 seconds and 60°C for 30 seconds.

The SYBR Green reaction contained: 10 µl of IQSYBR Green Supermix (Bio-RAD), 0.8 µl of forward and reverse primers (5 µM each) of each target gene, 2 µl cDNA and 7.2 µl of water. The real-time program included an initial denaturation period of 1.5 min at 95°C, 40 cycles at 95°C for 15 s, and 60°C for 30 s, followed by a melting step with ramping from 55°C to 95°C at a rate of 0.5°C/10 s.

The specificity of the amplified PCR products was confirmed by agarose gel electrophoresis and melting curve analysis.

The relative expressions of the studied genes were normalized based on the geometric mean of the three reference genes. The relative mRNA expression of tested genes was evaluated as fold of increase using the $2^{-\Delta\Delta CT}$ method referred to pVW-MSCs cultured in flask under standard 2d culture condition (control).

DAPI staining and immunofluorescence

To test cellular distribution in the different scaffolds, pVW-MSCs cultured for 72 hours were processed for labeling DNA in fluorescence with DAPI staining and alpha-tubulin immunofluorescence. In particular biomaterials were washed twice in DPBS then were fixed ON in cold 4% Formaldehyde Solution in PBS, pH 7,4 (Kalttek, Italy). Each sample was transferred into a 25% sucrose (Sigma-Aldrich, MO, USA) solution in PBS at 4°C for 24 hours to get cryoprotection. Finally, samples were embedded and freezed in OCT (Sakura Finetek, CA, USA). Ten micrometres sections were cut at a Leica CM1950 cryostat (Leica, Wetzlar, Germany) mounted on microscope's slides and stained with DAPI Staining Solution (Thermo Fischer). For immunofluorescence staining slides were completely dried at room temperature (RT), washed three times in PBS 1X for 5 minutes, permeabilized with Triton X-100 0,1% in PBS 1X for 1 hour then washed three times in PBS 1X for 5 minutes. For aspecific sites blocking slides were treated with 10% Normal Goat Serum in PBS 1X for 1 hour at RT then incubated ON in a humidified chamber with an anti alpha-tubulin antibody (Clone TU-01, Thermo Fisher Scientific, Waltham, MA, USA) diluted 1:250 in PBS 1X. In negative controls the primary antibody was omitted. At this point samples were washed three times in PBS 1X, incubated with anti-mouse FITC conjugate antibody (Sigma-Aldrich, St. Louis, MO, USA) diluted 1:100 in PBS 1X for 1 hour at RT in a humidified chamber. After two washes for 5 min in PBS 1X and one wash in distilled water for 5 minutes, coverslips were mounted on slides with Fluoreshield with PI (Sigma-Aldrich, St. Louis, MO, USA). Photomicrographs were obtained using a Nikon digital camera installed on a Nikon (Nikon Inc., Melville, NY, USA).

Statistical analysis

Three primary cell cultures derived from three different animals were used. Data represent the mean \pm SD (or \pm range of expression for qRT-PCR) of the three biological replicates. The data were analyzed by One-way analysis of variance (ANOVA) followed by the Tukey post hoc comparison Test. Differences of at least $p < 0.05$ were considered significant. Statistical analysis was carried out by using Graph Pad Prism 5.0 software.

RESULTS

Surface porosity evaluated by the morphometric analysis on ESEM images

The mean surface porosity of PLA scaffolds, evaluated on three random areas at 500 \times and 1000 \times was 45.49% (range 42.94-50.01%) and 40.08% (range 39.42-40.61%), respectively (**Figure 1a**). PLA-10CaSi-10DCPD scaffolds showed a mean porosity, evaluated on three random areas at 500 \times and 1000 \times magnifications was 31.51% (range 29.69-33.27%) and 26.94% (range 15.67-35.88%), respectively (Figure 1b). PCL scaffolds mean surface porosity, evaluated on three random areas at 500 \times and 1000 \times magnification, was 51.58% (range 49.25-54.16%) and 52.22% (range 47.18-59.11%), respectively (Figure 1c). PCL-10CaSi-10DCPD mean surface porosity, evaluated on three random areas at 500 \times and 1000 \times magnifications, was 41.42% (range 35.61-45.99%) and 41.65% (range 37.97-45.93%), respectively (**Figure 1d**).

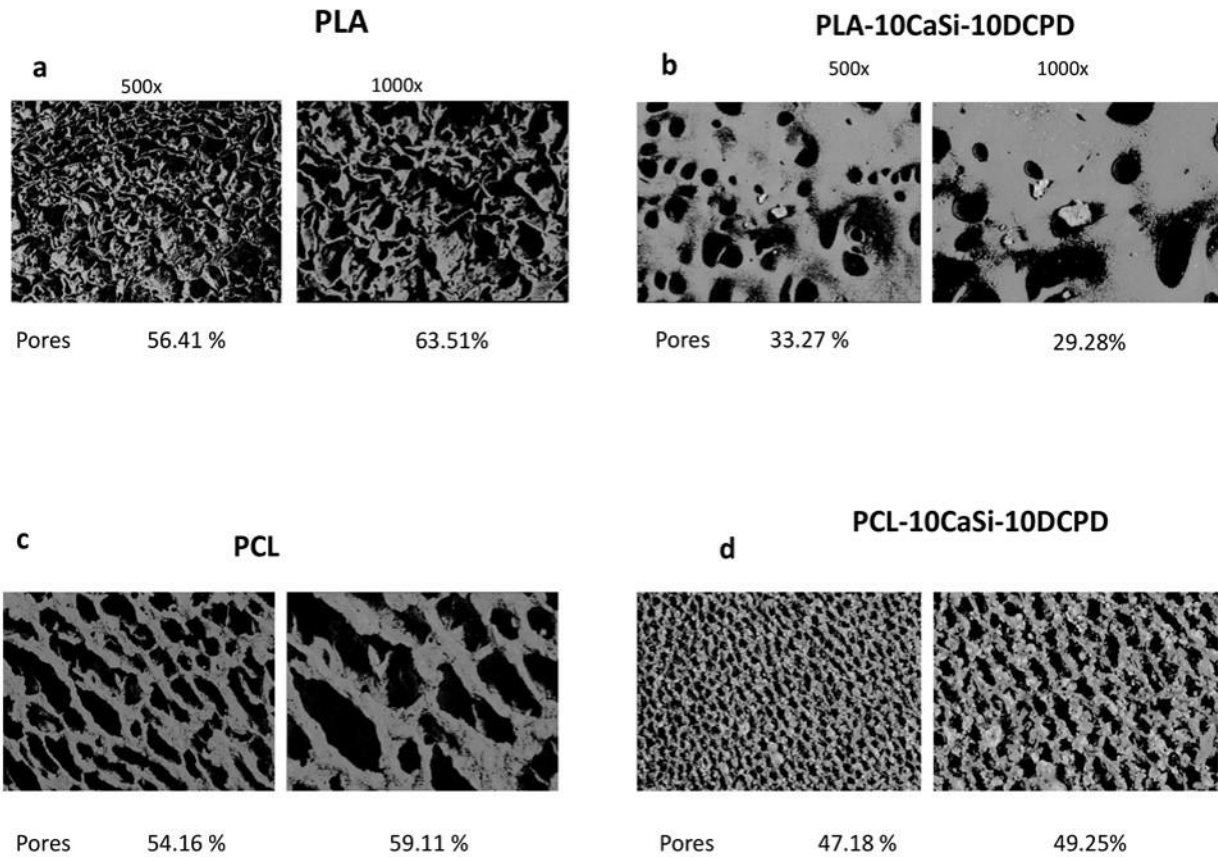


Figure 1 - Surface porosity evaluation of PLA (a,b) and PCL (c,d) scaffolds. PCL scaffolds reveal a more regular surface when compared to PLA scaffolds. The mineral doped formulations reveal lower surface porosity values.

Cytocompatibility

To investigate the pVW-MSCs ability to colonize biomaterials, we quantified the cell seeding efficiency (CSE). The results indicated a significant efficiency rate already at 24 h; both for PLA or PCL matrix ($\geq 90\%$), the presence of additives did not influence the cell seeding efficiency.

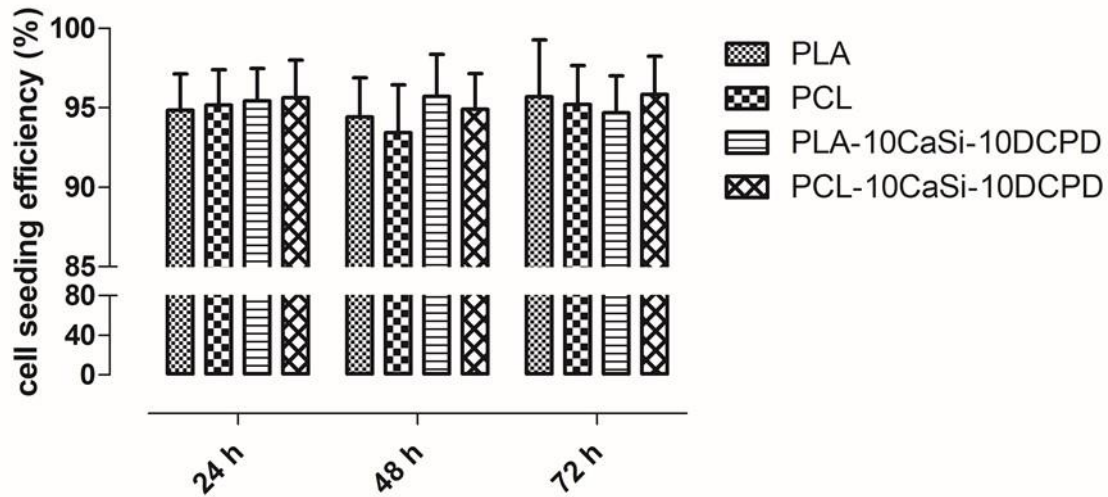


Figure 2 - Cell seeding efficiency. Cell seeding efficiency was performed by an indirect method. After 24 hours from the seeding cells did not attach to the scaffolds were quantified and cell seeding efficiency was calculated by the equation: $CSE (\%) = (1 - \text{cells}_u / \text{cells}_i) \times 100$. Data represent the mean \pm SD of three independent biological replicates (n=3) and were analysed using one-way ANOVA followed by the Tukey's post hoc comparison. No differences were detected among different scaffolds.

Metabolic activity

In order to measure the metabolic activity of pVW-MSCs grew on scaffolds, a MTT based assay method was performed on cells 24, 48 and 72 hours post seeding. Our results demonstrated that pVW-MSCs maintain a metabolically active state when seeded on all the materials, nevertheless, after 48 hours cells seeded on PLA and PLA-10CaSi-10DCPD showed higher metabolic activity compared to cells seeded on PCL or PCL-10CaSi-10DCPD.

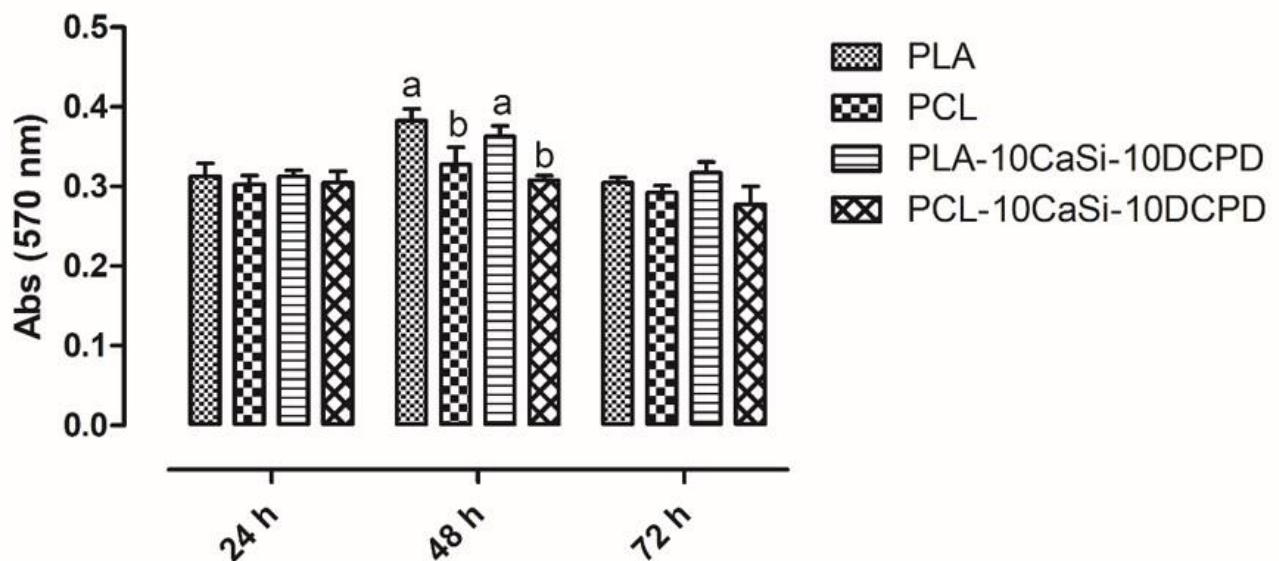


Figure 3 - Metabolic activity of pVW-MSCs seeded on different scaffolds after 24, 48 and 72 hours of culture was evaluated by MTT based assay. Data represent the mean±SD of three independent biological replicates (n=3) and were analysed using one-way ANOVA followed by the Tukey's post hoc comparison. Different letters indicate significant difference $p < 0.05$.

Effect of biomaterials on pVW-MSCs markers

pVW-MSCs cultured in PGM in presence of different scaffolds expressed all the studied genes (**Figure 4**). Moreover, qPCR analysis revealed a statistical significant downregulation of α -SMA in pVW-MSCs cultured on PCL scaffolds, in relation to the pVW-MSCs cultured under standard 2D condition (CTR) (**Figure 4**). The presence of CaSi and DCPD additives restored the basal level. On the contrary PDGFR- β was always decreased in both scaffolds in presence of CaSi and DCPD.

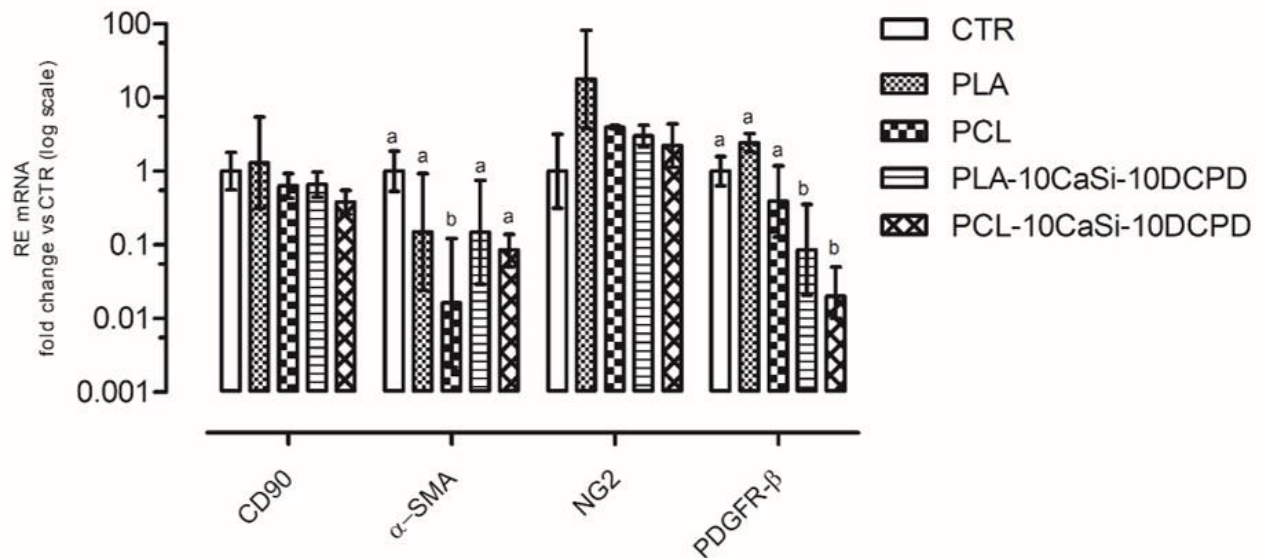


Figure 4 - CD90, α SMA, NG2 and PDGFR- β gene expression in pVW-MSCs evaluated after 72h of culture in presence of different scaffolds or in 2D standard culture condition (CTR). Data represent mean \pm range of relative expression (RE) of three biological replicates (n=3). Data were analysed using one-way ANOVA followed by the Tukey's post hoc comparison test. Different letters above the bars indicate significant differences ($p < 0.05$).

pVW-MSCs distribution on different scaffolds

DAPI staining and immunofluorescence assay for alpha-tubulin confirmed cellular presence on both kind of scaffold. Interestingly, a difference in cellular distribution was observed. In PLA-10CaSi-10DCPD scaffold pVW-MSCs grew individually with interconnection by cytoplasmic prolongations (**Figures 5c, e**), in contrast, in PCL-10CaSi-DCPD scaffolds, pVW-MSCs grew in spherical cluster (**Figure 5d, e**). The same distribution was observed also in pVW-MSCs cultured on the non-doped scaffolds (data not shown).

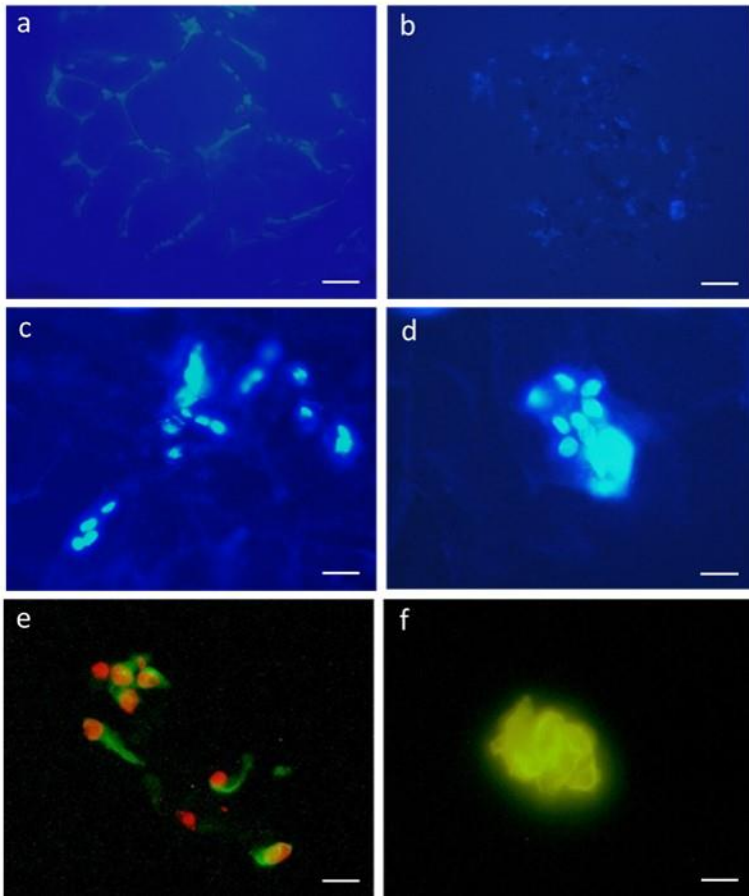


Figure 5 - DAPI staining (a-d) PLA-10CaSi-10DCPD (a) and PCL-10CaSi-10DCPD (b) without cells and in the presence of cultured cells (72 h): PLA-10CaSi-10DCPD (c), PCL-10CaSi-10DCPD (d). Immunofluorescence analysis for alpha-tubulin of cultured cells (72 h) on PLA-10CaSi-10DCPD (e) and PCL-10CaSi-10DCPD (f). Scale bar = 10 μm for a, b and 20 μm for c-f.

DISCUSSION

Hybrid biomaterials composed of biodegradable synthetic polymers and inorganic materials showed suitable property to use for biomedical application, also in the field of engineered tissue.

Biodegradable synthetic polymers such as based on poly- α -hydroxyl acids (as PLA and PCL) are currently used for scaffold design due to their biocompatibility, degradation into non-toxic components, long shelf-life, easy process ability, low cost and possibility to be customized/adapted to the surgical site (Armentano *et al.* 2010, Tajbakhsh *et al.* 2017). Highly porous Poly-lactic acid scaffolds doped with bioactive calcium silicates and calcium phosphates have been produced (Gandolfi *et al.* 2018) and it was demonstrated the ability to be cultured oral derived mesenchymal stem cells and to stimulate their shift through osteogenic lineage (Tatullo *et al.* 2019). Calcium silicates/Poly- ϵ -caprolactone 3D printed scaffolds were produced for dental pulp tissues revascularization purposes and showed good dental pulp stem cells proliferation and osteogenic differentiation (Ho *et al.* 2017).

Being Vascularization a crucial factor when approaching any engineered tissue, new scaffolds, able of promoting local angiogenesis, could represent a multi-approach strategy to obtain best result in engineered tissue.

In the present study pVW-MSCs have been cultured on 3D biodegradable highly porous scaffolds based on PLA and PCL doped with high amounts (20% w/w) of reactive biointeractive mineral fillers (CaSi and DCPD). The used vascular stem cells derived from the thoracic aorta (Zaniboni *et al.* 2014) represent an excellent model to test the angiogenic/anti angiogenic potential of different materials (Bernardini *et al.* 2016).

The results presented in this paper clearly demonstrated that both experimental PLA- and PCL-based scaffolds support pVW-MSCs grow and colonization; pVW-MSCs grown on all the scaffolds studied were metabolically active throughout the experimental time (72 hours). Interestingly, at 48 hours, pVW-MSCs cultured on PLA based scaffold showed an increase of metabolic activity respect to PCL based scaffold regardless of the presence of the additives. The difference in metabolic profile showed for PLA based scaffolds must be further investigated, considering that a different metabolic activity could represent a stem cells differentiation fate towards different specific lineages.

We previously demonstrated (Zaniboni *et al.* 2015) that pVW-MSCs cultured in 2D are characterized by a typical gene expression profile including mesenchymal stem cell markers, such as CD90 and pericyte markers such as: alpha-SMA, PDGFR- β and NG2. Similarly, pVW-MSCs cultured on all the experimental 3D scaffolds, continued to express these markers suggesting the possibility of a successful long-lasting colonization. However, some main differences in the expression level of the abovementioned genes has been revealed: PLA and PCL scaffolds determined a reduction of alpha-SMA, while the same scaffold with calcium silicates (CaSi) and dicalcium phosphate dihydrate (DCPD) mineral fillers restored the alpha-SMA expression level.

Otherwise, PDGF-receptor β was significantly reduced in scaffolds enriched with reactive minerals CaSi and DCPD. These results are particularly attractive and further investigation increasing time of culturing could explain if the different level of expression of these markers could be associated with different spontaneous differentiation.

The distribution of pVW-MSCs cultured on the experimental 3D scaffolds showed an individual cell growth on PLA-10CaSi-10DCPD whilst on PCL-10CaSi-10DCPD cells grown as compact clusters, which resemble the spheroids that could be obtained by hanging drop culture of pVW-MSC. The difference in gene expression could be related to this different distribution, in fact is well known that MSCs phenotype is dramatically changed when culture condition shifts from 2D to 3D and also depends on the approaches utilized to generate the spheroids (Han *et al.* 2019).

Overall with the present paper we demonstrated the possibility of culturing pVW-MSCs on 3D biodegradable highly porous mineral doped poly- α -hydroxy acids scaffolds. pVW-MSCs spontaneously colonize these biomaterials and maintain a general undifferentiated phenotype in the first 72 h of culture with slight differences with control 2D culture. However, further studies, with longer growth kinetics, are needed to investigate the differentiated fate of these cells grown on this 3D culture system.

CONCLUSIONS

Being VW-MSCs an excellent *in vitro* model to study vascular remodelling, due to their strong angiogenic attitude, the possibility of culturing pVW-MSCs on these biodegradable scaffolds represents a strategy for biomedical tissue engineering.

In conclusion, the property of the experimental scaffolds to be colonized by vascular stem cells demonstrated the potential of the scaffolds to allow/induce the formation of new vessels and their potential application in tissue regeneration as in mandibular and maxilla bone defects.

REFERENCES

Armentano I, Dottori M, Fortunati E, Mattioli S, Kenny JM. Biodegradable polymer matrix Nanocomposites for tissue engineering: A review. *Polym Degradation Stab* 2010;95:2126-2146.

Bernardini C, Zannoni A, Bertocchi M, Bianchi F, Salaroli R, Botelho G, Forni M. Deleterious effects of tributyltin on porcine vascular stem cells physiology. *Comp Biochem Physiol C Toxicol Pharmacol* 2016;185–186, 38–44.

Castilla Bolaños MA, Buttigieg J, Briceño Triana JC. Development and characterization of a novel porous small intestine submucosa-hydroxyapatite scaffold for bone regeneration. *Mater Sci Eng C Mater Biol Appl* 2017;1;72:519-525.

Chen Y, Chen S, Kawazoe N, Chen G. Promoted Angiogenesis and Osteogenesis by Dexamethasone-loaded Calcium Phosphate Nanoparticles/Collagen Composite Scaffolds with Microgroove Networks. *Sci Rep*. 2018;20;8:14143.

Ciavarella C, Fittipaldi S, Pasquinelli G. CoCl₂ Administration to Vascular MSC Cultures as an In Vitro Hypoxic System to Study Stem Cell Survival and Angiogenesis. *Methods Mol Biol* 2016;1516:309-317.

Day RM. Bioactive glass stimulates the secretion of angiogenic growth factors and angiogenesis in vitro. *Tissue Eng* 2005;11:768-77.

Dozza B, Lesci IG, Duchi S et al. When size matters: Differences in demineralized bone matrix particles affect collagen structure, mesenchymal stem cell behavior, and osteogenic potential. *J Biomed Mater Res A* 2017;105, 1019–1033.

Gandolfi MG, Spagnuolo G, Siboni F, Procino A, Riveccio V, Pelliccioni GA, Prati C, Rengo S. Calcium silicate/calcium phosphate biphasic cements for vital pulp therapy: chemical-physical properties and human pulp cells response. *Clin Oral Investig* 2015;19:2075-2089.

Gandolfi MG, Zamparini F, Degli Esposti M, Chiellini F, Aparicio C, Fava F, Fabbri P, Taddei P, Prati C. Polylactic acid-based porous scaffolds doped with calcium silicate and dicalcium phosphate dihydrate designed for biomedical application. *Mat Sci Eng C* 2018;82:163-181.

Han HW, Hou YT, Hsu SH. Angiogenic potential of co-spheroids of neural stem cells and endothelial cells in injectable gelatin-based hydrogel. *Mat Sci Eng C-Mater* 2019;99, 140–149.

Tajbakhsh S, Hajiali F. A comprehensive study on the fabrication and properties of biocomposites of poly(lactic acid)/ceramics for bone tissue engineering. *Mat Sci Eng C-Mater* 2017;70:897-912.

Tatullo M, Spagnuolo G, Codispoti B, Zamparini F, Zhang A, Degli Esposti M, Aparicio C, Rengo C, Nuzzolese M, Manzoli L, Fava F, Prati C, Fabbri P, Gandolfi MG. PLA-Based Mineral-Doped Scaffolds Seeded with Human Periapical Cyst-Derived MSCs: A Promising Tool for Regenerative Healing in Dentistry. *Materials* 2019, 12, 597.

Zaniboni A, Bernardini C, Alessandri M, Mangano C, Zannoni A, Bianchi F, Sarli G, Calzà L, Bacci ML, Forni M. Cells derived from porcine aorta tunica media show mesenchymal stromal-like cell properties in in vitro culture. *Am J Physiol Cell Physiol* 2014 15;306:C322-33.

Zaniboni A, Bernardini C, Bertocchi M, Zannoni A, Bianchi F, Avallone G, Mangano C, Sarli G, Calzà L, Bacci ML, Forni M. In vitro differentiation of porcine aortic vascular precursor cells to endothelial and vascular smooth muscle cells. *Am J Physiol Cell Physiol* 2015 1;309:C320-31.

4. Conclusions

The present project aimed to analyse several protocols for the rehabilitation of periapical bone defects and to develop strategies to achieve peri implant hard and soft tissue stability. These protocols will be particularly important in the future since the consistent increase of population aging, demanding less traumatic and predictable approaches.

The present study is structured on two main topics: the study of bone remodeling mechanisms around implants in the early stages of integration and the evaluation and characterization of CaSi-based cements for periapical bone defects.

Clinical studies allowed us to assess which factors are most involved in bone remodeling and long-term bone loss processes. Several minimally invasive protocols were also evaluated to maintain bone and soft tissue stability.

Concerning the degree of mineralization of the implant-bone interface, critical for a long-term prognosis of implant rehabilitations, loading procedures effectively influences its mineralization. It can be deduced that it is possible to obtain a satisfactory result in terms of bone stability through the use of less invasive approaches, such as secondary surgeries to expose the implant neck or open flap techniques.

At the same time research was conducted on materials and techniques in the endodontic field for a complete resolution of the periapical bone defects. The new hydraulic CaSi based materials were characterized in their chemical-physical abilities and compared to traditional sealers. A new generation of bio-interactive materials emerged that may be used to additionally preserve the endodontic affected tooth, rather than extract it.

The bio-interactivity and bioactivity of these materials lead to the final phase of the project, in which CaSi powders were used as fillers for scaffolds production. The advantage of these fillers also lies in the osteoconductive and osteoinductive properties recently demonstrated.

Chemical-physical and micromorphological properties were then analysed following different CaSi-Polymers (PLA or CaSi) formulations to characterize these materials.

In order to evaluate the potential biological interactions of these materials, two different mesenchymal stem cell populations were evaluated. The osteogenic potential of materials has been examined by the proliferation and differentiation of human periapical cysts MSC; angiogenetic potential via porcine vascular wall MSC. The MSC populations tested therefore demonstrated greater activity and growth on the most loaded samples.

These results show that the scaffolds with the highest concentration of minerals fillers demonstrate high alkalization activity, calcium release and high porosity. Furthermore the degradation of the polymer is balanced by the apatite forming ability of the material, favoring the replacement of the scaffold with new bone-like mineralized tissue.

The materials developed and tested in this project have shown encouraging results for their future use and are promising for further research and studies in animal models.